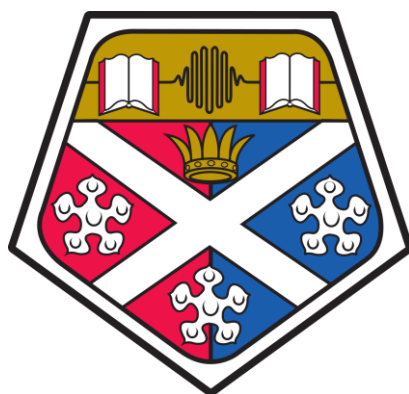


University of Strathclyde
Doctoral Thesis

Hydrothermal Synthesis of Binder-Free Tungsten-Tungsten Oxide Electrodes for Electrochemical Energy Storage



Author:

Thomas J.R. Cadden

Supervisor:

Dr Edward Brightman

Second Supervisor:

Professor Sudipta Roy

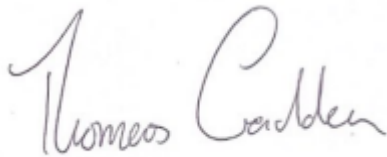
A thesis submitted in the fulfilment of the requirements for the degree of Doctor of
Philosophy in the Department of Chemical and Process Engineering

Declaration of Authorship

This thesis is the result of the author's original research. It has been composed by the author and has not previously been submitted for examination which has led to the award of a degree.

The copyright of this thesis belongs to the author under the terms of the United Kingdom Copyright Acts as qualified by the University of Strathclyde Regulation 3.50. Due acknowledgment must always be made of the use of any material contained in, or derived from, this thesis.

Signed:

A handwritten signature in black ink that reads "Thomas Cadden". The signature is written in a cursive style with a large initial 'T'.

27/01/24

Abstract

Binder-free metal-metal oxide architectures are a widely reported, highly promising electrode design for catalytic, semi-conducting, and sensing applications. Despite the wealth of existing literature on the synthesis of metal-metal oxide electrodes and, separately, the well-documented pseudocapacitive intercalation of cations in transition metal oxides, no attempt has been made to integrate such a design for applications in batteries or supercapacitors. This design streamlines fabrication and post-life recycling by limiting materials, reduces demand on transition metals, and may be expected to deliver excellent performance as the active charge storage layer is directly bonded to the current collecting material.

Tungsten oxide (WO_3) and conjugate metal tungsten (W) were considered an excellent initial test case for binder-free energy storage electrodes, with extensive literature to draw from in both these areas. Tungsten oxide is an emergent pseudocapacitive energy storage material, capable of reversibly intercalating protons within its structure upon simultaneous transfer of charge. In particular, the metastable hexagonal crystal phase has been shown to possess excellent kinetics owed to a tunnel structure, achieving attractive specific capacitances of over 300 Fg^{-1} . Similarly, the synthesis and characterisation of tungsten-tungsten oxide electrodes are widely reported in fields such as electrochromism, photocatalysis and gas-sensing. The purpose of this project is to merge these two areas, taking a first step into appraising binder-free electrodes for energy storage using a base case of tungsten-tungsten oxide (W-WO_3) electrodes; delivering full physical and electrochemical characterisation of W-WO_3 electrodes whilst using the learnings to inform future work.

In this study, eight sets of W-WO_3 electrodes were synthesised using a hydrothermal reaction pathway adapted from existing literature using four different capping agents with sodium tungstate, successfully growing hexagonal- WO_3 upon the surface of tungsten foil. It was demonstrated that a ratio of tungstate to cation is critical in delivering the hexagonal crystal structure and the interplay between anion and cation in solution was scrutinised. The energy storage characteristics of the hexagonal- WO_3 electrodes were studied through electrochemical potentiodynamic and galvanostatic investigation as well as potentiation impedance spectroscopy (PEIS). The electrochemical data was thoroughly analysed the extent of pseudocapacitive charge storage quantified, and capacities reported of up to 1.4 mAh/cm^2 at 1 mVs^{-1} and gravimetric capacitances of 178 Fg^{-1} . X-ray Diffractometry (XRD) and Scanning Electron Microscopy (SEM) were used to analyse the crystal phase and microstructure of each of the synthesised electrodes. The nature of the physical surface was linked to the electrochemical performance of each electrode; rubidium sulphate was found to be a particularly effective capping agent delivering the best-performing electrodes of the

sample, attributed to a unique nano-urchin morphology with a high surface area porous structure.

The hydrothermal synthesis scheme was then empirically analysed by systematic removal of reactants and changing reaction conditions to better understand the factors controlling the growth mechanism of WO_3 . The output result of each change was quantified using electrochemical potentiodynamic characterisation as a measure of electrochemical activity and SEM as a method of observing the physical change. It was found that the absence of sodium tungstate resulted in thinner coatings and the formation of the monoclinic phase. An acid-only hydrothermal reaction in the absence of both sodium tungstate and capping agent produced an electrode with highly promising performance, pointing to a key design trade-off between thin oxide layers possessing better kinetics but less capacity than thicker ones.

To give perspective to the merits and inadequacies of the binder-free W-WO_3 design, a straightforward comparison between the synthesised electrodes and conventional powder-based electrodes was completed, using the tungsten oxide powders produced as a by-product from each reaction of the initial synthesis scheme. The physical nature of the powders underwent thorough examination through XRD and SEM analyses, revealing each has a hexagonal crystal structure. The microstructure of each powder exhibited significant similarities to the binder-free electrodes synthesized under identical conditions. Using potentiodynamic and galvanostatic characterisation, the powders were found to have superior electrochemical performance than the binder-free foils, higher gravimetric capacities, and better capacity retention at faster rates of charge/discharge. The improved performance is ascribed to the thin layer of active material better facilitating ion movement and charge transfer. A final investigation applied the synthetic procedure used on tungsten foil to molybdenum instead, of the element above tungsten in the periodic table. The resultant foil exceeded the performance of the WO_3 powder and W-WO_3 electrodes documented pointing to an exciting avenue of future binder-free research.

Acknowledgements

I start by thanking my two supervisors Dr Edward Brightman and Prof. Sudipta Roy for their invaluable expertise and guidance that has supported me through this project. I am grateful for their support and mentorship, as well as the fantastic opportunities they have provided me throughout my studies.

I would like to extend my appreciation to James Kelly and Maider Olasolo in the AMRL; and Paul Edwards in Physics for their invaluable assistance with the various physical characterisation techniques used in this work. In addition, thank you to all the technicians Chris, Michael, Cammy, Liam, and Ian for all your help.

This journey of sorts would not have been the same without the camaraderie of all the brilliant folk I have met along the way: James, Christine, Robbie, Stuart, Grace, Andrew, Eleni, John, Pamela, Lewis, Shahin and all the others along the way. I would like to especially thank Shaon Debnath whose kindness, sense of humour and stories brightened the lab during the pandemic, and I wish him, and all the other guys, all the best for the future.

I am obligated to say big up the Berkeley boys: Jamie, Calum and Edward who have put up with me being a dour so and so at times throughout completing this. While I am at it, I suppose I may as well extend this sentiment to the Ravi and Iona crowd who have all been a welcome distraction from the world of tungsten oxide.

I thank my Mum, my Dad and my brother Ed, whose support and encouragement has been a constant source of strength throughout – I love you all.

Finally, I dedicate this to my Grandparents Rena and Roy McArthur; and Clare and Patrick Cadden whose graft has provided me with all the opportunities in life and education that was not available to them.

Contents

1	Introduction.....	1
1.1	Background.....	1
1.2	Research Aims.....	4
1.3	Electrochemical Energy Storage Fundamentals	6
1.3.1	Overview	6
1.3.2	Capacitance	7
1.3.3	Helmholtz Electrochemical Double Layer	9
1.3.4	Faradaic Reactions	13
2	Literature Review.....	24
2.1	Metal Oxide Supercapacitors.....	24
2.2	Tungsten Trioxide (WO ₃).....	26
2.2.1	Crystal Phases & Chemical Properties	26
2.2.2	Proton Intercalation in WO ₃	31
2.2.3	Tungsten-Tungsten Oxide Electrode Architectures (W-WO ₃).....	32
2.2.4	Pseudocapacitive Charge Storage in WO ₃	35
2.2.5	Summary	38
3	Materials & Methodology	40
3.1	Initial Synthesis Pathway Overview.....	40
3.2	Synthesis Methods	41
3.2.1	Acid Pretreatment Seeding Step.....	41
3.2.2	Hydrothermal Synthesis	44
3.2.3	Synthesis Procedures and Conditions	49
3.3	Material Characterisation	54
3.3.1	Scanning Electron Microscope (SEM) and Energy Dispersive X-ray (EDX)	54
3.3.2	Xray Diffraction (XRD).....	58
3.4	Electrochemical Characterisation Methods.....	61
3.4.1	Three Electrode Cell (Half-Cell) Procedure, Equipment and Conditions.....	61
3.4.2	Working Electrode Development: Plug Electrode Holder Development & Procedure..	62
3.4.3	Electrode Preparation	67
3.4.4	Cyclic Voltammetry (CV)	70
3.4.5	Galvanostatic Experimentation - Galvanostatic Cycling (GCD).....	75
3.4.6	Electrochemical Impedance Spectroscopy (EIS).....	78

3.4.7	Computational Processing & Analysis (Python).....	80
4	<i>Electrochemical Characterisation of W-WO₃ electrodes.....</i>	81
4.1	Introduction.....	81
4.2	Potentiodynamic Characterisation	81
4.3	Galvanostatic Characterisation	89
4.4	Electrochemical Impedance Spectroscopy.....	100
4.5	Summary of Performance	105
5	<i>Physical Characterisation of W-WO₃ Electrodes</i>	108
5.1	Introduction.....	108
5.2	Appearance of foils.....	108
5.3	Crystal structure	109
5.4	Microstructure (SEM imaging) planar to surface.....	114
5.5	Microstructure (EDX imaging) cross section.....	129
5.6	Foil Stability	132
5.7	Growth Mechanism.....	134
5.7.1	Capping agents	134
5.7.2	Role of Anion.....	136
5.7.3	Impact of Seed Layer	139
5.8	Conclusion	140
6	<i>Systematic Review of Hydrothermal Reaction Scheme</i>	142
6.1	Introduction.....	142
6.2	Iterative removal of synthesis parameters.....	144
6.2.1	Iteration 1 – removing sodium tungstate.....	144
6.2.2	Iteration 2 – is acidic pH needed?.....	147
6.2.3	Iteration 3 – isolating substrate type from one another.....	149
6.2.4	Iteration 4 – effect of acid only	154
6.3	Conclusion	168
7	<i>Characterisation of Powder Based WO₃ Electrodes.....</i>	171
7.1	Introduction.....	171
7.2	Electrochemical Characterisation of Powder Electrodes	171

7.2.1	CV Comparison of Powder Based Electrodes with Binder Free Electrodes	171
7.2.2	GCD Comparison between binder-free and powder electrodes	174
7.2.3	Ease of Manufacture & Stability of Powder-Based Electrodes	178
7.3	Physical Characterisation of Powders	179
7.3.1	Appearance of powders	179
7.3.2	Crystal Structure.....	179
7.3.3	Microstructure of powders	181
7.4	Summary	187
8	Conclusions & Future Work.....	188
8.1	Conclusions	188
8.2	Future Work.....	191
8.2.1	WO ₃ and W-WO ₃ for energy storage	191
8.2.2	Quantification of Hydrothermal Synthesis	191
8.2.3	Binder Free Electrodes	191
8.2.4	Molybdenum-Molybdenum Oxide	192
9	References	195
10	Appendices	

Table of Figures

Figure 1 Ragone Diagram of Electrochemical Devices. Taken from [5].....	6
Figure 2 Schematic of how capacitor stores electrical charge across a dielectric barrier.....	8
Figure 3 Schematic of electric capacitor's response to a) Cyclic Voltammetry and b) Galvanostatic Discharge	9
Figure 4 Solid-Solution interface when solid is not polarised adapted from [13]	10
Figure 5 Structure of the Helmholtz electrochemical double layer, adapted from [13]	11
Figure 6 Schematic measured response of electrochemical double layer capacitor (EDLC) from a) Cyclic Voltammetry and b) Galvanostatic Discharge. Adapted from [4].	13
Figure 7 A metal wire in an aqueous salt solution containing cations and anions. Adapted from [15].....	13
Figure 8 Schematic of a Redox Pseudocapacitance Process characterised by CV. Adapted from [9], [12].....	19
Figure 9 Schematic measured response of pseudocapacitive material from a) Cyclic Voltammetry and b) Galvanostatic Discharge. Adapted from [10].....	21
Figure 10 Schematic measured response of Battery-like process from a) cyclic voltammetry and b) Galvanostatic discharge. Adapted from [10].....	22
Figure 11 Pourbaix Diagram of Tungsten Phases. Taken from [4]	27
Figure 12 Schematic of anhydrous monoclinic and hexagonal WO_3 phases	29
Figure 13 Initial Synthesis Pathway Overview Schematic	40
Figure 14 Photo (left) & Schematic (right) of Acid Treatment Set Up: Oil bath magnetically stirred with immersed round bottom flask and condenser attached housed within fume cupboard. Temperature set by a thermocirculator bath with electronic control	42
Figure 15 Schematic accompanied with real photos of how seeding step progresses adapted from mechanism proposed in [50]	43
Figure 16 XRD spectra for 0, 15 and 30-minute acid treatments in preliminary experiments	43
Figure 17 Cyclic Voltammetry Data for 0, 15 and 30-minute acid treatments in preliminary experiments at 10 mVs^{-1}	44
Figure 18 Image of Stainless-Steel Screw Top Autoclave (left) and PTFE bomb/liner (right)	48
Figure 19 Oven used for hydrothermal synthesis	49
Figure 20 Schematic of emissions from electron beam depending upon the interaction volume of specimen. Adapted from [88], [89].....	55
Figure 21 Schematic of low Vacuum / Wet Mode Operation where a gas (often water vapour) is introduced into the chamber and collides with emitted electrons, producing positive ions	

which dissipate negative charge which may accumulate upon the surface. Adapted from [88].
..... 56

Figure 22 example images of samples studied mounted on stubs held in a stage; mounted directly upon a stage; and epoxy set to expose the cross sectional view of the foil 57

Figure 23 Schematic Diagram of Diffraction of X-rays by a crystal where Bragg's Law is satisfied. Adapted from [42], [91]. 58

Figure 24 Schematic of Powder XRD operation. Adapted from [91] 59

Figure 25 Schematic of grazing incidence XRD operation. Adapted from [92]. 59

Figure 26 Image of foil sample taped to aluminium block for grazing incidence XRD 61

Figure 27 Biologic SP-300 Potentiostat used in all experimentation 61

Figure 28 3-electrode cell configuration used in electrochemical characterisation a) Schematic b) Real set-up 62

Figure 29 Schematic of plug (left) and clip (right) electrode 63

Figure 30 Development of plug electrode from shop bought compression gland (left), saw-cut compression gland to remove open end (centre) and stainless-steel plug sat inside altered part with connecting wire and O-rings to improve sealing and tightening. 63

Figure 31 Schematic of plug electrode aperture 64

Figure 32 Schematic of different components of plug electrode 64

Figure 33 Schematic of plug electrode suspended in electrolyte to avoid short circuiting with the back current collector 65

Figure 34 CV of Seeded Substrate, S in clip electrode (left) and plug electrode (right). 65

Figure 35 IR-Correction of Seeded Sample in Plug Electrode (Figure 34 – right) 66

Figure 36 Images of typical ink preparation. The left image shows before sonication and the right image shows post sonication. 69

Figure 37 Image of freshly dropped “wet” ink coating (left) and air dried “dry” ink coating (right) 69

Figure 38 Theory of potentiodynamic experiment – Cyclic Voltammetry 70

Figure 39 Calculated K1 and K2 Plotted. 73

Figure 40 Dunn Method Modelled data before and after editing boundaries. 74

Figure 41 Theory of Galvanostatic Charge-Discharge Cycling Experiment 75

Figure 42 Example GCD data with modelled straight lines overlaid. 77

Figure 43 Example of further GCD analysis: The left figure shows edited data whereby the potential window may be reduced, and the straight line refitted; and the right shows the breakpoint analysis where instead the data is fitted as two lines not one. 77

Figure 44 Cyclic Voltammograms of all 8 samples at a sweep rate of 1 mVs⁻¹ a) NaCl samples b) Na₂SO₄ c) Rb₂SO₄ and d) (NH₄)₂SO₄ and tabulated below is the the average stored charge, capacity measured in mA/cm², across the recorded data set 82

Figure 45 Cyclic Voltammograms of all 8 samples at a sweep rate of 20 mVs ⁻¹ a) NaCl samples b) Na ₂ SO ₄ c) Rb ₂ SO ₄ and d) (NH ₄) ₂ SO ₄	84
Figure 46 Calculated capacity values in mAcm ² from Cyclic Voltammograms	85
Figure 47 Example of analytical plots used to find k ₁ and k ₂ for the Dunn method for example sample S4	87
Figure 48 Graphical representation of the Dunn Method analysis on sample S4 (first run) displaying: the capacitive controlled k ₁ v current at A) 1 mVs ⁻¹ and C) 20 mVs ⁻¹ ; and the diffusion controlled current k ₂ v ^{1/2} at B) 1 mVs ⁻¹ and D) 20 mVs ⁻¹	88
Figure 49 Capacitive component of charge stored as a percentage of total stored charge ..	89
Figure 50 GCD curves for samples W4 and S4 at 5, 10 and 20 mAcm ⁻² with post experiment specific current density. Note the y-axis is inverted to show charging being positive gradient and discharge negative gradient. The discharge capacity for each GCD curve displayed is tabulated below the figures.	90
<i>Figure 51 Mean magnitude of Ohmic Drop as a function of current density of experiment; the associated mean DCIR for each data set across all currents is provided in the legend</i>	91
Figure 52 GCD Curve of W4 from Figure 50 with perfect triangle line and Root Mean Square Error (RMSE) fitting provided in the legend	93
Figure 53 Charging curve of W4 showing the real data potential window, ΔE, shortened and the data refitted to the ideal case of a linear curve	93
<i>Figure 54 discharge curve of W4 showing the real data potential window, ΔE, shortened and the data refitted to the ideal case of a linear curve</i>	94
Figure 55 discharge curve of W4 showing the real data potential window, ΔE, shortened and the data refitted from ohmic drop point to the ideal case of a linear curve	94
Figure 56 Average Root Mean Square Error between the discharge curve and modelled purely capacitive line across all W4 Samples at reduced potential windows	95
<i>Figure 57 Piecewise linear regression of discharge curve featuring a break point.....</i>	95
Figure 58 Average Root Mean Square Error between the discharge curve and linear regression fitting across all W4 Samples at reduced potential windows	96
<i>Figure 59 Piecewise linear regression of charge curve featuring a break point</i>	97
Figure 60 Mean Areal Capacity (mAhcm ⁻²) versus Areal Current Density (mAcm ⁻²)	97
Figure 61 Scatter graph of Specific Capacity (mAh g ⁻¹) versus Specific Current Density (Ag ⁻¹)	98
Figure 62 Ragone Diagram of Dataset.....	99
<i>Figure 63 OCV values of samples at which impedance spectra was opened</i>	100
Figure 64 Equivalent Circuit fitted used to fit the recorded EIS data	101

Figure 65 Nyquist Plots for sample S4 (02): left hand side shows fitting from Zfit between 1Hz and 100 kHz; the right hand side shows the Zfit fitting between 10 mHz and 100 kHz using the fixed parameters for La1 and R1 found from left hand fitting	102
Figure 66 Bode Diagram for sample S4	104
Figure 67 Resistance of R1 from fitted equivalent circuit across the sample range plotted with dots and the average DCIR values from GCD data denoted by x.....	105
Figure 68 Photos of as synthesised hydrothermally grown electrodes with capping agent. In each photo the sample on the left is grown from a pristine tungsten substrate; the sample on the right is grown from a seeded substrate.....	108
Figure 69 Schematic of tunnelated M ⁺ in h-WO ₃ bronze. Adapted from [46], [111], [112]..	109
Figure 70 XRD of all hydrothermally deposited samples	110
<i>Figure 71 XRD reduced 2θ and renormalized</i>	111
Figure 72 XRD Spectra of samples W1, S1, W2 and S2 synthesised with Sodium based capping agents (NaCl and Na ₂ SO ₄) respectively	112
<i>Figure 73 XRD Spectra of samples W3 and S3 synthesised with ammonium sulphate</i>	113
<i>Figure 74 XRD Spectra of samples W4 and S4 synthesised with rubidium sulphate</i>	114
Figure 75 SEM Micrograph of Tungsten Foil Substrate. This is the only image taken on a W-Filament SEM.	115
Figure 76 SEM Micrographs of Seeded Substrate S	115
Figure 77 SEM Micrographs of samples W1 and S1 obtained through hydrothermal reaction using NaCl as a capping agent	116
Figure 78 SEM Micrograph of S1 obtained from hydrothermal reaction with NaCl as capping agent. A less magnified image is shown to show the uniformity of the surface.....	116
Figure 79 SEM Micrograph of W1 obtained from hydrothermal reaction with NaCl as capping agent. A less magnified image is shown to show the uniformity of the surface.....	117
<i>Figure 80 SEM Micrographs of samples W2 and S2 obtained through hydrothermal reaction using Na₂SO₄ as a capping agent</i>	118
Figure 81 SEM Micrograph of W2 obtained from hydrothermal reaction with Na ₂ SO ₄ as capping agent. A higher magnification is given of the flat plane region of the oxide layer..	118
<i>Figure 82 SEM Micrographs of sample W2 displaying two distinct areas within the clump region</i>	119
Figure 83 SEM Micrograph of sample S2 obtained through hydrothermal reaction with Na ₂ SO ₄ as capping agent, displaying the flat region	119
Figure 84 SEM Micrograph of sample S2 obtained through hydrothermal reaction with Na ₂ SO ₄ as capping agent, displaying a closer image of rosebud like structures protruding from the surface.....	120

Figure 85 SEM Micrographs of the top oxide layer in sample S3 using different magnifications	121
<i>Figure 86 SEM Micrographs of the top oxide layer in sample W3 using different magnifications</i>	<i>122</i>
Figure 87 SEM Micrographs of substrate beneath oxide layer in sample W3	122
Figure 88 The surface beneath oxide in S3.....	123
Figure 89 SEM Micrographs of samples W4 (left) and S4 (right). Both are grown using Rb_2SO_4 as capping agent, though sodium ions are also in solution from sodium tungstate.....	125
Figure 90 SEM Micrographs of nanoplates which form in W4 (left) and S4 (right).....	126
Figure 91 Highest magnification SEM Micrographs of nanoplate features W4 (left) and S4 (right)	126
Figure 92 SEM Micrograph of W4 at 3 different magnifications	127
Figure 93 SEM Micrograph of S4 at 3 different magnifications	128
Figure 94 NaCl directed samples cross sectional micrograph with EDX colour map	129
Figure 95 Rb_2SO_4 directed samples cross sectional micrograph with EDX colour map	130
Figure 96 Mechanisms for delamination a) drying out b) surface tension/pH change c) passing charge.....	132
Figure 97 Position and Direction of Oxygen Dipoles of hexagonal WO_3 Crystal	135
Figure 98 Schematic of hexagonal- WO_3 lattice showing two perspectives: planar view of top face and cross section of side face.	137
<i>Figure 99 Schematic of tungstate ion exchanging with chloride ions.....</i>	<i>138</i>
Figure 100 Schematic of tungstate ion exchanging with sulphate ion.....	138
Figure 101 Overview of 2 step synthesis scheme with hydrothermal reaction key parameters in bubble	142
Figure 102 Photographs of NaCl directed samples W1 & S1 in comparison to 'NaCl directed samples without Na_2WO_4 '	145
Figure 103 Micrographs of samples W5 and S5.....	145
Figure 104 Cyclic Voltammetry of iteration 1 samples against substrates W and S. The tabulated capacities of substrate S, W5 and S5 are tabulated below.	146
Figure 105 Photographs of samples W6 and S6; foils synthesised in deionised water at pH ~5.5	147
Figure 106 Micrographs of samples W6 and S6.....	148
Figure 107 Cyclic Voltammetry of iteration 1 samples made at pH of 2 (W5, S5) against iteration 2 samples hydrothermally treated in deionised water at a pH of ~5.5 (W6, S6) at 1 mVs^{-1} (left) and 20 mVs^{-1} (right). The stored capacities for the displayed CVs are tabulated below the figures.....	149

Figure 108 Cyclic Voltammetry of Seeded Substrate against iteration 2 samples hydrothermally treated in deionised water at a pH of ~5.5 (W6, S6) at 1 mVs ⁻¹ (left) and 20 mVs ⁻¹ (right). The capacities for the CVs in the figure are tabulated below the figure.	149
Figure 109 Schematic of hypothesised WO ₄ ²⁻ diffusion from high concentration seeded foil to low concentration pristine tungsten foil during the hydrothermal reaction	150
Figure 110 Photographs of iteration 1 samples (W5, S5) synthesised in the same autoclave; and of iteration 3 samples W7 and S7 using the same conditions but synthesised in their own isolated autoclave	151
Figure 111 Micrographs of samples W7 and S7.....	151
Figure 112 Comparison of Pristine Foils Cyclic Voltammetry of iteration 1 (W5) against iteration 4 (W7) at scan rates of 1 mVs ⁻¹ and 20 mVs ⁻¹ . The areal capacities for the displayed CV figures are tabulated below.	152
Figure 113 Comparison of Seeded Foils Cyclic Voltammetry of iteration 1 (S5) against iteration 4 (S7) at scan rates of 1 mVs ⁻¹ and 20 mVs ⁻¹	152
Figure 114 Areal Capacity values (mAhcm ⁻²) versus sweep rate for iteration 1 samples W5, S5 and iteration 3 samples W7 and S7	153
Figure 115 Comparison of Seeded Foils Cyclic Voltammetry of samples S7, S8 and S9 at scan rates of 1 mVs ⁻¹ and 20 mVs ⁻¹	154
Figure 116 Mean Areal Capacity values (mAhcm ⁻²) versus sweep rate for sample S7, S8 & S9	155
Figure 117 Cyclic Voltammograms of S9 (left) and S4 (right) at scan rates of 1-100 mVs ⁻¹ . The areal capacities of each CV is tabulated below the figure.....	156
Figure 118 Cyclic voltammograms of samples S4 and S9 compared at 1 mVs ⁻¹ (left) and 100 mVs ⁻¹ (right). The areal capacities for the presented CVs are tabulated below the figure. .	156
Figure 119 Mean Areal Capacity values (mAhcm ⁻²) of monoclinic versus hexagonal samples	157
Figure 120 Average Areal Capacitance of samples S8 and S9 versus sweep rate.....	158
Figure 121 Grazing incidence angle 2° XRD Spectra of Seeded Substrate “S” with three hydrothermally produced samples S7, S8 and S9. The reference patterns for tungsten metal and two hydrated tungsten oxide phases are shown for reference	159
Figure 122 Grazing incidence angle 2° XRD Spectra of Seeded Substrate “S” with three hydrothermally produced samples S7, S8 and S9. The reference patterns for monoclinic-WO ₃ and orthorhombic-WO ₃ (H ₂ O) _{0.33} are given. The tungsten metal peak from the substrate is denoted by a red square	161
Figure 123 Schematic of monoclinic and orthorhombic WO ₃ lattice shapes	162
Figure 124 Photographs of as-synthesised foils made with only acid	163
Figure 125 Micrographs of S8 and S9 at a scale of 100 μm	163

Figure 126 Micrographs of purely HCl directed samples at 10 μm and 2 μm scales.....	164
Figure 127 Micrographs of purely H_2SO_4 directed samples at 10 μm and 2 μm scales	164
Figure 128 Schematic of double layer which balances charge of orthorhombic- WO_3 when Chlorine and Sulphate ions are present including growth rates	166
Figure 129 SEM micrographs of S9 post electrochemical characterisation	167
Figure 130 Zoomed out micrograph (left) and photograph (right) of S9 electrode post electrochemical characterisation	168
Figure 131 Cyclic Voltammograms of powder samples at 1 mVs^{-1} (left) and 20 mVs^{-1} (right). The areal capacities are tabulated below the figures.....	172
Figure 132 Cyclic Voltammograms of W, S and P electrode types for capping agents a) NaCl b) Na_2SO_4 c) $(\text{NH}_4)_2\text{SO}_4$ d) Rb_2SO_4 . The areal capacities of the presented CV data is tabulated below the figures.....	173
Figure 133 Cyclic Voltammograms of W1, S1 and P1 electrode types for capping agents NaCl at four different sweep rates. The areal capacities are tabulated below the figures.....	174
Figure 134 Gravimetric Capacity (mAhg^{-1}) versus sweep rate (mVs^{-1})	174
Figure 135 GCD Curve of a P3 sample as representative of the powder dataset. The tabulated specific discharge capacity for the curves is shown below the figure.....	175
Figure 136 Potential at which ohmic drops against current density used in the galvanostatic charge-discharge cycling: the binder-free samples grouped by a blue polygon & the powder-based samples grouped by a yellow polygon	176
Figure 137 Gravimetric Discharge Capacity (mAhg^{-1}) against areal current density (left) and specific current density (right) for binder-free samples and powder-based samples.....	176
Figure 138 Ragone Diagram of all hexagonal M_xWO_3 samples produced in this work by gravimetric values (left) and areal values (right)	177
Figure 139 Photos of powders in sample holders for XRD	179
Figure 140 XRD Spectra of samples P1, P2, P3, P4 synthesised as a secondary product in the bulk solution with Na_2WO_4 using the capping agent NaCl, Na_2SO_4 , $(\text{NH}_4)_2\text{SO}_4$ and Rb_2SO_4 respectively.....	180
Figure 141 SEM Micrographs of powder P1 obtained through hydrothermal reaction using NaCl as a capping agent.....	182
Figure 142 SEM Micrographs of powder P2 obtained through hydrothermal reaction using Na_2SO_4 as a capping agent.....	183
Figure 143 SEM Micrographs of powder P3 obtained through hydrothermal reaction using $(\text{NH}_4)_2\text{SO}_4$ as a capping agent	184
Figure 144 SEM Micrographs of powder P4 obtained through hydrothermal reaction using $(\text{NH}_4)_2\text{SO}_4$ as a capping agent	185

Figure 145 Left; Cyclic Voltammogram of Mo-MoO_x synthesised in 69°C, 1.5M HNO₃ for 20 minutes made from 0.05mm molybdenum Foil from Sigma Aldrich. Right: an SEM image of as-synthesised Mo-MoO_x electrode 193

Table of Tables

Table 1 Select Table of Reported Metal Oxide Supercapacitor Electrodes Performance, Scarcity and Price as of October 2024. Where the metal ore price is given it is marked by an asterisk *	24
Table 2 Select Properties of Tungsten Oxide, WO_3	27
Table 3 Lattice Parameters of Tungsten Oxide Polymorphs.....	30
Table 4 Tungsten- Tungsten Oxide ($W-WO_3$) synthesis procedures, phase, microstructure, and application from literature	32
Table 5 WO_3 as active supercapacitor electrode material on various substrates	35
Table 6 Quantified Reaction Parameters from four reference papers.....	46
Table 7 Notation for identifying samples made through specific conditions used through Thesis	49
Table 8 Hydrothermal Synthesis Conditions synthesised with sodium tungstate.....	50
Table 9 Powder Electrode Synthesis Conditions synthesised from sodium tungstate.....	51
Table 10 Hydrothermal Synthesis Conditions related to 3.2.3.3	52
Table 11 XRD experimental conditions	60
Table 12 <i>Circuit Elements considered for circuit fitting</i> [105], [107], [108], [109].....	79
Table 13 Values used in Impedance Spectroscopy measurement.	80
Table 14 Reaction Parameters, sample names and colour coding used for hexagonal $W-WO_3$ binder free samples.	81
Table 15 Mean and Standard deviation of DCIR values found from the Galvanostatic Discharge data.....	92
Table 16 Fitting parameters for S4 (02) from Zfit between 1Hz and 100 kHz	102
Table 17 Fitting parameters for sample S4 (02) from Zfit between 10mHz and 100 kHz using the fixed values of L1, a1 and R1 from the first step.....	103
Table 18 Reference table for iterations reaction parameters and corresponding label/colour	143
Table 19 Reference table for powder sample's powder Capping Agent and corresponding label & colour	171

1 Introduction

1.1 Background

Green energy generation, storage and wider electrification is central to the UK government's plan for economic recovery from the COVID-19 pandemic, with climate targets expedited to promote change and reduce emissions [1]. These aims resonate with the wider world's efforts to decarbonise society in meeting global climate change targets agreed to in the Paris Accords at COP21. Green energy generation methods, such as solar and wind, are mature technologies already providing significant contributions to the UK's energy demand. However, generating capacity is often curtailed or backed up by fossil-fuelled reserve generators due to their intermittent nature and because the grid currently has insufficient energy storage capacity to allow for grid balancing. The UK government understands the urgency and potential of this sector and considers energy storage a "high priority," investing millions of pounds into energy storage research and commercialisation projects. Electrochemical energy storage is a particular focus, with research into battery, supercapacitor and electrolyser technologies receiving considerable attention and funding. Government funding and initiatives, such as The Faraday Institution, seek to commercialise battery and supercapacitor devices that offer economical, effective energy storage to achieve further integration of renewable energy sources into the grid.

Grid balancing refers to the continuous, dynamic nature of electrical supply and demand the grid infrastructure faces daily. The three key factors are fluctuating demand, intermittent sources (renewables) and outages. Out with incentive pricing, the fluctuations in energy must be mitigated through controlling energy generation, where possible, and through energy storage, storing energy during low demand to be used later.

Renewable energy generation is inherently intermittent and unstable, dependent upon natural processes which vary on a short-term basis with diurnal weather variation and a long-term basis with seasonal variation. It is not feasible to control the output of renewable generation, and so it is increasingly for energy storage to step in to accommodate the variable nature of renewable energy sources and ensure a reliable and consistent power supply.

On a daily basis, the energy infrastructure must be capable of storing excess generation to be later drawn by the grid at peak usage times. Similarly, over seasonal timescales, energy must be stored during summer months, where solar and wind generation is more effective, to be accessed months later in winter when heating and general energy requirements are greater. These two timescales, as a top-level simplification, will necessitate different energy storage technologies suited to either rapid response or long duration, respectively. From a grid balancing perspective, the battery or whatever long-term energy storage device is used will,

regardless of timescale, benefit from being coupled to an auxiliary high-power, or high rate, energy storage device capable of damping transient supply, reacting to rapid changes in demand, and providing back-up or bridging power in cases of supply dropout or emergency. Such a requirement can be served by large capacitors called supercapacitors or ultracapacitors, whose features provide resilience, reliability, and confidence in renewable grids and extend the lifetime of the battery they are coupled to.

Supercapacitors, beyond grid balancing, find applications across diverse sectors, either independently or often as part of hybrid systems. In the medical field, supercapacitors power critical devices such as defibrillators and pace-makers; in industrial settings they ensure stable voltage in variable-frequency drives crucial for manufacturing processes and provide quick peaking power for heavy machinery; Internet of Things devices, including smart door cameras and security cameras, leverage supercapacitors to reduce battery cycling, minimizing maintenance needs; and finally in electric and hybrid vehicles supercapacitors are integrated to enhance acceleration and capture braking energy, reducing wear on batteries. The diverse potential applications make supercapacitors a wide and burgeoning branch of energy storage research, offering highly promising and even already commercial solutions to the challenges of electrification and wider technological development.

Supercapacitor types may be split into electrochemical double layer capacitors (EDLCs), pseudocapacitors and hybrids. EDLCs are easy-to-fabricate, cheap devices with two active carbon electrodes which physically adsorb and desorb ions in the electrolyte, offering long cycle lives and fast charging rates but a low energy density. Pseudocapacitor devices are more expensive, being made of two transition metal oxide electrodes which store energy by transferring ions to and from the electrolyte with a highly reversible faradaic reaction. These faradaic reactions deliver higher energy densities and capacitances than EDLCs. Finally, there are hybrid or composite devices which combine EDLC, pseudocapacitor and battery electrode characteristics to achieve the desired performance.

Pseudocapacitor materials are less established than EDLCs and have enjoyed much interest in the last two decades because of their enormous potential. Able to store 10-100 times more energy by mass than EDLCs and able to charge/discharge faster than battery technologies, pseudocapacitors are well suited to various high-power applications [2]. Pseudocapacitance was first discovered in ruthenium oxide, and its behaviour has been well documented, however, this material will never realise a commercial prospect given ruthenium's scarcity and demand in other catalytic applications. Research has instead moved on to explore other promising pseudocapacitor materials. Various conducting polymers have been reported but the predominant focus of pseudocapacitance research is transition metal oxides such as nickel oxide, manganese oxide and cobalt oxide. These materials, already commercialised as

lithium-ion battery materials, can be tuned to deliver a more pseudocapacitive response whilst retaining a high energy density making them exciting options moving forward.

Finally, there is an opportunity to consider the end life of the device from the outset by carefully deciding how it is fabricated to better facilitate the recycling of spent cells whilst retaining excellent performance.

In the spirit of this, this study aims to take early steps in exploring the potential of “binder-free” electrode architectures for pseudocapacitive energy storage employ a single transition metal and its conjugate oxide as a functional pseudocapacitive electrode. Conventional electrode design may be condensed to three considerations: (1) the active charge storage material; (2) the current collecting material; and (3) the binder material which keeps (1) active material adhered to (2) current collector. This work investigates the effect of combining steps one and two whilst simultaneously removing the third consideration, the binder material, through instead growing the active material, a transition metal oxide (TMO_x), directly from the substrate, the conjugate metal (M-MO_x) and evaluating the performance.

Tungsten Oxide (WO_3) and its conjugate metal tungsten (W) were theoretically an ideal starting candidate for binder-free electrode research because of the wealth of existing literature on both WO_3 as a pseudocapacitive energy storage material and procedures to synthesise W- WO_3 for gas sensing and semiconducting applications. These W- WO_3 electrodes offer several theoretical advantages over conventional fabrication.

The proposed design features a straightforward and scalable architecture, with the oxide growth initiated directly from the surface. In this configuration, the entire mass of the electrode actively participates in charge storage, enhancing the overall efficiency of the system. Notably, the direct bond between the current collector (W) and the active charge storage material, tungsten trioxide (WO_3), serves to minimise electrical conduction losses, thereby optimizing performance.

A distinctive attribute of this design is the deliberate restriction of transition metals exclusively to tungsten, obviating the need for additional current-collecting materials like aluminium or copper which may lead to a cheaper cell. This deliberate simplification of materials streamlines the system and holds promise for facilitating post-life recycling efforts with only tungsten oxide and tungsten metal to recover.

Similarly, the use of protons as the charge-carrying ions makes the system lithium-free, reducing the cost of the electrolyte required and allowing for safer aqueous operation using cheaper electrolytes.

These potential benefits must be tempered with the cost, geopolitical importance and scarcity of tungsten itself. It is obvious due to the scarcity and vital use in other industries, tungsten will not realise a future as a battery or supercapacitor material [3]. That being said, for the

reasons outlined above it makes an interesting base case for a binder-free supercapacitor electrode – certainly within academic interest.

In summary, the integration of current collector (W) and pseudocapacitive charge storage material (WO_3) in the proposed energy storage electrodes aligns with principles of simplicity, scalability, and safety. The proposed electrode offers an interesting base case into the concept from which further work can be developed.

1.2 Research Aims

Developing and commercialising a range of novel supercapacitors is, as discussed, crucial to decarbonising society to meet global climate goals. Transition metal oxide pseudocapacitors are an emergent, and exciting branch of supercapacitor research. With a superior energy density to EDLCs and a greater power density than batteries, pseudocapacitors have a hybrid performance suitable for a range of applications.

Their development, like that of lithium-ion batteries, has hitherto centred upon synthesising a functional TMO powder and binding this to a conductive substrate to form an electrode [4], [5]. Taking a different approach, and instead growing the functional TMO from its conjugate metal to form a pseudocapacitive, binder-free electrode offers a simple, scalable, and sustainable method of electrode fabrication which warrants investigation.

This research project is an initial exploration of binder-free energy storage electrodes, centring on the examination of tungsten-tungsten oxide (W- WO_3) electrodes as a foundational case study. The synthesis of these electrodes was studied under diverse conditions, and the resulting electrodes were comprehensively characterised. Each synthesis iteration was guided by specific, detailed objectives outlined within individual results chapters and related to the overarching aims listed here.

The overarching objectives of this study encompassed several key areas:

- First, to grow the hexagonal phase of tungsten oxide directly from a tungsten foil in a binder-free configuration and thoroughly characterise the resulting electrodes.
- Second, to explore the influence of the present cations and anions in the hydrothermal reaction mixture on the resulting W- WO_3 electrodes.
- Third, to understand the influence of a seed layer in a hydrothermal reaction and whether a favourable surface epitaxy from a seed layer (monoclinic, orthogonal) can be exploited to better adhere a more functional (hexagonal) layer on the surface.
- Fourth, to systematically investigate the reagents employed in the hydrothermal reaction aimed to enhance understanding of the reaction and identify promising synthesis routes.
- Fifth, to offer a comparative analysis between the binder-free electrodes and conventionally produced powder-based WO_3 electrodes.

- Sixth, to critically review the binder-free electrodes synthesised in this study to discern promising routes and general principles for future investigations.

In outlining the central aims of this research, each objective contributes to a comprehensive exploration of binder-free electrochemical energy storage electrodes, with the outcomes serving to inform both the specific case of W-WO₃ electrodes and the broader picture of future binder-free electrode and pseudocapacitor research.

1.3 Electrochemical Energy Storage Fundamentals

1.3.1 Overview

Capacitor, battery, and supercapacitor devices share a common cell structure of two separated electrodes within a cell casing, connected to one another by an external circuit. The similarities end here, with each device possessing different properties which determine its characteristics and performance which may be characterised as a function of energy density and power density. In other words, the magnitude of energy that the cell can store versus the rate at which this energy can be released. These values can be normalised by mass, by area and by volume and presented in a Ragone diagram. An example Ragone diagram taken from J. Miller's Chapter "Market and Applications of Electrochemical Capacitors" from the book "Supercapacitors: Materials, Systems, and Applications" is displayed in Figure 1 [6].

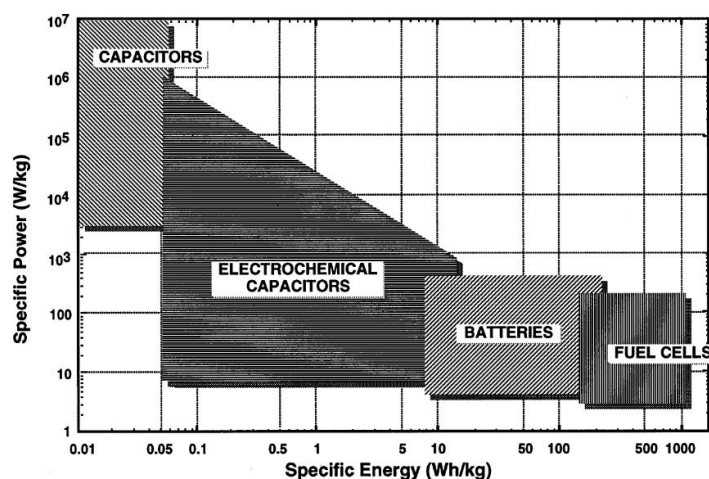


Figure 1 Ragone Diagram of Electrochemical Devices. Taken from [6]

Capacitors are elementary electric components which store electrical energy as an electric field formed across a dielectric barrier with no chemical reaction taking place. It has a positive and negative electrode which separates charge as electrons and positive holes when a potential difference is applied between the electrodes, with no conduction permitted through the dielectric. The charged particles arrange themselves as thin layers held at the surface of each electrode and, as such, may accumulate and dissipate rapidly. The stored energy may be continuously increased with increasing potential until the breakdown of the separation mechanism (vacuum or dielectric) which occurs at much greater voltages than the electrochemical limit faced by batteries [7]. This allows capacitors to operate with much larger voltages than batteries. Capacitors are ubiquitous in electrical circuits with capacitances spanning several orders of magnitude, with applications ranging from noise filtering to voltage conversion. The energy stored in a conventional capacitor is of the order of 0.01 to 0.05 Wh/kg but with power densities of above 10⁴ W/kg. This places capacitors at the top left, high power but low energy density, of the Ragone diagram.

Batteries are galvanic electrochemical cells which store and generate electrical energy through chemical redox reactions. A battery has a positive and negative electrode, separated by an ion-conducting electrolyte, where oxidation and reduction reactions occur simultaneously. The nature of the employed redox reactions dictates whether a cell is categorised as a primary or secondary battery. Primary batteries use an irreversible redox couple making them single-use, non-rechargeable batteries useful in low-drain electronic devices, examples include alkaline and zinc-carbon batteries. Secondary batteries use reversible redox couple allowing the battery to be charged and discharged over multiple cycles. Rechargeable, secondary batteries, such as lithium-ion and lead-acid, are far more versatile than primary cells and may be used in a host of applications from electric cars to personal electronics. The energy and power density of batteries is the inverse of capacitors, where batteries have a high energy density in the region of 10-100 Wh/kg but a low power density of 10^2 to 10^3 W/kg. This places batteries at the bottom right of the Ragone figure.

An electrochemical capacitor, commonly called a supercapacitor, is an all-encompassing term which describes any device which stores charge through a reversible electrochemical mechanism which delivers the characteristic electrical response of an electrical capacitor [8]. The categorisation of supercapacitors is more ambiguous than capacitors and batteries with a range of mechanisms used in a range of electrode/cell configurations. The two prominent mechanisms are electrochemical double layer capacitance and pseudocapacitance, which itself can be split into surface redox deposition pseudocapacitance, redox pseudocapacitance and intercalation pseudocapacitance discussed in more detail in section 1.3.4. Supercapacitors occupy the middle ground of the Ragone diagram with a lower energy density but faster charge-discharge capabilities than batteries. They characteristically function over smaller voltage windows than batteries but benefit from much longer cycle life [2], [9], [10].

For further discussion of the electrochemical energy storage processes occurring in batteries and supercapacitors, it is first necessary to define capacitance and discuss the electrical response capacitance delivers from characterisation. From this basis, electrochemical concepts may be introduced to fully define the charge storage mechanism of each device. This section makes use of model cyclic voltammetry (CV) and galvanostatic discharge data to describe various processes, a fuller explanation of these techniques may be seen in 3.4 of the methodology section.

1.3.2 Capacitance

A schematic for a capacitor is shown in Figure 2, composed of two electrodes separated by a dielectric barrier. The dielectric is an electrically insulating barrier which allows for the formation of an electric field. Polarizing the electrodes either side of the dielectric creates an electric field which drives the electrons and holes of the system to separate and accumulate upon the surface of the electrodes to balance the total system charge. In the case of the

diagram the sum of charge on the negative electrode $-Q$ is equal in magnitude to that on the positive electrode Q . This separation is driven by a potential difference applied across the electrodes of a voltage V .

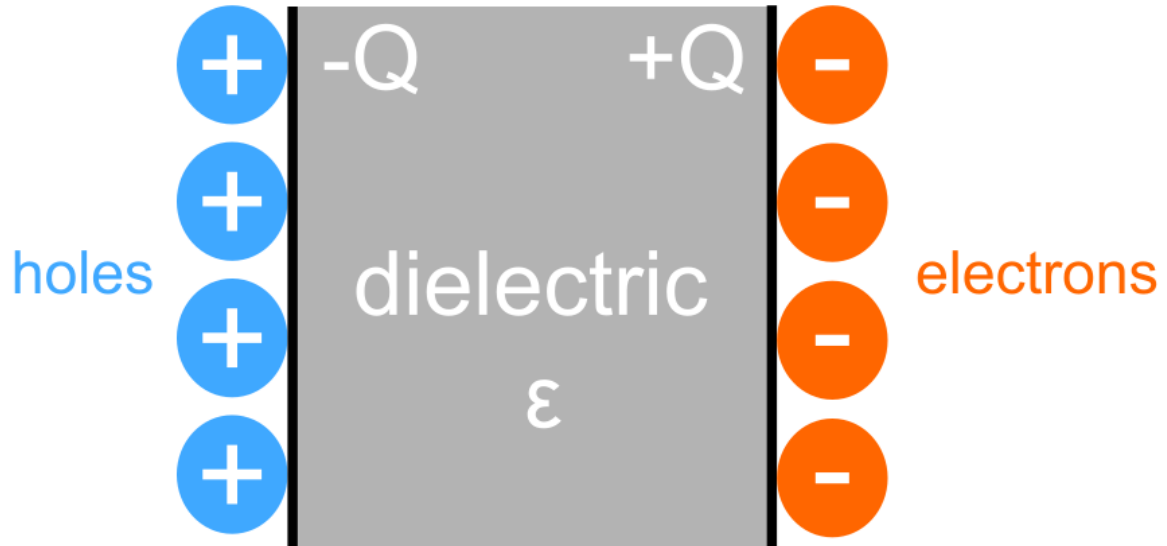


Figure 2 Schematic of how capacitor stores electrical charge across a dielectric barrier

The quotient of separated, or stored, electrostatic charge held by the capacitor at the applied voltage is defined as the capacitance C , and is an intrinsic property of a capacitor [7]:

$$C = \frac{Q}{V} = \frac{\Delta Q}{\Delta V} \quad 1$$

Where C is capacitance in farads, Q is charge in coulombs and V is potential in volts. Equation 1 describes a linear dependency between potential applied and charge separated/stored: a positive increase in applied potential V must induce an increase in separated charge Q which satisfies the capacitor's capacitance C .

The electrical energy available to a capacitor is proportional to the square of the operating potential difference [7]:

$$-\Delta G = \frac{1}{2} C \Delta V^2 = \frac{1}{2} Q \Delta V \quad 2$$

Where $-\Delta G$ is the Gibbs free energy stored in joules, ΔV is the potential difference across the capacitor measured in volts and C is the capacitance measured in farads. The expression may be instead written in terms of the charge passed, Q , by substituting in the definition of capacitance from equation 1.

The schematic in Figure 2 visualises how the separated charge is entirely held at the surface of the electrode; no charge is transferred between the electrode and the circuit, and no chemical reaction takes place. The surface-held nature of the charge means it may

dynamically and rapidly accumulate or dissipate according to subtle changes in the electric field. This affords capacitors fast rates of charge and discharge.

The response delivered from an electrical capacitor when characterised with cyclic voltammetry and galvanostatic discharge experiment are shown in Figure 3 and this response arises from equation 1. A CV experiment sweeps across potentials (V) within a range at a constant rate with respect to time (V per second). The resulting graph from such an experiment, as may be seen in Figure 3 a), is a rectangular shape plot. Considering equation 1, a change in voltage corresponds to a linear change in separated charge, measured as a current, whilst satisfying the law of capacitance. This means as the experiment sweeps to larger potentials a constant current evolves which satisfies the capacitance of the measured device. When the experiment then switches to sweep in the opposite direction, the current immediately switches to an equal magnitude but negative current. This creates the typical rectangular shape CV of a capacitor.

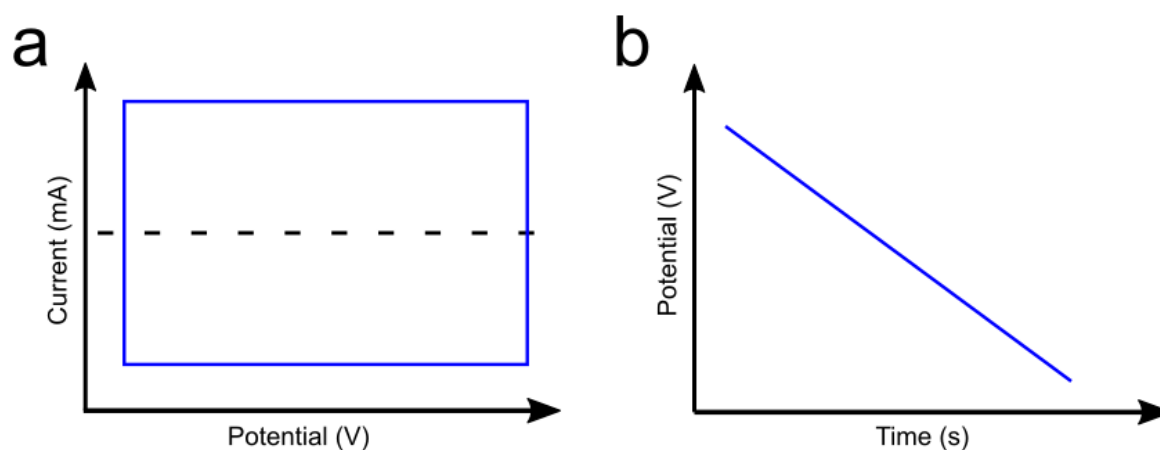


Figure 3 Schematic of electric capacitor's response to a) Cyclic Voltammetry and b) Galvanostatic Discharge

Figure 3 b) shows the discharge for the same model capacitor. This experiment draws a constant current from the capacitor (Q per second) and as time goes on the potential difference drops linearly from the maximum potential to zero. This exemplifies the same process seen in the CV data. The constant rate of change in charge results in a constant drop in potential V across the capacitor until there is no more separated charge. By definition then, it can be seen that the measured response of capacitance is a strictly linear phenomenon: there must be a direct proportionality between the change in potential and the amount of passed charge [10], [11], [12].

1.3.3 Helmholtz Electrochemical Double Layer

Capacitance may be said to occur in any system where a monolayer of particles can reversibly (de-)coat a surface, analogous to a Langmuir isotherm, from which a current may be measured [13]. Instances, where this occurs in electrochemical systems, require a simple base case to be introduced and discussed.

Consider a simple system where a solid is immersed in an electroneutral salt solution composed of cations M^+ and anions A^- and where charge transfer between the solid metal and a salt solution is not permitted. Say the present anions A^- have a higher propensity to be nearer the interface than the cations M^+ [14] then it can be expected the anions will arrange themselves closer to the solid than the cations. These anions may be considered bound to the solid surface and their accumulated presence creates a driving force for cations to diffuse to their surface to balance the excess of negative charge at this surface. This arrangement of ions is called a double layer, and this first case is visualised in the top example of Figure 4.

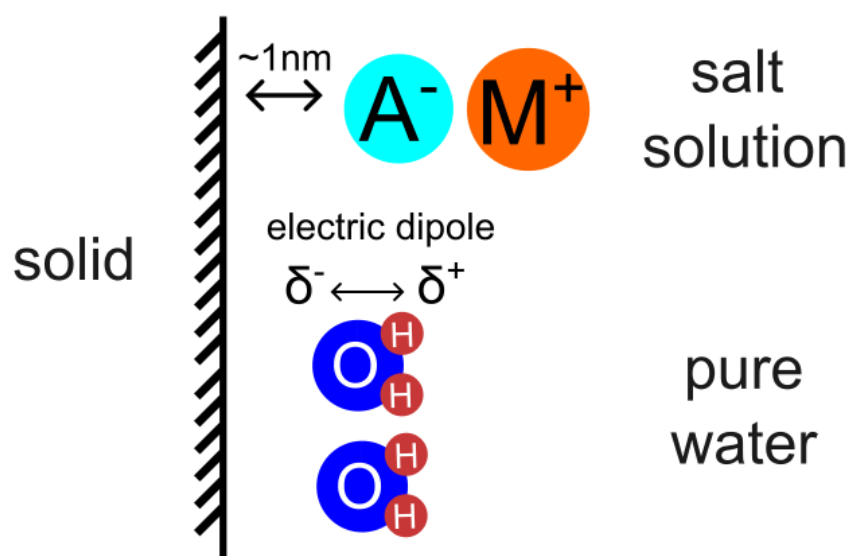


Figure 4 Solid-Solution interface when solid is not polarised adapted from [14]

A double layer does not however require salt solutions to form and may be formed from pure polar solvents such as water. The bottom section of Figure 4 shows a schematic of an unpolarised electrode in pure water. In this second case, the dipole moment of a water molecule is sufficient to create internal charge separation, driving the water molecules to orientate themselves such that the delta-negative oxygen atom is closer to the solid surface than the delta-positive hydrogens [14].

These examples have not yet involved polarising the electrode whereby the charge on the metal surface at the interface may be varied experimentally. Once polarised, ions in solution seek to balance the charge differential of the system by arranging themselves into double layers. Consider a case where there are two metals immersed in solution with a potential difference applied between them without an appreciable current arising from doing so [14]. Understanding where the potential drop occurs in this example is key to the nature of the electrochemical double layer. Firstly, in the absence of current, there is no possible ohmic potential drop which excludes the conductive elements, the metal electrodes, and the solution, from consideration. The drop therefore may only occur at the interface between the metal and solution, in the double layer. If the described electrode system may vary surface charge and

potential without concomitant reactions occurring, it is called the ideally polarizable electrode. A model of the Helmholtz electrochemical double layer formed at such an electrode is shown in Figure 5 and helps explain how capacitance arises from the formation of the double layer.

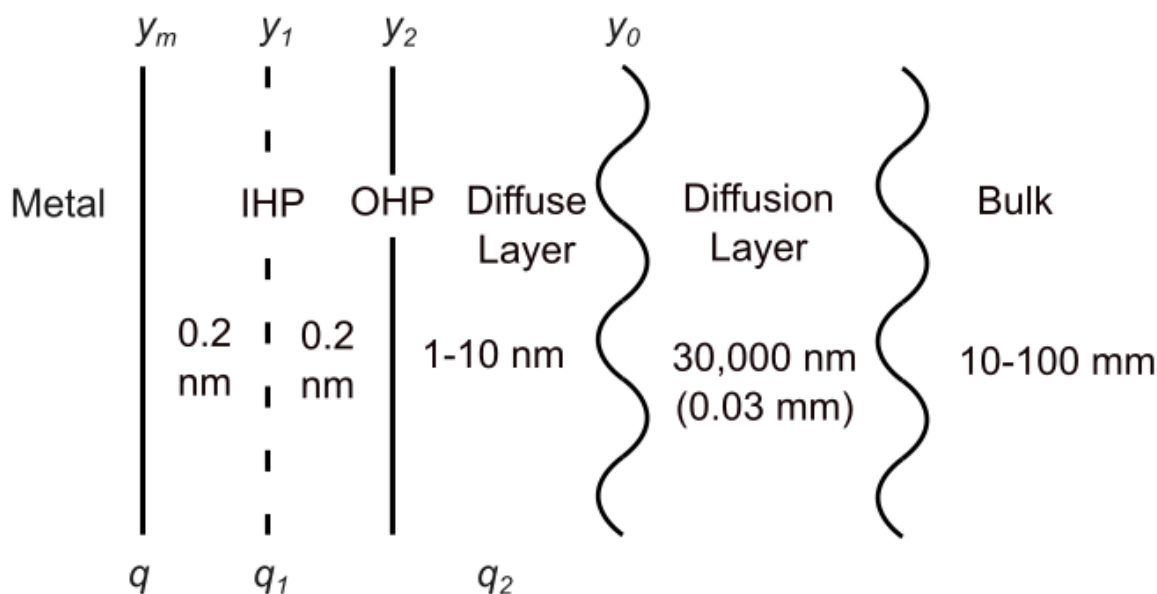


Figure 5 Structure of the Helmholtz electrochemical double layer, adapted from [14]

The metal surface has a charge q which interfaces with the solution. The inner Helmholtz plane (IHP) is the interfacial region where ions or molecules adsorb, or are immediately adjacent, to the charged surface in an ordered arrangement and is designated a charge q_1 . The outer Helmholtz plane (OHP) describes the boundary at which the influence of the charged metal surface on the solution diminishes. Beyond the OHP is the diffuse layer constituted of dispersed, unordered, and solvated ions present in the electrolyte except with a net electrical charge q_2 which creates an ionic gradient across the layer. The diffusion layer is similar to the diffuse layer, composed of the same salts and may have a concentration gradient of salt, but is electrically neutral. The interfacial region between metal and solution in the model is electrically neutral in nature ($q = q_1 + q_2$).

If the model above was expanded to include two ideally polarizable electrodes in a solution, and an applied current, transferring charge from one to the other, renders the electrodes equal but opposite charges from one another then a current will also be established in the solution, where charge moves from the solution side of one double layer to the other until an equilibrium point is reached where both double layers have equal and opposite total charge of $q_1 + q_2$. At this point, each interfacial region and the system, as a whole, is electrically neutral. However, the applied current has separated charge within each double layer equal to create a non-zero charge of q (i.e. $q_1 + q_2$). The charge separation seen in the double layers is capacitive, analogous to electrostatically held charge in an electrical capacitor, wherein the charge passed is proportional to the potential difference across the interfacial region. The capacitive

nature of the double layer is a feature of all electrochemical characterisation and is also critical to understanding the charge-storage mechanisms employed by batteries and supercapacitors.

1.3.3.1 Electrochemical Double Layer Capacitors (EDLCs)

The electrochemical double layer has been employed by commercial supercapacitor devices which use symmetrical, high surface area carbon electrodes which reversibly adsorb and desorb ions in an organic solution, chosen for the larger potential window than aqueous solutions. The limit of energy stored by these materials is defined by their electrochemical surface area and porosity and as such the focus of research into these devices is to develop highly porous, high surface area carbon nano-powders which may bind as much charge as possible [12], [15].

As discussed, each electrode/electrolyte interface has an electrochemical double layer and so a full-cell device corresponds to two capacitors in series with one another:

$$\frac{1}{C_T} = \frac{1}{C_A} + \frac{1}{C_B} \quad 3$$

Where C_T is the total capacitance of the capacitors C_A and C_B in series, where all capacitance values are measured in farads. The capacitance of a symmetrical supercapacitor device may be evaluated by determining the capacitance of a single electrode using the following formula:

$$C_T = \frac{1}{2} C_A \quad 4$$

The energy stored by an EDLC is then the same as that of an electrical capacitor shown in Equation 2. Figure 6 shows the response of an EDLC electrode when characterised through CV and galvanostatic discharge. The shape of the data is similar to an electrical capacitor as may be expected; however, they are not identical. The EDLC electrode has a quasi-rectangular CV and a quasi-linear discharge curve indicating a less-pure capacitive process which is impaired by losses in energy not experienced in the electrical capacitor.

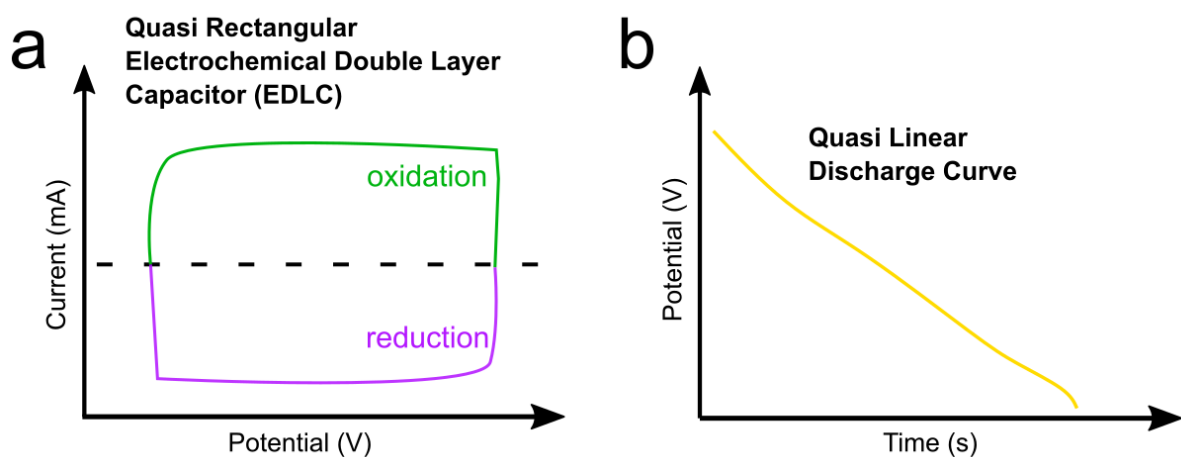


Figure 6 Schematic measured response of electrochemical double layer capacitor (EDLC) from a) Cyclic Voltammetry and b) Galvanostatic Discharge. Adapted from [4].

The differences between the response of a capacitor and an electrochemical double layer capacitor can be explained by the differences in how charge moves to and from the electrode surfaces. When an electrical capacitor is charged, losses are only possible through the resistances in the circuitry which may be expected to be minimal. The EDLC on the other hand experiences further losses through the more resistive movement of ions in the electrolyte compared to electrons in a metal. In addition, there is a greater risk of self-discharge in EDLC than in electric capacitors because the electrolyte permits movement of the ions unlike the fully insulating dielectric.

Despite these differences, the behaviour evinced from these graphs is close enough to pure capacitance to use the law of capacitance to calculate a capacitance from equation 1. This is a crucial point in the discussion of supercapacitors and is referenced extensively through the introduction and results chapters.

1.3.4 Faradaic Reactions

1.3.4.1 Introduction

A faradaic reaction is an electrochemical reaction involving the exchange of charge between two species. In a faradaic reaction, charge transfer occurs at the electrode-electrolyte interface, where one species is oxidised, transferring its electrons to another; the other species is reduced by accepting the transferred electrons. As before, a simple case may be used to introduce key fundamentals of faradaic reactions.

Take a similar case as before where there is a metal immersed in an electroneutral salt solution, though in this instance the electrolyte is instead made of iron ions Fe^{2+} and Fe^{3+} and anion A^- ; and crucially charge transfer is now permitted between the electrolyte and electrode. A schematic of this case is shown in Figure 7.

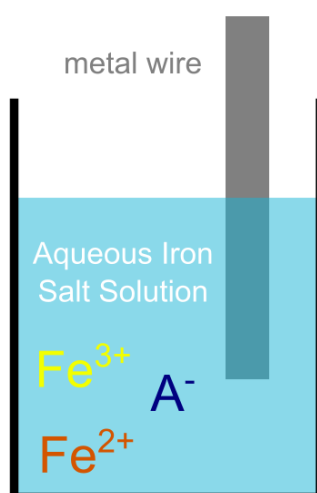
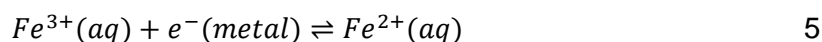


Figure 7 A metal wire in an aqueous salt solution containing cations and anions. Adapted from [16]

The conductive, immersed metal wire may now supply an electron to or drain electrons from the iron ions in the electrolyte [16]. For instance, an electron could transfer from the metal electrode to the solution turning Fe^{3+} into Fe^{2+} ; or vice-versa from solution to metal with the concomitant change of Fe^{2+} to Fe^{3+} . These two forward and reverse processes will occur continually from when the metal is immersed in the solution, occurring simultaneously and at the same rate [16].

This system can be said to be at equilibrium such that there is no net gain of one or the other species defined by the relationship:



This equilibrium describes how electrons must be transferred to and from the metal depending on the relative concentrations of the iron species. If the equilibrium leans to the left, then the metal must accept electrons from the solution creating a net negative charge; to the right, it must donate more to the solution creating a net positive charge. Both cases result in a driving force for charge separation between metal wire and solution; hence creating a potential difference between the metal and solution [16].

This simple example introduces faradaic charge transfer between ions in the electrolyte and solid electrode and explains how the equilibrium established in such a system creates a measurable potential upon the electrode. This system is quite different from the physical processes described in relation to electrical capacitors and the electrochemical double layer, charge has been transferred between species through a chemical reaction.

1.3.4.2 Batteries & General Nernst Equation

A faradaic reaction may be understood further from a thermodynamic perspective. The Gibbs free energy can be derived from the 1st and 2nd laws of thermodynamics, at constant pressure and temperature, as the maximum electrical work that can be obtained from a faradaic reaction (i.e. non-mechanical work) [7] :

$$\Delta G = -\delta w_{elec} \quad 6$$

The Gibbs free energy of the reaction ΔG in Joules per mole is the work associated with moving a charge, Q measured in coulombs, across an electrical potential, E , measured in Volts:

$$-\Delta G = Q\Delta V \quad 7$$

This expression governs a battery cell which uses a faradaic redox couple to store energy where Q is the charge stored by a battery in coulombs and ΔV is the cell's potential difference in Volts. It is worth noting that the available energy of a battery is double that of an electrical or electrochemical double layer capacitor. This is because when charging a pure double-layer capacitor any additional charge stored must first do electrical work against the existing charge density accumulated upon the electrodes which simultaneously increases the potential difference ΔV [13]. This is not the case in a battery where a theoretical constant potential

difference exists between each electrode regardless of the state of charge of the battery [13]. One consequence of this is the maximum energy stored by a battery is limited by the redox potentials of the materials it is composed of - usually a 1-4V potential window [7].

Faraday's second law of electrolysis relates the amount of charge passed by an electrochemical reaction, Q , to the moles of product generated, N , using the moles of electrons n and Faraday's constant, F , which gives the charge of a mole of electrons:

$$Q = nFN \quad 8$$

A standard Gibbs free energy per mole may be then calculated from a standard electrode potential for faradaic reaction measured under standard conditions:

$$\Delta G^\circ = -nFE^\circ \quad 9$$

This equation relates the standard Gibbs free energy ΔG° (Joules/mole) to the standard cell potential E° (V) using n and F as defined earlier and provides insight into the spontaneity of a reaction under standard conditions. If ΔG° is negative the reaction would proceed spontaneously and if positive, then energy must be supplied to drive the reaction.

Every chemical reaction tends to an equilibrium value, which defines the extent to which the reaction proceeds between reactants and products. This equilibrium determines the relative concentrations of reactants and products when the system reaches a state of balance. The equilibrium position is characterized by the equilibrium constant, which describes the ratio of product and reactant activities at equilibrium. The standard Gibbs free energy change, ΔG , is linked to this equilibrium through the relationship:

$$\Delta G^\circ = -RT \ln K \quad 10$$

Equation 10 shows the relationship between the standard Gibbs free energy change (ΔG°) and the equilibrium constant (K) for a reaction. Here, R is the universal gas constant, and T is the absolute temperature in Kelvin. The equation implies that the free energy change determines how far a reaction is from equilibrium: a negative ΔG indicates a spontaneous reaction, while K reflects the balance between reactants and products at equilibrium.

When the system is at equilibrium, $\Delta G=0$, and the reaction quotient - defined as the unitless quotient of the activities of products over the activities of reactants each raised to the power of their respective stoichiometric coefficients - equals the equilibrium constant, K . When the system is not at equilibrium, the Gibbs free energy is expressed in terms of the reaction quotient as follows:

$$G = G^\circ + RT \ln \frac{\prod a_{products}^v}{\prod a_{reactants}^v} \quad 11$$

Where G is the Gibbs free energy in Joules per mole, G° is the standard Gibbs free energy in Joules per mole, R is the universal gas constant in joules per mole per Kelvin, T is the system temperature in Kelvin and the logarithmic term is the unitless reaction quotient.

This equation shows how the Gibbs free energy changes as the reaction progresses and how the system's tendency to reach equilibrium drives the reaction. As the reaction quotient approaches the equilibrium constant, ΔG approaches zero, mathematically showing reaction is at equilibrium and no further net change in the concentrations of reactants and products will occur. Through substitution equation 11 may be written in terms of potential, and an expression can be obtained for electrochemical reactions:

$$E = E^0 - \frac{RT}{nF} \ln \frac{\Pi a_{red}^{\nu}}{\Pi a_{ox}^{\nu}} \quad 12$$

One now can relate the theoretical cell potential E in Volts with the standard potential E^0 in Volts with the given reaction conditions. The reaction quotient is now expressed in reduced and oxidised species to fit with electrochemical reaction terminology for a half-cell. This expression is called the Nernst equation and is the general form of the equation [12]. Similar to the relationship between Gibbs free energy and reaction progress, the Nernst equation describes how the theoretical cell potential E is related to the standard electrode potential and the activities of reactants and products in the system. As an electrochemical reaction proceeds at a given rate controlled with an electrical current, products are formed, and reactants are consumed changing the equilibrium potential. Alternatively, if a potential is applied to an electrode then this acts as a driving force for the quotient to change to return the system to equilibrium, which involves the transfer of charge, measurable as an electrical current. This is the thermodynamic basis of electrochemical experimentation, controlling the current or the potential, and measuring the response in the other. A final comment on the Nernst equation is the extents of the reaction. For a reversible reaction, if the term $\frac{\Pi a_{red}^{\nu}}{\Pi a_{ox}^{\nu}} > 1$ then the $\frac{RT}{nF} \ln \frac{\Pi a_{red}^{\nu}}{\Pi a_{ox}^{\nu}}$ is positive which means the electrode potential is lower than that of the standard potential. Conversely, if the term $\frac{\Pi a_{red}^{\nu}}{\Pi a_{ox}^{\nu}} < 1$ then the electrode potential is raised due to the higher activity of the oxidised species. If one were to instead apply a cell potential below the standard potential this would drive the reaction from oxidised to reduced species; and similarly, if one were to apply a potential greater than the standard potential there would be a drive from reduced species to oxidised.

Most reversible redox reactions therefore operate around a redox potential close to that of the standard redox potential. The real potential of an operating cell also depends on the kinetic and mass transport over-potentials for the reaction i.e. the necessary activation energy required for the charge transfer reaction and real-world losses due to diffusion of reactants to the electrode surface.

1.3.4.3 Intercalation Nernst Equation

Intercalation is a highly reversible faradaic reaction whereby cations are (de-)inserted into a lattice interstitial site with the concomitant reduction or oxidation of the host material without any irreversible crystallographic phase change [2]. An interstitial site refers to the spaces or gaps within the crystal lattice of a host material where the mobile ion can be reversibly inserted, and the intercalated ions are considered delocalised within the host matrix, not fixed to a site. The Nernst equation for an intercalation reaction may be shown to be a function of the quotient of free and filled interstitial sites X [2]:

$$E = E^0 + \frac{RT}{F} \ln \frac{X}{(1 - X)} \quad 13$$

Intercalation occurs in transition metal oxides (TMOs) and stems from their semiconducting valence state. Specifically, the atomic bonding in TMOs transforms individual atomic orbitals into sub-orbitals of similar energies grouped into larger energy bands: one lower energy band, or valence band, consisting of filled, delocalised orbitals and a higher energy band, the conduction band, consisting of unoccupied orbitals [2], [10], [17]. This valence structure means that electron transfer may occur across a range of similar potentials, which is reflected by equation 13: a slight change in X corresponds to a slight change in E . In addition, when transfer does occur these electrons are shared across many atoms allowing for non-stoichiometric (i.e. fractional stoichiometric) levels of charge transfer [10].

A feature of this is that there are two fixed limits to intercalation at 0 to 100 % filled interstitial sites, and therefore equation 13 is only valid within a certain potential window. Beyond this range other faradaic reactions would occur. It is possible that if the potential window is extended too far, the active metal oxide material itself may undergo a redox change which is certainly undesirable as this redox change could lead to an irreversible phase changes of the TMO material structure itself [18]. Intercalation occurs across substantial potential windows ($\Delta E > 0.5V$) and is a common underlying mechanism in many battery and supercapacitor materials.

In a CV experiment one changes the potential and measures the resultant current. For an intercalation system, a gradual change in potential would drive a gradual change in X which physically means a gradual change in intercalated species and transferred electrons compared to the initial starting potential. Experimentally when measured, this can manifest as a near constant current for a given change of potential which is similar in appearance to the CV of a capacitor or EDLC shown earlier in Figure 3 and Figure 6 respectively. For this reason, intercalation materials are described as showing pseudocapacitance, where their faradaic reaction experimentally exhibits aspects which could be interpreted as capacitive. However, the experimental result to achieve this effect is highly dependent on the nature of the material and the experimental conditions used. In other words, an intercalation material may be

pseudocapacitive in one set of conditions but not in another. The next section discusses this in more detail along with other pseudocapacitive charge storage mechanisms, close to but distinct from intercalation.

1.3.4.4 Pseudocapacitance & the Nernst Equation

As introduced in the preceding paragraph, pseudocapacitance is a subset of faradaic reactions which are most simply defined as faradaic reactions that when studied experimentally deliver the signal as if a capacitive process is occurring. It is by definition faradaic; current must pass across the double layer transferring between electrode and electrolyte, only in a pseudocapacitive electrode the derivative of evolved charge affected by a change in potential shows linear proportionality, satisfying the law of capacitance (equation 1). This capacitance is distinct from the electrostatic process employed in EDLCs and hence is called pseudocapacitance [13].

There are three recognised faradaic mechanisms which have been shown to deliver pseudocapacitive features when characterised: (1) redox pseudocapacitance (2) surface pseudocapacitance and (3) intercalation pseudocapacitance.

These faradaic reactions exhibit unique characteristics that deviate from the general Nernst equation (equation 12) and thus demand alternative forms of the Nernst equation, like the one given for intercalation (equation 13). These types of reactions share key similarities: they occur over narrow potential ranges, and their reaction kinetics are both fast and reversible, allowing for rapid response to changes in potential. The Nernst equations for these forms of pseudocapacitance share similar surface adsorption mechanisms to the intercalation Nernst equation discussed earlier [13]. The next section begins by introducing the types of pseudocapacitance, followed by a discussion on the nature of pseudocapacitance and the factors that influence it.

1.3.4.4.1 Redox Pseudocapacitance

Chapter 10 of Conway's 'Electrochemical Capacitors Based on Pseudocapacitance' provides a full mathematical derivation of how some reversible redox reactions, thermodynamically governed by the Nernst equation with respect to electrode potential, can display mathematical pseudocapacitance within a very narrow potential range [13]. Examples include the highly reversible ferri-ferrocyanide but may extend to any highly reversible inorganic redox couple. The Nernst equation for such a reaction is:

$$E = E^0 + \frac{RT}{F} \ln \frac{\chi}{(1 - \chi)} \quad 14$$

Where the χ is a term for the quotient of oxidised and reduced species [Ox]/[Red] for the specific reaction. Where such a redox reaction which fits equation 14 is present, a redox pseudocapacitance system may typically deliver a cyclic voltammetry as shown in Figure 8 which is quite different from the CVs of a capacitor or EDLC discussed earlier.

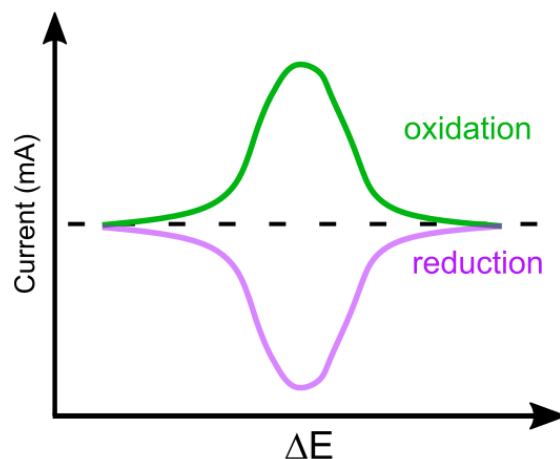


Figure 8 Schematic of a Redox Pseudocapacitance Process characterised by CV. Adapted from [10], [13]

Conway originally outlined the process shown by the CV above as “redox pseudocapacitance” because mathematically it can be shown there is proportionality between the change in potential and consequent current evolved satisfying the law of capacitance, and secondly the immediate switch in current direction with scan direction. This is a view shared by other respected reviewers in literature who agree with this characterisation [2], [13]. Regardless, Conway notes that in most cases redox-pseudocapacitance unfortunately only occurs across small potential ranges (less than 200mV [13]) and therefore is not useful as an energy storage mechanism. For this reason, no further discussion is offered of redox pseudocapacitance.

1.3.4.4.2 Surface redox pseudocapacitance

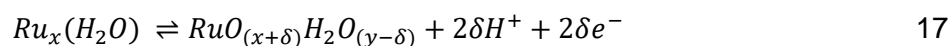
Surface redox pseudocapacitance is an adsorption or deposition process whereby a monolayer of cations in solution are adsorbed to the surface of a noble metal through the transfer of delocalised electrons to adsorbed species, often called underpotential deposition [2], [13]:



This adsorption process is well understood in catalytic noble metals like platinum, iridium, and ruthenium as the preliminary step of hydrogen evolution [13], [19]. This process is analogous to a monolayer sorption process where charge is held at the surface of an electrode and hence may be modelled by the Langmuir-type isotherm. This occurs in several electrochemical reactions including the electrodeposition of copper or lead upon noble metal surfaces [13]. It may be shown that the Nernst equation for this process may be written in terms of free adsorption sites, θ , as denoted in a Langmuir isotherm [13]:

$$E = E^0 + \frac{RT}{F} \ln \frac{\theta}{(1 - \theta)} \quad 16$$

Indeed, it was this mechanism through which pseudocapacitance was first reported in ruthenium oxide (RuO_2) [20]. Hydrous ruthenium oxide may be pseudocapacitively charged and discharged between a wide potential range of 1.4 V. This is due to the metallic-type conductivity of RuO_2 that facilitates electron transfer through the lattice and the hydrous structure facilitates ionic proton transfer too, making the entire bulk of the electrode conductive. Protons can reversibly insert into a hydrous RuO_2 surface film through the reaction [13]:



This top-level, simplified reaction does not show the succession of redox couples which occur across the potential range as ruthenium reduces from Ru^{4+} or Ru^{6+} to Ru^{2+} leading to the fully charged state. The reaction proceeds through several oxidation states of ruthenium which occurs at many distinct but overlapping potentials throughout the electrode surface which creates a quasi-rectangular shaped CV.

The proton may be said to intercalate within the layer but with a key distinction from the proton and lithium-ion intercalation that occurs in transition metal oxides: the protons intercalated in hydrous RuO_2 are on localised oxygen atoms or water molecules; the protons intercalated in transition metal oxides are delocalised, free to move within the bulk lattice [13].

Though the gravimetric capacitances reported are extremely high, the expense and scarcity of the noble metals displaying this behaviour, as well as the limited potential window it occurs, make surface redox deposition an unlikely mechanism for commercial supercapacitor electrodes.

1.3.4.4.3 Factors which influence pseudocapacitance

A key element to pseudocapacitance is that materials capable of exhibiting it only do so under strict conditions and within certain potential ranges. Out with these conditions the material's charge storage mechanism is no longer pseudocapacitive. This leads to an over-reporting of pseudocapacitive materials which have been shown in other work to be truly pseudocapacitive but in the reported data display results which fall short of the definition. Another way of phrasing this is that a material's intrinsic properties make it capable of intercalating or undergoing surface redox to deliver a pseudocapacitive response. However, the microstructure of the material, the potential window used and the electrolyte composition among other variables may influence whether the specific result is or is not pseudocapacitive. This section will discuss the factors which influence pseudocapacitance .

Firstly by looking at the Nernst equations which govern intercalation and surface redox reactions (equation 13 and 15 respectively) they follow a general formula where there is a ratio of free to filled sites that determines the reaction potential. The important differentiation here is what is meant by a "site" in each process: a sorption site, a reacted surface site or an

interstitial intercalation site (delocalised) respectively. In all cases these are surface area-dependent processes and how the redox-active ions diffuse to these sites will dictate the electrochemical response of the materials when studied.

A first example which could be considered is a metal oxide pseudocapacitive material which can intercalate cations in and out of its structure. A typical result of CV and GCD analysis from such a material is shown in Figure 9.

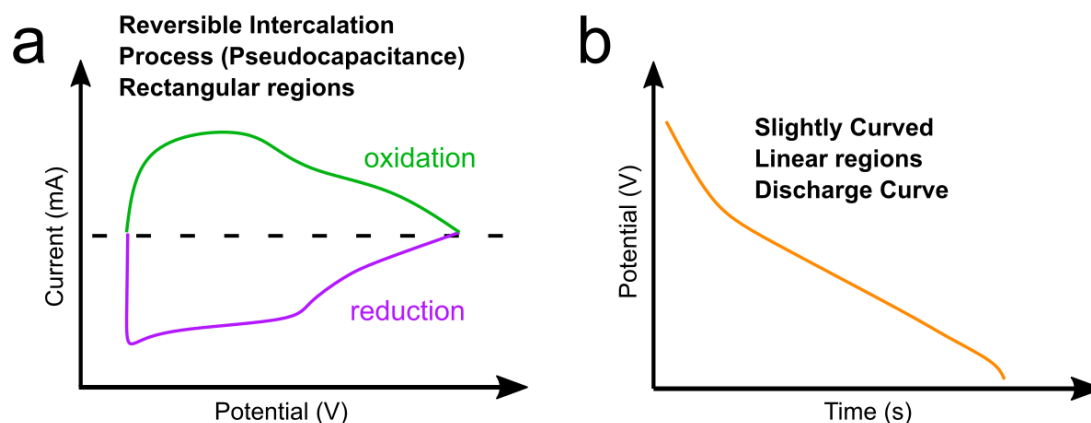


Figure 9 Schematic measured response of pseudocapacitive material from a) Cyclic Voltammetry and b) Galvanostatic Discharge. Adapted from [11].

The cyclic voltammetry (CV) can be described as box-like with no clearly identifiable peaks, indeed one may fit a rectangle within the boundaries of the reduction and oxidation curves. In addition, upon changing the sweep direction of the CV, the current changes immediately with the switch in potential creating a flat back to the figure. This is an important feature in creating the box-like pseudocapacitive shape. The discharge curve can be said to be less linear than that of a capacitor or EDLC but is approximately a single straight line. To summarise, the presented graphs of Figure 9 are not purely capacitive, but neither are they dissimilar. This dialectic is at the foundation as to why there is a great deal of misunderstanding and misreporting of pseudocapacitive behaviour in literature, with the central question: would it be appropriate to calculate a “capacitance” value from the data presented in Figure 9? As the whole data presented does not fit the definition of capacitance it would be inappropriate and instead a capacity can be reported. However, the CV does have capacitive features which the author could find a capacitance for, or alternatively the experiment could reduce the potential window and attain a truly pseudocapacitive graph from which to calculate a capacitance. Confusingly, it is still appropriate to call this material pseudocapacitive because, as discussed, regions of the CV are capacitive. Some authors calculate a capacitance from such data by approximating the CV to rectangle and the discharge to a straight line [10], [21]. However, it is this authors opinion that the entire figure is not capacitive and following a strict definition a capacity should be determined from the presented data. Nevertheless, efforts can be made to

quantify how capacitive the response is and to understand how close to capacitance the response is. These analytical methods are methods are outlined in 3.4.

Published authors often use a looser definition of pseudocapacitance to calculate a capacitance from data like Figure 9 and reporting of such data leads to misleading, inflated capacitance values which should be instead reported as capacities [22], [23], [24], [25], [26]. These red herrings make compiling and comparing relevant pseudocapacitive data difficult because one cannot immediately trust the value being presented. Indeed, some of the values reported in Table 5 may not fully fit the strict definition. In response to such published works, some authors have encouraged changing the terminology for clarity and understanding and even suggested other names such as “supercapattery” [10], [27].

A second example can now be considered to draw comparison to Figure 9 and draw the distinction between pseudocapacitive data and what is often described as battery-like or Nernstian characterisation data in reported literature. Figure 10 shows the characterisation data of the same metal oxide pseudocapacitive material that can reversibly intercalate ions only now the studied electrode was fabricated in a substantially different way: a much larger surface area was used, a larger mass loading of active material is coated creating a thicker layer and a wider potential window was used in studying the electrode through CV.

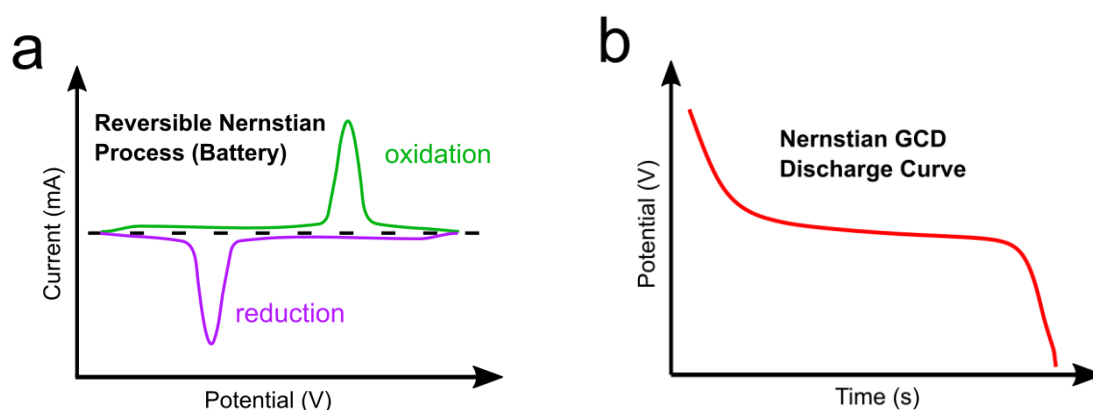


Figure 10 Schematic measured response of Battery-like process from a) cyclic voltammetry and b) Galvanostatic discharge. Adapted from [11].

The CV here shows that there are two distinct onset potentials which initiate a measured reduction and oxidation current, respectively. In both reactions current rises to a maximum at a given potential before dropping to zero forming a narrow peak. The discharge curve of this material is no longer an approximate straight line but has three clear sections: a drop from maximum to a plateau voltage, the plateau and then a rapid drop to a minimum potential. The peaked CV and the plateau-shaped discharge curve may be said to be well characterised by a single potential i.e. the potential where the current is maximised in the CV and the plateau potential of the discharge. This is in stark contrast to the pseudocapacitive data presented in Figure 9 which are better described as a range of potentials not a single characteristic one.

For this reason authors call the data in Figure 10 Nernstian, or battery-like, because the current profile of the electrode is well described as a single peak occurring at an onset potential as predicted by the general Nernst equation. [10], [11], [12].

As mentioned, this electrode employs intercalation to store charge, so why in this instance is it Nernstian/Battery-like and not pseudocapacitive? For intercalation to be pseudocapacitive, the rate at which the surface redox reactions can occur must be rapid and therefore mass transport to and from the surface must be rapid. The intercalation exhibited in Figure 10 which does not show pseudocapacitance can be interpreted as being limited by mass-transport i.e. ion diffusion which is influenced by the electrode's microstructure and its internal electrical conductivity. In the example, a higher mass loading increases resistance because both electrons and ions have longer pathways to travel.

The rate of diffusion is also influenced by the charge-storage ion, which is determined by the electrolyte formulation. Protons, for instance, are more likely to bestow a pseudocapacitive response than larger cations like sodium or potassium because their small size allows for more rapid diffusion [28]. Protons can rapidly migrate within the bulk of the oxide lattice through Grotthuss hopping (if the oxide is hydrated) or along lattice sites and as such the charging mechanism for some materials has been described as a 3-dimensional sorption process which develops a capacitor-like response [13], [17], [28]. Nevertheless, pseudocapacitance may still be seen with other ions with many such Li-ion battery electrodes exhibiting the behaviour [13], [29].

In summary, an active material may deliver a pseudocapacitive or battery like response depending on experimental conditions and how the electrode is fabricated. Furthermore, any intercalation material may be described by the Nernst equation, however the most appropriate variation of the Nernst equation applied depends on the observed behaviour. Ultimately, the desired application, battery or supercapacitor, is what is critical in deciding the how to prepare the active material in order to achieve the desired characterisation response. The data shown in Figure 10 is that of an electrode designed to function as a battery electrode: to store as much charge as possible and discharge at a given rate, not to display pseudocapacitance. Conversely, the pseudocapacitive response displayed in Figure 9 is attained from preparing the active material in such a way to create the conditions for rapid ion diffusion.

2 Literature Review

2.1 Metal Oxide Supercapacitors

Since Conway's seminal work outlining the pseudocapacitance noticed in ruthenium oxide (RuO_2) in 1962 [20] there has been extensive development in pseudocapacitive metal oxide research. Ruthenium oxide (RuO_2) is a high-performing pseudocapacitive material owed to its unique properties: quasi-metallic conductivity, hydrated lattice structure, and wide potential window of up to 1.4V afforded by the multiple valence states [13]. Ruthenium is, however, an extremely expensive, scarce element and therefore will never realise a commercial future as a widespread pseudocapacitive electrode: it is important to consider the performance in conjunction with the scarcity of the material to identify promising chemistries. This data for various pseudocapacitive TMOs is displayed in Table 1, with the spot prices accurate to October 2024.

*Table 1 Select Table of Reported Metal Oxide Supercapacitor Electrodes Performance, Scarcity and Price as of October 2024. Where the metal ore price is given, it is marked by an asterisk *.*

Oxide	Pseudocapacitance Type	Reported Capacitance Fg^{-1}	Global Reserve of Transition Metal (Tonnes)	Metal Commodity Price (USD/tonne - * denotes metal ore price)	Source
$\text{RuO}_2 \cdot 0.5\text{H}_2\text{O}$	Surface Redox	900 at 2 mVs^{-1}	5000 [30]	15.59 M	[31]
Anhydrous RuO_2		0.75 at 2 mVs^{-1}			
IrO_2	Surface Redox and intercalation	645 at 0.25 mAcm^{-2}	n/a	149 M	[31]
MnO_2	Intercalation & Surface Redox	400-500 various rates	3.2 billion [30]	496*	[32], [33]
$\text{CuO}_x\text{-SnO}_2$	Surface Redox	662 at 0.3 Ag^{-1}	5 billion [34] (copper) 4.6 million [34]	Cu: 9,963 Sn: 33,709	[32], [33]

NiO	Surface Redox	300 at 5mVs ⁻¹	>100 million [34]	17,905	[32], [33]
TiO ₂	Intercalation	200 mF/cm ² at 1mAcm ² (areal capacity)	>2 billion [34]	18,600*	[35]
Co ₃ O ₄	Intercalation	472 at 2 mVs ⁻¹	8.3 million [34]	24, 500	[33]
MoO ₃	Intercalation	238 at 2mVs ⁻¹	19 million [30]	48,215	[33]
WO ₃	Intercalation	510 at 2mVs ⁻¹	3.8 million [36]	19,590*	[35]

The electrochemical data in Table 1 states the pseudocapacitance mechanism employed and the reported capacitance value calculated from its characterisation. The CVs that led to these capacitances being calculated have been checked to ensure the quoted value may indeed be termed as a capacitance in line with the previous discussion.

It is quite clear that RuO₂•0.5H₂O is the best-performing metal oxide. This performance is owed to its hydrated, amorphous structure which facilitates proton movement throughout the entire bulk of the material [19]. This is in stark contrast to anhydrous, crystalline RuO₂ which has a tiny capacitance because the layers of oxide are inaccessible to protons [19]. This is not unique to ruthenium oxide, the level of hydration of oxide is critical to the pseudocapacitive other metal oxides including WO₃ and is discussed in greater detail in section 2.2.2 [17], [37]. Though the other metal oxides cannot match RuO₂ they can show relatively high capacitances above 200 Fg⁻¹. There is no standard method as to how this capacitance value has been produced and reported making comparison challenging. A standardisation of how sweep rates or current densities are used to deliver the value would aid this comparison.

The global reserve tonnage and commodity spot price of each conjugate metal, or metal ore, are given as a metric of scarcity. The platinum group metals, ruthenium and iridium, are the most scarce of those tabulated. These metals have more important roles in catalysis which means they will never be suitable for commercial pseudocapacitor applications despite their attractive performance. This is reflected by their price per tonne which is measured in millions of USD.

The other metals are considerably more abundant. Manganese oxide for instance has a billion tonnes of available ore and encouraging capacitances between 400 and 500 Fg⁻¹ depending on the experimental conditions. Unfortunately for the purposes of this research, metals like manganese and chromium at a thickness of around 0.05 mm are sold upon a plastic support material which may limit the potential synthesis methods to create metal-metal oxide

architectures and so must be discounted from this work. Nickel, titanium, molybdenum, and tungsten are all credible candidates for this investigation because the foil is stable enough to be sold as foil.

There were two considerations to choose which metal and conjugate oxide to study. The first was which of these pairings has lots of existing literature on synthesis methods of metal-metal oxide architectures and the second which of these oxides has been well established as a pseudo capacitor. Tungsten and tungsten oxide was found to meet both of these criteria.

Tungsten-tungsten oxide ($W-WO_3$) electrodes are an already established electrode design in fields such as sensors [38], catalysis, electrochromic and photochromic devices [39], [40], and semiconductors [41]. The range of potential applications has driven extensive research into the synthesis of nanostructured WO_3 with many morphologies and phases reported [39]. Secondly, tungsten oxide's ability to pseudocapacitively intercalate protons, rapidly and reversibly, within its lattice structure is well-reported and makes tungsten oxide an emergent supercapacitor electrode material.

One should acknowledge, as mentioned in the introduction, that a tungsten oxide supercapacitor electrode will likely remain of academic interest rather than being commercially viable. Tungsten is a critical element used across various essential industries, and its supply is limited, with significant geopolitical concerns surrounding its availability [3]. These factors make tungsten unsuitable for widespread commercial use in supercapacitor technology, as the risks associated with its supply chain likely outweigh its potential benefits in this application.

The synthesis of tungsten-tungsten oxide structures and separately the application of tungsten oxide as a supercapacitor electrode have both seen rapid development recently. These areas of materials research have however largely progressed in parallel, the idea of using a $W-WO_3$ as a supercapacitor electrode has not been appraised. With so many possible synthesis methods already documented it appeared an ideal choice to investigate binder-free electrodes.

2.2 Tungsten Trioxide (WO_3)

2.2.1 Crystal Phases & Chemical Properties

Tungsten is a dense, heavy transition metal known for its high melting point and exceptional hardness. It has many oxidation states ranging from -2 to +6 leading to a wide range of potential oxides [5]. Inspecting the Pourbaix diagram for tungsten in Figure 11 there are three oxides theoretically possible from anodizing tungsten metal, WO_3 (VI) is the spontaneous passive phase. Other known tungsten oxides are W_2O_3 (III), WO_2 (IV) and W_2O_5 (V) which all may be synthesised from WO_3 . Each of these tungsten oxides have unique properties offering many avenues to investigate for electrochemical applications [5].

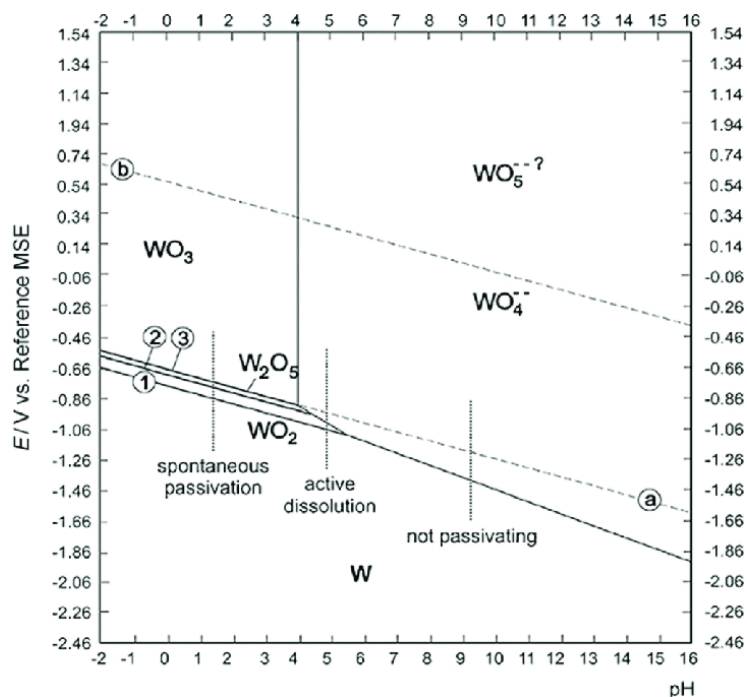
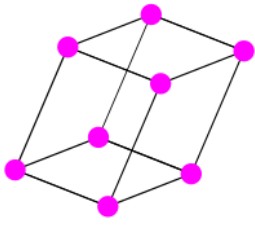
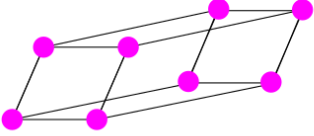
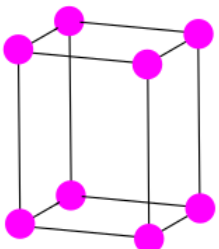
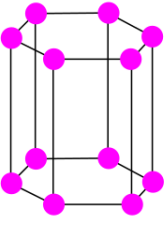


Figure 11 Pourbaix Diagram of Tungsten Phases. Taken from [5]

Tungsten trioxide (WO_3) has been employed for various applications including gas sensors, fuel cell catalysts, electrochromic devices, and photoelectric water splitting. WO_3 exists in various polymorphic forms which are stable within temperature regions and can reversibly exchange between forms [39], [42]. Table 2 shows the structure, properties, and synthesis method of several key phases of WO_3 found in the literature.

Table 2 Select Properties of Tungsten Oxide, WO_3

Phase	Stable Temp Range (°C)	Synthesis Techniques	Crystal Structure (adapted from [43])
Monoclinic [44] (m- WO_3)	17-330	Oxidation, hydrothermal	<p>monoclinic</p>  <p>Angles A=B= 90°; C≠90°</p> <p>Lengths a≠b≠c</p>

Triclinic [5]	-43 – 17	Oxidation	<p>triclinic</p>  <p>Angles no axis are perpendicular to one another</p> <p>Lengths $a \neq b \neq c$</p>
Orthorhombic [45] (o-WO ₃)	330- 730	Oxidation followed by annealing	<p>orthorhombic</p>  <p>Angles $A=B=C 90^\circ$</p> <p>Lengths $a \neq b \neq c$</p>
Hexagonal (h-WO ₃) [44]	RT – 420	Hydrothermal / Solvothermal	<p>hexagonal</p>  <p>hexagonal lattice sites form face from which perpendicular axis extends</p>

The monoclinic structure (m-WO₃) is the ubiquitous phase and is formed through the thermal oxidation of tungsten metal. The m-WO₃ polymorph, made up of corner-sharing WO₆ octahedra, forms a rigid tunnel structure [46]. The monoclinic phase is what spontaneously passivates the tungsten metal surface from thermal oxidation and anodization.

The orthorhombic and triclinic phases of WO₃ are closely related to the monoclinic, with the crystal structure able to shift between these phases upon changes in temperature or hydration state [17], [37], [46]. The orthorhombic phase may readily passivate the tungsten surface under certain anodization conditions.

The hexagonal tungsten oxide (h-WO₃) is a metastable phase that may be synthesised hydrothermally, or solvothermally, from tungsten salts [42]. This metastable structure is also composed of WO₆ octahedra, but through this reaction, they form hexagonal rings instead of corner-sharing. This hexagonal tunnel is stabilised by a central cation as may be seen in Figure 12 which must be present in the hydrothermal reaction. This hexagonal phase is stable up to around 420 °C at which point the structure becomes unstable and decomposes to the

monoclinic phase, this temperature is variably dependent upon the precise hydration state and cation which stabilises the central tunnel [39], [46], [47]. It has been shown in hexagonal ammonium tungsten bronzes that not all tunnels necessarily need to be supported with the cation but there is a minimum amount required [47].

Comparing monoclinic and hexagonal structure as shown Figure 12 one may see why the hexagonal phase has been reported as the best performing phase of WO_3 compared to the other monoclinic type phases. The hexagonal tunnels, filled with a tunnelated cation (Na^+ , K^+ , Rb^+ , NH_4^+ etc), are both hydrated and larger than the anhydrous monoclinic tunnels. These large central tunnels are then also bisected by smaller diamond-shaped tunnels creating a network with a much greater surface area than that of the other phases. This network structure allows for the facile transport and uptake of ions, especially protons, making the hexagonal phase the prominent focus of tungsten oxide energy storage research [5], [48], [49].

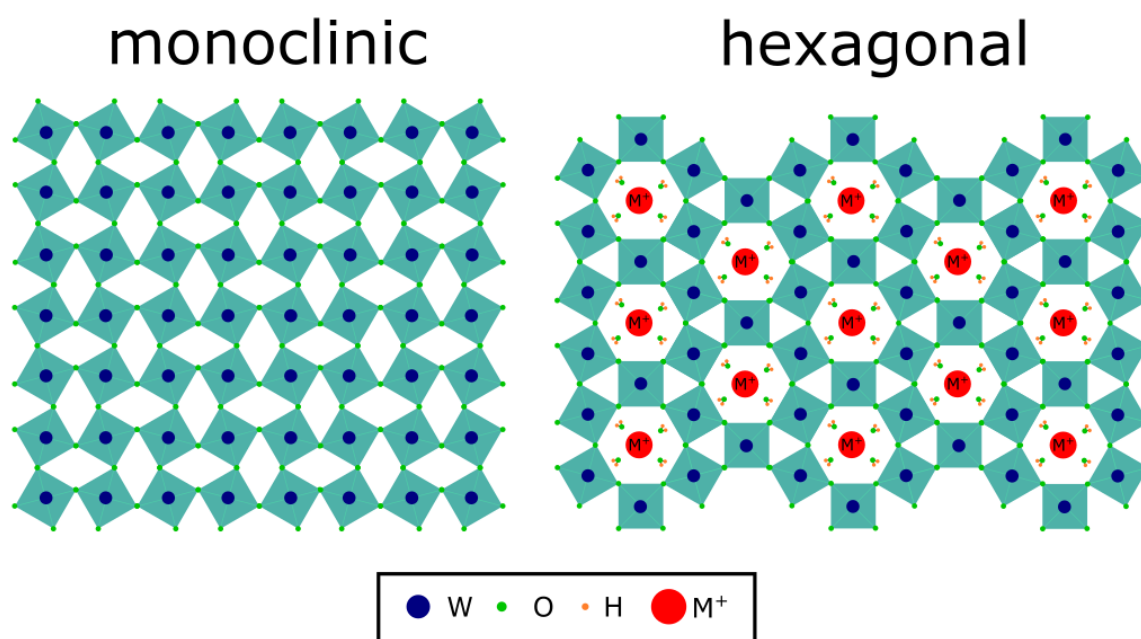


Figure 12 Schematic of anhydrous monoclinic and hexagonal WO_3 phases

The performance as a supercapacitor electrode is not solely determined by the phase alone, the hydrated nature and morphology of the sample are critical in delivering good intercalation performance. Reminiscent of the RuO_2 data, authors have studied the effect of how structural water allows monoclinic- WO_3 lattice to shift its structure when intercalating protons transforming the electrochemical response from a battery-like material to a supercapacitor [17], [37]. Many authors have reported many different morphologies of WO_3 in monoclinic, orthorhombic, and hexagonal phases discussed in section 2.2.4.

A final point can be made on the shared features of the monoclinic and hexagonal lattice structures and how this could be exploited for binder free electrodes. Zheng et al. noted that their synthesised monoclinic- WO_3 on an FTO substrate shared similar lattice parameters to

that of the hexagonal-WO₃ powder [50]. The lattice parameters for these samples may be seen from PDF 01-072-1465 and 01-085-2460, respectively. They found that the seed layer could greatly influence the morphology of a hydrothermally grown hexagonal WO₃ and experimented with different monoclinic loadings to tune the resultant layer. They propose that the monoclinic surface provides an epitaxial surface (better than FTO) for the hexagonal crystal to grow. However, the XRD data presented shows limited, if any, signs of monoclinic oxide remaining post hydrothermal synthesis leaving the question open of whether the hexagonal layer grows upon the monoclinic surface or does the monoclinic layer instead change to hexagonal phase?

The lattice parameters of tungsten metal and the monoclinic, orthorhombic, and hexagonal phases are tabulated below.

Table 3 Lattice Parameters of Tungsten Oxide Polymorphs. The PDF reference values are from the AMRL Diffraction database if not otherwise referenced.

Structure	Lattice Parameters						PDF
	a (Å)	b (Å)	c (Å)	α (deg)	β (deg)	γ (deg)	
Monoclinic-WO ₃	7.3	7.53	7.66	90	90.76	90	01-072-1465 [50]
Tungstite Orthorhombic- WO ₃ (H ₂ O)	5.247	10.7851	5.14	90	90	90	00-018-1418
Hydrotungstite Monoclinic- WO ₃ ·(H ₂ O) ₂	7.45	6.92	3.72	90	90.37	90	01-085-4030
hex-WO ₃	7.32	7.32	7.66	90	90	120	01-085-2460 [50]
Hex-Na _{0.2} WO ₃	7.4818	7.4818	7.614	90	90	120	00-046-0173
Hex-Rb _{0.2} WO ₃	7.4042	7.4042	7.5376	90	90	120	01-076-507
Hex-(NH ₄) _{0.25} WO ₃	7.388	7.388	7.551	90	90	120	01-073-1084
Cubic-W	3.155	3.155	3.155	90	90	90	00-001-1203

Following the hypothesis put forward by Zheng et al, an anhydrous monoclinic or hydrated monoclinic (hydrotungstite) seed layer appears to provide a good epitaxy from which a more functional hexagonal layer could grow. The lattice parameters of four different hexagonal tungsten bronzes (sodium, ammonium, and rubidium) all share relatively similar a and b, α and β parameters.

There is a significant lattice change between the tungstite orthorhombic lattice with one stoichiometric water molecule versus hydro-tungstite monoclinic lattice with two waters. It

would therefore be desirable from an epitaxial standpoint to produce the hydrotungstite. Even still, this tungstite surface would provide a high surface area surface for hexagonal to grow from which may lead to an enhanced hexagonal layer than simply growing from a pristine tungsten surface [51].

To summarise the WO_3 phases from a binder-free perspective, the phases which spontaneously passivate the surface of tungsten metal happen to not be the most effective at storing charge. The hexagonal phase, formed through hydrothermal reactions, offers superior charge storage performance but more involved synthesis methods. Furthermore, there seems an opportunity to provide a more favourable surface for the hexagonal layer to grow by providing a seed layer instead of the pristine tungsten foil surface because a monoclinic – and less so an orthorhombic surface – have a closer epitaxy than pristine tungsten.

2.2.2 Proton Intercalation in WO_3

All phases of tungsten oxide (WO_3) are able to accommodate protons within their interstitial sites upon reduction, intercalating the H^+ between lattice molecules without disrupting the crystal structure. The hexagonal phase, across many studies, can store more charge than other phases because of its superior surface area afforded by a metastable tunnel network (Table 5) – and the synthesis scheme was designed to grow it. Additionally, it was demonstrated by Mitchell et al that the hydration state of WO_3 influences the pseudocapacitive behaviour of WO_3 even when they have the same lattice structures [17], [37]. Anhydrous monoclinic WO_3 can store far less charge than hydrous monoclinic $WO_3 \cdot (H_2O)_2$ which was ascribed to the superior proton conduction and the lattice's ability to shift. This is logical as proton movement is a function of available proton-conducting pathways and hydration adds sites for Grotthuss mechanism hopping in addition to hopping between interstitial sites. Interestingly, the single hydrated phase $WO_3 \cdot (H_2O)_2$ takes an orthorhombic lattice shape and too delivered a higher capacity than the anhydrous state.

The reversible charge storage mechanism in tungsten oxide, within a limited potential window, may be described using the following:



Where the value x indicates the number of protons incorporated into the structure ($0 < x < 1$). The charge storage mechanism of hydrated WO_3 bronzes may be more accurately described as:



Where M^+ is the tunneled cation, α is the stoichiometric coefficient of tunneled M^+ cations, n is the stoichiometric coefficient of structural water, x is the number of protons incorporated into the structure ($0 < x < 1$).

Regardless of the presence of M^+ , proton intercalation within WO_3 structures occurs through a two-step process: (1) hopping: protons hop into the oxide's lattice through available sites; and (2) intercalation: protons intercalate into available interstitial sites with the concomitant reduction of W^{6+} to W^{5+} driven by an electron transferring from the circuit to oxide. This is the relevant charge storage mechanism and will be referred to throughout the electrochemical results.

2.2.3 Tungsten-Tungsten Oxide Electrode Architectures ($W-WO_3$)

Tungsten-tungsten oxide ($W-WO_3$) electrode architectures are one promising avenue of tungsten oxide research that has received much attention lately. A nanostructured oxide surface is cultivated directly upon tungsten foil through thermal oxidation [52], chemical oxidation [51] or anodization [53] creating a novel electrode where the metal current collector and the active surface material are chemically bonded. This design possesses excellent conductivity, versatility and is simple to manufacture. Table 4 gives an overview of preparation methods of synthesising $W-WO_3$ architectures in literature and the related applications.

Table 4 Tungsten- Tungsten Oxide ($W-WO_3$) synthesis procedures, phase, microstructure, and application from literature

WO₃ Crystal Structure	Microstructure	Preparation Method	Application	Ref
monoclinic	nanorods	Thermal oxidation followed by hydrothermal synthesis using capping agent CTAB	electrochromic devices	[54]
not stated	nanoporous Layer	Anodization in oxalic acid bath	photoelectrochemical	[55]
monoclinic	nanosheets	Anodization in H_2SO_4	lithium-ion batteries: binder-free anode	[56]
monoclinic	Triple layer: nanorods; nanoparticles; nanoflakes	Anodization in HNO_3 and NH_4F	photoelectrochemical solar energy conversion	[53]

hexagonal	nanotrees – trunks and branches	Hydrothermal synthesis using the capping agent (NH ₄) ₂ SO ₄	smart surfaces	[57]
hexagonal	nanotrees	Thermal oxidation followed by hydrothermal synthesis using capping agent RbSO ₄	sensors, displays and electrochromic devices	[58]
hexagonal	nanotrees	Thermal oxidation followed by hydrothermal synthesis using capping agent RbSO ₄ and oxalic acid	electrochromic devices, sensors, batteries and photocatalysis	[52]
monoclinic	nanoflake arrays	Thermal oxidation followed by hydrothermal synthesis using capping agent PEG	photochemical water splitting/ photoanodes	[59]
orthorhombic- WO ₃ ·H ₂ O (pre calcination) & monoclinic- WO ₃ (post calcination)	nanoflakes	Hydrothermal synthesis using HNO ₃ and HCl followed by sintering at 500 °C	photochemical water splitting/ photoanodes	[60]
orthorhombic- WO ₃ ·H ₂ O & monoclinic- WO ₃ ·2H ₂ O (pre calcination) & m-WO ₃ (post calcination)	platelike	Hydrothermal nitric acid treatment at 100-180 °C followed by Calcination	photochemical water splitting/ photoanodes	[61]
monoclinic	nanorods	Thermal oxidation followed by hydrothermal synthesis	photochemical water splitting and wastewater treatment	[62]

		using capping agent PEG		
monoclinic	nanorods	Chemical Oxidation using HNO ₃ followed by annealing	Electrochromic devices, sensors, batteries and photoanodes	[51]
monoclinic	urchin like	Thermal oxidation followed by hydrothermal synthesis using capping agent Rb ₂ SO ₄ and oxalic acid	Supercapacitor scaffold material – V ₂ O ₅ active electrode material	[63]

The preparation methods in Table 5 may be split into two categories: surface oxidation creating a monoclinic or orthorhombic surface; and hydrothermal growth where nanostructured hexagonal or orthorhombic WO₃ crystals are grown or deposited on the metal surface.

Surface oxidation of tungsten foil creates a direct bond between metal and oxide and may be achieved through annealing at temperatures between 400-500 °C in an oxygenated atmosphere, nitric acid treatment of tungsten foils at temperatures over 50 °C, or anodization of a tungsten foil in an acidic electrolyte. One feature of thermal oxidation is that it creates an anhydrous monoclinic layer. This may be favourable for epitaxial growth of hexagonal WO₃, but the anhydrous nature was known to be ill-performing as an energy storage electrode [37], [50].

Hydrothermal synthesis deposits WO₃ particles directly upon the tungsten substrate in an autoclave reactor without forming a chemical bond. Nitric acid oxidation, anodization and hydrothermal-seeding techniques offer greater control over the thickness, type and surface of the oxide layer formed than thermal oxidation of foils. On the other hand, hydrothermal processes are harder to scale and are more complex to optimise.

Of the remaining procedures, nitric acid oxidation offers the most scalable process with hydrothermally seeded foils limited by the size of the autoclave used and anodization a more complex concept. Nitric acid oxidation is a facile and well-reported procedure and is currently the most promising choice for creating W-WO₃ electrodes on a mass scale. This method is known to produce hydrated orthorhombic-WO₃ surfaces which have been shown to have good electrochemical performance [17], [37], [51].

Despite the wealth of literature surrounding W-WO₃ architectures, papers investigating this electrode design rarely identify this as an energy storage electrode and, as may be seen from Table 4, have a more general theme of materials discovery. Moreover, when the W-WO₃ electrode has been identified as a potential EES electrode, it has not yet been suggested to

incorporate tungsten oxide as the principal charge storage material of the electrode [63]. This is likely because the anhydrous monoclinic surface formed when oxidizing W-foil is unremarkable as a charge storage material itself as described earlier. Its electrical conductivity, ease of manufacture and simplicity do make it a promising design of current collecting electrode scaffold for a high-performing EES active layer. The surface structure of the monoclinic layer is sensitive to thermal annealing enabling a range of morphologies to be created, illustrated by Table 4. Thermal post-treatment is then a technique which may be used to “tune” the surface to better support an active material.

2.2.4 Pseudocapacitive Charge Storage in WO₃

Tungsten oxide’s potential as a charge storage material has been explored out-with the W-WO₃ electrode design, showing high capacitances and good cyclability. Table 5 shows a selection of key performance data, structural properties, and methods of fabrication of recently reported WO₃-based supercapacitor electrodes.

Table 5 WO₃ as active supercapacitor electrode material on various substrates

WO ₃ Structure		Active Material	Electrode Fabrication	Capacitance (Fg ⁻¹)	Capacitance Retained post cycling		Ref
Crystal Phase	Morphology				Cycles	%	
amorphous	mesoporous	WO ₃	Carbon black slurry/ glass carbon	199 Fg ⁻¹ at 1mAcm ⁻¹	1200	95.00%	[23]
oxygen deficient	amorphous/ mesoporous	WO _{3-x}	Carbon	*175 Fg ⁻¹ at 2mVs ⁻¹	1000	133.00%	[64]
hexagonal	nanopillars	WO ₃	Acetylene black, PTFE, ethanol /stainless steel	421.8 F g ⁻¹ 0.5 A g ⁻¹	1000	100.00%	[65]
hexagonal	unspecified	WO ₃	Single-wall carbon nanotubes	*510 Fg ⁻¹ at 2mVs ⁻¹	5000	87.00%	[44]

monoclinic	unspecified	WO ₃	Single-wall carbon nanotubes	*232 Fg ⁻¹ at 2mVs ⁻¹	5000	79.00%	[44]
hexagonal	nanowires	WO ₃	Grown on Titanium foil	183 at 1Ag ⁻¹	1500	91.90%	[66]
hexagonal	nanowires	PANI-WO ₃	Grown on Titanium foil	278 F/g at 1Ag ⁻¹	1500	92.20%	[66]
hexagonal	nanofibers	WO ₃	Grown on Copper Foil	436 F/g at 1Ag ⁻¹	5000	93.00%	[67]
nickel doped WO ₃	urchin like	Ni-WO ₃	Isopropanol, water slurry/ glass carbon	557 F/g at 1Ag ⁻¹	4000	85.00%	[68]
monoclinic	urchin like	WO ₃	Isopropanol, water slurry/ glass carbon	475 F/g at 1Ag ⁻¹	not given	not given	[68]
hexagonal	Nanofiber	WO ₃ / Graphite Composite	PTFE & Carbon Black slurry/ Nickel foam	85.7 F g ⁻¹ at 0.7 A g ⁻¹	1000	85%	[69]
monoclinic	Nanograin thin film	WO ₃	Grown on ITO Glass	228 Fg ⁻¹ at 0.25A g ⁻¹	2000	75%	[70]
orthorhombic	Nano-flowers	WO ₃ ·H ₂ O/ Graphite Composite	PTFE & Carbon Black slurry/ Nickel foam	92 Fg ⁻¹ at 4 Ag ⁻¹	900	80%	[71]
hexagonal	Nano-fibres	WO ₃ / Graphite Composite	Acetylene & PTFE slurry /Nickel foam	274 F g ⁻¹ at 0.7 A g ⁻¹	1000	75%	[72]
Not stated	microspheres	WO ₃ /CuO Composite	Not stated	284 Fg ⁻¹ at 1 Ag ⁻¹	1500	85.2%	[73]
hexagonal	Nanorods	WO ₃	Acetylene black, PVDF & ethanol/ stainless steel	319 Fg ⁻¹ at 0.7Ag ⁻¹	6000	83.2%	[74]

monoclinic	nanocubes	WO ₃	Nafion, PVD, Carbon black/ carbon cloth	*175 Fg ⁻¹ at 20mV/s	4000	82%	[49]
hexagonal	Nanoplates	WO ₃	PTFE slurry/ glassy carbon substrate	*229 Fg ⁻¹ at 20mV/s	4000	90%	
orthorhombic	Nano cubes	WO ₃		*204 Fg ⁻¹ at 20mV/s	4000	94%	
tetragonal	Nanoplates	WO ₃		*123 Fg ⁻¹ at 20mV/s	4000	76%	
hexagonal	Nanorods	WO ₃ / Carbon Nanofibers		385 Fg ⁻¹ at 0.5 Ag ⁻¹	Not given	Not given	[75]

The majority of electrodes in Table 5 employ hexagonal-WO₃ as the active charge storage material, recognizing its superior performance for ion transport and intercalation over other crystal phases. Lohande et al indeed compared four of the crystalline phases of WO₃ using the same electrode fabrication method and found hexagonal-WO₃ possessed the highest capacitance [49].

It is, however, not as simple as simply stating hexagonal phase is desirable, because of the vast variation within the microstructures of the hexagonal phase itself. Changing key parameters in hydrothermal synthesis namely the capping agent and concentration, the reaction pH, the reaction time, and reaction temperature define the tunnelated cation, the hydration state, and the microstructure present in the obtained hexagonal-WO₃ powder.

This may be seen in the array of microstructures given in Table 5 which are delivered from the various conditions used. The aspect ratio of these reported microstructures defines the surface area of the oxide which in turn determines the ability to intercalate protons and therein the performance.

Table 2 also shows the range of electrode fabrication techniques used across literature, which determine the phase and microstructure and therein the performance. None of the reported supercapacitor electrodes found in this literature survey implement a W-WO₃ electrode architecture. The reported electrodes in Table 5 instead look for a high surface area scaffold that can support the active WO₃ nanoparticle or create an ink which is then coated upon a flat substrate. The one exception to this is Wang et al [63] who hydrothermally synthesised W-WO₃ electrodes as a current collector for supercapacitors. This functioned as a support for a vanadium oxide (V₂O₅) active material. This does not feature in Table 5 as WO₃ was not the

principal charge storage material. The idea to use W-WO₃ as an electrode scaffold was first proposed by Widenkvist et al who synthesised the electrodes using nitric acid, though again WO₃ was not outlined as the principal charge storage material [51]. As discussed, Zheng et al also recognised the potential to provide a seed layer of monoclinic WO₃ which may provide epitaxial surface for subsequent hexagonal WO₃ growth from a hydrothermal reaction within the field of electrochromism not as a battery material [50].

2.2.5 Summary

In summary, many metal oxides and conjugate metals were reviewed, appraising their suitability as binder-free metal-metal oxide electrodes. From the metal oxide's pseudocapacitive behaviour and the reported synthesis methods in the literature, tungsten-tungsten oxide emerges as a promising candidate for a binder-free electrode case study. Tungsten oxide's excellent performance as a pseudocapacitive material has been well researched and a selection of the existing literature in Table 5 was discussed. Tungsten-tungsten oxide electrodes are also a well-established area of research evinced by the range of synthesis methods displayed in Table 4. The diverse synthesis methods for fabricating W-WO₃ electrodes were discussed and informed a promising pathway to synthesise the binder-free all-tungsten energy storage electrodes. The key findings from the literature survey were as follows:

- Hexagonal tungsten oxide is the superior polymorph in terms of charge storage owing to a higher oxide surface area and 3-dimensional pathways for proton movement.
- The hydrothermal reaction conditions are critical in determining the phase and microstructure of the resulting oxide. The capping agent and its concentration in particular show the largest influence.
- A hydrated lattice structure, where possible, is desirable for enhanced proton intercalation owing to confined water layers allowing for structural transformations not possible in the anhydrous layer and to facilitate proton transport.
- Hexagonal tungsten oxide has a more similar crystal structure to the monoclinic phase than to cubic tungsten metal or the orthorhombic phase and so a monoclinic seed layer may provide better epitaxy to grow a functional layer.
- The hydrated structure grown from a tungsten foil using nitric acid treatment is the orthorhombic phase tungstite (orthorhombic- WO₃·H₂O) which has good charge storage performance but does not match the epitaxy of the hexagonal phase as much as the monoclinic.
- There is insufficient evidence whether a seed layer provides epitaxial growth from which a hexagonal layer grows from or whether it would be consumed by the reaction.

- Nevertheless, a seed layer has been shown to be able to provide better controlled and more tuneable surfaces than using a pristine substrate.

Considering these points, it was hypothesised that a seed layer is desirable and that the reaction conditions should be altered to deliver a hexagonal phase. Following this, a two-step approach was devised which first seeded a pristine tungsten foil and then grew a hexagonal phase using hydrothermal synthesis. The details of this are presented in the following chapter.

3 Materials & Methodology

3.1 Initial Synthesis Pathway Overview

The literature review highlighted hexagonal tungsten oxide as the most effective polymorph, but also suggested that a seed layer of a different phase, such as monoclinic or orthorhombic, could be advantageous in promoting good epitaxial growth of the hexagonal layer. An initial experimental procedure was devised following three key steps and is shown in Figure 13.

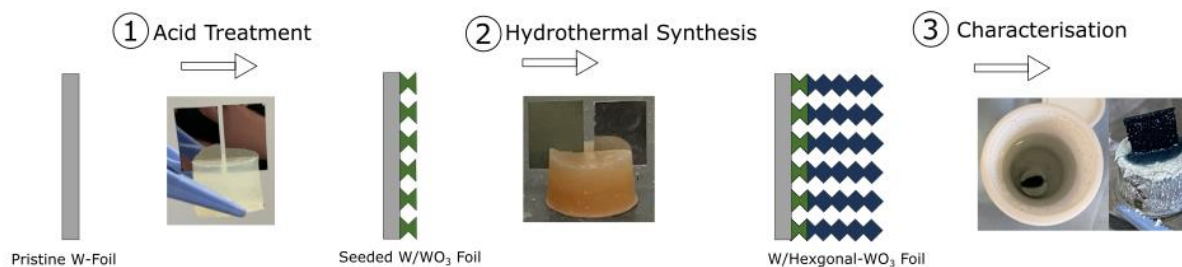


Figure 13 Initial Synthesis Pathway Overview Schematic

The pathway can be summarised as follows:

- The first step would use a seeding pre-treatment to create a WO_3 which may provide a better surface for hexagonal WO_3 to grow. This step was developed from the work of Widenkvist et al [51] and chosen over other routes such as anodisation and thermal oxidation because it created a hydrated layer which was identified as desirable for proton intercalation. This would be at the expense of better epitaxy for the hexagonal phase. A pragmatic reason also contributed here as the experimental work during the COVID-19 pandemic limited access to labs with furnaces capable of creating the monoclinic phase.
- The second step would be to grow the desired hexagonal WO_3 using hydrothermal synthesis. A range of capping agents would be used to study their effect on the resulting oxide and to measure the effect of the pre-treatment seeding step, a pristine tungsten substrate would be used alongside a seeded foil to measure the difference. The hydrothermal synthesis parameters were adapted of existing procedures in literature outlined in section 3.2.2 .
- The third, and most involved, step is the characterisation which can be split into subcategories of electrochemical and material. The electrochemical gives the functionality and performance of the layer and the physical or material seeks to explain the former through discussing the microstructure and crystal phase.

This was deemed to be the most auspicious route to creating a good performing binder free electrode and each of these steps is discussed in greater detail.

3.2 Synthesis Methods

3.2.1 Acid Pretreatment Seeding Step

3.2.1.1 Principle

Tungsten is a robust and chemically resistant metal requiring elevated temperatures or powerful oxidising reagents to achieve oxidation. The most facile way to produce a seed layer in the laboratory was to use nitric acid at elevated temperatures (>50°C) to oxidise the surface to create W-WO₃ [51], [76], [77]. The high temperature and low pH of nitric acid place the reaction in the top left WO₃ (passive) region of the Pourbaix diagram (Figure 11). This occurs through tungsten metal rapidly solvating to WO₄²⁻ before being dehydrated to WO₃ through the reaction [51]:



An alternative and more complex reaction scheme (anodization) has been proposed involving oxygen vacancies migrating from the metal/film interface to the surface and reacting with adsorbed surface water [78]. However, experimentally equation 20 describes the observed experimental results in literature [51]. For instance, it was reported in the literature, and verified in preliminary experiments, that if the nitric acid were stirred no oxide would form on the surface which supports a dissolution and growth mechanism [51].

The temperature of the reaction is critical: the rate of tungsten dissolution and tungstate nucleation increases with temperature leading to a greater number of smaller crystallites as opposed to lower temperatures where there are a few larger crystallites [51]. The reaction occurs rapidly with a colour change occurring after 10 minutes depending on the reaction temperature used.

3.2.1.2 Materials

99.95% tungsten foil (CAS: 7440-33-7) of thickness 0.05 mm as rolled was purchased from Sigma Aldrich in either 50x50 mm or 100x100 mm sized squares. The whole sheet was marked into a grid using a steel ruler and a Stanley blade before being cut into 10x15 mm sized coupons using scissors.

1.5 M nitric acid solution was prepared from 70% stock solution (Sigma Aldrich) and deionised water in a fume cupboard.

3.2.1.3 Equipment & Experimental Procedure

The “seeded substrate” of tungsten-tungsten oxide (W-WO₃) was prepared by treating pristine 0.05 mm thick tungsten foil (W) in 1.5 M nitric acid (HNO₃) at 75 °C. Before entering the reaction, the tungsten metal coupon was degreased with isopropanol, rinsed with deionised water, and dried using a stream of nitrogen.

A temperature of 75 °C was found to rapidly produce an oxide layer with a good electrochemical response in preliminary trials and so was chosen as the reaction temperature.

Figure 14 shows the experimental set-up for the acid treatment step: the nitric acid was held in a round bottom reaction flask with condenser, and the acid was heated in a stirred oil bath to 75 °C set by a pumped water bath. The acid was left in the oil bath for 30 minutes to equilibrate and at this point, the solution was assumed to reach the oil bath temperature.



Figure 14 Photo (left) & Schematic (right) of Acid Treatment Set Up: Oil bath magnetically stirred with immersed round bottom flask and condenser attached housed within fume cupboard. Temperature set by a thermocirculator bath with electronic control

At this stage up to 2 cleaned foils, held in a silicone rubber sample holder for handling purposes, were dropped into the heated acid and left for the desired time. Once the set time had expired the hot solution was carefully decanted into a beaker and the foils were removed with tweezers. The foils were quickly immersed in deionised water to slow any remaining oxidation reaction from residual acid and rinsed multiple times in deionised water. The synthesised foils were then stored underwater to keep the oxide surface hydrated.

A schematic with corresponding real photographs of the progression of the seeding experiment with respect to time is shown in Figure 15 where a distinct colour change from metal grey to green is observed, consistent with other reports in the literature, and indicated the seeding oxidation reaction had occurred [51]. This process occurs at the surface of the substrate and as such it was essential that the acid solution was not stirred. If the acid was stirred it was found no green layer appeared and if left long enough the entire foil eventually dissolved entirely into solution.

There is a significant difference between the pristine W-foil and the seeded W- $\text{WO}_3 \cdot \text{H}_2\text{O}$ foil materially and electrochemically; this difference can be shown using Cyclic Voltammetry and X-ray diffraction.

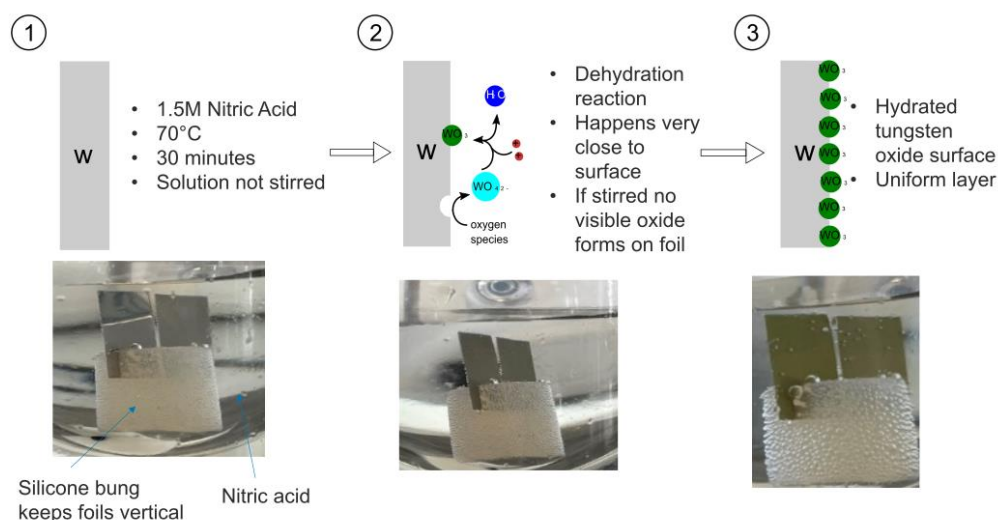


Figure 15 Schematic accompanied with real photos of how seeding step progresses adapted from mechanism proposed in [51]

To determine a suitable length of exposure time for foils in the acid, three settings were tried in preliminary testing: zero minutes (i.e. pristine W-foil), 15 minutes and 30 minutes in nitric acid. The XRD spectra recorded for foils made at each of these conditions are presented in Figure 16.

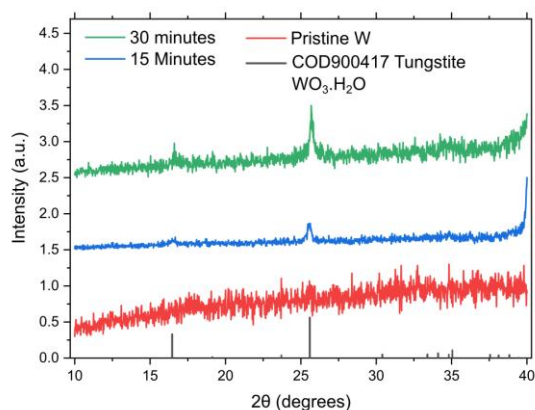


Figure 16 XRD spectra for 0, 15 and 30-minute acid treatments in preliminary experiments

The X-ray diffractograms for 15 and 30-minute treatments share peaks and can be indexed to Tungstite (orthorhombic- $\text{WO}_3 \cdot \text{H}_2\text{O}$). This data was cut and renormalized from the original data because W-metal peaks from 2θ of 41° and greater make the tungstite peaks difficult to resolve. It was therefore decided to reduce the seeding step to a binary choice of seeded or unseeded (W-Pristine foil).

The CV data recorded using a scan rate of 10 mVs^{-1} for each of the substrate types is shown in Figure 17. The cell used to record this data is outlined in section 3.4.1. There is a clear difference in activity between the pristine W-foil and each of the acid-treated samples. This further confirms the visual and XRD indicators that a tungsten oxide surface was successfully synthesised through seeding.

There is no substantial difference between the CV data recorded between the 15-minute (purple line) and 30-minute (orange line) acid treatments which suggests a point of passivation is reached by 15 minutes [51], [78]. That is to say, the seed layer of tungstite produced inhibits any further oxidation of the foil beneath. The reproducibility of the data at each setting also gave confidence in the reproducibility of the synthesis scheme.

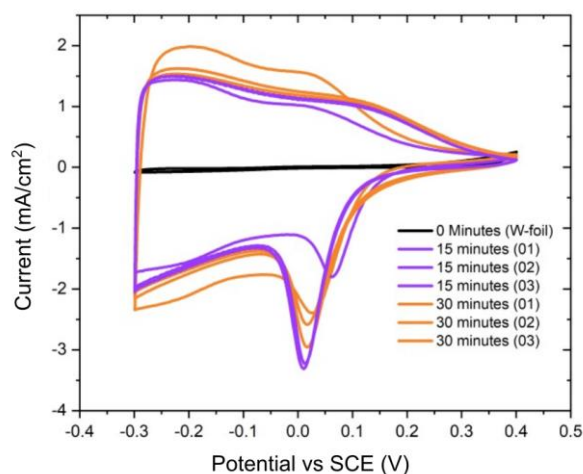


Figure 17 Cyclic Voltammetry Data for 0, 15 and 30-minute acid treatments in preliminary experiments at 10 mVs^{-1}

3.2.2 Hydrothermal Synthesis

3.2.2.1 Operating Principle of Hydrothermal Synthesis

Hydrothermal, or solvothermal, syntheses are a widely used, varied and increasingly important route of inorganic synthesis [79]. They are defined as any synthesis reaction which occurs at a temperature above the solvent's boiling point (i.e. $100 \text{ }^\circ\text{C}$ for aqueous solutions) and operates at a pressure of between 1-100 MPa in a sealed vessel or autoclave [79].

These are distinct from solid-state reactions: no reaction occurs at the interface between solid and solution; rather the reaction between ions or molecules all occurs within the solution. This critical difference allows for new materials including unique metastable phases of inorganic compounds to be synthesised that are otherwise not possible through solid-state chemistry [79].

The high temperature and pressure environment within the autoclave may be categorised into subcritical hydrothermal ($100\text{-}240 \text{ }^\circ\text{C}$) and supercritical ($>240 \text{ }^\circ\text{C}$) reactions [79]. The non-ideal and non-equilibrium conditions created within the reaction vessel, in conjunction with increased reaction rates are the driving force behind the unique compounds which can be obtained [79].

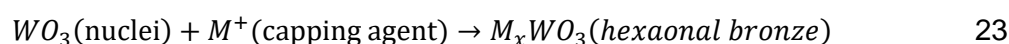
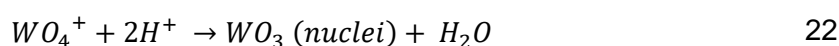
The pressure and kinetics within the hydrothermal reaction are all a function of the reaction temperature and the fill factor of the vessel (i.e. the volume of solvent / total reactor volume) and these must be considered carefully for safe operation [79]. An upper limit pressure inside the vessel may be estimated by assuming: the volume of reactants is entirely solvent, that the

thermal expansion of the liquid is consistent with values in literature; the non-solvent volume is air (approximated to an ideal gas), and the temperature of the reaction is well controlled. The estimated pressure should be within the pressure rating of the purchased autoclave.

3.2.2.2 Quantification of Hydrothermal Parameters to deliver Hexagonal WO_3

Hydrothermal synthesis of hexagonal tungsten bronze ($h-M_x-WO_3$) powders from sodium tungstate dihydrate ($Na_2WO_4 \cdot 2H_2O$) is a well-established procedure in literature. A number of experimental factors have been reported to influence this, but particular focus has often been given to the capping agent employed. The approach outlined here begins with discussing the established growth theory. It then moves on to quantifying the existing synthesis schemes through a ratio of cation to tungstate ion to identify starting points for the synthesis.

The hydrothermal reaction may be explained on a top-level basis through the following reactions:



Literature is consistent in the discussion of two phases of growth: nucleation (equation 22) and subsequent growth (equation 23) which are driven by different processes [80], [81], [82], [83], [84]. Nucleation is a dehydration reaction driven by the low pH of the solution. The pH determines the rate at which tungstate dehydrates to tungsten oxide nuclei and thusly defines the number of particles available to form hexagonal WO_3 in solution. A higher pH has a slow rate of nuclei formation forming a small number of large nuclei; a lower pH has a fast rate of nuclei formation forming many smaller nuclei. The concentration of nuclei formed then impacts how these nuclei interact together in subsequent growth and impacts the final microstructure. Subsequent growth is a more complex process controlled and is a function of many things: cation concentration, cation properties, the rate of nucleation, the anion in solution, microstructure agglomeration and Ostwald ripening.

The theory of how cations function as “capping agents” which influence crystal growth is well documented in the literature [80], [81], [82], [83], [84]. In most reported versions of this synthesis, the capping agent added is ascribed as the influential parameter shaping the WO_3 microstructure. A cation may interact with the growing hexagonal- WO_3 lattice through (i) adsorption onto crystal sites stabilizing or inhibiting growth in certain directions including stabilising the tunnel structure and (ii) electrostatic interactions with double-layer ions which influence aggregation and subsequent growth processes.

Subsequent growth processes include aggregation or agglomeration of microstructures where when structures have large surface areas, they seek to reduce the surface area to a lower energy state by adjoining to one another. Ostwald ripening is a different mechanism with the

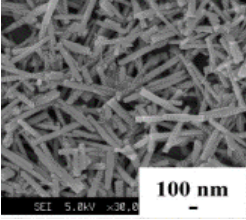
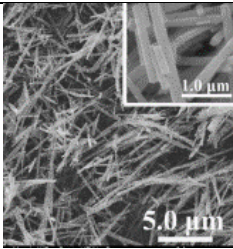
same goal of reducing the system energy: small high surface area crystals dissolve and re-deposit upon larger crystals reducing the entire surface energy. These processes are influenced by the double-layer properties of the growing crystal.

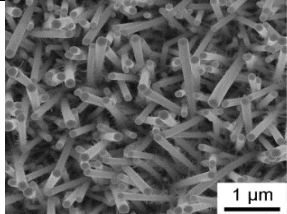
In many cases literature accredits [83], [84], [85], [86], [87] the resulting phase and nanostructure to the sole action of the capping agent added in the synthesis whilst ignoring any contribution of sodium ions from the sodium tungstate may have. Taking a different tack and viewing the obtained hexagonal phase and microstructure as the product of a dual effect of sodium and other cations (i.e. Na^+ and M^+) an empirical analysis was completed upon existing reported literature to identify a promising general reaction scheme. The reaction procedure of four papers which synthesised hexagonal tungsten bronze from Na_2WO_4 using similar temperatures, pressures, and pH but with different capping agents (NaCl , Na_2SO_4 , Rb_2SO_4 and NH_4SO_4) was quantified. In short, a ratio R was found from the reported procedure:

$$R = \frac{\text{Total Moles of Cation}}{\text{Moles of Tungstate}} = \frac{N_{\text{Na}^+} + N_{\text{M}^+}}{N_{\text{WO}_4^{2-}}} \quad 24$$

Where the total moles of cation present are the sum of sodium from sodium tungstate together with the moles of M^+ ($=\text{Na}^+$, Rb^+ or NH_4^+) from the relevant capping agent. The calculated R numbers are tabulated in Table 6 along with SEM micrographs from the publications, which all display the formation of distinct nanorod structures.

Table 6 Quantified Reaction Parameters from four reference papers.

Capping Agent	pH	R Number	Obtained Phase	SEM Micrograph from Source	Source
NaCl	2	4-6	hexagonal		[87]
Na_2SO_4	2	4-6	hexagonal		[80]

$(\text{NH}_4)_2\text{SO}_4$	1	6-10	hexagonal		[88]
Rb_2SO_4	2	5-8	hexagonal		[84]

A more detailed table may be seen in Appendix C and it is clear the reaction parameters are not the same: different reaction times are used, and the ammonium procedure uses a different pH. However, from this simple quantitative analysis it can be seen that the R numbers used in these reports overlap, and furthermore, all of these procedures have delivered similar nanorod microstructures. The value of $R=6$ fits comfortably within the range of each of these procedures, hence this was selected as the R-value most likely to obtain the hexagonal phase. Sodium tungstate, as the tungstate source in the reaction, is suitable for hydrothermal synthesis because it is water soluble. This enables the decoupling of the control over the rate of WO_3 nucleation (set by the pH) and how the subsequent growth proceeds (capping agent, concentration, anion) allowing for a range of morphologies to be produced.

In addition to the cation being used, the anion was also critically analysed. The authors cited above have mixed anions used in the synthesis (different counter anions used in acid and capping agent) and neglect to discuss this effect despite other authors discussing the influence of the anions in solution [80]. To clarify the role of individual anions on the growth of the tungsten bronze, the reactions were simplified to use identical counter-anions on the acid and capping agent.

Finally, it is unclear from the literature whether it is the cation's properties or its interaction with the anion that is influential in growing hexagonal tungsten bronze. To investigate the interplay between cation and anion, NaCl with HCl and separately Na_2SO_4 with H_2SO_4 were used as two of the experimental conditions. This limits the ions as much as possible to a binary pairing (i.e. Na^+ and Cl^- or Na^+ and SO_4^{2-}) in the reaction allowing for the role of anion to be studied.

3.2.2.3 Materials

The hydrothermal synthesis when growing an active layer used W-pristine foil substrates made as described in section 3.2.1.2 Materials, and seeded foil substrates were synthesised as described in the larger 3.2.1 section.

All chemicals and reagents were purchased from Sigma Aldrich:

- Sodium tungstate dihydrate $\text{Na}_2\text{WO}_4 \cdot 2\text{H}_2\text{O}$ (CAS: 10213-10-2)
- Sodium chloride NaCl (CAS: 7647-14-5)
- Sodium sulphate Na_2SO_4 (CAS: 7757-82-6)
- Ammonium sulphate $(\text{NH}_4)_2\text{SO}_4$ (CAS: 7783-20-2)
- Rubidium sulphate Rb_2SO_4 (CAS: 7488-54-2)
- 95-97% sulphuric acid H_2SO_4 (CAS: 7664-93-9) which was diluted to 2M using deionised water
- 37% hydrochloric acid HCl (CAS: 7647-01-0) which was diluted to 2M using deionised water.

3.2.2.4 Equipment



Figure 18 Image of Stainless-Steel Screw Top Autoclave (left) and PTFE bomb/liner (right)

Hydrothermal synthesis was performed in a Huanyu stainless steel autoclave with a polytetrafluoroethylene (PTFE) liner, also known as a bomb. This is a simple design where the reaction mixture is decanted into the PTFE vessel which sits on a removable stainless-steel plate at the bottom of the stainless-steel autoclave casing. Another removable stainless-steel block sits on top of the PTFE lid, sealing the PTFE lid as the casing's lid is tightened. The bottom of the autoclave casing has machined flats at the bottom to grip a vice, and the top of the stainless-steel lid has a hole for a rod so that the autoclave may be tightened. The autoclave was designed to be heated/cooled at a maximum rate of $5^\circ\text{C}/\text{min}$ and so a heating rate of $3^\circ\text{C}/\text{min}$ was chosen to be well within this limit.

The oven used was a Binder FD56 (Figure 19) which was programmed to increase from 40°C to 180°C at $3^\circ\text{C}/\text{min}$ and to hold the temperature for 24 hours at which point the heating shuts off and the oven cools naturally overnight. No controlled cooling was possible.



Figure 19 Oven used for hydrothermal synthesis

The pH was measured before the reaction started using a Mettler Toledo SevenMulti dual conductivity and pH meter with a Mettler Toledo pH probe. The meter was periodically calibrated using three pH buffer solutions from Thermo Scientific Orion Solutions: 4.01, 7.00 and 10.01. The deionised water for all experiments was taken from a Millipore Elix Water Purifier and 30L holding vessel.

3.2.3 Synthesis Procedures and Conditions

It was revealed in preliminary findings that the hydrothermal synthesis had a more pronounced effect on the resulting foil compared to the seeding time in the pre-treatment phase. However, a significant difference was observed between foils synthesized from seeded and unseeded substrates. Consequently, a binary approach using either seeded (30-minute treatment) or unseeded substrates is focussed on throughout the work. As the hydrothermal process and capping agent play crucial roles in determining the final electrode, an exploration of the impact of varying the capping agent salt on the electrode's structure and performance was undertaken using four different capping agents.

A notation was devised to aid understanding of each synthesis iteration and is summarised in Table 7.

Table 7 Notation for identifying samples made through specific conditions used through Thesis.

Sample Simple	Meaning
S	A seeded foil - made using the procedure outlined in 3.2.1 - was the substrate used in the hydrothermal synthesis

W	A pristine tungsten foil – degreased and cleaned but with no further treatment – was used in the hydrothermal synthesis.
Integer following W or S (1, 2 ...n)	Corresponds to the hydrothermal synthesis conditions used in that specific iteration. Where these are used there is a table provided in each chapter which outlines the specific reaction conditions for the chapter. For the samples characterised in Chapter 4 and 5 please see Table 8 and Table 14. For samples characterised in Chapter 6 please see Table 10 and Table 18. For the samples characterised in Chapter 7 please see Table 9 and Table 19.

The original synthesis scheme was derived from closely looking at the literature to develop a relationship between obtaining the hexagonal phase and the concentrations of tungstate (WO_4^{2-}) and capping agent cation (M^+) in the reaction [80], [84], [87], [88]. Subsequent synthesis schemes build upon the learnings from the results of the original scheme.

3.2.3.1 Foil electrodes synthesised with sodium tungstate

The $\text{W-M}_x\text{WO}_3$ electrodes were synthesised using a hydrothermal reaction of sodium tungstate and a chosen capping agent. The procedure was identical except for the capping agent and acid employed. The quantities of reagents used may be seen in Table 8.

Table 8 Hydrothermal Synthesis Conditions synthesised with sodium tungstate.

Sample	Sodium Tungstate	Capping Agent	Substrate	Capping Agent mass	Acid
W1	2.2 g	NaCl	Pristine W-Foil	1.559 g,	HCl (pH 2)
S1	7.48×10^{-3} mol		Seeded W- WO_3	0.0267 mol (R = 6)	
W2	2.2 g	Na_2SO_4	Pristine W-Foil	1.895 g,	H_2SO_4 (pH 2)
S2	7.48×10^{-3} mol		Seeded W- WO_3	0.0133 mol (R = 6)	

W3	2.2 g	$(\text{NH}_4)_2\text{SO}_4$	Pristine W-Foil	1.787 g,	H_2SO_4 (pH 2)
S3	7.48×10^{-3} mol		Seeded W- WO_3	0.0133 mol (R = 6)	
W4	2.2 g	Rb_2SO_4	Pristine W-Foil	3.562,	H_2SO_4 (pH 2)
S4	7.48×10^{-3} mol		Seeded W- WO_3	0.0133 mol (R = 6)	

The reaction mixture was prepared by firstly dissolving $\text{Na}_2\text{WO}_4 \cdot 2\text{H}_2\text{O}$ (2.2 g, 0.0067 mol) of sodium tungstate into 56 ml of magnetically stirred deionised water contained in a PTFE bomb. This volume was chosen as the additional volume from the added acid would bring the volume to $60 \text{ ml} \pm 0.5 \text{ ml}$. Once dissolved, the pH of the solution was reduced to pH 2 by the relevant acid (Table 8) and a white precipitate is visible from the dehydration reaction.

Next, the relevant capping agent was dissolved in solution. Once dissolved, the magnetic stirrer was removed and the two substrates, one seeded and one pristine foil, held vertically in a silicone sample holder were lowered into the reaction mixture, ensuring the base was wide enough to prevent the samples from falling over. The bottom corner of the pristine tungsten foil was clipped with scissors to allow for simple identification of each sample post-synthesis. The lid for the PTFE bomb was secured and it was transferred to the stainless-steel autoclave. The autoclave was sealed by hand and placed in an oven. The autoclave was heated at $3 \text{ }^\circ\text{C}/\text{min}$ from $40 \text{ }^\circ\text{C}$ to $180 \text{ }^\circ\text{C}$ and held at $180 \text{ }^\circ\text{C}$ until the reaction time was complete (table). Once the time had completed the oven was switched off and the vessel was allowed to cool overnight before being opened using the vice in the lab. If necessary, a wrench may be used to loosen the autoclave lid.

The samples were either removed immediately for characterisation or moved into a storage solution (pH 2 of the same acid) which was found to best preserve the as-synthesised foils.

3.2.3.2 Powder Electrodes from Na_2WO_4

The hexagonal WO_3 powder was synthesised in the same reaction described and the key reaction conditions are held in Table 9. The powder that had precipitated and was at the bottom of the PTFE bomb was collected by pouring the reaction liquor through a fibreglass filter paper.

Table 9 Powder Electrode Synthesis Conditions synthesised from sodium tungstate.

Sample	Capping Agent	Type	Capping Agent mass	Acid	Temperature ($^\circ\text{C}$)	Reaction Time (hrs)
--------	---------------	------	--------------------	------	----------------------------------	---------------------

P1	NaCl	Powder	1.559 g, 0.0267 mol (R = 6)	HCl (pH 2)	180	24
P2	Na ₂ SO ₄	Powder	1.895 g, 0.0133 mol (R = 6)	H ₂ SO ₄ (pH 2)		
P3	(NH ₄) ₂ SO ₄	Powder	1.895 g, 0.0133 mol (R = 6)	H ₂ SO ₄ (pH 2)		
P4	Rb ₂ SO ₄	Powder	3.562, 0.0133 mol (R = 6)	H ₂ SO ₄ (pH 2)		

The powder was periodically washed with deionised water (50-60ml) throughout the day and then was left in a fume cupboard and allowed to dry overnight without any external vacuum or heating applied to the filtering process. This was done to ensure that the samples retained structural water with the view to improving performance and retaining the obtained structure. The washing was intended to remove any capping agent salt which remained. The powder was then transferred from filter paper to a glass vial which was labelled and stored ready for when ink coating would be prepared.

3.2.3.3 Further Foil Electrodes Synthesis

An iterative process was used to review the initial reaction scheme discussed previously to better understand the hydrothermal reaction and attempt optimisation. The results of these iterations are presented in Chapter 6 'Systematic Review of Hydrothermal Reaction Scheme' and were synthesised in a similar fashion to 3.2.3.1 with a general two simplifications. Firstly, no sodium tungstate was added to the reaction with the view to synthesising a thinner layer of oxide, and secondly, only sodium chloride was used as a capping agent where the iteration called for the use of a capping agent. This reduced the amount of synthesis required whilst still allowing the factors of interest to be investigated. The procedures for each iteration are given in Table 10.

Table 10 Hydrothermal Synthesis Conditions related to 3.2.3.3

Iteration	Samples	Procedure
#1	W5, S5	Motivation: investigate the effect of removing sodium tungstate from the reaction upon growing foils
		56 ml of deionised water was added directly to the PTFE bomb and the pH was adjusted to a value of 2 using 2M HCl. 1 gram of NaCl

		was added to the reaction mixture and allowed to dissolve. A Seeded and Pristine foil were then added to the bomb held by a silicone sample holder. The reaction was heated at 3°C/min to 180°C and held for 24 hours before being allowed to cool naturally. The samples were removed, rinsed, and characterised as synthesised.
#2	W6, S6	Motivation: determine whether pH in solution requires to be as low as 2 for an effective layer
		56 ml of deionised water was added directly to the PTFE bomb and the pH was left unaltered (~5.6). 1 gram of NaCl was added to the reaction mixture and allowed to dissolve. A Seeded and Pristine foil were then added to the bomb held by a silicone sample holder. The reaction was heated at 3°C/min to 180°C and held for 24 hours before being allowed to cool naturally. The samples were removed, rinsed, and characterised as synthesised.
#3	W7, S7	Motivation: determine the influence of different substrates on each other's growth in shared autoclave
		Two identical reaction mixtures were prepared in two different PTFE bombs: in each 56 ml of deionised water was added directly to the PTFE bomb and the pH was adjusted to a value of 2 using 2M HCl. 1 gram of NaCl was added to the reaction mixtures and allowed to dissolve. A Seeded foil was then added to one bomb held by a silicone sample holder; conversely, a pristine unseeded foil was added to the other. The two autoclaves were heated at 3°C/min to 180°C and held for 24 hours before being allowed to cool naturally. The samples were removed, rinsed, and characterised as synthesised.
#4	S8, S9	Motivation: investigate the effect of using no capping agent in the reaction
		Two similar reaction mixtures were prepared in two different PTFE bombs: in each 56 ml of deionised water was added directly to the PTFE bomb and the pH was adjusted to a value of 2 using 2M HCl in one and 2M H ₂ SO ₄ in the other. No Capping agent was added to either mixture. A Seeded foil on its own was then added to each bomb held by a silicone sample holder. The two autoclaves were heated at 3°C/min to 180°C and held for 24 hours before being allowed to cool

		naturally. The samples were removed, rinsed, and characterised as synthesised.
--	--	--

3.3 Material Characterisation

3.3.1 Scanning Electron Microscope (SEM) and Energy Dispersive X-ray (EDX)

3.3.1.1 *Operating principle*

The microstructure of synthesised samples, both foils and powders, was studied and characterised using Scanning Electron Microscopy (SEM) – a versatile materials characterisation technique which can generate detailed images of a material’s topography irrespective of the material’s thickness or composition [89].

SEM operates by directing a focussed beam of electrons upon a sample under vacuum conditions and measuring various emissions from the ensuing collision [89]. A visualisation of these different emissions is given in Figure 20.

The emission type is a function of the orbital level of the electron which has been affected by the beam impact. The secondary electrons refer to those knocked out of the outermost orbital by the incident electron, and these may be used to create an image of the sample’s surface [89]. Backscattered electrons refer to the case where an incident electron interacts with the nuclei of an atom but does not eject any additional electrons [89], [90]. These electrons may also be used to generate an image which offers slightly different details given the electron interrogates the atoms of the sample to a deeper level [89], [91].

When incident electrons eject electrons of higher energy shells, other electrons rapidly shift to fill the shell vacancy to balance the atom’s charge and simultaneously emit x-ray radiation. Because the energy of the emitted X-rays is intrinsically linked to the electron orbitals of atoms, an energy-dispersive X-ray (EDX) detector can interpret the emitted spectra and identify the chemical composition of the sample [89].

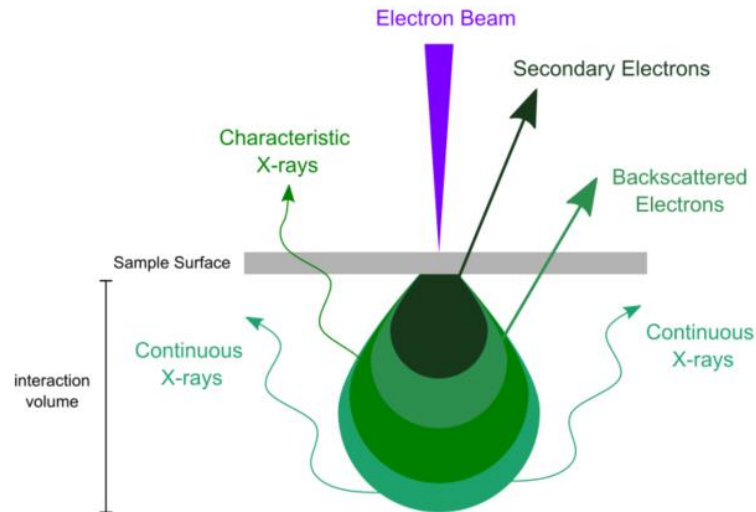


Figure 20 Schematic of emissions from electron beam depending upon the interaction volume of specimen. Adapted from [89], [90]

The beam of electrons may either be produced by heating a tungsten filament (W-filament SEM) or a field emission gun (FE-SEM) which results in a better resolution of image because it can create a higher density electron beam [89]. Regardless of how it is generated, the beam is trained upon the sample using an anode, electromagnets and condenser lenses and moves across an area of the sample in a raster pattern, generating the image [89].

Where charging of the sample occurs from electrons not dissipating, water vapour to a pressure of around 0.5mbar is introduced to the chamber which is called low-vacuum or wet mode [89]. A schematic of how low-vacuum mode operation dissipates charges is shown in Figure 21 and may be summarised as follows: electrons emitted from the sample attempt to travel to the positively charged detector, they collide with gas molecules present which generates positive ions and additional electrons which continue onwards, creating a cascade effect, the positive ions migrating to the sample surface dissipate any accumulated charge [89]. The incident beam is so narrow and energy-dense that it experiences little scattering from the gas molecules.

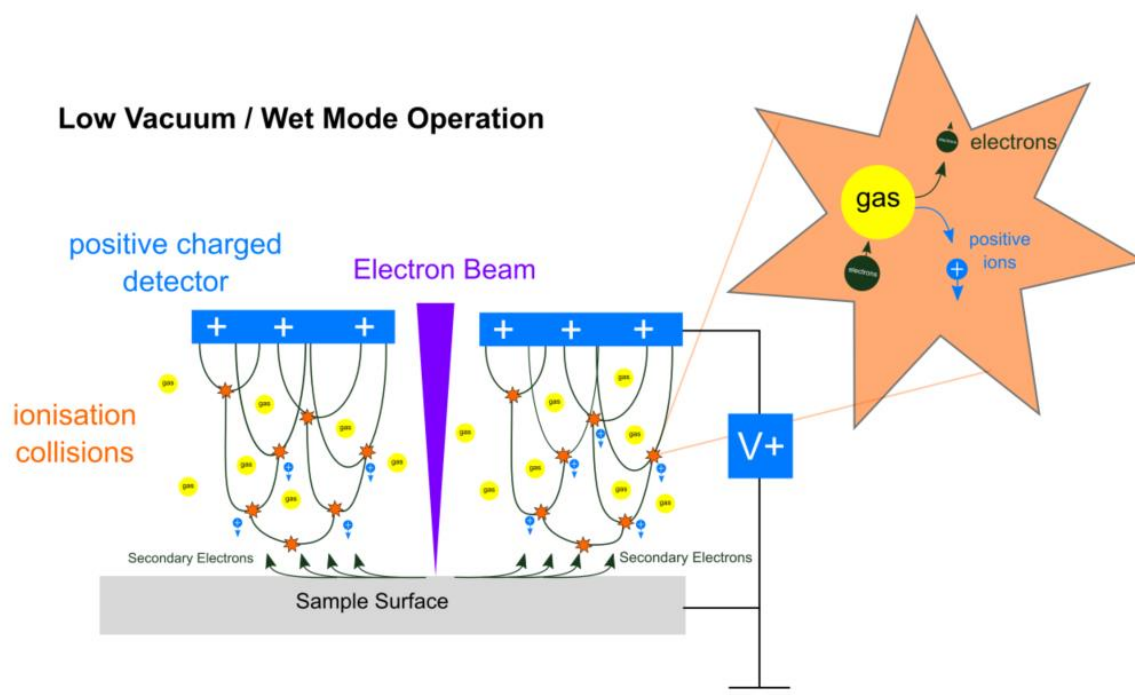


Figure 21 Schematic of low Vacuum / Wet Mode Operation where a gas (often water vapour) is introduced into the chamber and collides with emitted electrons, producing positive ions which dissipate negative charge which may accumulate upon the surface. Adapted from [89].

3.3.1.2 SEM & EDX Experimental Procedure

Micrographs were taken using the Field Emission Environmental SEM “FEI Quanta 250 FEG-ESEM” with a limited number taken using a tungsten-source SEM “JEOL JSM-IT100 InTouchScope”. The sample preparation was identical using both apparatuses and although these microscopes use different software, and focussing parameters/jargon, the principle in how micrographs were taken was also identical:

- (a) The sample(s) of interest was mounted either directly upon a stage using silver paint or a carbon sticky tab or mounted upon a stub using a carbon sticky tab which itself sat in a groove on the stage. Examples of this may be seen in Figure 22. When foil samples were being studied, effort was made to remove the oxide on the mount-facing side to improve conductivity. Critically, it is important to check by blowing pressurised gas over the sample to see if the exposed oxide is well enough adhered so that it will not fly off from the initial agitation the samples experience when reaching the vacuum. When cross-sectional micrographs were being studied the epoxy block was placed upon the stage, its weight alone would keep it in place.

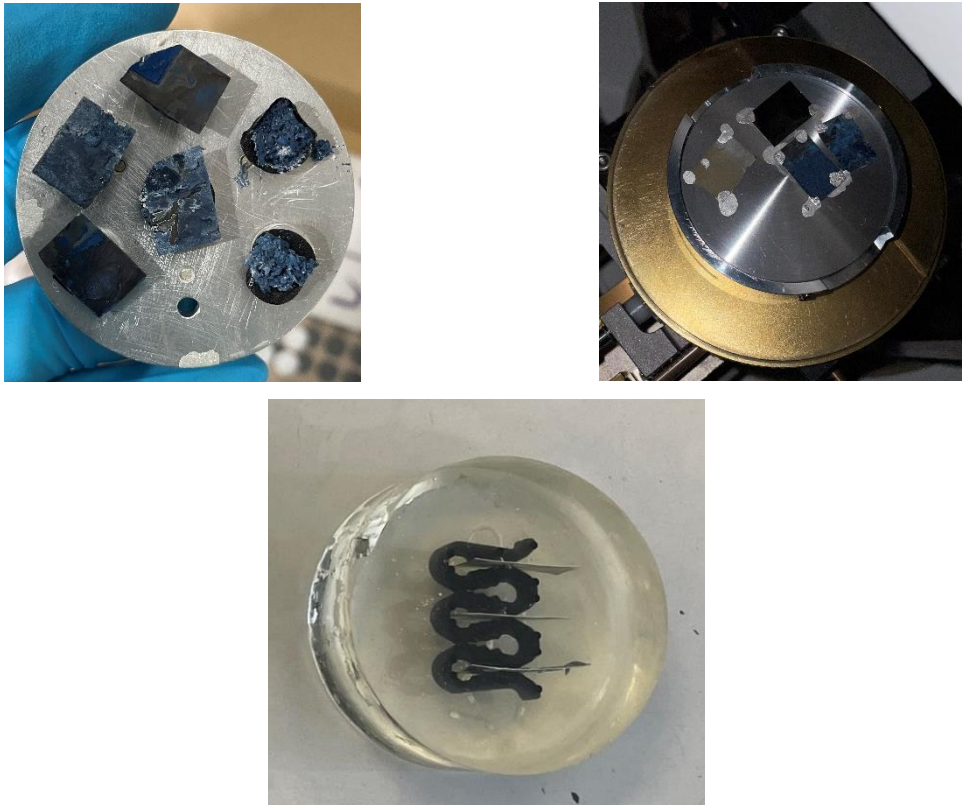


Figure 22 example images of samples studied mounted on stubs held in a stage; mounted directly upon a stage; and epoxy set to expose the cross-sectional view of the foil

- (b) Once the samples were mounted into the chamber of the respective SEM unit, a high vacuum setting was applied, and the system would reach high vacuum after a few minutes. The epoxy set samples were only viewed in low-vacuum because the epoxy is prone to charging.
- (c) The following steps were followed in order to take a micrograph of sufficient resolution:
- Starting with low beam energy, usually 5.00 kV, an attempt was made to gain focus at low magnification using rough focussing before increasing magnification and seeing if features were visible.
 - The brightness and contrast settings were adjusted to maximise what may be seen.
 - Astigmatism, fine focus, beam shift and lens alignment were all then adjusted to optimise the image on screen [91]
 - If the image was satisfactory then it was taken and saved. If not, another beam energy was chosen and steps i to iv were iterated through once more; in the case of FE-SEM images, the beam size may also be adjusted, and the steps iterated through again.
- (d) If the image was still not satisfactory and the settings in (c) had been exhausted, efforts were made to reduce charging in the system by using a low-vacuum mode with water

vapour added to the chamber. Further efforts may be made to improve conduction between sample and stage by using more silver paint [89], [91]

- (e) EDX Procedure: if an EDX spectra were desired for the given sample, the energy of the beam was increased further to 15kV and higher, as well as widening the beam spot to ensure as much excitation of sample electrons as possible. The micrograph was focussed as well as possible and an EDX map was recorded of the given area. This data was interpreted with Oxford Aztec software.

3.3.2 Xray Diffraction (XRD)

3.3.2.1 XRD Operating principle

XRD is a non-destructive technique which uses X-rays to determine the arrangement of atoms within a crystal allowing for the crystal phase of the synthesised samples to be determined [43]. It accomplishes this by firing an X-ray beam at a sample and measuring only the emitted X-rays where Bragg's Law is satisfied [43], [92].

Bragg's law, described by (25), states that constructive interference may only occur in scattered X-rays when they are diffracted at the same angle as they entered because they have passed through a crystal where all atoms are spaced in a regular, repeatable way [43].

$$n\lambda = 2d \sin\theta \quad (25)$$

The value n is the order of reflection, d is the interplanar spacing of the crystal lattice, λ is the x-ray wavelength and θ is the angle of incidence the x-ray enters the crystal. A visualisation of this relationship is presented in Figure 23.

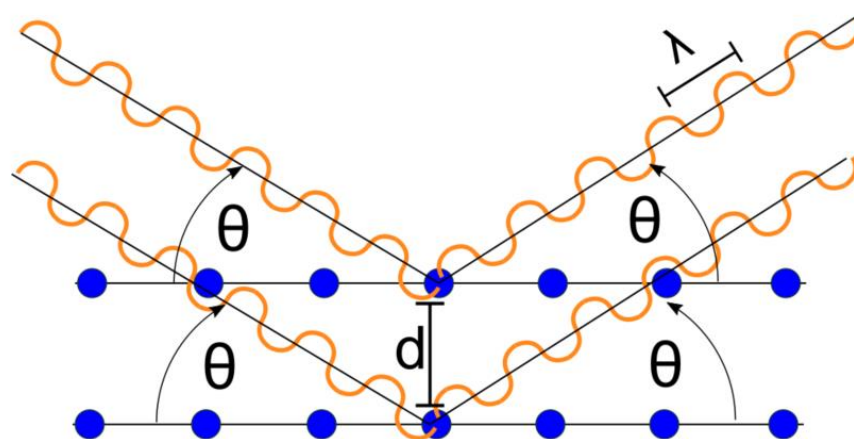


Figure 23 Schematic Diagram of Diffraction of X-rays by a crystal where Bragg's Law is satisfied. Adapted from [43], [92].

The diffracted beams, sharing a wavelength and exit angle, constructively interfere and their amplitude is boosted to the summation of all the relevant X-rays. Since the angle between the

incident and diffracted beam is always 2θ , this value is used as a reference for measured intensity values.

A schematic of the conventional, powder XRD apparatus is shown in Figure 24. An X-ray source emitting a given wavelength and a detector opposite the emitter rotate around a sample over a preset 2θ range at a given rate (degrees/time) and the intensity of X-rays at each 2θ value is recorded. The X-rays are produced from a tungsten filament which generates them when heated using a high voltage [92].

Conventional XRD

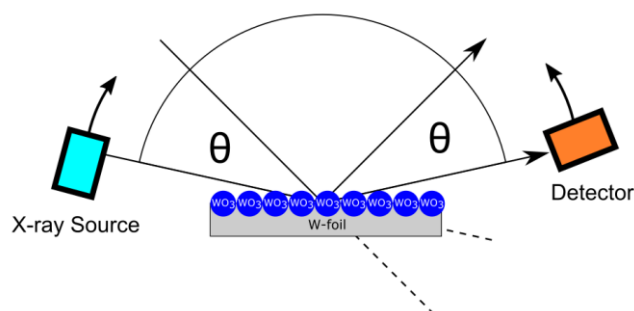


Figure 24 Schematic of Powder XRD operation. Adapted from [92]

Grazing incidence, or low angle, XRD was also employed in this work because of the nature of the thin oxide coatings on some of the samples. It uses the same operating principle but a different configuration between the X-ray source and detector: the X-ray source remains fixed at a predetermined angle of incidence and the detector moves around the sample to measure the intensities at different 2θ values as may be seen in Figure 25 [92]. Before the measurement is taken, the angle of incidence and stage height must be moved in the z-direction and rocked over minute angles in an automated process run by the apparatus to determine the angle at which best interrogates the surface oxide, not the substrate.

Grazing Incidence XRD

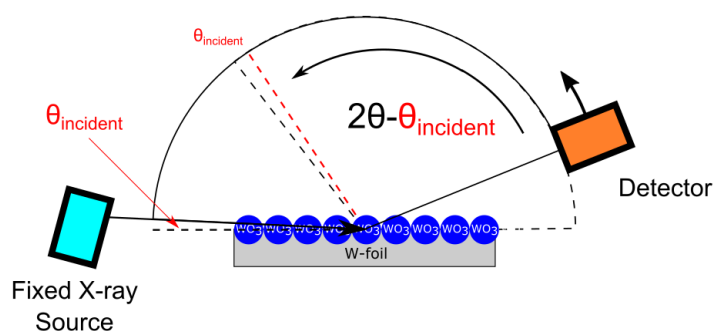


Figure 25 Schematic of grazing incidence XRD operation. Adapted from [93]

The data produced from these techniques is directly comparable given both are beam intensities recorded in terms of 2θ position.

3.3.2.2 XRD Experimental Procedure

Conventional XRD was completed at the Advanced Materials Research Laboratory (AMRL) using a BRUKER D8 ADVANCE X-Ray Diffractometer with the help of Dr Maider Olasolo. The grazing incidence measurements were completed on the author's behalf by Dr Alan Martin and Ms Rachel Feeney at the Continuous Manufacture and Crystallisation Materials Characterisation (CMAC) laboratory using a Bruker D8 Discover instrument.

All measurements used a Cu-K α source with a 0.6 mm anti-divergence slit and a 10.5 mm opening aperture. The key parameters used for different samples are summarised in Table 11.

Table 11 XRD experimental conditions

Samples	Sample Type	XRD Type	2 θ Range (degrees)	Scan Rate (Degrees/min)	Sample Preparation Method
P1, P2, P3, P4	Powder	Conventional	10-50	2	The powder was transferred into an aluminium sample holder and flattened with a spatula
W, S, S1, S2, S3, S4	Foil	Conventional	10-80	2	Placed directly upon stage
S, S7, S8, S9	Foil	Grazing Incidence	10-55	0.48	Taped with strong double-sided sticky tape upon an aluminium substrate to ensure the sample was perfectly flat (Figure 26)

An example of how the samples were prepared for grazing incidence XRD is shown in Figure 26 where double-sided sticky tape was used to ensure the substrate was perfectly flat. The beam orientation before the measurement is sensitive to bends in the substrate and this method was found to work well. Peaks from the aluminium mounting block were unavoidable and the tape was found to produce none.

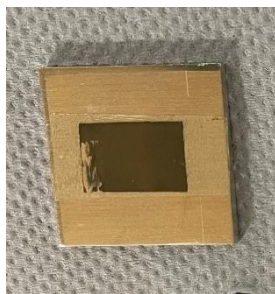


Figure 26 Image of foil sample taped to aluminium block for grazing incidence XRD

3.3.2.3 Analysis of XRD Spectra

Diffraction data was analysed using Diffrac.Eva software:

- (a) the background noise was removed, and the baseline corrected of the diffractogram.
- (b) the 'Search' function of the software which compares the recorded spectra with crystallographic database entries held in the ICDD Powder Diffraction File 2 database as well as the open-source COD database was then used for phase identification.
- (c) Each peak of the spectra was identified by limiting the search to only known elements i.e. tungsten, oxygen, capping agent chemicals, and aluminium for mount.
- (d) the recorded as well as the database data was outputted to text files for plotting in external software.

3.4 Electrochemical Characterisation Methods

3.4.1 Three Electrode Cell (Half-Cell) Procedure, Equipment and Conditions

All electrochemical data presented was recorded using the Biologic SP-300 potentiostat, shown in Figure 27, and the data itself was logged using Biologic's software EC-Lab.



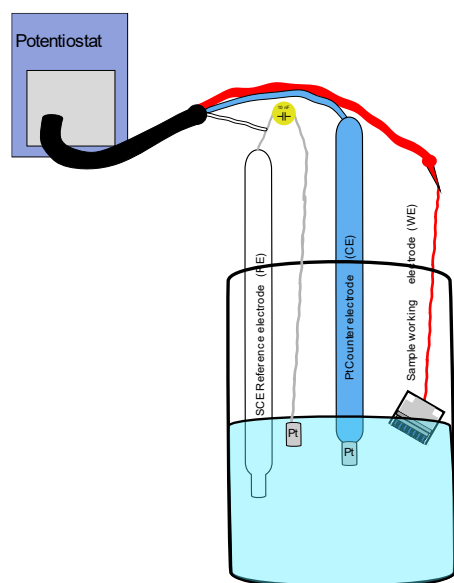
Figure 27 Biologic SP-300 Potentiostat used in all experimentation

A schematic and image of the three-electrode (or half) cell may be seen below on the left and right of Figure 28 respectively. The three-electrode set-up used the following electrodes and electrolyte:

- the as-synthesised sample as a working electrode (WE, red wire)
- a platinum counter electrode (CE, blue wire)
- a saturated calomel reference electrode (SCE, white wire)

- a 0.5 M H₂SO₄ electrolyte.

a)



b)



Figure 28 3-electrode cell configuration used in electrochemical characterisation a) Schematic b) Real set-up

A second platinum wire was also submerged and was connected to a 10 nF electrical capacitor in parallel with the reference [94]. This was necessary to avoid high-frequency artefacts which distort impedance spectra recorded for a highly capacitive working electrode [94]. This bypass capacitor allows the reference electrode to maintain a constant voltage reference while the reactance it experiences decreases with increasing frequency [94]. This artefact stems from the high impedance of the reference electrode and “stray capacitances” from the voltage amplifier within the potentiostat and reference electrode wire [95].

Once the cell was set up, a preset programme of electrochemical experiments was run sequentially. The exact experiments are discussed in the following sections of the methodology. When this program was finished, the sample was removed and processed to obtain a mass as per the destructive testing method discussed in section 3.4.2.3.

3.4.2 Working Electrode Development: Plug Electrode Holder Development & Procedure

All electrochemical characterisation was completed on the as-synthesised foils which, other than being rinsed, required no further processing. The samples are composed of only the 0.05 mm tungsten foil (Sigma Aldrich) as the current collector and the hydrothermal tungsten bronze deposit (M_xWO_3) as the active charge storage material.

The characterisation was intended to be completed with an existing “clip sample holder” which clipped to the top of the sample leaving the double-sided as-synthesised electrode suspended in the electrolyte. The clip electrode was a PTFE screw clip which had a platinum metal contact which could connect to the foil, these electrodes have a surface area of 2cm², and a schematic

may be seen on the right of Figure 29. However, the frequent delamination made characterisation impossible to replicate and it was necessary to develop something specific.

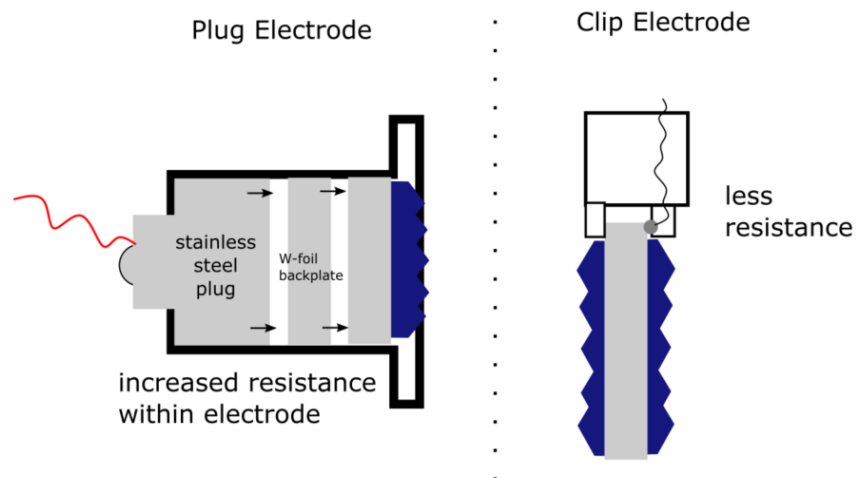


Figure 29 Schematic of plug (left) and clip (right) electrode

The “plug electrode,” left of Figure 29, was developed in conjunction with the department workshop technician Mr Liam Kirkwood. It was adapted from PVC 20mm Compression Glands (MK, purchased from B&Q) used in electrical cabling, a nylon mesh (Amazon), Viton® O-rings (Fisher Scientific) and stainless steel 316 back plugs made bespoke in the workshop.

The front of the PVC compression gland (Figure 30 A) was removed leaving a large circle front face with an opening and a threaded chamber at the back (Figure 30 B). The back screw of the compression gland could then be tightened to secure the sample. The scraped and polished sample was placed facedown upon the electrode surface (Figure 30 C) and then a pristine-tungsten backplate was specifically cut to fit behind these and placed on top of that to keep it in place (Figure 30 D).

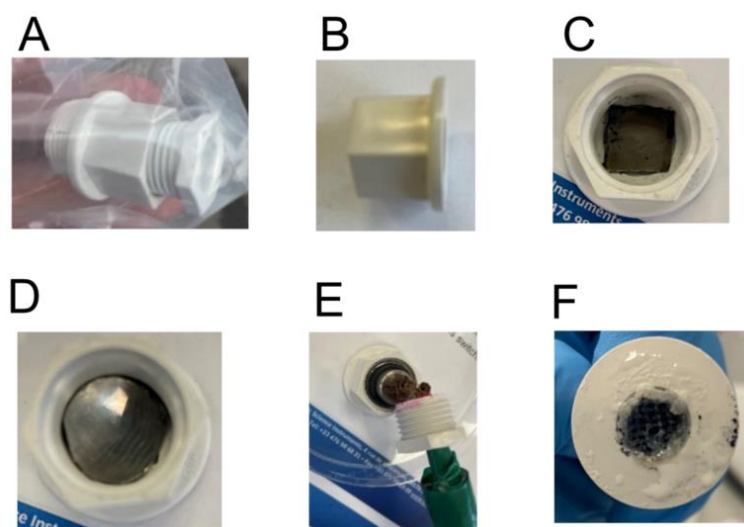


Figure 30 Development of plug electrode from shop bought compression gland (left), saw-cut compression gland to remove open end (centre) and stainless-steel plug sat inside altered part with connecting wire and O-rings to improve sealing and tightening.

A stainless-steel plug was machined in the department workshop by Mr Liam Kirkwood with a screw and washer to grip a wire (Figure 30 E). Viton O-rings were added to improve the sealing around the plug and ensure good conductivity throughout the electrode (Figure 30 – E).

There was a plastic casing and mesh, on which the as synthesised sample sat with one face polished to expose a tungsten metal contact (Figure 30 F). The nylon mesh was cut to the size of the opening and epoxied within the circle itself.

These electrodes have a working surface area of 1.038 cm^2 exposed ignoring the nylon mesh which blocks a small proportion of the overall area.

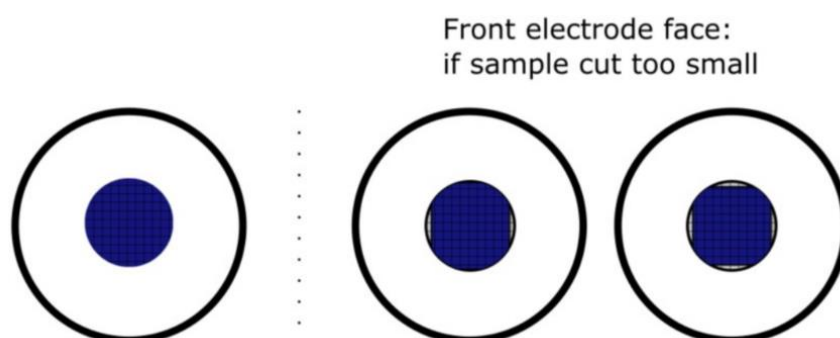


Figure 31 Schematic of plug electrode aperture

The schematic presented in Figure 31 displays the pitfalls of cutting the samples by hand. A small mistake may lead to exposed tungsten foil which will interact differently with the electrolyte. This was unavoidable given they are cut by eye and the reproducibility of the recorded data deemed this tolerable.

A full schematic of the various parts of the bespoke plug electrode is given in Figure 32.

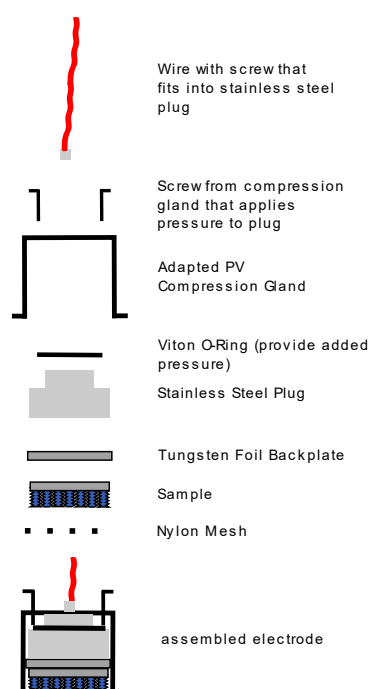


Figure 32 Schematic of different components of plug electrode

The nylon mesh provides enough physical compression for the oxide to stay adhered to the foil, and the adapted compression gland allows for sufficient pressure to be placed on the metal foil so that there is an electrical connection through the electrode. One limitation of this electrode is that the back has no insulation, which is to say the copper wire screwed into the back of the stainless-steel plug was exposed. This meant the full electrode could not be submerged in the electrolyte because this metal surface may then interact with the solution. The only method around this was to instead suspend the electrode as presented in the schematic of Figure 33.

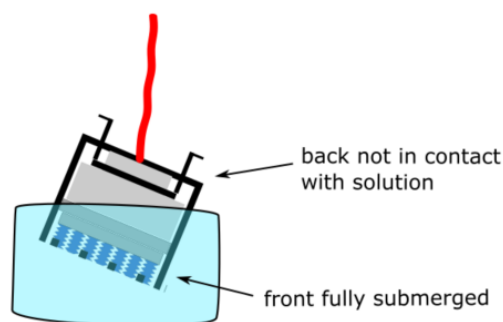


Figure 33 Schematic of plug electrode suspended in electrolyte to avoid short circuiting with the back current collector

3.4.2.1 Plug Electrode in comparison with Clip Electrode

The Seeded Substrate (S) oxide layer (no hydrothermal treatment) was very well adhered to the surface unlike many of the samples presented in this work. This sample allowed for a direct comparison between the clip and plug electrodes to be made by recording cyclic voltammograms using each. The recorded spectra are presented in Figure 34.

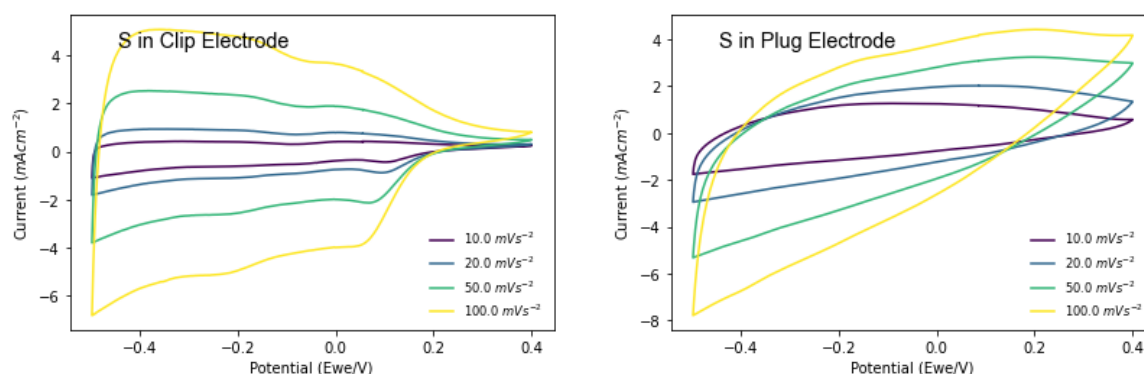


Figure 34 CV of Seeded Substrate, S in clip electrode (left) and plug electrode (right)

The first notable difference is that the clip electrode captures more detail than the plug electrode, and the plug electrode loses resolution. They share a similar shape however the plug loses evidence of redox peaks in both sweeps. This may be from a greater electrical resistance between contacts in the electrode. This electrical resistance manifests in the plug

electrode data as a skew that worsens with an increased scan rate. This is not present in the clip electrode. Finally, the current reaches a lower minimum as a result of the skew.

It is clear that the clip electrode would provide a more detailed CV than achieved with the plug, but the stability issues of the hexagonal layer necessitated the plug holder for characterisation. The impedance spectra modelled to fit the plug electrode sample (Figure 34 - right) may be seen in Appendix E, and the fitted ohmic resistance was found to be 4.7Ω . This value was used to create an IR-corrected CV displayed in Figure 35 which reduces the skew without removing it completely, steepening the back of the reverse anodic sweep.

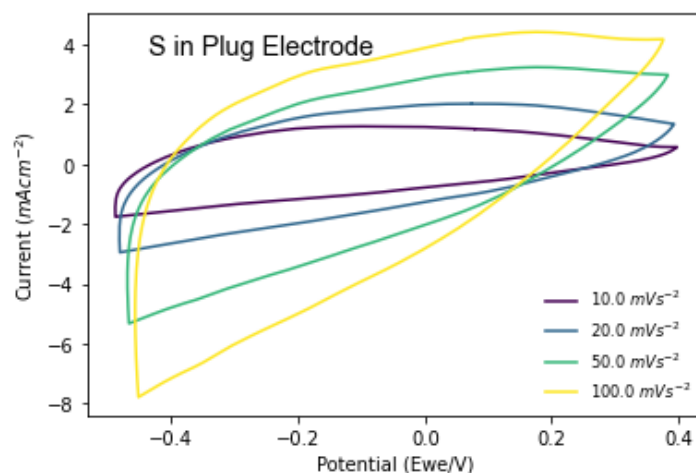


Figure 35 IR-Correction of Seeded Sample in Plug Electrode (Figure 34 – right)

The data in this report is not IR-corrected because the data was recorded without accounting for it at the time of measurement. Correcting post-measurement would shorten the potential window for each CV recorded and such a shifting potential window for each experiment would require far greater computation to estimate each sample's performance. It is an accepted limitation of the work that the plug electrode is not an ideal apparatus for precise electrochemical characterisation whilst still being functional enough to allow evaluation of the material's performance.

3.4.2.2 Delamination

The fragility of the electrodes makes them challenging to work with; care must be taken with each stage of cleaning, storing, and characterising them once synthesised. The oxide surface is prone to delaminating from the foil through a range of mechanisms including:

1. Drying out – when the oxide is removed from the reaction liquor it is hydrated and adhered to the surface. If the foil is left exposed to air, the oxide dries out and this results in oxide delaminating. To solve this, the sample was placed into a pH 2 acidic solution to store it ahead of testing.
2. Surface tension – when the electrode leaves or enters a solution the surface tension is often sufficient to cause delamination. To get around this whenever a sample was removed from a solution a dropper was used to carefully remove the liquid; conversely,

if it was being placed in a beaker for storage it was placed in an empty beaker and the liquid was dropped in using a plastic dropper.

3. Passing current – when electrochemical characterisation occurs, the test will cause the intercalation to and from the oxide. Though the oxide will not change phase, this action has been enough to prompt delamination, presumably due to a lattice volume change upon intercalation/deintercalation. It was noted that the electrodes maintained their integrity for longer when passing current in the solution they were made, pH 2, and when they were not allowed to dry out. It was decided to evaluate the electrodes as synthesised, i.e. wet, to minimise this. However, it was also necessary to characterise the electrodes in the bespoke electrode holder.

3.4.2.3 *Destructive Testing*

Due to the fragility of the electrodes outlined in section 3.4.2.2 and the decision to test the electrodes wet, it was impossible to measure an active mass of WO_3 prior to characterisation. It would not have been possible due to the uncertainty in the amount of liquid water retained on the foils at the time at which they were weighed, removing the possibility of standardisation. The mass of the active material is critical to characterising the performance of the electrode, however, and so measuring a dry, comparable mass was necessary to compare results with other reported electrodes.

Considering this, the method of characterising is considered 'destructive' in that a sample was made, characterised, and then dried out in an oven to remove any water before weighing. This caused the oxide to delaminate from the substrate rendering it unusable again. The mass of the substrate was measured before synthesis and subtracted from the as-synthesised dry mass.

A further drawback of this method is that when completing galvanostatic measurements it was impossible to set a current density normalised by active mass i.e. 1 A/g, 2 A/g etc. Instead, a set range of currents was used, and the actual current densities were evaluated post-characterisation. This makes direct comparison of samples and those reported in literature challenging but enables trends to be observed.

The most frustrating aspect of this method is of course that samples are not retained. They cannot be characterised again after an ageing period or from completing post-treatments, so multiple repeats were therefore conducted.

3.4.3 *Electrode Preparation*

3.4.3.1 *Binder-Free Foil Electrodes*

These electrodes were characterised as synthesised from the pre-described methods. However, some steps were required to prepare the sample for the electrode holder:

1. The foil was gently rinsed often with a dropping pipette.

2. The 10 mm x 15 mm coupon was then cut down to 10 mm x 10 mm so that it would fit into the plug electrode holder.
3. One face of the oxide was removed to expose the tungsten metal beneath to improve conduction with the back plug.
 - a. In most cases the oxide was so loosely adhered a cotton bud could remove the oxide before a gentle sanding was completed to polish the surface and remove any non-visible oxide.
 - b. The seeded substrate, as well as S8 and S9 required rough (1200 grit) and then finer (4000 grit) intensive sanding to remove the oxide. The sandpaper was loosely folded to create a round, almost flat sandpaper surface. The foil was held between the thumb and index finger from diagonal corners and carefully drawn up and down to remove the oxide from the back side.
4. The prepared sample was lowered into the plug electrode using tweezers so that the active face pointed out the front opening.
5. A tungsten foil (0.05 mm) circular backplane was then placed over this, and the plug electrode was assembled as outlined in section 3.4.1

3.4.3.2 Powder-based Electrodes

The powder-based electrodes were prepared by forming an ink from the hexagonal-WO₃ powder and a mixture of solvent. Once prepared, a given volume was dropped upon a tungsten substrate. The ink was composed of:

- The washed & filtered M_xWO₃ powder
- 99.5% 1-propanol from ThermoFischer Scientific (CAS: 71-23-8)
- Deionised water
- Nafion solution (5 wt% in mixed alcohols) from Sigma Aldrich

The ink was prepared in a small plastic reaction vial and sonicated using a Sonics VC5050 Ultrasonic Processor. Firstly 0.01 g of powder was accurately measured into the vial. Using micropipettes, 33.33 μL of deionised water then 133.33 μL of 1-propanol and finally 33.33 μL of 5 wt% Nafion solution were added to the reaction vial (1 part water: 4 parts 1-propanol : 1-part Nafion 5wt%). The vial was held in a small plastic vice to ensure it was vertical and the mixture was ultrasonically agitated using the fine-tip probe. A 10-minute set programme was used which sonicated the mixture using a pulse of 5 seconds at the max amplitude (40% on the instrument) followed by 1 second being off. The mixture transitioned from two distinct phases into one coherent ink as may be seen in before (left image) and post-sonication (right) images presented in Figure 36. The resulting ink was a thin, creamy consistency which held the colour of the tungsten oxide powder.

Once the sonication was completed, 60 μL of the ink was carefully drawn with a micropipette and was dropped carefully onto a pre-weighed, degreased pristine tungsten metal coupon cut to 10 mm x 10 mm. One drop was allowed to spread before another was added to prevent it from spilling over the edge.

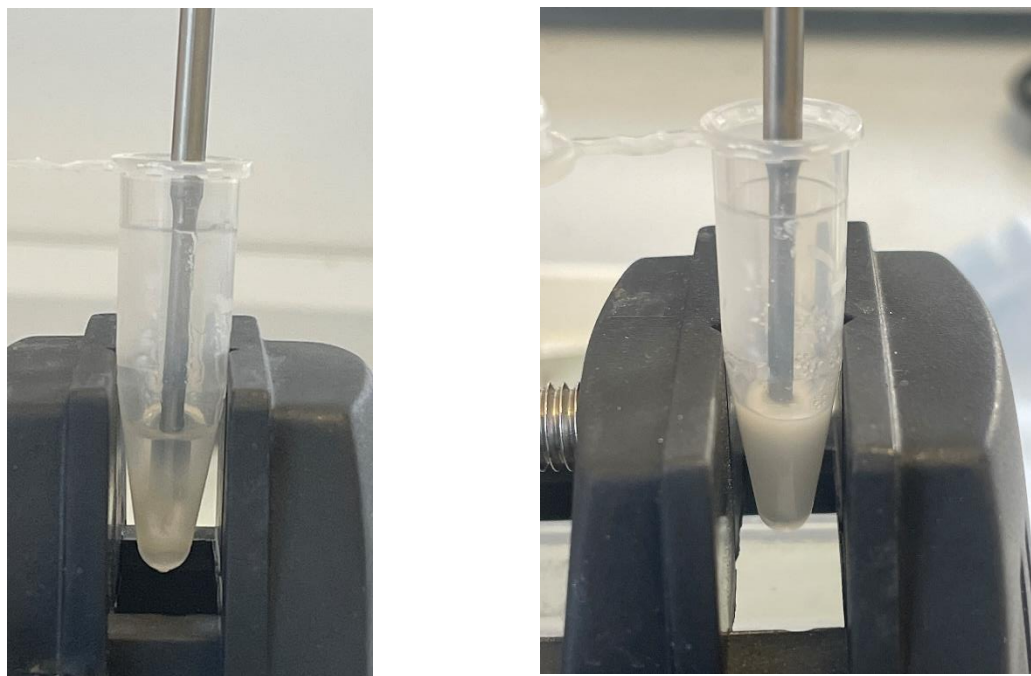


Figure 36 Images of typical ink preparation. The left image shows before sonication and the right image shows post sonication.

The ink now on the surface of the tungsten foil was allowed to dry in ambient air for around 1 hour. An image of the freshly coated ink and the dried ink on the tungsten substrate may be seen in Figure 37. What may be seen is that there is adequate coverage in the centre of the electrode, and the edges and corners of the tungsten substrate are still visible.



Figure 37 Image of freshly dropped “wet” ink coating (left) and air dried “dry” ink coating (right)

There is an unavoidable “coffee-stain” effect which occurs from the spreading of the ink across the substrate, but the coverage was deemed acceptable. Once dried, the sample was weighed to measure the active mass coated upon the foil. From the proportions of solvent to tungsten oxide used in the prepared ink an active material mass was evaluated. The calculation, with stated assumptions, may be seen in Appendix C.

Once this was calculated, the potentiostat programme was adjusted to account for the new mass and the sample was then tested immediately. It is worth noting that these foils were stable enough to be stored in a dry environment until characterisation, the limits of this were never investigated.

3.4.4 Cyclic Voltammetry (CV)

3.4.4.1 Operating Principle

This potentiodynamic experiment changes the potential of the working electrode in relation to the reference electrode at a chosen constant rate (a sweep rate or scan rate) between two fixed limiting potentials and measures the current evolved. A schematic is provided in Figure 38 displaying the change in potential and the output data.

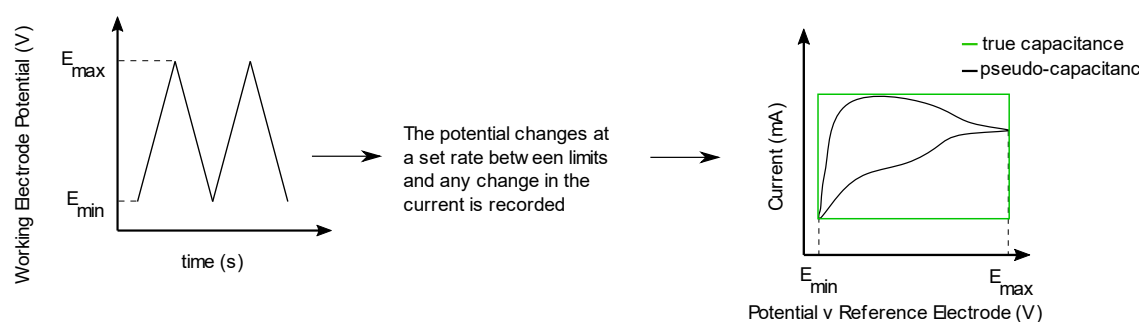


Figure 38 Theory of potentiodynamic experiment – Cyclic Voltammetry

The left of Figure 38 shows how the potential changes linearly with time between two potential limits. The potentiostat is a digital device and so in reality this change in potential is a sequential curve of incremental steps. Whether the triangle displayed is a good assumption is dictated by the sweep rate used which determines the size of each step change.

The right of Figure 38 shows two different sets of CV data on the same graph, a green line for a true capacitor and a black line showing a hypothetical intercalation pseudocapacitance electrode. Both of these graphs show that as the potential changes along the x-axis, a current may develop. The mechanism evolving the current in each of these cases is different and requires analysis and understanding to identify the cause. In the case of the black intercalation line a non-zero line indicates that a charge transfer reaction is occurring at that potential; where no or little current develops it is clear no charge transfer is occurring.

The rate of change in potential used in CV experiments affects the driving force for processes in the system: a high rate rapidly polarises the electrode; a slow rate slowly polarises the electrode. As discussed in section 1.3, ions in the electrolyte have different properties, including different charge and rates of diffusion, and interact differently with the electrodes in the system. It can therefore be expected they will react quite differently depending on the rate of polarisation of the electrode. This means that different processes may occur depending upon the rate used in the CV experiment. This results in a different response in the recorded

CV data for different sweep rates used and the observed development of the cyclic voltammograms with sweep rate is useful in understanding the working electrode kinetics. With respect to this, 6 scan rates were used: 1, 5, 10, 20, 50 and 100 mVs⁻¹ between potential limits of -0.5 V and +0.4 V vs SCE. Three cycles were recorded at each sweep rate to examine the consistency at each. The initial cycle after increasing the sweep rate may show a dramatic increase in current because of the initial instantaneous step change in potential and so was not chosen for plotting and analysis. Instead, the third (final) cycle of each CV experiment was used as this was taken to be the most equilibrated of the cycles taken; it was most adjusted to the electrolyte conditions and sweep rate used.

3.4.4.2 Calculating a Capacity/Capacitance from Cyclic Voltammetry

The area of a perfectly reversible cyclic voltammogram is directly proportional to the charge stored by the electrode in a three-electrode half-cell configuration:

$$\text{Charge Stored} \propto \text{Area of Cyclic Voltammogram}$$

This relationship may be used to evaluate a capacity by dividing the area by the sweep rate used in the experiment using 26:

$$Q = \int_{E_{min}}^{E_{max}} i(E) \partial V v^{-1} \quad 26$$

Where Q is the charge stored, or capacity, in coulombs, i (A) is the current at a given potential E (V), v is the sweep rate in (Vs⁻¹) and m is the mass of the active charge storage material. This value may then be normalised to provide a specific capacity (charge per unit mass) or an areal capacity (charge per unit area) so that it may be compared with similar materials.

Capacitance, C, measured in farads is defined as the charge passed, Q, across a potential difference, E and as defined in equation 1. Substituting Q from equation 26 into equation 1 allows for a capacitance to be calculated from a cyclic voltammogram:

$$C = \frac{\int_{E_{min}}^{E_{max}} I(E) \partial V}{v \Delta E} \quad 27$$

Where ΔE is the potential window in volts, the top line is the charge in coulombs, v is the experimental sweep rate used in V/s.

The capacitance of a two-electrode, symmetrical cell may be approximated as two capacitors in series, whereby charging occurs at one interface whilst discharging simultaneously occurs at the second interface. The total capacitance of two capacitors in series is the sum of their reciprocal individual capacities ($C_{total} = 1/C_1 + 1/C_2$) which changes equation 27 to 28 [10]:

$$C_{\text{symmetrical cell}} = \frac{\int_{E_{\text{min}}}^{E_{\text{max}}} I(E) \partial V}{v \Delta E} \times \frac{1}{2} \quad 28$$

It should be clearly stated that in equations 27 and 28, the nomenclature uses ΔE which is the potential window ($\Delta E = E_{\text{max}} - E_{\text{min}}$) which reinforces the idea that pseudo capacitance is present over a limited potential range, after which non-pseudocapacitive charge transfer may occur.

3.4.4.3 Estimating capacitive contribution to charge storage from CV data

As discussed in section 1.3, pseudocapacitance stems from monolayer adsorption of ions onto a high surface area electrode; or from fast faradaic reactions that occur over many, similar potentials creating an apparent proportionality between potential and charge stored over that particular voltage window [2], [7], [11], [20], [96], [97]. This faradaic reaction can be differentiated into redox pseudocapacitance occurring at local surface sites and intercalation pseudocapacitance where ions intercalate, a diffusion-type process, into the delocalised bulk structure of a redox-active material [96]. It was also noted that these faradaic reactions are not inherently pseudocapacitive; they are contingent upon the electrode/electrolyte couple and the reaction kinetics. It is therefore of interest to investigate what contribution towards the total stored charge of a studied electrode is pseudocapacitively stored. A method of CV analysis was proposed by Dunn et al to quantify the pseudocapacitive contribution [98]. The base assumption is that stored or discharged current from an electrode is a summation of faradaic and capacitive processes which may be mathematically separated [2], [98], [99]. The Dunn method states that faradaic reactions and capacitive processes are scan-rate dependent but are described by distinct functions which can be analytically separated from a CV. The Dunn method models intercalation as a diffusion-limited process where the rate of intercalation, measured experimentally as current, has a square root dependency with respect to time as can be shown through Fick's second law [13]. The current evolved from a capacitive process on the other hand, governed by equation 1, and has a linear dependency with respect to time. These assumptions can be written algebraically as the total current from a CV experiment being equal to the summation of capacitive currents and faradaic intercalation [2], [99], [100]:

$$i(V) = k_1 v + k_2 v^{1/2} \quad 29$$

Where $i(V)$ is the current at a given potential, k_1 is a linear constant, v the experimental sweep rate and k_2 the root square constant. This expression can be solved analytically, by dividing through by $v^{1/2}$ on both sides to deliver a straight-line formula:

$$\frac{i(V)}{v^{1/2}} = k_1 v^{1/2} + k_2 \quad 30$$

If several CV experiments are completed across a range of sweep rates, then the above expression can be solved as a set of simultaneous equations. A final assumption that is made is that capacitive processes above scan rates of 20 mVs^{-1} are of a magnitude that devalues

this analysis and so only sweep rates of 1 to 20 mVs⁻¹ are used. The simultaneous equations for a given potential of -0.3V at these scan rates are shown below by way of illustration:

$$\frac{i(-0.3V)}{1^{1/2}} = k_1 1^{1/2} + k_2 \quad (1 \text{ mV/s})$$

$$\frac{i(-0.3V)}{5^{1/2}} = k_1 5^{1/2} + k_2 \quad (5 \text{ mV/s})$$

$$\frac{i(-0.3V)}{10^{1/2}} = k_1 10^{1/2} + k_2 \quad (10 \text{ mV/s})$$

$$\frac{i(-0.3V)}{20^{1/2}} = k_1 20^{1/2} + k_2 \quad (20 \text{ mV/s})$$

This can be graphed on a plot of $i/v^{1/2}$ vs $v^{1/2}$ to calculate k_1 (gradient) and k_2 (intercept) for any given potential V . A table may then be produced of values of k_1 (gradient) and k_2 (intercept) at each distinct potential taken from the CV datasets. The more points computed, the greater the resolution of any plot produced. The full analysis is completed at potential steps of $dE = 0.001 \text{ V}$ i.e., around 900 data points for each cathodic and anodic sweep (sweeping over a range of 0.9 V). In Figure 39 increments of 0.1V have been plotted to illustrate how this works, any more than this and the graph becomes looking very cluttered.

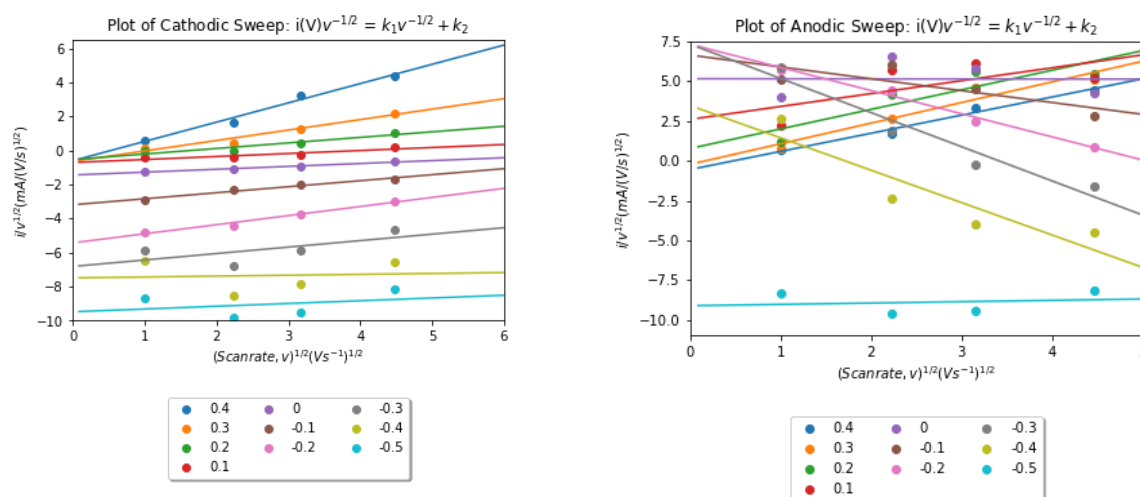


Figure 39 Calculated K_1 and K_2 Plotted

Through this method values of k_1 and k_2 are now determined for each potential and plugging these values back into the component parts of equation 29 a “capacitive” component (k_1v) and a “faradaic” component ($k_2v^{1/2}$) of the current may be plotted. The established method of visualising the results of this data is not to plot the calculated component current but rather to present it as a percentage of the real current. One does this through manipulating equation 29 through the following steps:

	$\frac{i}{k_1 v + k_2 v^{1/2}} = \frac{k_1 v}{k_1 v + k_2 v^{1/2}} + \frac{k_2 v^{1/2}}{k_1 v + k_2 v^{1/2}}$	29.1
--	---	------

	$1 = \frac{k_1 v}{k_1 v + k_2 v^{\frac{1}{2}}} + \frac{k_2 v^{\frac{1}{2}}}{k_1 v + k_2 v^{\frac{1}{2}}}$	29.2
	$i(V) = \frac{k_1 v}{k_1 v + k_2 v^{\frac{1}{2}}} \cdot i(V) + \frac{k_2 v^{\frac{1}{2}}}{k_1 v + k_2 v^{\frac{1}{2}}} \cdot i(V)$	29.3
	$i(V) = \text{Capacitive}\% \cdot i(V) + \text{Faradaic}\% \cdot i(V)$	29.4

It is then possible to plot the percentage influence of these components on top of the real data of the CV. These modelled curves often need adaptations to present the data, particularly at the edges of the CV. Figure 40 displays the same example of Dunn method modelling before and after editing the data for the boundaries. If the real recorded data were more rectangular then this would be unnecessary as any calculated-percentage current would likely fall within the real data. However, the pointed shape of these CVs means that sometimes the modelled current may breach the boundary line of the real data. The key consequence of this is that in curtailing the modelled data the areas of these modelled regions changes, removing modelled values at the endpoints. For instance, looking at the left graph of Figure 40, the modelled capacitive region has a negative peak around -0.45 V whilst the diffusion-controlled line rises out with the real plot area. The modelling is saying that the tip is capacitive, but this is not what is shown on the post-edited graph where automated cutting of the data relies on the plot boundary, so this region is misrepresented.

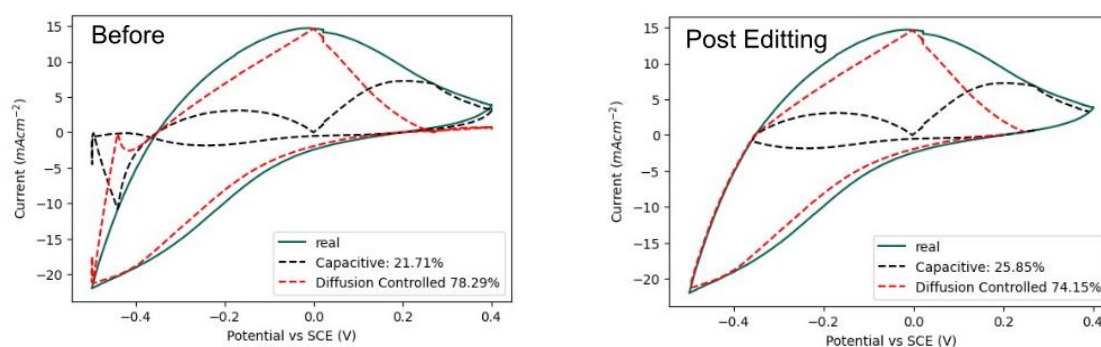


Figure 40 Dunn Method Modelled data before and after editing boundaries

This is a known issue with the Dunn method where CVs which are not suitably rectangular are less suited to this analysis [101]. Whilst, indeed, the calculated values ascribed to each of these plots may not be meaningful themselves, this analysis does allow a visual representation of capacitive and diffusion-controlled regions and for trends to be recognised across CVs [101].

3.4.5 Galvanostatic Experimentation - Galvanostatic Cycling (GCD)

3.4.5.1 Operating Principle of GCD

Any Galvanostatic technique supplies a controlled current to the working electrode, and the reference electrode measures the resulting changes in the electrode potential. In galvanostatic cycling a constant positive current is applied, followed by a negative current (or vice versa), switching once a set limiting potential has been reached as visualised in Figure 41. This may be repeated over any number of cycles.

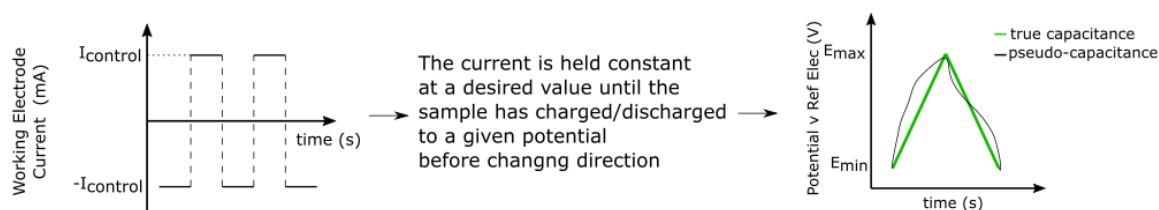


Figure 41 Theory of Galvanostatic Charge-Discharge Cycling Experiment

In this investigation, a negative current is deemed to be the charging step while a positive current discharged the working electrode, given tungsten oxide's half-cell, equation 18. The charge passed by this electrode may then be calculated from the following equation [96]:

$$Q_{\text{capacity}} = \int_{t_{\min}}^{t_{\max}} i(t) \partial t = \sum_{t_{\min}}^{t_{\max}} dQ (= Idt) \quad 31$$

where t is the charge or discharge time in seconds, the current is variable as a function of time, I is a galvanostatic set current and Q is the charge passed. The specific charge or discharge capacity in (Cg^{-1}) or areal capacity (Ccm^{-2}) for any half-cell may be calculated from:

$$Q_{\text{specific capacity}} = Im^{-1} \int_{t_{\min}}^{t_{\max}} \partial t \text{ or } Q_{\text{areal capacity}} = IA^{-1} \int_{t_{\min}}^{t_{\max}} \partial t \quad 32$$

where m is the mass of active material and A is the area of electrode used in the experiment. Similar as in calculations from cyclic voltammetry this value may be converted to a capacitance, where appropriate. By the definition of capacitance, the rate of change of charge must be proportional to change in potential as described by the green line in Figure 41. To satisfy this a linear charging or discharging curve must be seen in galvanostatic cycling. When this occurs, a capacitance may be calculated by substituting this equation into the capacitance equation [96]:

$$C = \frac{I m^{-1} \Delta t}{\Delta E} \quad 33$$

Where I is current, m is the mass of the active material, Δt is the linear change in time and ΔE is the change of potential. It is critical to notice that the change in potential is linear with respect to time. This equation may not be used to calculate a capacitance with a non-linear discharge curve [10].

The energy stored by an electrode may be evaluated from a GCD curve and also from the following equation [99]:

$$W = i \int_{V_{min}}^{V_{max}} V(t) \partial t \quad 34$$

Where W is the electrode's energy from the charge or discharge cycle, the voltage is V , and the time of charge or discharge is t . An average power, P , may then be evaluated by dividing the Energy, W , by the time of charge or discharge, t :

$$P = \frac{W}{t_{charge/discharge}} \quad 35$$

3.4.5.2 Linearity Analysis of GCD

As discussed, when presenting 33, a capacitance may only be calculated where the GCD curve is linear, or approximately linear. It was deemed important to have some method of quantifying how linear GCD data was and therefore indicate whether a capacity or a capacitance should be reported. How linear a GCD curve is has been discussed by some respected authors in good detail [10], [11], [97], [99]. However, there is no established method of quantifying the linearity of a pseudocapacitance curve in these works. This is mathematically possible, and the concept of quantifying linearity has been applied to electrochemical systems before [102].

Several approaches were taken to quantify the linearity of the GCD curves which either took the isolated discharge curve and fitted a straight line between the max and min position or took the full charge-discharge cycle and overlaid a triangle formed between the two minima and maximum state of charge.

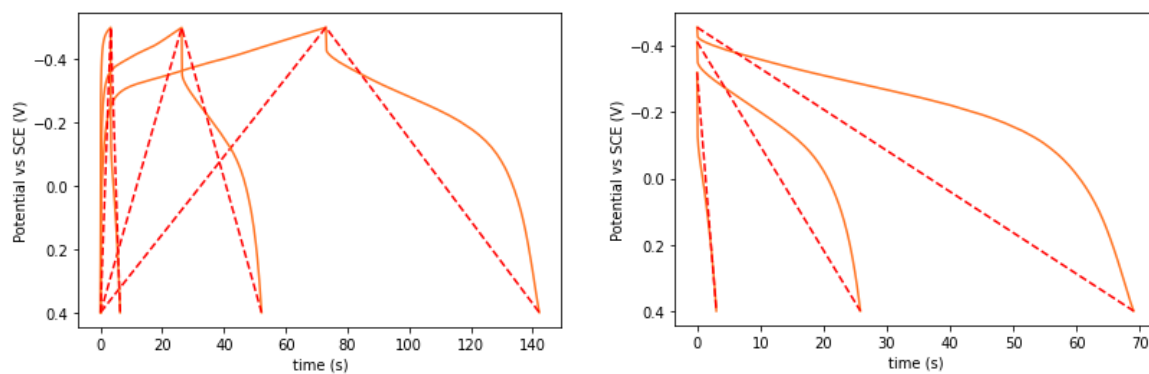


Figure 42 Example GCD data with modelled straight lines overlaid

Two more complex analyses were also completed. The first reduced the potential window of each experiment by trimming the data to a smaller potential window and refitting the straight lines to gauge the suitability of the potential window. An example of this is shown on the left of Figure 43. The other instead approximated the modelled fitting as two lines, not a single line using a breakpoint mathematical method from the Python library “PiecewiseLinFit”, a function which identifies the optimal breakpoint position to approximate real data with a series of straight lines [103] and an example of this may be seen in right of Figure 43.

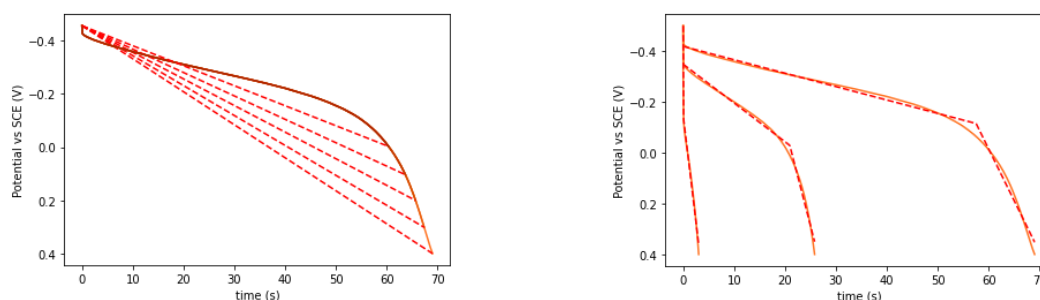


Figure 43 Example of further GCD analysis: The left figure shows edited data whereby the potential window may be reduced, and the straight line refitted; and the right shows the breakpoint analysis where instead the data is fitted as two lines not one.

The linearity analysis employed the statistical comparison method root mean square error (RMSE) to compare observed values with modelled values [104]. RMSE takes any data set and evaluates a single value to quantify the linearity through [104]:

- Evaluating the residual error between observed and modelled values
- Squaring the residual errors to deliver a positive value.
- Determining a mean average value of errors across the dataset
- And finally square rooting this value to produce a single value which describes the similarities of the two lines on average in the same unit of the compared data.
- This means that the smaller the RMSE the closer the match between the modelled and observed data.

3.4.6 Electrochemical Impedance Spectroscopy (EIS)

3.4.6.1 Operating Principle

Impedance is a measure of the opposition that a circuit presents to the flow of alternating current (AC). It is a complex quantity that includes both resistance and reactance: the resistance represents the opposition of the flow of current due to the resistive elements like resistors; the reactance represents the opposition to the flow of alternating current from the circuit's reactive elements such as capacitors and inductors. Electrochemical impedance describes the same opposition to the flow of alternating current signals within an electrochemical system. As discussed in 1.3 Electrochemical Energy Storage Fundamentals, an electrochemical circuit features an electrolyte, an interface and reactions which may all be modelled as if they were an electrical circuit through electrochemical impedance spectroscopy.

Electrochemical impedance spectroscopy in principle is a technique that applies a small periodic stimulation signal and measures the response signal of an electrochemical system over a range of sequential frequencies. This is completed over multiple cycles with the view to achieving a steady state response. In this work, potentiostatic impedance spectroscopy (PEIS) is what is specifically used, and this technique applies a small stimulation potential signal of different frequencies and measures the corresponding current signal response [105]. The input voltage signal is sent as a function of frequency, and the subsequent current signal is measured as a function of frequency. The impedance, therefore, analogous to electrical resistance in a DC circuit, is the quotient of voltage as a function of frequency over current as a function of frequency, algebraically expressed as [106]:

$$Z(\omega) = \frac{V(\omega)}{I(\omega)} \quad 36$$

Where $Z(\omega)$ is the impedance, $V(\omega)$ the voltage and $I(\omega)$ the current all expressed as a function of frequency. The impedance of the measured current signal is described mathematically as having a real and complex component: a real component owing to the ohmic resistance present in the studied system which is not a function of frequency; and a complex part from the system's "reactance" which describes the storage or release of energy from the system by processes, including inductors and capacitors, which are dependent upon the frequency [105], [107]. The reactance causes a shift in the phase of the measured current signal and must be represented mathematically as imaginary numbers [105].

The experiment uses a range of frequencies (10 mHz – 100 kHz) and because electrochemical processes are sensitive to this frequency, different processes dominate different ends of this range [105]. Each electrochemical process within the electrode may be modelled as a circuit element and a full circuit system produced to characterise the observed behaviour as a whole [105], [106], [108]. The following circuit elements were employed to find the most suitable

circuit model for the electrodes characterised by impedance spectroscopy. Common variables used throughout table 12 are j the imaginary unit equal to the square root of negative one and the angular frequency denoted as omega, ω . Other components are identified in the description provided.

Table 12 *Circuit Elements considered for circuit fitting* [106], [108], [109], [110]

Circuit Element	Impedance Equation	Description
Resistor	$Z = R$	Where Z is the impedance in Ω and R is resistance in Ω . A resistor's impedance is independent of frequency, linearly contributing to a potential drop depending on the resistance value. The complex component of a resistor is equal to zero.
Capacitor	$Z = \frac{1}{j\omega C}$	Where Z is impedance measured in Ω , j is the imaginary unit, ω is the angular frequency in s^{-1} and C is the capacitance in Farads. A capacitor is a reactive element and therefore is dependent upon the frequency. The impedance has an inverse relationship with the capacitance of the capacitor.
Constant Phase Element (CPE)	$Z = \frac{1}{Q(j\omega)^\alpha}$	Where Z is impedance in Ohms, Q is a constant in $\Omega \cdot s^\alpha$, j is the imaginary unit and ω the angular frequency in s^{-1} . A constant phase element describes a non-ideal capacitor where the exponent alpha characterises the phase shift of the response, quantifying how ideal the capacitor is [106]. If alpha is 1 then the CPE acts as a regular capacitor; if it is 0 then the element becomes a constant value acting as a pure resistor. Q is a constant that allows flexibility in representing the non-ideal capacitor behaviour. The name constant phase describes how, depending on the value of alpha, the resultant complex component is generated with a constant phase relationship.

Warburg Element	$Z = \sigma \frac{(1 - j)}{\sqrt{\omega}}$	Where σ is the Warburg Coefficient in $\Omega \cdot s^{-1/2}$, j is the imaginary unit and ω is the angular frequency in inverse seconds. At low frequencies, diffusion is the dominant process and the Warburg impedance dominates. At high frequencies, diffusion is more rapid and the impedance decreases.
-----------------	--	---

3.4.6.2 Measurement & Analysis of data

The impedance data was measured at the beginning of a preset programme of electrochemical characterisation techniques and recorded at the open circuit voltage. The full set of conditions are displayed in Table 13.

Table 13 Values used in Impedance Spectroscopy measurement.

Low Frequency	High Frequency	Set Potential (V)	Points per Decade
10 mHz	100 kHz	Open Circuit Voltage (OCV)	6

The impedance data was analysed using the open-source Python package Impedance.py which allows Bode, Nyquist and circuit fitting within the Python environment [108]. This package uses a preprocessing function to fit Nyquist data whereby all values below the x-axis are removed. A Python script was developed to accept EC-Lab text files (.mpt) to read these in and output the circuit fitting with 5 inputted circuit diagrams using the impedance.py package.

A Nyquist displays the response signal of the current in the frequency domain, plotting the real (ohmic) part of the response on the x-axis, $Re(Z)$ and the imaginary, complex part on an inverted y-axis, $-Im(Z)$. The intercepts of the x-axis correspond to ohmic resistances experienced in the electrode. All other data at negative or positive values of $Im(Z)$ map reactive processes which can be positive $Im(Z)$ values from inductance; and negative $-Im(Z)$ values from capacitance. The y-axis is inverted so that capacitive elements are plotted in a positive direction to aid interpretation. The processes occurring on a Nyquist should be considered to be occurring concurrently.

3.4.7 Computational Processing & Analysis (Python)

Python is a high-level, interpreted, and general-purpose programming language that was used extensively to process, plot and analyse the data presented in this work. The electrochemical characterisation completed by the potentiostat was outputted as EC-Lab text files (.mpt) and Python scripts were self-developed to process these using Spyder from the Anaconda Distribution. Most packages used were within that distribution with the key exception of Impedance.py which was used extensively for the analysis of the impedance spectra.

4 Electrochemical Characterisation of W-WO₃ electrodes

4.1 Introduction

This chapter sees W-WO₃ electrodes prepared in 8 different conditions electrochemically characterised using cyclic voltammetry, galvanostatic charge-discharge cycling and impedance spectroscopy. The discussion may from time to time refer to the same electrode's physical characterisation in chapter 5 and the intercalation mechanism previously described in section 2.2.2 Proton Intercalation in WO₃.

The samples are discussed in relation to the reaction conditions they were synthesised in according to the following table where the letter denotes the substrate type, and the number refers to the capping agent used. A colour coding is used throughout to indicate what sample is being discussed. Each capping agent has a colour (blue, orange, purple, green) with the tone pale for W-substrate samples and darker if S-substrate is used.

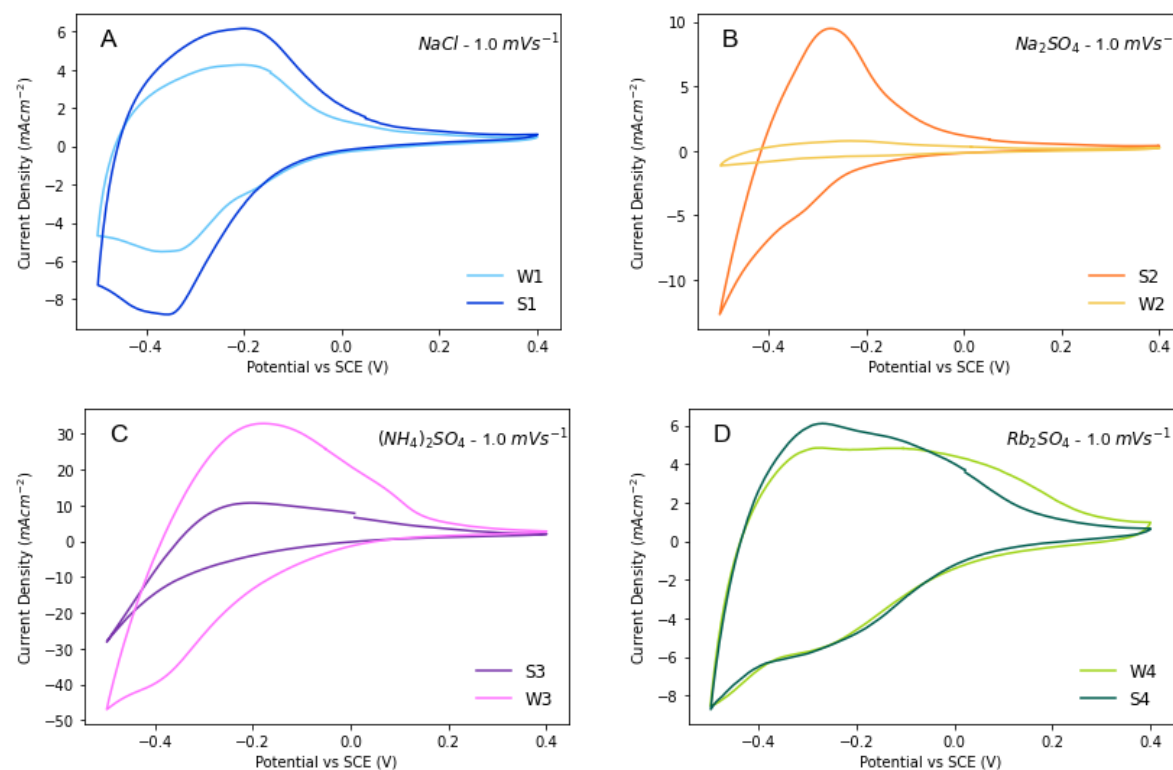
Table 14 Reaction Parameters, sample names and colour coding used for hexagonal W-WO₃ binder free samples.

Pristine Tungsten Foil Substrate	W		Seeded Substrate (Tungstite surface)	S	
Tungsten Foil Substrates (W)			Tungstite Seeded Substrates (S)		
Sample	Capping Agent	Colour	Sample	Capping Agent	Colour
W1	NaCl		S1	NaCl	
W2	Na ₂ SO ₄		S2	Na ₂ SO ₄	
W3	(NH ₄) ₂ SO ₄		S3	(NH ₄) ₂ SO ₄	
W4	Rb ₂ SO ₄		S4	Rb ₂ SO ₄	

4.2 Potentiodynamic Characterisation

The Cyclic Voltammetry (CV) recorded at the slowest scan rate used (1 mVs⁻¹) for each sample is displayed in Figure 44. These figures allow for comparison to be made between the capping agent and substrates used. At this low scan rate, 1 mVs⁻¹, all the CVs are a shape consistent with highly reversible, intercalation processes. The sodium chloride and rubidium sulphate-directed samples (Figure 44 A and D) show what may be described as pseudocapacitive shapes [11]. As the current in all samples tapers to around zero past 0.2V vs SCE, it may be expected that a shortening of the potential window to 0.2 V vs SCE (or

lower) these samples would show a more rectangular-shaped CV response like the seeded substrate in Figure 34.



Sample	W1	S1	W2	S2	W3	S3	W4	S4
Capacity (mAh/cm ²)	0.89	1.28	0.15	0.98	5.72	1.70	1.45	1.41

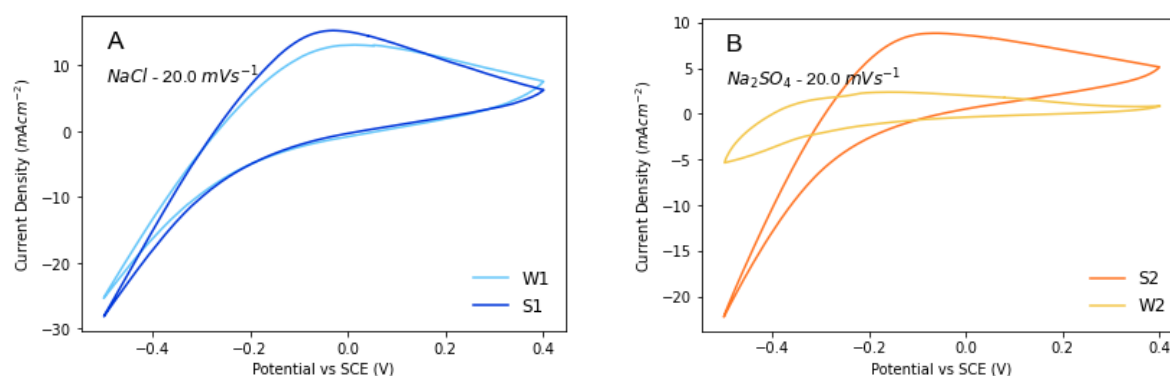
Figure 44 Cyclic Voltammograms of all 8 samples at a sweep rate of 1 mVs⁻¹ a) NaCl samples b) Na₂SO₄ c) Rb₂SO₄ and d) (NH₄)₂SO₄ and tabulated below is the average stored charge, capacity measured in mA/cm², across the recorded data set

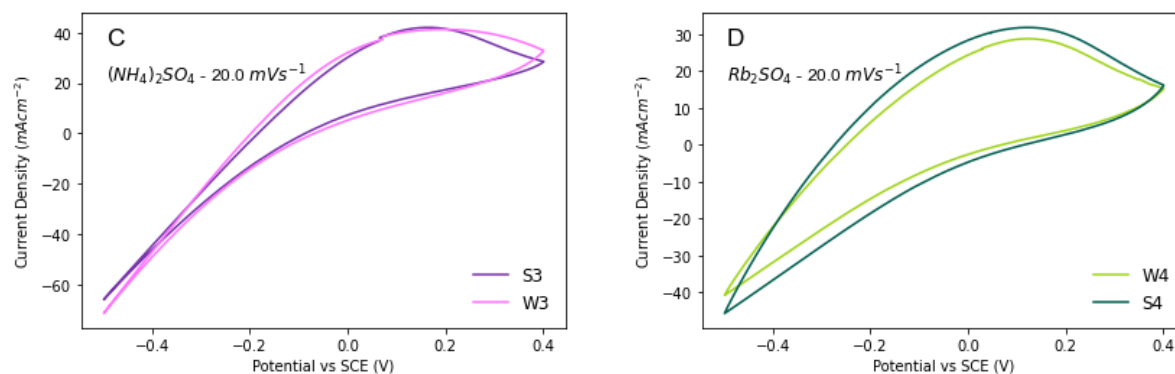
The area of a CV is proportional to the charge stored by the electrode and may be taken as a measure of the electrochemical activity of each sample. Looking first at the sodium-directed samples in Figure 44 A and B, the Seeded samples have a larger area and therefore electrochemical activity than their pristine tungsten foil counterparts. This can be linked to the microstructure discussed in section 5.4. In the case of S2 and W2, this result is not surprising at all from inspecting Figure 68 in section 5.2 because the tungsten substrate sample barely has a visible covering. Sample W3 has a larger activity than S3 as may be seen in Figure 44 C and produces the largest capacity of all the studied foils. These foils were particularly challenging to characterise given the strange nature of the oxide and resulted in irreproducible results. The high areal capacities they delivered is owed to their larger mass loading compared to other samples – see Appendix F. The W3 sample produced a current density of magnitude 5 times greater than the other samples. Finally, the rubidium-directed samples can be seen in D of the figure, and it is clear that seeding had the least effect on the electrochemical performance of these samples reflected by the congruent CVs produced. The shape of these

CVs is most consistent with a pseudocapacitive intercalation system, where the current can be seen to plateau or approach plateau forming an expansively shaped CV. These rubidium samples produced the highest capacity of reproducible samples so were deemed the most successful of those synthesised using the procedure.

The rubidium directed samples, W4 and S4, delivered the most pseudocapacitive shaped CVs at 1 mVs⁻¹. These samples were chosen to calculate a specific capacitance (F/g) using equation 27 for the purposes of comparing with samples from the literature values reported in Table 5. The W4 sample delivered an average specific capacitance of 113.57 Fg⁻¹ and S4 a higher value of 186.65 Fg⁻¹ – when the outlier of S4_03 was removed. The highest average capacitance from this chapter, S4, is on the lower end of the WO₃ specific capacitances from literature presented in section 2.2.4. Considering that the literature values were measured at faster scan rates and that some of the reported hexagonal-WO₃ capacitances from literature are above 300 Fg⁻¹, it can be concluded that the binder free electrodes shown here are not as effective as their powder-based counterparts in literature. Further discussion on this is given later in Chapter 7.

Figure 45 shows the CV for the same samples at a higher sweep rate. Increasing the sweep rate further to 20 mVs⁻¹ is akin to increasing the rate of charging-discharging and resulted in quite different CV shapes as previously seen. It may be seen in all samples, to some extent more than others, that a skew develops which appears to rotate the whole CV by a few degrees which is indicative of the ohmic resistance increasing with sweep rate. The increased ohmic resistance of the studied electrodes arises from the electrical resistance of the sample holder – shown in 3.4.2.1 - and the increasing ionic resistance of ineffective proton diffusion at faster sweep rates.





Sample	W1	S1	W2	S2	W3	S3	W4	S4
Capacity (mAh/cm ²)	0.1	0.11	0.03	0.07	0.2	0.17	0.23	0.29

Figure 45 Cyclic Voltammograms of all 8 samples at a sweep rate of 20 mVs⁻¹ a) NaCl samples b) Na₂SO₄ c) Rb₂SO₄ and d) (NH₄)₂SO₄

As the sweep rate increases, the driving force on the protons also rises. The potential of the tungsten bronze shifts more rapidly, and protons move at a faster pace to satisfy the charge imbalance. This increased number of protons moving leads to greater congestion, resulting in higher resistance and less intercalated protons. The higher ohmic resistance evident in these CVs at 20 mVs⁻¹ shows that the electrode is not effective at allowing proton movement into the bronze so that they may be intercalated. The departure from a pseudocapacitive shape to a pointed shape, still typical of intercalation, is more prevalent in some samples than others. The change in CV shape between Figure 44 and Figure 45 is more profound in blocks B and C than in A and D. In fact, block D featuring the rubidium-directed samples W4 and S4 suffers far less from this resistivity issue than the other presented samples. It may be inferred from this that the W4 and S4 allow faster proton diffusion than the others. This is quite apparent from the microstructural data presented in the subsequent chapter.

The discussed trend between increased rate of charging and increased ohmic resistance is clear from looking at the full complement of CVs for these samples that may be seen in Appendix F. This trend may be seen through calculating the charge stored by each sample using equation 37 and plotting this value against the sweep rate used in the experiment.

$$Q_{\text{mAh/cm}^2} = \frac{CV_{\text{area}} (\text{mA} \cdot \text{V})}{\text{scan rate} (\text{mV/s})} \cdot \frac{1}{3.6} \cdot \frac{1}{\text{electrode surface area}} \quad 37$$

Where Q is the areal capacity in mAh/cm², the CV area is the area between the curve of the CV in mAV, the scan rate is the scan rate used in the experiment set in mV/s, 3.6 is a factor to convert Coulombs into mAh and the electrode surface area is the surface area of the electrode used in the experiment measured in cm².

The much-discussed goal of this thesis is to synthesise pseudocapacitive materials so why not convert the CV area to a capacitance? Many of the CV results above may not be interpreted as pseudocapacitive because they do not show a quasi-linear proportionality between potential and evolved current; a capacitance is not valid for the entire dataset. Instead, a capacity can be calculated and that is what is presented in Figure 46. A charge stored in mAh/cm² was calculated at each sweep rate for each sample across three experimental runs. The median values for the three experimental runs are plotted in Figure 46.

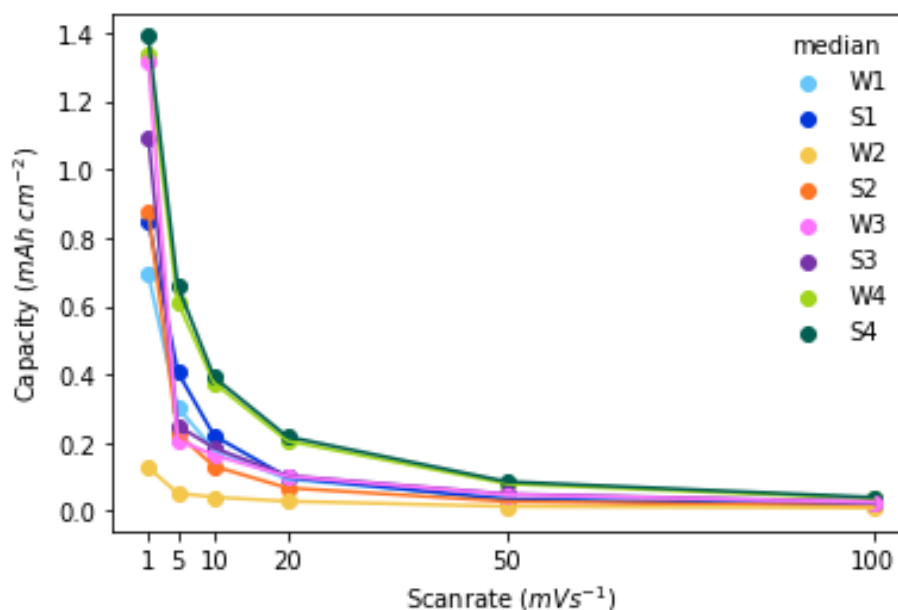


Figure 46 Calculated capacity values in mAh cm² from Cyclic Voltammograms

There is a steep decline in capacity across all samples moving from 1 to 5 mVs⁻¹ which then flattens out beyond 20 mVs⁻¹. As noted from the CVs, the samples W4 and S4 do not suffer from the same loss in capacity as the other samples. Though at 50 and 100 mVs⁻¹ they do approach similar values as the other samples.

The characteristic drop in capacity across all the samples can be discussed from the perspective of the two-step charge mechanism: protons (1) hop into the lattice and (2) intercalate into available interstitial sites. Intercalation requires protons being available at the surface to intercalate, it is dependent on diffusion moving the protons to the sites. The mechanism from which protons can absorb to interstitial sites is an intrinsic property to the tungsten bronze being studied. That is to say, the charge-transfer resistance between an interstitial site and a proton is the same regardless of how protons diffuse to and from it. Nevertheless, the proton needs to be available at the surface to be intercalated and to be there depends upon the diffusion of protons through the oxide surface. As outlined when discussing the Dunn analysis method, the rate of intercalation may be modelled as a diffusion-limited process with a square root dependency compared to double-layer formation - a linearly

dependent process. This means at faster rates of charging the double layer current may be expected to increase faster than that of intercalation; and as consequence, the rapidly forming double layers prohibit diffusion to the surface for intercalation to occur. Intercalation is a function of oxide electrical and ionic conductivity, hydration, and microstructure of the WO₃. Of these, the microstructure is the predominant factor which separates all eight electrodes, and what may be seen from Chapter 5 is that the sample microstructures align well with the electrochemical performance.

Looking at Figure 46, the lowest sweep rate capacity is highest where the rate of intercalation is not impeded by the movement of ions. The microstructure and crystal phase provide sufficient networks and porosity for the ions to move and give sufficient time for protons to fill all the interstitial sites available. Increasing to 5 mVs⁻¹ there is a drop in capacity to half that recorded at 1 mVs⁻¹. The higher rate of change in potential drove more ions to move creating ionic resistance to diffusion as double layers are established, blocking protons access to some pores of the oxide, and limiting intercalation to larger pore interstitial sites. A further change to 20 mVs⁻¹ and beyond exacerbates this further. The number of ions moving creates rapidly formed double layers across areas of the bronze, blocking proton movement further to the extent that intercalation becomes limited to very few, negligible, sites.

To summarise, the CV results may be explained as follows: increasing the sweep rate causes protons and other ions in solution to move faster to satisfy the charge requirement and these ions rapidly form electrochemical double layers. These double layers provide an impenetrable barrier to protons, prohibiting them from intercalating and the capacity drops. The current measured in the experiments rises with sweep rate as more ions in solution are mobilised to form the double layer, increasing ion movement leads to an increased ohmic resistance.

To further elucidate the collapse in capacity, the Dunn analysis method [2], [101] was completed on the data using a self-developed Python script. A full description is given in the Methodology. This method may be explained by focusing firstly upon an example dataset of the S4 sample, the most pseudocapacitive by CV shape, before reviewing the whole dataset's key metrics. The graphical representation of finding k_1 and k_2 parameters for the Dunn method, as described in section 3.4.4.3, for sample S4 shown in Figure 47. For a purely capacitive sample, with a rectangular or quasi-rectangular shape, the analysis would only be necessary to be completed on one scan, as the symmetry infers reversible processes are occurring. This does not apply to these unsymmetrical cyclic voltammograms and thus it was necessary to find k_1 and k_2 values for each cathodic sweep (forward charging reaction of Figure 47 left) and anodic sweep (backwards discharging reaction of Figure 47 right).

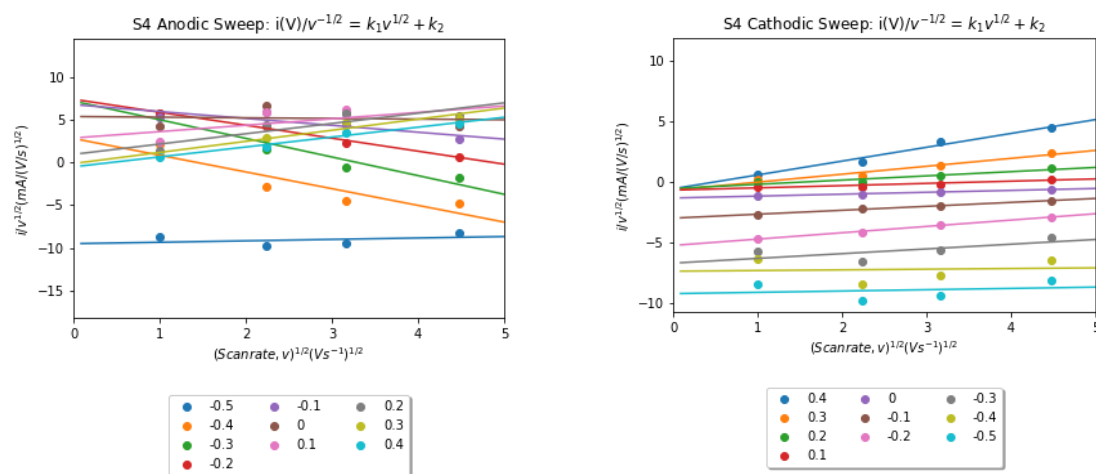


Figure 47 Example of analytical plots used to find k_1 and k_2 for the Dunn method for example sample S4

The k_1 (capacitive element) and k_2 (diffusion-controlled element) values obtained from the above graphs may then be used to plot an illustrative, modelled CV that can visualise the capacitive and diffusion-controlled regions of the original CV data. The graphical representation of this is shown in Figure 48 at two different scan rates.

Figure 48 A & B show the capacitive and diffusion-controlled contributions to the energy stored by the bronzes, respectively. The capacitive contribution is negligible on the cathodic charging sweep sitting around 0V, though, it does then grow in the anodic sweep to become completely dominant beyond 0.2 V. This implies that the charging of the layer faces a lower ohmic resistance than the discharge which is interesting. The step back of the CV upon discharge indicates a fast process, as protons are released from their adsorbed sites. It would make sense therefore that these protons would block one another, increasing proton congestion and increasing the ohmic resistance. In the charging case, however, the protons gradually enter the bronze, unimpeded and intercalate as desired. The “capacitive nose” is present in all the characterised samples and by being purely capacitive means that there are no protons left to de-intercalate. This region will be made of surface-held anions forming a double layer. It can therefore be said the samples have been overcharged and the positive end of the potential window needs to be curtailed.

From 0.2 V to -0.5 V, the experimental data at 1 mVs⁻¹ fits extremely well with the diffusion-controlled processes. This is interesting for two reasons: firstly, this diffusion-limiting process, intercalation, must be so rapid that it exhibits a pseudocapacitive shape. Secondly, it may be said at this sweep rate the rate of proton hopping into the bronze is slower or comparable to intercalation into the WO₃ lattice. This is because capacitive effects only occur in the described “nose” and upon discharge.

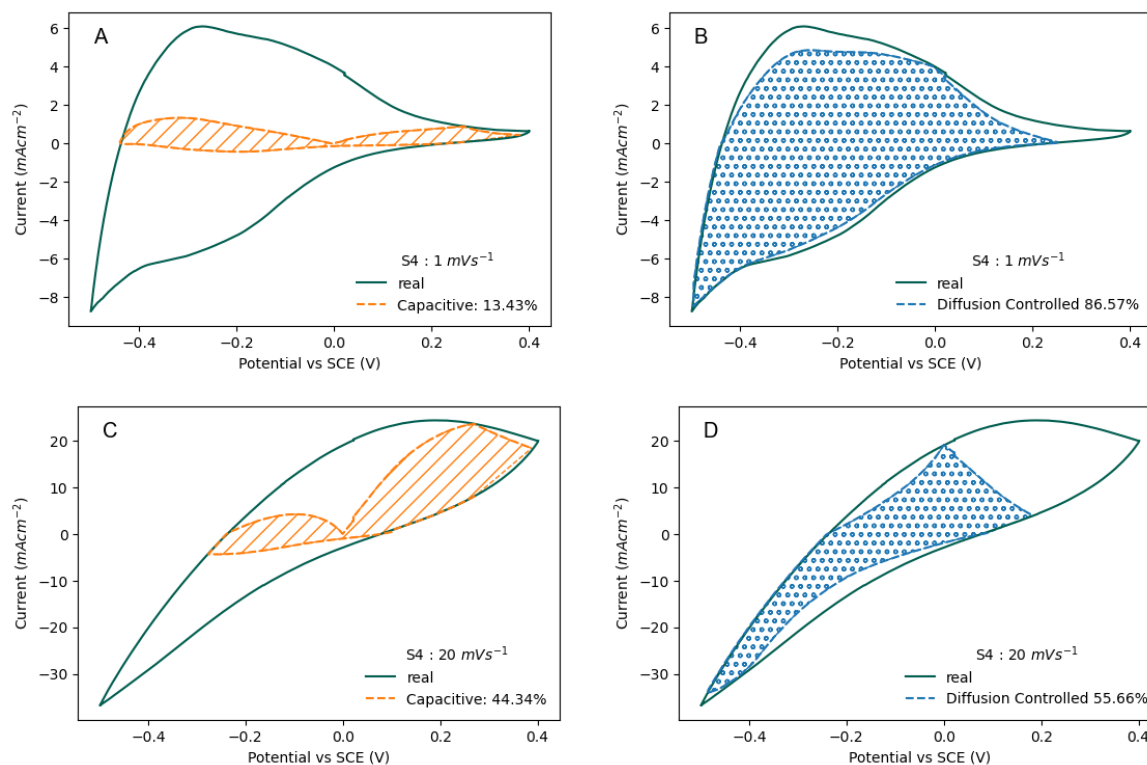


Figure 48 Graphical representation of the Dunn Method analysis on sample S4 (first run) displaying: the capacitive controlled k_1v current at A) 1 mVs^{-1} and C) 20 mVs^{-1} ; and the diffusion controlled current $k_2v^{1/2}$ at B) 1 mVs^{-1} and D) 20 mVs^{-1}

It is perhaps obvious looking at Figure 48, and from the previous discussion of intercalation, that at higher scan rates the capacitive element, linearly dependent, will dominate more than the diffusion-controlled, square root of the scan rate function. It is quite apparent from graphs C and D of Figure 48 that the capacitive element has increased. It is now a non-zero value in the cathodic sweep and the “capacitive nose” is more prevalent. It follows, given the previous discussion, that with faster charging the increased diffusion of protons would create more capacitive effects that appear in the cathodic sweep. The larger cathodic nose is driven by the fact fewer protons have intercalated than in the first instance, and so to reach these potentials the system forms a double layer sooner, at potentials closer to 0 V.

How the capacitive element of the entire dataset varied with sweep rate may be seen in Figure 49 presented in a 3-D graph. The discussed increase in capacitive behaviour occurs in all samples, consistent with the explanation given.

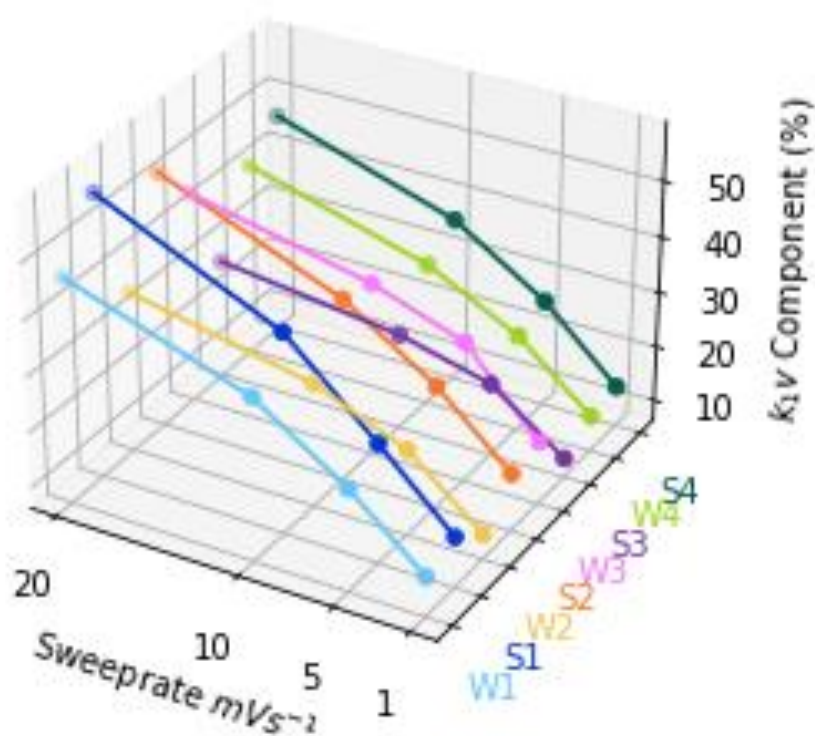
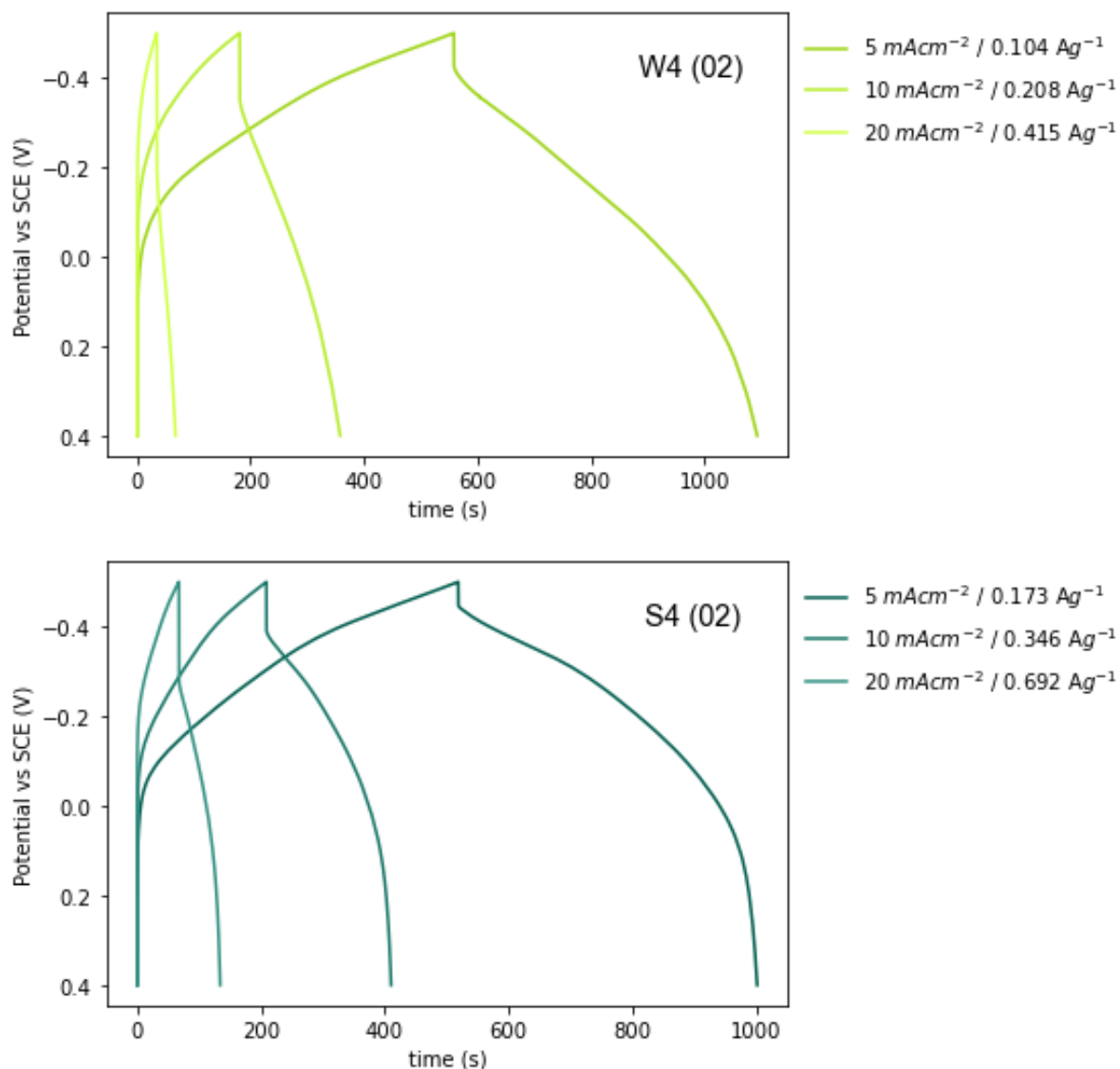


Figure 49 Capacitive component of charge stored as a percentage of total stored charge

It should be noted that Dunn analysis is not completed above 20 mVs⁻¹. The strength of this technique is in visualising at what potentials these processes become more important and in providing an estimate of what percentage of the charge stored is related to capacitive-like or intercalation-like mechanisms. Beyond 20 mVs⁻¹ the effect of concentration polarisation and the increased ohmic drop losses make the analysis less valuable.

4.3 Galvanostatic Characterisation

For a pseudocapacitive material to be correctly labelled, it must show a quasi-rectangular CV and a quasi-linear galvanostatic charge-discharge (GCD) profile. Both these shapes indicate proportionality between the charge passed and the change in potential, satisfying the definition of capacitance. The GCD curves (full dataset may be seen in section Appendix G) follow a highly similar shape across all samples indicating similar charge-discharge kinetics across the samples regardless of synthesis conditions. The y-axis of the GCDs was inverted so that the charging and discharging cycles could be intuitively viewed. The best-performing samples W4 and S4 are discussed here, displayed in Figure 50, as representative of the whole dataset.



Sample	Discharge Capacity mAcm ⁻²		
	5 mAcm ⁻²	10 mAcm ⁻²	20 mAcm ⁻²
W4	0.77	0.51	0.19
S4	0.70	0.58	0.38

Figure 50 GCD curves for samples W4 and S4 at 5, 10 and 20 mAcm⁻² with post experiment specific current density. Note the y-axis is inverted to show charging being positive gradient and discharge negative gradient. The discharge capacity for each GCD curve displayed is tabulated below the figures.

The GCD curve shares some similar features which can be described from full discharged (0 seconds) through to the peak of charge back to full discharged (maximum time). There is a steep increase from time 0 to around 0.1V depending on the current density of the experiment. This region corresponds to the fully discharged state of fully unoccupied interstitial sites, and the exit of surface-held anions, to first intercalated protons. There is then an angled, steady decrease in potential to a minimum peak. This region relates to the intercalation of protons within the WO₃ bronze. This charging region has a straight element to it which shows

proportionality between the faradaic charge passed and the change in the potential, a necessary characteristic of a pseudocapacitive material. Through the peak, there is a linear drop of various magnitudes depending on the current density called the ohmic drop. This is caused by the current being switched instantaneously so the system reacts accordingly. The discharge curve again has a straight region until it reaches around 0V and steeply approaches the positive maximum.

The first feature to discuss in detail is the prominent ohmic drop, the steep drop-off in potential observed when the switch is made from the charge to discharge cycle. This instantaneous drop is called the direct current internal resistance (DCIR) and is a measure of the ohmic resistance of the material at discharge. The gradient of this graph provides the resistance encountered from the ohmic drop experienced at galvanostatic discharge ($V = (|I_{\text{charge}}| + |I_{\text{discharge}}|) \cdot R$) to be estimated. Since the magnitude of I_{charge} and $I_{\text{discharge}}$ were the same in this experiment we can use $2 \cdot I$ to calculate R from the measured voltage drop [111]. The mean magnitude of each sample's ohmic drop plotted against the current density is displayed in Figure 51. For all samples there is a clear proportionality between the size of the ohmic drop and the rising current densities, analogous to skew observed in CV data that develops with sweep rate. Sample W2 was removed from the analysis because the DCIR values found from the analysis were significantly different from the dataset below and made no physical sense.

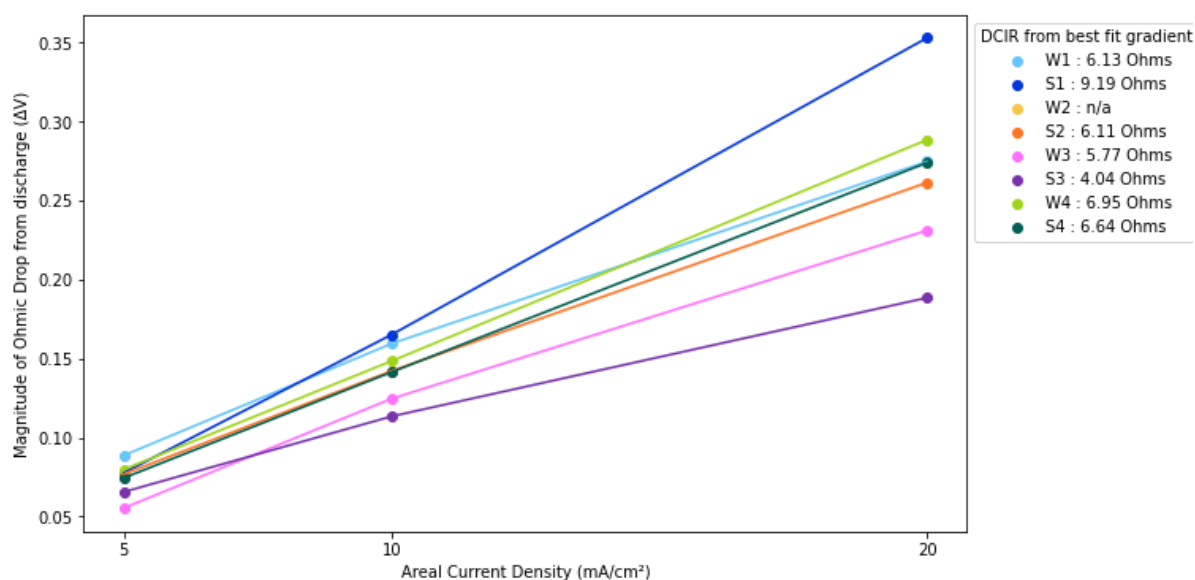


Figure 51 Mean magnitude of Ohmic Drop as a function of current density of experiment; the associated mean DCIR for each data set across all currents is provided in the legend

Table 15 displays the mean DCIR and associated standard deviations calculated for the dataset. Some of the calculated values are approximately similar to the DCIR values found from the best line fitting seen in the legend of Figure 51, but others have large standard deviations.

The seeded samples produce a larger standard deviation than the pristine tungsten samples but it is unclear whether this is linked to the nature of the foils or a coincidental result. Interestingly, there is some consistency to the DCIR values within each sample type, with the sodium chloride directed foils producing the largest and the ammonium delivering the lowest.

Table 15 Mean and Standard deviation of DCIR values found from the Galvanostatic Discharge data

Sample	W1	S1	W2	S2	W3	S3	W4	S4
Mean DCIR	8.04	8.35	N/A	7.11	5.85	5.65	7.54	7.12
Standard deviation DCIR	0.99	2.06	N/A	0.59	0.35	2.38	0.69	1.46

The increasing size of the ohmic drop with current displays a significant ohmic resistance experienced by the studied electrodes. A few samples cycled at 1 mAcm⁻² (F.1) displayed no apparent ohmic drop which can be attributed to a lower IR drop at the sweep rate. It should be noted the effect seen in Figure 51 is observed within the charging curve also, where a steep line stems from 0.4V to progressively lower potentials. This region relates to the “nose” discussed in the CV section whereby the charge storage mechanism was found to be capacitive.

As with the CV data, it is of interest to evaluate how pseudocapacitive the data truly is. Outlined in section 1.3.4, a capacitive charging curve is a perfect linear triangle whereas a battery curve features a plateau region. The GCD data presented is some intermediate with linear and non-linear regions and there is a question of how best to quantify this, can one measure the linearity of the GCD data and use this to estimate how pseudocapacitive the data is?

The most straightforward approach is to compare the data with a triangle. As discussed, true capacitor exhibits a perfect triangle when charged and discharged due to the linear proportionality between the charge passed and the change in potential. Figure 52 displays a plot of a triangle over the experimental data and the calculated root mean square error (RMSE) between the triangle and the figure is shown in the legend. RMSE is a common method for model validation which quantifies the discrepancy between predicted and observed values by computing the square root of the average of the squared differences, outputting a measure of model performance in the original units of the response variable, in this case, volts. These RMSE values are large in relation to the measured units indicating poor fitting to a perfect triangle which worsens with current density, driven by the ohmic drop effect and the clear elbow to the curve.

This may be obvious upon fast inspection of the GCD data, with a more lopsided bell shape present. It is clearly worthwhile to look at the charge and discharge components separately and to look at the linearity across different regions of the curve.

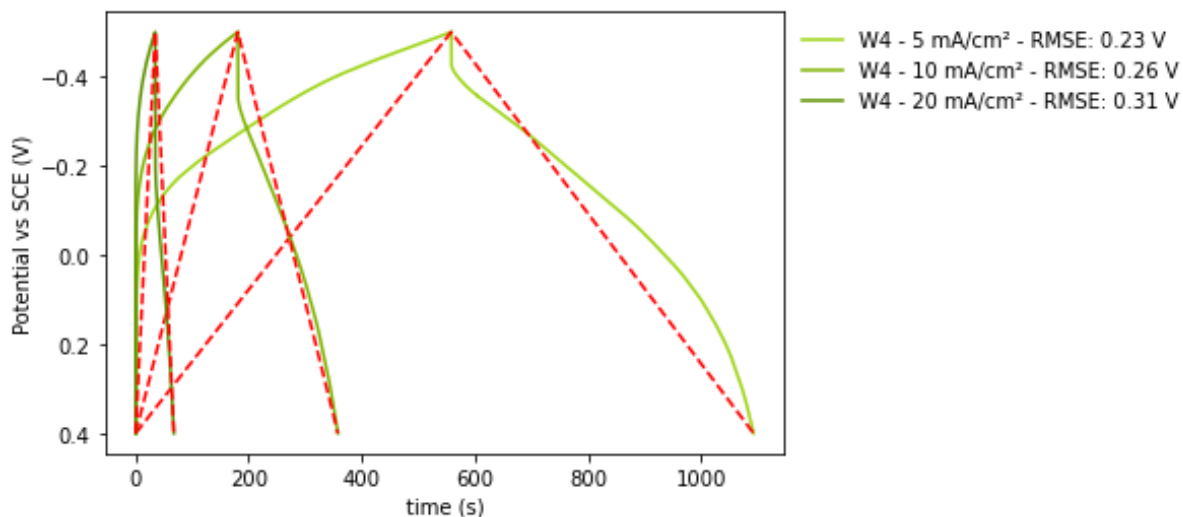


Figure 52 GCD Curve of W4 from Figure 50 with perfect triangle line and Root Mean Square Error (RMSE) fitting provided in the legend

The charging section is looked at first in Figure 53 and compared to a straight line between the potential limits. The data after the positive potential limit was cut by increments of 0.1 V, replotted and refitted again to a straight line. The graph therefore has the real curve and 5 red dotted lines each offering analysis between the maximum state of charge -0.5V and a positive limit between 0.4 and 0V. What is clear is that the fit of the straight line improves as the potential window is retroactively cut down to between 0 and -0.5V. This region is what is most pseudocapacitive and as mentioned with the CVs, reducing this potential window in future would lead to more pseudocapacitive behaviour in future.

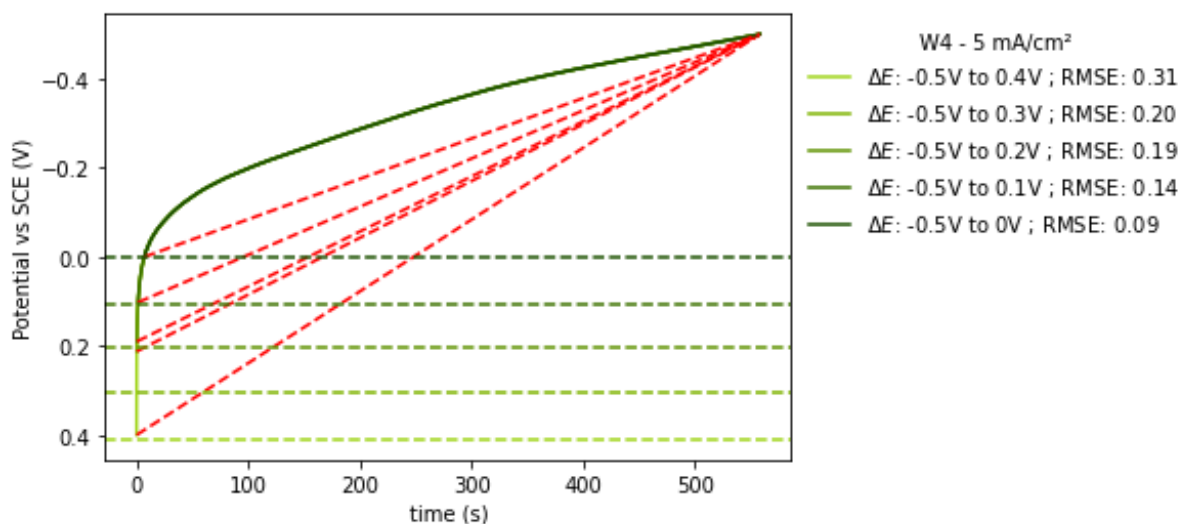


Figure 53 Charging curve of W4 showing the real data potential window, ΔE , shortened and the data refitted to the ideal case of a linear curve

An identical analysis was then applied to the discharge curve. What is noticeable here is the RMSE values are a lot lower than those produced in the charge curve. The discharge curve

appears to be more capacitive in that regard. There is a similar trend in this data, as the potential window is reduced there is an improvement in fit from the experimental conditions.

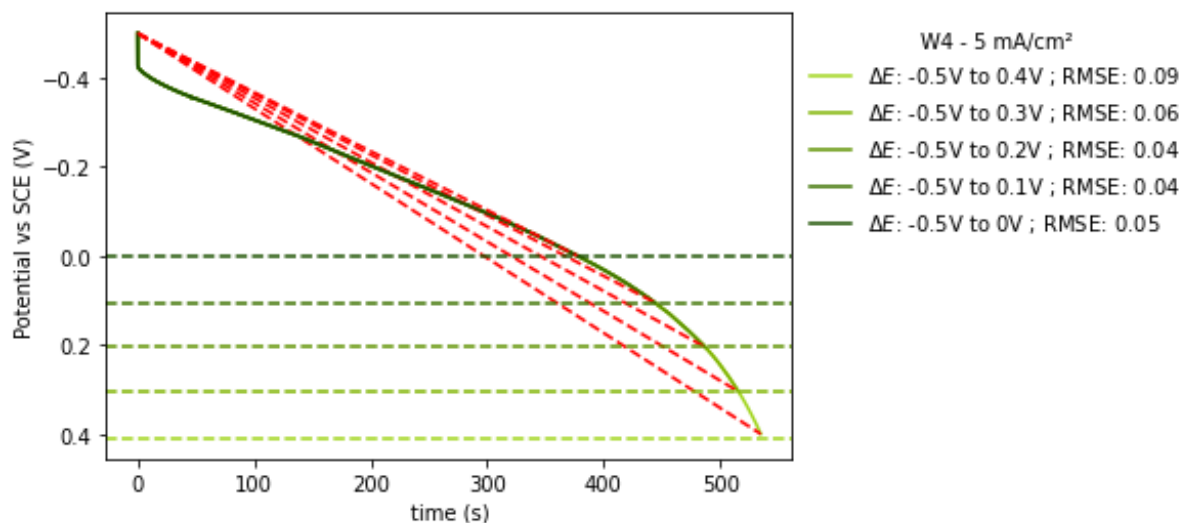


Figure 54 discharge curve of W4 showing the real data potential window, ΔE , shortened and the data refitted to the ideal case of a linear curve

This data is plotted from the top of the ohmic drop, and this itself may be influencing the analysis disproportionately. If instead the ohmic drop present in the discharge curve in Figure 54 is accounted for and the same fitting is repeated from the point the potential drops to, the graph turns into Figure 55. This fitting from this point to reduced potential windows of a discharge limit of 0V is truly pseudocapacitive because the very low RMSE value indicates the real data is quasi-linear in nature. This result, as with the charging curve, is further evidence that the potential limits need adjustment for pseudocapacitive performance.

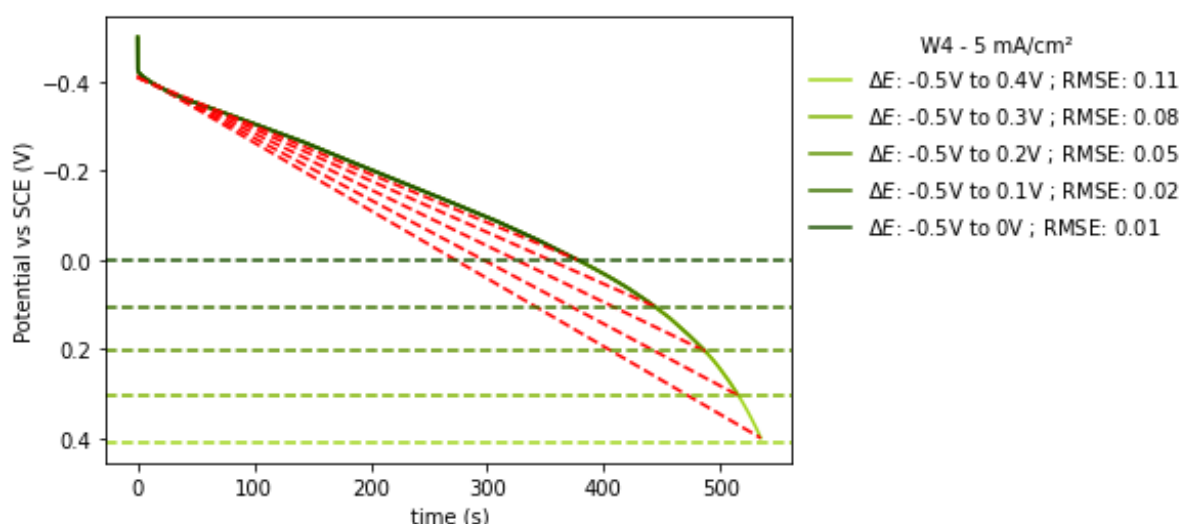


Figure 55 discharge curve of W4 showing the real data potential window, ΔE , shortened and the data refitted from ohmic drop point to the ideal case of a linear curve

This analytical method was then repeated across all current densities with the RMSE measure of fit calculated for each new potential window. An average value was calculated for the three iterations of each sample, and this is plotted against the current density in Figure 56.

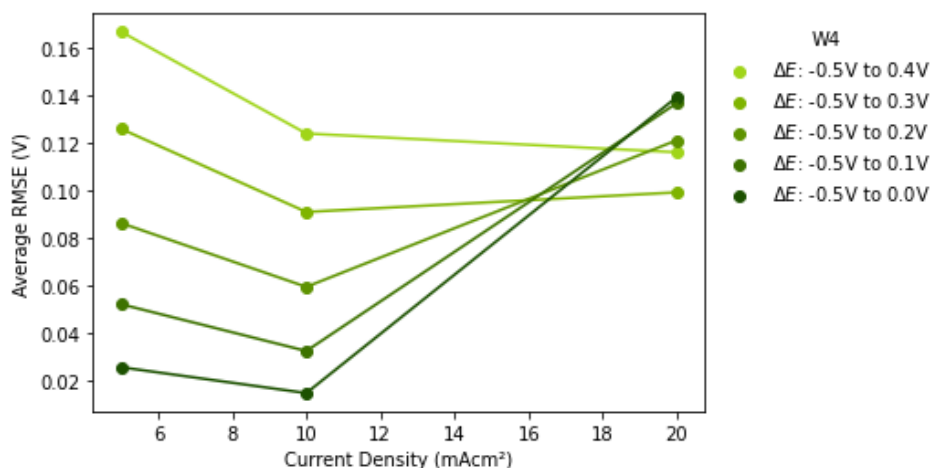


Figure 56 Average Root Mean Square Error between the discharge curve and modelled purely capacitive line across all W4 Samples at reduced potential windows

From looking at Figure 56 it may be reasoned that 20 mAcm⁻² was far beyond the material's limit and resulted in little intercalative charge storage. It may also be a consequence of the resolution in data captured by the potentiostat. In other words, the amount of data points captured by the potentiostat was insufficient for this analysis given the speed of the reaction being measured. The method used by the Python script did not have sufficient points to identify the ohmic drop in these cases - making analysis of 20 mAcm⁻² impossible.

Discounting the 20 mAcm⁻² values a clear trend is then identifiable; reducing the potential window's limit to 0.0 V brought a lower RMSE than the full window 0.4V indicating closer to linear, pseudocapacitive behaviour. This supports, as with the CV Dunn-method analysis, that the foils were characterised using too large a potential window and that the behaviour here could be truly pseudocapacitive with an adjustment to less than 0.2V.

Fitting the discharge to two lines using piecewise linear regression with an algorithm to identify the optimal breakpoint in the data, was implemented to further analyse the data. An example of the result of this is shown in Figure 57.

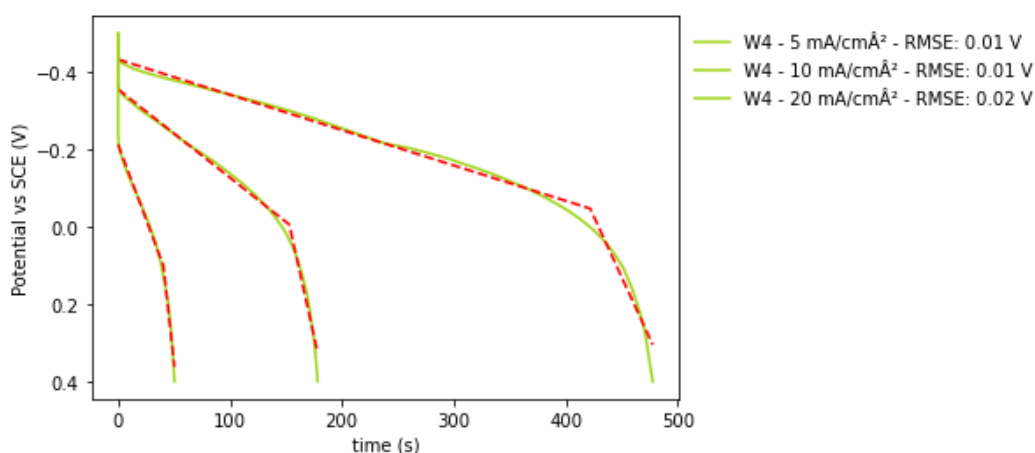


Figure 57 Piecewise linear regression of discharge curve featuring a break point

This method of analysis is helpful in trying to identify different straight-line regions in the dataset and indeed, as may be seen in Figure 57, two may be identified. The ohmic drop marks the beginning of the first which has been discussed as being the linear de-intercalation process. However, this method of analysis further identifies where the de-intercalation ends, and the changing gradient of the line marks a new process taking over. This region of the curve describes where all the interstitial sites are now becoming empty and solution anions are moving to balance surface charge in a double-layer capacitive process.

The calculated the average RMSE for this model comparison value for each new potential window at each sweep rate is presented in Figure 58. This RMSE from the breakpoint linear regression modelling better matches the real data by a factor of ten times compared to a simple straight-line analysis. This analysis does not cover the full data set like the straight line must, instead fitting two lines as best it can. For instance, in Figure 57 it is clear the ohmic drop is ignored and the maximum positive potential is not reached. This technique has been successful in quantitatively identifying the faradaic discharging and capacitive over-discharging regions of the GCD. The useful discharging region has a shallow gradient across a moderate amount of time which shows that charge is passing, and protons are being de-intercalated; conversely, the over-charging region is a steep line over miniscule periods of time showing little charge is being passed.

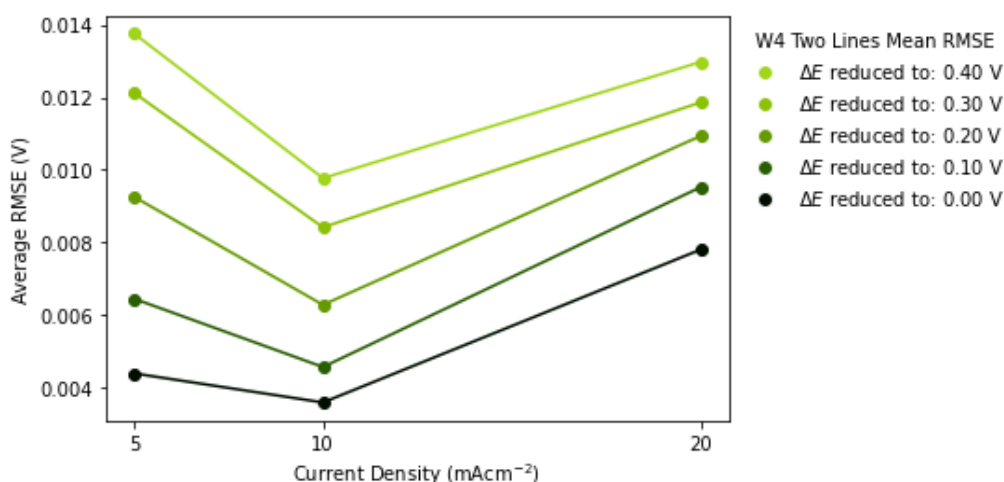


Figure 58 Average Root Mean Square Error between the discharge curve and linear regression fitting across all W4 Samples at reduced potential windows

Using the same approach on the charging curve, a similar result comes out from the data and can be seen in Figure 59. The charging curve again fits the 2-line linear regression model (Figure 59) better than the simpler linear case, and the charge storage mechanism may be summarised in three regions.

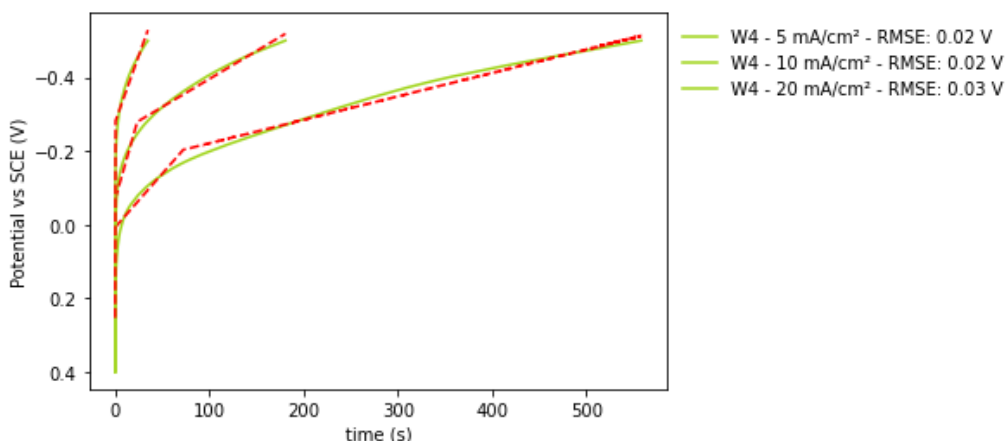


Figure 59 Piecewise linear regression of charge curve featuring a break point

The charge curve, regardless of current density, begins with a steep jolt from 0.4V to below 0.0V which is analogous to the ohmic drop experienced on the discharge. Both of these ohmic drops are caused by surface-held ions rapidly moving from the surface upon the change in current between cycles. In this case, the drop is made more profound by the fact no protons are any longer in the layer because it is over-discharged as discussed in the CV analysis. The next phase of the charging process is modelled to a small straight line which captures the bend from the vertical ohmic process to the beginning of intercalation. This process initially occurs rapidly before plateauing to a straight line where intercalation steadily occurs until the top potential. It should be noted that in the fastest current density, 20 mAcm⁻¹, the transition between intercalation beginning and the steady plateau disappears with a loss in resolution and that the regression approximates these two parts as one line.

Areal and specific capacities may be determined from GCD discharge curves using the equations outlined in section 3.4.5. The areal capacity presented below in Figure 60 follows a very similar profile to those calculated from CVs in Figure 46, where an increased rate of charging is accompanied with a drop in capacity.

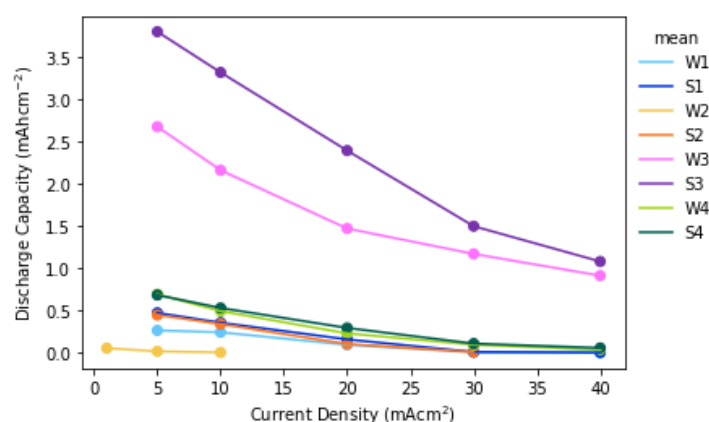


Figure 60 Mean Areal Capacity (mAhcm⁻²) versus Areal Current Density (mAcm⁻²)

The ammonium-directed samples here show a far superior performance; however, this is a mean value which is highly distorted by one, unreproducible result due to the colloidal nature

of the ammonium-based samples and their much higher mass loading. It points to hexagonal (NH₄)_xWO₃ having encouraging performance in principle but the physical nature of W3 and S3 synthesised in this work are too problematic to work with.

The dry mass of the samples could be measured post characterisation allowing for a capacity and current by mass to be calculated and is presented in Figure 61. The visible active mass was scraped off onto a glass dish and dried in an oven. The mass of the glass dish was weighed post-treatment and the mass was estimated to 2 decimal places. It is acknowledged that this method, though straightforward, may not contribute to the scattering observed. This graph helps to show the spread of performance across all the samples and also the variance in current densities that evolve from growing the active layer as opposed to coating a known mass. The rubidium sulphate-directed samples S4 and W4 show closer grouping than other samples which have far more outliers. The W1 and S1 samples deliver some of the higher specific capacities of the dataset, higher than even the best performing on an areal basis W4 and S4.

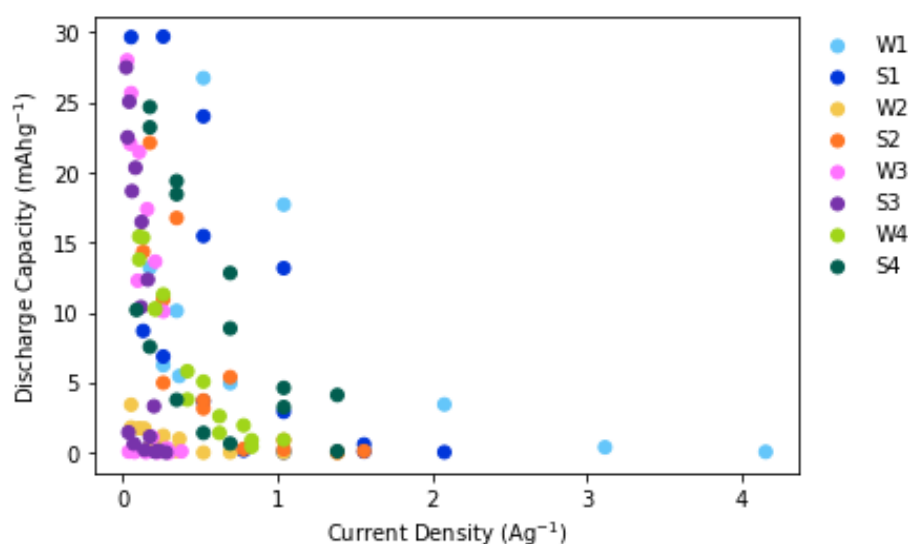


Figure 61 Scatter graph of Specific Capacity (mAh g⁻¹) versus Specific Current Density (Ag⁻¹)

Similarly to the CV data, a capacitance can be calculated from the discharge curves for the purpose of comparing the performance with values from literature displayed in Table 5, with the caveat, again, that these non-linear curves do not satisfy the definition of pseudocapacitance. The specific capacitance values calculated using equation 33 are shown in full in Appendix. These follow the trend of the capacities displayed in Figure 61 only that they are scaled by the capacity over the potential difference according the definition of capacitance (equation 1). The sodium chloride directed sample S1 delivered the highest specific capacitance at 118.72 Fg⁻¹ at a current density of 0.26 Ag⁻¹. Similar to the comparison of the specific capacitance found from the CV analysis, this capacitance is of a similar magnitude to those given in Table 5 albeit recorded at a much lower current density. If one

reduces the dataset to current densities of 1 Ag⁻¹ then the highest capacity drops considerably to between 10-70 Fg⁻¹. It can be concluded, again, that these binder free electrodes do not match the performance of powder based WO₃ electrodes found in literature.

A final visualisation of the discharge curve data is a comparison of the energy versus power density of the samples and is shown in Figure 62. The sodium chloride-based samples W1 and S1, as well as the rubidium-directed samples W4 and S4, are again the best performing of the samples presented, occupying the top right region of the dataset. The calculated values presented in the Ragone diagram fall within the established range of supercapacitor, or supercapattery electrodes found in literature [10].

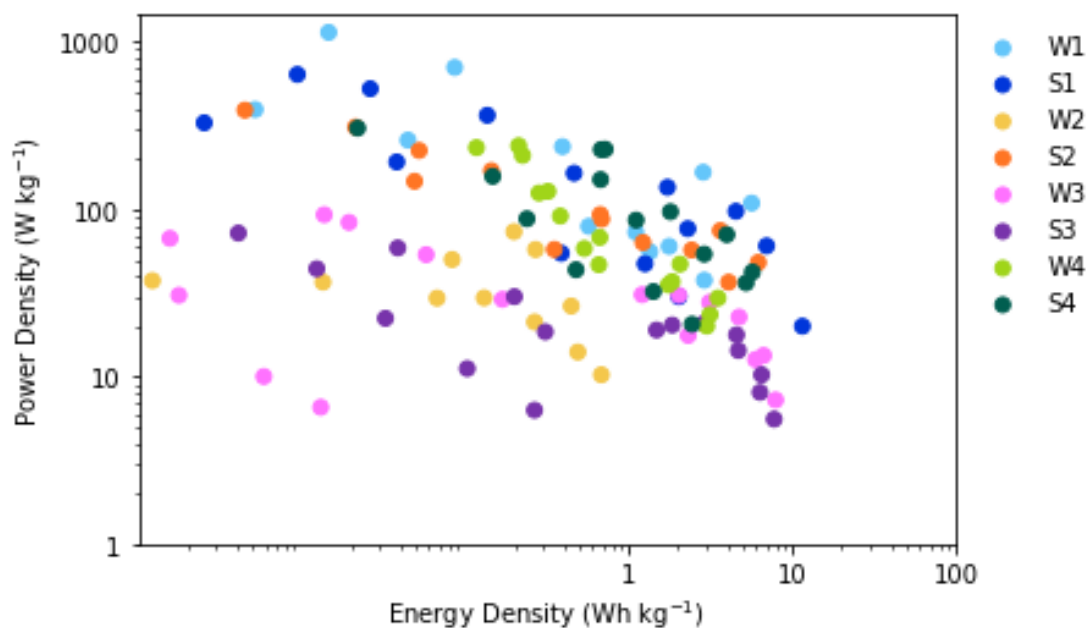


Figure 62 Ragone Diagram of Dataset

4.4 Electrochemical Impedance Spectroscopy

Potentiostatic Electrochemical Impedance Spectroscopy (PEIS) was measured at the beginning of the electrochemical characterisation sequence to provide further insight to the energy storage process. This was recorded before any other more intrusive, sometimes damaging (see section 5.6), galvanostatic or potentiodynamic process was performed. Like all the experimentation this technique was measured at uncontrolled room temperature. The PEIS method first recorded the open circuit potential and this was an opportunity to see how the lack of temperature control impacted the experiment. If temperature had a significant impact, a large variance in OCV for each individual sample could be expected. These OCV values, Figure 63, were within a similar range between 0.0 and 0.1V vs SCE though one considerable outlier exists in the S2 sample, and this was removed from the subsequent analysis.

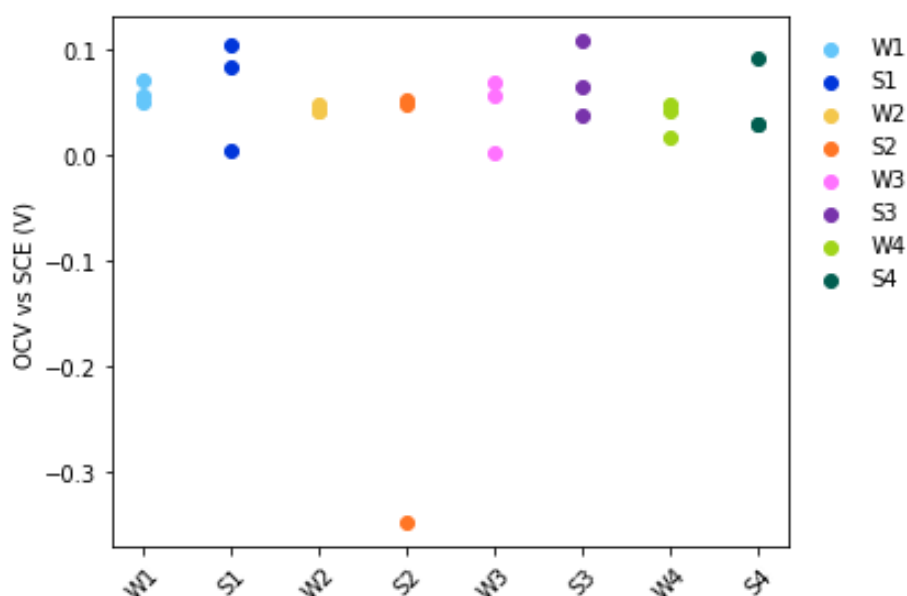


Figure 63 OCV values of samples at which impedance spectra was opened

The measured OCV was quite consistent across the whole dataset with one notable outlier in S2. This suggests that hydrothermal synthesis produced samples to a similar state of charge i.e. regardless of the synthesis scheme the resulting WO₃ was on the discharged end of the potential window.

The impedance analysis software Zfit from Biologic's EC-Lab was used to fit the impedance spectra with a two-step approach: firstly, an initial fit was performed on a narrow range of the data (between 1 Hz up to 100 kHz) to find suitable values for the high-frequency circuit parameters. The values obtained for the non-ideal inductor (La1) and the ohmic resistor (R1) were then fixed and the fitting was then re-run across the full range to find best fit values for the remaining parameters. An example of the results of this methodology is shown here with sample S4 before the results of the whole dataset as a whole are comparatively discussed.

The full range of spectra and fitting data from the analysis can be seen in Appendix H. The equivalent circuit used to fit the data is shown in Figure 64.

Equivalent Circuit

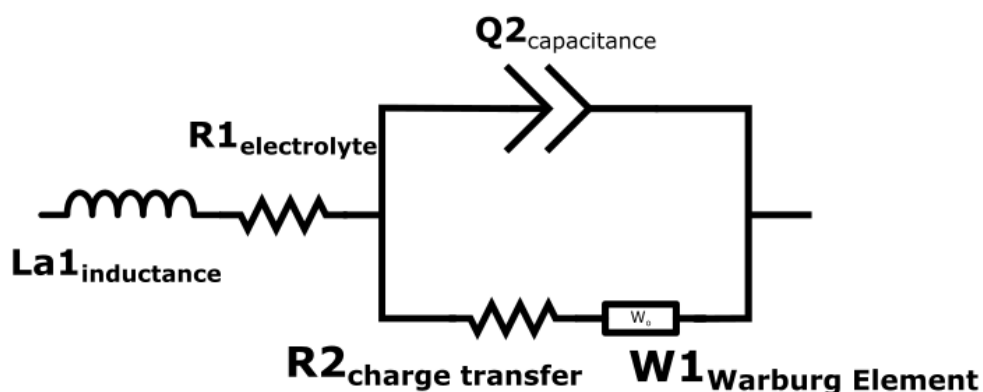


Figure 64 Equivalent Circuit fitted used to fit the recorded EIS data

The circuit is made up of 5 components which are defined from left to right in the schematic. The first element is a modified inductor element which accounts for non-ideal inductance which was observed in the data and assumed to arise from the leads and electrical connections of the experimental setup. In series with the inductor element is a resistor which represents the ohmic resistance of the electrolyte. Following these elements is a parallel section which models the charge storage mechanism of the electrode, where protons simultaneously must diffuse to the surface (represented by W1) through the electrochemical double layer (Q2) at which point charge is transferred between electrode and electrolyte through an electrochemical reaction which overcomes a charge transfer resistance (R2). The element Q2 is a constant phase element (CPE) which models non-ideal capacitive behaviour arising from the nonuniform microstructure of the samples. All of these elements have different responses to the frequency of the measurement: the Warburg element dominates the impedance at low frequencies due to the longer timescales of diffusion; whereas the CPE and modified inductance element are more influential at intermediate and high frequencies because the impedance of a capacitive element decreases with increasing frequency whilst the inductor's reactance increases.

The first analysis reduced the frequency range to between 1 Hz – 100 kHz to fit the predominantly high frequency influenced elements La1 and R1. Once these values were fitted with good confidence, they were fixed and the range extended to the full frequency range (10mHz to 100kHz). The Nyquist plots for the first and second fitting of sample S4 (02) is shown in the figure below:

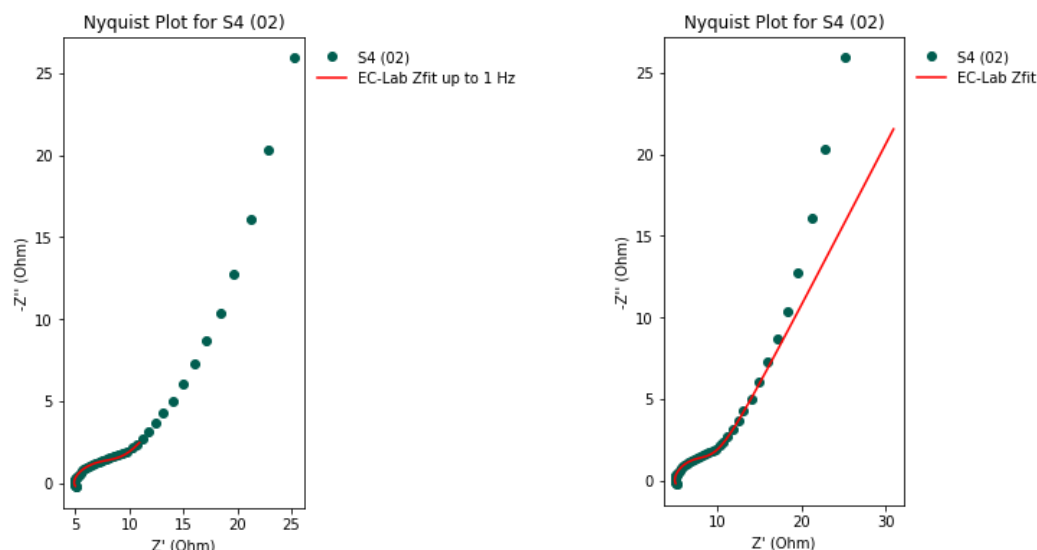


Figure 65 Nyquist Plots for sample S4 (02): left hand side shows fitting from Zfit between 1Hz and 100 kHz; the right hand side shows the Zfit fitting between 10 mHz and 100 kHz using the fixed parameters for La1 and R1 found from left hand fitting

The fitting parameters for the Nyquist plot on the left side of Figure 65 are shown below in Table 16. It can be seen that the standard errors for this particular fitting are a reasonable magnitude in relation to the fitted value. This is reflected in the Nyquist plot where the shape of the modelled curve well describes the dataset.

It can be seen that the standard errors for this particular fitting are a reasonable magnitude in relation to the fitted value. This is reflected in the Nyquist plot where the shape of the modelled curve well describes the dataset.

Table 16 Fitting parameters for S4 (02) from Zfit between 1Hz and 100 kHz

circuit parameter	value	standard error	unit
L1	0.143	0.073	H.s ^(a-1)
a1	0.173	0.027	
R1	3.532	0.245	Ohm
Q2	0.015	0.0	F.s ^(a - 1)
a2	0.42	0.008	
R2	7.805	0.277	Ohm
s1	6.697	0.055	Ohm.s ^{-1/2}

The subsequent step of refitting the values with fixed L1, a1 and R1 parameters but across the full frequency range of the measurement delivered the following set of fitting parameters shown in Table 17.

Table 17 Fitting parameters for sample S4 (02) from Zfit between 10mHz and 100 kHz using the fixed values of L1, a1 and R1 from the first step.

circuit parameter	value	standard error	unit
L1	0.143	0.073	H.s ^(a-1)
a1	0.173	0.027	
R1	3.532	0.245	Ohm
Q2	0.011	0.002	F.s ^(a - 1)
a2	0.456	0.019	
R2	6.753	0.525	Ohm
s1	5.987	0.275	Ohm.s ^{-1/2}

The standard error of the elements that were not fixed (Q2, a2, R2 and s1) increase as these low frequency influenced elements are now required to fit to the full spectra. At the lower frequencies, diffusion becomes the dominant process and is mostly described by the semi-infinite Warburg element. As this low-frequency tail of the Nyquist bends to a steeper angle than the Warburg element is capable of we see that the standard errors increase. This suggests another element could be added to improve the fitting of the lower-frequency points but this raises the question: which element could be added which makes sense within the physical system? There is a danger of using too many elements so that the fitting produces very low standard errors without any physical meaning.

The Bode diagram for the same sample is shown in Figure 66. The magnitude and phase of the modelled fit is consistent with the real data at low frequencies but departs from the real data as the frequency increases. This is a relatively consistent trend across the samples as can be seen in appendix H.

Not all the samples, though, were able to be fitted with acceptable standard errors. Appendix H.2.1 groups the errors which are larger than the value by circuit element and again states whether the error is 5 times larger than the calculated value. This analysis identified the Warburg element and R2 describing the charge transfer resistance as the two most problematic of the circuit elements. Some of the errors are to order of 10¹⁵⁺ indicating significant uncertainty in the fitting and point to unreliable experimental measurement. It is unlikely other Warburg elements would aid the fitting in these samples given the other EIS spectra fitted using the semi-infinite Warburg delivered more sensible fitting results. The modified inductor (La1), ohmic resistor (R1) and CPE (Q2) only resulted in a few samples which produced a larger error than the fitted value and none of these were to orders of excessively large values giving confidence in the accuracy of these fitted values.

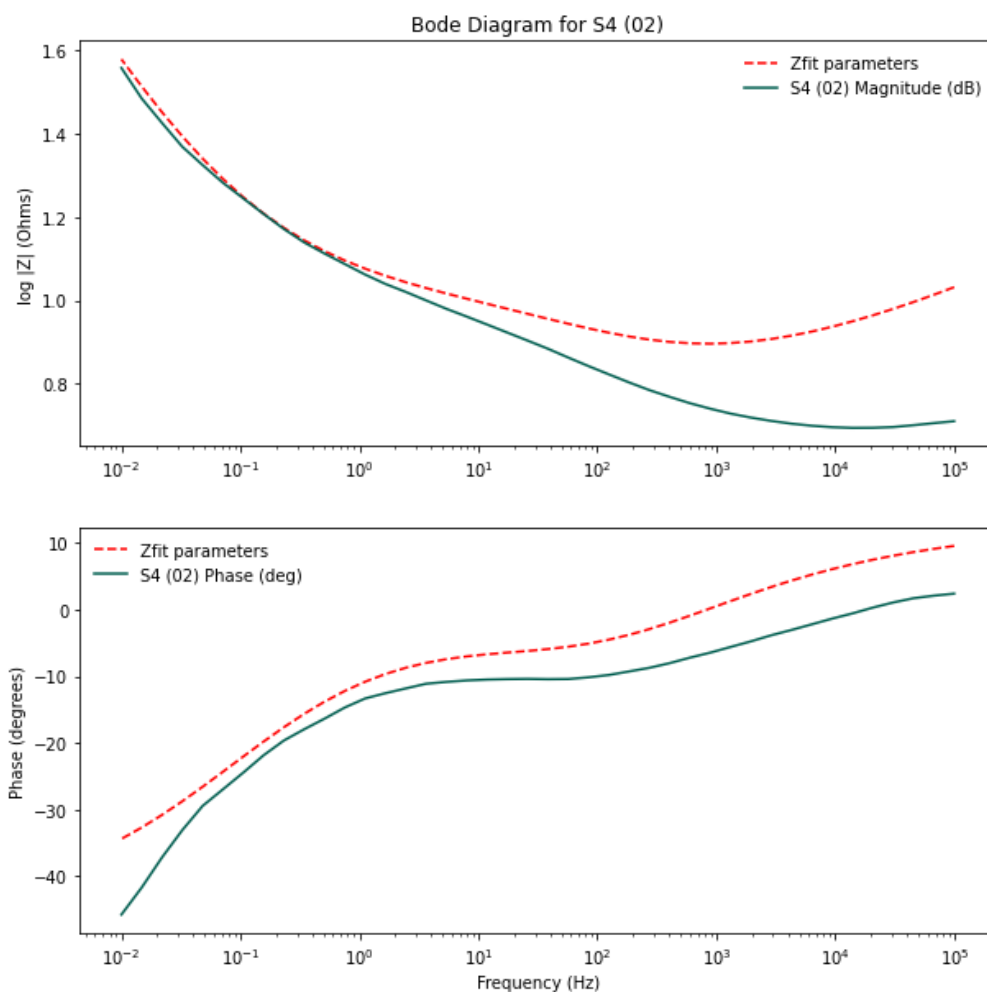


Figure 66 Bode Diagram for sample S4

As discussed, the fitting values for the ohmic produced errors within sensible tolerances so this data can be compared with the DCIR values found from the ohmic drop analysis from the galvanostatic charge-discharge analysis. The ohmic resistances derived from the equivalent circuit fitting for each sample are shown in Figure 67. The ohmic resistances found from PEIS spectra are predominantly between 4 Ω – 6 Ω with a few outliers above and below this range. The DCIR values are of a magnitude of 6 Ω – 8 Ω which is higher than what was found from the equivalent circuit fitting. One possible explanation for the difference is that the ohmic drop is measured at a full state of charge whereas the EIS measurement was conducted at a low state of charge at open circuit. Protons diffusing in and around the fully charged electrode at -0.5V vs SCE will have higher ionic resistance due to less free interstitial sites for hopping being available than at open circuit where there is more free sites. In other words, the resistance of the electrode is affected by the state of charge (SOC) though further work would be required to verify this is the cause.

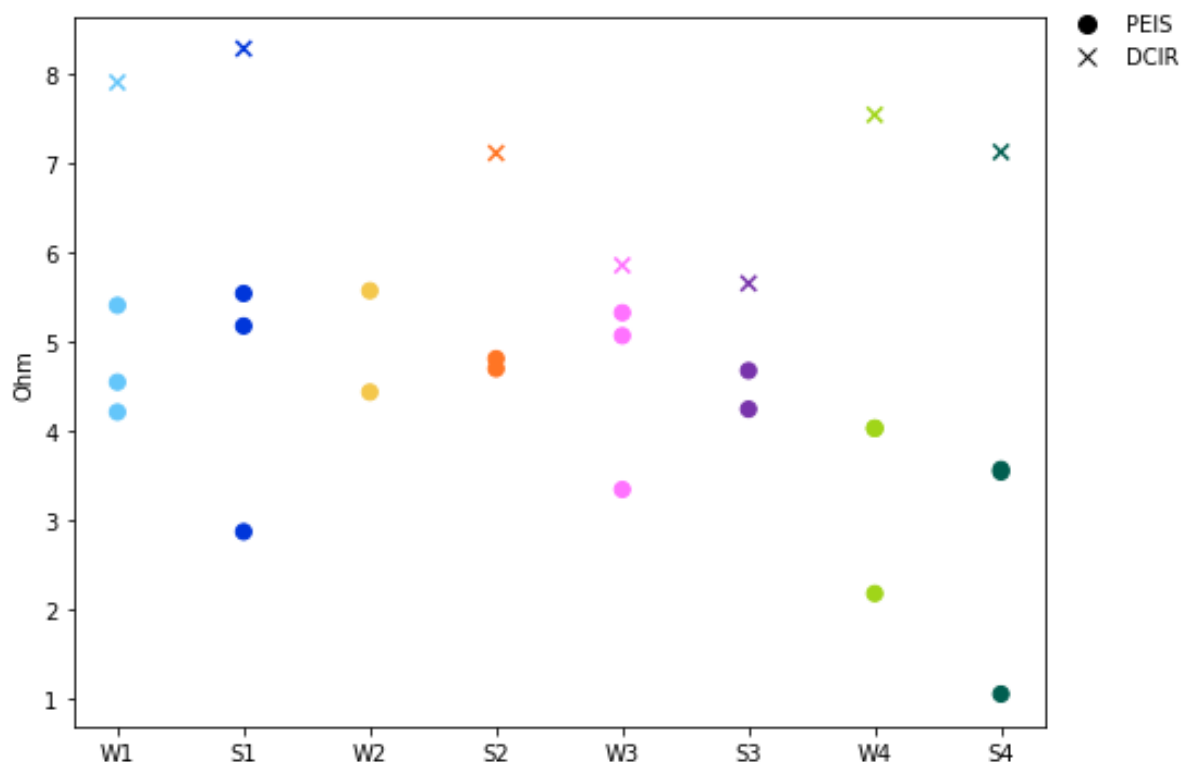


Figure 67 Resistance of R1 from fitted equivalent circuit across the sample range plotted with dots and the average DCIR values from GCD data denoted by x

The Electrochemical Impedance Spectroscopy (EIS) analysis encountered challenges due to the poor quality of some of the recorded data, which was quite varied even with different runs of the same sample type. The fitting resulted in large standard errors, particularly in the fitting of low frequency dominated elements like the Warburg. This variability compromised the overall reliability of the EIS analysis. The best agreement was found for samples which had the largest fitting errors, which gives low confidence in this comparison. The ohmic resistance of the solution was an element which broadly returned fitting values with low error, with values lower than obtained from GCD experiments. This may be due to the state of charge varying the resistances. Despite these issues, some of the recorded data was successfully fitted to the equivalent circuit model, indicating that while the results were not uniformly robust, a subset of the data delivered sensible fitting parameters.

4.5 Summary of Performance

The reported binder-free tungsten-tungsten oxide electrodes were evaluated using cyclic voltammetry (CV), galvanostatic charge-discharge (GCD), and electrochemical impedance spectroscopy (EIS) to assess their performance as energy storage electrodes and to understand the extent of pseudocapacitive charge storage behaviour in the data. The key findings from each technique are summarised as follows:

- The cyclic voltammograms of numerous samples did show proportionality between potential and charged passed at low scan rates, in line with pseudocapacitive

behaviour. A maximum capacitance of 186 Fg⁻¹ measured at 1 mVs⁻¹ was found to be lower than other reported tungsten oxide electrodes in literature. Upon increasing the sweep rate above 5 mVs⁻¹ the shape became a more pointed CV and noticeably suffered from high ohmic resistances. The pseudocapacitance was probed using the Dunn method and the capacitive proportion of the stored charge was found to increase with sweep rate with a simultaneous drop in faradaically stored charge. This was attributed to increased congestion from proton movement at higher sweep rates and the poor electrical conduction of the electrode. From this analysis it was demonstrated that the “nose” at the most positive potential end of the CV was entirely capacitive and indicates the potential window of the CVs extended beyond the intercalation region.

- The GCD data similarly showed some proportionality between charge passed and potential within some regions. As noted with the CV data, the GCD curves showed that the samples were “over-discharged” to positive potentials. The charge-discharge curves were shown to be more linear, and therefore more pseudocapacitive, when the potential window of the figure was reduced 0.4V vs SCE to 0.2V. The GCD curves suffered from large ohmic drops upon switching the current between charging and discharging cycles and may have benefitted from resting for a brief period between these. As with the CV analysis, the capacitances calculated from the data were found to be lower than those reported of powder-based tungsten oxide electrodes found in literature.
- The PEIS data was quite varied and challenging data to interpret. The recorded data was varied even within repeats of samples and made fitting challenging. Some elements, especially those dominant in the low frequency region, produced large errors. Nevertheless the data was fitted to an equivalent circuit and some partial conclusions were drawn: the ohmic resistances were to the same order of magnitude of the DCIR analysis from the GCD data but generally were lower.

In summary, whether the charge storage measured in these tungsten oxide electrodes may be correctly described as pseudocapacitive proved a complex question to answer. The data pointed to a pseudocapacitive performance when slow charging rates were employed during the measurement. However, the pseudocapacitive aspects in the data disappear upon faster rates of charge transfer due to a compounded effect of protons encountering greater congestion and therein ohmic resistance as they diffuse to the surface of the electrode and from the poor electrical conductivity of the working electrode. The deterioration in pseudocapacitance with increasing rates of charging and discharging was accompanied with a collapse in capacity in all the samples. Even still, the derived capacitances at low rates of charging and discharging were lower than other reported tungsten oxide electrodes in literature. The relatively lower capacitances, drop in performance with scan rate and the

pragmatic difficulty in handling and characterizing these electrodes delivered an unsatisfactory performance.

5 Physical Characterisation of W-WO₃ Electrodes

5.1 Introduction

This chapter provides a thorough physical characterisation of the eight distinct hydrothermally enhanced W-M_xWO₃ electrodes discussed in Chapter 4. The physical characterisation features a discussion of the appearance, crystal structure and microstructure of the samples, and seeks to explain how these properties have influenced their electrochemical performance. Some attention is given to explaining how the structures were formed from their given reaction conditions, in particular the pairing of conjugate anions and cations from salt and acids present, in the growth mechanism section. For consistency, the same labelling and colour scheme for samples outlined in Table 14 of section 4.1 is used where appropriate to identify samples on the graphs.

5.2 Appearance of foils

An obvious indicator of the impact the capping agent cation had upon the as-synthesised electrodes is their visual appearance. Figure 68 below shows photographs of each of the hydrothermal products produced. On the left of each photo is the deposit grown on a pristine tungsten foil and the right is the deposit grown on a seeded foil.

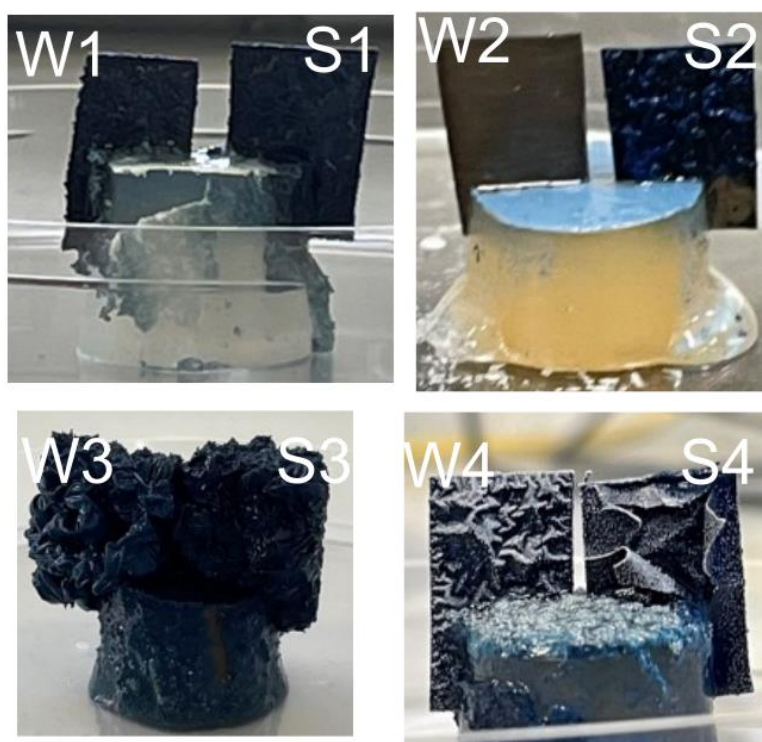


Figure 68 Photos of as synthesised hydrothermally grown electrodes with capping agent. In each photo the sample on the left is grown from a pristine tungsten substrate; the sample on the right is grown from a seeded substrate.

The choice of directing agent (or capping agent) present in hydrothermal synthesis drastically altered the nature of the deposited layer as may be seen in the photographs in Figure 68. The

sodium-directed samples formed a sputtered powder-like deposit (those in the top row). In the case of sodium chloride (samples W1 and S1), the samples looked very similar and were only indistinguishable from the intentional cutting of the corner of the pristine tungsten substrate pre-synthesis. The substrate used in the case of the sodium sulphate samples may easily be identified as the seeded foil had greater coverage than the pristine. The sample S2 was very similar to the W1 and S1 samples to the eye but was less well adhered.

In comparison, those made with ammonium sulphate (W3 and S3) produced larger colloidal layers which were continuous structures cocooning the substrate, very loosely adhered. The oxide on occasion may slide from the substrate underneath. These structures, like those made from NaCl, were indistinguishable from one another. Although these colloidal oxides appear very close to one another it should be noted they were not adjoined and in no instances were found to be adjoined.

The final capping agent to be used was rubidium sulphate and this produced glossy smooth films across the surface, quite different from the others. These films often rose outwardly from the surface as may be seen in the image of S4, though this also occurred in the W4 samples made from pristine substrates. Indeed, these samples, like those made from ammonium sulphate and sodium chloride, were identical to one another by the human eye and had to be distinguished using the cut substrate corner.

One thing that these layers shared was their unstable fragility, delaminating from the substrate through a range of mechanisms: drying out, surface tension, moving between different pH solutions. A careful handling and storage procedure was necessary to complete the electrochemical studies and the characterisation featured in this chapter.

5.3 Crystal structure

A schematic of the hexagonal crystal structure of tungsten oxide is visualised in Figure 69 which may be seen to be stabilised with a central “tunnelled” cation M⁺ and potentially water molecules too.

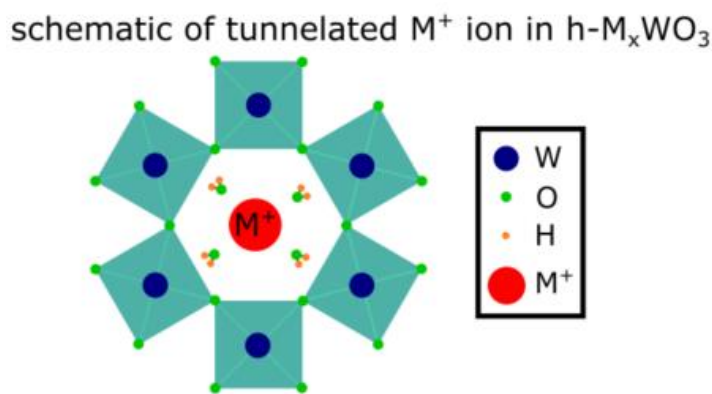


Figure 69 Schematic of tunnelled M⁺ in h-WO₃ bronze. Adapted from [47], [112], [113]

Powder X-ray Diffraction was used to identify the crystal phase of the hydrothermal deposits and the obtained spectra for the 10 foil samples may be seen in Figure 70. The oxide was scraped off one side of the sample so that the oxide surface could lie flat on the XRD instrument stage, and each was scanned as if it were a powder sample. Given each sample had a different thickness, this resulted in each scan delivering a different intensity.

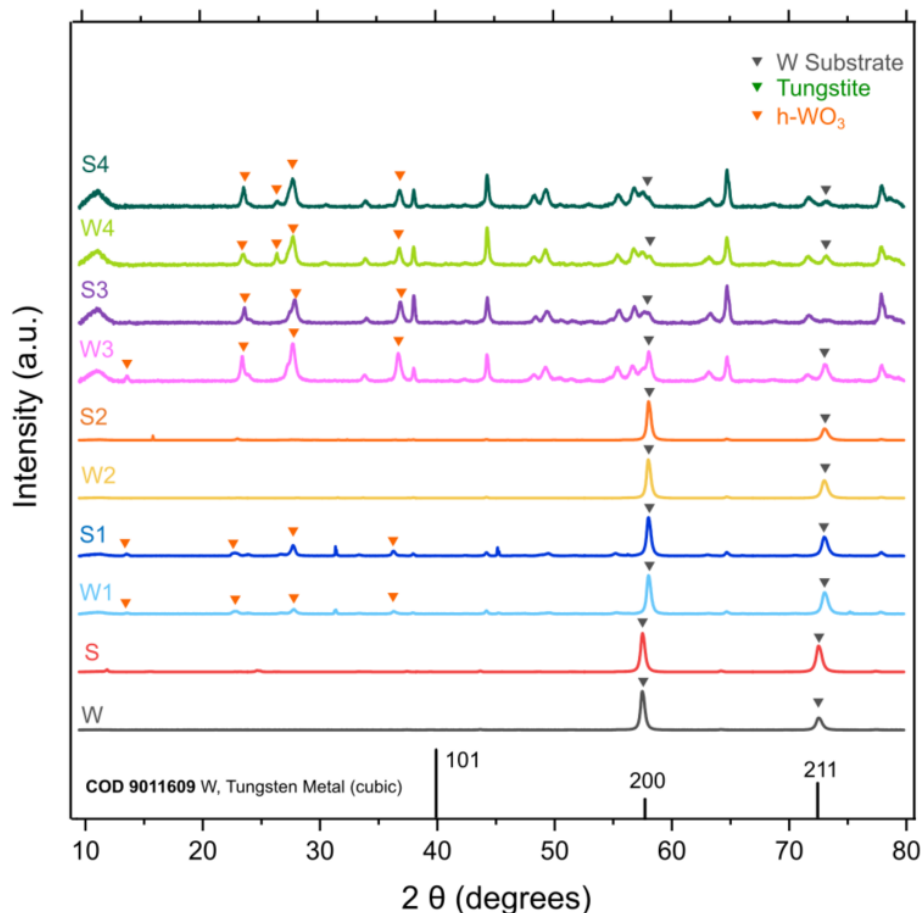


Figure 70 XRD of all hydrothermally deposited samples

For instance, there is a significant difference in the measured intensity between the rubidium and ammonium-directed samples (top four lines) and the rest of the samples despite the same scanning conditions being used. This may be explained from viewing the images in Figure 68 and XRD theory.

Using conventional powder XRD on these samples, a flat sample is desirable because it ensures uniform scattering of the incident X-ray beam, and a thick layer of oxide is also desirable so that the beam interacts with more oxide and less substrate.

The rubidium and ammonium-directed samples have large deposits but uneven surfaces, and this results in artefacts at the beginning of the scan. These samples do show far stronger oxide peak intensities, due to the thicker oxide deposits giving the x-ray beam more interaction than the thinner deposits. This does point to the powder XRD method being suboptimal to characterise these oxide layer samples, particularly over the 2θ range used.

There are two large peaks from the tungsten foil given at 58° and 73°. The relative intensity of these peaks makes it difficult to identify oxide peaks. Given the hexagonal peaks of interest mostly fall before 50° the data was trimmed to between 10° and 50° on the 2θ axis and renormalized. This was completed to make the best use of the available data by magnifying the 2θ region of interest and the resulting graph may be seen in Figure 71. Once this was completed, the spectra obtained for each of the bronzes become more similar, sharing similar features, and allowing for peaks to be identified.

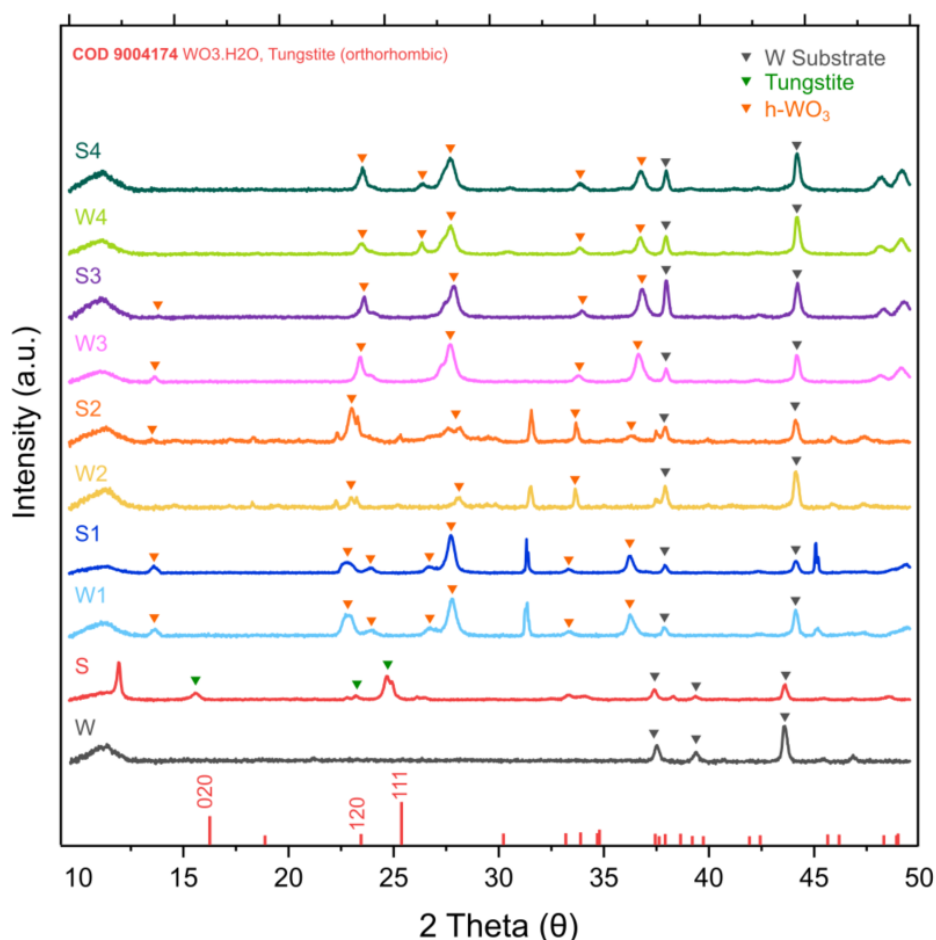


Figure 71 XRD reduced 2θ and renormalized

The seeded substrate, S is identifiable as tungstite, hydrated WO₃·H₂O lattice that is stretched by water molecules into an orthorhombic shape – the powder diffraction file of which may be seen along the bottom of the figure, as well as Figure 17 in section 3.2.1.3 of the Methodology. The lattice parameters of S were given in Table 3 Lattice Parameters of Tungsten Oxide Polymorphs in section 2.2.1. The crystal parameters for the tungstite phase were identified as being less suited to epitaxial hexagonal growth than other monoclinic phases however a decision was made to not alter this surface. The first reason was in the event the surface persisted through the hydrothermal reaction then the hydrated structure which has excellent proton intercalation properties would be preserved. The second was that access to furnace

equipment during the COVID-19 was limited and thus there was no way to convert the structure to anhydrous monoclinic.

From the figure it is clear that only a single phase of WO₃ can be detected in the hydrothermal products, with no identifiable tungstite peaks. This is an indication that the tungstite does not persist through the reaction. More sensitive XRD would be required to confirm its disappearance to confirm this.

The following sections now look more closely at each spectra above in sequence of the cation used in the synthesis.

5.3.1.1 Sodium Tungsten Bronze (Samples W1-2, S1-2)

The samples directed by sodium ions, either sodium chloride or sulphate, are displayed in *Figure 72* and one can identify the presence of hexagonal sodium tungsten bronze from comparison with PDF 01-081-0577. This is one of several hexagonal-Na_xWO₃ powder diffraction files, with different values of x and water content, which may be applied to these samples because they share identical peaks. To deliver these values further elemental analysis would be required to give an accurate value to the sodium content.

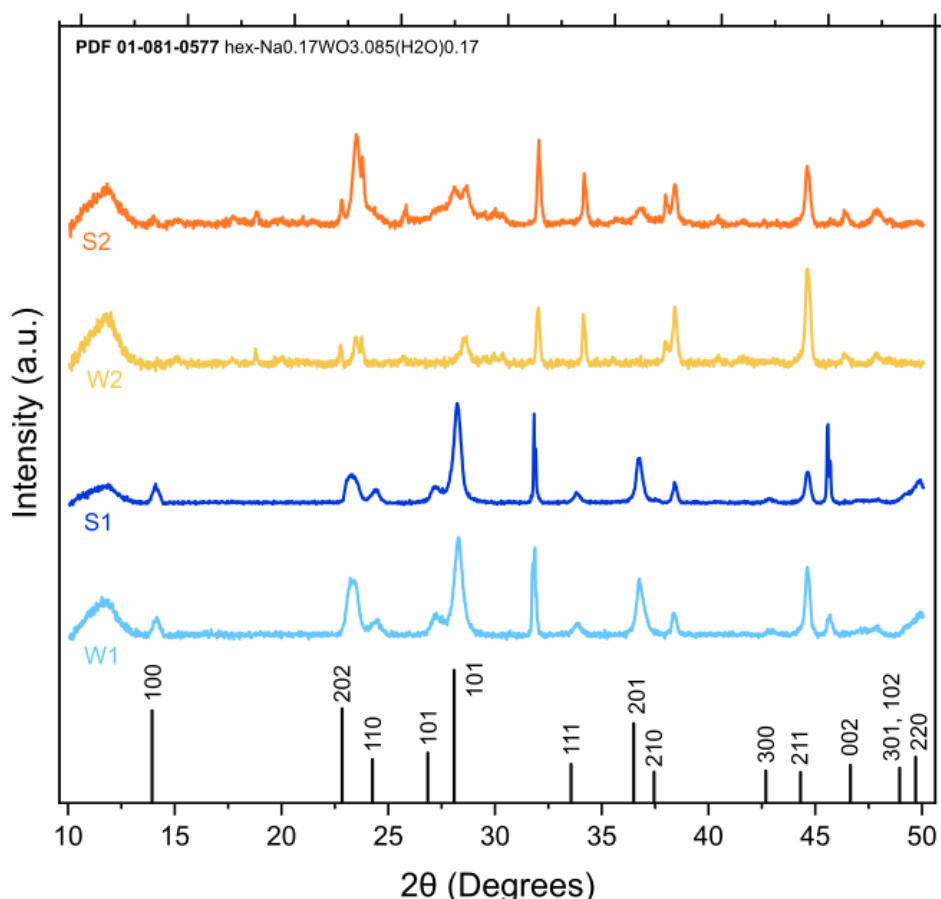


Figure 72 XRD Spectra of samples W1, S1, W2 and S2 synthesised with Sodium based capping agents (NaCl and Na₂SO₄) respectively

These samples display a sharp peak at 32 degrees which does not feature on any of the other samples, including substrates and may not be indexed to any other phase of WO₃. It is

possible that there was residual sodium salt present in the sample, despite washing. Sodium sulphate (131) and sodium chloride (200) both share a strong peak at 32 degrees supporting this [114]. The samples were washed gently in water and dried in ambient air before the measurement was taken but even still it is possible some remained in the sample.

5.3.1.2 Ammonium & Rubidium Tungsten Bronze (W3-4, S3-4)

The individual spectra of the W3 and S3 samples, made with ammonium sulphate as a capping agent, may be seen in Figure 73 and can be indexed to hexagonal ammonium tungsten bronze (HATB) PDF 00-042-0452. Similarly, as with the NaCl samples, there are multiple HATB PDFs which may be applied to the data and without further analysis it is impossible to provide a more accurate identification.

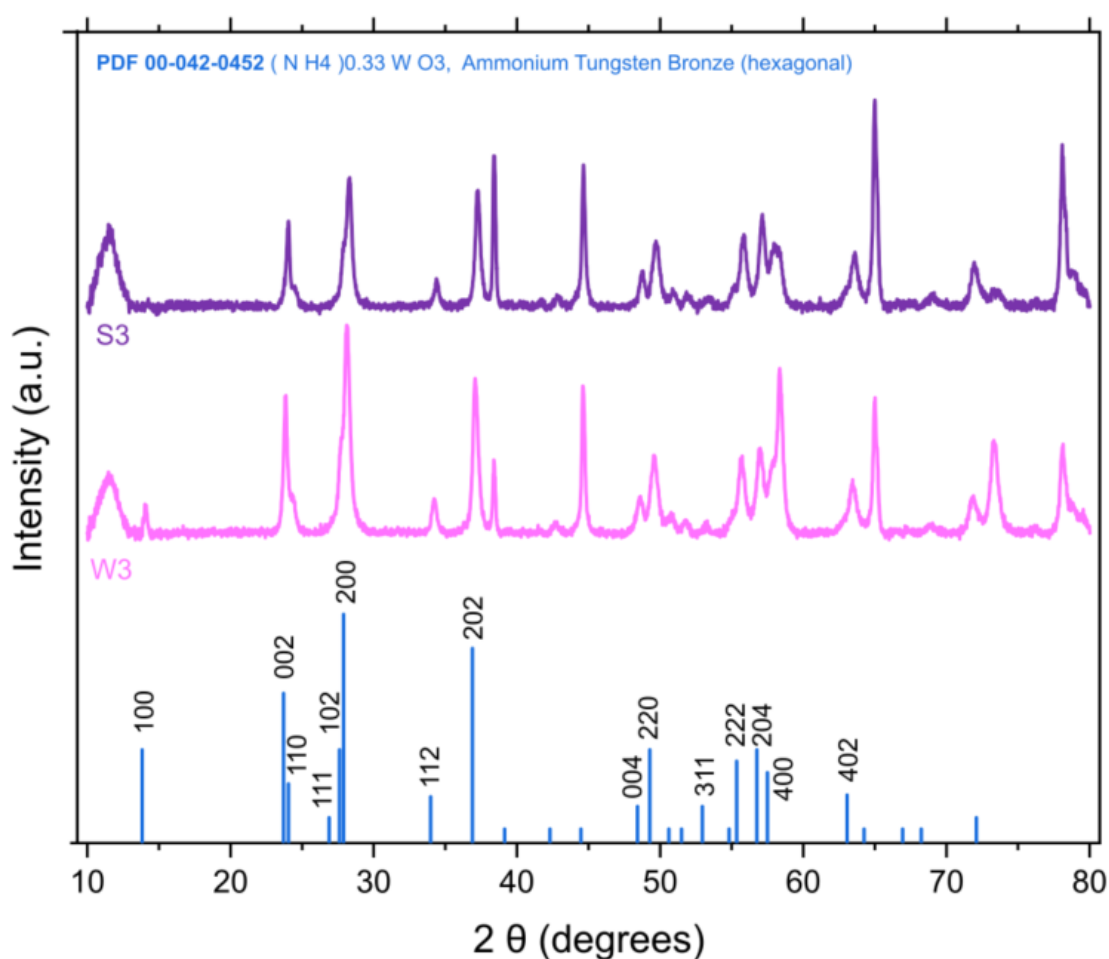


Figure 73 XRD Spectra of samples W3 and S3 synthesised with ammonium sulphate

Finally, the individual spectra of the rubidium-directed samples, W4 and S4, are shown in Figure 74. Like the other samples the spectra are well indexed to the rubidium tungsten bronze PDF provided (01-070-0803) and it may be noted that the spectra are nearly identical to that of the reported sample from which this synthesis procedure was adapted [84].

The rubidium and ammonium-directed samples' spectra have sharper peaks than their sodium counterparts which may be taken to show a higher degree of crystallinity however it seems more likely that this is due to their characteristically thicker deposits interacting more with the X-ray beam. [115].

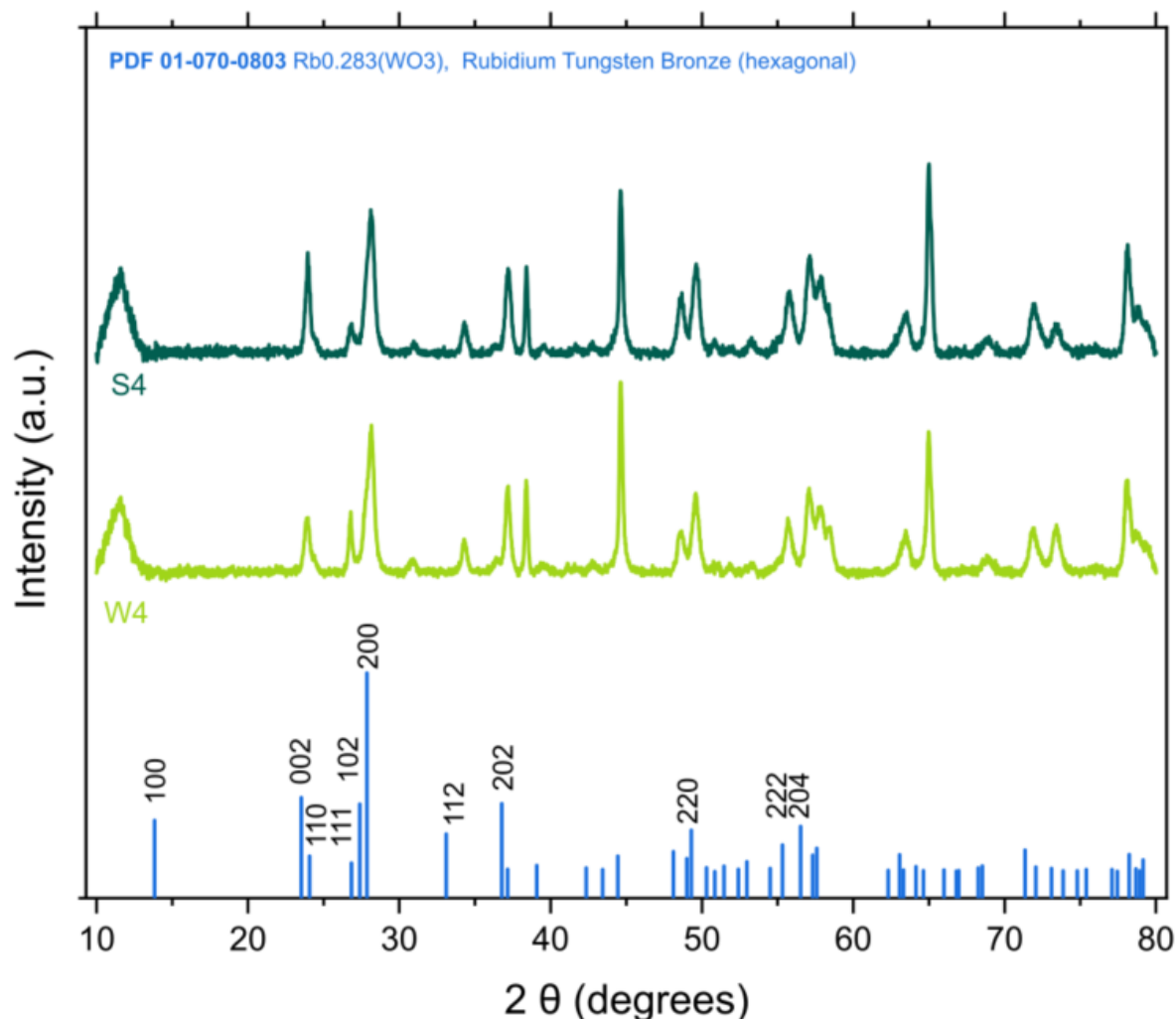


Figure 74 XRD Spectra of samples W4 and S4 synthesised with rubidium sulphate

5.4 Microstructure (SEM imaging) planar to surface

The microstructure of the obtained foils from the hydrothermal reaction was characterised using Field Emission Scanning Electron Microscopy (FE-SEM or SEM) in two configurations: planar to the surface which shows the morphology of the surface oxide, and as a cross-section showing the junction between W-substrate and WO₃. This section details and discusses the planar results with cross-sectional results presented in section 5.5.

These SEM images were taken from as synthesised samples except in the cases of W3 and S3. Given their colloidal nature, the ammonium-directed samples required the layer to be removed, dried, and stuck down to avoid loose material that may have damaged the instrument under vacuum. This will be discussed in the W3 and S3 Sections.

5.4.1.1 Substrates

It is important to first characterise the surface of the substrates used in the investigation so that the observed change delivered by the hydrothermal reaction may be fully understood. The micrographs of pristine tungsten foil and the seeded substrate (orthorhombic oxide surface) are shown in Figure 75 and Figure 76 respectively.

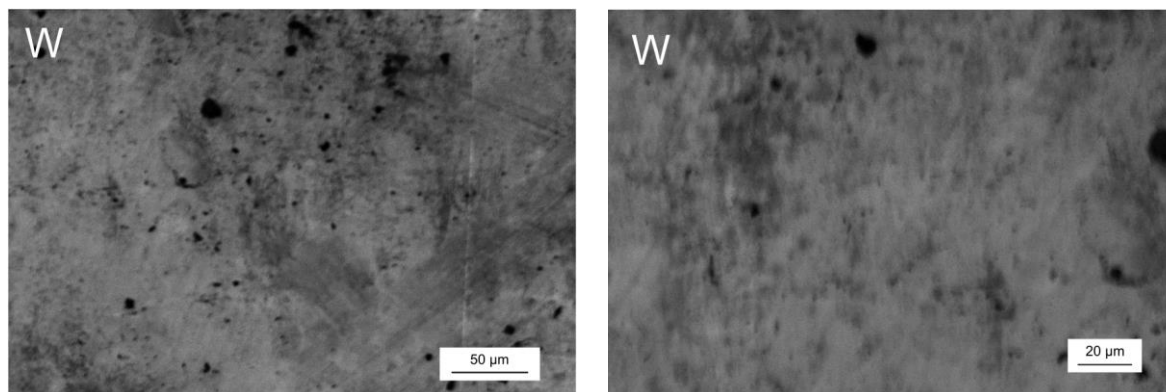


Figure 75 SEM Micrograph of Tungsten Foil Substrate. This is the only image taken on a W-Filament SEM.

The pristine tungsten foil has a flat, featureless surface. The marks on the surface may come from handling the foil during the measurement. In stark contrast to this is the highly textured surface of the Seeded foil where many oxide structures are normal to the surface plane.

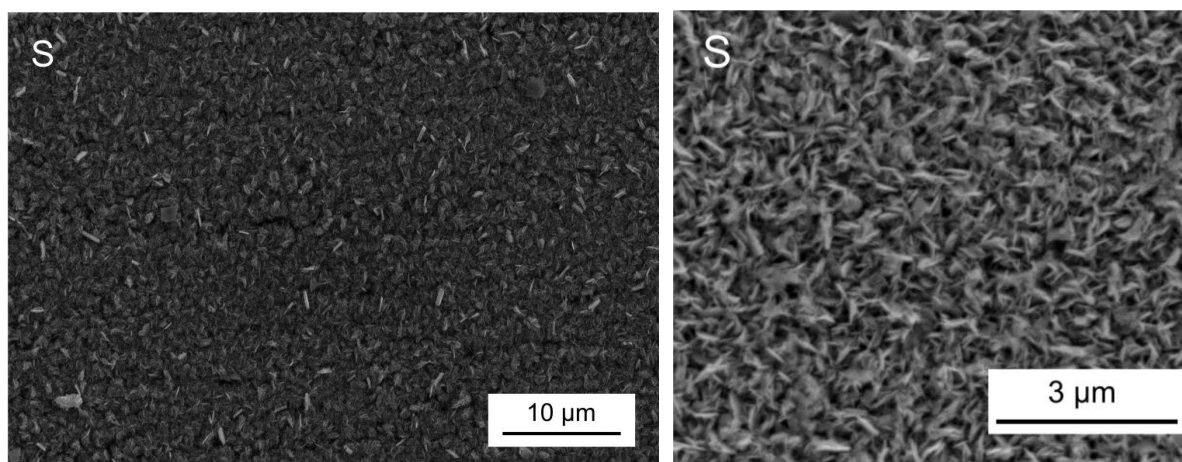


Figure 76 SEM Micrographs of Seeded Substrate S

This surface is similar to the surface obtained from Widenkvist et al [51], the procedure from which the seeding step used here was taken. The jagged tungstite crystals protrude perpendicular to the surface of the oxide. There is wide coverage of the whole surface, and it may be seen from the micrograph on the left of Figure 76 that this is a consistent surface.

A key distinction referred to throughout the following discussion is that of the initial states these substrates enter the hydrothermal reaction. The pristine foil, as may be seen in Figure 75, has no visible oxide surface. On the other hand, the seeded foil, S, has thousands of existing WO₃ crystals at its surface from the onset of the reaction. As identified from the XRD data, this seed layer of oxide is expected to dissolve in hydrothermal conditions and these substrates will

have substantially different local concentration of crystals (S high, W low) at the onset which will influence the growth.

5.4.1.2 NaCl Directed Samples W1 and S1

The planar view micrographs of samples W1 and S1 are displayed in Figure 77. At a 500 nm scale, it may be seen that each of the samples are composed of thin nanorods, though neither show uniform aspect ratios or epitaxy. These base nanorods have conglomerated on the microscale into a fibrous structure, of which the density of these fibres drastically increases when a seeded substrate is used.

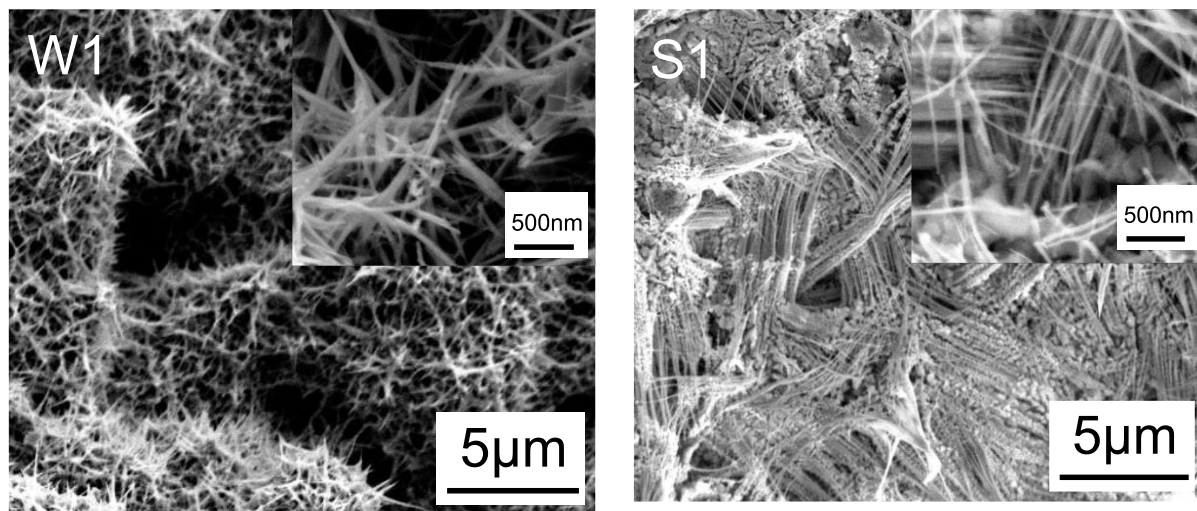


Figure 77 SEM Micrographs of samples W1 and S1 obtained through hydrothermal reaction using NaCl as a capping agent

Figure 78 shows a less magnified image of the S1 surface and it can be seen the dense, fibrous structure of Figure 77 repeats over the surface. These nanorods appear to rise out of the surface like in the Substrate S but have grown too large and have collapsed into one another.

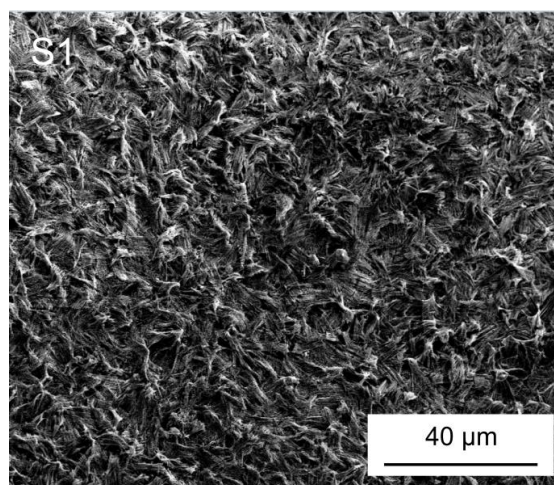


Figure 78 SEM Micrograph of S1 obtained from hydrothermal reaction with NaCl as capping agent. A less magnified image is shown to show the uniformity of the surface

This surface is quite different from that obtained from a W-pristine tungsten sample made in the same conditions, presented in Figure 79. This surface is less cohesive and is instead composed of various-sized clumps, or particles, of oxide. Some of these, to the bottom right of the image, are quite large. It should be noted that the larger and smaller particles were composed of the same microstructure seen in Figure 77 when zoomed in.

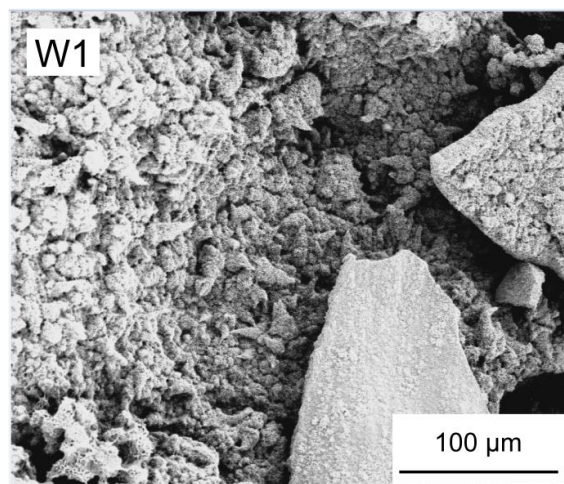


Figure 79 SEM Micrograph of W1 obtained from hydrothermal reaction with NaCl as capping agent. A less magnified image is shown to show the uniformity of the surface

What is interesting is that the samples W1 and S1 were identical to the human eye and were both composed of thin spindles as a base structural unit. However, the way that these base units manifest into larger structures is quite different and because the only difference in the synthesis procedure was the substrate surface it can be reasoned the size, geometry and placement of structures grow according to the initial surface concentration of WO₃ at the beginning of the reaction. The seeded sample, with a high concentration of available surface WO₃ nuclei, produced a more regular, cohesive surface oxide layer than the low-concentration WO₃ pristine tungsten foil. The possible mechanism for this is discussed in further detail in the growth mechanism section.

The seeded sample, S1, displayed better electrochemical performance than W1 too and this again must be accredited to the more regular surface structure providing a higher active surface area. The large uneven particles present in W1 reduce the available surface area which interfaces with the electrolyte in contrast to the more regular pattern S1.

5.4.1.3 Na₂SO₄ Directed Samples W2 and S2

The micrographs of samples W2 and S2 are displayed in Figure 80. Akin to the sodium chloride samples, there is more of an apparent uniformity in the seeded sample with repeating structures than in the unseeded sample. However, this manifests quite differently when using sodium sulphate: there are flat planar regions from which emerge microspheres, or clumps of agglomerated microspheres. The uniformity of the S2 materialises as clear spacing and a

consistent shape. The unseeded sample W2 will be discussed first before S2 and a comparison of the two.

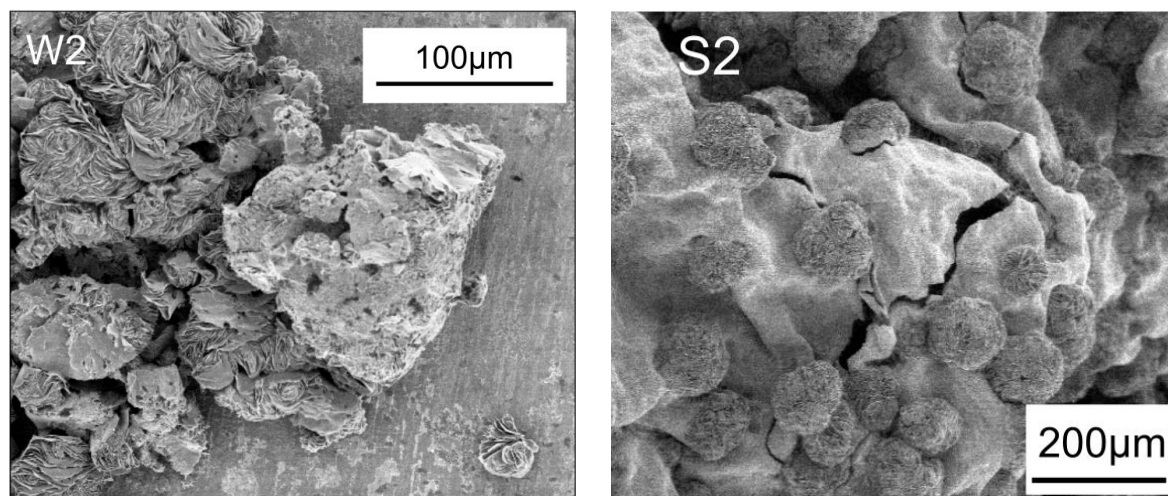


Figure 80 SEM Micrographs of samples W2 and S2 obtained through hydrothermal reaction using Na₂SO₄ as a capping agent

A closer magnification of the flat planar region on the right-hand side of the W2 image presented in Figure 80, is displayed below in Figure 81. This surface from 100 μm down to 1 μm scale is a flat but continuous layer. It is distinct from the pristine foil that enters the reactor (Figure 75) thus it seems likely this is an oxidised surface made of a very flat oxide structure.

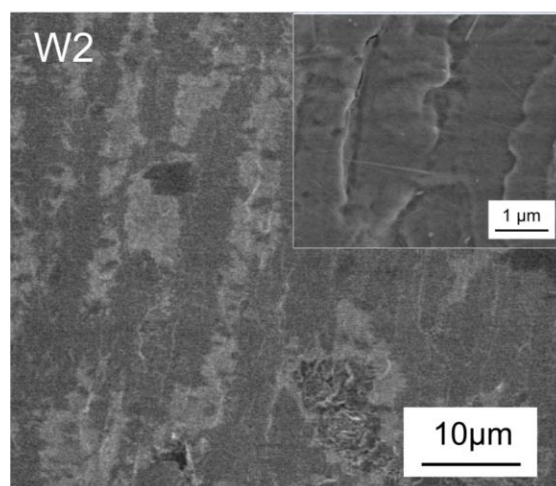


Figure 81 SEM Micrograph of W2 obtained from hydrothermal reaction with Na₂SO₄ as capping agent. A higher magnification is given of the flat plane region of the oxide layer.

The region on the left of Figure 80 appears to be clumps or particles of oxide. A closer magnification of this region is given in Figure 82: the left image shows string-like nanorods and plates agglomerated together in a random distribution; the right image shows a close-up of the more spherical-like particles which are composed of plates, reminiscent of petals of a rosebud. Flowerlike and nanoplate structures are widely reported in WO₃ powder research [71] composed of plate-like structures assembled radially around an axis, resulting in a flower-

like morphology. This manifests as different structures, including WO₃ flowers grown on FTO glass [85] and well-aligned orthorhmic-WO₃ plates grown from a seeded tungsten substrate [59]. However, the structures presented here are quite distinct from those found in the literature, showing a rosebud structure which is confined within a spherical particle.

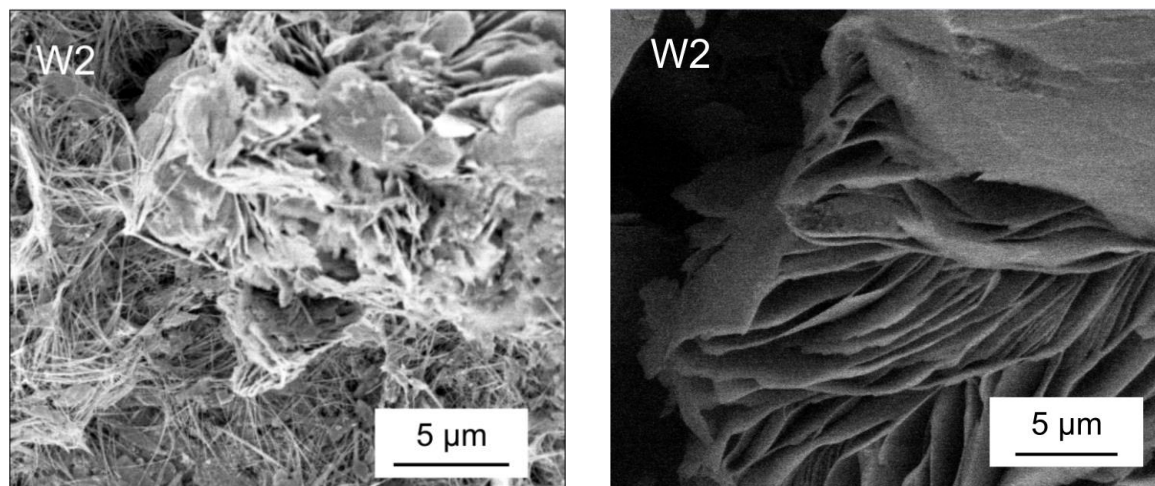


Figure 82 SEM Micrographs of sample W2 displaying two distinct areas within the clump region

Analysing the S2 sample with a similar approach as W2, one may look at the surface regions and the protruding particles present in S2 (right micrograph of Figure 80). Taking first the zoomed-in image of the surface region of S2 shown in Figure 80, the surface is immediately more interesting than the counterpart layer seen in W2 (Figure 81). Here there is a textured array of nanowires that appear to have coalesced into a fibrous structure just as seen in S1.

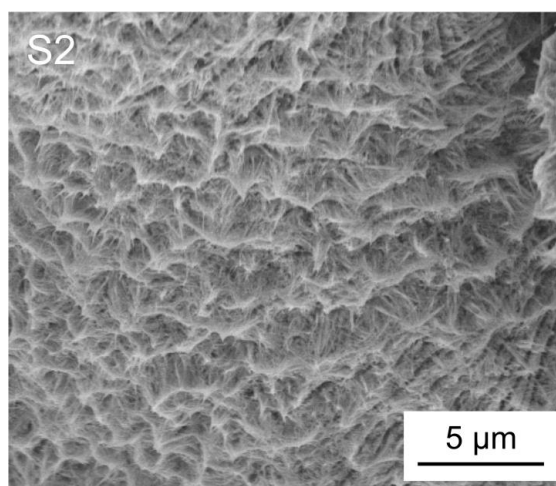


Figure 83 SEM Micrograph of sample S2 obtained through hydrothermal reaction with Na₂SO₄ as capping agent, displaying the flat region

The particles which protrude from this surface in S2, as mentioned, are more regularly sized particles than those present in W2. A more magnified image of these is shown in Figure 84 and like W2 it may be seen they are composed of nanoplates. What is distinct from the W2 sample is the spacing between each rosebud and their more uniform size. Where there is agglomeration between these rosebuds, the edges of individual spheres may still be identified.

It is interesting that again the Seeded substrate has produced a more uniform surface than the pristine foil. This establishes a trend which is discussed further in the growth mechanism section of the chapter. What may be clearly explained is the superior performance of S2 compared to W2: the S2 surface is textured, covered in a nanorod surface layer dotted with many similar shaped nanospheres; the W2 surface is plain, and the particles clumped together creating a low-surface area electrode.

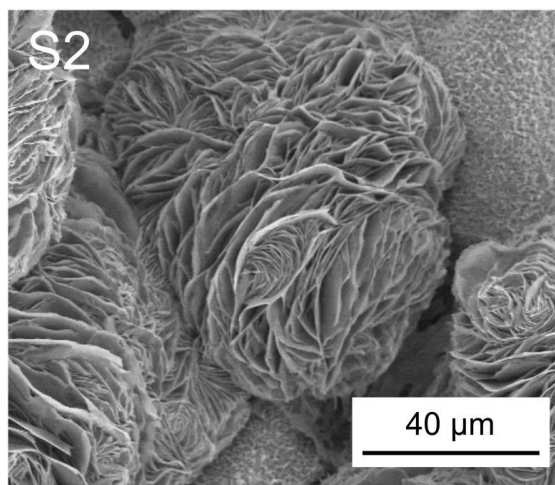


Figure 84 SEM Micrograph of sample S2 obtained through hydrothermal reaction with Na₂SO₄ as capping agent, displaying a closer image of rosebud-like structures protruding from the surface

At this juncture, a further comparison may be made between NaCl-directed samples (W1 & S1) and the Na₂SO₄ samples (W2 & S2). In particular, comment may be made upon the role of the anion, chloride, or sulphate, in solution because it was the only changed variable between these groups of samples.

The first comment to make is that the sulphate ion synthesis resulted in much less coverage of the pristine substrate than the chloride ion equivalent, visible both by eye, Figure 68, and in the micrographs. The greater coverage resulted in W1 having superior electrochemical performance compared to W2. It is unclear as to what aspect of sulphate drives this but may lie in sulphate's interaction with the W-foil surface.

Secondly, the anion in solution has a profound influence upon the microstructure which is obtained from the hydrothermal reaction. Chloride samples produced solely nanowires as a base structural unit from which larger structures are made; sulphate was capable of producing nanowires and nanoplates as structural units. Geometrically, the difference between a nanowire and a nanoplate is whether the structure is confined to grow in one direction or two. Specifically, if the lattice can grow anisotropically in one direction, a nanowire forms where a

single lattice facet favourably extends, or anisotropically in two directions, a nanoplate is formed where the lattice promotes growth in two directions.

Based on the results observed here one may summarise that sulphate permits lateral growth; chloride prohibits lateral growth. A possible mechanism for explaining this is speculated upon in the growth mechanism section.

5.4.1.4 (NH₄)₂SO₄ Directed Samples W3 and S3

The ammonium-directed sample had somewhat different bulk physical properties to the other samples prepared in this section (an image may be seen in Figure 68), which made handling difficult and necessitated a slightly different characterisation procedure. The layer was very hydrated, almost colloidal in nature and it was not adhered to the surface. The hexagonal (NH₄)_xWO₃ would slide off like a sheath, if allowed, under its weight and was extremely fragile as if held together by the surface tension of colloidal water. The micrographs of the top layer were taken by scraping the top surface off and letting it dry in ambient air before attaching it to a carbon adhesive pad for SEM imaging.

Upon removal of the oxide, it was apparent that the substrate underneath was not simply pristine tungsten but itself had an oxide surface. These two areas were examined, the top oxide surface and the foil beneath in both the unseeded (W3) and seeded case (S3). It is also worth noting in W3 and S3 that there is no longer a single cation in solution, from the capping agent, but also the Na⁺ present from the sodium tungstate. The total concentration of M⁺ ions was kept constant as discussed in more detail in the methodology section 3.2.2.2.

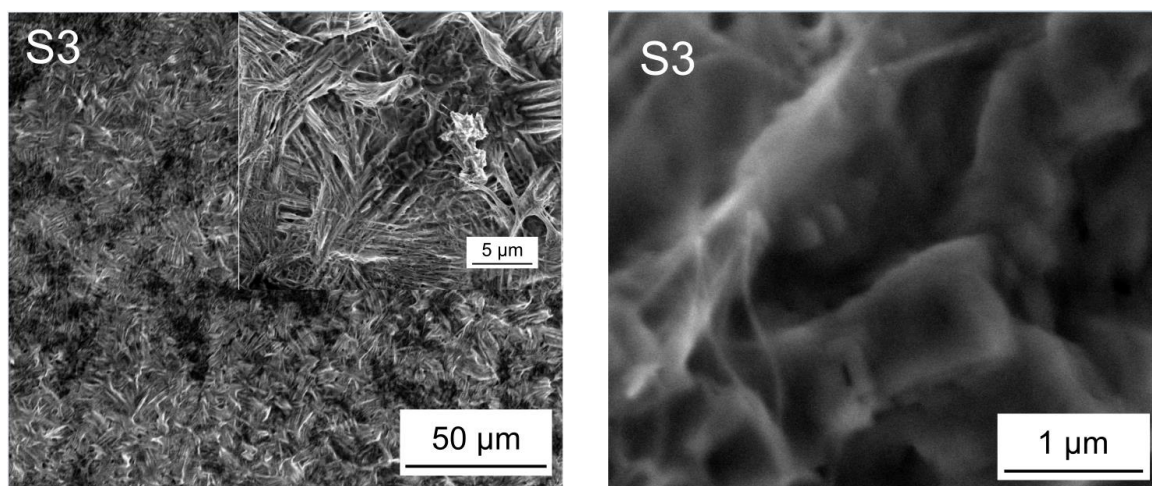


Figure 85 SEM Micrographs of the top oxide layer in sample S3 using different magnifications

Figure 86 shows the top layer of oxide present on the seeded sample at three different magnifications. The images on the left show a dense fibrous-looking layer remarkably like those obtained from the sodium chloride sample S1. It is difficult to say whether these are nanoplate-like structures or if they are the result of nanorods agglomerating together. Using a higher magnification (right image of Figure 86), one can see that both these are present; there appear to be thick nanoplate-like structures which are intersected by much thinner nanorods.

Despite the ammonium-directed layer looking identical to the eye (Figure 68), the observed microstructure of these layers is quite different, as was seen in the sodium chloride-directed samples. Figure 85 displays the top layer oxide surface produced from S3 and it is quite different from the top layer that covered W3. The W3 has a continuous surface with larger particles present upon the surface, and this continuous layer may be seen to be comprised of spindly nanorod structures. In the right image of Figure 85, there is an obvious distinction between nanorods and flatter, nanorod-type structures. Unlike the nanoplates in W2 and S2 which show some order, these structures show no organised arrangement, they are disorderedly interconnected.

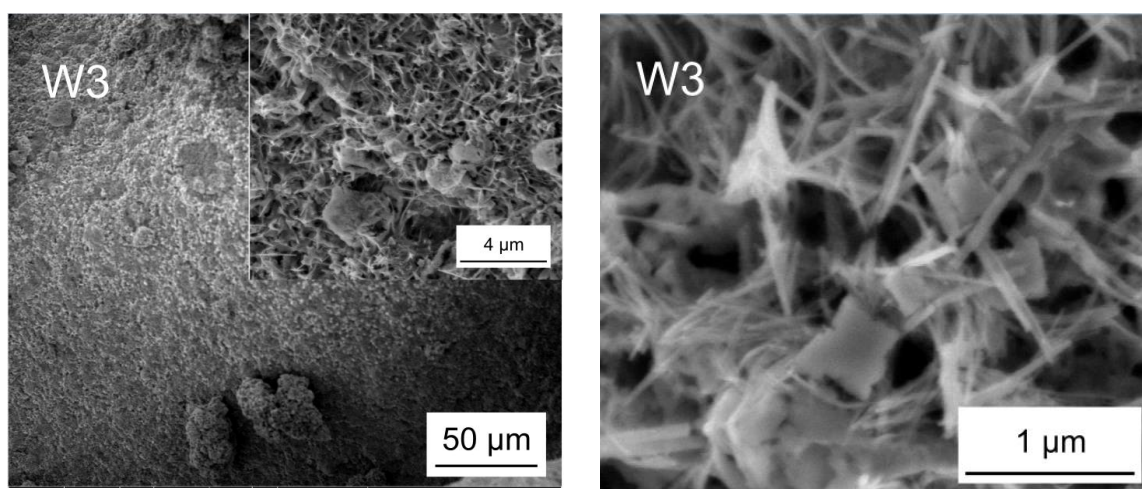


Figure 86 SEM Micrographs of the top oxide layer in sample W3 using different magnifications

The remaining oxide surface left on the substrate beneath these unadhered top layers is now discussed. Figure 87 shows the pristine W-Foil surface and it is reminiscent of the W2 surface, an almost continuous film of tungsten oxide which is peppered with smaller structures. It is unclear whether these particles are remnants from the top layer being removed or whether they exist separately from that layer.

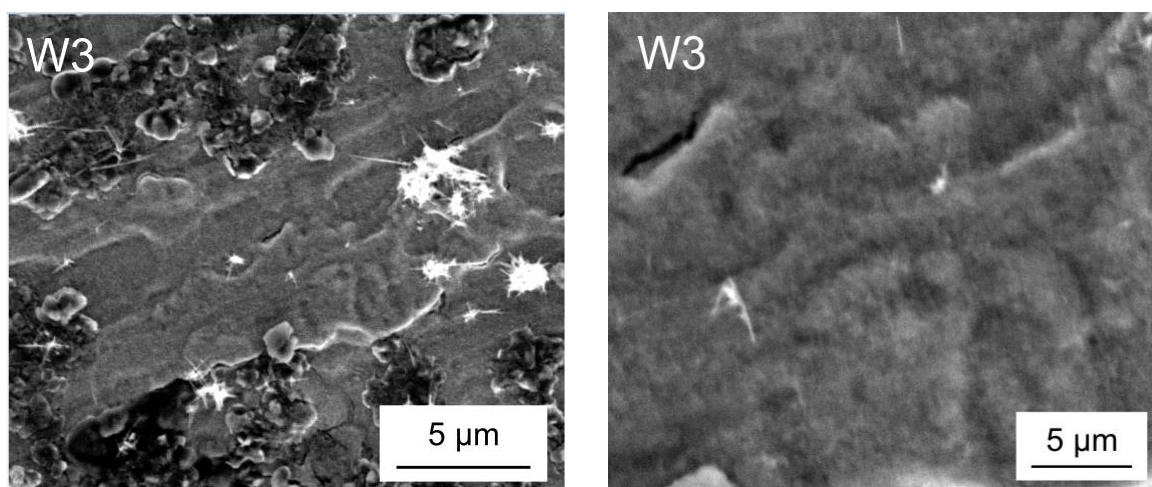


Figure 87 SEM Micrographs of substrate beneath oxide layer in sample W3

Looking now underneath the oxide layer to the substrate of S3 beneath there is a quite different microstructure to that seen in W3. Figure 88 in stark contrast to Figure 87 has quite a textured surface of nanorods upon the surface. There are regions of no growth like in W3, which may be a result of the top oxide layer being removed or maybe the way it grows. The seeded surface in this sample has achieved quite uniform nanorods, more so than in S1 and S2. The answer to this possibly lies in the unique pH and cation conditions created underneath a larger WO₃ blanket. It is difficult to analyse this further and would be left to further experimentation.

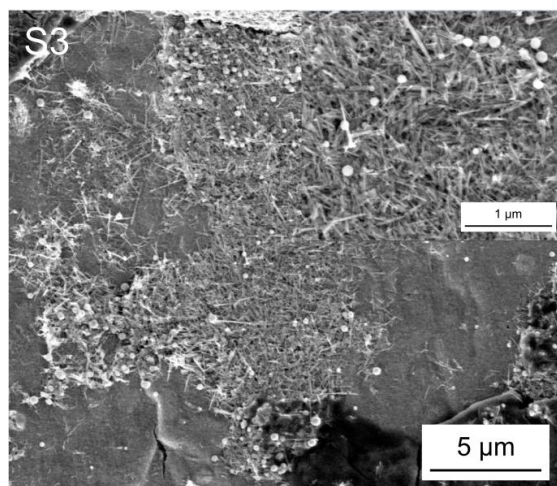


Figure 88 The surface beneath oxide in S3

These samples introduced ammonium ions to the reaction mixture, different from the purely sodium-driven synthesis before. The first remarkable thing is that considering W3 and S3 are identical to the eye the microstructures are quite distinguishable. This of course was the same for the sodium chloride-directed samples W1 and S1, and the samples W3 and S3 share similarities: the seeded samples produced uniform, dense fibrous structures, and the pristine W-foil samples had coherent surfaces peppered with dense structures.

Similarities between the surface beneath the W3 and S3 top layer, and the sodium sulphate samples W2 and S2 may also be drawn. The W2 and W3 samples share flat continuous film-like surfaces, the seeded samples conversely have a textured surface clearly showing oxide structures. These samples share sulphate as the anion in solution and its presence must again be noted as a possible cause of this. Moreover, the presence of sulphate ions in W3 and S3 again led to the formation of lateral growth structures that were not present in any chloride ion structures.

However, it is the role of ammonium ion which has undoubtedly led to the extraordinary differences between the sodium-driven samples. Ammonium is reported to be the most stabilising cation for the hexagonal tungsten oxide crystal [116]. This is a dual effect of its large ionic radius (~50% larger than Na⁺) and high interaction energy with the hexagonal-WO₃ crystal's tunnel [116]. The modelling work explains once in the tunnel, the ion's mobility slows

drastically in comparison to the smaller cations such as lithium, sodium, and protons to the extent it may even be considered permanently in the tunnel [116].

The synthesis of W3 and S3 involved reaction conditions where both sodium and ammonium influenced the oxide's growth. Based on ammonium's reported interaction with the hexagonal lattice and the presented results here, it is suggested that these ions played distinct roles in the oxide's growth. The ammonium ion has a preference for stabilising the hexagonal-WO₃ tunnel and once it is slow to leave; the sodium ion is unlikely to fulfil the role of tunnel stabilising ion and is limited to a roll mediating the double layer surrounding the growing crystals influencing their morphology. In other words, the ammonium is dominant in stabilising the lattice structure; the sodium may only contribute to directing the microstructure[47], [116].

This however would not explain the moist, colloidal, and bulky structure obtained which is drastically different. If sodium is limited to the morphology, why does it not match samples W1-2 and S1-2? This unique structure is proposed to come from ammonium's interaction with water molecules. Unlike sodium and other alkali metal-based capping agents, ammonium's four hydrogen atoms are capable of hydrogen bonding in addition to electrostatic interaction. Ammonium is capable of much stronger bonds with water molecules than sodium and thus pulls more water molecules into the growing oxide creating a far more hydrated structure. Whether these water molecules are held within the tunnels themselves or confined between layers of oxide is unknown. However, this would be consistent with the observed gel-like behaviour of the layer. This hydrated nature may well also explain why the surface was not adhered but detached, cocooning the substrate.

These samples, though interesting and unique, are a frustration to work with. The layer was extraordinarily challenging to use as an electrode. The electrochemical data of these samples was unreliable and makes difficult to link the microstructure to the observed electrochemical performance. The role of ammonium in WO₃ hydrothermal synthesis is quite interesting and may warrant further investigation.

5.4.1.5 Rb₂SO₄ Directed Samples W4 and S4

The final iteration of the four capping agents investigated was rubidium sulphate. Rubidium is a larger alkali metal cation than sodium but of a comparable size to ammonium. The results here offer further insight into the interplay between hexagonal-WO₃ and large cations with different properties. The samples reported here are grown from two cations in solution, rubidium from the capping agent and sodium from tungstate salt. As ever the total cation concentration was kept the same as outlined in section 3.2.2.2.

The observed microstructure of W4 and S4 are remarkably similar and presented together in Figure 89 at a scale of 100 μm. The hexagonal tungsten oxide directed with the addition of rubidium grows into what other authors have reported as nano-urchins, a morphology found in Mo-doped monoclinic-W₁₈O₄₉ [117], hexagonal-WO₃ powder using Rb₂SO₄ [83] (which

states nanorods form using K₂SO₄ and more platelike nano-urchin h-WO₃ using Na₂SO₄ [85]. Hexagonal WO₃ nano tree films, similar to those obtained here without the urchin structures, were grown from a tungsten foil using Rb₂SO₄ in different conditions [58]. Gu et al found these structures may be synthesised within a limited concentration window of rubidium sulphate and proposed a mechanism whereby microspheres spontaneously form from particles in solution to reduce their surface area. The proposed mechanism continued to say that these spherical particles then provide favourable sites for subsequent growth of nanorods which give the appearance of an urchin [83].

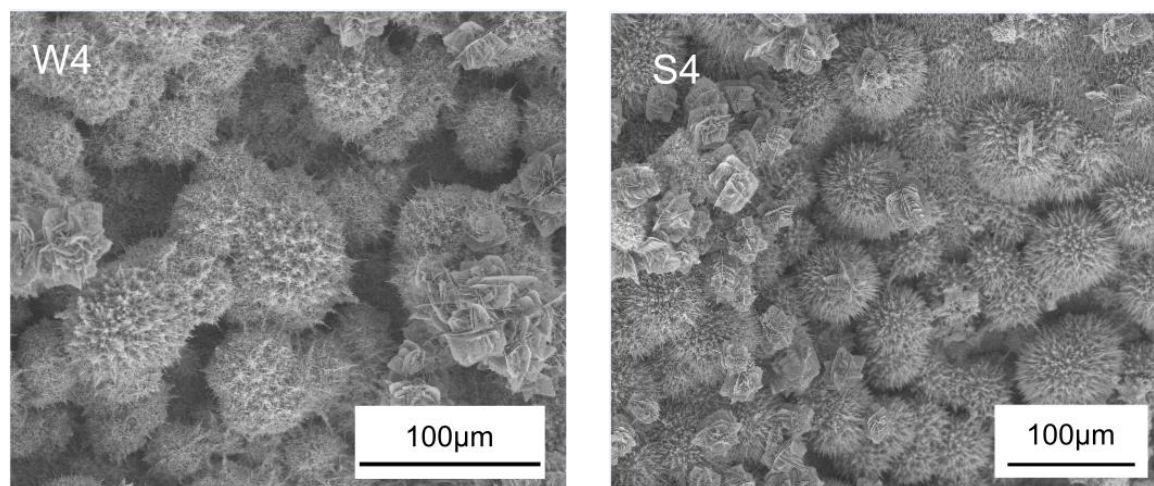


Figure 89 SEM Micrographs of samples W4 (left) and S4 (right). Both are grown using Rb₂SO₄ as capping agent, though sodium ions are also in solution from sodium tungstate

The average size of the spheres obtained is similar around 70µm, though measurement is difficult given the clear levels of the spheres. The seeded substrate does appear to have less well-defined spheres than W4 with spheres scattered on the surface of a more continuous nanoforest. W4 has no such continuous layer, with distinctly defined spherical particles.

Applying the Gu-mechanism this may be explained as follows, in the seeded sample, S4, there is a large concentration of WO₃ at the surface and therefore lots of the nanospheres form very quickly. These would rapidly agglomerate into larger structures to reduce their area whilst still leaving a surface to promote subsequent growth of nanowires and appear to be a nanoforest [83]. In the converse case of the pristine substrate there is a low concentration of WO₃ nuclei at the surface and so oxide that forms upon this substrate likely comes from crystals that have grown organically in the bulk solution. These bulk particles grow distinct particles and as they coat the W-substrate they are arranged as in the left of Figure 89. It is accepted this is theoretical and would require further synthesis at timed intervals to obtain snapshots of this growth.

A feature present in both W4 and S4 is where the oxide forms nanoplates instead of “urchin prickles” with magnified examples shown in Figure 90. What is immediately clear, with reference to the scales, is that the W4 feature is of a larger size than S4. Considering Figure

89 it does appear that this would be consistent across the layers. These nanoplates are arranged quite differently from those found in the sodium sulphate samples W2 and S2, possessing more angular junctions than the rosebud formations. These structures only form atop the urchins which would mean they form last in the reaction. Why lateral growth is promoted in the final stages of the reaction is interesting and would require further investigation.

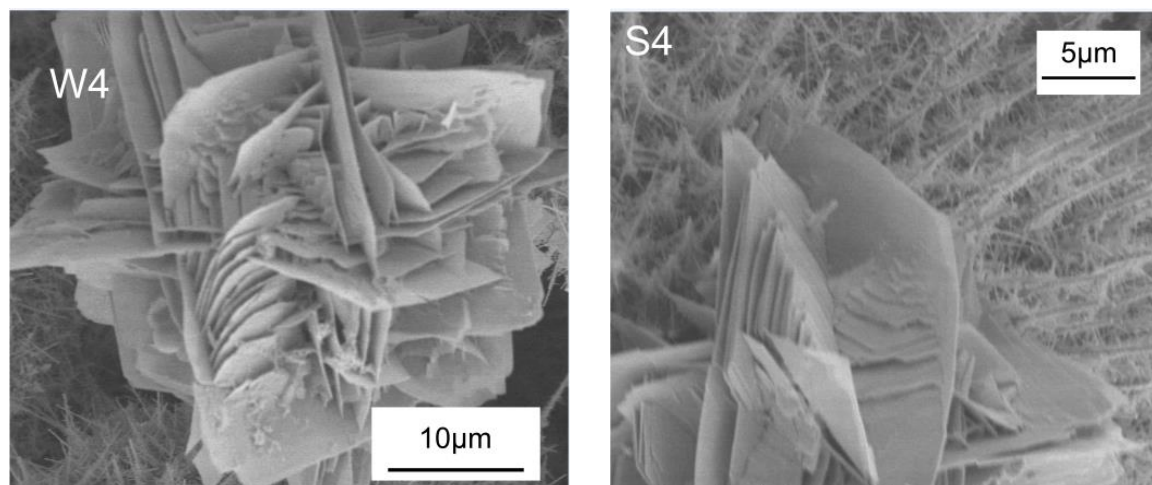


Figure 90 SEM Micrographs of nanoplates which form in W4 (left) and S4 (right).

Finally, Gu et al [83] found that over a certain rubidium ion concentration, the nanoplates that were reported were composed of highly aligned nanowires. It is clear in this instance, upon the highest magnification (Figure 91), that no nanowire feature is visible in either.

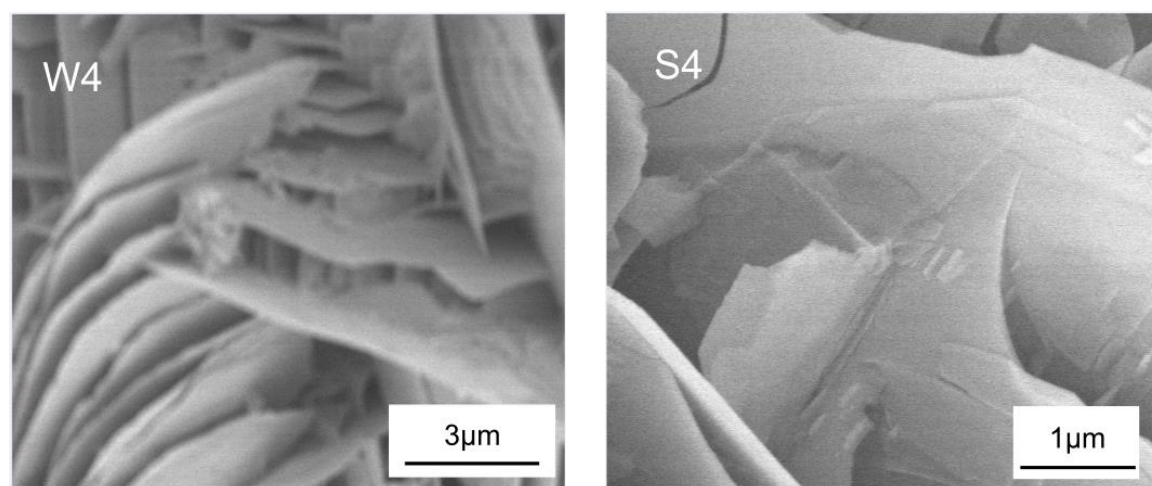


Figure 91 Highest magnification SEM Micrographs of nanoplate features W4 (left) and S4 (right)

Taking a more magnified look at the nanorods which make up the urchins, it is clear these are the most uniform and well-defined nanostructures obtained from the results presented in this chapter. In the micrographs of the W4 urchins in Figure 92, the urchins are composed of nanorods or trees, which have central trunks from which branches grow. The main trunk of these features rise radially to a central point. The microstructure is identical to S4 as may be seen in Figure 93.

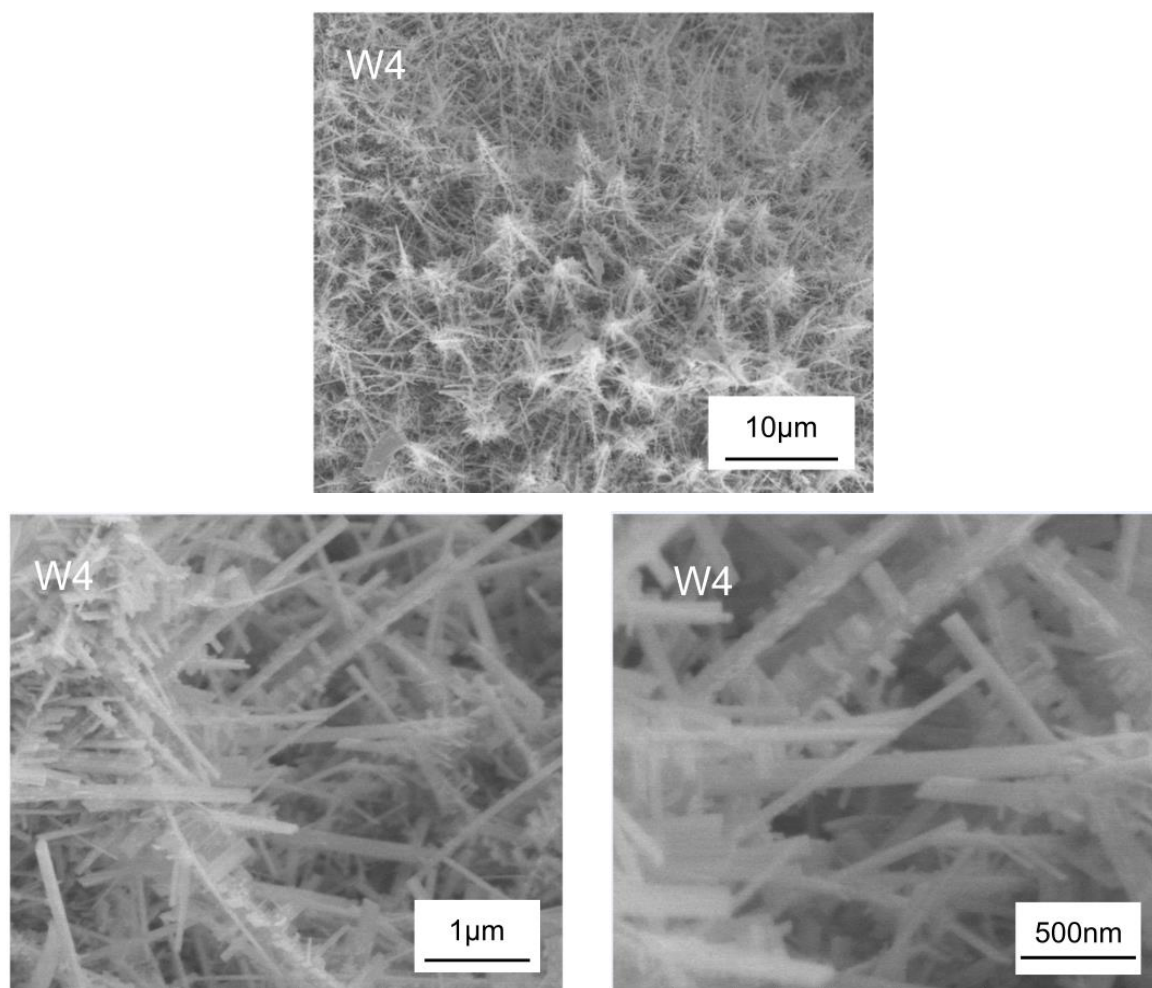


Figure 92 SEM Micrograph of W4 at 3 different magnifications

These highly ordered networks of nanorods proved to have the best electrochemical performance of chapter 4 and this is perhaps obvious when comparing the microstructures of W4 and S4 with those presented previously. Often in other samples, there are long nanorod structures which seem to have collapsed or agglomerated together which reduces surface area and therein limits intercalation in and out of the bronze. This is not the case here; the rubidium samples' structures will be both porous and high surface area which affords them the highest capacities reported.

What is more, the rubidium samples were found to lose their capacitance at a slower rate than the other samples. Their clear superior porosity compared to the other samples makes clear that the ions have an easier time diffusion to and from the surface. In simpler terms, there is less ionic resistance to proton movement in the well-ordered, open arrays here than in the unordered or collapsed network structures presented earlier.

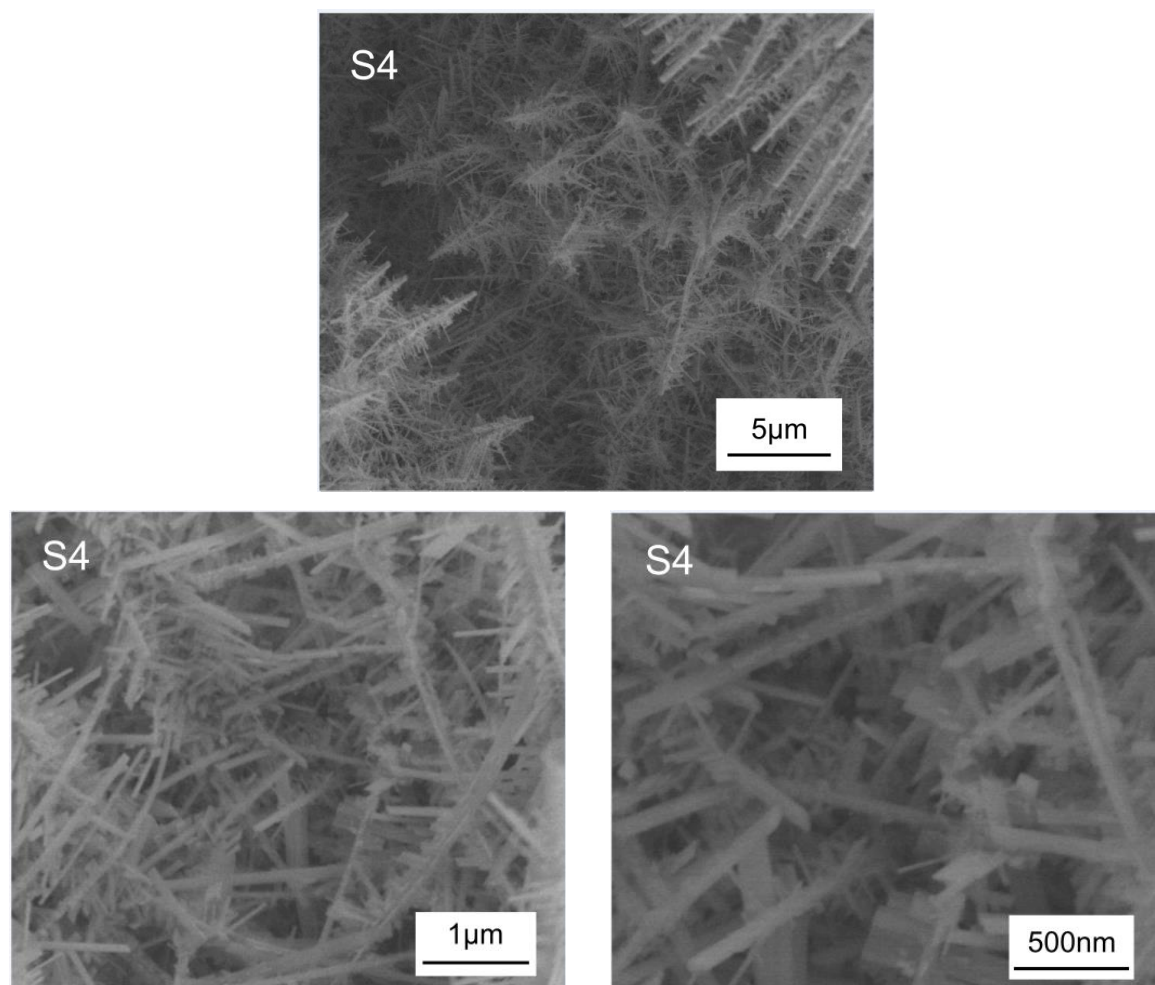


Figure 93 SEM Micrograph of S4 at 3 different magnifications

A final aspect of their electrochemical performance worth mentioning is how similar it is between the seeded and unseeded samples. W4 and S4 are not only the most well-orientated structures but also the most similar to one another. That is to say that the seeding step had less of an influence on the final rubidium-directed structure compared to the other samples. This was particularly noticeable comparing the similarities of W4 and S4 and the seeded and unseeded samples made from sodium chloride and sodium sulphate which had noticeably different performances.

The presence of the ammonium produced quite different microstructures but to a lesser extent than the sodium salts. Each substrate in the case of ammonium resulted in quite similar electrochemical performance, with the caveat its electrochemical characterisation was especially challenging. Both large cation synthesis conditions resulted in similar microstructures being delivered and therein similar electrochemical performance. It seems that because larger cations are more effective at stabilising the tunnel, they may be considered dominant in the growth process to a degree that lessens other factors [116].

In summary, the addition of rubidium, like ammonium before, has had a profoundly beneficial effect on the microstructures obtained from the reaction. Its presence reduced the influence

of the seeding step on the electrochemical performance by creating unique urchin structures. As to why this is, is discussed in more general terms in the growth mechanism section.

5.5 Microstructure (EDX imaging) cross section

5.5.1.1 Presence of Cation

Each of the synthesised samples was set in epoxy to expose the cross-section and micrographic and Energy-Dispersive X-ray (EDX) data was recorded for each to detect the presence of the cation used in the synthesis. The images produced from these do not have consistent colours throughout the dataset and are described in turn for improved clarity.

The micrographs for NaCl-directed samples, W1 and S1, are shown in Figure 94. The boundary between W-metal and WO₃ is distinct from the evident boundary in morphology. It would be expected that oxygen, the red colour in Figure 94, should be present throughout the oxide region but it is not evident due to the method of how the EDX creates these maps. The software is instructed on what elements may be present from the synthesis method and best matches the recorded X-ray energies to this data. Oxygen and sodium, light elements, produce low-energy x-rays which can readily absorb into the sample making detection more difficult and their energies may be masked by higher energy x-rays from elements like the tungsten.

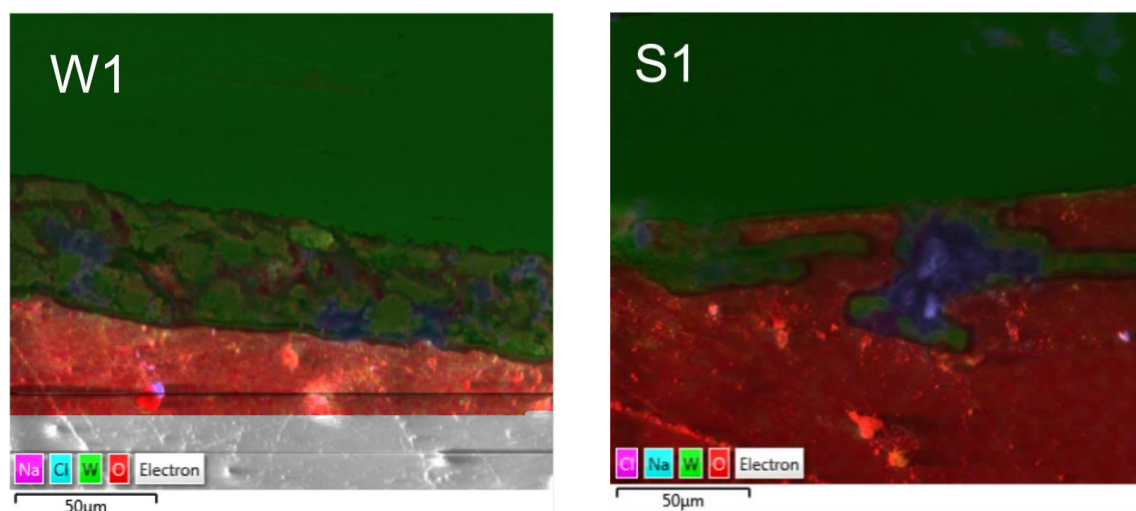


Figure 94 NaCl directed samples cross sectional micrograph with EDX colour map

An additional drawback of EDX with these particular samples is the epoxy setting will charge under the electron beam which will distort the acquired spectra, as well as make lighter element detection more challenging.

Despite these drawbacks, sodium may be identified in the oxide region within the oxide layer of both samples. Crucially, it may be seen that sodium is present deep into the layer which shows its presence throughout the oxide structure. This means that either, it is present as a tunnelled ion or that it has been intercalated within the bronze. The XRD results indicated that only the hexagonal phase of WO₃ was present in the samples and given this phase is

known to require a stabilising tunnel ion, it seems extremely likely that is what these sodium ions are.

It was challenging to identify the presence of a cation in the sodium sulphate (H.1) and ammonium sulphate (H.1) directed samples due to the drawbacks EDX suffers from on epoxy set samples. This is especially the case of ammonium where observation of nitrogen atoms proved impossible.

Detection was possible in the rubidium-directed samples, which produced a far clearer EDX spectrum than the others. The EDX map of samples W4 and S4 is presented in Figure 95 below.

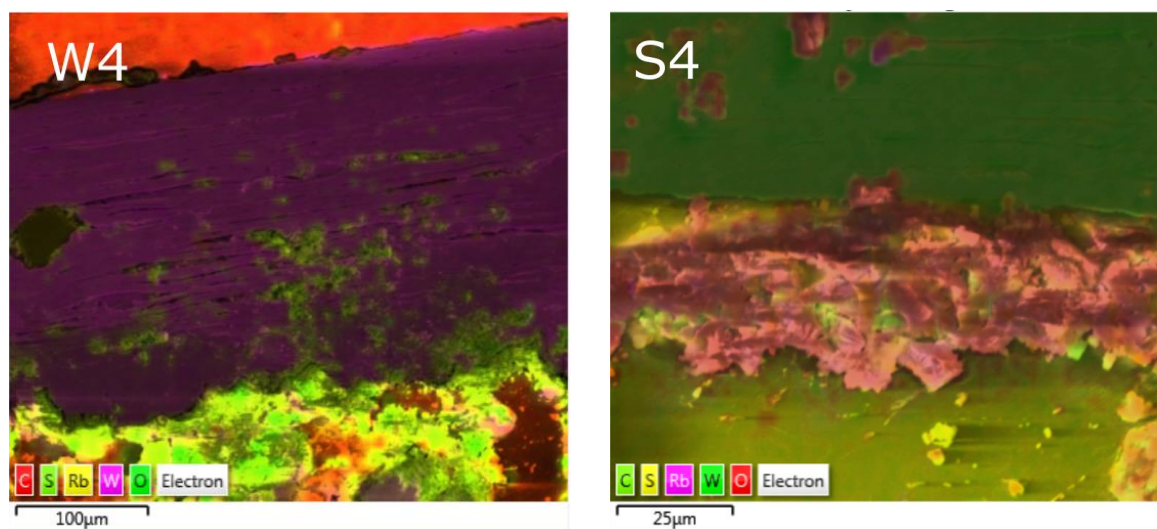


Figure 95 Rb₂SO₄ directed samples cross sectional micrograph with EDX colour map

In both these EDX maps the oxide layer displays a strong presence of rubidium and also, especially in the W4 spectra, sulphur. These samples are more effective at differentiating oxygen than in Figure 94 which is down to less charging occurring during the measurement. It is unsurprising that rubidium, the heaviest of all cations used in the synthesis, gives the strongest indicator of its presence from EDX.

Again, the presence of rubidium may be identified throughout the whole bulk of the obtained oxide not just at the surface. This shows that, as with W1 and S1, the capping agent cation is integral to the hexagonal tunnel structure.

It was of interest to identify whether the seed layer would remain adhered, unchanged in any way through the reaction and provide an epitaxial surface to direct growth creating a bilayer of oxides; or whether it would dissolve into solution given the hydrothermal conditions, re-nucleate upon the tungsten surface and grow a monolayer. The full physical characterisation leans towards the latter for the following reasons. Firstly, the XRD identified pure tungsten, the substrate, and one hexagonal tungsten bronze on the surface. Secondly, the cross-sectional SEM images show no evidence of two different structures, i.e. these phases would have different microstructures. Further XRD which better interrogates the surface, such as

grazing incidence XRD, would be required to confirm the disappearance of the seed layer. If this holds, then the epitaxy of a seeded surface is not so important for the resulting layer. More important would be the particle size and distribution of the seed layer entering the hydrothermal reaction.

5.5.1.2 Oxidation occurring within layers of Tungsten foil substrate.

Whilst taking these cross-sectional EDX maps it was noticed that the tungsten metal foil in some samples showed an expanded layered structure in which oxidation appeared to have occurred between the layers, like it had been prised open. The EDX map of W4 in Figure 95 shows this quite clearly, where there are identifiable layers of tungsten metal with oxide clumps growing in the open space between the layers. This feature was unexpected and was identified in a few samples including W1, S3 and S4 (H.1).

The mechanism for this occurring is quite unclear from the results although one simple conclusion may be drawn. There was no apparent correlation between the varied experimental conditions (i.e. capping agent or substrate type used) and the interlayer oxidation occurring. What is consistent across all of these is the hydrothermal conditions employed, the high temperature and pressure, and the pH. It may be concluded these reaction conditions themselves are sufficient to drive oxidation between the nanoscale gaps which will be present in the tungsten metal substrate.

Intra-substrate oxidation is quite undesirable because the oxide formed will be electrochemically active. The stability issue that these electrodes suffer is noted to be highly pH sensitive, in that these electrodes maintain their layer within pH 2 but have been observed to delaminate in stronger or weaker acids. The pH will drive the concentration of protons which intercalate from the concentration gradient between solution and electrode, and the intercalation/deintercalation will be accompanied by an expansion/contraction from the new ions entering the bronze. This same effect is observed in charging and discharging the electrodes. This oxide within the substrate itself expanding or contracting, bending the electrode, could be a feature which leads to delamination.

A final comment is that tungsten is a notoriously robust metal, resistant to corrosion. If a hydrothermal procedure can prise open the layers and oxidise the space between, then it is likely this would occur with any other metal used in a similar procedure. It may be the case that the effect of this may be limited through using shorter reaction times but the presence at all is of concern.

5.5.1.3 Estimating thickness of oxide

The cross-sectional analysis intended to be able to measure the thicknesses of the oxide of each synthesis condition and determine whether the substrate is consumed in the reaction. However, the results of this were found to be inconclusive. This may be condensed to two

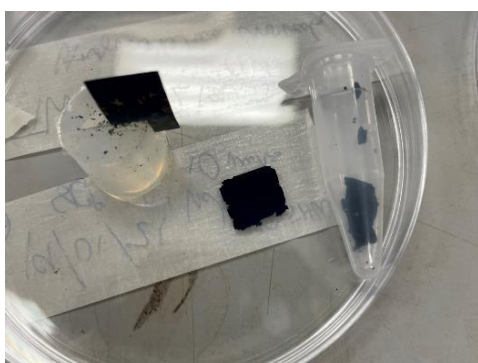
points: (1) the pristine W-foil known by manufacture (and micrometre gauge) to be 50 μm in thickness was measured by the SEM measurement to be 149 μm ; (2) if this was taken to be the “baseline” in error, i.e. the value from which all other thicknesses could be based off then this would make sense. However, the substrate of one sample was found to be 250 μm which would mean the substrate had generated mass in the reaction which is inconceivable. The expansion from interlayer oxidation discussed above would not alone cause this. It was therefore viewed as fruitless to pursue further analysis of these results in this regard. The table of measured values may be found in (H.1) for completeness. It was not established as to what caused this but the epoxy setting itself may be prone to tilting, even slightly, the samples which would then result in experimental error.

5.6 Foil Stability

Handling and characterisation of these foils was made challenging by the poor of these foil electrodes. This section aims to detail the challenges encountered and offers insight into expected challenges to overcome in binder-free electrodes.

The binder-free electrodes characterised here suffer from the delamination of the tungsten bronze from the tungsten substrate. This occurs through many mechanisms, the results of which are illustrated in Figure 96.

a)



b)



c)



Figure 96 Mechanisms for delamination a) drying out b) surface tension/pH change c) passing charge

The first mechanism recognised that if the sample were left to dry in ambient air, the sample would “dry out” and delaminate from the substrate. To prevent this the samples were stored in solution until characterisation.

The second reason for delamination became prominent from the solution to drying out. As the sample was placed from one solution into another it would have to contend with surface tension. The force of which was sufficient on occasion to remove the surface oxide.

A third method of delamination was found when the samples were moved between solutions of differing pH values. For instance, the sample being moved from dilute acid storage solutions (pH 2) to concentrated acids used in characterisation (0.5M Sulphuric acid) would prompt the layer to delaminate. The increased concentration of protons creates a driving force for protons in solution to move into lattice channels causing a swelling.

The fourth and final mechanism of delamination is intercalation itself. The concomitant expansion/contraction the lattice experiences when intercalating/de-intercalating protons over the course of the characterisation creates stress in the layer and results in surface oxide being removed. Some layers would initially appear to be adhering to the surface but once any charge-transfer-inducing characterisation was started they would on occasion would delaminate. This was not to say the full layer was removed, but often regions of the substrate or potentially just a few loose particles departed the surface. These loose particles may have been dislodged from the abrasion experienced as the foil was loaded and tightened into the working electrode holder. A final and crucial point to mention is the intra-substrate oxidation identified in some samples (Figure 95) would exacerbate this effect by causing the substrate itself to move with the intercalation.

All of these mechanisms point to poor adhesion between the hexagonal oxide and metal substrate and make their characterisation challenging.

These issues demanded a storage system to be thought out, maintaining the samples at a pH of 2, and for a bespoke working electrode sample holder to be developed for 3-electrode characterisation. There was a desire to perform two-electrode characterisation however multiple attempts to create a device using several inbuilt designs were unsuccessful and a decision was made to move on.

The ammonium tungsten bronze (ATB) samples W3 and S3 stood out as the most prone to delamination, indeed the layer could be considered already delaminated on removal from the reaction. It is then not surprising that the electrochemical characterisation was quite irreproducible. The ATB layer was a moist, almost colloidal consistency which when placed into the bespoke holder and tightened would compress and collapse. This meant that standardising the loading and tightening within the electrode was impossible. This is not to say samples the other samples were stable, only more so in direct comparison to W3 and S3.

As described in the methodology, the method for loading the samples into the electrode holder required one side of the oxide to be removed with a cotton bud. This would remove all oxide visible. In contrast, wiping a cotton bud over the seeded substrate would remove none. This comparison is useful in explaining how loosely adhered the hexagonal phase was to the substrate and is a good indicator that the hexagonal phase is ill-suited to being the active phase of a robust binder-free electrode.

5.7 Growth Mechanism

5.7.1 Capping agents

The role of cations in directing the growth of tungsten oxide is widely reported in the literature, with most papers cited in Table 5 outlining identical growth mechanisms based on surface energy anisotropy theory: lattice facets have unique surface energies, some higher and some lower, and thermodynamically the lattice is driven to reduce its surface energy as much as possible [82], [87]. During hydrothermal crystal growth, a negatively charged lattice facet can lower its energy either by extending the lattice or by binding to positively charged capping agents. These cations preferentially bind to specific facets, reducing the growth rate perpendicular to those facets by stabilizing them. Conversely, facets where the cations bind less strongly experience faster crystal growth in the normal direction, leading to anisotropic development of the crystal. This section applies the theory to observed microstructures presented investigated in this work.

One paper by Zheng et al models the growing tungsten bronze system to a hexagonal prism with negatively charged faces and makes some approximations to provide a simple explanation to the developing microstructures [84]. The charge of each oxygen dipole is considered equal in magnitude and each face is taken as the summation of the charge of the dipoles of oxygen atoms exposed at each of the faces. Following these assumptions, it can be said the negative charges on the top and bottom faces are identical in magnitude; similarly, each side face of the hexagonal prism has an identical negative charge. Following this logic, the strength of negative charges on the bottom and top faces of the prism are less than each side face because the side faces (double the exposed O^{δ-}) have double the number of dipoles. This dipole arrangement is visualised in Figure 98 and is based off a schematic presented in [84].

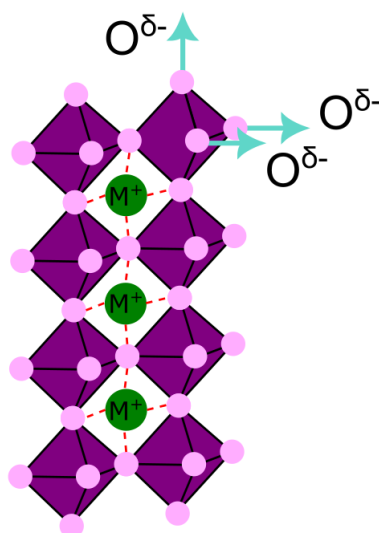


Figure 97 Position and Direction of Oxygen Dipoles of hexagonal WO₃ Crystal

The consequence of dipole arrangement to the growth of the hexagonal-WO₃ lattice is that cations preferentially bind to the side facets more than the top face, prohibiting tungstate (WO₄²⁻) ions from reaching side and making lattice growth more likely from the top face. The capping agent in solution therefore selectively promotes growth from the top face instead of the side faces, extending the lattice anisotropically in one direction forming a nanorod.

This theory aligns well with what was seen in W1 and S1 where nanowires were exclusively formed but not so well for the other samples which had mixed microstructures. The system is more complex. Some comments may be drawn on the difference in cation properties and the resulting microstructure before one must introduce the role of the anion and substrate surface into the system analysis as discussed in sections 5.7.2 and 5.7.3 respectively.

The cations present in the reaction were protons, sodium, rubidium, and ammonium which have quite different properties. Protons are small and mobile, highly suited to intercalation but may not influence growth or stability as much when larger ions are present which can displace them. Sodium, a medium-sized ion with good mobility and strong interaction with the hexagonal lattice can stabilise the hexagonal phase, unlike a proton, though it still has sufficient mobility to be able to flow through the prism. There are then ammonium and rubidium, larger ions still that are well suited to tunnel stabilisation because their large radii effectively fill the centre of the hexagon [116]. These were found to create drastically different structures to the pure sodium cases. These ions are large enough and have a powerful interaction with the WO₃ lattice so they may be said to move very slowly through the oxide tunnel in comparison to sodium and protons. In ammonium's case, it created a very hydrated layer. It may be speculated that this was due to hydrogen bonding of ammonium pulling more water molecules into the lattice structure than possible with alkali metals. Rubidium created unique nano-urchin morphologies which were highly similar to the structures reported by Gu

et al [83] who proposed a mechanism which was discussed in detail in section 5.4.1.5. In short, the rubidium ions' affinity for the centre of the hexagonal prism is so profound it stabilises the bronze rapidly forming microspheres of high surface area. These spheres then provide sites for nanorod growth.

A last point must be made on the dual impact of present cations upon the nature of samples W3, S3, W4 and S4. These samples were not made from one single capping agent ion but two, the chosen cation and sodium. Given the affinity of large ions to stabilise the WO₃ tunnel and their slow movement through it, one can assume that these ions permanently stay there to draw further comment. If rubidium and ammonium are fixed in the tunnel, their relative concentration in solution drops in comparison to sodium. It is then proposed that the two chosen ions fulfil distinct roles: the large cation stabilises and the smaller mediates subsequent growth through defining aggregation processes. This could point to an unexplored strategy in tungsten oxide nanostructure synthesis: select a blend of cations to enhance certain properties of the oxide whilst maintaining the overall cation ratio.

For instance, one may potentially tailor hexagonal-WO₃ synthesis for maximum surface area by selecting a cation large enough to stabilise the hexagonal tunnel (NH₄⁺, Rb⁺, K⁺) whilst pairing it with a specific capping agent salt that grows the desired crystal. Another example would be using a finely controlled amount of ammonium sulphate to increase the hydration properties of the obtained oxide. This would make an interesting avenue for future investigation.

5.7.2 Role of Anion

The role that the anion plays in determining the morphology of tungsten oxide formed through hydrothermal synthesis is often neglected in the literature, with the effect of the cation given far more credence. Its role was probed by comparing the samples made from sodium chloride (W1, S1) and sodium sulphate (W2, S2) which shared identical reaction conditions except for the employed anion.

Anions can influence the growth and morphology of WO₃ nanostructures through multiple mechanisms. While direct interaction with the WO₃ lattice is possible, anions have a significant role in determining the electrostatic double layer around the growing crystal, influencing the potential microstructures. As described, the growing WO₃ lattice creates negative dipoles around the oxygen atoms which then attract cations in solution to balance the charge which in turn attracts anions in solution. This mechanism so far has only considered the cation roles in adsorbing to the lattice, not the role of the anion in the subsequent double layer.

Extending this analogy to the double layer the role of the anion may be speculated on, including the differences between chloride and sulphate-mediated growth. It is clear that this double layer will have different properties if it is composed of chloride or sulphate ions have different properties. The sulphate ion's ionic radii in an aqueous solution are much larger

(0.242 nm) than the chloride ion (0.18 nm) and form much larger complex structures holding two sodium ions to chloride's one [118]. A schematic describing a generalised system between WO₃ lattice, proton, anion, and the cation is shown in Figure 98, developed starting from a schematic from Zheng et al [84]. This figure illustrates a double layer forming on the side of the growing lattice but also considers the entirety of the double layer surrounding the prism. Protons accumulate near the lattice, anions move to balance their charge, and finally, cations move to these forming the double layer.

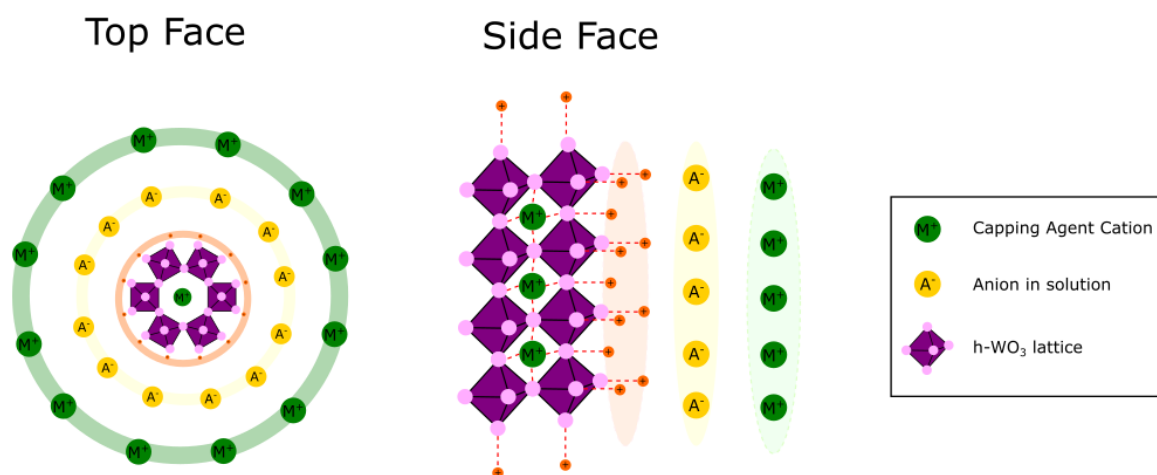


Figure 98 Schematic of hexagonal-WO₃ lattice showing two perspectives: planar view of top face and cross section of side face.

It should be noted this schematic shows protons interacting with the WO₃ lattice, and not the capping agent cation in solution for simplicity. In reality, cations like sodium, rubidium and ammonium would compete and exchange readily with the protons for these sites. The “top face” view of the system is used now to discuss the differences between a sulphate and chloride system.

Taking chloride first the ratio of chloride to protons in solution is one to one and as visualised by Figure 99, a tungstate would have to dislodge and exchange with two chlorides to satisfy the charge requirement of the double layer. Chloride ions have a small ionic radius and therein a high charge density can be expected to form strong electrostatic interactions with the WO₃ lattice. This strong interaction between chloride and proton creates a strong double layer at the side of the lattice. This compounded by the requirement for two chlorides to exchange for one tungstate to extend the lattice makes lateral growth far less likely than growth from the top face. The cumulative energy of the side double layer is much larger relative to the top and in the chloride-only system, nanorods formation is promoted and indeed are the only microstructure present in W1 and S1. This fits well with the nanorod formation already outlined [80], [81], [82], [83], [84]

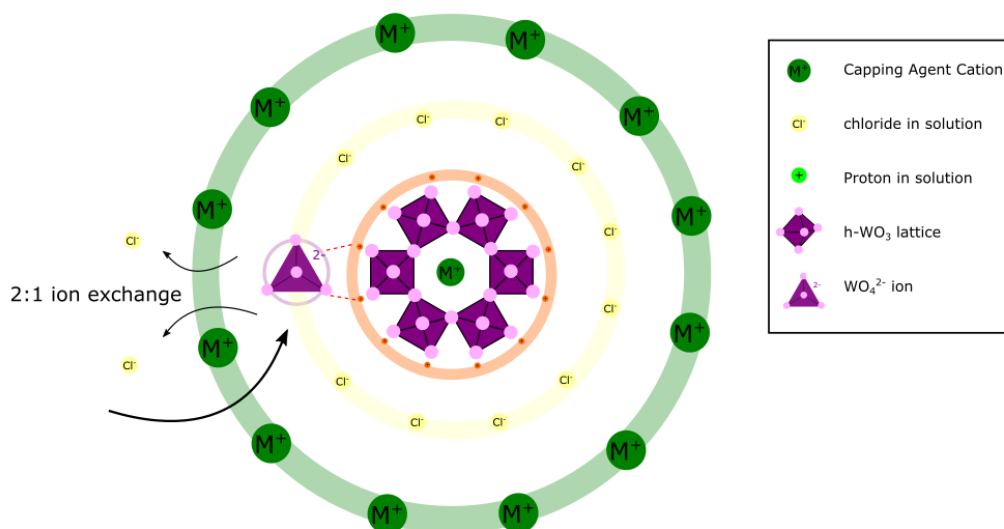


Figure 99 Schematic of tungstate ion exchanging with chloride ions

The presented WO₃ microstructures directed from sulphate systems did not fit with purely nanorod formation, however, with lateral growth structures such as the rosebuds identified in W2 and S2. A speculative explanation for the lateral growth observed may be made by visualising the sulphate-mediated double layer, and the resulting schematic is presented in Figure 100.

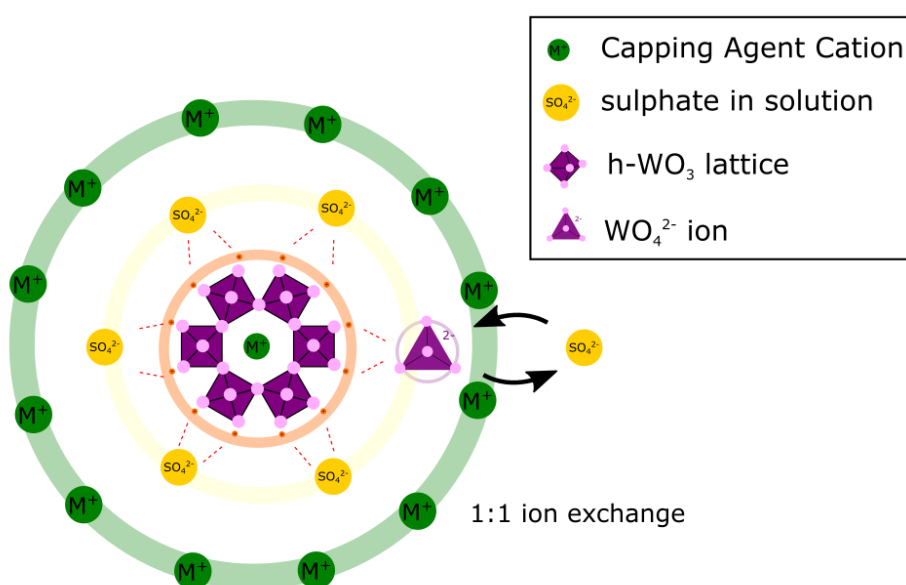


Figure 100 Schematic of tungstate ion exchanging with sulphate ion

In this system, there is now a ratio of protons to sulphate ions of two to one, which is identical to the ratio of tungstate ions to protons or sodium. This means sulphate balances the double-layer charge with half the number of ions. Sulphate also has a lower charge density than chloride ions 5 and 8 C mm⁻³ respectively [119]. Considering this it may be said that the

sulphate-mediated double layer is composed of weaker interactions and more penetrable than that formed from chloride ions. It is more likely that tungstate ions can access the side of the growing lattice and adjoin in a sulphate system than it is in a chloride system.

In other words, the sulphate-mediated double layer is more susceptible to lateral growth than the chloride case. Nevertheless, the system still promotes nanorod formation because of the well-discussed inherent difference in double-layer energy between the side face compared to the top face [84]. This explains why both nanorods and lateral structures are observed in samples W2 and S2.

Finally, the anions present in the reaction appeared to have an impact on the rate of corrosion of the pristine tungsten substrate. The hydrochloric acid system resulted in extensive nanorod coverage in W1 compared to more limited coverage in W2. It may be inferred then that the chloride ion creates a more corrosive environment for the tungsten substrate surface than the sulphate.

5.7.3 Impact of Seed Layer

The seeding process resulted in different resulting morphologies compared to unseeded substrates, with varied effects across the different capping agents. A consistent finding was that the seeding step is more advantageous in obtaining a uniform oxide microstructure than that made from the pristine foil. This can be explained by the understood from understanding the relative concentrations of tungsten oxide nuclei formed at the seeded and pristine surface at the beginning of the reaction.

The seeded substrate provides the reaction with solvated tungstate at the surface of the substrate at the start of the reaction. When the reaction begins the tungstate rapidly nucleates forming lots of small tungsten oxide nuclei at the surface. In the pristine case, tungsten oxide nucleation must form spontaneously from either dehydration of WO₄²⁻ from solution near the surface or from the tungsten metal oxidising in the hydrothermal conditions. This factor alone means that the seeded surface will produce a more uniform surface because it has a high concentration of tungsten oxide nuclei everywhere across the substrate; the pristine foil is dependent upon other processes that will have local fluctuations.

Furthermore, during the subsequent growth of the hexagonal crystals, they extend anisotropically, directed by the capping agent [80], [81], [82], [83], [84]. The seeded substrate with lots of small nuclei will form a high density of high surface area structures [82], [87]. These will seek to reduce their surface energy through agglomeration. The seeded samples therefore developed denser structures that were observed consistent with the results.

A follow-up question arises to this, why do the nanoplate structures form on the extremities of the surface in some seeded samples (like S2, and S4) whereas nanorods form closer to the surface? A speculative answer to this may lie in considering the initial seeded surface and then the subsequent evolving surface during the reaction. At the beginning of the reaction,

there is the first phase of hexagonal growth where there are many orthorhombic WO₃ particles at the surface which can become soluble in hydrothermal conditions. Once they solvate and are directed by a capping agent to form hexagonal-WO₃ crystals there is a high density of WO₃ crystals formed rapidly. The high density of these and the proximity of the crystal side face will create a strong double-layer energy which makes lateral growth less likely resulting in many nanorods.

Subsequently, there is a second phase of growth upon this surface where the formed oxide provides a surface from which new structures can form from tungstate ions from the solution. These oxide structures are no longer defined by the high concentration of crystals found at the surface and instead will grow according to the bulk solution characteristics.

The first phase of growth may be viewed as either consuming or reorientating surface particles which form nanowires. These may agglomerate into larger microstructures but keep the characteristic nanowire shape. However, once the available WO₃ from the surface has been consumed and reorientated into the hexagonal phase, any further growth on the surface will come from bulk tungstate ions joining in a second phase either as deposited but partially formed structures or growing directly from exposed sites. If formed in solution their microstructure would understandably be different to those formed during the first phase.

This idea is supported by the micrographs obtained by W2 which does not produce nanowires upon the surface (Figure 81) whatsoever because growth may only occur on W2 from the tungstate ions in solution or if some tungsten particles oxidise into solution. Neither of these processes will create a high enough density to prohibit lateral growth as in the case of S2 where the high density of formed tungsten oxide crystals makes nanorods more likely.

5.8 Conclusion

This chapter delivered a thorough physical characterisation of eight distinct hydrothermally grown tungsten-tungsten oxide (W-M_xWO₃) electrodes, discussed how the reaction conditions influenced their nature and linked their microstructure to the electrochemical performance in discussed in chapter 4. The oxide layers of each foil were found to have a different appearance depending on the capping agent and substrate used in the reaction. The crystal structure of the surface oxide was determined to be hexagonal tungsten bronze in all cases and the EDX imaging identified the presence of the tunnelated cation. Much discussion was given to the microstructure of the foils, and this was found to vary with changing reaction conditions, and the growth mechanism speculated upon.

This work analysed the reaction schemes of four published papers and quantified the capping agent concentrations use to find a ratio of 6 capping agent cations (M⁺) to one tungstate ion (WO₄²⁻) which in each had successfully delivered the hexagonal phase of tungsten oxide regardless of capping agent used. The decision to use this ratio for all the capping agent

iterations synthesis was well vindicated as the hexagonal phase was produced in each. Moreover, without any further optimisation, the synthesis delivered highly orientated nanowires in the case of W4 and S4 and a unique rosebud structure in S2. This approach of quantifying existing reaction schemes in literature has proved useful in finding a useful starting point from which it may be expected to optimise the structures further.

A clear trend emerged between the microstructure of the foils and their performance. The rubidium sulphate-directed samples were found to have highly ordered micro-urchin morphology which correlated well with their superior electrochemical performance compared to the other samples. This microstructure better facilitated ion movement between nanowires leading to enhanced intercalation. The sodium chloride samples also gave good relative performance owed to the nanowire structure. If the S1 sample could be made "less dense" to improve the porosity and surface area this sample could well be as effective as W4 and S4.

The synthesis scheme set out to grow hexagonal WO₃ from a tungsten foil substrate and succeeded in doing so. It found no evidence that the seed layer persisted through the hydrothermal synthesis making it unlikely that surface epitaxy may be used to direct hexagonal-WO₃ growth but instead found that instead the concentration, or loading, of seed crystals influences the resulting hexagonal phase. Further investigation would be required to confirm this.

The working assumption was made that the best-performing phase in powder-based tungsten oxide charge storage would also perform well in the binder-free architecture. This was found to be incorrect with the hexagonal binder free electrodes suffering from poor stability and lacklustre performance as energy storage electrodes. This is not to say that the binder-free electrode in principle is misguided but that in deciding what phase to grow upon the substrate, the most stable, adherent phase of oxide upon its conjugate metal should take precedence over the best performing polymorph in any powder-based study.

6 Systematic Review of Hydrothermal Reaction Scheme

6.1 Introduction

Chapters 4 & 5 detailed the electrochemical and physical characterisation of W-hexagonal- M_xWO_3 electrodes synthesised through hydrothermal reaction. The synthesis was successful in synthesising the desired crystal phase of tungsten oxide, but these electrodes were found to be prone to delamination and suffer from high ohmic resistances which contributed to underwhelming performance. This chapter focussed on reviewing the synthesis scheme used to better understand if it may be altered to produce more effective binder-free foils.

It is important to first understand the employed synthesis scheme used in these two chapters is summarised in the schematic in Figure 101. Though very unstable and poor performing, significant understanding was made surrounding the effect of the seeding step and the roles of cation and anion on the phase and microstructure of the hydrothermal product.

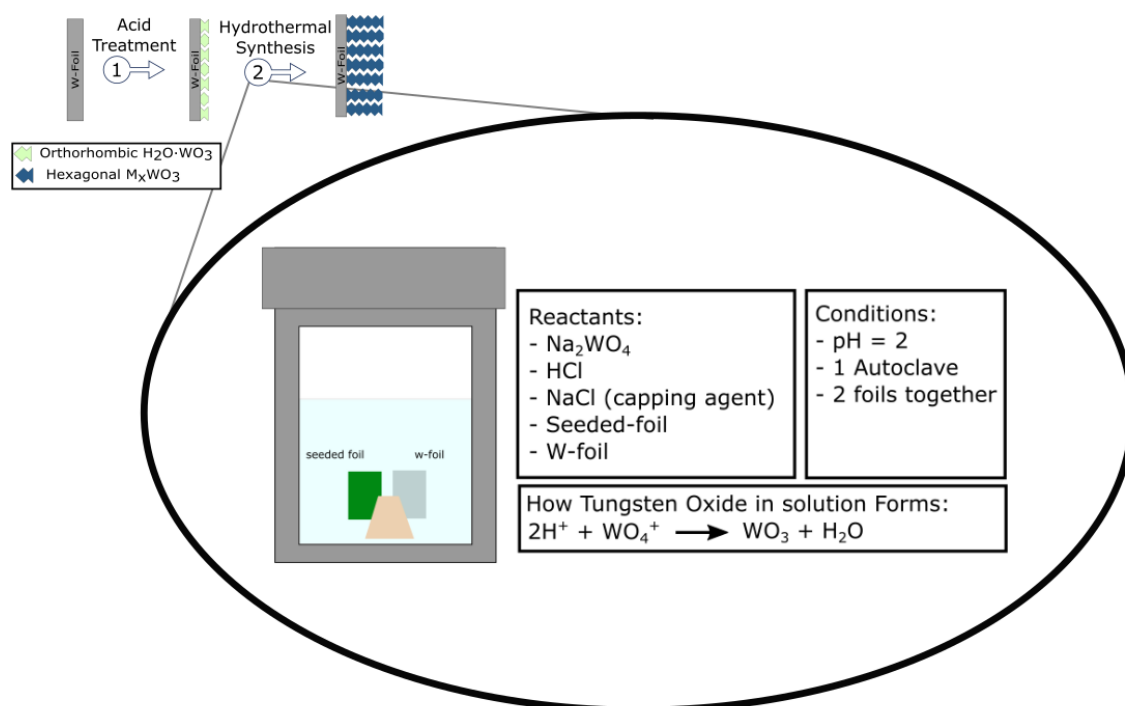


Figure 101 Overview of 2 step synthesis scheme with hydrothermal reaction key parameters in bubble

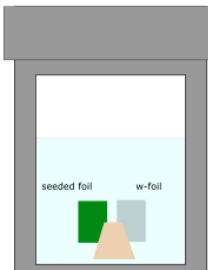
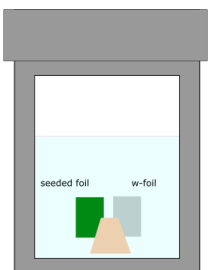
These results hitherto have used sodium tungstate (Na_2WO_4) as an additional tungstate source above that contributed by the substrates in the reaction. This resulted in thick oxide layers being deposited. If no additional tungstate source was added to the reaction an oxide surface may only be formed from oxidation of the W-substrate or re-organisation of the surface oxide entering the reaction from the seeded substrate. Based on previous results, a thinner coating is desirable to prevent delamination and improve conductivity, improving performance and stability.

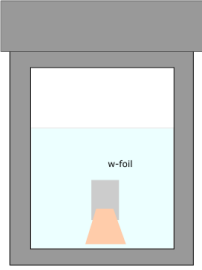
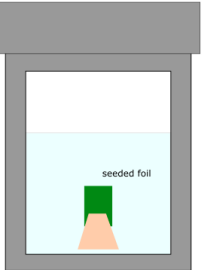
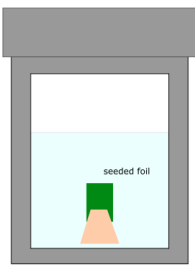
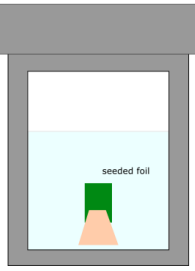
This chapter systematically iterates through hydrothermal reaction parameters and measures the result of the change using CV and SEM. Each iteration of the developing synthesis scheme is detailed within this chapter to clarify the variable under investigation, the over-arching synthesis scheme is outlined in the methodology.

Cyclic voltammetry of each sample is used as a direct measure of each iteration's electrochemical activity, given that the area of the CV is directly proportional to the charge stored. The SEM images complement the electrochemical data by explaining the observed change in performance. As such, the data within this chapter is presented by iteration, not by type of characterisation as previously.

Each sample synthesised at each iteration discussed throughout this chapter is summarised in Table 18 for reference. The substrates are the same as in previous chapters, pristine tungsten foil and W-WO₃ seeded foil, and maintain their labels W and S, respectively. To distinguish the samples from those discussed in previous chapters, the samples are labelled by their substrate type followed by a number beginning with 5 i.e. a continuation from the sample numbering in the preceding chapter.

Table 18 Reference table for iterations reaction parameters and corresponding label/colour

Iteration #	Sample Label	Synthesis Conditions	Colour
	W	Pristine tungsten foil	Black
	S	See 3.2.1 Acid Pretreatment Seeding Step	Red
1	W5	 <div style="display: flex; justify-content: space-between;"> <div style="border: 1px solid black; padding: 5px;"> Reactants: - Na₂WO₄ - HCl - NaCl (capping agent) - monoclinic-WO₃ - W-foil </div> <div style="border: 1px solid black; padding: 5px;"> Conditions: - pH = 2 - 1 Autoclave - 2 foils together </div> </div>	Purple
	S5		Blue
2	W6	 <div style="display: flex; justify-content: space-between;"> <div style="border: 1px solid black; padding: 5px;"> Reactants: - Na₂WO₄ - HCl - now just water - NaCl (capping agent) - W-WO₃ - W-foil </div> <div style="border: 1px solid black; padding: 5px;"> Conditions: - pH = X ≈ 5.6 - 1 Autoclave - 2 foils together </div> </div>	Green
	S6		Yellow

3	W7		Reactants: - Na₂WO₄ - HCl - NaCl (capping agent) - W-foil	Conditions: - pH = 2 - foil isolated in its own autoclave	Orange
	S7		Reactants: - Na₂WO₄ - HCl - NaCl (capping agent) - W-WO ₃	Conditions: - pH = 2 - foil isolate in its own autoclave	
4	S8		Reactants: - Na₂WO₄ - HCl - NaCl (capping agent) - W-WO ₃	Conditions: - pH = 2 - foil isolate in its own autoclave	Orange
	S9		Reactants: - Na₂WO₄ - HCl - H₂SO₄ - NaCl (capping agent) - W-WO ₃	Conditions: - pH = 2 - foil isolate in its own autoclave	

6.2 Iterative removal of synthesis parameters

6.2.1 Iteration 1 – removing sodium tungstate

The starting point for this analysis was to conduct the hydrothermal reaction using all the reaction parameters as before except with the removal of sodium tungstate. The reaction parameters used in this iteration, and all those that follow in this chapter, are visualised in Table 18.

Images of NaCl-directed samples (W1, S1) and the Iteration 1 samples are shown in Figure 102 a and b, respectively. Upon removing sodium tungstate from the reaction mixture there is an obvious change in the visual appearance of samples W5 and S5 compared to W1 and S1. Sodium tungstate produces a thicker oxide layer than without as expected because there is more available tungstate to grow or deposit a layer. In Figure 102 b) the tungsten substrate

sample, W5, has a thin, barely visible coating; Sample S5 has a more opaque coating though still recognisably thinner than S1. The surfaces of W5 and S5 were both moist, and the visible layer could be removed with a soft wipe.

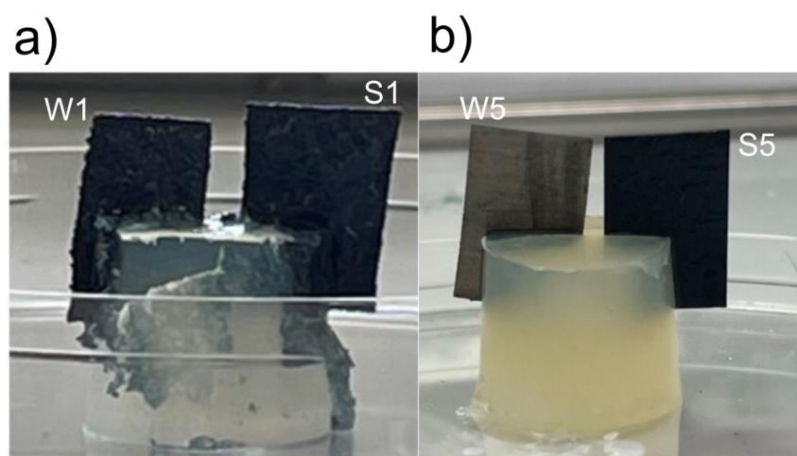


Figure 102 Photographs of NaCl directed samples W1 & S1 in comparison to 'NaCl directed samples without Na_2WO_4 '

The micrographs of these samples, displayed in Figure 103, correlate well with the photographs above. The W5 sample has no discernible microstructures, and any oxide on its surface must be extremely thin. This could also indicate that the corrosion rate of tungsten substrate is quite low in these conditions, given no oxide products form visible microstructures. Of course, the corrosion products may have remained in the reaction solution and further investigation of this would be required.

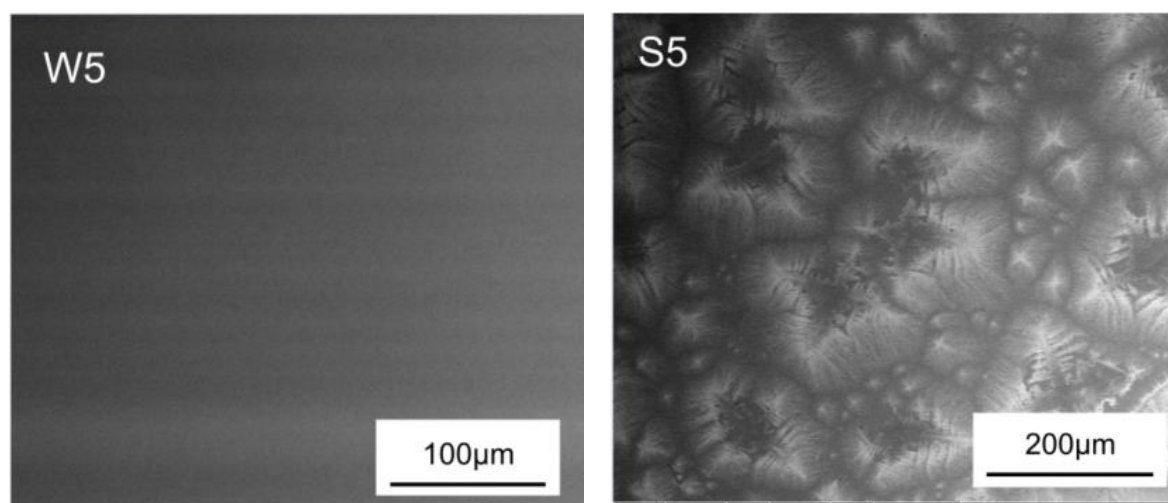
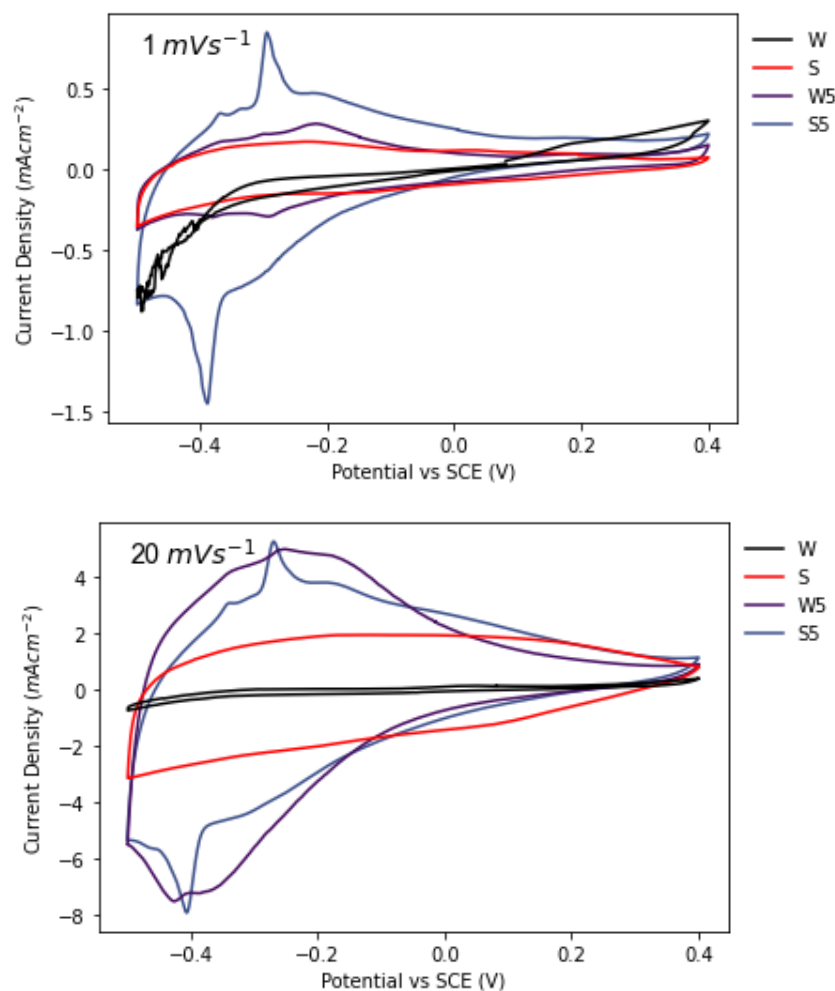


Figure 103 Micrographs of samples W5 and S5

The S5 micrograph forms dune-like patterns, quite different from the initial seeded substrate microstructure. This indicates that the sodium chloride in solution has a significant effect in directing the reshaping of surface tungsten oxide. No XRD was completed on the sample so it cannot be commented upon what phase was produced. However, some comments may be drawn on the capping agent's effects. The 1 g of sodium chloride added would make the ratio of Na^+ ions to WO_4^{2-} higher than the 6:1 required for hexagonal growth as shown. The

fact this level of NaCl has altered the surface oxide may leave the possibility open for a thin layer of hexagonal phase to be synthesised in this way. If a mass of surface WO_3 particle could be found per cm^2 then an appropriate concentration of capping agent could be added to create a micro-thin layer of hexagonal phase oxide. Alternatively, this could be explored empirically adding far smaller concentrations of sodium than used here.



Sweep rate (mV/s)	Areal Capacity (mAhcm^{-2})		
	S	W5	S5
1	0.053	0.083	0.131
20	0.037	0.060	0.055

Figure 104 Cyclic Voltammetry of iteration 1 samples against substrates W and S. The tabulated capacities of substrate S, W5 and S5 are tabulated below.

The electrochemical activity, estimated through CV, of these samples was compared with the substrates to show how the layers had developed. Figure 104 displays the CV curves recorded for samples W5 and S5, plotted alongside the two substrates. At 1 mVs^{-1} , S5 produces the largest area of CV and therefore the greatest activity, more than the seeded substrate and W5. Increasing this further to 20 mVs^{-1} , samples W5 and S5 expand whilst maintaining characteristic features, in line with pseudocapacitive materials. Interestingly, the W5 sample shows the largest area despite so little is apparent on the surface. It can be

surmised that an extremely thin oxide layer of W5 would better compensate for the tungsten oxide's poor electrical conductivity and the resultant electrode would have a lower ohmic resistance. The reduced ohmic resistance and consequent improved pseudocapacitive behaviour observed in these samples showed the removal of sodium tungstate is a promising step, leading to thinner, better performing W-WO₃ electrodes and warranted further investigation.

6.2.2 Iteration 2 – is acidic pH needed?

The pH value of all hydrothermal reactions thus far had been set to 2 given this pH was prevalent in literature for optimal phase or microstructure in powder-based WO₃ studies. However, it was important to understand if its influence was as crucial in W-WO₃ systems. This iterative step used unbuffered deionised water (pH ~5.5) without any added acid to investigate the resultant effect. The pH was this value due to dissolved carbon dioxide forming weak carbonic acid. Tungsten's Pourbaix diagram, in Figure 11, indicates that at this pH, tungsten oxide will dissolve into solution forming WO₄²⁻ ions and so two pristine tungsten foils could be expected. This iteration may be viewed as a control experiment in demonstrating the necessary effect of the acid.

The images of these synthesised samples are shown in Figure 105 and the similarity between both W6 and S6 with W5 is immediately apparent when comparing with Figure 102. The S6 sample formed in water has a much thinner oxide layer in which the substrate is still visible than the S5 sample. As discussed, it is clear in the case of S6 that the majority of tungsten oxide entering the reaction is dissolved from the surface of the seeded substrate and diffuses into the bulk. However, it is interesting that there remains a visible layer upon each of these substrates regardless.

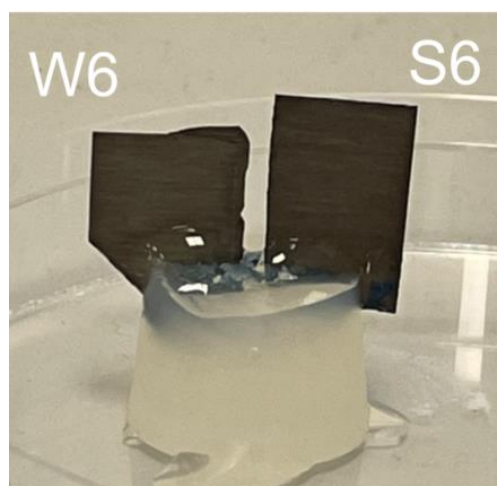


Figure 105 Photographs of samples W6 and S6; foils synthesised in deionised water at pH ~5.5

Inspecting these samples' micrographs in Figure 106 it is clear that, despite appearing quite similar to the eye, samples W6 and S6 are quite distinct. Mirroring the first iteration in

section 6.2.1, the seeded sample S6 has a dune-like microstructure and the tungsten foil sample has no apparent microstructure. Different in this case is that both of these samples have large black cubic structures upon the surface which are likely crystallised sodium chloride from the solution.

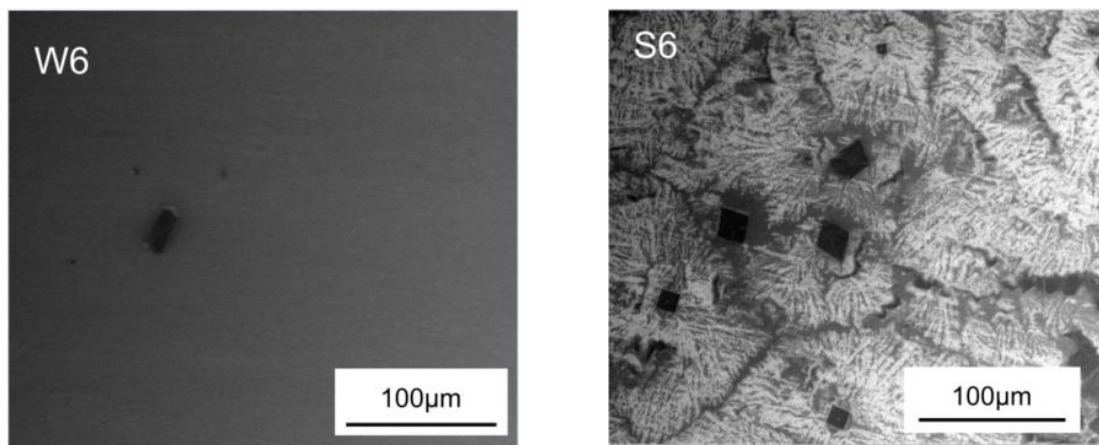
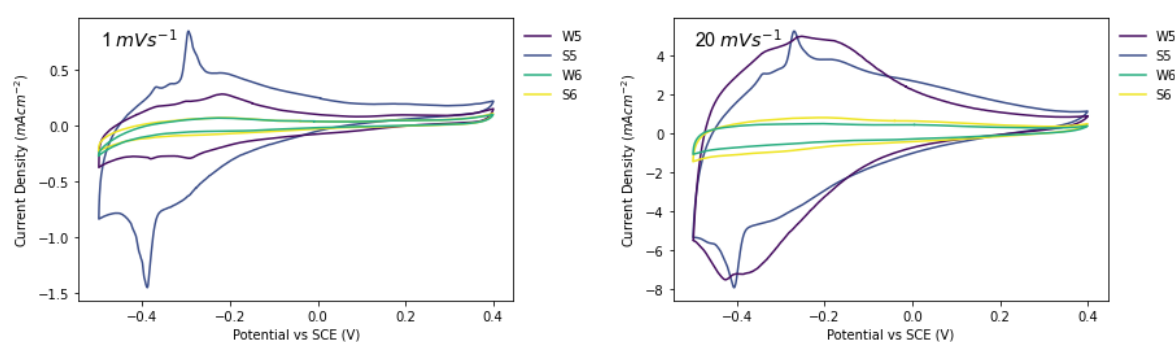


Figure 106 Micrographs of samples W6 and S6

Two explanations can be speculated upon for why an oxide surface persists in these conditions. The first is that the pH of the solution during hydrothermal conditions is lower than what is measured at room temperature because the dissociation of acid in solution increases with temperature, shifting the point of the Pourbaix to the left and retaining surface oxide. Secondly, the dissolution of oxide from the surface occurs in an unstirred, stagnant solution so it is likely a high concentration exists close to the substrate surface. Once the oven ends its programme, the reaction mixture cools to room temperature and the oxide precipitates out of solution, and intermolecular forces draw it to the substrate surface creating the loosely adhered surface observed.

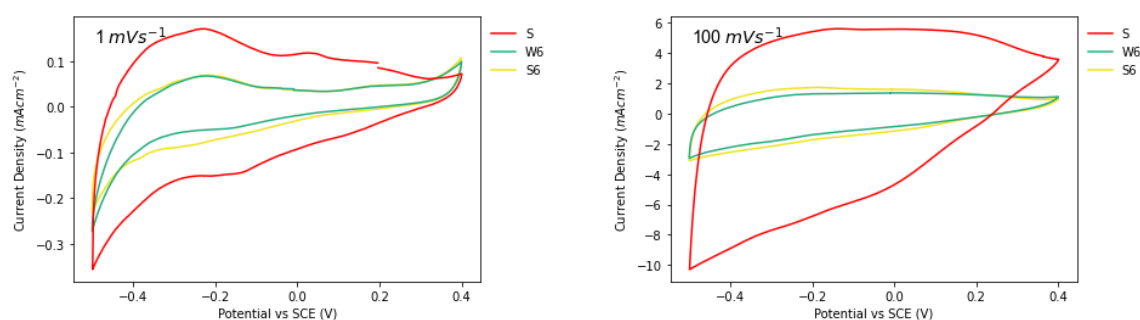


Sweep rate (mV/s)	Areal Capacity (mA _h cm ⁻²)			
	W5	S5	W6	S6
1	0.083	0.131	0.017	0.025
20	0.060	0.055	0.009	0.013

Figure 107 Cyclic Voltammetry of iteration 1 samples made at pH of 2 (W5, S5) against iteration 2 samples hydrothermally treated in deionised water at a pH of ~5.5 (W6, S6) at 1 mVs⁻¹ (left) and 20 mVs⁻¹ (right). The stored capacities for the displayed CVs are tabulated below the figures.

The electrochemical performance of these samples was quite different from W5 and S5. Figure 108 compares the CV of this iteration (W6, S6) with those synthesised at pH 2 and there is a clear drop in electrochemical activity. Even upon increase to 20 mVs⁻¹ (and higher) the W6 and S6 samples show little growth in the CV area. The yellow line of S6 is marginally larger than that of W6, which shows that some of the tungsten oxide from the seeding step remained on the surface but ultimately most dissolved off.

This reduced performance is made starker still when comparing the W6 and S6 samples with the seeded substrate. Figure 108 shows that the seeded substrate possesses a far greater activity than both these hydrothermally treated foils and confirms oxide has been dissolved. The shape of CV remaining is still consistent with tungsten oxide, albeit producing much smaller currents.



Sweep rate mV/s	Areal Capacity (mAhcm ⁻²)		
	S	W6	S6
1	0.053	0.017	0.025
100	0.022	0.009	0.007

Figure 108 Cyclic Voltammetry of Seeded Substrate against iteration 2 samples hydrothermally treated in deionised water at a pH of ~5.5 (W6, S6) at 1 mVs⁻¹ (left) and 20 mVs⁻¹ (right). The capacities for the CVs in the figure are tabulated below the figure.

It is clear from this iteration that the thin layer formed in the hydrothermal reaction with the removal of sodium tungstate is sensitive to pH. This iteration really acts as a control experiment to demonstrate that oxide development in the reaction is not solely from the temperature and pressure of the system. It would be of interest to vary the pH value closer to the value of 2 to ensure that the levels of dissolution here do not occur.

6.2.3 Iteration 3 – isolating substrate type from one another

Hitherto, an assumption has been made throughout the hydrothermal synthesis results presented that the two substrates do not interfere with one another. From a theoretical perspective, the substrates will interact differently with the solution. As discussed in section

1.3, the surface of an uncharged electrode influences the propensity for some ions in the solution to move closer to the electrode than others, meaning both will establish different double layers. Secondly, as discussed in great detail in Chapter 5 there is a difference in concentration of WO_3 between the Seeded and Pristine Foils at the beginning of the reaction. This iteration attempts to elucidate whether zero interference between substrates is a fair assumption or whether the described differences between the substrates, and their proximity invalidate it.

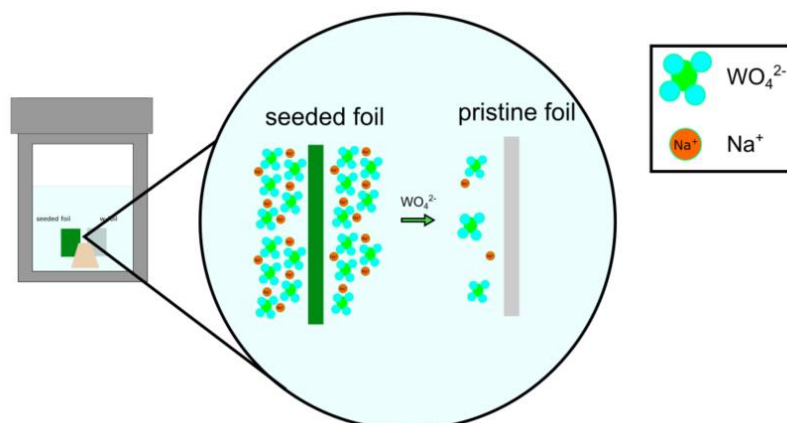


Figure 109 Schematic of hypothesised WO_4^{2-} diffusion from high concentration seeded foil to low concentration pristine tungsten foil during the hydrothermal reaction

Moreover, such an interference may not have been significant in the original synthesis scheme when sodium tungstate was present because there was a high concentration of WO_4^{2-} close to the surface regardless of what substrate is used. This is plainly not the case when sodium tungstate is left out of the reaction mixture, the only available WO_4^{2-} comes from that on the seeded substrate and that which may be created through oxidation of either substrate. It can be expected that the concentration gradient of solvated tungstate ions may diffuse from high-concentration seeded foil to low-concentration pristine foil as visualised in Figure 109.

The synthesis presented here isolates the pristine substrate in one autoclave and the seeded substrate in another blocking any influence between the samples. The size of influence can then be estimated through comparing those formed in a single autoclave. The visual appearance of these two cases can be seen in Figure 110.

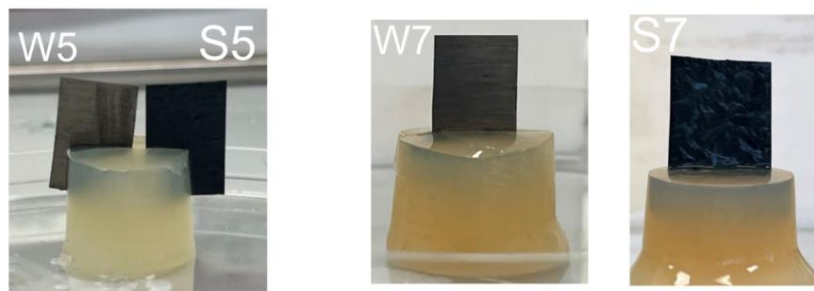
a) Same Autoclave b) Separate Autoclave

Figure 110 Photographs of iteration 1 samples (W5, S5) synthesised in the same autoclave; and of iteration 3 samples W7 and S7 using the same conditions but synthesised in their own isolated autoclave

Upon isolating the substrate types to their own autoclave there is a distinct change in the surface of the seeded substrate (S7) compared with that made in the same autoclave (S5). The S7 sample has a smoother oxide coating, reminiscent of the rubidium sulphate samples W4 and S4. In comparison, there is a more sputtered particle finish on the S5. The W7 sample made from a pristine foil is similar to W5 and W6.

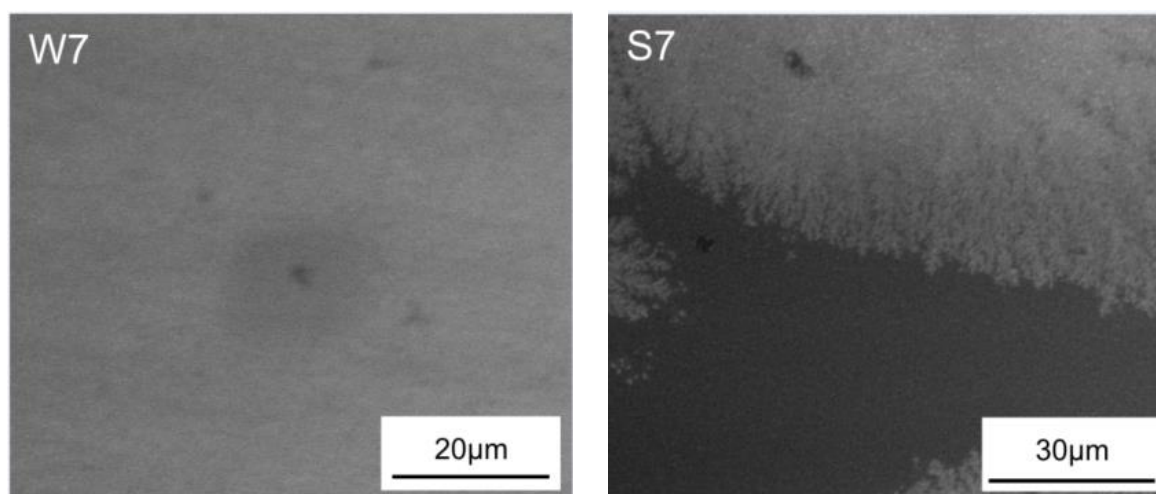
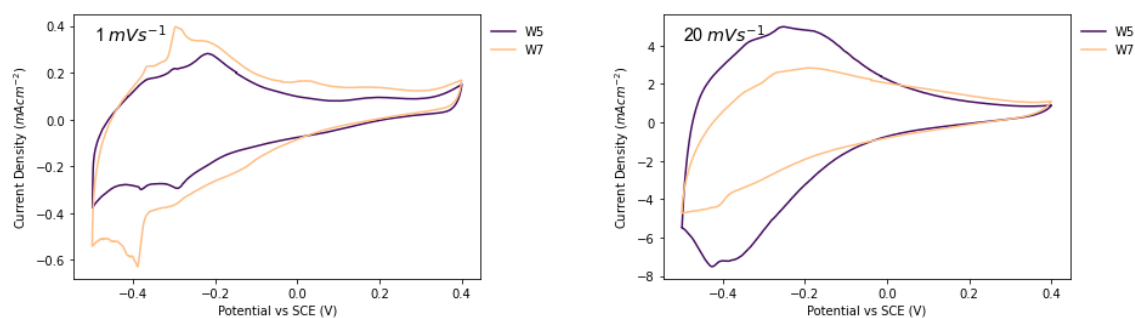


Figure 111 Micrographs of samples W7 and S7

The micrographs of samples W7 and S7 are shown in Figure 111. Again, the microstructures observed are consistent with the samples so far presented in this chapter: W7 has no discernible microstructure and the S7 has a thin microstructure coating with a “dune” like effect.

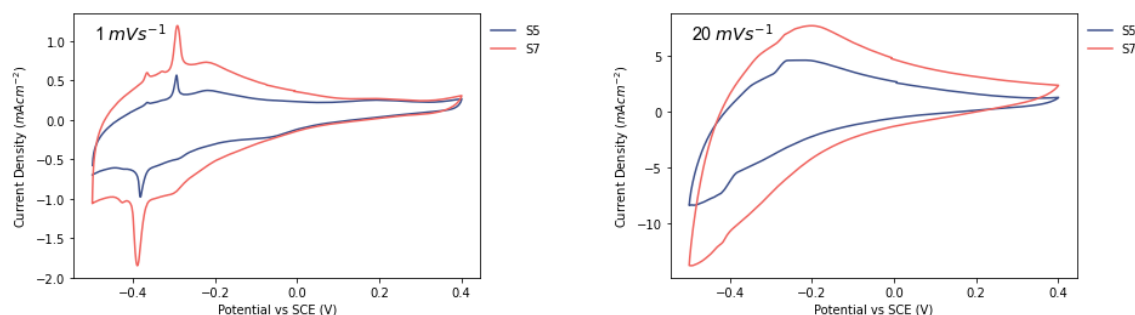
The difference between foils synthesized in shared and isolated autoclaves is made plain when comparing the CVs from the respective substrate types. Figure 112 shows the CV recorded at 1 and 20 mVs⁻¹ for the unseeded sample in the same autoclave (W5) and separate autoclaves (W7).



Scan Rate (mVs ⁻¹)	Areal Capacity (mAhcm ⁻²)	
	W5	W7
1	0.083	0.156
20	0.060	0.038

Figure 112 Comparison of Pristine Foils Cyclic Voltammetry of iteration 1 (W5) against iteration 4 (W7) at scan rates of 1 mVs⁻¹ and 20 mVs⁻¹. The areal capacities for the displayed CV figures are tabulated below.

At the low sweep rate of 1 mVs⁻¹, the area of the isolated foil's CV is larger but of comparable size than that of the shared one. This result flips as the sweep rate increases to 20 mVs⁻¹ where the foil synthesized in the shared autoclave becomes much more active, achieving a peak current double the magnitude. It is unclear why the lowest scan rate showed higher activity in W7, the isolated autoclaved. This trend was consistent across all repeats, as may be seen in Appendix L, which is interesting but difficult to interpret. It can be said the pristine foil sample's electrochemical performance benefited from sharing an autoclave with a seeded foil.



Scan Rate (mVs ⁻¹)	Areal Capacity (mAhcm ⁻²)	
	S5	S7
1	0.131	0.231
20	0.055	0.085

Figure 113 Comparison of Seeded Foils Cyclic Voltammetry of iteration 1 (S5) against iteration 4 (S7) at scan rates of 1 mVs⁻¹ and 20 mVs⁻¹

The seeded foils too displayed a noticeable change in the CV area when the foil was isolated. The CVs recorded at 1 and 20 mVs⁻¹ for shared autoclave sample S5 and isolated sample S7 area are shown in Figure 113. The shape of the response is similar to that of those synthesised in the same autoclave, but different current densities are achieved. The isolation of the seeded

foil led to a greater area and therein better activity than the seeded foil synthesised in a shared reactor.

Figure 114 presents the mean capacities calculated across multiple runs of the synthesis at each sweep rate allowing a trend to be seen. The seeded sample S7 seems to benefit from isolation, gaining capacity which means the pristine foils harmed their performance. The shared-autoclave sample S5 and isolated S7 have similar capacities beyond 20 mVs^{-1} . Low sweep rates, as outlined in the previous discussion, allow intercalation to proceed uninhibited but larger sweep rates become dominated by other processes which prevent intercalation. The net effect of isolation on the samples is therefore diminished beyond 20 mVs^{-1} because intercalation cannot proceed anyway.

The isolated W7 sample also has a higher capacity at lower sweep rates than the seeded sample, which suggests that isolation improved the performance. As discussed, this is puzzling, and no explanation can be offered, unless it is due to experimental uncertainty.

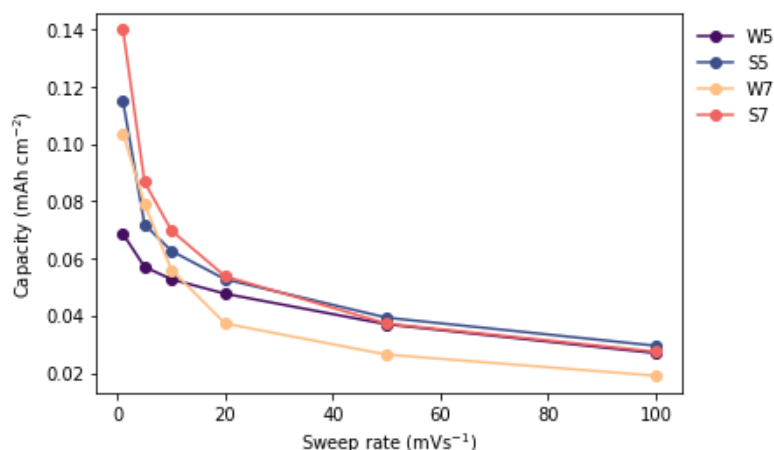


Figure 114 Areal Capacity values (mAhcm^{-2}) versus sweep rate for iteration 1 samples W5, S5 and iteration 3 samples W7 and S7

The concentration transfer mechanism outlined in Figure 109 is supported in the case of the seeded substrates because isolation was found to improve the capacity. However, the pristine w-foil data here are not definitive.

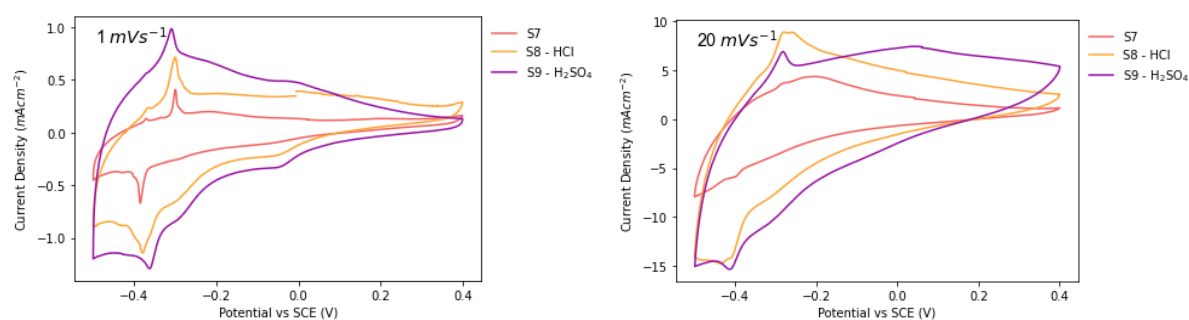
From reviewing the full complement of CVs recorded, it is clear that there is a noticeable greater variance in the area of these CVs compared with samples synthesized in the presence of sodium tungstate. This may be attributed to the seeding step being the sole determinant of WO_3 concentration pre-hydrothermal synthesis whereas the addition of Na_2WO_4 increases tungstate concentrations to a level which diminishes the effect of seed layer variance in the product's performance. That is to say, variance in the seeding step is amplified by the hydrothermal synthesis. A clear conclusion from this iteration is that pristine W-foil samples formed without sodium tungstate have much poorer performance than the seeded samples.

6.2.4 Iteration 4 – effect of acid only

Until this point, all of the synthesised W-WO₃ have employed a capping agent salt and an acid because of the much-discussed dual effect that may be achieved by having both. This section removes the capping agent, simplifying the reaction parameters to the seeded foil i.e. W-orthorhombic-WO₃ and an acid: hydrochloric or sulphuric acid. This dramatically simplified synthesis scheme shines a light on the role of protons and anions on the resulting microstructure by limiting the reaction to seeded substrate and acid. In this instance, the acid may be considered as the capping agent. The hydrochloric acid-directed sample is S8 and the sulphuric acid-directed sample is S9.

6.2.4.1 Iteration 4 - Electrochemical Characterisation

The electrochemical activity of these samples was a significant improvement to the other iterations in this chapter. The CV of the acid-directed samples is shown in Figure 115, where both S8 (HCl) and S9 (H₂SO₄) produce much larger areas than iterations current best S7.



Scan Rate (mVs ⁻¹)	Areal Capacity (mAhcm ⁻²)		
	S7	S8	S9
1	0.231	0.242	0.283
20	0.085	0.097	0.110

Figure 115 Comparison of Seeded Foils Cyclic Voltammetry of samples S7, S8 and S9 at scan rates of 1 mVs⁻¹ and 20 mVs⁻¹

The S8 and S9 samples share similar shapes of CV which is expected given their shared crystal phase and similar morphologies presented in the following section 6.2.4.2. The shape of the CV expands with increasing scan rate, retaining much of the features visible at the low scan rate and without much evidence of increased ohmic resistance. The S9 sample is made from sulphuric acid which creates the greater area and can be said to be the more active of the two.

This trend is more apparent when reviewing the averaged mean capacity versus sweep rate across three or more experimental runs as presented in Figure 116. The S9 sample has a superior capacity, and retention of the capacity, over the rest of the samples in this iteration. The S8 sample does have a better capacity than S7 at low scan rates but this drops away, and they mirror each other beyond 20 mVs⁻¹. This shows the sodium chloride added in the

case of S7 had a detrimental effect on the electrode. Reasons for this are discussed with the physical characterisation of S8.

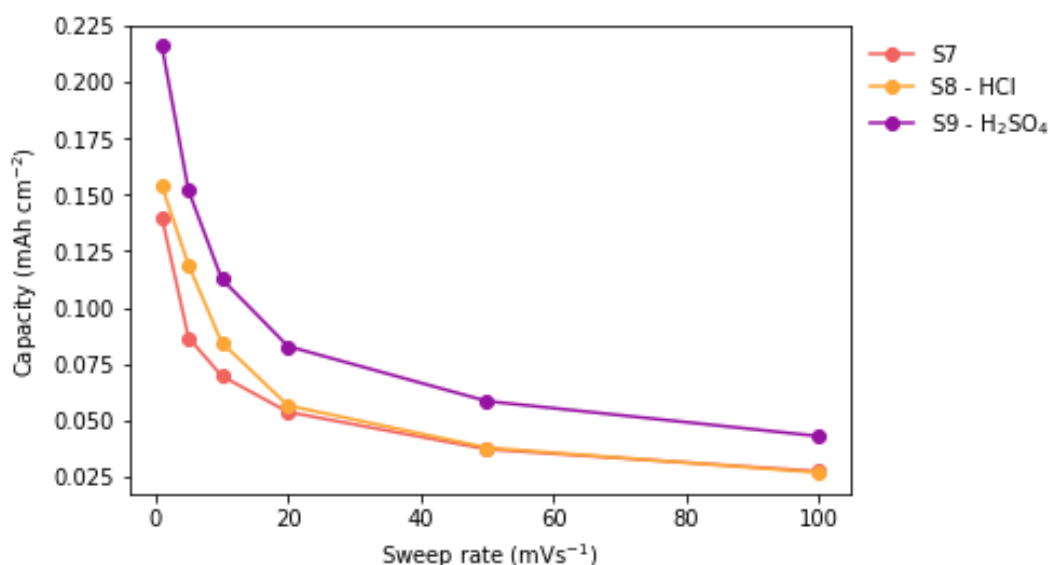
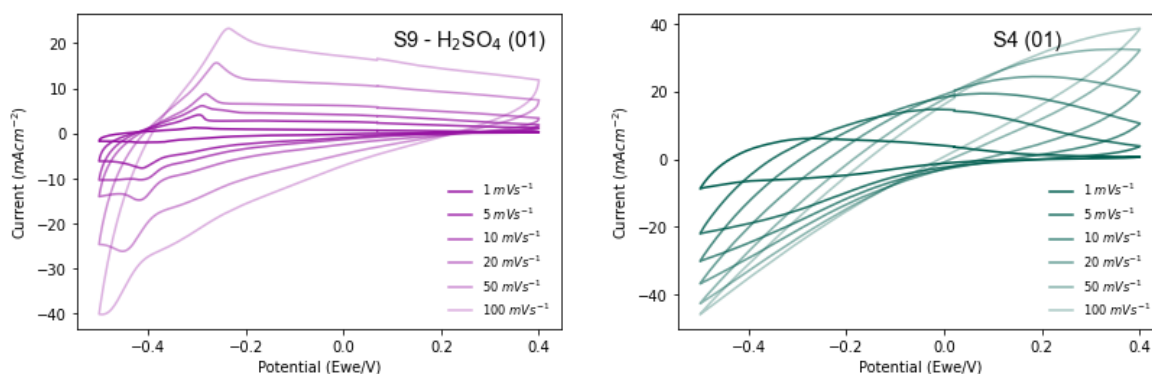


Figure 116 Mean Areal Capacity values (mAhcm⁻²) versus sweep rate for sample S7, S8 & S9

The positive performance of S9 warrants comparison with the hexagonal-WO₃ samples produced in previous chapters. The best-performing hexagonal-WO₃ foils were made from rubidium sulphate and so sample S4 is taken as the representative best-performing sample of the hexagonal-WO₃ samples for the purposes of this discussion. This discussion may be made in terms of hexagonal vs monoclinic because as discussed in 6.2.4.2.1 the phase of S9 is monoclinic.

Cyclic Voltammetry is used again to compare the performance of these samples. The left of Figure 117 shows S9 and the right shows S4. These CVs reach similar peak current densities, a cathodic minimum of -40 mAcm⁻² and an anodic maximum of over 20. There are sizeable differences in the data beyond that.



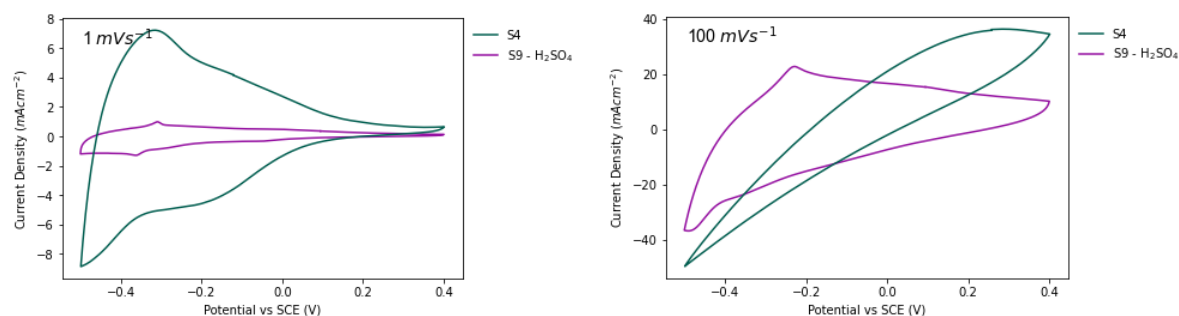
Scan Rate (mVs ⁻¹)	Areal Capacity (mAhcm ⁻²)	
	S9	S4
1	0.215	0.155
5	0.15	0.115
10	0.11	0.085
20	0.08	0.055
50	0.055	0.035
100	0.04	0.025

1	0.283	1.411
5	0.196	0.661
10	0.15	0.392
20	0.11	0.194
50	0.078	0.065
100	0.057	0.026

Figure 117 Cyclic Voltammograms of S9 (left) and S4 (right) at scan rates of 1-100 mVs^{-1} . The areal capacity of each CV is tabulated below the figure.

In the case of S9, the shape and area of the CV progressively increase with the sweep rate, retaining its shape and identifiable redox peaks. This is not the case in S4: as the sweep rate increases a skew progressively develops from an increased ohmic resistance. It can be concluded that S9 has a lower ohmic resistance in the electrode than S4 which, as discussed, may be attributed to the thinner layer of oxide negating poor electrical conductivity of the oxide and possibly to the sample holder.

Further comparison is made easier by analysing the CVs one on top of the other. Figure 118 contains the CVs for S4 and S9 at the lowest and highest scan rates used, 1 mVs^{-1} and 100 mVs^{-1} , respectively.



Scan Rate (mVs^{-1})	Areal Capacity (mAhcm^{-2})	
	S9	S4
1	0.283	1.411
20	0.11	0.194

Figure 118 Cyclic voltammograms of samples S4 and S9 compared at 1 mVs^{-1} (left) and 100 mVs^{-1} (right). The areal capacities for the presented CVs are tabulated below the figure.

At 1 mVs^{-1} , it is evident that the hexagonal phase, S4, is much more active than the monoclinic- WO_3 made with H_2SO_4 by a magnitude of 4 times. However, as the sweep rate is increased to 100 mVs^{-1} the pseudocapacitance of S4 degrades entirely, losing its pseudocapacitive shape. Conversely, the expanded CV area that accompanies the increasing scan rate observed in S9 exhibits a key property of any pseudocapacitive material: there is proportionality between the charge passed and the increase in sweep rate [97].

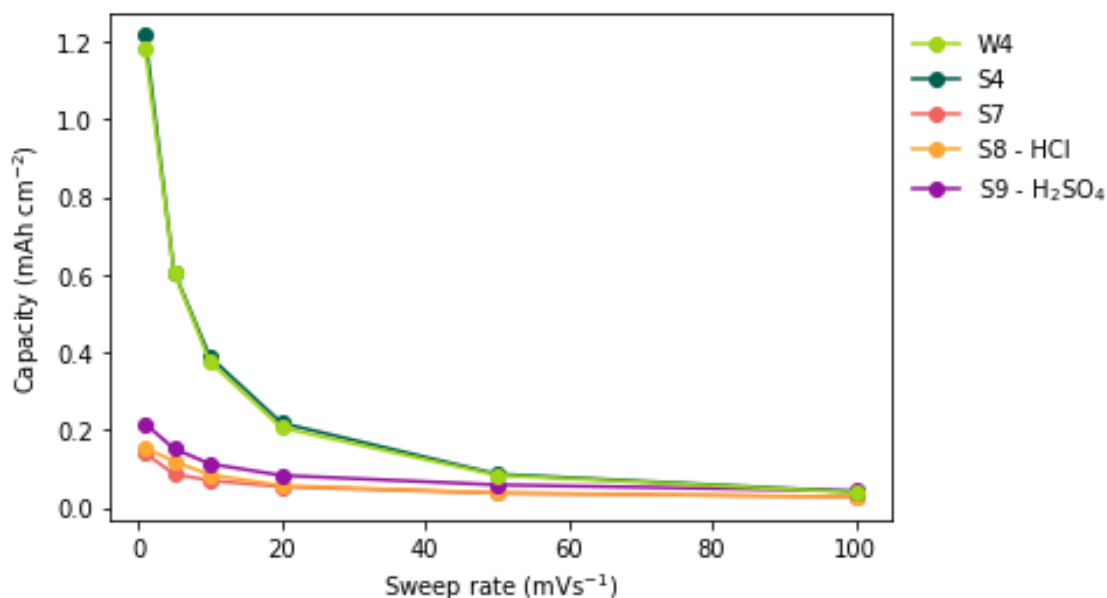


Figure 119 Mean Areal Capacity values (mAhcm²) of monoclinic versus hexagonal samples

An updated version of Figure 116 to show the samples against rubidium sulphate samples is presented in Figure 119 and it may be clearly seen despite the more pseudocapacitive behaviour shown by the monoclinic samples, their capacity is considerably lower than the hexagonal phase.

To summarise the difference between these sample types one must consider the crystal structure and the microstructure. The hexagonal phase, as noted, is best suited to charge storage because of its large channels offering faster proton transport and surface area for intercalation. However, the crystal function alone does not dictate if the electrodes performance is pseudocapacitive or not. The thickness and microstructure of the grown oxide surface will define how fast diffusion may occur and the electrical resistance from metal to the top of the oxide surface. Figure 119 and the previous discussion identify an inverse relationship between pseudocapacitance and the magnitude of capacity driven by the thickness of the layer. A thick layer can store more charge but in a less pseudocapacitive way than a thin layer which stores less charge but in a truly pseudocapacitive manner. Optimising these for a desired function is crucial for further binder free electrode studies.

Despite the enhanced pseudocapacitance of the S9 sample, it possessed a much smaller capacity than S4 due to the lower loading on the S9 foil. If the mass loading could be accurately measured or estimated, samples S8 and S9 would be expected deliver a higher specific capacitance and capacity than the W4 and S4 samples, and considerably so at higher sweep rates.

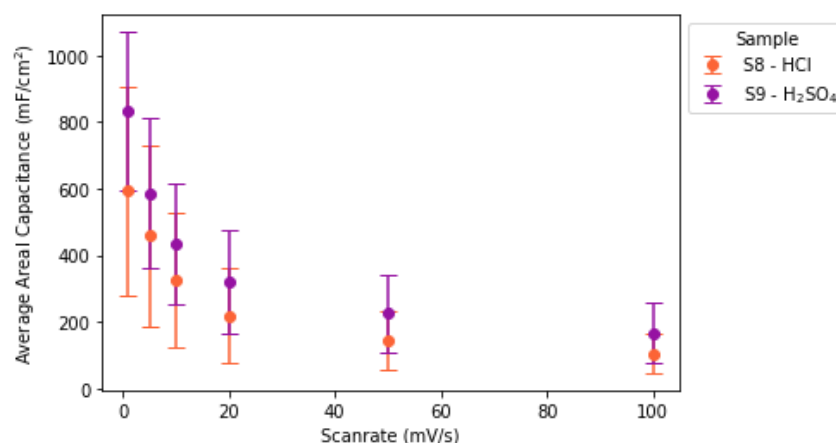


Figure 120 Average Areal Capacitance of samples S8 and S9 versus sweep rate

In the absence of a mass loading, an areal capacitance can instead be calculated using equation 27 and compared with literature. The calculated mean areal capacitances for S8 and S9 are presented in Figure 120. The variance of these values at scan rates below 20 mVs⁻¹ are quite large as shown by the error bars. Nevertheless, even the lowest of these values give large areal capacitances of over 200 mFcm⁻² at 20 mv/s and up to 800-1000 mFcm⁻² when 1 mVs⁻¹ is used. These values are of the same order of magnitude as WO₃ areal capacitances reported in literature where Liu et al reported 2552 mFcm⁻² at 1 mVs⁻¹ and Xu et al reported 240 mFcm⁻² at 10 mVs⁻¹ [120], [121]. The areal capacities of S8 and S9 may be viewed as quite promising as the capacitances reported would be expected to improve further with reaction optimisation and exploration using different oxidising agents.

6.2.4.2 Iteration 4 - Physical Characterisation

6.2.4.2.1 Grazing Incidence XRD

These samples made without sodium tungstate were much thinner than those made with, and so the more surface-sensitive grazing incidence XRD technique was used. The crystal structure of samples S7, S8 and S9 was determined using grazing incidence XRD. At the same time the seeded substrate, S was re-examined using this more sensitive technique. The obtained spectra for each sample along with PDF patterns for cubic tungsten (00-001-1204), hydro tungstite (00-18-1420) and orthorhombic tungstite (00-018-1418) are shown in Figure 121.

This technique provides far better resolution of the seeded substrate than the previously presented XRD spectra. There is a clear peak at 40.416° which comes from tungsten substrate present in all the samples to varying extent, although it is hardly visible in S7.

Considering the seeded substrate “S” first, the strongest peak is at 25.502 which is flanked by two broad, doublet peaks which are related to lattice parameters (111). This strongest line is consistent with the hydrated orthorhombic-WO₃·H₂O known as tungstite and similar spectra were obtained in other studies [51], [71], [122]. The peaks at 12.8°, 24° and 27° are not present

in the tungstite spectra but are present in “hydro tungstite” which is the dihydrate monoclinic phase $\text{WO}_3 \cdot 2\text{H}_2\text{O}$ (Figure 121 and another hydro tungstite spectra in Appendix N) which may indicate both are formed [61], [123].

Indeed, the CV recorded for the seeded spectra is strikingly similar to the well-performing $\text{WO}_3 \cdot 2\text{H}_2\text{O}$ electrodes of Mitchell *et al.* [37]. This would require further optical studies to ascertain for certain, however, this result points to a mixed hydrated phase being produced with nitric acid which was not picked up by conventional XRD.

The samples S7, S8 and S9 are all quite similar to one another and do share some peaks with the Seeded Substrate, S. They are though evidently a different phase to that of the Seeded Substrate.

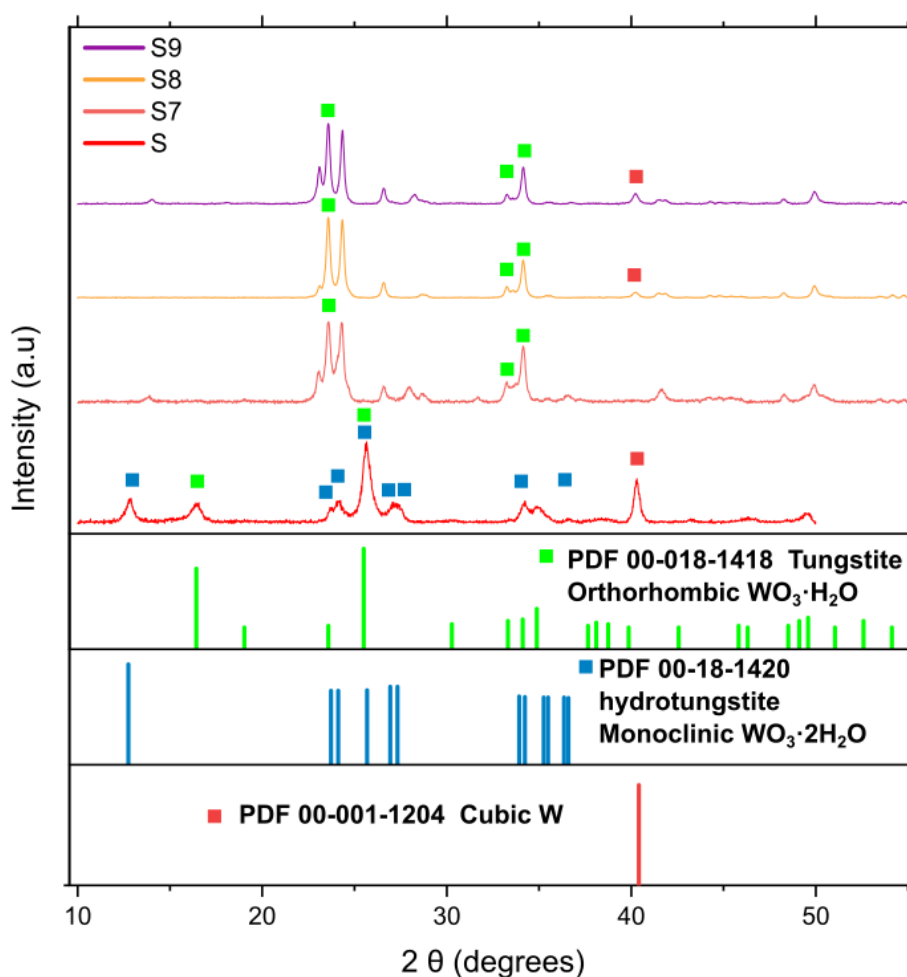
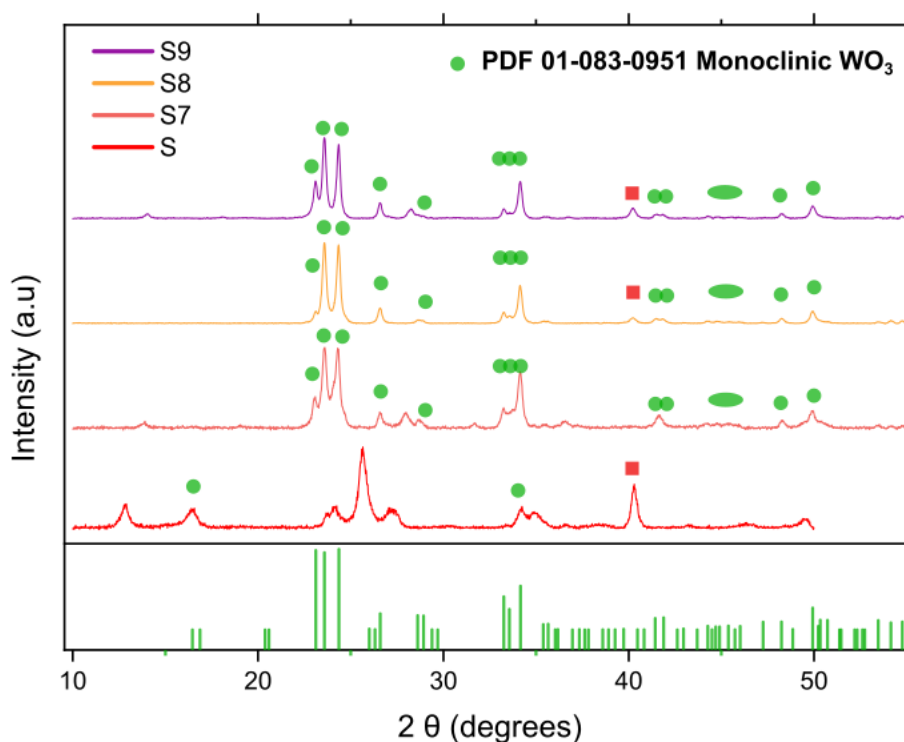


Figure 121 Grazing incidence angle 2° XRD Spectra of Seeded Substrate “S” with three hydrothermally produced samples S7, S8 and S9. The reference patterns for tungsten metal and two hydrated tungsten oxide phases are shown for reference

Figure 122 provides the recorded spectra again but provides different PDF patterns for comparison. The top graph of the figure has the PDF 01-083-0951 for monoclinic- WO_3 , and the bottom shows PDF 97-001-5514 reference for hydrated orthorhombic- $\text{WO}_3(\text{H}_2\text{O})_{0.33}$.

The presence of the monoclinic phase, the top XRD spectra in Figure 122, may be immediately identified through the triplet peak at 23.118° , 23.583° and 24.365° correlated to (0,0,2), (0,2,0) and (2, 0, 0) miller indices. The weakest of these indices is (0, 0, 2) at 23.118° which indicates the (0, 2, 0) and (2, 0, 0) planes perpendicular to the surface are preferred as the crystal grows rather than lateral growth parallel to it. This result is supported in the SEM micrographs where formations extend from the surface.

The second largest peaks between $33\text{--}34^\circ$ again are well indexed to the monoclinic phase. However, these peaks are also consistent with many Powder Diffraction Database (PDF) spectra related to the orthorhombic- WO_3 of varying hydration levels i.e. water confined between the lattice (Appendix N).



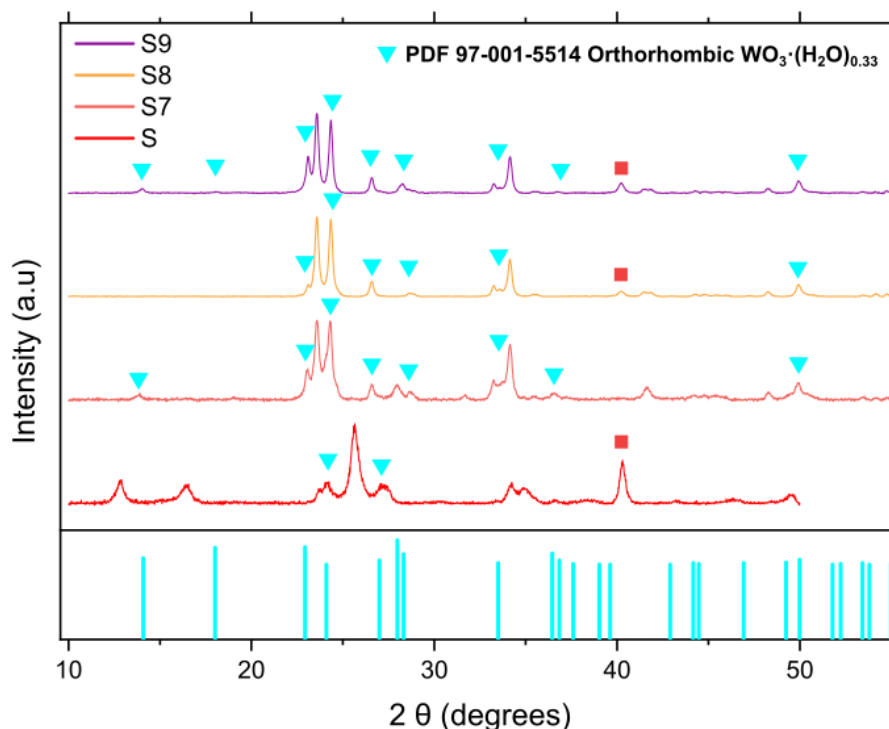


Figure 122 Grazing incidence angle 2° XRD Spectra of Seeded Substrate "S" with three hydrothermally produced samples S7, S8 and S9. The reference patterns for monoclinic- WO_3 and orthorhombic- $\text{WO}_3(\text{H}_2\text{O})_{0.33}$ are given. The tungsten metal peak from the substrate is denoted by a red square

Further to this some peaks are inconsistent with a pure monoclinic phase: peaks at 14° , 18° , 28° , and 36° present particularly in S7 and S9 spectra are consistent with hydrated orthorhombic- $\text{WO}_3(\text{H}_2\text{O})_{0.33}$ not monoclinic- WO_3 . Interestingly, the S8 sample, formed with HCl, only shows the peak at 28° , which may be interpreted as the chloride anion being less favourable to orthorhombic formation than SO_4^{2-} – consistent with some studies into anion influence on orthorhombic WO_3 growth [45], [124].

These peaks are interesting because they are indexed to orthorhombic planes perpendicular, or close to perpendicular, to the substrate. The 14° correlates to (0, 2, 0) of the orthorhombic phase, which is analogous to the 23.582° peak in the anhydrous monoclinic phase. Similarly, the 28° peak corresponds to (2, 2, 0) indices in the perpendicular direction, unique to the orthorhombic phase, however, a stronger peak for monoclinic (2, 2, 0) is present at 34° .

Finally, the 36° peak corresponds to (2, 2, 2) which is not quite perpendicular but is angled from the surface. Its matching monoclinic peak is at 41.886° and again is relatively much larger than the orthorhombic counterpart. Their presence indicates that there are some orthorhombic-shaped crystals present. The magnitude of these peaks, however, compared to the monoclinic equivalents is small which suggests the structure is monoclinic. Very similar, though much noisier, spectra to those obtained from S7, S8 and S9 have been identified as orthorhombic- WO_3 in [45], [49], [125] and the anhydrous orthorhombic- WO_3 phase again is

well indexed to the S7, S8 and S9 spectra (Appendix N). On the other hand, similar spectra have been reported as monoclinic- WO_3 [56] indicating the challenge in identification.

Figure 123 shows a schematic of monoclinic and orthorhombic lattice shapes with defining characteristics. Though these are similar they have been found to have drastically different performance as charge storage electrodes [49] and so the difference is important.

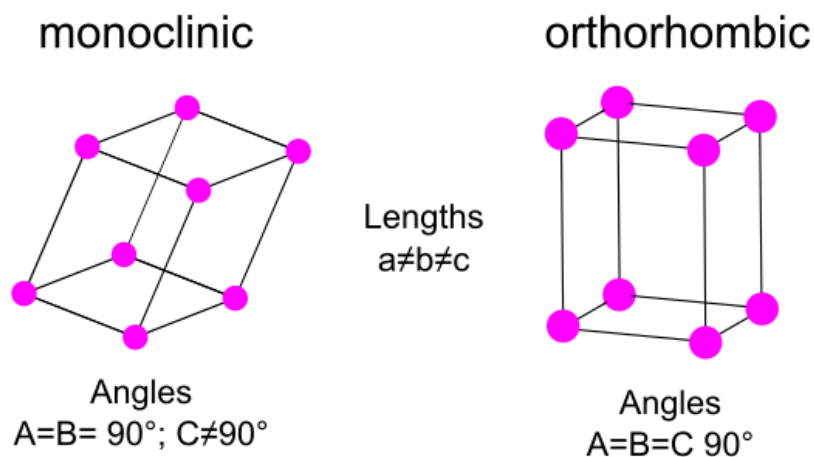


Figure 123 Schematic of monoclinic and orthorhombic WO_3 lattice shapes

The angle at which the monoclinic lattice deviates from 90° is less than a degree, for instance, it is 90.89° PDF 01-083-0951 displayed in Figure 122. It is therefore of no surprise that they share similar XRD spectra, and it is challenging to isolate one from the other.

It is known there is a temperature-dependent relationship upon WO_3 phase when calcining powders: Monoclinic $\text{WO}_3 \cdot 2\text{H}_2\text{O} >$ Orthorhombic $\text{WO}_3 \cdot \text{H}_2\text{O} >$ monoclinic WO_3 when different temperatures are used [17], [60]. It is then quite conceivable that the synthesis has produced a mixed-phase monoclinic-orthorhombic phase whereby confined structural water leads to both phases in the layer. It is also possible that the water content confined to the lattice is unique to this synthesis method and has rendered a partially hydrated phase close to that of orthorhombic- $\text{WO}_3(\text{H}_2\text{O})_{0.33}$. It is unlikely that the seed layer persists forming a bilayer of two phases, given that its strongest peaks entirely disappear.

In summary, the presence of the triplet peak is compelling to say that the monoclinic phase has been produced. However, there is evidence that some hydrated orthorhombic- WO_3 is present and more research beyond this result would be necessary to fully characterize the phase.

6.2.4.2.2 Appearance of S8 and S9

The images of cut portions of as-synthesised S8 and S9 may be seen in Figure 124.

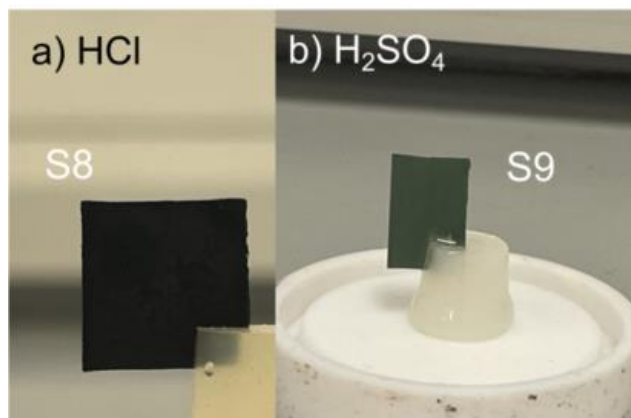


Figure 124 Photographs of as-synthesised foils made with only acid

Both have a flat, uniform surface which makes them appear closer to the Seeded Substrate (S) than any hydrothermally altered sample. An obvious observation is that the S8 samples were coloured blue when removed from the reaction, indicating a high extent of intercalation, whereas H₂SO₄ were green, indicating little intercalation. However, the explanation for why this occurs is uncertain.

It is worth commenting that these samples were easily the most stable, physically, of which were synthesised using the autoclave. The oxide of all previously discussed samples, with the exception of S the seeded substrate, could be wiped with a cotton bud and the remaining oxide surface removed with minimal, gentle sanding to expose the tungsten substrate. These samples, however, demanded two rigorous sanding procedures to expose the metal beneath, using rough then smooth sandpaper to remove the oxide. This is not the whole picture though, and their stability is discussed in full in section 6.2.4.2.4 'Post Electrochemical Characterisation SEM of S9'.

6.2.4.2.3 Microstructure of S8 and S9

A micrograph of S8 and S9 at 100 μm is shown in Figure 125. There is clear uniformity to both of these surfaces on the microscale as with the visual appearance.

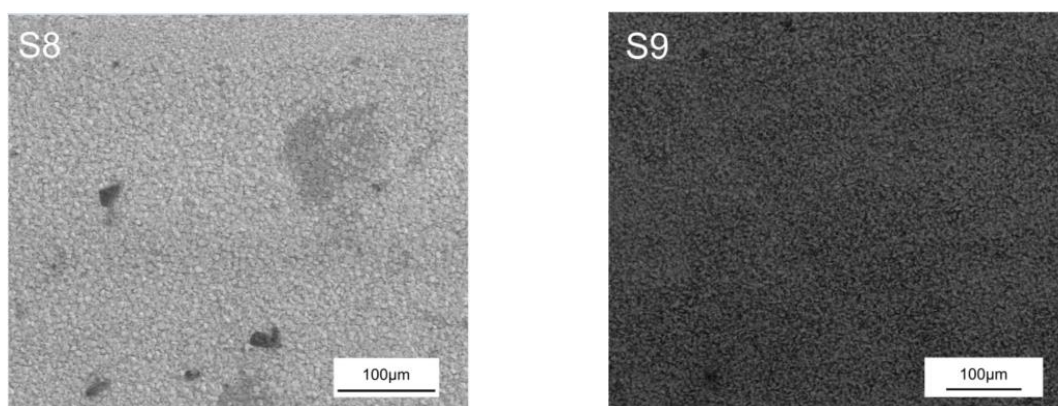


Figure 125 Micrographs of S8 and S9 at a scale of 100 μm

The surface of the purely HCl directed sample S8 is shown in two micrographs in Figure 126 at two levels of magnification. The image on the left shows a uniform surface composed of cubic microstructures, although there is a more amorphous structure to the left of the image which is less clear. A closer image of the cube structures, it becomes apparent these cubes are made up of nanorod-like structures which have agglomerated together.

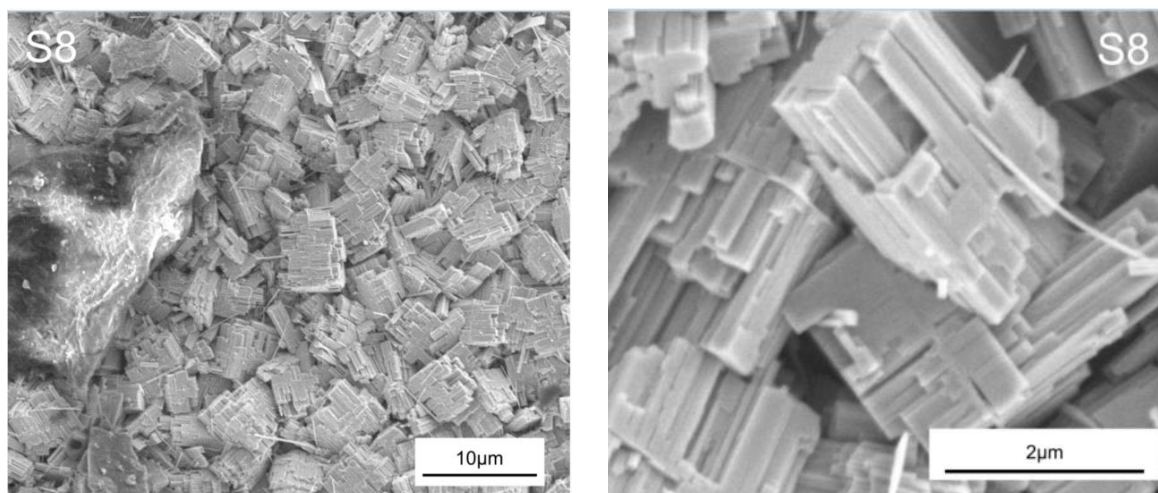


Figure 126 Micrographs of purely HCl directed samples at 10 μm and 2 μm scales

Similarly, the surface morphology of the sulphuric acid-directed samples S9 may be seen in Figure 127. The microstructure of S9, though still cube-like, is quite distinct from S8 made with HCl. In this case, the S9 block-like structures are interceded with plates angling out of the central block. This gives the S9 structure a larger more porous surface area than S8. The superior activity in S9 is accredited to the greater surface from these angular nanoplates emerging from the nano-cubes. The more regular cube formations in S8 lack these high surface area wedges and have a lower surface area and activity as a consequence.

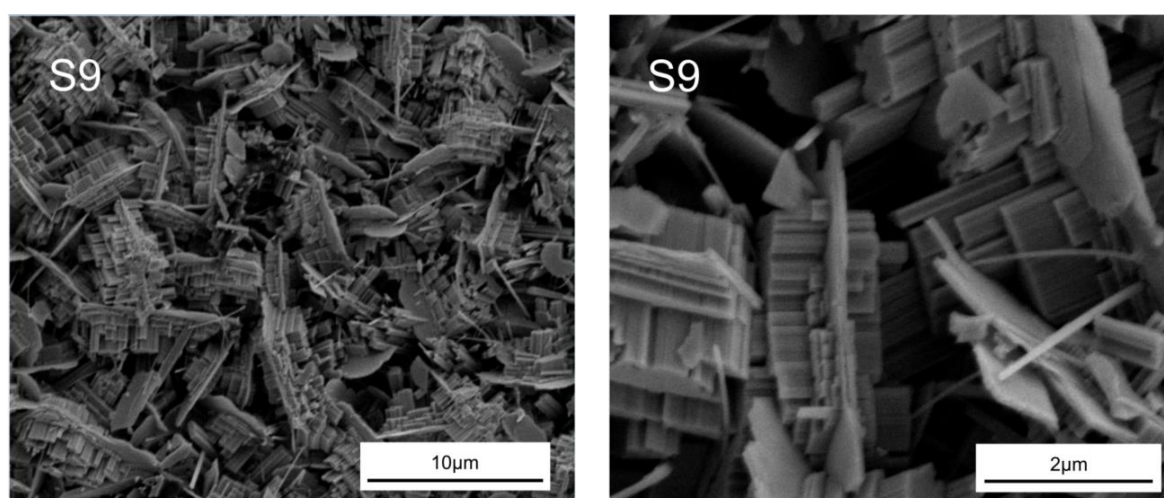


Figure 127 Micrographs of purely H_2SO_4 directed samples at 10 μm and 2 μm scales

The synthesis of cuboidal WO_3 powders across different phases, predominantly without an added capping agent and at a pH below 1.2, has been widely reported using sodium tungstate

(Na_2WO_4) [49], [87], [126], [127]. However, the existing literature presents varying explanations for this phenomenon. and this warrants further analysis to shed light on how the phase and morphology of S8 and S9 are formed.

The most consistent explanation for the morphologies observed in S8 and S9 comes from a report suggesting that the monoclinic phase forms from the decomposition of the orthorhombic phase [126]. Here, the authors report the orthorhombic phase redissolves into solution over time, dehydrates, and undergoes Ostwald ripening, leading to the expansion of the microstructure into monoclinic- WO_3 . This explanation, focusing on reaction temperature and residence time, is consistent with our findings in terms of crystal phase and morphology and offers insights into the possible detection of orthorhombic- WO_3 in S7 and S9.

This suggests in the absence of a cation to support the hexagonal tunnel, that the reaction time of 24 hours leads to the formation of monoclinic- WO_3 regardless of the conditions used. This explains the resultant phase but not the microstructure; it is clear the changing anion in solution has strongly influenced the growth of WO_3 .

The orthorhombic and monoclinic lattices grow in a layered structure where each tungsten atom is octahedrally coordinated by six oxygen atoms, forming a 3D network of corner-sharing WO_6 octahedra with confined water between these layers [17]. The way in which these layers agglomerate together into microstructures is then determined by the ions in solution. The acid determines the properties of the double layer formed between lattice, intercalated proton, and anion; and may itself bind to lattice sites. Organic acids have been studied in this context [45], [124] where organic and hydroxyl groups may be added to deliver the orthorhombic phase with the suggestion some anions selectively bind to the orthorhombic lattice over other phases. Further computational research would be necessary to illuminate the direct interaction between anion and lattice. The results of this work demonstrate chloride, sulphate, and nitrate influence both morphology and phase.

The cube-like morphology presented in the results here may be explained by making comments about the differences in the double layers formed with chloride and sulphate in the reaction, similar to as discussed in section 5.7. A speculative mechanism for how the double layer determines the microstructure is shown in Figure 128.

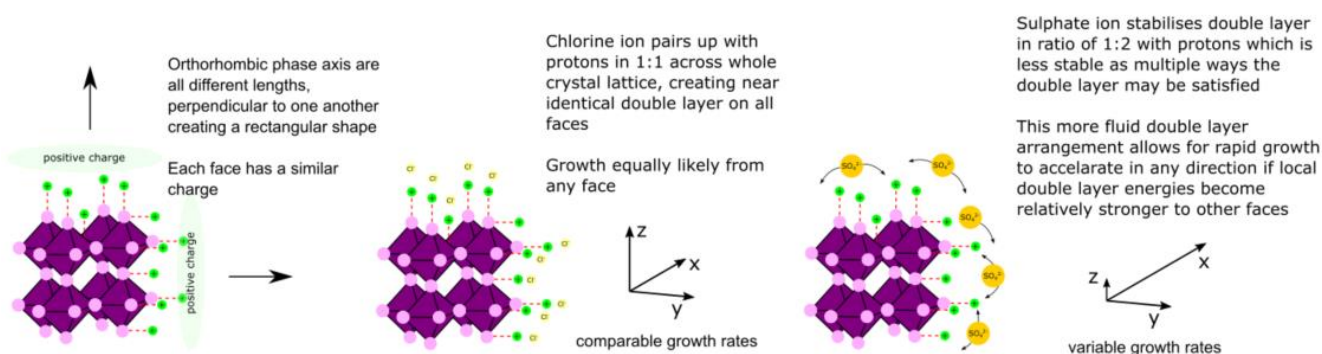


Figure 128 Schematic of double layer which balances charge of orthorhombic-WO₃ when Chlorine and Sulphate ions are present including growth rates

The orthorhombic lattice by definition has all perpendicular axes of different lengths; the monoclinic phase differs by having two perpendicular axes and one almost perpendicular. These geometries share similar dipole properties in that each face has a comparable negative charge to another, as visualised to the left of Figure 128. The protons in solution move to this charge and bring anions with them forming a double layer of similar energy on each face. This is quite different to the previously covered hexagonal phase on which the side of the hexagonal prism would have a higher positive charge than the top face.

As a consequence of this, the anions present become critical in determining what face of the monoclinic or orthorhombic WO₃ lattice will grow. The HCl-directed orthorhombic-WO₃ samples, S8, have a chloride ion of a single negative charge which balances the charge of each proton held by the lattice, creating a uniform energy barrier to the double layer surrounding the crystal. This makes growth from any face equally likely, as tungstate ions would have to displace ions held by a similar energy regardless to interact with the crystal. This creates the nano-cube structure of the S8 samples in Figure 126.

The sulphuric acid on the other hand has a double negative charge and thus needs to balance the charge of two protons held by the lattice. This makes the double layer inherently more unstable because there are multiple ways the charge may be balanced and will lead to ions dynamically shifting in the double layer.

On occasion, this movement of ions could result in local minima and maxima energies in the double layer. If a local minimum appears it will enable the oxide to rapidly grow from this point. If this occurs in the x-direction, then the rapid extension in the x-direction simultaneously grows the xz plane and xy plane increasing the double-layer energy of those faces. As the x-axis grows it increasingly prohibits growth in the y and z direction. This mechanism would explain how cube-like nanostructures with nanoplates jutting out which may be seen in Figure 127. In short, and as described in 5.7.2, the weakly bonded divalent sulphate ion enables lateral growth because of how it mediates the double layer, the stronger, monovalent chloride ion does not.

Comparing these results with the relevant literature some comments may be made on the synthesis. Firstly, limiting the cations in solution to protons increases the influence of anion upon the microstructure. Secondly, the presence of an orthorhombic phase detected when H₂SO₄ is used instead of HCl indicates careful selection of anion may retain more orthorhombic tungsten oxide hydrate. This is a favourable outcome given orthorhombic superior reported charge storage properties [37], [49] over anhydrous monoclinic. The anion has been shown to selectively promote orthorhombic formation evinced by Figure 122 and numerous other reported studies [45], [124]. Ultimately, the hydrothermal reaction drives the

orthorhombic phase to monoclinic and if the orthorhombic phase is desired another synthesis scheme needs to be employed.

6.2.4.2.4 Post Electrochemical Characterisation SEM of S9

As previously discussed, the S8 and S9 foils were the most stable of the hydrothermally produced samples. However, they were not immune to delamination which often occurred as they were cycled. Some SEM images were taken of S9 post-characterisation to ascertain what occurred on the microscale are presented in Figure 129.

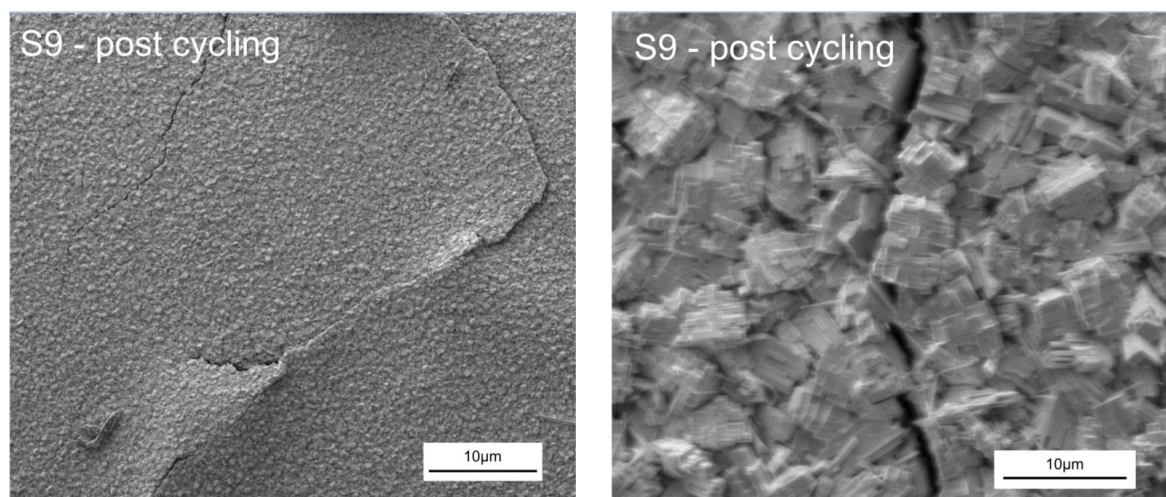


Figure 129 SEM micrographs of S9 post electrochemical characterisation

The dense, continuous layer that was present in Figure 125 (right) and Figure 127 has cracked and appears to be shifting over one another like tectonic plates. The right image of Figure 129 shows a thick break and it may be seen how these components would fit together. It is quite clear the microstructure post-cycling is unchanged with cube-like structures still present. A lesser magnification micrograph with an accompanying photograph is shown in Figure 130 to show the scale of the cracking on the micro and macro scales.

On this scale, it is clear the damage that is done to the electrode. The nature of the oxide altered after being cycled moving from a dense, robust coating that required sanding to be removed, to a moist, poorly adhered layer that would wipe off, and delaminate. The root cause of the cracking can be attributed to the already described swelling and contraction the lattice experiences with the concomitant intercalation and deintercalation of protons. It also suggests that the transition between fully intercalated to proton-free state draws water, or H_2SO_4 , into the lattice making it more hydrated and far less likely able to remain on the surface.

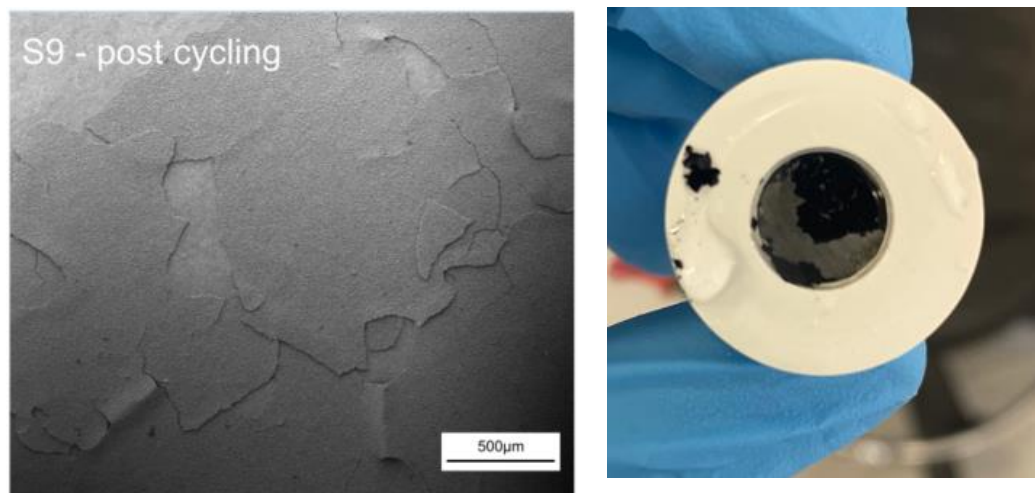


Figure 130 Zoomed out micrograph (left) and photograph (right) of S9 electrode post electrochemical characterisation

It would be remiss to not add the considerable mechanical stress these samples were subjected to when preparing for characterisation to this discussion. To expose a tungsten metal surface upon one side for electrical connection with the sample holder necessitated extensive sanding with different grades of sandpaper. It is quite reasonable to assume this warped the substrate and contributed to destabilizing the oxide surface.

6.3 Conclusion

The original synthesis scheme was systematically studied by removing and blocking certain parameters. Through changing conditions of the synthesis and characterising the resultant foil electrodes using Cyclic Voltammetry and SEM, several interesting points were uncovered in each iteration:

- The first iteration removed sodium tungstate and found a thinner layer of oxide developed which was to be expected. There was an enhancement in the activity of these foils compared to the substrates which pointed to a more simple and fruitful synthesis procedure.
- The second iteration sought to find whether the pH was critical in the oxide formation, as it is in powder WO_3 synthesis, or whether a change to the oxide may be achieved through the hydrothermal temperature and pressure solely. This was completed by comparing the synthesis at a pH of 2 versus using only deionised water. Hydrothermally treating the substrates in deionised water stripped the seeded oxide from the surface and led to poorly performing electrodes, with the little activity measured coming from the oxide which persisted through the reaction. This supports the notion identified in Chapter 5 that the seed layer does not provide epitaxial surface for a hexagonal phase as it itself changes during the reaction.
- The third iteration challenged an assumption made throughout the research presented so far, that having two substrates within the same reaction would lead to interference

with one another. It was found that there was a noticeable difference between samples produced in isolated autoclaves and shared autoclaves. Consequently, the seeded substrate was only considered moving forward because of its superior performance over the pristine substrate.

- The fourth and final iteration simplified the hydrothermal reaction conditions to the seeded substrate and an acid solution, removing any capping agent effect. This created conditions where the proton and anion in solution would solely determine the nature of the oxide. This was found to be the best-performing and most promising synthesis route of all the iterative steps. Their areal capacitances were found to be to the same order of magnitude as other WO_3 electrodes from literature, although mass loading could not be determined for a complete comparison. It was found that changing the anion could dramatically alter the morphology and to a lesser extent the phase which opens a highly promising synthesis route which may improve their areal capacitance further.
- The monoclinic- WO_3 foils reported in the fourth step were found to be more stable than the hexagonal phase samples but able to store less charge due to a lower mass loading. Nevertheless, with many acids to be investigated and the pH, temperature, and reaction time optimised, this is a highly appealing synthesis route requiring minimal reactants and is easy to control.

The question arises: can a thin layer of hexagonal- WO_3 be grown on the W-foil surface without the need for a tungsten salt, like Na_2WO_4 ? Such an electrode design would pair the benefits of a thin oxide layer with the theoretical performance of the hexagonal polymorph. The results do not conclude definitively either way whether the hexagonal phase is possible on removing Na_2WO_4 from the hydrothermal reaction. A highly accurate concentration of cation such as Na^+ would have to be added and be tailored to the pH of the solution – it seems the 1g of NaCl added in this work was too much.

The hexagonal phase binder-free electrodes have a higher areal capacity than the monoclinic counterparts, as may be seen in Figure 119. However, the retention of pseudocapacitive performance seen within the S8 and S9 Samples not present in hexagonal binder-free electrodes draws a focus to the benefit of having thin layer coatings.

A thin layer of hexagonal- WO_3 would hypothetically make the highest capacity and best performing W- WO_3 electrode by keeping the hexagonal phase's superior intercalation properties whilst negating the resistive effects encountered with a thicker deposit.

However, finding the optimal capping agent concentration in conjunction with pH, temperature and reaction time adds another level of complexity to finding a high-performance electrode. Additionally, the poor adhesion the hexagonal phase has shown in this work suggests that the

phase is fundamentally ill-suited to being the active material in W-WO₃ architectures, with the caveat that this may be improved if the layer is thin enough.

7 Characterisation of Powder Based WO₃ Electrodes

7.1 Introduction

This chapter intends to give perspective on the binder-free electrode architecture by comparing their performance with that of more conventional hexagonal-WO₃ powder-based electrodes formed by making an ink with the active powder, which is then coated upon the conductive substrate, in this case, tungsten foil. These inks were produced using the powders that were formed as a by-product of synthesising the W-hexagonal-M_xWO₃ electrodes. Since the powder is formed simultaneously from the surrounding solution in identical conditions it makes for a good comparison between the solution and surface oxides. Four powders were characterised, one for each of the capping agents. Each was given its own label, beginning with P and the number corresponding to the capping agent, and a colour so that it may be identified in the data. These can be seen in Table 19.

Table 19 Reference table for powder sample's powder Capping Agent and corresponding label & colour

Sample Label	Capping Agent	Acid	Colour
P1	NaCl	HCl	Dark Blue
P2	Na ₂ SO ₄	H ₂ SO ₄	Brown
P3	(NH ₄) ₂ SO ₄	H ₂ SO ₄	Light Purple
P4	Rb ₂ SO ₄	H ₂ SO ₄	Green

The comparative analysis between the binder-free electrodes and these powder-based WO₃ electrodes sought to determine the better electrochemical performance and stability and link that to the physical characteristics, answering the fourth research aim of the report. The results of this analysis were useful in identifying promising routes of binder-free electrode research and suggesting general principles for future investigations.

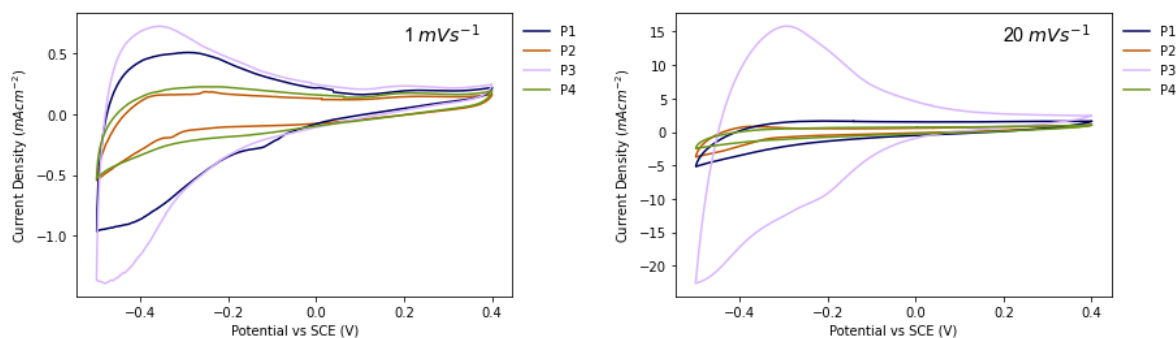
7.2 Electrochemical Characterisation of Powder Electrodes

7.2.1 CV Comparison of Powder Based Electrodes with Binder Free Electrodes

The CV for each of the powder-based samples per unit area at 1 and 20 mVs⁻¹ is presented in Figure 131. It may be immediately seen that the P3 sample (directed by ammonium sulphate) has the highest activity of any of the powders. What is more, it retains its shape with the increasing sweep rate which is visible even up to 50 mVs⁻¹ (Appendix M.3 & M.5) and certainly displays less of a resistivity developing within the samples with increasing sweep rate.

This of course could be attributed to the ink formation method used. Each powder was collected, and dried at room temperature and an ink was formed using a specific amount of WO₃ powder (~1mg) regardless of M cation known to be present. This means there is an inherent bias, especially against rubidium samples over sodium and ammonium which have

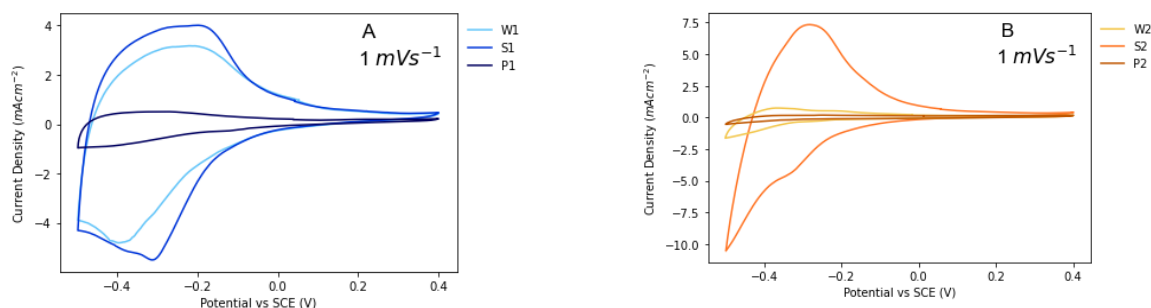
smaller gram formula masses. Ammonium, with the smallest mass, would be expected to have the greatest mass of WO₃ upon the electrode so perhaps it is not surprising it performed the best. This method was used because it was a straightforward way of comparing the mass of active material versus the mass of active material. If the x content in M_xWO₃ is unknown for each, a more sophisticated method could be used.

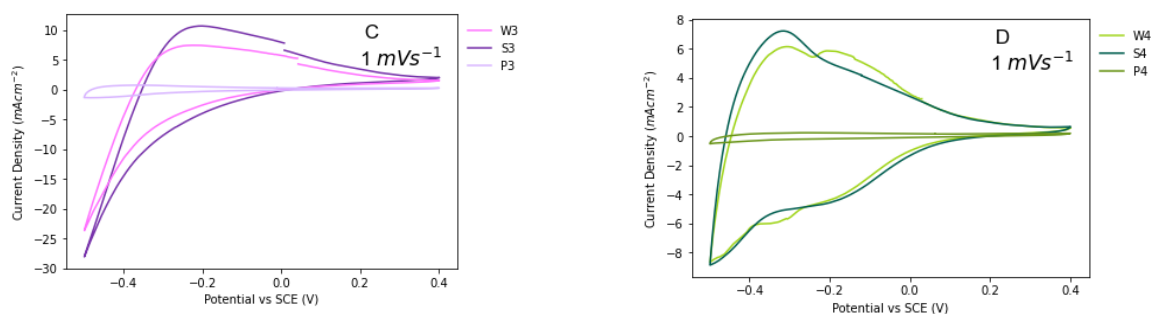


Scan Rate (mVs ⁻¹)	Areal Capacity (mAhcm ⁻²)			
	P1	P2	P3	P4
1	0.15	0.072	0.292	0.072
20	0.068	0.018	0.114	0.022

Figure 131 Cyclic Voltammograms of powder samples at 1 mVs⁻¹ (left) and 20mVs⁻¹ (right). The areal capacities are tabulated below the figures.

The performance of hydrothermally grown W-WO₃ electrodes may be put in perspective by offering another straightforward comparison between powder-based WO₃ electrodes made from the same reaction conditions. These simplified, and unoptimized, powder-based electrodes are useful in understanding the promise of the binder-free electrode architecture. Taking the simplest comparison available of powder-based versus binder-free on a per-area basis (Figure 132) it is quite clear that the binder-free electrodes are the more active than that of the powder electrode.

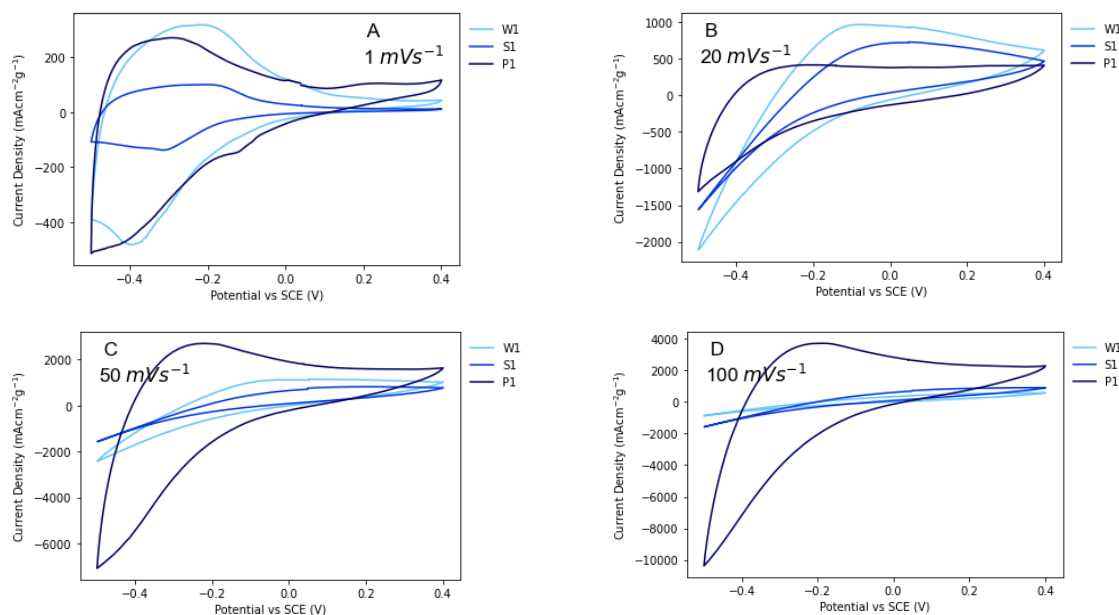




Scan rate (mVs ⁻¹)	Areal Capacity (mAhcm ⁻²)											
	W1	S1	P1	W2	S2	P2	W3	S3	P3	W4	S4	P4
1	0.89	1.28	0.15	0.15	0.98	0.07	5.72	1.70	0.29	1.45	1.41	0.07

Figure 132 Cyclic Voltammograms of W, S and P electrode types for capping agents a) NaCl b) Na₂SO₄ c) (NH₄)₂SO₄ d) Rb₂SO₄. The areal capacities of the presented CV data is tabulated below the figures.

This comparison, however, is misleading as the mass loadings of the binder-free samples are greater in the region of 10 or more times larger than the mass of the powder counterparts. If the data presented in Figure 132 is normalised by the active mass of WO₃ coated on each electrode, a vastly different trend becomes apparent. Taking the samples directed by NaCl as an example, the following CVs recorded using W1, S1 and P1 electrodes are presented in Figure 133.



Sweep rate (mVs ⁻¹)	Areal Capacity (mAhcm ⁻²)		
	W1	S1	P1
1	0.894	1.275	0.15
20	0.104	0.111	0.098
50	0.039	0.04	0.053

100	0.02	0.019	0.028
-----	------	-------	-------

Figure 133 Cyclic Voltammograms of W1, S1 and P1 electrode types for capping agents NaCl at four different sweep rates. The areal capacities are tabulated below the figures.

Looking at the slowest scan rate, 1 mVs⁻¹ in Figure 133 A, up to a scan rate of 20 mVs⁻¹ the current densities achieved from all the samples are comparable. At 20 mVs⁻¹ the binder-free samples, W1 and S1, achieve higher current densities than the powder samples albeit with a more distorted shape from the layer's ohmic resistance. Once 20 mVs⁻¹ has been surpassed the powder electrode P1 achieves much higher current densities than the W1 and S1 sample whilst retaining a shape of curve consistent with an intercalation system.

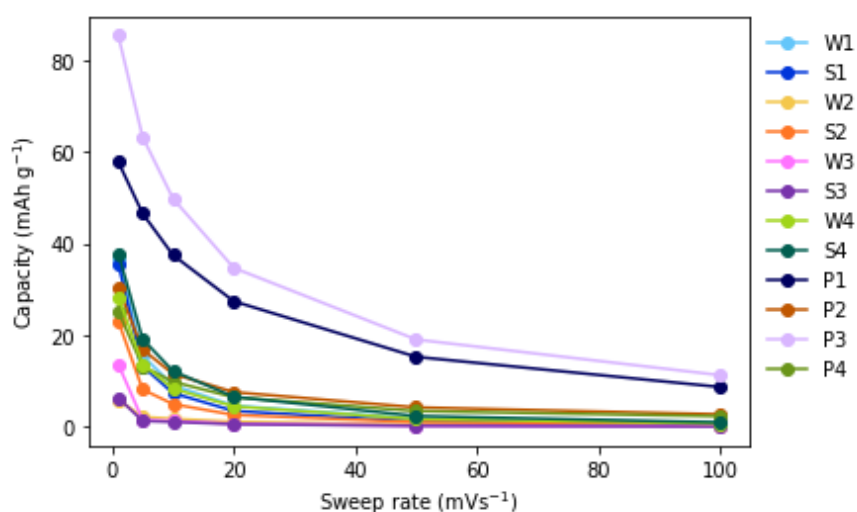


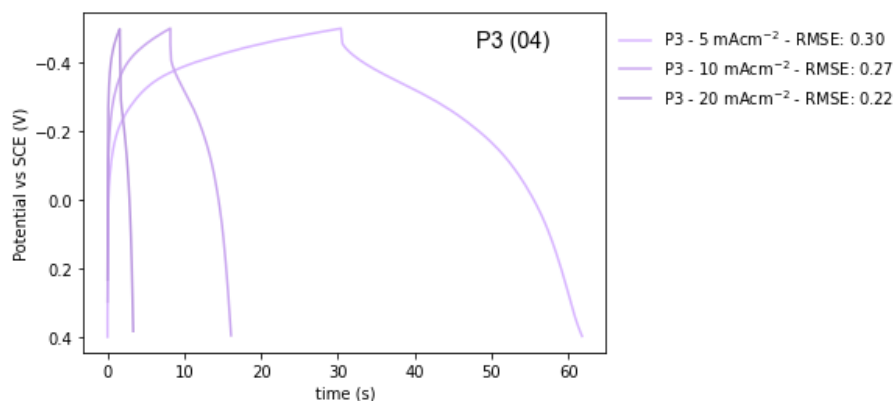
Figure 134 Gravimetric Capacity (mAhg⁻¹) versus sweep rate (mVs⁻¹)

Figure 134 makes this point clearer still, plotting the calculated gravimetric capacity (mAhg⁻¹) against an increasing sweep rate. All the powder samples produce a much larger gravimetric capacity than their binder-free counterparts. Most notably from Figure 131, the ammonium-directed powder-based electrode P3 performed extremely well with a top average capacity of 85 mAhg⁻¹ which drops to a capacity above the other presented samples at 100 mVs⁻¹. The sodium-based powder sample, P1, performed similarly well, with a lower top capacity around 60 mAhg⁻¹ but reaching a similar point to P3 at 100 mVs⁻¹. These two samples are quite encouraging, they experience the typical drop in capacity with sweep rate, but their structure still achieves intercalation at these rapid rates.

7.2.2 GCD Comparison between binder-free and powder electrodes

Figure 135 shows one of the obtained GCD curves for sample P3, the best-performing sample, as representative of all the samples. The powder electrodes' galvanostatic charge-discharge data was recorded in the same conditions as the binder-free samples and the full array of data may be seen in appendices O.6 and O.6.1. The shape of the GCD curves is consistent with those presented previously in section 4.3 with a pointed bell shape appearing.

The specific discharge capacity of P3 at 5 mAcm⁻² is the highest capacity presented of the WO₃ samples discussed in this work. As discussed later in this discussion, see Figure 137, the specific capacities of the powder and hydrothermally grown samples are similar.



Current Density (mAcm ⁻²)	Specific Discharge Capacity (mAhg ⁻¹)
5	64.87
10	56.48
20	44.37

Figure 135 GCD Curve of a P3 sample as representative of the powder dataset. The tabulated specific discharge capacity for the curves is shown below the figure.

The DCIR is evident upon switching cycles and can be compared directly with the binder-free samples. Figure 136 displays the potential reached by the ohmic drop as a function of current density, the blue polygon on the left groups the hexagonal binder free samples and the yellow on the right groups the powder-based samples.

The magnitude of the drop can be interpreted as a measure of resistance in the sample. It is evident that the powder-based samples have a much lower ohmic drop compared to the binder-free electrodes, and across a much larger current range, with the drop more often than not falling only to -0.4V or less. The binder-free electrodes, for which the current density was much lower, dropped to much lower values past -0.4V.

The smaller drop in the powder samples is a function of the comparatively much smaller mass loading, and therein thickness of coating, of the powder coatings over the grown ones. This thins the distance between the current collector and the active material allowing for good electrical conduction throughout the electrode, reducing the impact of the active material's lower conductivity. What is more, the characteristic length protons must diffuse within the bronze before intercalating is reduced, perhaps even facilitated by the Nafion which binds the powder to the current collector.

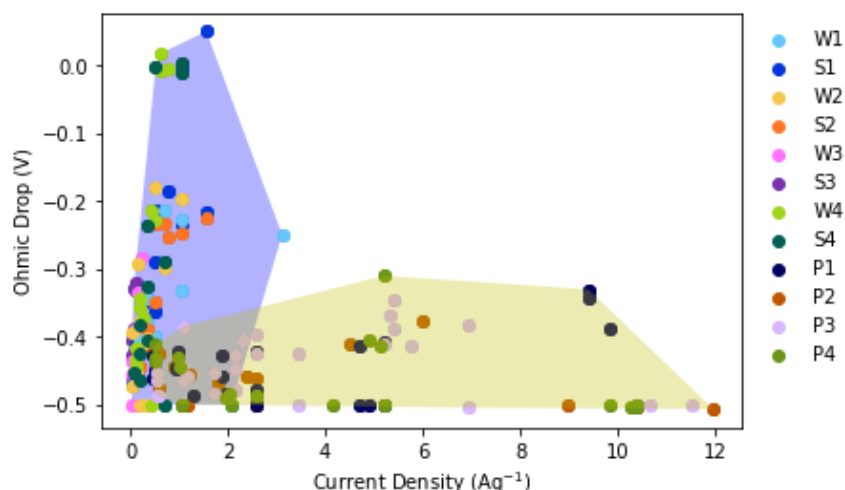


Figure 136 Potential at which ohmic drops against current density used in the galvanostatic charge-discharge cycling: the binder-free samples grouped by a blue polygon & the powder-based samples grouped by a yellow polygon

The gravimetric capacities of the powder and binder-free electrodes were compared against the current density set by area and mass basis. The average specific discharge capacity (mAhg⁻¹) of the samples as a function of areal current densities is shown in the left graph of Figure 137. The capacities calculated from the charge-discharge cycling offer a less clear trend than those calculated from the CV data (Figure 134). Powder sample P3 displays the highest recorded capacity of all samples at a low current density but this declines faster with increasing current density than the other best-performing binder-free samples.

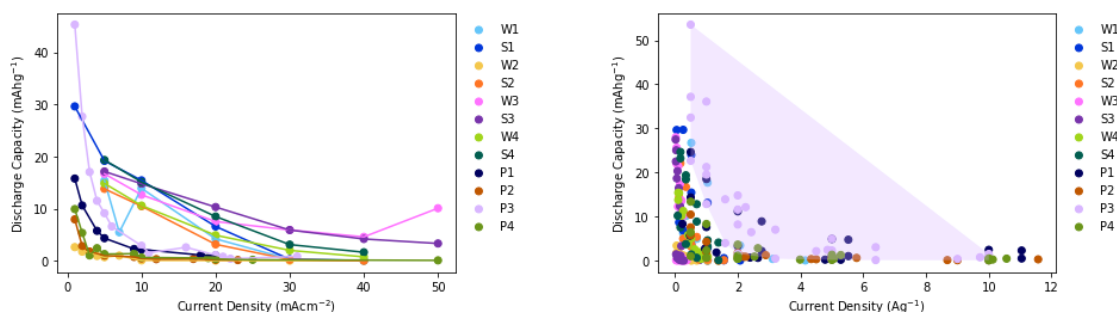


Figure 137 Gravimetric Discharge Capacity (mAhg⁻¹) against areal current density (left) and specific current density (right) for binder-free samples and powder-based samples

The gravimetric current density used in the binder-free characterisation is measured and not set because the loading is unknown. For this reason, an average value may not be calculated for the specific current density (Ag⁻¹) as each characterisation had a slightly different mass loading and therein a different current density. Instead, a scatter graph was plotted, shown on the right of Figure 137, to display the full dataset. It may be seen from this graph that the capacities of sample P3 are the highest and depreciate slower than the other samples. This is highlighted with a pink polygon mapping these data points.

The GCD data allows for energy and power density to be estimated from the 3-electrode cell setup and these values can be used to create a Ragone diagram normalised by unit mass

and by unit area. The result of this analysis is presented in Figure 138. Using the same colours of blue for binder-free hexagonal electrodes and yellow for powder-based hexagonal electrodes, the sample performance is mapped on the Ragone to identify a trend in the full dataset.

The gravimetric energy and power densities are displayed in the left graph of Figure 138 and the yellow powder-based region occupies the top of the figure, and the blue binder-free region occupies the bottom area. This shows that the powder-based samples possess the better performance of the two occupying both the high power and high energy regions. Interestingly, both data sets expand across similar energy-density ranges, though this is a function of tungsten oxide's intrinsic ability to store charge per unit mass. The power density however is more dependent on the electrode surface and its diffusion characteristics which separates the two electrode types here.

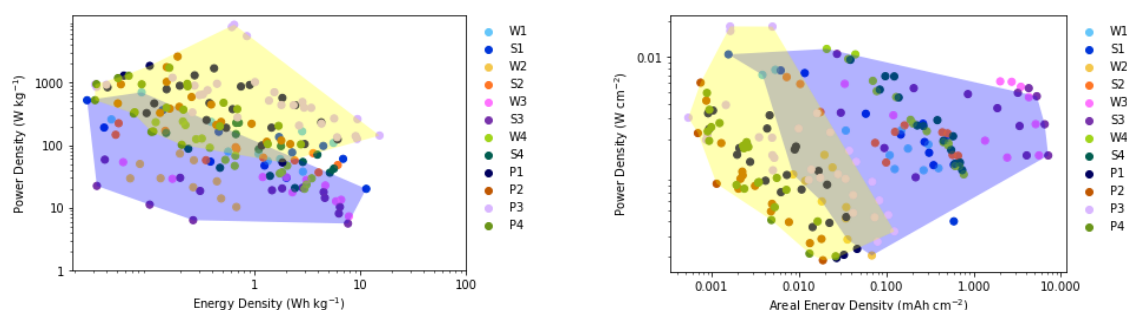


Figure 138 Ragone Diagram of all hexagonal $M_x\text{WO}_3$ samples produced in this work by gravimetric values (left) and areal values (right)

Considering the data now from an area perspective it can be seen the blue, binder-free region sits on the high energy density right-hand side of the graph and the powder samples in yellow to the left. Imagining the active material as a cuboid on the surface of the substrate, the area for each electrode type is the same but with quite different thicknesses. It therefore follows the thicker of the two, the binder-free electrodes, would have a superior energy density than the thinner, powder-based layer. This is made clearer by looking at the W3 and S3 ammonium samples which have the highest energy density correlated to the highest mass loading of any sample measured.

The two electrode types, in this case, do share similar power densities, in fact, the power density per square centimetre is lower for the powder samples than the binder-free ones. Power is a rate of energy over time. In the case of the binder-free samples the numerator, unnormalized by mass in this case, is much larger than the powder samples delivering a larger power per unit area.

These Ragone diagrams and the discussion highlight some key problems with thin film electrode development and how samples may be accurately compared. The gravimetric capacities are inherently sensitive to the way the mass of the electrodes is recorded and in

the case of the hexagonal binder-free samples were only accurate to 0.01 of a gram, leading to underestimation of the capacity.

Another related issue is that it was sometimes impossible to estimate a sample's active material mass as there was no method sensitive enough available. For instance, the encouraging CVs produced by S9, and indeed the simple Seeded Substrate S, would deliver attractive gravimetric capacities because of the thin mass loading present and perhaps perform better than the powder samples. It is therefore obvious that for the successful development of these electrodes, facile yet robust methods are developed and available to researchers to estimate the mass or thickness of active material grown on the substrate. Alternatively, it may be necessary to evaluate reported or commercial electrodes and determine an internal areal capacity standard which may be used as a comparison.

Nevertheless, the inferior capacities and gravimetric energy and power densities are a clear indication that the hexagonal-WO₃ binder-free electrodes presented in this work are unable to compete with similar WO₃ powder-based electrodes. The thickness and morphology of the hexagonal samples presented in this work result in high resistivities developing between the electrode surface and the current collector. At low rates of charge transfer, this is tolerable because the rate of potential change is comparable to the rate of proton intercalation within the oxide. At higher sweep rates, however, the rate overwhelms the ability of the binder-free electrode to intercalate protons and this manifests as a skewed, pointed shape on the cyclic voltammogram.

The powder samples, on the other hand, benefit from having a thin layer coating the current collector which minimises any intrinsic electrical resistivity of the tungsten bronze and negates the material's poor electrical conductivity on account of the thin coating. It should be expected that the powder electrode performance could be improved further by optimising the ink preparation.

7.2.3 Ease of Manufacture & Stability of Powder-Based Electrodes

The powder-based electrodes presented in this Chapter were easier to work with than the binder-free foils. The goal of this work was to couple the current collector and active material together for ease of manufacture. It was found that de-coupling these elements through making a powder which can then be subsequently coated upon the current collector resulted in more stable, robust electrodes.

The powder electrodes' greater stability reduced the likelihood of breaking or damaging a sample which saved time re-synthesising damaged samples. This is an attractive quality of being able to independently control the synthesis of active material and then separately the electrode preparation for characterisation.

The powder-based electrodes were better adhered to the tungsten substrate than their corresponding binder-free samples. The stability issues encountered when using

hydrothermally grown $\text{W-M}_x\text{WO}_3$ electrodes have already been discussed in section 5.6 “Foil Stability”. The observed improvement in stability when no sodium tungstate was used in the hydrothermal reaction was noted, but these electrodes have less capacity than the powder electrodes with more problems of their own too. The improved stability in the Powder electrodes is attributed to the small mass loading of active material in conjunction with the Nafion polymer in the ink which acts as a proton-conducting adhesive.

7.3 Physical Characterisation of Powders

7.3.1 Appearance of powders

Images of the powders obtained from the four experiments are shown in Figure 139. These powders were obtained by filtering the reaction solution through glass microfiber filter paper overnight and allowed to dry in the ambient air.

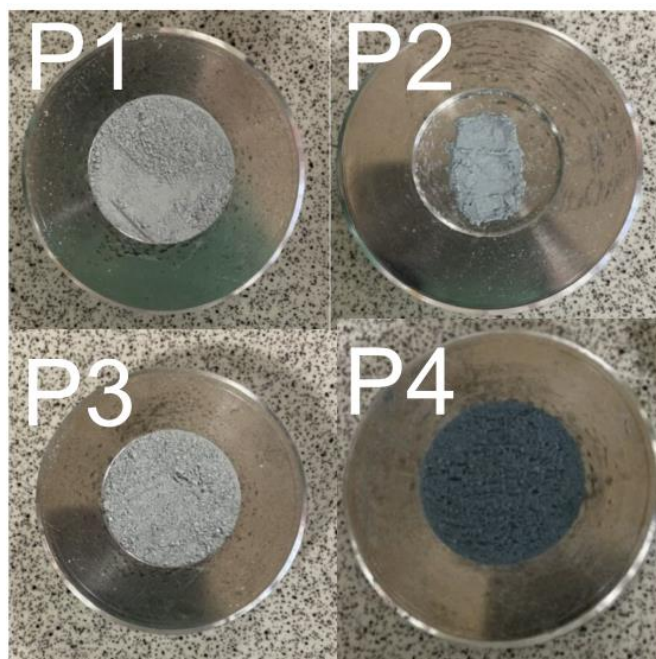


Figure 139 Photos of powders in sample holders for XRD

Where the W-WO_3 foil samples were distinguishable by the shape and finish of the surface oxide layer, these powders are easily distinguishable by their colour. Specifically, the shade or tone of the blue. The range in blue colours are an immediate indication of the change in bandgap that comes with a different ion, or different concentration of ions, being hosted in the bronze [128]. The sodium Samples P1 and P2 produced light blues of different tones and the ammonium sample P3 gave a little more of a green tint to the light blue. P4 is quite distinct in these samples, the addition of rubidium to the tungsten oxide gives rise to a dark blue tone.

7.3.2 Crystal Structure

Powder X-ray diffraction was used to identify the crystal phase of the WO_3 powders synthesised in the hydrothermal synthesis as a secondary product. The spectra for all four powders and several reference PDF spectra are shown in Figure 140.

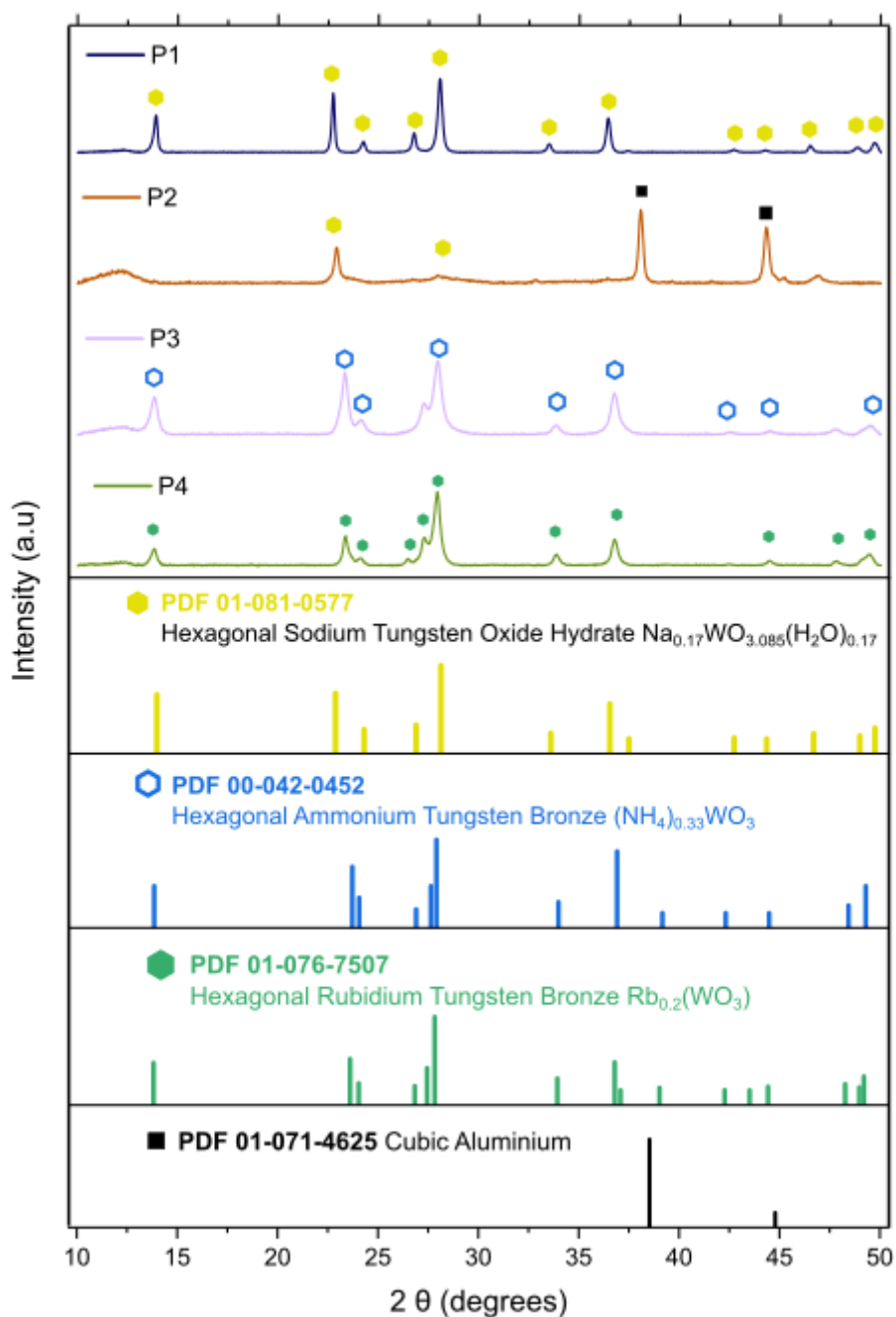


Figure 140 XRD Spectra of samples P1, P2, P3, P4 synthesised as a secondary product in the bulk solution with Na_2WO_4 using the capping agent NaCl , Na_2SO_4 , $(\text{NH}_4)_2\text{SO}_4$ and Rb_2SO_4 respectively

The P2 Spectra is unexpectedly quite a different shape from the others, and this may be accounted to a poor measurement. The powder samples were held and flattened in an aluminium sample holder, an image of this may be seen in Figure 139. What is clear is that the P2 sample does not fill the area and there is aluminium exposed. There were no alternative holders available at the time. This appears clearly in the XRD with two peaks at 38.52° and 44.78° . Regardless of this 22.837° peak is identifiable and on closer inspection as is the 28.087° peak. Deleting these peaks and re-normalising the data some more hexagonal- WO_3 peaks become more visible (Appendix J). In addition, the Binder Free electrodes synthesised

in the same reaction conditions with sodium sulphate produced hexagonal WO₃ surfaces. It is therefore with some confidence this powder is identified as hexagonal-WO₃. A repeat of this experiment would be worthwhile.

The P1, P3 and P4 spectra are all similar sharing a common shape immediately recognisable as the hexagonal phase. The P1 spectra show an excellent match to hexagonal sodium tungsten bronze (PDF 01-081-0577) in both peak position and intensity. Similarly, to the previous discussion, the exact bronze would require elemental composition to be completed to confirm this.

P3 and P4 are similar to the hexagonal ammonium and rubidium tungsten bronze reference patterns, respectively. There are some minor differences in these patterns, and this may be accounted for by a different cation concentration from the reference pattern. A different cation concentration results in differences in how the lattice stretches and thus changes the lattice parameters and spectra produced. For instance, both ATB and RTB reference patterns share three increasingly large peaks between 26.8° and 28°. These are present in the P4 spectra but are offset by a fraction of a degree; in P3's case, the smallest of these peaks is not present. It is quite plausible that there is also a mixture of sodium in addition to the main capping agent cation in these samples, which again creates a unique lattice structure. Without further XRF or EDX scans to evaluate the cation concentration it is impossible to comment any further.

The XRD spectra obtained here further vindicates the synthesis scheme developed through quantifying existing experimental procedures. A ratio of six capping agent cations to one tungstate ion in solution has been demonstrated to deliver the hexagonal phase.

7.3.3 Microstructure of powders

7.3.3.1 P1 – directed by NaCl.

The obtained microstructure of sodium chloride-directed hexagonal tungsten bronze powder P1 may be seen in Figure 141. The powder is made up of well-formed nanorods which have agglomerated together into larger blocks which has been found previously by [82], [83], [87]. Other authors have successfully tuned the aspect ratio of these nanorods by altering the capping agent concentration, pH, reaction time and temperature [82], [87]. The microstructure achieved in these samples is uniform given the simplified approach of using a pH of 2 and capping agent ratio of 6.

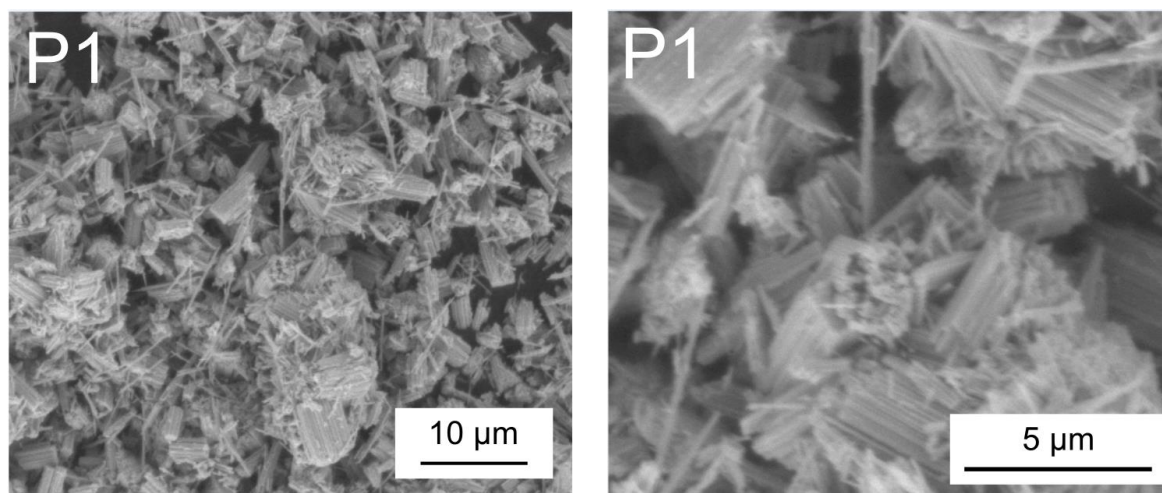


Figure 141 SEM Micrographs of powder P1 obtained through hydrothermal reaction using NaCl as a capping agent

The structure of the P1 oxide powder may be said to be similar to W1 and S1 in (Figure 77) as far as both are composed of nanorods. The P1 nanorods formations are grown in the bulk solution and are shorter, and thicker than the string-like, fibrous formations that form on the substrate surface. The nanorods in P1 have agglomerated in block-like structures whilst retaining their identifiable nanorod shape; the W1 and S1 created fewer regular formations. As discussed in relation to W1 and S1, the conditions of oxide growth in the bulk solution are different to that close to the substrate surface because of the relative concentrations of tungsten oxide crystals which nucleate during the reaction. This is fully discussed in section 5.7.

The electrochemical performance of these powders was found to be good relative to P2 and P4, with only P3 delivering a larger capacity. This shows that these short, well-formed nanorods give a high surface area and porosity which facilitates proton movement and intercalation. From this starting point, the synthesis could be refined to prevent agglomeration to leave distinct nanorods and an even greater capacity would be expected.

7.3.3.2 P2 – directed by Na₂SO₄.

Two micrographs of the powder grown with sodium sulphate as capping agent are presented in Figure 142. As expected, the hexagonal tungsten oxide microstructure obtained is quite different from sodium chloride. There are no discernible nanorods present in the microstructure and instead lots of rosebud-like particles formed. These appear to be formed of nanoplate formations.

The particles are similar to the “rosebud” formations found peppered over the surface of W2 and S2 (Figure 80). It is possible that the particles seen in Figure 142 have adjoined the surface of the substrates in W2 and S2 however, this seems unlikely given the shape of the rosebuds on each of the substrates are quite different. As discussed in section 5.7, these rosebud formations have been reported elsewhere in tungsten oxide research. In addition, a

lateral growth mechanism was proposed that shows the sulphate ion leads to nanoplate growth through its mediation of the double layer. The large faces of these nanoplates agglomerate to stabilise the high-energy surfaces and extend out leading to these rotund, rosebud particles.

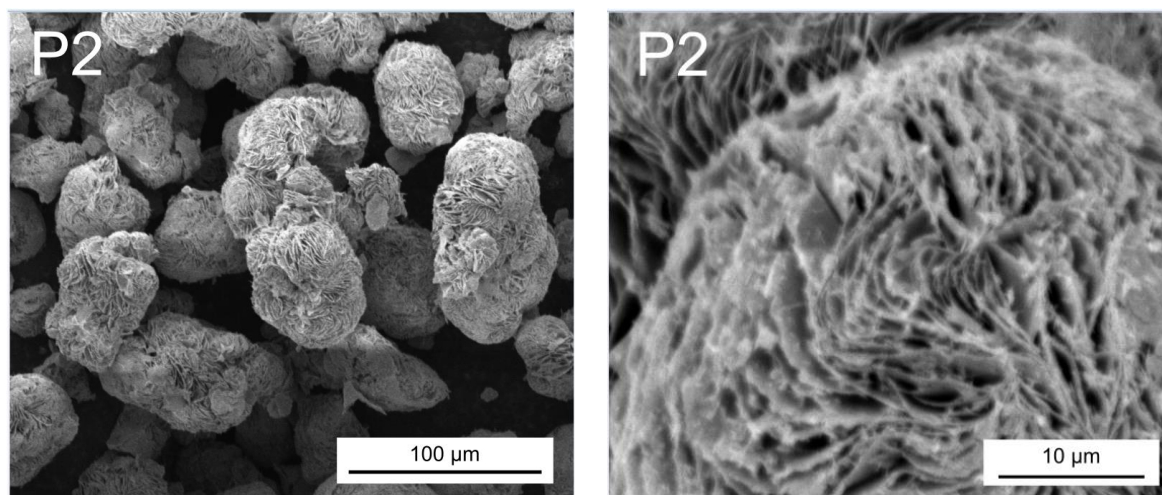


Figure 142 SEM Micrographs of powder P2 obtained through hydrothermal reaction using Na₂SO₄ as a capping agent

The electrochemical performance of P2 was poor relative to the other powders which may be linked to the high agglomeration of the rosebuds to one another reducing the surface area. The densely packed nanoplates also look too close to facilitate effective ion movement which leads to the low capacity.

The rosebuds are less spherical than those obtained on the surface of S2 which implies that these particles could be tuned to give a higher surface area. In the discussion of S2, it was stated that the rosebud formations grow later in the hydrothermal synthesis because they are atop the already-developed surface. Following this, because the rosebuds formed in the bulk will establish earlier in the reaction, they may be said to have had too much time to agglomerate into larger structures. It may then be expected that with optimisation, the surface area and performance of the sodium sulphate-directed rosebud particles could be improved by reducing the reaction time limit agglomeration.

7.3.3.3 P3 – directed by (NH₄)₂SO₄.

The powder obtained in the hydrothermal synthesis reaction with ammonium sulphate is displayed in Figure 143. The image on the left makes the powder appear clumpy and formless however upon greater magnification it becomes apparent that these structures are densely packed, spindly nanorod formations.

Similar spindly structures have been reported using KSO₄ and the formation of these was accredited to the mediating effect of the sulphate ion [83]. The author notes such spindles appeared only in trials with K or NH₄ suggesting that the large ionic radii of these structures promote these structures [83]. Of course, the large cation rubidium produces quite different

structures, so the ionic size is not the only factor at play. There is little evidence of lateral growth, but the image resolution is insufficient to certify this, and further images would be required.

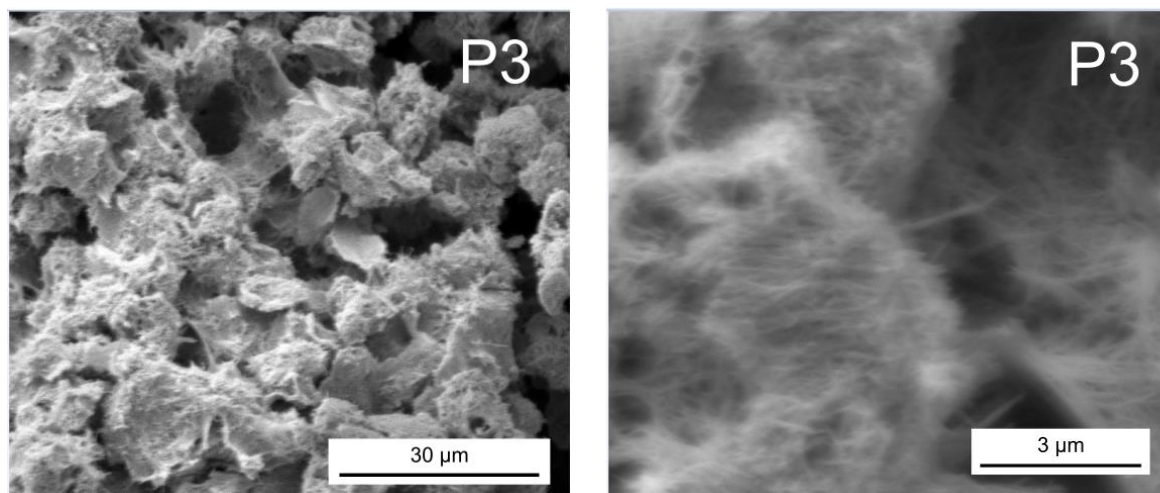


Figure 143 SEM Micrographs of powder P3 obtained through hydrothermal reaction using (NH₄)₂SO₄ as a capping agent

Despite the clumpy appearance at the 30 µm scale, sample P3 was found to be the best-performing electrode characterised. It delivered the highest capacity and the characteristic decline in capacity with charging rate was considerably lower than all other samples. It owes this performance to the thin, spindly microstructure observed here. These high aspect ratio spindles provide a large surface area for intercalation to occur; and the seeming lack of agglomeration provides the gaps between each spindle, increasing the porosity and facilitating ion movement to and from the oxide.

A final point to consider in this regard is the tunnelled ion in P3 is ammonium which has quite different properties to alkali metals sodium and rubidium. As a molecule which allows hydrogen bonding, it may be expected to occupy the hexagonal tunnel different to alkali metals in a way that better facilitates hydrogen movement. Whether this is protons hopping via ammonium molecules or an increased water concentration in the bronze, it does appear the hexagonal ammonium tungsten bronze is more auspicious for energy storage than others.

7.3.3.4 P4 – directed by (Rb₂SO₄)

The microstructure of the rubidium sulphate-directed powder P4 may be seen in Figure 144. The powder is made up of distinguishable particles that have clumped together. The higher magnification micrograph on the right of Figure 144 shows the “nano-urchin” microstructure of these particles is similar to that of the oxide formed on substrates in the same reaction (W4 and S4). The discussion offered in section 5.4.1.5 well explains the growth of these urchin structures observed in the powder. In short, the nucleated particles are stabilised enough by rubidium to form nanospheres which agglomerate rapidly into microspheres to minimise their surface area. These provide sites for subsequent growth of nanorod crystals to grow from [83].

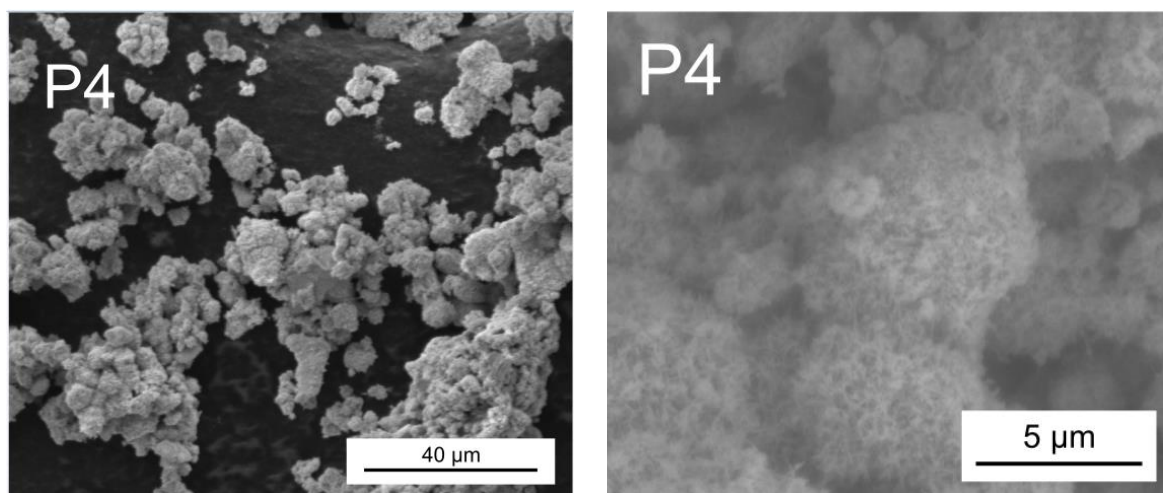


Figure 144 SEM Micrographs of powder P4 obtained through hydrothermal reaction using (NH₄)₂SO₄ as a capping agent

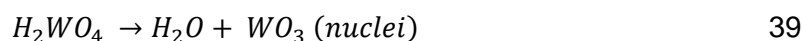
These micro-urchins have a high surface area microstructure which would be expected to deliver good energy storage performance. However, the performance of P4 was lacklustre in comparison to the other powders which was more surprising given the encouraging performance of W4 and S4. As discussed earlier, this may be down to the lower mass loading of P4 electrodes compared to other powder electrodes because of the higher molar mass of rubidium. Even still, the P4 powder presented here has a lower surface area than it could from agglomeration of these nano-urchins. Efforts to reduce this in the synthesis would improve capacity and performance.

7.3.3.5 Growth Mechanism of WO₃ Powders

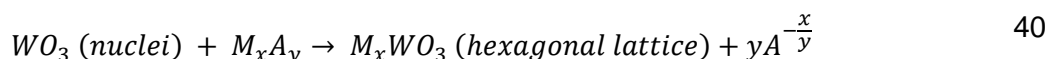
The growth of hexagonal WO₃ from sodium tungstate is well documented by many sources, including those which the synthesis scheme is based upon [80], [84], [87], [88]. A generalised scheme, adapted from these sources, for cation M⁺ and anion A⁻ is discussed here in relation to how hexagonal tungsten oxide grows. At room temperature before even hydrothermal synthesis begins, protons from the acid undergo a neutralisation reaction (38) and form tungstic acid, also known as tungsten trioxide hydrate (H₂O·WO₃). This product is insoluble and precipitates into solution, often forming a milky colour.



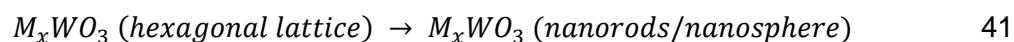
Once the hydrothermal reaction begins, the neutralisation above shifts further to the right creating more tungstic acid still. The previously insoluble tungstic acid becomes soluble, and the supersaturation drives nucleation through a dehydration reaction, equation 39. The concentration of acid governs the rate of the first step and therein the concentration of WO₃ in solution.



Tungstic acid can be written as H₂O·WO₃ and so where the dehydration reaction is required for the nuclei to aggregate together into a lattice is unknown. Regardless, the hexagonal phase may form if there are cations present in the correct concentration and energy (governed by reaction Temperature & Pressure) through stabilising the tunnel structure.



The hexagonal lattice structure may now extend in a subsequent growth step. The microstructure developed is governed by the properties of the anion and cations present. The hexagonal prism shape inherently favours nanorods given the disparity in double-layer energies between top and side facets.



Once nanorods begin forming, the concentration of ions in solution determines the aspect ratio of these nanorods, or nanospheres in the case of rubidium. This is a complex step, where the rate of nucleation of WO₃, dictated by the concentration of protons in solution, defines how many nanorods begin growing. A high rate of nucleation creates lots of small WO₃ nuclei which will develop many, narrow nanorods; a low rate of nucleation creates few larger WO₃ nuclei forming fewer, thick nanorods.

The size and shape of these nanorods then dictates how they arrange themselves into larger structures. For instance, the more nanorods formed the faster the agglomeration will occur as these microstructures seek to reduce their surface area. The fewer thicker nanorods have a smaller total surface area and so would slowly agglomerate as there is a less powerful driving force.

In powder synthesis the rate of nucleation is as described, set by the pH and relative concentrations of sodium tungstate in the bulk solution. This is quite different from the substrate cases where in the seeded case the nucleation is determined by the surface WO₃ dissolving at the beginning of the reaction; the pristine case is different too where the substrate itself could be expected to create a local concentration as its surface may attract or repel reactants in solution. In each case, the powder microstructure was found to be quite different from the related oxide surfaces of the substrates which support this description.

7.4 Summary

This chapter describes the electrochemical performance and physical characterisation of the hexagonal phase M_xWO_3 powders made as a by-product in the hydrothermal reaction when synthesising binder-free electrodes. Obtaining the hexagonal crystal structure further supports the quantification of existing synthesis schemes to streamline the synthesis of desired phases. The microstructure of the powder samples showed substantial base similarities with those grown upon the substrates. However, it was also clear the substrate surface created sufficiently different conditions from powder growing in the bulk to develop different microstructures. The effect of this was linked to the various concentrations at the substrate surfaces and within the bulk solution.

Powder-based electrodes were found to have several advantages over their binder-free counterparts. They were more robust and easier to handle, making storage and testing far more straightforward. Their performance too was better, achieving a higher gravimetric capacity and crucially these capacities diminished at a much slower rate with increasing charging rate. These advantages can be attributed to the much thinner layer of oxide coated on the powder-based electrodes in comparison to the hydrothermally grown W-WO_3 electrodes, and further work to investigate thicker coatings may be worthwhile. A thin coating of active material reduces resistive losses in both ion movement and charge transfer simply by reducing the volume through which the ions must move in the oxide and the distance over which electrons must conduct between oxide and metal. In addition, the thin layer ensures internal stress in the layer is minimised making it more likely the material stays adhered. Of course, the additional binder material also helps in this regard.

8 Conclusions & Future Work

8.1 Conclusions

This work set out to appraise the concept of binder-free electrodes to be used as pseudocapacitive energy storage electrodes. This was completed through synthesising and thoroughly characterising 11 binder-free electrodes and comparing them with 4 more conventional powder-based electrodes.

The first two chapters saw the electrochemical and physical characterisation of eight tungsten-hexagonal-tungsten oxide electrodes. The synthesis itself was a success in being able to demonstrate hexagonal-WO₃ grown upon a tungsten substrate from a two-step synthesis scheme developed from existing literature. The synthesis scheme derived the necessary relative quantities of tungstate and cation in solution to deliver a certain phase. It was found that the first “seeding” step did not influence the crystal lattice produced through epitaxial growth but was beneficial in obtaining more favourable, uniform microstructures than unseeded substrates. This can be ascribed to the high concentration of WO₃ seed crystals present in the reaction providing a higher rate of nucleation than in the pristine foils. The effect of cation and anion present in the reaction solution was studied by using four different “capping agents” with complementary acid and a prospective growth mechanism put forward. In short, cations dictate whether the hexagonal phase is formed by stabilising the tunnel structure while anions influence the subsequent growth by mediating the double layer surrounding the growing lattice.

These same eight electrodes were electrochemically characterised using cyclic voltammetry, galvanostatic charge-discharge cycling and impedance spectroscopy. All electrodes were functional as energy storage electrodes, capable of reversibly intercalating protons into the lattice structure. The behaviour was not strictly pseudocapacitive and their performance was instead predominantly characterised using capacities. The instability of the oxide upon the tungsten surface demanded a bespoke sample holder to be developed which, despite allowing characterisation, suffered from a high internal ohmic resistance itself. The samples formed from rubidium sulphate and sulphuric acid were found to be the best performing of the eight electrodes synthesised, which was attributed to the unique, high surface area urchin-like microstructure obtained from this set of conditions. The rubidium directed sample S4 delivered the highest specific capacitance of 186 Fg⁻¹ measured at 1 mVs⁻¹ but this was lower than most powder-based tungsten oxide electrodes reported in literature. In all these samples the oxide layer was found to be too unstable to be put into a device and did not warrant further investigation.

The hydrothermal reaction used to synthesise the hexagonal-WO₃ electrodes was systematically reviewed by removing reagents and measuring the effect using cyclic voltammetry and SEM. It was found that placing a seeded foil in an autoclave with only acid at pH 2 resulted in a promising electrode architecture using a more simple, scalable process. The anion was again shown to dramatically influence the obtained microstructure by promoting or prohibiting lateral growth from certain lattice facets supporting the same analysis previously described. These electrodes were far more stable than the hexagonal-WO₃ counterparts and much more active than the seed-layer foils. Sample S9 delivered an areal capacitance of 800-1000 mFcm⁻² when 1 mVs⁻¹ which was on the upper end of other areal capacitances of tungsten oxide electrodes in literature. With further optimisation of reaction parameters this value could be expected to rise. This result made clear that the thickness and stability of oxide upon the conjugate metal is of more importance than what phase is best performing from the literature survey of powder based electrodes.

The last chapter of this work offered a straightforward comparison between hexagonal-WO₃ powder/ink electrodes and the binder-free hexagonal-WO₃ electrodes. This powder was synthesised as a byproduct of the binder-free synthesis. These were found, without any further optimisation of the ink, to be more stable and perform better electrochemically than the binder-free samples on a weight-for-weight basis. It was concluded that hexagonal-WO₃ layers formed in the initial synthesis were not a viable route for binder-free electrode synthesis.

The results and discussion made significant understanding of the hydrothermal reaction and to understand the merits of the synthesis with a view to binder-free electrode development.

When designing any electrochemical energy storage electrode, one must consider three key aspects: (1) the current collecting material, (2) the employed charge storage material and (3) the adhesion of these two parts. The proposed advantage of binder-free electrodes is that no additional adhesion is required because the active material is self-supporting upon the conjugate metal it has been grown from.

The success of this regarding all the W-WO₃ electrodes presented in this thesis is mixed, the results do outline some considerations which should be made when designing synthesis schemes for other M-MO_x systems and do point to the most promising W-WO₃ hydrothermal synthesis routes.

The stability of the oxide upon the conjugate metal is a function of its phase, morphology, and thickness. The results of this work suggest the thickness may be more important than the other two as the adhesion of oxide to W-foil substrate decreased with oxide thickness. The thickness of grown oxide creates the critical trade-off which will determine the oxide performance: a thin oxide layer will have better adhesion and less electrical resistance; however, the thickness determines the overall capacity of the electrode.

The key design condition for exploration of M-MO_x electrodes should therefore not be to select the phase which achieves the highest capacity in powder-based studies, but instead, find the oxide phase and morphology which allows the thickest layer of stable oxide to adhere.

Considering this, the most promising path forward for hydrothermally enhanced W-WO₃ electrodes appears to be simplifying the reactants to solely a seeded foil and a specific acid, chosen for its anion. It may be possible to blend acids to introduce anions to influence phase and others to influence morphology. This simplified reaction scheme, with investigation and optimisation, seems to offer the most viable pathway to realising these as energy storage electrodes. It seems quite possible given further investigation, that a hydrothermal reaction could produce a layer of hydrated orthorhombic-WO₃ which balances thickness, stability, and performance in a highly effective proton storage electrode.

8.2 Future Work

8.2.1 WO_3 and W- WO_3 for energy storage

Tungsten-Tungsten Oxide (W- WO_3) electrodes were investigated as a starting case for binder-free electrodes. A highly simplified hydrothermal reaction using only an acid at elevated temperature and pressure was found to deliver the most promising of the binder-free electrodes. However, even these are unlikely to realise a commercial future given the scarcity of tungsten metal and its gravimetric density.

Hexagonal- WO_3 as a powder-based electrode is more plausible than W- WO_3 because it is more straightforward to synthesise and the array of microstructures that can be made. If one were to continue with WO_3 synthesis research there is scope to explore the effect of synthesis of WO_3 powders using mono-, di- and tri-protic acids and their complementary salts to show how the lateral growth develops. Furthermore, the potential of “blending” capping agents would be interesting to see whether the properties may be enhanced further i.e. (lesser amounts of ammonium to fill and hydrate tunnels with more sodium to grow uniform high surface area structures).

8.2.2 Quantification of Hydrothermal Synthesis

The simple qualitative approach used in this research proved quite fruitful in delivering the desired hexagonal phase of WO_3 with interesting microstructures. This was based upon four published papers when there now exist hundreds of papers on WO_3 synthesis alone.

Many of these discuss how five key factors: cation, anion, pH, temperature, and time have been altered to deliver a phase and microstructure associated with each condition. With the advent of widespread AI, processing this and creating a database which links reaction conditions to phase and microstructure seems quite feasible. The power of this would allow for trends to be identified, synthesis to be streamlined and opportunities to be identified.

From such an empirical, qualitative database a desired phase and microstructure could be synthesised which would function as a starting point to be optimised further. Naturally, this becomes as complex as one desires as more factors are added but the central and most interesting point is that existing literature can already deliver a “best guess” starting point saving time-intensive synthesis.

8.2.3 Binder Free Electrodes

Tungsten and tungsten oxide are unlikely to realise a future as a binder-free electrode given the performance outlined here. The work presented here is useful in providing some general learnings which can be taken forward into subsequent binder-free electrode research.

Firstly, any development should consider which oxide readily forms on the surface of the metal without complex hydrothermal reactions. The focus should be on optimising this surface oxide

for performance instead of trying to synthesise a particular phase which is less inclined to stay adhered.

Secondly, and related to point one, hydrothermal synthesis should be removed. This may seem strange given the discussion of hydrothermal synthesis in this report, but its use was not productive. More importantly, its use actually removes a key theoretical advantage these electrodes hold over conventional powder-based electrodes: hydrothermal synthesis is inherently a batch process where instead a continuous oxidation method could be used on binder-free electrodes. A continuous process would simplify fabrication and make these electrodes more cost-effective.

Finally, by applying the first point the scope for improving the active material is limited to the most stably adhered oxide. The task is then a case of synthesising as an effective surface oxide as possible through optimising the employed oxidation process. The room for development lies in altering the initial substrate before it is oxidised. This could be as simple as using thinner or more textured substrates; or more complex ideas where the substrate to be oxidised is composed of conducting metal A coated in another metal B where A is chosen for its conductivity and B is chosen for the oxide it produces.

8.2.4 Molybdenum-Molybdenum Oxide

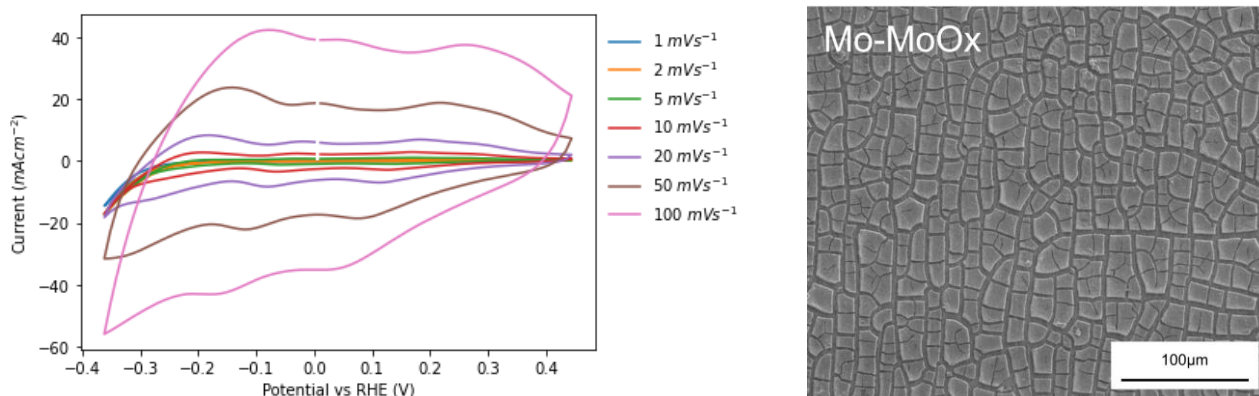
The introduction discussed which metals were theoretical contenders for binder-free electrode architectures. Molybdenum, which sits above tungsten in the periodic table, is a more abundant (Table 1) and lighter metal than tungsten. It also has been noted as a promising pseudocapacitive material [129], [130]. Molybdenum does not have the same wealth of synthesis literature regarding Mo-MoO_x and so was not as attractive as tungsten for the purposes of this work.

It was, though, of interest to see whether the synthesis used here would be effective on molybdenum foil and to provide preliminary data as to its suitability as a binder-free electrode. A Mo-MoO_x electrode was synthesised using the same procedure outlined in 3.2.1 Acid Pretreatment Seeding Step. The preliminary results were promising, and so more extensive experiments were performed. These experiments were in part conducted by William Johnson, an MEng master's student under supervision.

As mentioned, several Mo-MoO_x electrodes were synthesised using the same nitric acid seeding step as performed throughout this work. The resultant electrodes were more pseudocapacitive and stable than any of the aforementioned tungsten-based samples described in this work – including the hexagonal phase foils. Considering this one-step procedure avoided using hydrothermal synthesis this is a really exciting finding and deserves further investigation.

A cyclic voltammetry across many sweep rates for one of the Mo-MoO_x electrodes can be seen on the left of Figure 145. The shape of CV is truly pseudocapacitive, expanding with

sweep rate without any evidence of increased ohmic resistance. It is hypothesised this is delivered by an intercalation system; however further work is required to validate these initial findings because the phase was difficult to ascertain.



Scan rate (mVs ⁻¹)	Capacity (mAhcm ⁻²)	Capacitance (mFcm ⁻²)
1	0.003	14.22
2	0.01	45.51
5	0.052	232.18
10	0.087	391.28
20	0.117	526.17
50	0.135	605.6
100	0.125	561.21

Figure 145 Left; Cyclic Voltammogram of Mo-MoO_x synthesised in 69°C, 1.5M HNO₃ for 20 minutes made from 0.05mm molybdenum Foil from Sigma Aldrich. Right: an SEM image of as-synthesised Mo-MoO_x electrode

As may be seen in the tabulated values, the capacitance of these studied samples actually grows with scan rate. However, hydrogen evolution reaction (HER) was evident on these samples and also in the low scan rate data. With further research the potential window could be identified and accurate capacitances calculated. Even still, if the above CV data is retrospectively curtailed to a reduced potential limit of -0.2V with no HER peaks (Appendix P2) the resulting areal capacitance is found to be 596 mFcm⁻² at 50 mV/s. This is a considerably higher value than any of the reported samples in this work and to the areal capacitances for tungsten oxide electrodes reported in literature of around 240 mFcm⁻² at 10 mV/s [120], [121]. When this sample was studied with SEM (Figure 145 Right) it was found to be composed of islands upon the substrate, remarkably different from the polycrystalline surface made when the same treatment was performed on tungsten foil. Reminiscent of a dried riverbed, this surface morphology requires more characterisation to determine how it relates to the observed pseudocapacitance performance.

As mentioned, efforts to determine the oxide present by grazing incidence XRD and X-ray reflectivity were fruitless. The unique microstructure considered as “islands on a substrate”

surface [115] seems to be the cause of this. A first step in such research would be to determine whether dioxide, trioxide or a mixture has been formed. There is much scope to develop this material further to optimise performance using “low tech” methods such as abrasion of the foil pre-oxidation to increase surface area and use of lower pH (higher H^+ concentration).

9 References

- [1] UK Gov, 'UK sets ambitious new climate target ahead of UN Summit', Press release. Accessed: Apr. 23, 2021. [Online]. Available: <https://www.gov.uk/government/news/uk-sets-ambitious-new-climate-target-ahead-of-un-summit>
- [2] V. Augustyn, P. Simon, and B. Dunn, 'Pseudocapacitive oxide materials for high-rate electrochemical energy storage', 2014, *Royal Society of Chemistry*. doi: 10.1039/c3ee44164d.
- [3] UK Gov, 'Accelerate, Collaborate and Enhance: Our New Approach to Critical Minerals'. Accessed: Oct. 27, 2024. [Online]. Available: <https://www.gov.uk/government/publications/uk-critical-mineral-strategy/4acf2ca4-70cf-4834-a081-cf16b7c66959>
- [4] M. Y. Ho, P. S. Khiew, D. Isa, T. K. Tan, W. S. Chiu, and C. H. Chia, 'A review of metal oxide composite electrode materials for electrochemical capacitors', *Nano*, vol. 9, no. 6, pp. 1–25, 2014, doi: 10.1142/S1793292014300023.
- [5] P. A. Shinde and S. C. Jun, 'Review on Recent Progress in the Development of Tungsten Oxide Based Electrodes for Electrochemical Energy Storage', *ChemSusChem*, vol. 13, no. 1, pp. 11–38, 2020, doi: 10.1002/cssc.201902071.
- [6] J. R. Miller, 'Market and Applications of Electrochemical Capacitors', *Supercapacitors: Materials, Systems, and Applications*, vol. 45, pp. 509–526, 2013, doi: 10.1002/9783527646661.ch14.
- [7] B. E. Conway, 'Transition from "Supercapacitor" to "Battery" Behavior in Electrochemical Energy Storage', *J Electrochem Soc*, vol. 138, no. 6, pp. 1539–1548, 1991, doi: 10.1149/1.2085829.
- [8] A. Eftekhari and M. Mohamedi, 'Tailoring pseudocapacitive materials from a mechanistic perspective', 2017, *Elsevier Ltd*. doi: 10.1016/j.mtener.2017.10.009.
- [9] X. Liu, S. Chen, Z. Xiong, K. Li, and Y. Zhang, 'Tungsten oxide-based nanomaterials for supercapacitors: Mechanism, fabrication, characterization, multifunctionality, and electrochemical performance', *Prog Mater Sci*, vol. 130, no. 2021, p. 100978, 2022, doi: 10.1016/j.pmatsci.2022.100978.
- [10] G. Z. Chen, 'Supercapacitor and supercapattery as emerging electrochemical energy stores', *International Materials Reviews*, vol. 62, no. 4, pp. 173–202, 2017, doi: 10.1080/09506608.2016.1240914.
- [11] Y. Gogotsi and R. M. Penner, 'Energy Storage in Nanomaterials - Capacitive, Pseudocapacitive, or Battery-like?', *ACS Nano*, vol. 12, no. 3, American Chemical Society, pp. 2081–2083, Mar. 27, 2018. doi: 10.1021/acsnano.8b01914.

- [12] J. N. H. Thomas F. Fuller, *Electrochemical engineering: An overview of its contributions and promising features*, vol. 82, no. 12. 2004. doi: 10.1205/cerd.82.12.1571.58046.
- [13] B. E. Conway, *Electrochemical Capacitors Based on Pseudocapacitance*. 1999. doi: 10.1007/978-1-4757-3058-6_10.
- [14] J. Newman and K. E. Thomas-Alyea, *Electrochemical Systems*, 3rd ed. John Wiley & Sons, Incorporated, 2012.
- [15] Y. Kumar, S. Rawal, B. Joshi, and S. A. Hashmi, 'Background, fundamental understanding and progress in electrochemical capacitors', *Journal of Solid State Electrochemistry*, vol. 23, no. 3, pp. 667–692, 2019, doi: 10.1007/s10008-018-4160-3.
- [16] R. G. Compton and G. H. W. Sanders, *Electrode Potentials*. Oxford: Oxford University Press, 2009.
- [17] J. B. Mitchell *et al.*, 'Confined Interlayer Water Promotes Structural Stability for High-Rate Electrochemical Proton Intercalation in Tungsten Oxide Hydrates', *ACS Energy Lett*, vol. 4, no. 12, pp. 2805–2812, 2019, doi: 10.1021/acsenergylett.9b02040.
- [18] T. Nguyen and M. de F. Montemor, 'Metal Oxide and Hydroxide–Based Aqueous Supercapacitors: From Charge Storage Mechanisms and Functional Electrode Engineering to Need-Tailored Devices', *Advanced Science*, vol. 6, no. 9, 2019, doi: 10.1002/advs.201801797.
- [19] J. W. Long, K. E. Swider, C. I. Merzbacher, and D. R. Rolison, 'Voltammetric Characterization of Ruthenium Oxide-Based Aerogels and Other RuO₂ Solids: The Nature of Capacitance in Nanostructured Materials', *Langmuir*, vol. 15, no. 3, pp. 780–784, 1999, doi: 10.1021/la980785a.
- [20] B. E. Conway and E. Gileadi, 'Kinetic theory of pseudo-capacitance and electrode reactions at appreciable surface coverage', *Transactions of the Faraday Society*, vol. 58, pp. 2493–2509, 1962, doi: 10.1039/tf9625802493.
- [21] Y. Wang, Y. Song, and Y. Xia, 'Electrochemical capacitors: Mechanism, materials, systems, characterization and applications', 2016, *Royal Society of Chemistry*. doi: 10.1039/c5cs00580a.
- [22] B. Zhao *et al.*, 'Monolayer graphene/NiO nanosheets with two-dimension structure for supercapacitors', *J Mater Chem*, vol. 21, no. 46, pp. 18792–18798, 2011, doi: 10.1039/c1jm13016a.
- [23] S. Yoon, E. Kang, J. K. Kim, C. W. Lee, and J. Lee, 'Development of high-performance supercapacitor electrodes using novel ordered mesoporous tungsten oxide materials with high electrical conductivity', *Chemical Communications*, vol. 47, no. 3, pp. 1021–1023, 2011, doi: 10.1039/c0cc03594g.
- [24] H. Wang, W. Zhang, H. Chen, and Zheng Weitao, 'SCIENCE CHINA Special Topic: Electrochemical Energy Storage Towards unlocking high-performance of

- supercapacitors: From layered transition-metal hydroxide electrode to redox electrolyte', *Sci China Tech Sci*, vol. 58, pp. 1779–1798, 2015, doi: 10.1007/s11431-015-5930-0.
- [25] B. Saravanakumar *et al.*, 'Enhanced pseudocapacitive performance of SnO₂, Zn-SnO₂, and Ag-SnO₂ nanoparticles', *Ionics (Kiel)*, vol. 24, no. 12, pp. 4081–4092, 2018, doi: 10.1007/s11581-018-2727-8.
- [26] Q. Li, Y. F. Zhang, X. R. Han, C. Ju, and Z. L. Wang, 'A comparison of MoO₃ nanorods and C / MoO₃ nanocomposites for high-performance supercapacitor electrode', vol. 18, no. 7, pp. 413–420, 2021.
- [27] T. Brousse, D. Bélanger, and J. W. Long, 'To be or not to be pseudocapacitive?', *J Electrochem Soc*, vol. 162, no. 5, pp. A5185–A5189, 2015, doi: 10.1149/2.0201505jes.
- [28] T. Xu *et al.*, 'Electrochemical Proton Storage: From Fundamental Understanding to Materials to Devices', *Nanomicro Lett*, vol. 14, no. 1, pp. 1–23, 2022, doi: 10.1007/s40820-022-00864-y.
- [29] V. Augustyn *et al.*, 'High-rate electrochemical energy storage through Li + intercalation pseudocapacitance', *Nat Mater*, vol. 12, no. 6, pp. 518–522, 2013, doi: 10.1038/nmat3601.
- [30] 'Minor Metals Trade Association (mmta)'. [Online]. Available: <https://mmta.co.uk/metals/>
- [31] 'Johnson Matthey: PM Management'. Accessed: Oct. 05, 2024. [Online]. Available: <https://matthey.com/products-and-markets/pgms-and-circularity/pgm-management>
- [32] 'Trading Economics', Trading Economics. Accessed: Oct. 05, 2024. [Online]. Available: <https://tradingeconomics.com/commodities>
- [33] 'London Metals Exchange', Accessed: Oct. 05, 2024. [Online]. Available: <https://www.lme.com/en/metals/ev/lme-molybdenum-platts#Trading+day+summary>
- [34] S. M. Jasinsk, *Mineral Commodity Summaries*. 2023.
- [35] 'Shanghai Metals Market (SMM)', Accessed: Oct. 05, 2024. [Online]. Available: <https://www.metal.com/Titanium>
- [36] 'Reserves of Tungsten Worldwide from 2010 to 2022'. [Online]. Available: <https://www.statista.com/statistics/1298382/tungsten-reserves-worldwide/#:~:text=The total global volume of,strongest materials found in nature.>
- [37] J. B. Mitchell, W. C. Lo, A. Genc, J. Lebeau, and V. Augustyn, 'Transition from Battery to Pseudocapacitor Behavior via Structural Water in Tungsten Oxide', *Chemistry of Materials*, vol. 29, no. 9, pp. 3928–3937, 2017, doi: 10.1021/acs.chemmater.6b05485.
- [38] J. R. Baylis, 'No Title', *Ind Eng Chem Res*, vol. 15, p. 852, 1923.

- [39] C. C. Mardare and A. W. Hassel, 'Review on the Versatility of Tungsten Oxide Coatings', *Physica Status Solidi (A) Applications and Materials Science*, vol. 216, no. 12, 2019, doi: 10.1002/pssa.201900047.
- [40] A. C. Marques *et al.*, 'Office paper platform for bioelectrochromic detection of electrochemically active bacteria using tungsten trioxide nanoprobcs', *Sci Rep*, vol. 5, no. 1, pp. 1–7, 2015, doi: 10.1038/srep09910.
- [41] L. Wang *et al.*, 'Hydrogen-treated mesoporous WO₃ as a reducing agent of CO₂ to fuels (CH₄ and CH₃OH) with enhanced photothermal catalytic performance', *J Mater Chem A Mater*, vol. 4, no. 14, pp. 5314–5322, 2016, doi: 10.1039/c5ta10180h.
- [42] B. Gerand, G. Nowogrocki, J. Guenot, and M. Figlarz, 'Structural study of a new hexagonal form of tungsten trioxide', *J Solid State Chem*, vol. 29, no. 3, pp. 429–434, 1979, doi: 10.1016/0022-4596(79)90199-3.
- [43] Y. Waseda, E. Matsubara, and K. Shinoda, *X-Ray Diffraction Crystallography; Introduction, examples and solved problems*. 2011.
- [44] W. Sun *et al.*, 'High Surface Area Tunnels in Hexagonal WO₃', *Nano Lett*, vol. 15, no. 7, pp. 4834–4838, 2015, doi: 10.1021/acs.nanolett.5b02013.
- [45] K. Ghosh, A. Roy, S. Tripathi, S. Ghule, A. K. Singh, and N. Ravishankar, 'Insights into nucleation, growth and phase selection of WO₃: morphology control and electrochromic properties †', *J. Mater. Chem. C*, vol. 5, p. 7307, 2017, doi: 10.1039/c7tc01714f.
- [46] N. Rayón-López *et al.*, 'High-temperature tungsten trioxides obtained by concentrated solar energy: physicochemical and electrochemical characterization', *Journal of Solid State Electrochemistry*, vol. 23, no. 3, pp. 707–716, 2019, doi: 10.1007/s10008-018-04167-4.
- [47] I. M. Szilágyi *et al.*, 'Stability and controlled composition of hexagonal WO₃', *Chemistry of Materials*, vol. 20, no. 12, pp. 4116–4125, 2008, doi: 10.1021/cm800668x.
- [48] K. Huang, Q. Pan, F. Yang, S. Ni, X. Wei, and D. He, 'Controllable synthesis of hexagonal WO₃ nanostructures and their application in lithium batteries', *J Phys D Appl Phys*, vol. 41, no. 15, 2008, doi: 10.1088/0022-3727/41/15/155417.
- [49] V. Lokhande, A. Lokhande, G. Namkoong, J. H. Kim, and T. Ji, 'Charge storage in WO₃ polymorphs and their application as supercapacitor electrode material', *Results Phys*, vol. 12, pp. 2012–2020, 2019, doi: 10.1016/j.rinp.2019.02.012.
- [50] F. Zheng, H. Lu, M. Guo, and M. Zhang, 'Effect of substrate pre-treatment on controllable synthesis of hexagonal WO₃ nanorod arrays and their electrochromic properties', *CrystEngComm*, vol. 15, no. 29, pp. 5828–5837, 2013, doi: 10.1039/c3ce40494c.

- [51] E. Widenkvist, R. A. Quinlan, B. C. Holloway, H. Grennberg, and U. Jansson, 'Synthesis of nanostructured tungsten oxide thin films', *Cryst Growth Des*, vol. 8, no. 10, pp. 3750–3753, 2008, doi: 10.1021/cg800383c.
- [52] J. Zhang, X. L. Wang, X. H. Xia, C. D. Gu, and J. P. Tu, 'Electrochromic behavior of WO₃ nanotree films prepared by hydrothermal oxidation', *Solar Energy Materials and Solar Cells*, vol. 95, no. 8, pp. 2107–2112, 2011, doi: 10.1016/j.solmat.2011.03.008.
- [53] H. Qi, J. Wolfe, D. Wang, H. J. Fan, D. Fichou, and Z. Chen, 'Triple-layered nanostructured WO₃ photoanodes with enhanced photocurrent generation and superior stability for photoelectrochemical solar energy conversion †', *Nanoscale*, vol. 6, 2014, doi: 10.1039/c4nr03982c.
- [54] C. Y. Ng, K. Abdul Razak, and Z. Lockman, 'WO₃ nanorods prepared by low-temperature seeded growth hydrothermal reaction', *J Alloys Compd*, vol. 588, pp. 585–591, 2014, doi: 10.1016/j.jallcom.2013.11.096.
- [55] A. Watcharenwong, W. Chanmanee, N. R. de Tacconi, C. R. Chenthamarakshan, P. Kajitvichyanukul, and K. Rajeshwar, 'Anodic growth of nanoporous WO₃ films: Morphology, photoelectrochemical response and photocatalytic activity for methylene blue and hexavalent chrome conversion', *Journal of Electroanalytical Chemistry*, vol. 612, no. 1, pp. 112–120, 2008, doi: 10.1016/j.jelechem.2007.09.030.
- [56] X. Yang *et al.*, 'Self-Assembly Growth of 3D WO₃ Framework with Interpenetrated Nanosheets as Binder-Free Anode for Lithium Ion Batteries', *J Electrochem Soc*, vol. 164, no. 12, pp. A2783–A2789, 2017, doi: 10.1149/2.1891712jes.
- [57] C. Gu, J. Zhang, and J. Tu, 'A strategy of fast reversible wettability changes of WO₃ surfaces between superhydrophilicity and superhydrophobicity', *J Colloid Interface Sci*, vol. 352, no. 2, pp. 573–579, 2010, doi: 10.1016/j.jcis.2010.08.064.
- [58] M. Shibuya and M. Miyauchi, 'Efficient electrochemical reaction in hexagonal WO₃ forests with a hierarchical nanostructure', *Chem Phys Lett*, vol. 473, no. 1–3, pp. 126–130, 2009, doi: 10.1016/j.cplett.2009.03.043.
- [59] Q. Chen *et al.*, 'Preparation of well-aligned WO₃ nanoflake arrays vertically grown on tungsten substrate as photoanode for photoelectrochemical water splitting', *Electrochem commun*, vol. 20, no. 1, pp. 153–156, 2012, doi: 10.1016/j.elecom.2012.03.043.
- [60] D. D. Qin *et al.*, 'Dense layers of vertically oriented WO₃ crystals as anodes for photoelectrochemical water oxidation', *Chemical Communications*, vol. 48, no. 5, pp. 729–731, 2012, doi: 10.1039/c1cc15691h.
- [61] F. Amano, M. Tian, G. Wu, B. Ohtani, and A. Chen, 'Facile Preparation of Platelike Tungsten Oxide Thin Film Electrodes with High Photoelectrode Activity', *ACS Appl Mater Interfaces*, vol. 3, no. 10, pp. 4047–4052, 2011, doi: 10.1021/am200897n.

- [62] Q. Zeng *et al.*, 'Highly-stable and efficient photocatalytic fuel cell based on an epitaxial TiO₂/WO₃/W nanothorn photoanode and enhanced radical reactions for simultaneous electricity production and wastewater treatment', *Appl Energy*, vol. 220, no. 800, pp. 127–137, 2018, doi: 10.1016/j.apenergy.2018.03.042.
- [63] F. Wang *et al.*, 'Construction of 3D V₂O₅/hydrogenated-WO₃ nanotrees on tungsten foil for high-performance pseudocapacitors', *Physical Chemistry Chemical Physics*, vol. 16, no. 24, pp. 12214–12220, 2014, doi: 10.1039/c4cp01200c.
- [64] Y. Zhou, S. Ko, C. W. Lee, S. G. Pyo, S. K. Kim, and S. Yoon, 'Enhanced charge storage by optimization of pore structure in nanocomposite between ordered mesoporous carbon and nanosized WO₃-x', *J Power Sources*, vol. 244, pp. 777–782, 2013, doi: 10.1016/j.jpowsour.2013.04.054.
- [65] M. Zhu, W. Meng, Y. Huang, Y. Huang, and C. Zhi, 'Proton-insertion-enhanced pseudocapacitance based on the assembly structure of tungsten oxide', *ACS Appl Mater Interfaces*, vol. 6, no. 21, pp. 18901–18910, 2014, doi: 10.1021/am504756u.
- [66] G. Yang, T. Takei, S. Yanagida, and N. Kumada, 'Hexagonal tungsten oxide-polyaniline hybrid electrodes for high-performance energy storage', *Appl Surf Sci*, vol. 498, p. 143872, 2019, doi: 10.1016/j.apsusc.2019.143872.
- [67] F. Zheng *et al.*, 'Facile preparation of WO₃ nano-fibers with super large aspect ratio for high performance supercapacitor', *J Alloys Compd*, vol. 772, pp. 933–942, 2019, doi: 10.1016/j.jallcom.2018.09.085.
- [68] T. Meng *et al.*, 'Electronic Structure Control of Tungsten Oxide Activated by Ni for Ultrahigh-Performance Supercapacitors', *Small*, vol. 14, no. 20, 2018, doi: 10.1002/sml.201800381.
- [69] C. Pau *et al.*, 'Synthesis of reduced graphene oxide / tungsten trioxide nanocomposite electrode for high electrochemical performance', *Ceram Int*, vol. 42, no. 11, pp. 13128–13135, 2016, doi: 10.1016/j.ceramint.2016.05.100.
- [70] A. I. Inamdar *et al.*, 'Solar Energy Materials & Solar Cells Highly efficient electro-optically tunable smart-supercapacitors using an oxygen-excess nanograin tungsten oxide thin film (a) (b)', *Solar Energy Materials and Solar Cells*, vol. 166, no. pp. 78–85, 2017, doi: 10.1016/j.solmat.2017.03.006.
- [71] L. Ma *et al.*, 'Hydrothermal preparation and supercapacitive performance of flower-like WO₃·H₂O/reduced graphene oxide composite', *Colloids Surf A Physicochem Eng Asp*, vol. 481, pp. 609–615, 2015, doi: 10.1016/j.colsurfa.2015.06.040.
- [72] C. P. P. Wong, K. M. Lee, and C. W. Lai, 'Hydrothermal preparation of reduced graphene oxide/tungsten trioxide nanocomposites with enhanced electrochemical performance', *Journal of Materials Science: Materials in Electronics*, vol. 28, no. 19, pp. 14554–14567, 2017, doi: 10.1007/s10854-017-7319-2.

- [73] J. Tian, B. Lin, Y. Sun, X. Zhang, and H. Yang, 'Porous WO₃@CuO composites derived from polyoxometalates@metal organic frameworks for supercapacitor', *Mater Lett*, vol. 206, pp. 91–94, 2017, doi: 10.1016/j.matlet.2017.06.116.
- [74] S. Yao, F. Qu, G. Wang, and X. Wu, 'Facile hydrothermal synthesis of WO₃ nanorods for photocatalysts and supercapacitors', *J Alloys Compd*, vol. 724, pp. 695–702, 2017, doi: 10.1016/j.jallcom.2017.07.123.
- [75] H. Peng, G. Ma, K. Sun, J. Mu, M. Luo, and Z. Lei, 'High-performance aqueous asymmetric supercapacitor based on carbon nanofibers network and tungsten trioxide nanorod bundles electrodes', *Electrochim Acta*, vol. 147, pp. 54–61, 2014, doi: 10.1016/j.electacta.2014.09.100.
- [76] R. S. Lillard, G. S. Kanner, and D. P. Butt, 'The Nature of Oxide Films on Tungsten in Acidic and Alkaline Solutions', *J Electrochem Soc*, vol. 145, no. 8, pp. 2718–2725, 1998, doi: 10.1149/1.1838704.
- [77] W. Burke, Ld; Dp, 'Enhanced oxide growth on tungsten in acid under potential cycling conditions', *J Electroanal Chem Interfacial Electrochem*, vol. 135, pp. 55–65, 1982.
- [78] V. Karastoyanov and M. Bojinov, 'Anodic oxidation of tungsten in sulphuric acid solution-Influence of hydrofluoric acid addition', *Mater Chem Phys*, vol. 112, no. 2, pp. 702–710, 2008, doi: 10.1016/j.matchemphys.2008.06.029.
- [79] S. Feng and L. Guanhua, *Hydrothermal and Solvothermal Syntheses*. Elsevier B.V., 2011. doi: 10.1016/B978-0-444-53599-3.10004-6.
- [80] T. Peng, D. Ke, J. Xiao, L. Wang, J. Hu, and L. Zan, 'Hexagonal phase WO₃ nanorods: Hydrothermal preparation, formation mechanism and its photocatalytic O₂ production under visible-light irradiation', *J Solid State Chem*, vol. 194, pp. 250–256, 2012, doi: 10.1016/j.jssc.2012.05.016.
- [81] A. Michailovski *et al.*, 'Morphological and kinetic studies on hexagonal tungstates', *Chemistry of Materials*, vol. 19, no. 2, pp. 185–197, 2007, doi: 10.1021/cm061020o.
- [82] J. Wang, E. Khoo, P. S. Lee, and J. Ma, 'Synthesis, assembly, and electrochromic properties of uniform crystalline WO₃ nanorods', *Journal of Physical Chemistry C*, vol. 112, no. 37, pp. 14306–14312, 2008, doi: 10.1021/jp804035r.
- [83] Z. Gu *et al.*, 'Controllable assembly of WO₃ nanorods/nanowires into hierarchical nanostructures', *Journal of Physical Chemistry B*, vol. 110, no. 47, pp. 23829–23836, 2006, doi: 10.1021/jp065170y.
- [84] F. Zheng *et al.*, 'Hydrothermal preparation, growth mechanism and supercapacitive properties of WO₃ nanorod arrays grown directly on a Cu substrate', *CrystEngComm*, vol. 18, no. 21, pp. 3891–3904, 2016, doi: 10.1039/c6ce00316h.

- [85] K. Christou *et al.*, 'Effect of solution chemistry on the characteristics of hydrothermally grown WO₃ for electroactive applications', in *Thin Solid Films*, Elsevier, 2015, pp. 333–337. doi: 10.1016/j.tsf.2015.03.045.
- [86] D. Sarkar, S. Mukherjee, S. Pal, D. D. Sarma, and A. Shukla, 'Hexagonal WO₃ nanorods as ambipolar electrode material in asymmetric WO₃/WO₃/MnO₂ supercapacitor', *J Electrochem Soc*, vol. 165, no. 10, pp. A2108–A2114, 2018, doi: 10.1149/2.0451810jes.
- [87] J. Wang, E. Khoo, P. S. Lee, and J. Ma, 'Controlled synthesis of WO₃ nanorods and their electrochromic properties in H₂SO₄ electrolyte', *Journal of Physical Chemistry C*, vol. 113, no. 22, pp. 9655–9658, 2009, doi: 10.1021/jp901650v.
- [88] P. A. Shinde, A. C. Lokhande, A. M. Patil, and C. D. Lokhande, 'Facile synthesis of self-assembled WO₃ nanorods for high-performance electrochemical capacitor', *J Alloys Compd*, vol. 770, pp. 1130–1137, 2019, doi: 10.1016/j.jallcom.2018.08.194.
- [89] B. D. Fahlman, 'What is Materials Chemistry? BT - Materials Chemistry', B. D. Fahlman, Ed., Dordrecht: Springer Netherlands, 2007, pp. 1–11. doi: 10.1007/978-1-4020-6120-2_1.
- [90] P. Estefania and V. Armas, 'Effect of Water on Copper Electrodeposition from Water-containing Deep Eutectic Solvents', no. January, 2019.
- [91] F. E. I. C. All, 'The Quanta FEG 250 / 450 / 650 User Operation Manual 4', no. 2009.
- [92] J. Epp, *X-Ray Diffraction (XRD) Techniques for Materials Characterization*. Elsevier Ltd, 2016. doi: 10.1016/B978-0-08-100040-3.00004-3.
- [93] P. P. T. C. Huang, 'GRAZING-INCIDENCE X-RAY TECHNIQUE FOR SURFACE, INTERFACE, AND THIN-FILM ANALYSIS', 1997.
- [94] Bio-logic Science Instruments and I. Introduction, 'EC-Lab – Application Note # 44 Equivalent model of an electrochemical cell including the reference electrode impedance and the potentiostat parasitics I – EIS BASICS EC-Lab – Application Note # 44', pp. 1–5, 2013.
- [95] A. T. Tran, F. Huet, K. Ngo, and P. Rousseau, 'Artefacts in electrochemical impedance measurement in electrolytic solutions due to the reference electrode', *Electrochim Acta*, vol. 56, no. 23, pp. 8034–8039, 2011, doi: 10.1016/j.electacta.2010.12.088.
- [96] B. E. Conway, V. Birss, and J. Wojtowicz, 'The role and utilization of pseudocapacitance for energy storage by supercapacitors', *J Power Sources*, vol. 66, no. 1–2, pp. 1–14, 1997, doi: 10.1016/S0378-7753(96)02474-3.
- [97] G. Z. Chen, 'Supercapattery: Merit merge of capacitive and Nernstian charge storage mechanisms', *Curr Opin Electrochem*, vol. 21, pp. 358–367, 2020, doi: 10.1016/j.coelec.2020.04.002.

- [98] J. Wang, J. Polleux, J. Lim, and B. Dunn, 'Pseudocapacitive Contributions to Electrochemical Energy Storage in TiO₂ (Anatase) Nanoparticles', vol. 2, pp. 14925–14931, 2007.
- [99] G. Z. Chen, 'Linear and non-linear pseudocapacitances with or without diffusion control', *Progress in Natural Science: Materials International*, vol. 31, no. 6, pp. 792–800, 2021, doi: 10.1016/j.pnsc.2021.10.011.
- [100] A. J. B. L. R. Faulkner, *Electrochemical Methods: Fundamentals and Applications*, 2nd ed. Wiley & Sons, 2001.
- [101] T. Liu, 'How to Differentiate Capacitances using Trasatti and Dunn Methods Some of the authors of this publication are also working on these related projects: energy storage View project Carbon Materials for Supercapacitors View project', no. 2018.
- [102] C. Fan, T. R. B. Grandjean, K. O'Regan, E. Kendrick, and W. D. Widanage, 'Understanding non-linearity in electrochemical systems using multisine-based non-linear characterization', *Transactions of the Institute of Measurement and Control*, 2021, doi: 10.1177/01423312211045991.
- [103] Charles Jekel, 'piecewise linear fit python documentation (pwfl py)'. [Online]. Available: https://jekel.me/piecewise_linear_fit_py/license.html
- [104] T. Chai and R. R. Draxler, 'Root mean square error (RMSE) or mean absolute error (MAE)? -Arguments against avoiding RMSE in the literature', *Geosci Model Dev*, vol. 7, no. 3, pp. 1247–1250, 2014, doi: 10.5194/gmd-7-1247-2014.
- [105] J. R. Macdonald and a J. Wiley, *Impedance Spectroscopy Theory, Experiment, and Applications*.
- [106] X. Z. Yuan, C. Song, H. Wang, and J. Zhang, *Electrochemical impedance spectroscopy in PEM fuel cells: Fundamentals and applications*. 2010. doi: 10.1007/978-1-84882-846-9.
- [107] B. A. Mei, O. Munteshari, J. Lau, B. Dunn, and L. Pilon, 'Physical Interpretations of Nyquist Plots for EDLC Electrodes and Devices', *Journal of Physical Chemistry C*, vol. 122, no. 1, pp. 194–206, 2018, doi: 10.1021/acs.jpcc.7b10582.
- [108] 'Impedance.py Documentation'. [Online]. Available: <https://impedancepy.readthedocs.io/en/latest/index.html>
- [109] M. D. Levi, Z. Lu, and D. Aurbach, 'Application of finite-diffusion models for the interpretation of chronoamperometric and electrochemical impedance responses of thin lithium insertion V₂O₅ electrodes', *Solid State Ion*, vol. 143, no. 3–4, pp. 309–318, 2001, doi: 10.1016/S0167-2738(01)00819-0.
- [110] H. C. Yu, S. B. Adler, S. A. Barnett, and K. Thornton, 'Simulation of the diffusional impedance and application to the characterization of electrodes with complex

- microstructures', *Electrochim Acta*, vol. 354, p. 136534, 2020, doi: 10.1016/j.electacta.2020.136534.
- [111] P. L. Taberna, P. Simon, and J. F. Fauvarque, 'Electrochemical Characteristics and Impedance Spectroscopy Studies of Carbon-Carbon Supercapacitors', *J Electrochem Soc*, vol. 150, no. 3, p. A292, 2003, doi: 10.1149/1.1543948.
- [112] Z. Chen *et al.*, 'Hierarchical Nanostructured WO₃ with Biomimetic Proton Channels and Mixed Ionic-Electronic Conductivity for Electrochemical Energy Storage', *Nano Lett*, vol. 15, no. 10, pp. 6802–6808, 2015, doi: 10.1021/acs.nanolett.5b02642.
- [113] T. Gao, B. P. Jelle, and A. Gustavsen, 'Synthesis and Characterization of Sodium Tungsten Bronze Nanorods for Electrochromic Smart Window Applications *', vol. 3, no. 7491, pp. 3–6, 2013.
- [114] L. Zhu *et al.*, 'Determination of NaCl and Na₂SO₄ Equilibrium Solubility in Cyclohexanol and Cyclohexanone Aqueous Solutions at 323.15 K', *J Chem Eng Data*, vol. 65, no. 4, pp. 1617–1626, 2020, doi: 10.1021/acs.jced.9b01035.
- [115] R. Lazzari, *Grazing incidence small-angle X-ray scattering from nanostructures*, vol. 770. 2009. doi: 10.1007/978-3-540-88588-7_7.
- [116] L. Chen, S. Lam, Q. Zeng, R. Amal, and A. Yu, 'Effect of cation intercalation on the growth of hexagonal WO₃ nanorods', *Journal of Physical Chemistry C*, vol. 116, no. 21, pp. 11722–11727, 2012, doi: 10.1021/jp301210q.
- [117] X. Zhong, Y. Sun, X. Chen, G. Zhuang, X. Li, and J. G. Wang, 'Mo Doping Induced More Active Sites in Urchin-Like W₁₈O₄₉ Nanostructure with Remarkably Enhanced Performance for Hydrogen Evolution Reaction', *Adv Funct Mater*, vol. 26, no. 32, pp. 5778–5786, 2016, doi: 10.1002/adfm.201601732.
- [118] Y. Marcus, 'Ionic radii in aqueous solutions', *Chem Rev*, vol. 88, no. 8, pp. 1475–1498, Dec. 1988, doi: 10.1021/cr00090a003.
- [119] Rayner-Canham, 'Charge Densities of Selected Ions', *Descriptive Inorganic Chemistry*, pp. 13–15, 1976.
- [120] X. D. Liu *et al.*, 'Oxygen vacancy-rich WO₃ heterophase structure: A trade-off between surface-limited pseudocapacitance and intercalation-limited behaviour', *Chemical Engineering Journal*, vol. 425, 2021, doi: 10.1016/j.cej.2021.131431.
- [121] W. Xu *et al.*, 'Preparation of WO₃ Nano-material Negative Electrode for Asymmetric Supercapacitor', 2018.
- [122] A. Di Paola, F. Di Quarto, and C. Sunseri, 'Electrochromism in Anodically Formed Tungsten Oxide Films', *J Electrochem Soc*, vol. 125, no. 8, pp. 1344–1347, 1978, doi: 10.1149/1.2131675.
- [123] J. B.; V. A. Mitchell, 'Supporting Information: Transition from Battery to Pseudocapacitor Behavior via Structural Water in Tungsten Oxide', 2017.

- [124] S. K. Biswas, J. O. Baeg, S. J. Moon, K. J. Kong, and W. W. So, 'Morphologically different WO₃ nanocrystals in photoelectrochemical water oxidation', *Journal of Nanoparticle Research*, vol. 14, no. 1, 2012, doi: 10.1007/s11051-011-0667-6.
- [125] R. Dhillip Kumar, Y. Andou, and S. Karuppuchamy, 'Facile synthesis of Co-WO₃/functionalized carbon nanotube nanocomposites for supercapacitor applications', *Journal of Materials Science: Materials in Electronics*, vol. 28, no. 7, pp. 5425–5434, 2017, doi: 10.1007/s10854-016-6203-9.
- [126] L. Wang, H. Hu, J. Xu, S. Zhu, A. Ding, and C. Deng, 'WO₃ nanocubes: Hydrothermal synthesis, growth mechanism, and photocatalytic performance', *J Mater Res*, vol. 34, no. 17, pp. 2955–2963, 2019, doi: 10.1557/jmr.2019.189.
- [127] H. F. Pang, Z. J. Li, X. Xiang, Y. Q. Fu, F. Placido, and X. T. Zu, 'Hierarchical structured tungsten oxide nanocrystals via hydrothermal route: Microstructure, formation mechanism and humidity sensing', *Appl Phys A Mater Sci Process*, vol. 112, no. 4, pp. 1033–1042, 2013, doi: 10.1007/s00339-012-7475-4.
- [128] K. Bange, 'Colouration of tungsten oxide films: A model for optically active coatings', *Solar Energy Materials & Solar Cells*, vol. 58, pp. 1–131, 1999.
- [129] V. S. Saji and C. W. Lee, 'Molybdenum, molybdenum oxides, and their electrochemistry', *ChemSusChem*, vol. 5, no. 7, pp. 1146–1161, 2012, doi: 10.1002/cssc.201100660.
- [130] X. Wang, Y. Xie, K. Tang, C. Wang, and C. Yan, 'Redox Chemistry of Molybdenum Trioxide for Ultrafast Hydrogen-Ion Storage', *Angewandte Chemie - International Edition*, vol. 57, no. 36, pp. 11569–11573, 2018, doi: 10.1002/anie.201803664.

10 Appendices

The appendices are labelled alphabetically to be distinct from numbered main body sections. These include full data sets for experiments referred to in the main body.

Appendix A Covid-19 Pandemic Impact Statement

I believe that the COVID-19 Pandemic, and specifically my department's response to it, significantly hampered the progress of this project. First and foremost, the department laboratories were completely closed for 6 months between March 2020 and September 2020 during the first year of the project with no access permitted, meaning no practical work could take place, significantly longer than any other department in the faculty of which opened largely as soon as feasibly possible.

Upon reopening, departmental rules often went far beyond any UK or Scottish government laws and guidelines to unnecessary extents. Firstly, for the next year, until September 2021, the department forbade the use of the kitchen facilities and office areas - denying access to hot food, hot water, a desk to work at, and the refrigerator even through winter. The kitchen room itself where one could take a break was 6 distanced tables covered in hazard tape for the duration which naturally made for an unpleasant space to eat your lunch. Secondly, practical training and supervision in the lab were actively prohibited meaning that everything in this report was entirely self-taught, managed, and arranged. Thirdly, the specific lab bench you worked from had to be booked and approved a day in advance, resulting in a great deal of lost time to overbearing bureaucracy if one forgot to book in. This frustration with this measure was acutely felt by those working within shared spaces. Fourthly, access to physical characterisation out with the department was severely limited and because the Department of Chemical & Process Engineering at Strathclyde does not have any form of in-house SEM or XRD at the time of writing, none of the characterisation was completed until 2022 – two and a half years from beginning the project. All of this may seem petty, it feels as much writing it, but I hope that it paints a rather miserable picture of general malaise students felt *trying to work* in the department. I say try because you were simultaneously being asked to deliver results and progress whilst being denied access to the training and equipment required to do so.

Reflecting upon this now, it did cause an inordinate amount of unnecessary stress. The University, to its credit, granted two months additional stipend for which I am incredibly grateful. I am also grateful for the support of my supervisors in challenging the working conditions. Those in the department making the decisions however I can say nothing positive about. No consideration to the students working under the rules was given, we were ignored and when we challenged the department patronised.

Appendix B Personal Output

B.1 Conferences

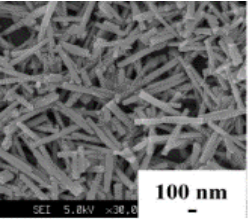
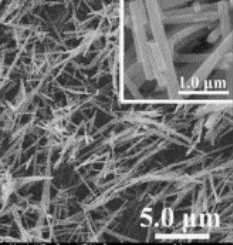
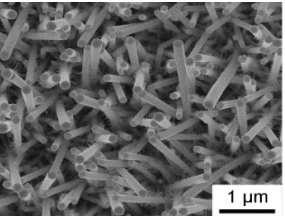
- ESEE2020 (delayed and placed online in 2021): presented a poster on preliminary results.
- UoS ChemEng internal Research Celebration Event 2021: delivered an oral presentation and was awarded best oral presentation.
- ESC242 in Atlanta, GA October 2022: delivered an oral presentation titled “Hydrothermally Enhanced W-WO₃ electrodes for pseudocapacitive energy storage”.

B.2 Papers

It is disappointing to not have published a paper from the work in this thesis as of submission, but two papers are in preparation with the intention of submitting for publication in 2024:

1. Cadden T, Brightman E, Roy S. Binder free tungsten-tungsten oxide electrodes for energy storage
2. Cadden T, Brightman E, Roy S. Effect of capping agent, pH, and substrate surface upon the hydrothermal growth of tungsten oxide from tungsten foils

Appendix C Quantification of Reaction Parameters

Capping Agent	pH	Temperature (°C)	Reaction Time (hr)	R Number	Obtained Phase	SEM IMAGE From Source	Source
NaCl	2	180	24	4-6	Hexagonal		[87]
Na ₂ SO ₄	2	180	24	4-6	Hexagonal		[80]
(NH ₄) ₂ SO ₄	1	180	12	6-10	Hexagonal		[88]
Rb ₂ SO ₄	2	180	8	5-8	Hexagonal		[84]

Appendix D Powder Ink Masses and calculated current densities.

Assuming all water and propanol (all solvent) evaporate given powder is dry. The only solids that remain are active material and Nafion.

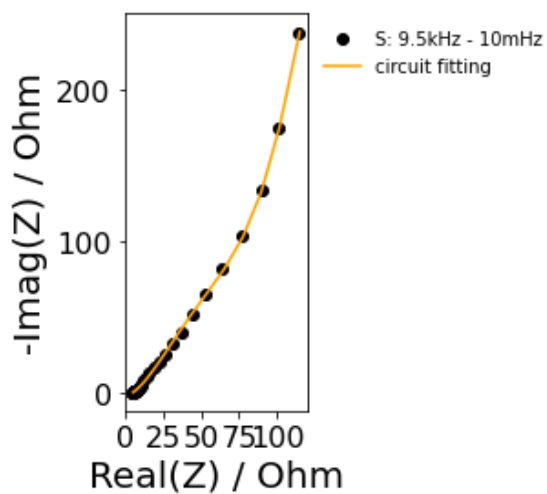
Calculated using 0.1 g of active material in ink.

Nafion mass (g) = 0.05 g Nafion/g Solution * 0.01035 g Solution/ μ l (measured in lab) * 33 μ l = 0.01707gNafion in ink

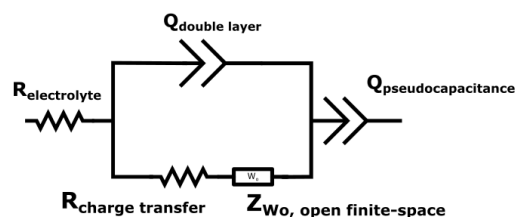
In well-mixed ink: $mass\ of\ WO_3 = \frac{0.1}{0.1+0.01707} = 0.85419\%$ of measured ink mass.

sample	Powder Mass in ink (g)	Foil (g)	ink coated foil (g)	measured mass	active mass (g)	Current Densities (A/g --> biologic mA)				
						0.5	1	2	5	10
NaCl_Powder_01	0.0101	0.1003	0.1025	0.0022	0.0019	0.940	1.879	3.758	9.396	18.792
NaCl_Powder_02	0.0111	0.1085	0.1131	0.0046	0.0039	1.965	3.929	7.859	19.646	39.293
NaCl_Powder_03	0.0103	0.0926	0.0948	0.0022	0.0019	0.940	1.879	3.758	9.396	18.792
Na2SO4_Powder_01	0.0104	0.1079	0.1107	0.0028	0.0024	1.196	2.392	4.783	11.959	23.917
Na2SO4_Powder_02	0.0108	0.1041	0.1068	0.0027	0.0023	1.153	2.306	4.613	11.532	23.063
Na2So4_Powder_03	0.0102	0.1079	0.1100	0.0021	0.0018	0.897	1.794	3.588	8.969	17.938
Rb2SO4_Powder_01	0.0104	0.0923	0.0984	0.0061	0.0052	2.605	5.211	10.421	26.053	52.106
Rb2SO4_Powder_02	0.0111	0.1042	0.1065	0.0023	0.0020	0.982	1.965	3.929	9.823	19.646
Rb2SO4_Powder_03	0.0101	0.0997	0.1021	0.0024	0.0021	1.025	2.050	4.100	10.250	20.501
NH42SO4_Powder_01	0.0101	0.1046	0.1073	0.0027	0.0023	1.153	2.306	4.613	11.532	23.063
NH42SO4_Powder_02	0.0102	0.0997	0.1035	0.0038	0.0032	1.623	3.246	6.492	16.230	32.459
NH42SO4_Powder_03	0.0111	0.0997	0.1022	0.0025	0.0021	1.068	2.135	4.271	10.677	21.355
NH42SO4_Powder_04	0.1050	0.0999	0.1037	0.0038	0.0032	1.623	3.246	6.492	16.230	32.459

Appendix E Impedance Fitting for V=IR Correction



Circuit

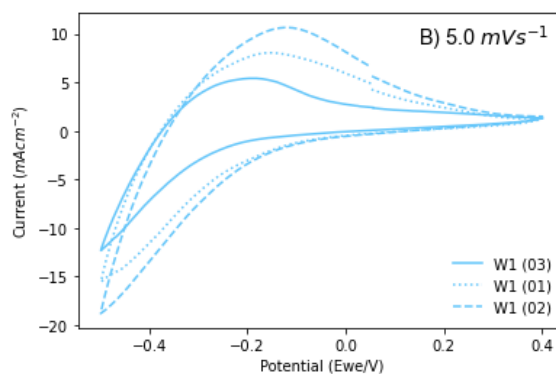
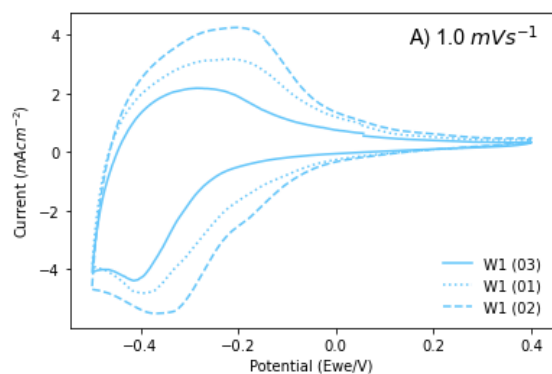


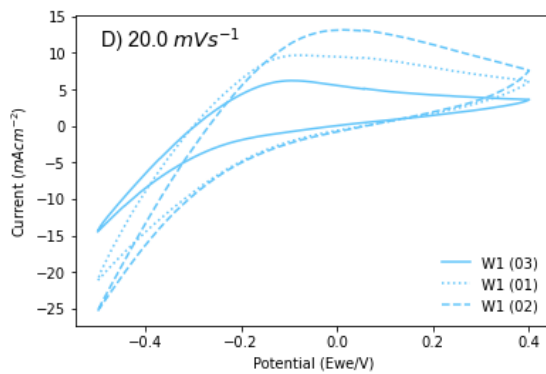
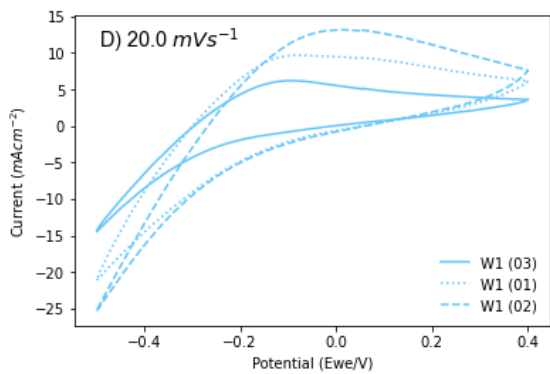
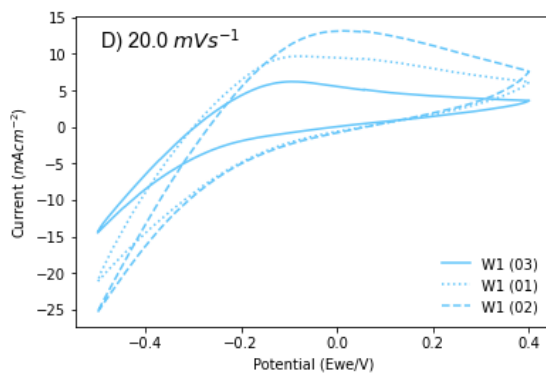
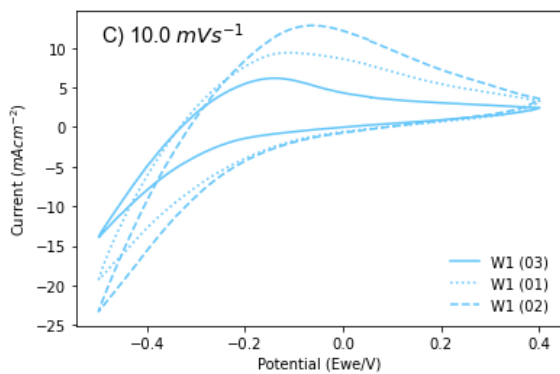
Sample	R_e (Ω)	R_{ct} (Ω)	Z_{wo} (Ω)	τ (seconds)	Q_{dl} ($F Hz^{-1}$)	α_{dl} (unitless)	Q_{ps} ($F Hz^{-1}$)	α_{ps} (unitless)
S	4.77	5.92	304.32	14.37	0.03	0.922	0.035	0.392
Confidence	0.28	173.93	234.22	17.44	0.028	0.11	0.008	0.043

Appendix F CV data from Chapter 4

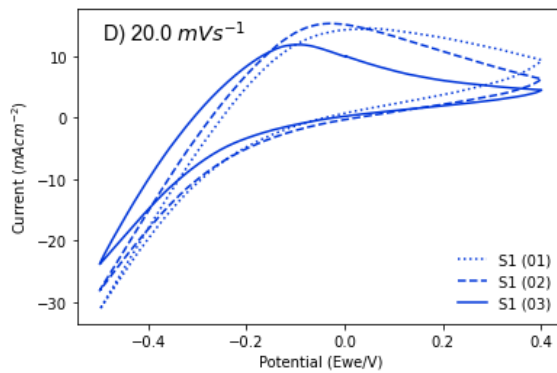
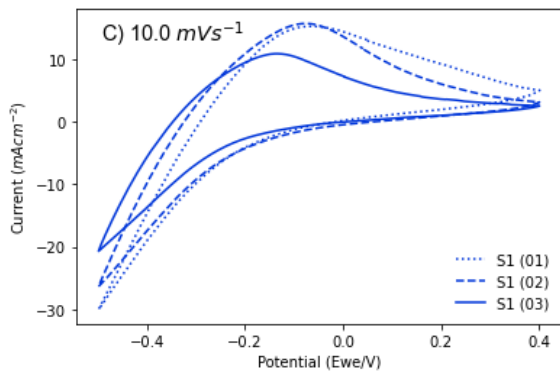
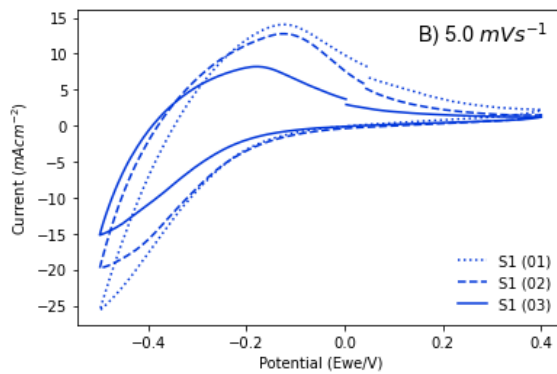
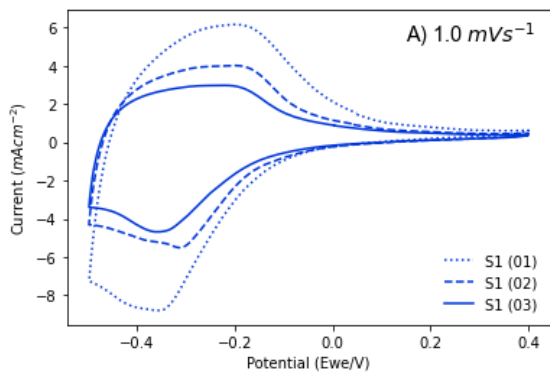
F.1 Sample Reproducibility

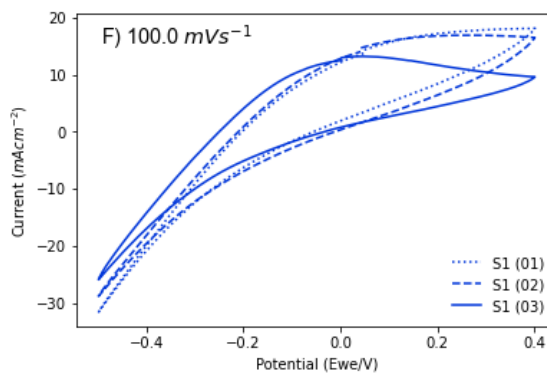
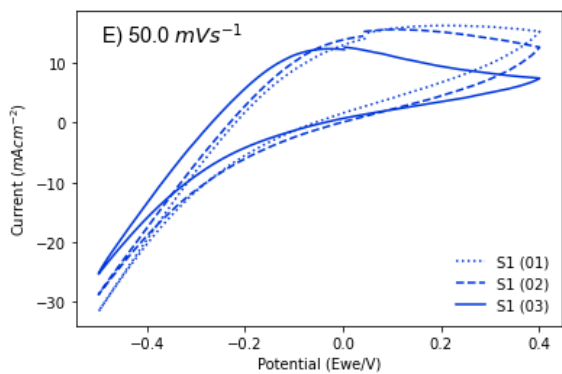
F.1.1 W1



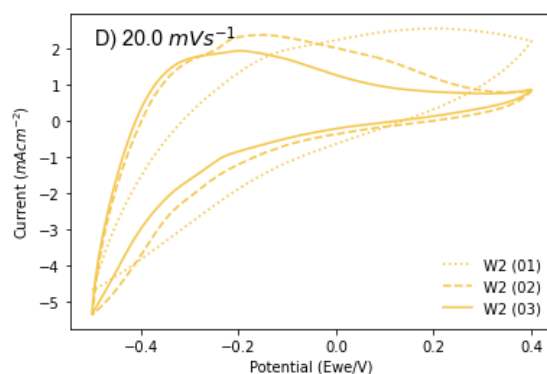
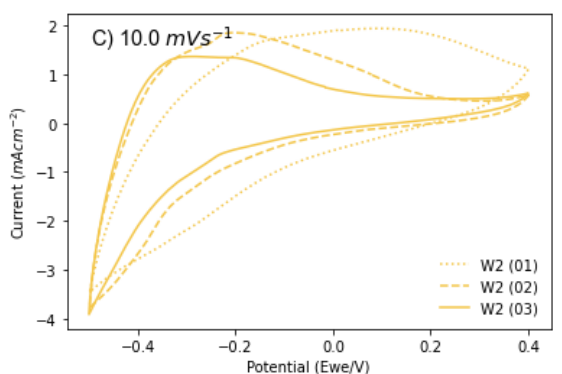
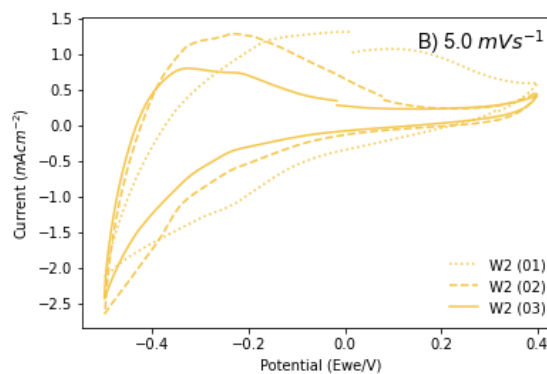
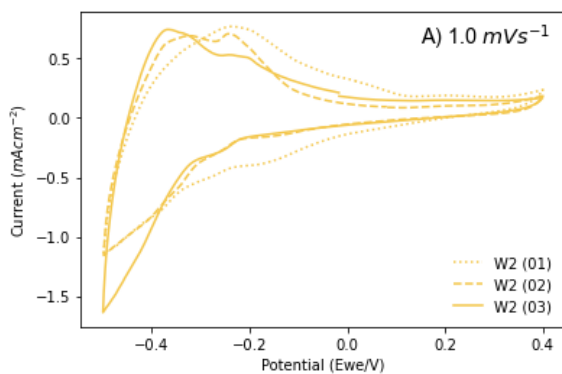


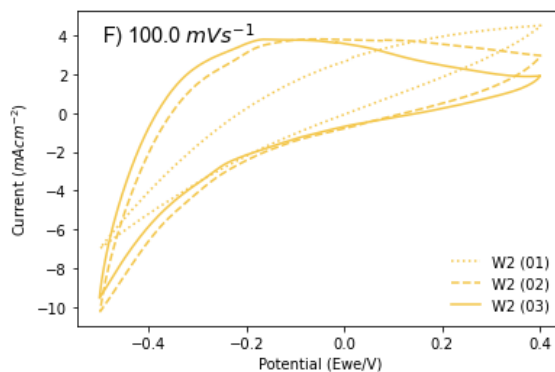
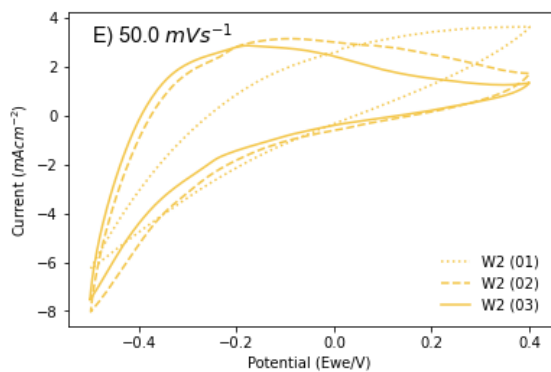
F.1.2 S1



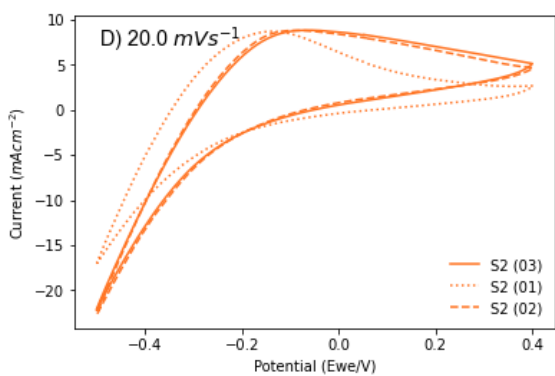
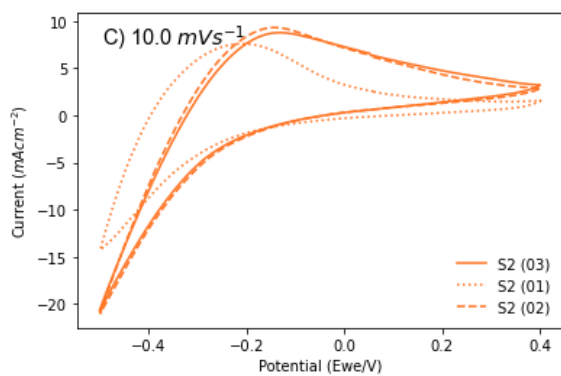
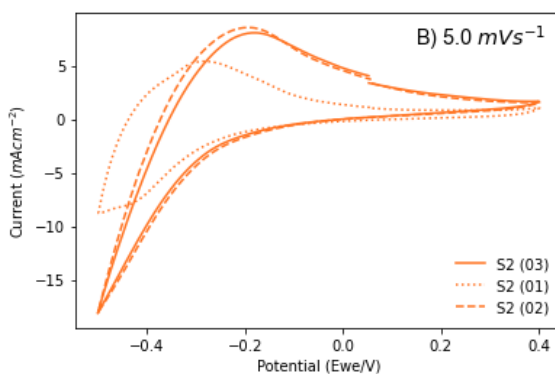
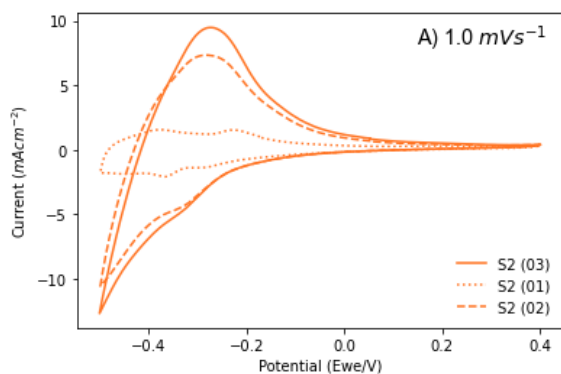


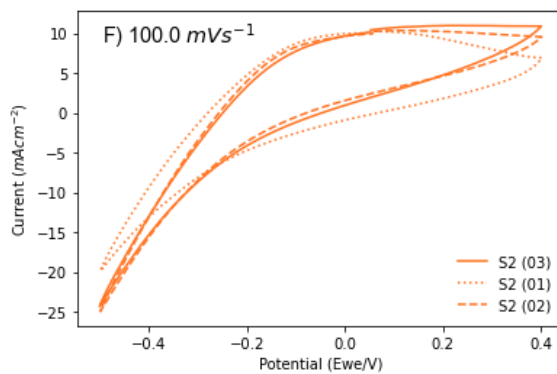
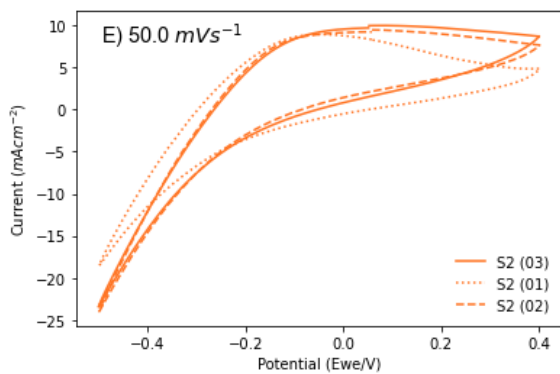
F.1.3 W2



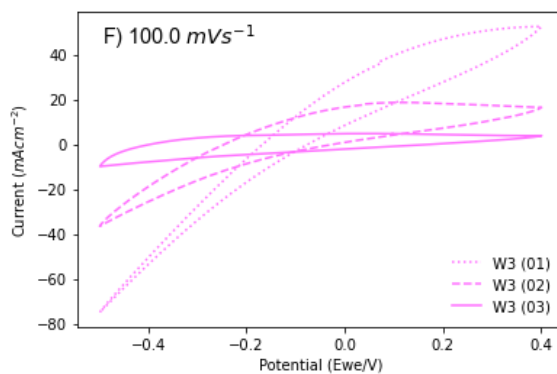
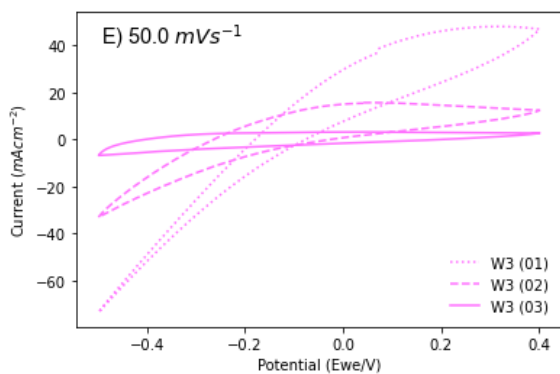
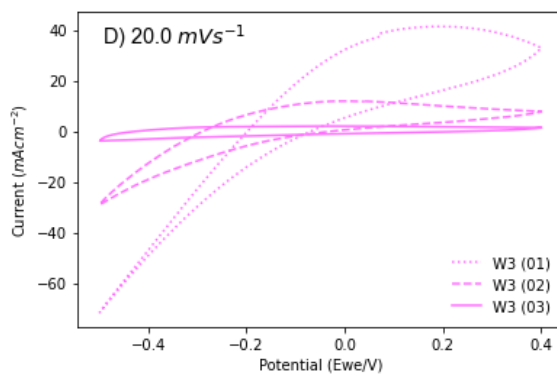
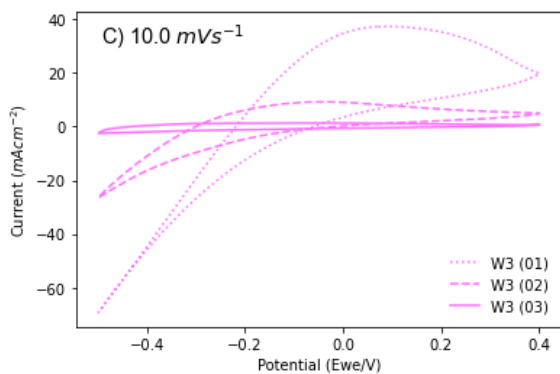
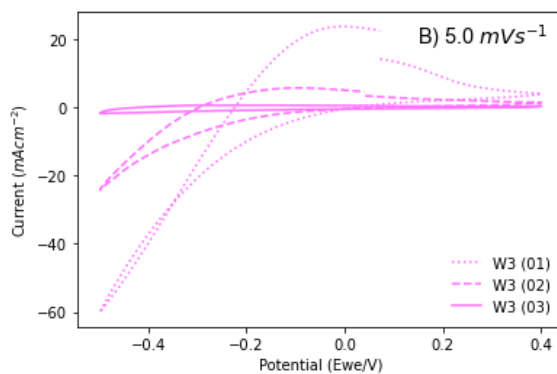
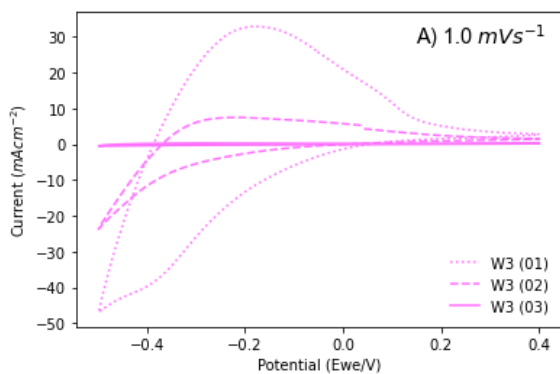


F.1.4 S2

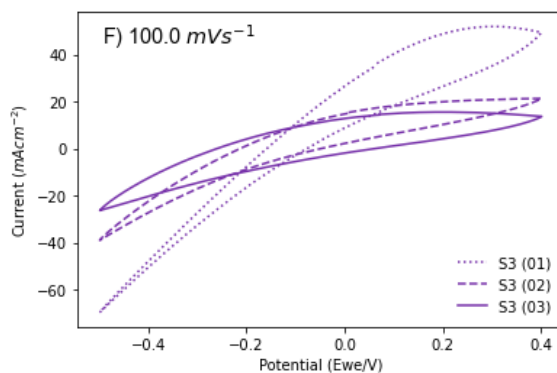
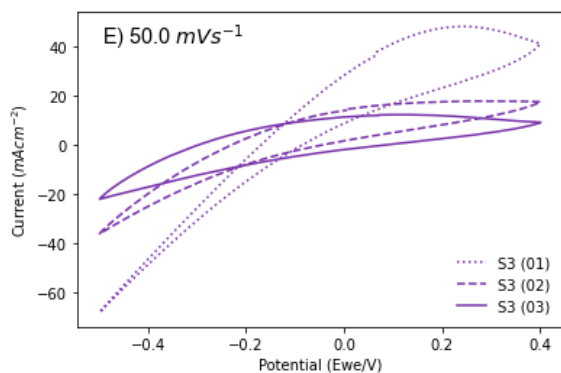
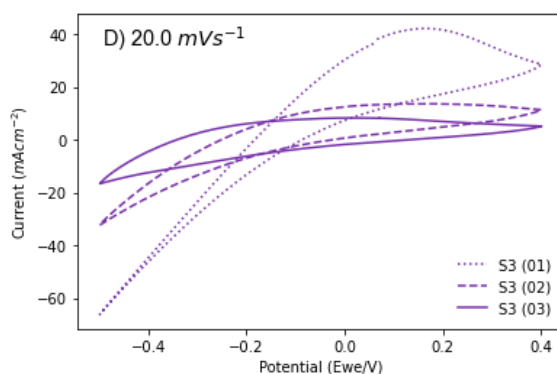
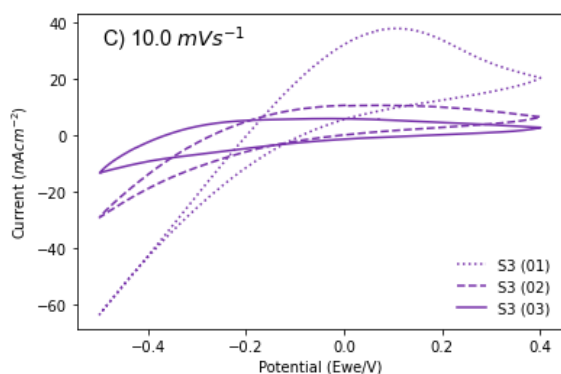
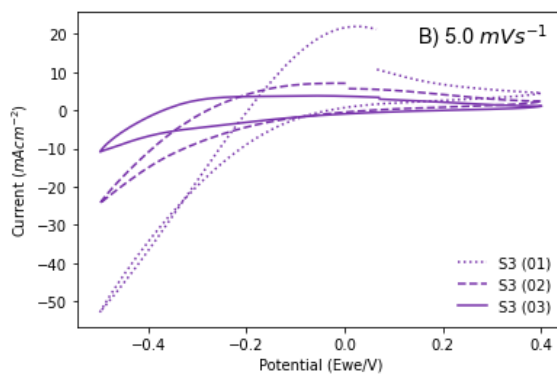
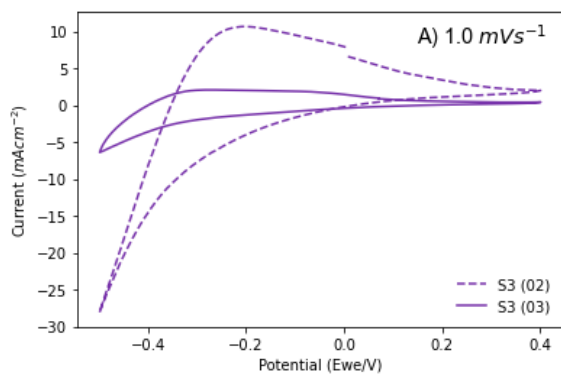




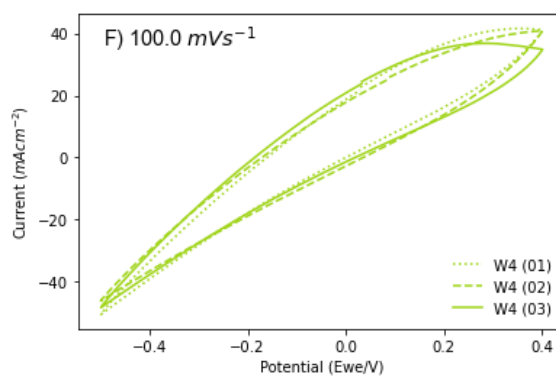
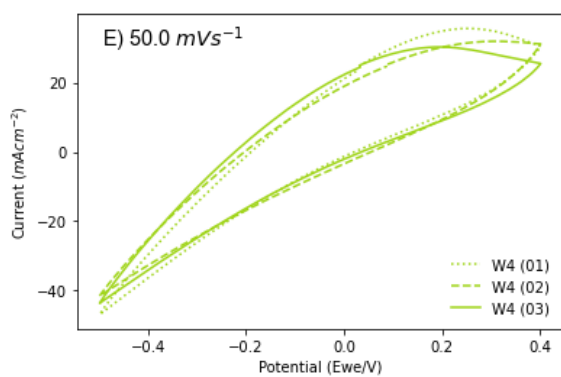
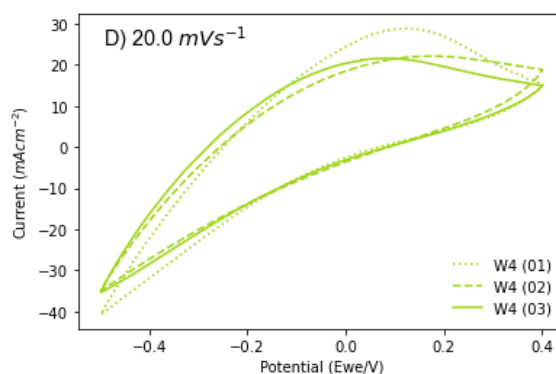
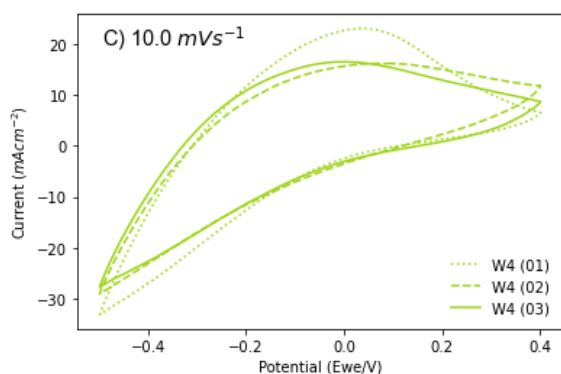
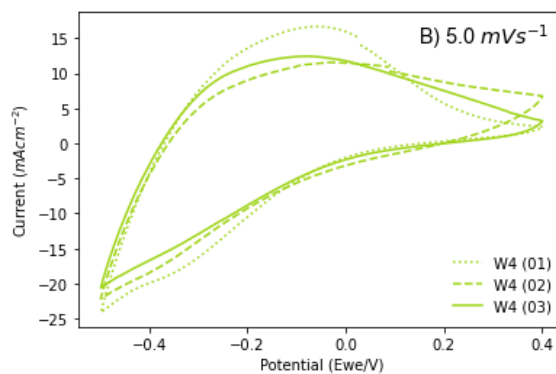
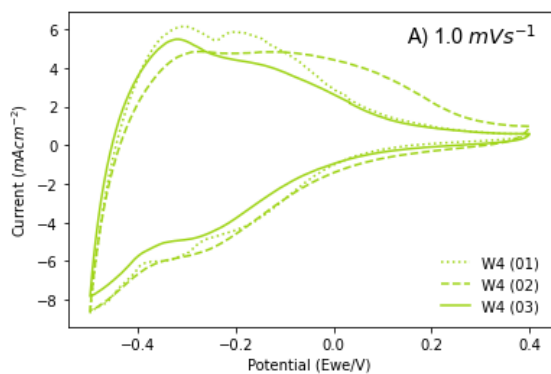
F.1.5 W3



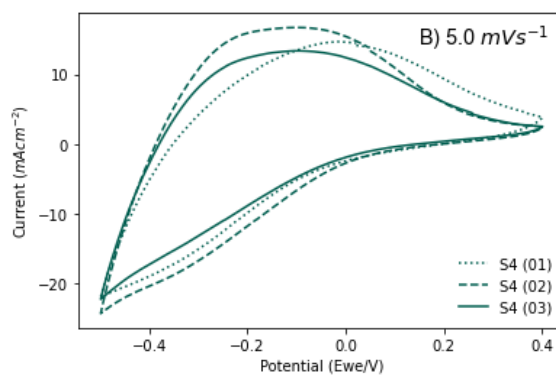
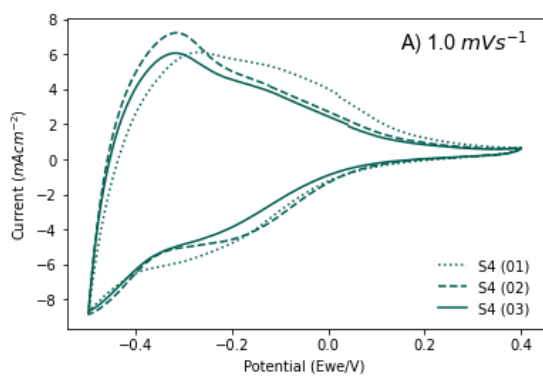
F.1.6 S3

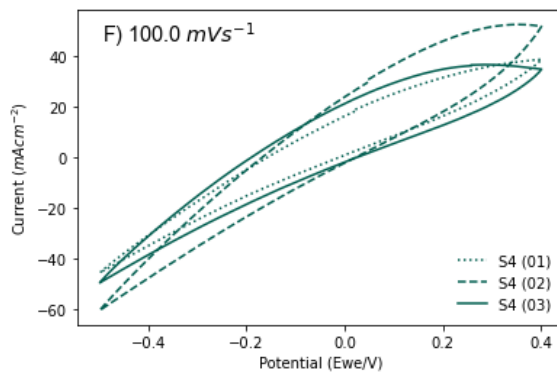
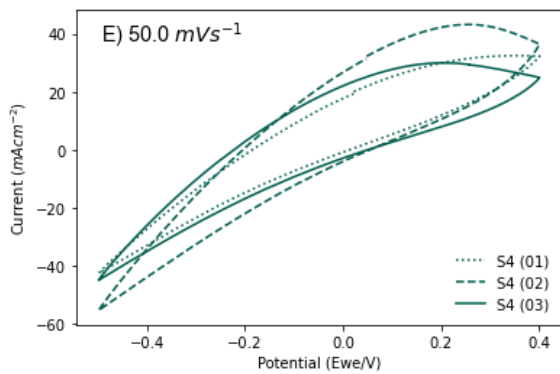
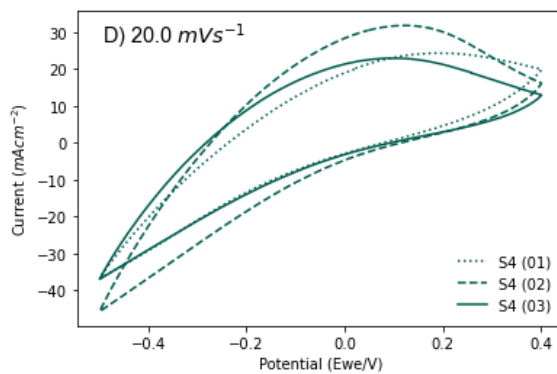
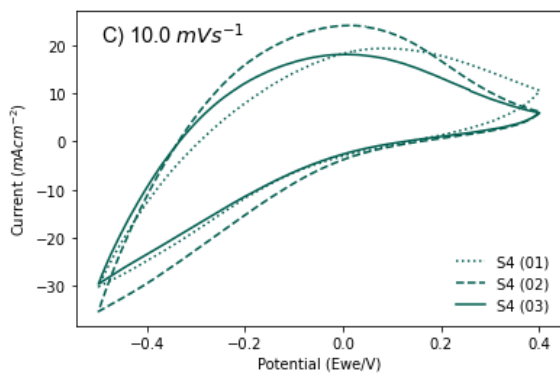


F.1.7 W4



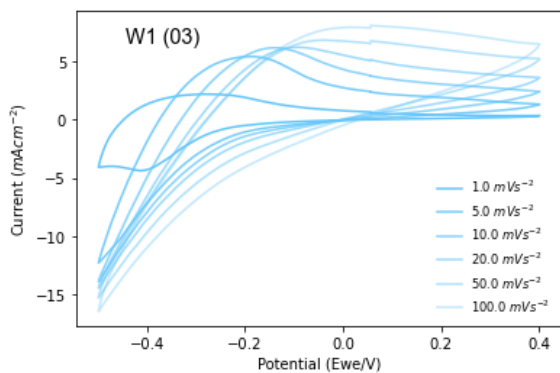
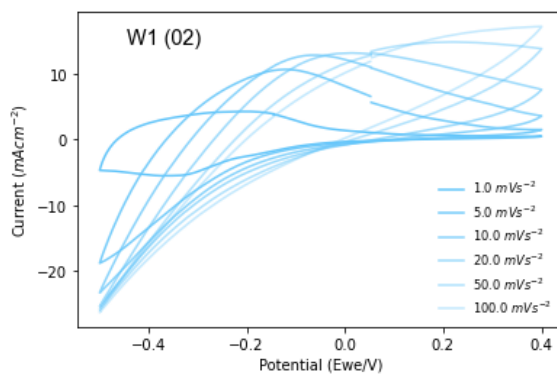
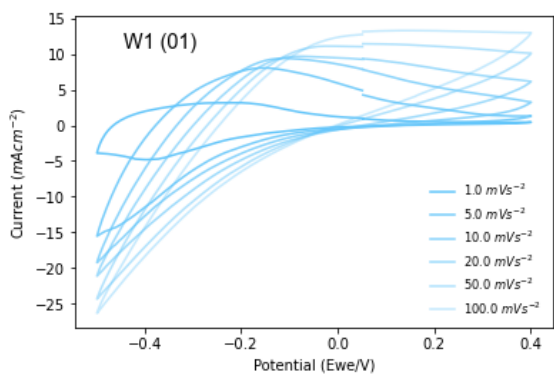
F.1.8 S4



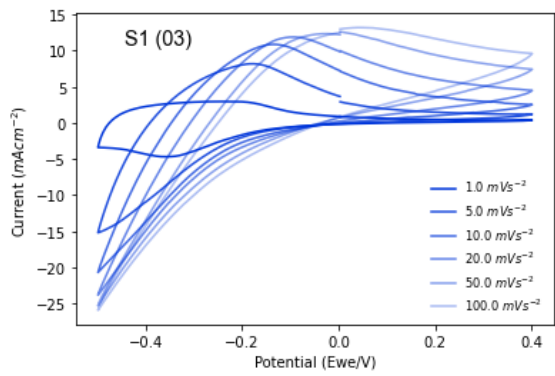
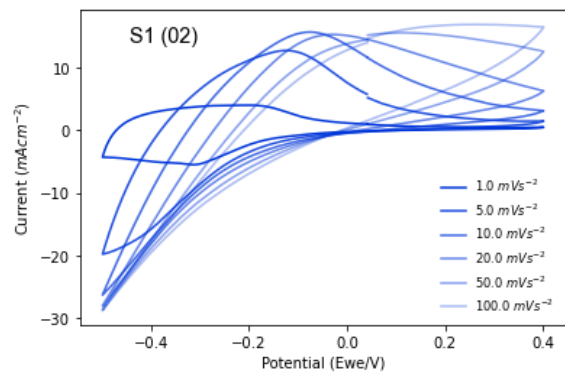
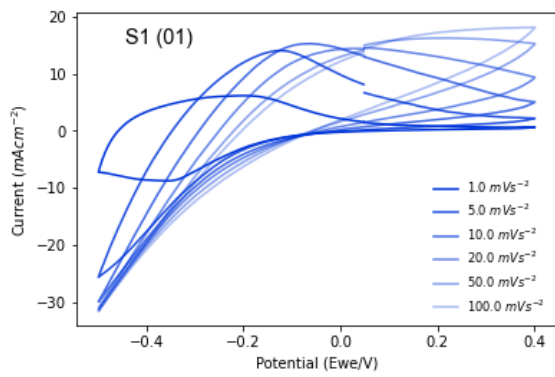


F.2 CV data of each sample

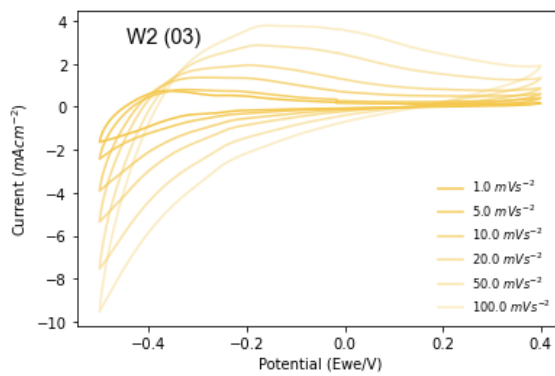
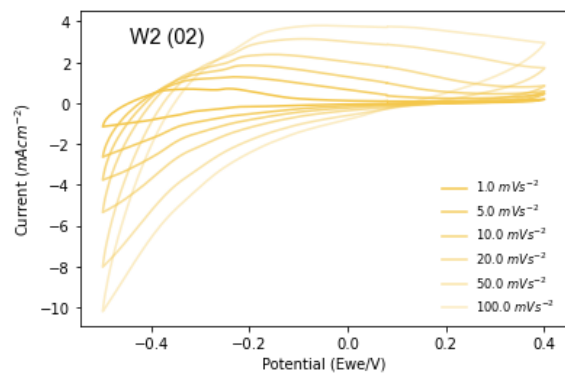
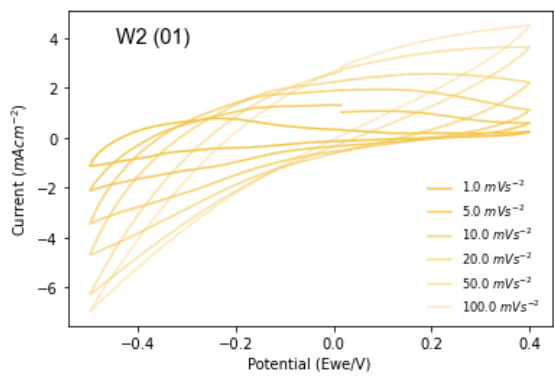
F.2.1 W1



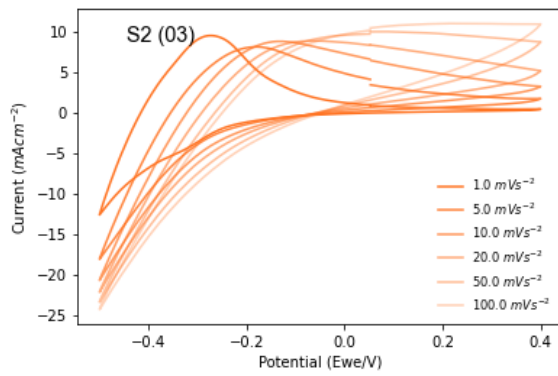
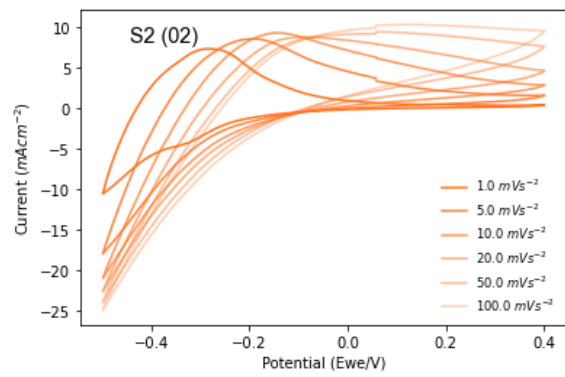
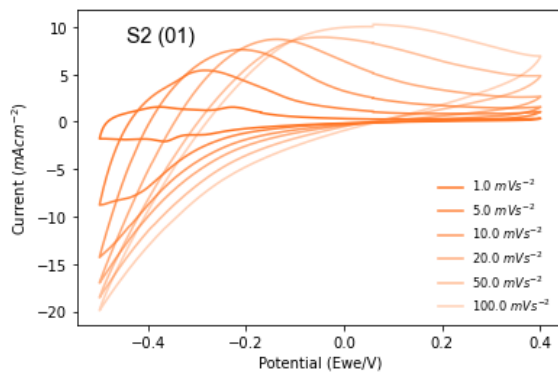
F.2.2 S1



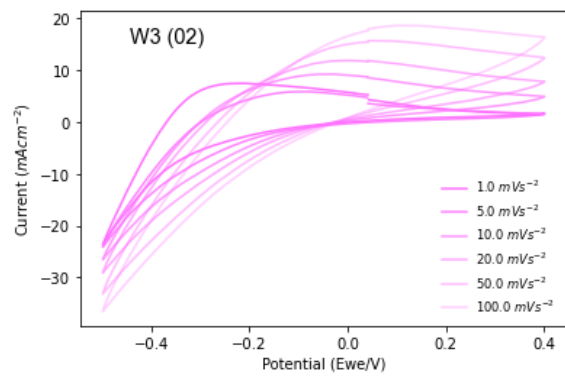
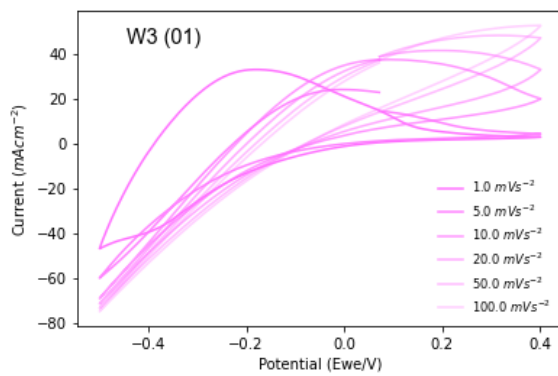
F.2.3 W2

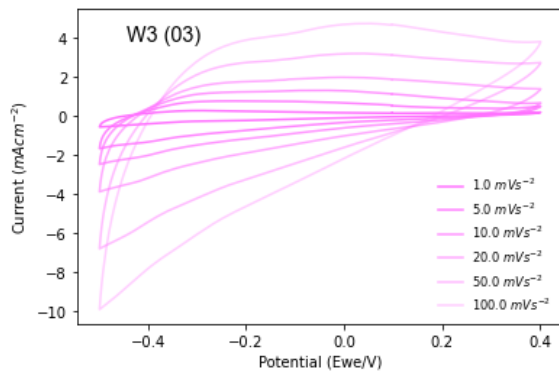


F.2.4 S2

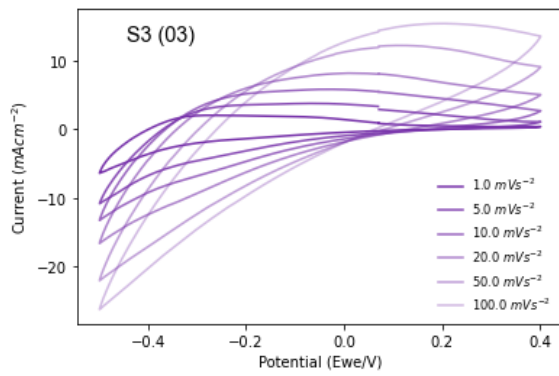


F.2.5 W3

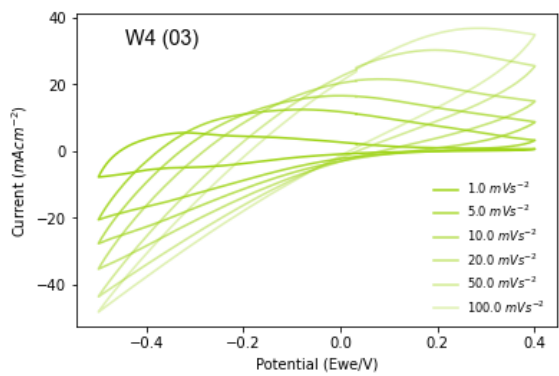
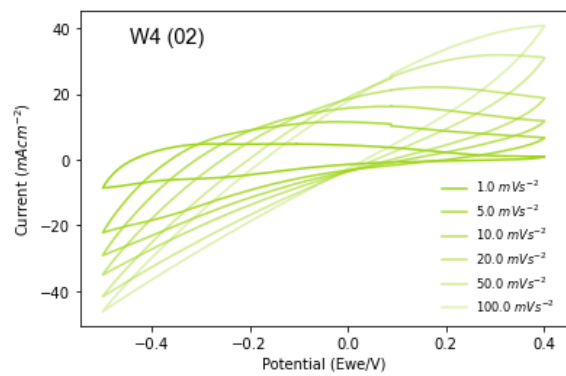
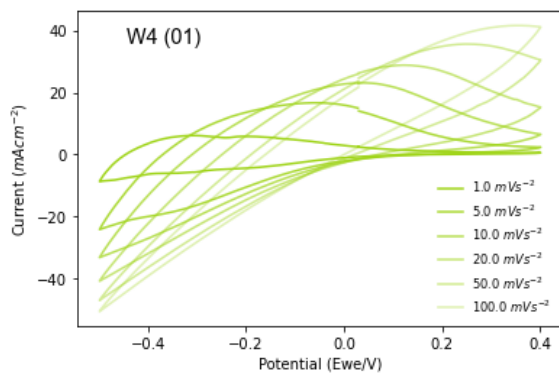




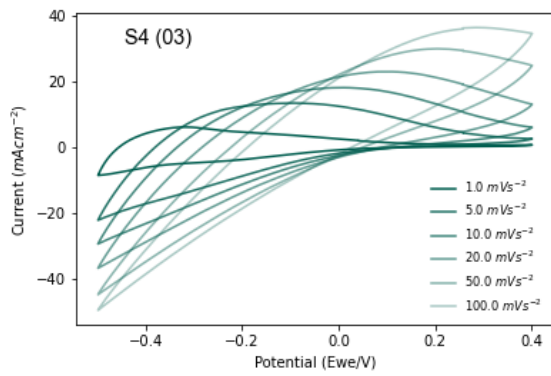
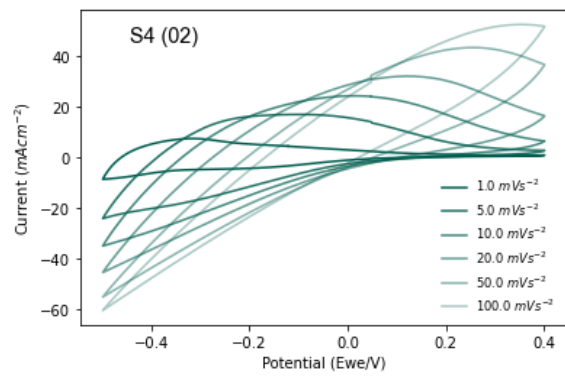
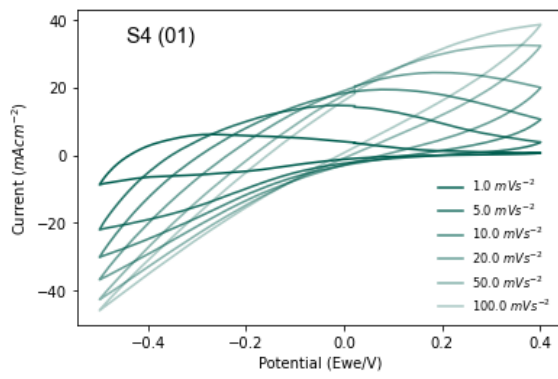
F.2.6 S3



F.2.7 W4



F.2.8 S4



F.3 Summary Table of Capacities and Capacitances from CV Data

Sample	Scanrate	Run	Scanrate/mVs	Area/mAV	Mass/g	Q/C	Capacity/mAhg	Capacitance/Fg	mAh/cm ²	C/cm ²	C/g
W1	1.00	01	1.00	2.50	0.01	2.50	69.44	277.78	0.69	2.50	250.00
W1	1.00	02	1.00	3.22	0.03	3.22	29.82	119.26	0.89	3.22	107.33
W1	1.00	03	1.00	1.58	0.04	1.58	10.97	43.89	0.44	1.58	39.50
W1	5.00	01	5.00	5.48	0.01	1.10	30.44	121.78	0.30	1.10	109.60
W1	5.00	02	5.00	6.50	0.03	1.30	12.04	48.15	0.36	1.30	43.33
W1	5.00	03	5.00	3.11	0.04	0.62	4.32	17.28	0.17	0.62	15.55
W1	10.00	01	10.00	6.46	0.01	0.65	17.94	71.78	0.18	0.65	64.60
W1	10.00	02	10.00	7.66	0.03	0.77	7.09	28.37	0.21	0.77	25.53
W1	10.00	03	10.00	3.28	0.04	0.33	2.28	9.11	0.09	0.33	8.20
W1	20.00	01	20.00	6.73	0.01	0.34	9.35	37.39	0.09	0.34	33.65
W1	20.00	02	20.00	7.47	0.03	0.37	3.46	13.83	0.10	0.37	12.45
W1	20.00	03	20.00	3.36	0.04	0.17	1.17	4.67	0.05	0.17	4.20
W1	50.00	01	50.00	7.07	0.01	0.14	3.93	15.71	0.04	0.14	14.14
W1	50.00	02	50.00	6.52	0.03	0.13	1.21	4.83	0.04	0.13	4.35
W1	50.00	03	50.00	4.01	0.04	0.08	0.56	2.23	0.02	0.08	2.01
W1	100.00	01	100.00	7.07	0.01	0.07	1.96	7.86	0.02	0.07	7.07
W1	100.00	02	100.00	5.73	0.03	0.06	0.53	2.12	0.02	0.06	1.91
W1	100.00	03	100.00	5.03	0.04	0.05	0.35	1.40	0.01	0.05	1.26
S1	1.00	01	1.00	4.59	0.02	4.59	63.75	255.00	1.28	4.59	229.50
S1	1.00	02	1.00	3.07	0.04	3.07	21.32	85.28	0.85	3.07	76.75

S1	1.00	03	1.00	2.37	0.03	2.37	21.94	87.78	0.66	2.37	79.00
S1	5.00	01	5.00	7.54	0.02	1.51	20.94	83.78	0.42	1.51	75.40
S1	5.00	02	5.00	7.35	0.04	1.47	10.21	40.83	0.41	1.47	36.75
S1	5.00	03	5.00	4.69	0.03	0.94	8.69	34.74	0.26	0.94	31.27
S1	10.00	01	10.00	7.94	0.02	0.79	11.03	44.11	0.22	0.79	39.70
S1	10.00	02	10.00	8.31	0.04	0.83	5.77	23.08	0.23	0.83	20.78
S1	10.00	03	10.00	5.89	0.03	0.59	5.45	21.82	0.16	0.59	19.63
S1	20.00	01	20.00	7.11	0.02	0.36	4.94	19.75	0.10	0.36	17.78
S1	20.00	02	20.00	7.96	0.04	0.40	2.76	11.06	0.11	0.40	9.95
S1	20.00	03	20.00	6.13	0.03	0.31	2.84	11.35	0.09	0.31	10.22
S1	50.00	01	50.00	6.12	0.02	0.12	1.70	6.80	0.03	0.12	6.12
S1	50.00	02	50.00	7.24	0.04	0.14	1.01	4.02	0.04	0.14	3.62
S1	50.00	03	50.00	6.10	0.03	0.12	1.13	4.52	0.03	0.12	4.07
S1	100.00	01	100.00	5.61	0.02	0.06	0.78	3.12	0.02	0.06	2.80
S1	100.00	02	100.00	6.70	0.04	0.07	0.47	1.86	0.02	0.07	1.67
S1	100.00	03	100.00	6.32	0.03	0.06	0.58	2.34	0.02	0.06	2.11
W2	1.00	01	1.00	0.55	0.02	0.55	7.64	30.56	0.15	0.55	27.50
W2	1.00	02	1.00	0.41	0.03	0.41	3.80	15.18	0.11	0.41	13.67
W2	1.00	03	1.00	0.46	0.02	0.46	6.39	25.56	0.13	0.46	23.00
W2	5.00	01	5.00	1.17	0.02	0.23	3.25	13.00	0.07	0.23	11.70
W2	5.00	02	5.00	0.94	0.03	0.19	1.74	6.96	0.05	0.19	6.27
W2	5.00	03	5.00	0.61	0.02	0.12	1.69	6.78	0.03	0.12	6.10
W2	10.00	01	10.00	1.86	0.02	0.19	2.58	10.33	0.05	0.19	9.30

W2	10.00	02	10.00	1.46	0.03	0.15	1.35	5.41	0.04	0.15	4.87
W2	10.00	03	10.00	1.10	0.02	0.11	1.53	6.11	0.03	0.11	5.50
W2	20.00	01	20.00	2.14	0.02	0.11	1.49	5.94	0.03	0.11	5.35
W2	20.00	02	20.00	2.07	0.03	0.10	0.96	3.83	0.03	0.10	3.45
W2	20.00	03	20.00	1.59	0.02	0.08	1.10	4.42	0.02	0.08	3.97
W2	50.00	01	50.00	1.98	0.02	0.04	0.55	2.20	0.01	0.04	1.98
W2	50.00	02	50.00	2.93	0.03	0.06	0.54	2.17	0.02	0.06	1.95
W2	50.00	03	50.00	2.45	0.02	0.05	0.68	2.72	0.01	0.05	2.45
W2	100.00	01	100.00	1.72	0.02	0.02	0.24	0.96	0.00	0.02	0.86
W2	100.00	02	100.00	3.51	0.03	0.04	0.33	1.30	0.01	0.04	1.17
W2	100.00	03	100.00	3.39	0.02	0.03	0.47	1.88	0.01	0.03	1.70
S2	1.00	01	1.00	1.10	0.02	1.10	15.28	61.11	0.31	1.10	55.00
S2	1.00	02	1.00	3.16	0.03	3.16	29.26	117.04	0.88	3.16	105.33
S2	1.00	03	1.00	3.54	0.03	3.54	32.78	131.11	0.98	3.54	118.00
S2	5.00	01	5.00	3.10	0.02	0.62	8.61	34.44	0.17	0.62	31.00
S2	5.00	02	5.00	4.56	0.03	0.91	8.44	33.78	0.25	0.91	30.40
S2	5.00	03	5.00	4.08	0.03	0.82	7.56	30.22	0.23	0.82	27.20
S2	10.00	01	10.00	4.37	0.02	0.44	6.07	24.28	0.12	0.44	21.85
S2	10.00	02	10.00	4.99	0.03	0.50	4.62	18.48	0.14	0.50	16.63
S2	10.00	03	10.00	4.72	0.03	0.47	4.37	17.48	0.13	0.47	15.73
S2	20.00	01	20.00	4.95	0.02	0.25	3.44	13.75	0.07	0.25	12.38
S2	20.00	02	20.00	4.82	0.03	0.24	2.23	8.92	0.07	0.24	8.03
S2	20.00	03	20.00	4.88	0.03	0.24	2.26	9.04	0.07	0.24	8.13

S2	50.00	01	50.00	5.44	0.02	0.11	1.51	6.04	0.03	0.11	5.44
S2	50.00	02	50.00	4.78	0.03	0.10	0.89	3.54	0.03	0.10	3.19
S2	50.00	03	50.00	5.08	0.03	0.10	0.94	3.76	0.03	0.10	3.39
S2	100.00	01	100.00	6.46	0.02	0.07	0.90	3.59	0.02	0.06	3.23
S2	100.00	02	100.00	4.90	0.03	0.05	0.45	1.82	0.01	0.05	1.63
S2	100.00	03	100.00	5.06	0.03	0.05	0.47	1.88	0.01	0.05	1.69
W3	1.00	01	1.00	20.58	0.20	20.58	28.58	114.33	5.72	20.58	102.90
W3	1.00	02	1.00	4.75	0.11	4.75	11.99	47.98	1.32	4.75	43.18
W3	1.00	03	1.00	0.28	0.14	0.28	0.56	2.22	0.08	0.28	2.00
W3	5.00	01	5.00	8.61	0.20	1.72	2.39	9.57	0.48	1.72	8.61
W3	5.00	02	5.00	3.77	0.11	0.75	1.90	7.62	0.21	0.75	6.85
W3	5.00	03	5.00	0.91	0.14	0.18	0.36	1.44	0.05	0.18	1.30
W3	10.00	01	10.00	15.25	0.20	1.52	2.12	8.47	0.42	1.52	7.62
W3	10.00	02	10.00	5.89	0.11	0.59	1.49	5.95	0.16	0.59	5.35
W3	10.00	03	10.00	1.55	0.14	0.15	0.31	1.23	0.04	0.16	1.11
W3	20.00	01	20.00	14.41	0.20	0.72	1.00	4.00	0.20	0.72	3.60
W3	20.00	02	20.00	7.32	0.11	0.37	0.92	3.70	0.10	0.37	3.33
W3	20.00	03	20.00	2.43	0.14	0.12	0.24	0.96	0.03	0.12	0.87
W3	50.00	01	50.00	12.25	0.20	0.24	0.34	1.36	0.07	0.24	1.22
W3	50.00	02	50.00	8.67	0.11	0.17	0.44	1.75	0.05	0.17	1.58
W3	50.00	03	50.00	3.81	0.14	0.08	0.15	0.60	0.02	0.08	0.54
W3	100.00	01	100.00	10.88	0.20	0.11	0.15	0.60	0.03	0.11	0.54
W3	100.00	02	100.00	9.39	0.11	0.09	0.24	0.95	0.03	0.09	0.85

W3	100.00	03	100.00	5.33	0.14	0.05	0.11	0.42	0.01	0.05	0.38
S3	1.00	02	1.00	6.11	0.18	6.11	9.43	37.72	1.70	6.11	33.94
S3	1.00	03	1.00	1.79	0.15	1.79	3.31	13.26	0.50	1.79	11.93
S3	5.00	01	5.00	5.98	0.26	1.20	1.28	5.11	0.33	1.20	4.60
S3	5.00	02	5.00	4.51	0.18	0.90	1.39	5.57	0.25	0.90	5.01
S3	5.00	03	5.00	3.66	0.15	0.73	1.36	5.42	0.20	0.73	4.88
S3	10.00	01	10.00	12.14	0.26	1.21	1.30	5.19	0.34	1.21	4.67
S3	10.00	02	10.00	6.66	0.18	0.67	1.03	4.11	0.19	0.67	3.70
S3	10.00	03	10.00	5.64	0.15	0.56	1.04	4.18	0.16	0.56	3.76
S3	20.00	01	20.00	12.18	0.26	0.61	0.65	2.60	0.17	0.61	2.34
S3	20.00	02	20.00	7.46	0.18	0.37	0.58	2.30	0.10	0.37	2.07
S3	20.00	03	20.00	7.25	0.15	0.36	0.67	2.68	0.10	0.36	2.42
S3	50.00	01	50.00	11.78	0.26	0.24	0.25	1.01	0.07	0.24	0.91
S3	50.00	02	50.00	7.60	0.18	0.15	0.23	0.94	0.04	0.15	0.85
S3	50.00	03	50.00	8.97	0.15	0.18	0.33	1.33	0.05	0.18	1.20
S3	100.00	01	100.00	11.03	0.26	0.11	0.12	0.47	0.03	0.11	0.42
S3	100.00	02	100.00	7.56	0.18	0.08	0.12	0.47	0.02	0.08	0.42
S3	100.00	03	100.00	9.67	0.15	0.10	0.18	0.72	0.03	0.10	0.64
W4	1.00	01	1.00	4.81	0.05	4.81	26.72	106.89	1.34	4.81	96.20
W4	1.00	02	1.00	5.21	0.05	5.21	28.94	115.78	1.45	5.21	104.20
W4	1.00	03	1.00	4.25	0.04	4.25	29.51	118.06	1.18	4.25	106.25
W4	5.00	01	5.00	12.34	0.05	2.47	13.71	54.84	0.69	2.47	49.36
W4	5.00	02	5.00	11.06	0.05	2.21	12.29	49.16	0.61	2.21	44.24

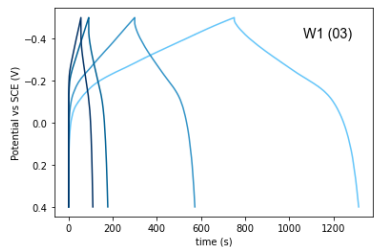
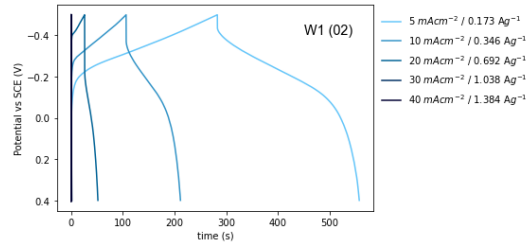
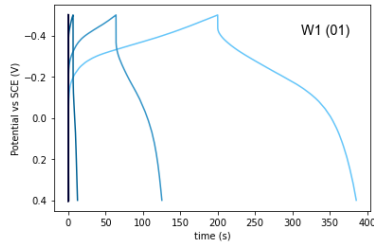
W4	5.00	03	5.00	10.92	0.04	2.18	15.17	60.67	0.61	2.18	54.60
W4	10.00	01	10.00	15.54	0.05	1.55	8.63	34.53	0.43	1.55	31.08
W4	10.00	02	10.00	12.90	0.05	1.29	7.17	28.67	0.36	1.29	25.80
W4	10.00	03	10.00	13.51	0.04	1.35	9.38	37.53	0.38	1.35	33.78
W4	20.00	01	20.00	16.31	0.05	0.81	4.53	18.12	0.23	0.82	16.31
W4	20.00	02	20.00	13.92	0.05	0.70	3.87	15.47	0.19	0.70	13.92
W4	20.00	03	20.00	14.81	0.04	0.74	5.14	20.57	0.21	0.74	18.51
W4	50.00	01	50.00	14.43	0.05	0.29	1.60	6.41	0.08	0.29	5.77
W4	50.00	02	50.00	14.08	0.05	0.28	1.56	6.26	0.08	0.28	5.63
W4	50.00	03	50.00	14.97	0.04	0.30	2.08	8.32	0.08	0.30	7.48
W4	100.00	01	100.00	12.17	0.05	0.12	0.68	2.70	0.03	0.12	2.43
W4	100.00	02	100.00	13.07	0.05	0.13	0.73	2.90	0.04	0.13	2.61
W4	100.00	03	100.00	13.99	0.04	0.14	0.97	3.89	0.04	0.14	3.50
S4	1.00	01	1.00	5.08	0.03	5.08	47.04	188.15	1.41	5.08	169.33
S4	1.00	02	1.00	5.01	0.03	5.01	46.39	185.56	1.39	5.01	167.00
S4	1.00	03	1.00	4.38	0.06	4.38	20.28	81.11	1.22	4.38	73.00
S4	5.00	01	5.00	11.89	0.03	2.38	22.02	88.08	0.66	2.38	79.27
S4	5.00	02	5.00	13.76	0.03	2.75	25.48	101.92	0.76	2.75	91.73
S4	5.00	03	5.00	10.95	0.06	2.19	10.14	40.56	0.61	2.19	36.50
S4	10.00	01	10.00	14.10	0.03	1.41	13.06	52.22	0.39	1.41	47.00
S4	10.00	02	10.00	18.53	0.03	1.85	17.16	68.63	0.51	1.85	61.77
S4	10.00	03	10.00	13.99	0.06	1.40	6.48	25.91	0.39	1.40	23.32
S4	20.00	01	20.00	13.99	0.03	0.70	6.48	25.91	0.19	0.70	23.32

S4	20.00	02	20.00	20.90	0.03	1.04	9.68	38.70	0.29	1.05	34.83
S4	20.00	03	20.00	15.68	0.06	0.78	3.63	14.52	0.22	0.78	13.07
S4	50.00	01	50.00	11.63	0.03	0.23	2.15	8.62	0.06	0.23	7.75
S4	50.00	02	50.00	19.73	0.03	0.40	3.65	14.62	0.11	0.39	13.15
S4	50.00	03	50.00	15.51	0.06	0.31	1.44	5.74	0.09	0.31	5.17
S4	100.00	01	100.00	9.52	0.03	0.10	0.88	3.52	0.03	0.10	3.17
S4	100.00	02	100.00	16.70	0.03	0.17	1.55	6.18	0.05	0.17	5.57
S4	100.00	03	100.00	14.46	0.06	0.14	0.67	2.68	0.04	0.14	2.41

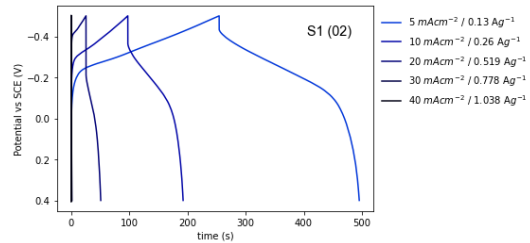
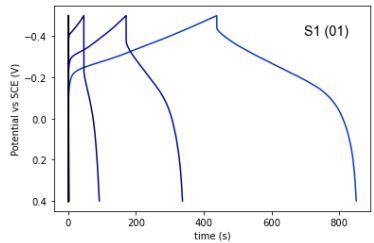
Appendix G GCD Data and Analysis Chapter 4

G.1 GCD data of each sample

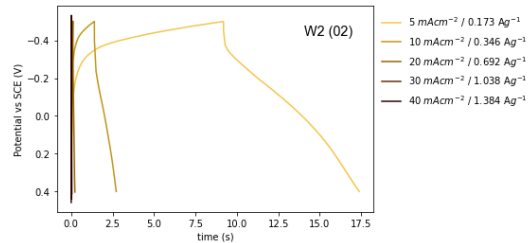
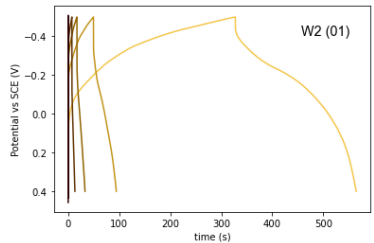
G.1.1 W1

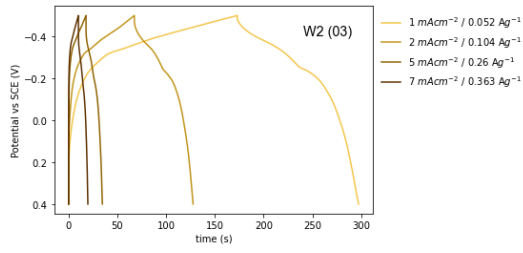


G.1.2 S1

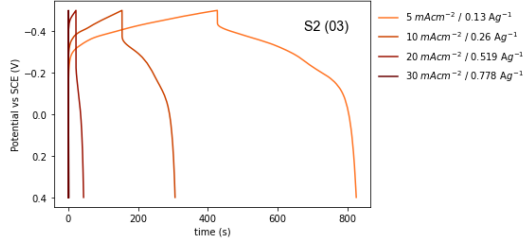
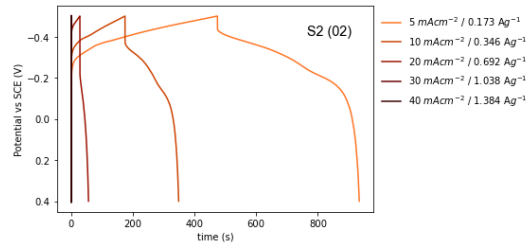
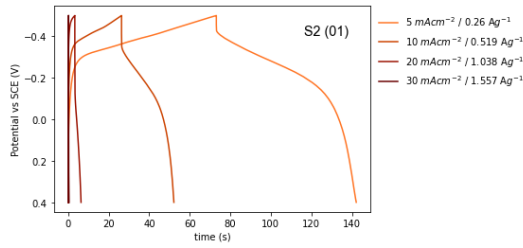


G.1.3 W2

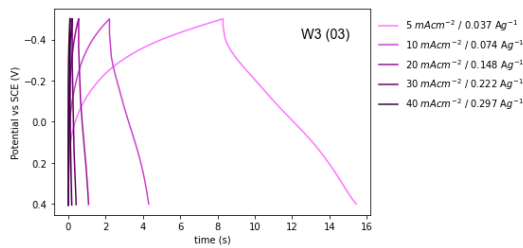
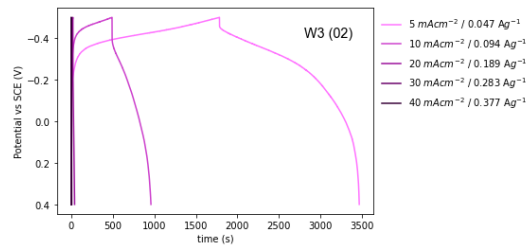
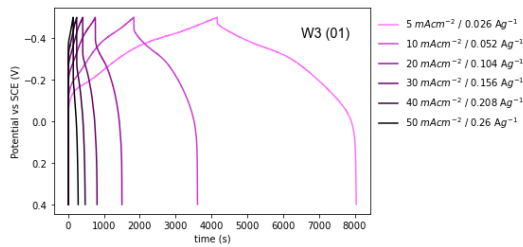




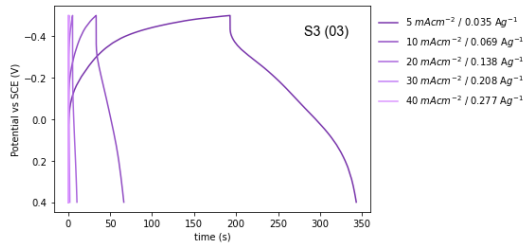
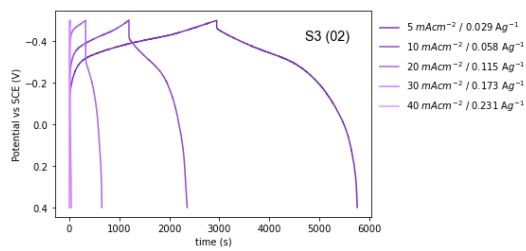
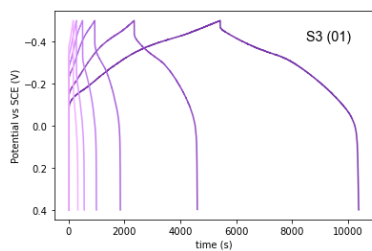
G.1.4 S2



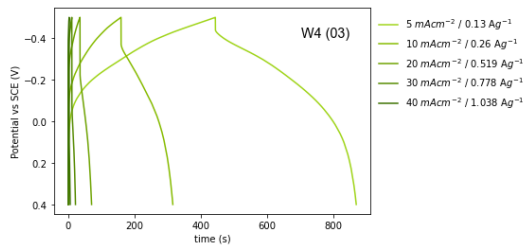
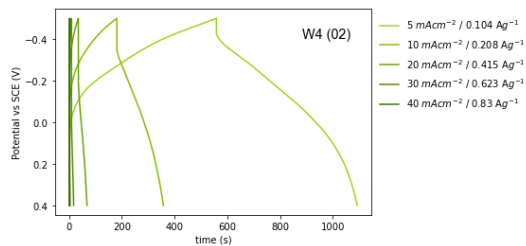
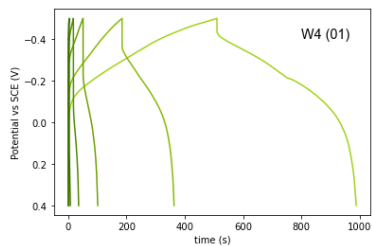
G.1.5 W3



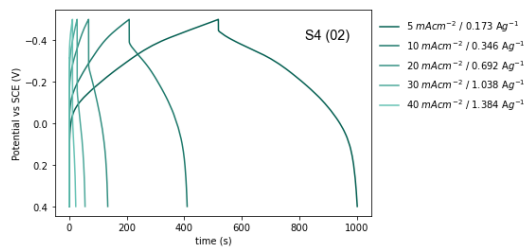
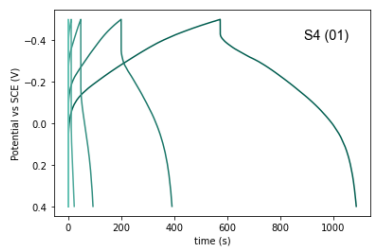
G.1.6 S3

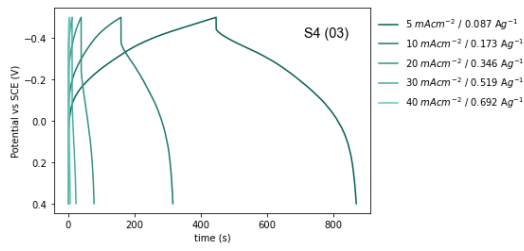


G.1.7 W4



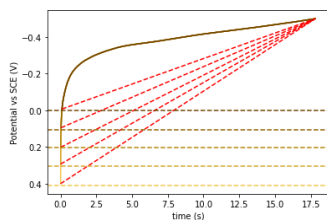
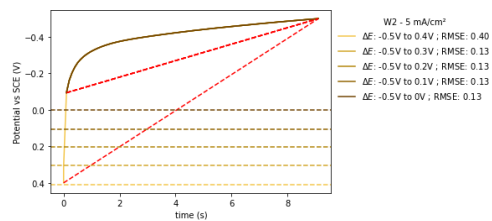
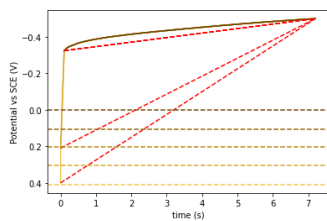
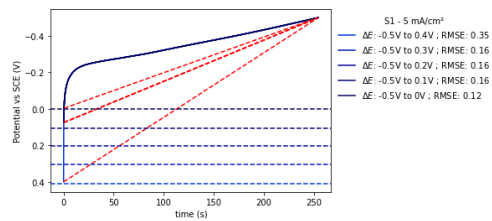
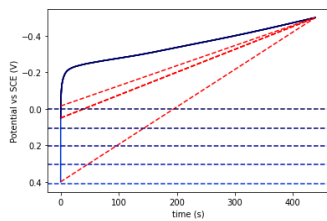
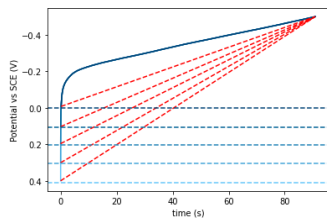
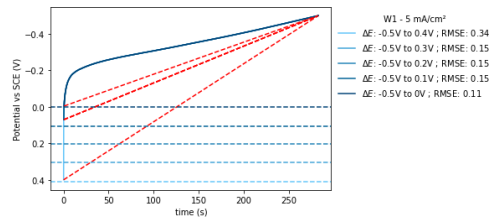
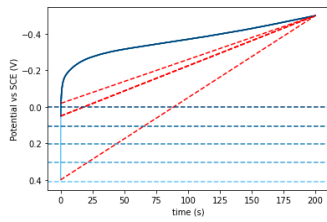
G.1.8 S4

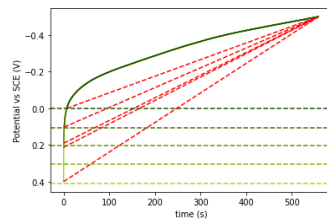
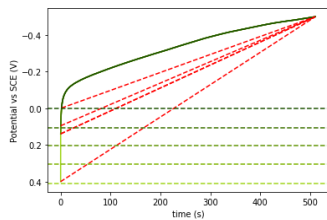
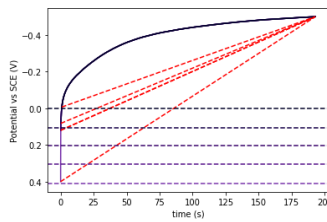
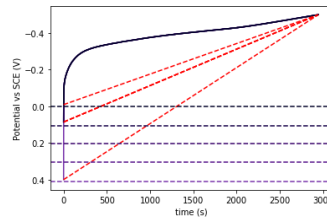
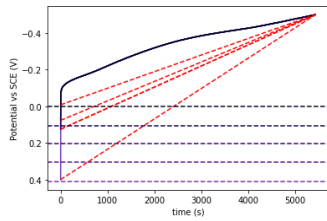
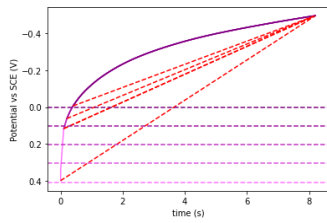
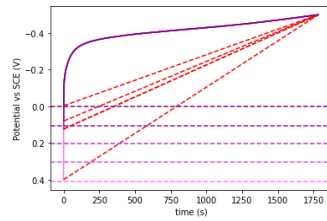
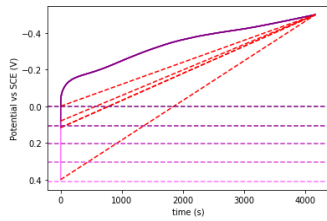
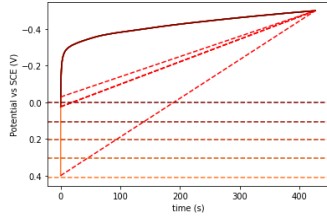
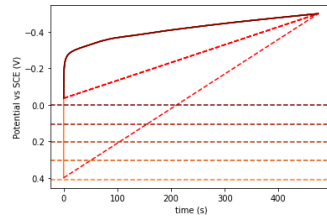
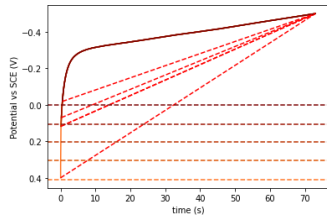


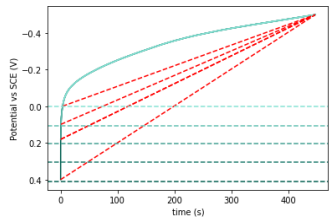
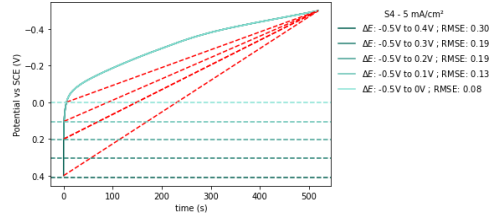
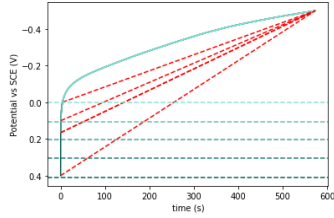
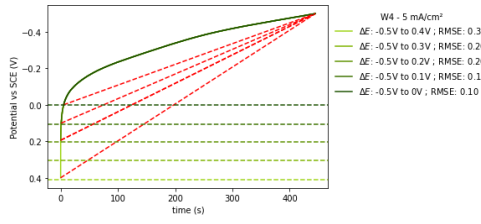


G.2 GCD fitting to pure capacitive lines

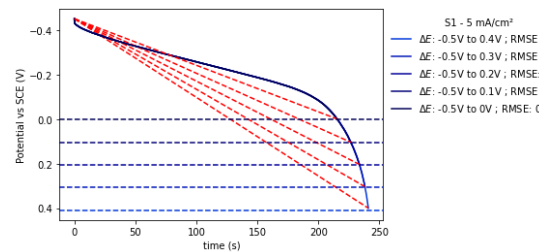
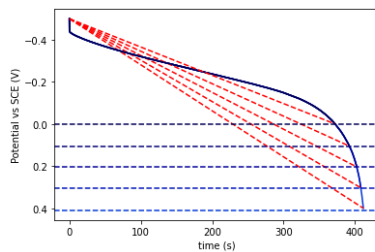
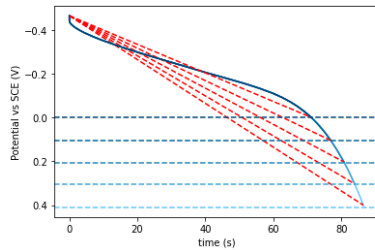
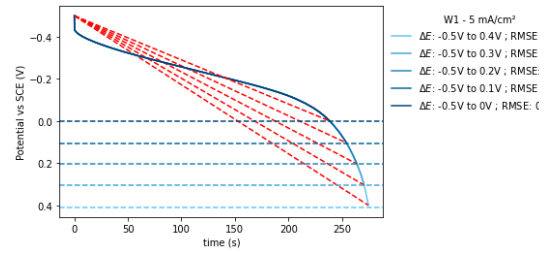
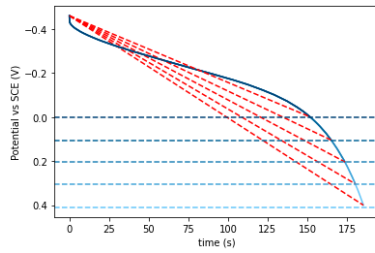
G.2.1 5 mA/cm² Charging Curve fitted to ideal capacitive line

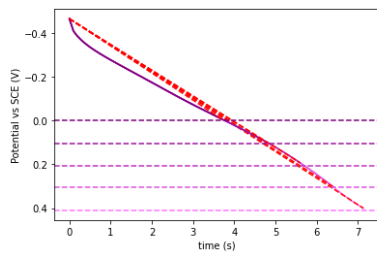
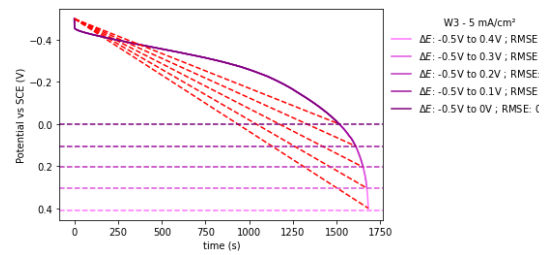
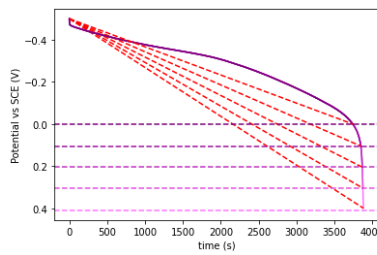
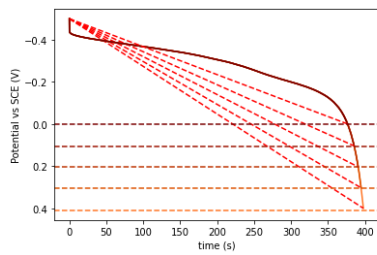
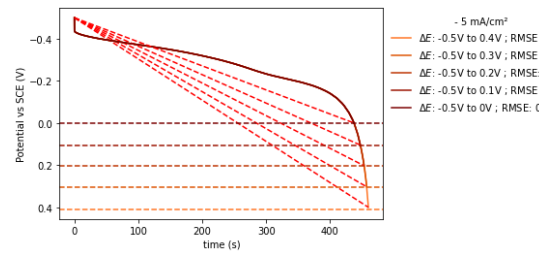
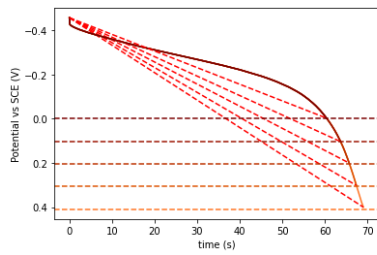
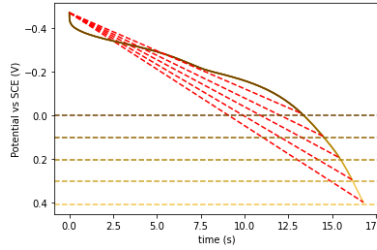
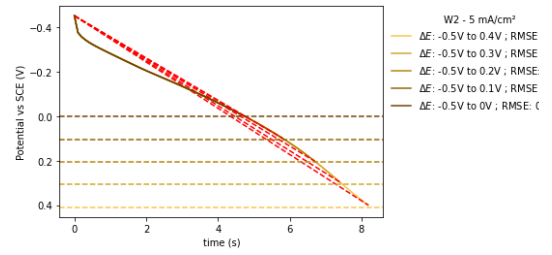
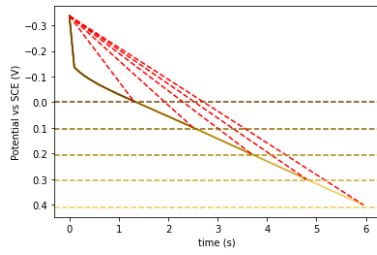




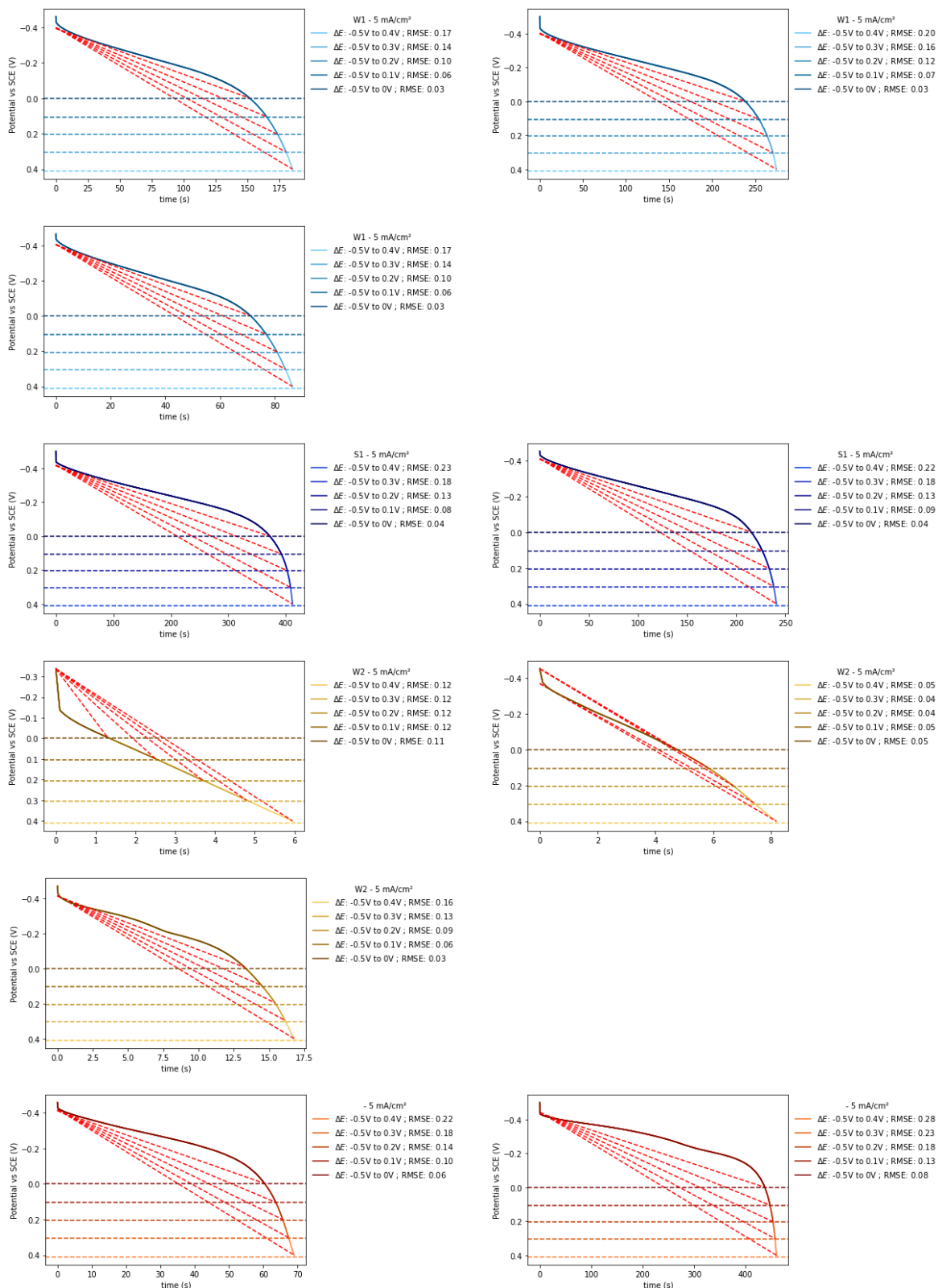


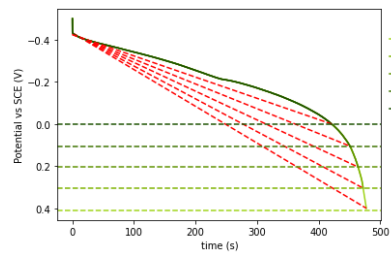
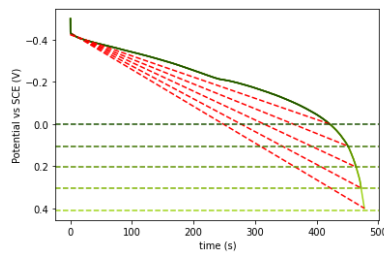
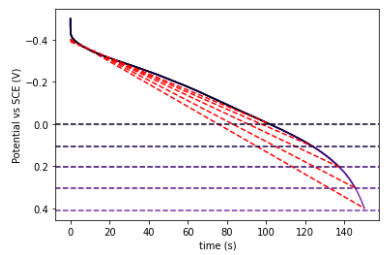
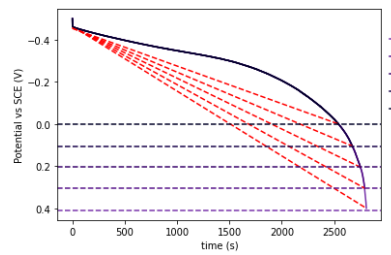
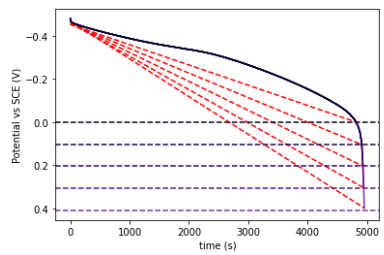
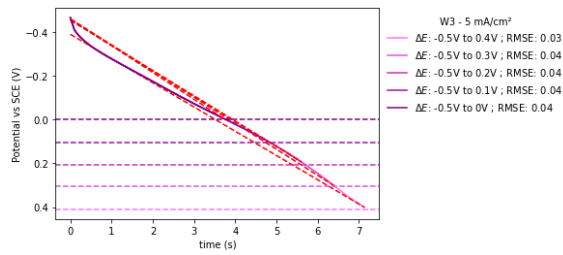
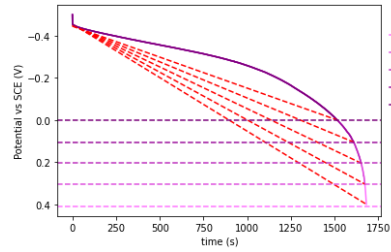
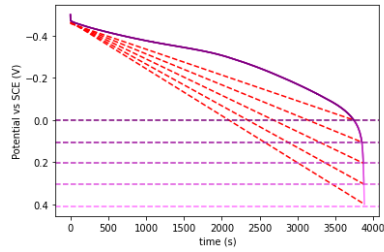
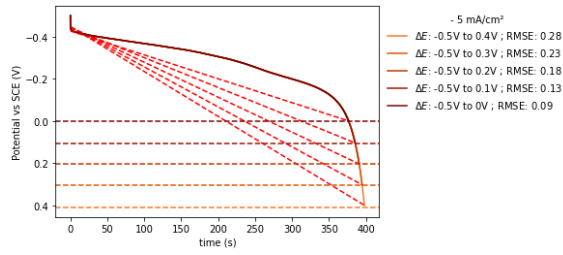
G.2.2 5 mAcm² Discharging Curve fitted to ideal capacitive line

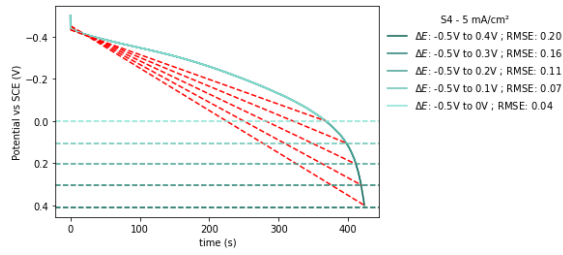
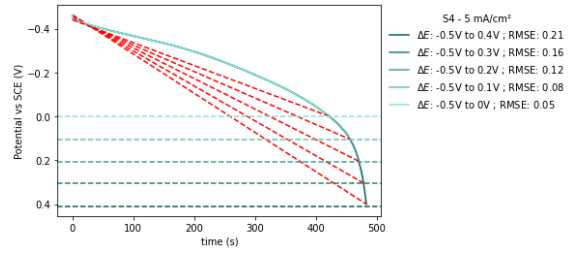
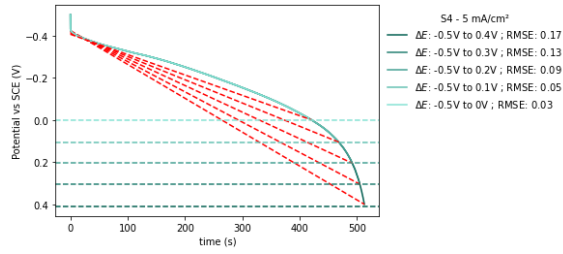
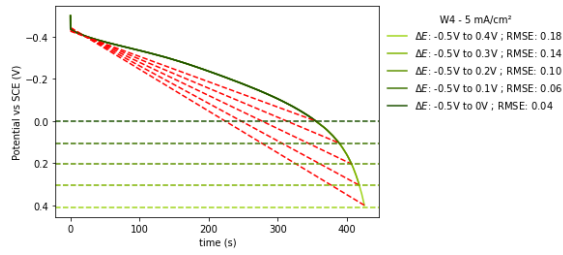




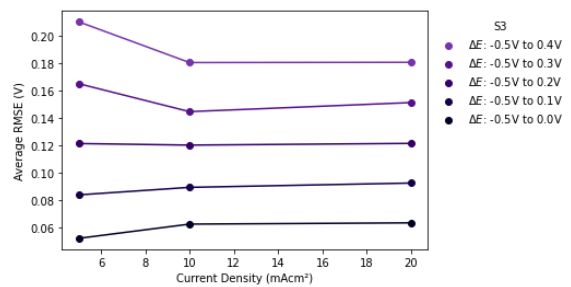
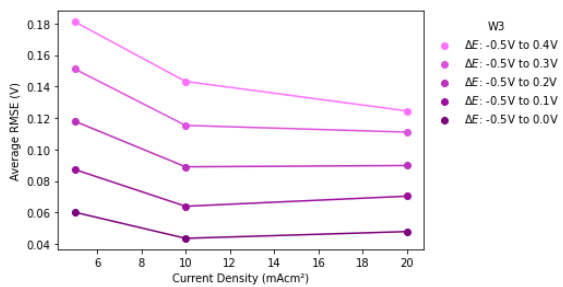
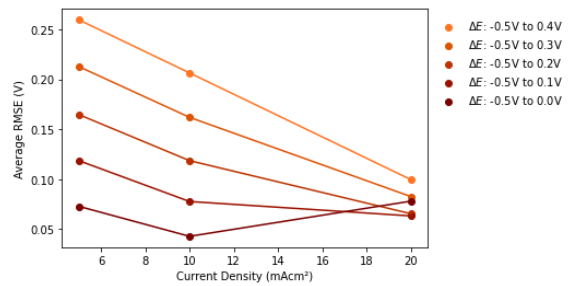
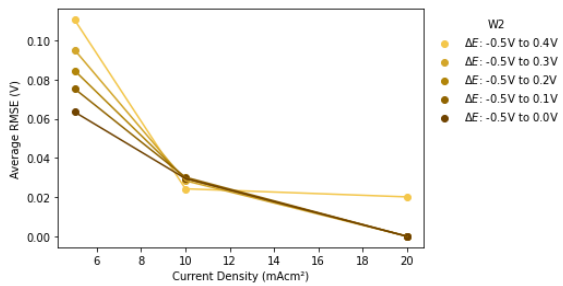
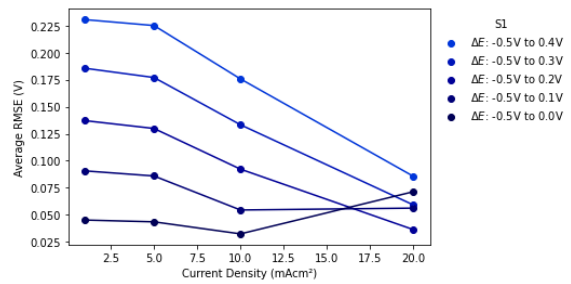
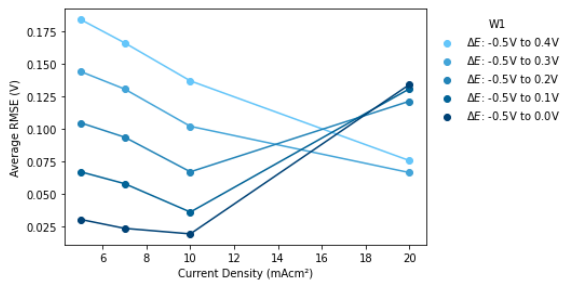
G.2.3 5 mA/cm² Discharge Curve Fitted to Ideal Capacitive Case from point of Ohmic Drop

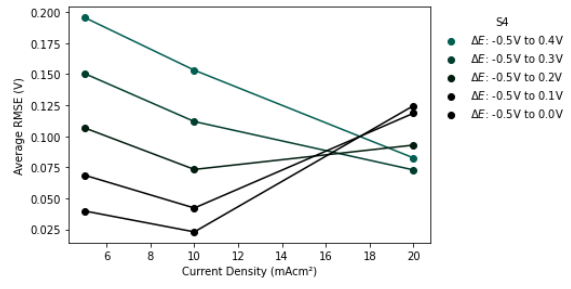
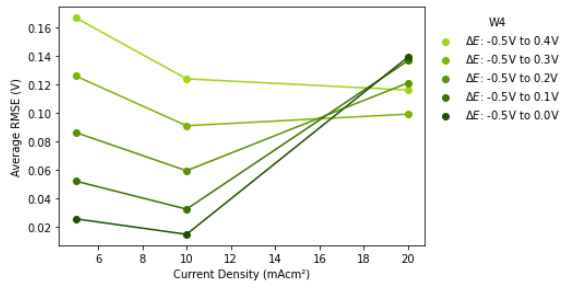






G.2.4 RMSE compared from point of Ohmic Drop





G.3 Summary Table of Capacities and Capacitances found from GCD data

Sample	Run	j Area mA/cm ²	j mass A/g	Capacity Charge mAh/cm ²	Capacity Discharge mAh/cm ²	Capacity Charge mAh/g	Capacity Discharge mAh/g	Discharge time/s	Charge time/s	mass/g	Discharge Capacitance (F/g)
W1	01	5	0.52	0.29	0.27	28.83	26.72	185.35	199.99	0.01	106.88
W1	02	5	0.17	0.41	0.4	13.6	13.2	274.73	282.97	0.03	52.81
W1	03	5	0.26	0.13	0.12	6.55	6.24	86.5	90.93	0.02	24.94
W1	03	7	0.36	0.11	0.11	5.62	5.46	54.12	55.72	0.02	21.85
W1	01	10	1.04	0.18	0.18	18.44	17.69	61.36	63.97	0.01	70.77
W1	02	10	0.35	0.31	0.3	10.22	10.11	105.24	106.35	0.03	40.46
W1	01	20	2.08	0.04	0.03	3.78	3.44	5.96	6.55	0.01	13.75
W1	02	20	0.69	0.15	0.15	5.0	4.95	25.77	26.0	0.03	19.81
W1	01	30	3.11	0.0	0.0	0.31	0.38	0.44	0.35	0.01	1.52
W1	02	30	1.04	0.01	0.01	0.17	0.18	0.62	0.61	0.03	0.72
W1	01	40	4.15	0.0	0.0	0.05	0.05	0.05	0.05	0.01	0.21
W1	02	40	1.38	0.0	0.0	0.02	0.02	0.05	0.05	0.03	0.07
S1	03	1	0.05	0.77	0.59	38.27	29.64	2056.12	2654.59	0.02	118.57
S1	01	5	0.26	0.63	0.59	31.61	29.68	411.75	438.48	0.02	118.72
S1	02	5	0.13	0.37	0.35	9.17	8.68	240.93	254.46	0.04	34.73
S1	01	10	0.52	0.49	0.48	24.64	23.99	166.39	170.91	0.02	95.95

S1	02	10	0.26	0.28	0.27	7.02	6.85	95.1	97.39	0.04	27.42
S1	03	10	0.52	0.32	0.31	15.86	15.45	107.19	110.02	0.02	61.81
S1	01	20	1.04	0.27	0.26	13.32	13.16	45.64	46.19	0.02	52.64
S1	02	20	0.52	0.15	0.15	3.67	3.66	25.37	25.49	0.04	14.63
S1	03	20	1.04	0.07	0.06	3.43	2.91	10.1	11.88	0.02	11.65
S1	01	30	1.56	0.01	0.01	0.6	0.58	1.35	1.39	0.02	2.33
S1	02	30	0.78	0.01	0.01	0.13	0.15	0.71	0.61	0.04	0.62
S1	03	30	1.56	0.0	0.0	0.04	0.08	0.18	0.08	0.02	0.31
S1	01	40	2.08	0.0	0.0	0.03	0.03	0.05	0.04	0.02	0.12
S1	02	40	1.04	0.0	0.0	0.01	0.01	0.03	0.03	0.04	0.03
W2	01	1	0.05	0.09	0.07	4.72	3.42	236.9	327.56	0.02	13.66
W2	03	1	0.05	0.05	0.04	2.49	1.79	124.48	173.06	0.02	7.18
W2	01	2	0.14	0.04	0.03	1.9	1.72	44.81	49.54	0.02	6.87
W2	03	2	0.1	0.04	0.03	1.94	1.74	60.31	67.39	0.02	6.96
W2	01	4	0.21	0.02	0.02	0.99	0.91	15.81	17.19	0.02	3.65
W2	01	5	0.26	0.01	0.01	0.53	0.43	5.95	7.28	0.02	1.72
W2	02	5	0.17	0.01	0.01	0.44	0.39	8.19	9.19	0.03	1.57
W2	03	5	0.26	0.03	0.02	1.29	1.21	16.78	17.83	0.02	4.84
W2	03	7	0.36	0.02	0.02	1.02	0.98	9.69	10.07	0.02	3.91
W2	01	10	0.52	0.0	0.0	0.0	0.0	0.01	0.01	0.02	0.0
W2	02	10	0.35	0.0	0.0	0.13	0.13	1.32	1.4	0.03	0.51

W2	02	20	0.69	0.0	0.0	0.02	0.02	0.12	0.1	0.03	0.09
W2	02	30	1.04	0.0	0.0	0.01	0.01	0.02	0.02	0.03	0.03
W2	02	40	1.38	0.0	0.0	0.0	0.0	0.01	0.01	0.03	0.01
S2	01	5	0.26	0.11	0.1	5.27	4.98	69.04	73.1	0.02	19.91
S2	02	5	0.17	0.68	0.66	22.79	22.1	459.86	474.27	0.03	88.4
S2	03	5	0.13	0.62	0.57	15.39	14.34	397.8	427.08	0.04	57.35
S2	01	10	0.52	0.08	0.07	3.8	3.72	25.83	26.33	0.02	14.89
S2	02	10	0.35	0.5	0.5	16.77	16.74	174.13	174.5	0.03	66.94
S2	03	10	0.26	0.44	0.44	11.11	10.95	151.91	154.17	0.04	43.8
S2	01	20	1.04	0.02	0.02	0.95	0.88	3.05	3.29	0.02	3.52
S2	02	20	0.69	0.16	0.16	5.43	5.39	28.02	28.25	0.03	21.55
S2	03	20	0.52	0.13	0.13	3.21	3.15	21.85	22.26	0.04	12.6
S2	01	30	1.56	0.0	0.0	0.08	0.11	0.25	0.19	0.02	0.43
S2	02	30	1.04	0.0	0.01	0.16	0.24	0.84	0.57	0.03	0.96
S2	03	30	0.78	0.01	0.01	0.19	0.26	1.2	0.89	0.04	1.04
S2	02	40	1.38	0.0	0.0	0.01	0.02	0.04	0.03	0.03	0.06
W3	01	5	0.03	6.0	5.6	29.98	27.99	3882.4	4158.81	0.2	111.94
W3	02	5	0.05	2.57	2.42	23.37	22.03	1681.13	1783.33	0.11	88.13
W3	03	5	0.04	0.01	0.01	0.09	0.07	7.14	8.29	0.14	0.29
W3	01	10	0.05	5.28	5.13	26.39	25.65	1779.2	1830.83	0.2	102.6
W3	02	10	0.09	1.42	1.35	12.88	12.27	467.94	491.52	0.11	49.06

W3	03	10	0.07	0.01	0.01	0.05	0.04	2.1	2.21	0.14	0.17
W3	01	20	0.1	4.37	4.29	21.84	21.44	743.66	757.52	0.2	85.77
W3	02	20	0.19	0.12	0.12	1.07	1.09	20.88	20.46	0.11	4.38
W3	03	20	0.15	0.0	0.0	0.02	0.02	0.53	0.56	0.14	0.09
W3	01	30	0.16	3.5	3.47	17.51	17.37	401.61	404.91	0.2	69.48
W3	02	30	0.28	0.03	0.03	0.25	0.3	3.86	3.23	0.11	1.22
W3	03	30	0.22	0.0	0.0	0.01	0.01	0.21	0.22	0.14	0.05
W3	01	40	0.21	2.74	2.73	13.7	13.63	236.34	237.61	0.2	54.52
W3	02	40	0.38	0.01	0.01	0.07	0.09	0.84	0.69	0.11	0.35
W3	03	40	0.3	0.0	0.0	0.01	0.01	0.08	0.11	0.14	0.03
W3	01	50	0.26	2.02	2.02	10.11	10.08	139.79	140.19	0.2	40.31
S3	01	5	0.02	7.82	7.15	30.08	27.48	4956.1	5425.25	0.26	109.92
S3	02	5	0.03	4.25	4.05	23.6	22.49	2808.62	2946.74	0.18	89.98
S3	03	5	0.03	0.28	0.22	1.85	1.45	150.36	192.85	0.15	5.78
S3	01	10	0.04	6.77	6.51	26.03	25.03	2257.4	2346.93	0.26	100.14
S3	02	10	0.06	3.44	3.36	19.12	18.66	1164.64	1193.46	0.18	74.62
S3	03	10	0.07	0.1	0.09	0.64	0.63	32.94	33.34	0.15	2.53
S3	01	20	0.08	5.39	5.28	20.73	20.32	916.25	934.76	0.26	81.29
S3	02	20	0.12	1.9	1.87	10.54	10.38	324.07	328.99	0.18	41.53
S3	03	20	0.14	0.03	0.03	0.2	0.2	5.23	5.26	0.15	0.8
S3	01	30	0.12	4.32	4.28	16.62	16.46	494.65	499.47	0.26	65.83

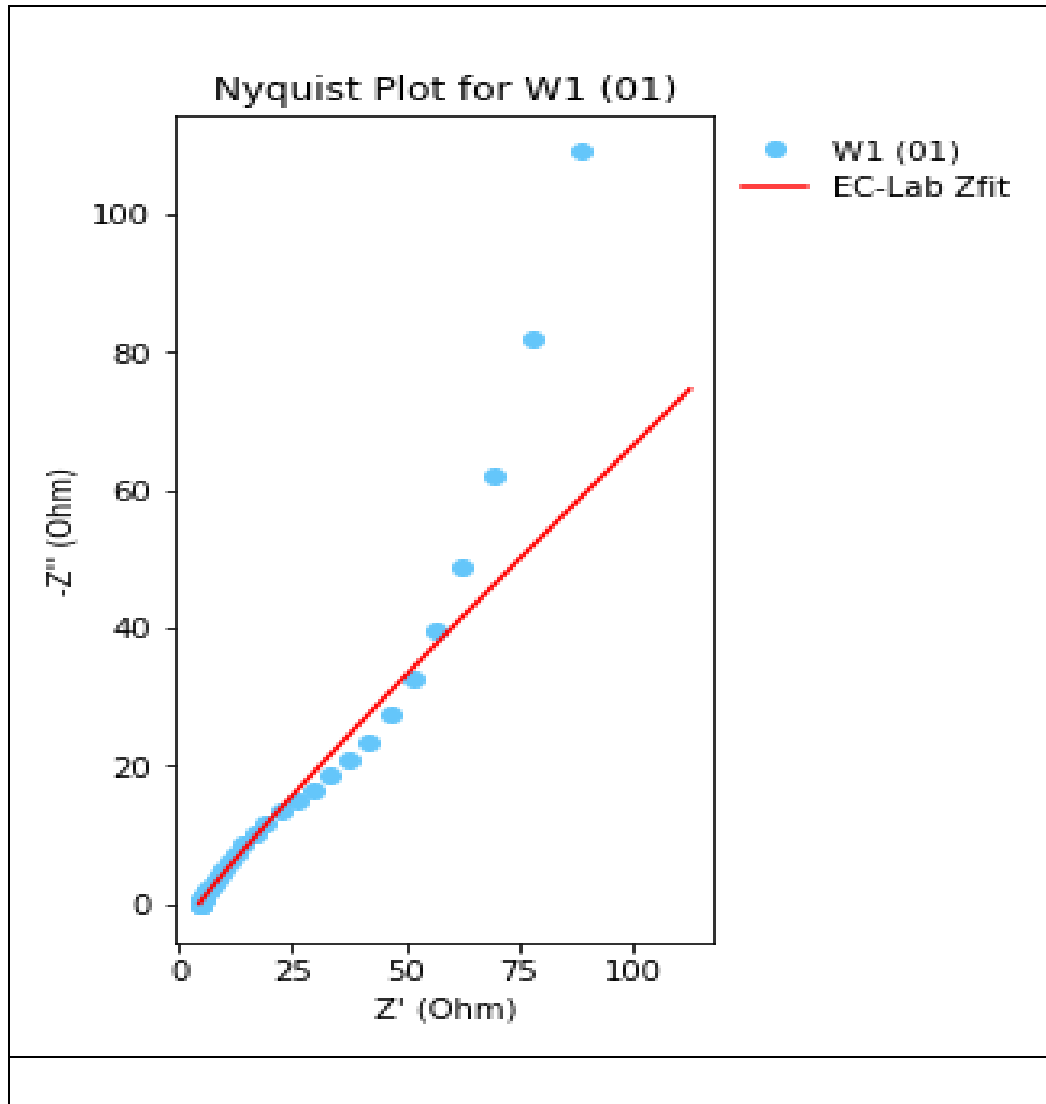
S3	02	30	0.17	0.17	0.21	0.96	1.14	23.82	20.07	0.18	4.58
S3	03	30	0.21	0.01	0.01	0.06	0.06	1.01	1.01	0.15	0.23
S3	01	40	0.16	3.22	3.21	12.37	12.34	278.27	278.91	0.26	49.37
S3	02	40	0.23	0.02	0.03	0.12	0.15	2.36	1.83	0.18	0.61
S3	03	40	0.28	0.0	0.0	0.02	0.02	0.2	0.2	0.15	0.06
S3	01	50	0.2	3.91	0.86	15.05	3.31	59.65	271.38	0.26	13.23
W4	01	5	0.1	0.74	0.69	14.71	13.77	477.64	510.13	0.05	55.09
W4	02	5	0.1	0.8	0.77	16.1	15.41	534.56	558.26	0.05	61.65
W4	03	5	0.13	0.64	0.61	16.03	15.34	425.71	444.66	0.04	61.37
W4	01	10	0.21	0.53	0.51	10.66	10.28	178.3	184.82	0.05	41.13
W4	02	10	0.21	0.52	0.51	10.42	10.21	177.08	180.75	0.05	40.85
W4	03	10	0.26	0.46	0.45	11.51	11.29	156.56	159.66	0.04	45.14
W4	01	20	0.42	0.29	0.29	5.89	5.81	50.35	51.04	0.05	23.23
W4	02	20	0.42	0.2	0.19	4.01	3.79	32.86	34.77	0.05	15.16
W4	03	20	0.52	0.21	0.2	5.14	5.06	35.12	35.65	0.04	20.25
W4	01	30	0.62	0.18	0.13	3.6	2.6	15.01	20.79	0.05	10.38
W4	02	30	0.62	0.08	0.07	1.53	1.4	8.11	8.82	0.05	5.61
W4	03	30	0.78	0.11	0.08	2.81	1.94	8.99	12.98	0.04	7.77
W4	01	40	0.83	0.04	0.04	0.83	0.88	3.83	3.6	0.05	3.54
W4	02	40	0.83	0.02	0.02	0.38	0.42	1.8	1.64	0.05	1.66
W4	03	40	1.04	0.03	0.04	0.86	0.92	3.18	2.97	0.04	3.66

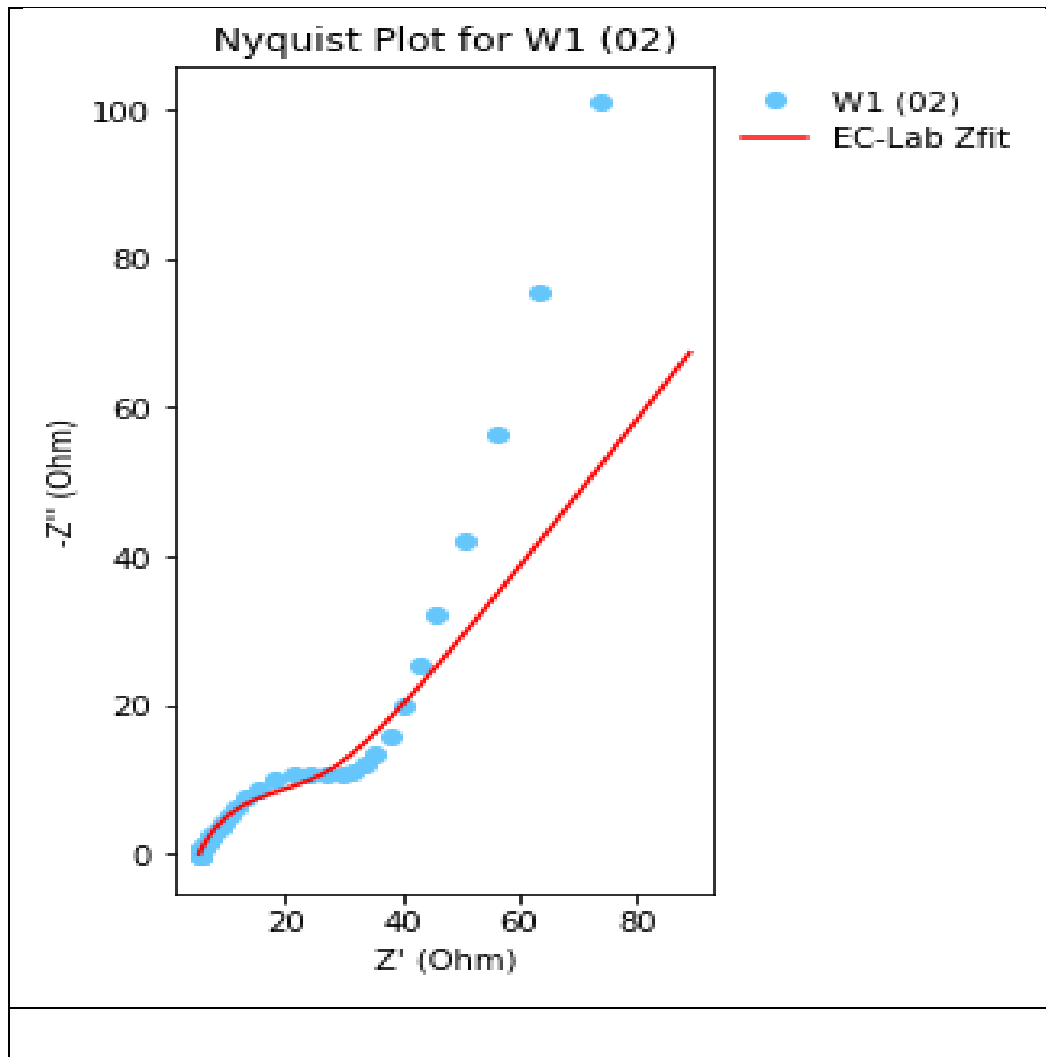
S4	01	5	0.17	0.83	0.74	27.55	24.66	513.11	573.33	0.03	98.63
S4	02	5	0.17	0.75	0.7	24.93	23.21	482.91	518.72	0.03	92.83
S4	03	5	0.09	0.64	0.61	10.74	10.18	423.57	446.94	0.06	40.71
S4	01	10	0.35	0.58	0.55	19.2	18.43	191.78	199.76	0.03	73.73
S4	02	10	0.35	0.6	0.58	20.06	19.37	201.57	208.71	0.03	77.49
S4	03	10	0.17	0.46	0.45	7.67	7.54	156.94	159.52	0.06	30.17
S4	01	20	0.69	0.27	0.27	9.13	8.86	46.12	47.49	0.03	35.46
S4	02	20	0.69	0.39	0.38	12.98	12.81	66.65	67.51	0.03	51.25
S4	03	20	0.35	0.23	0.23	3.77	3.77	39.17	39.19	0.06	15.06
S4	01	30	1.04	0.1	0.1	3.33	3.25	11.26	11.53	0.03	12.99
S4	02	30	1.04	0.34	0.14	11.28	4.62	16.02	39.13	0.03	18.47
S4	03	30	0.52	0.12	0.08	1.99	1.4	9.74	13.83	0.06	5.62
S4	01	40	1.38	0.01	0.0	0.17	0.1	0.26	0.43	0.03	0.4
S4	02	40	1.38	0.14	0.12	4.72	4.11	10.68	12.27	0.03	16.43
S4	03	40	0.69	0.04	0.04	0.62	0.65	3.36	3.21	0.06	2.58

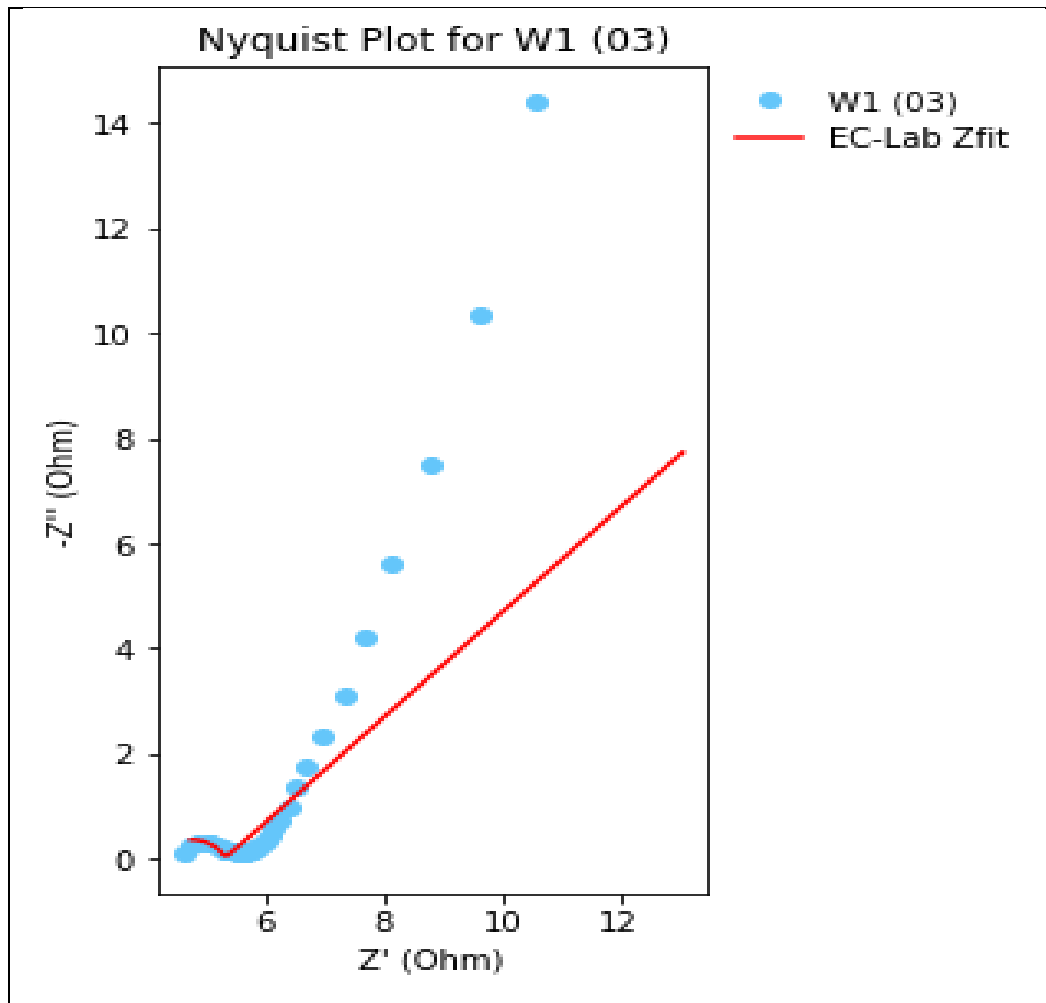
Appendix H Impedance data and analysis from Chapter 4

H.1 Nyquist Diagrams

W1 : Nyquist full

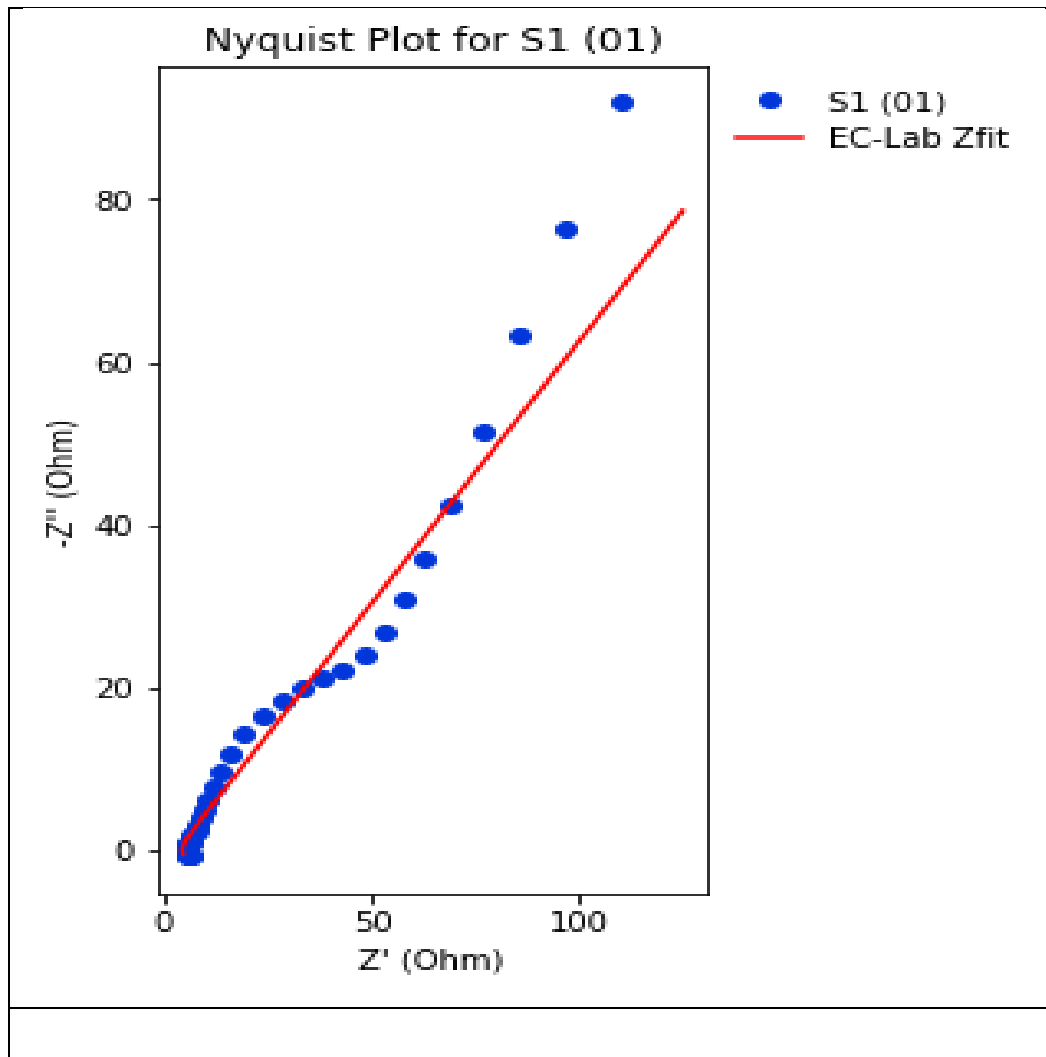


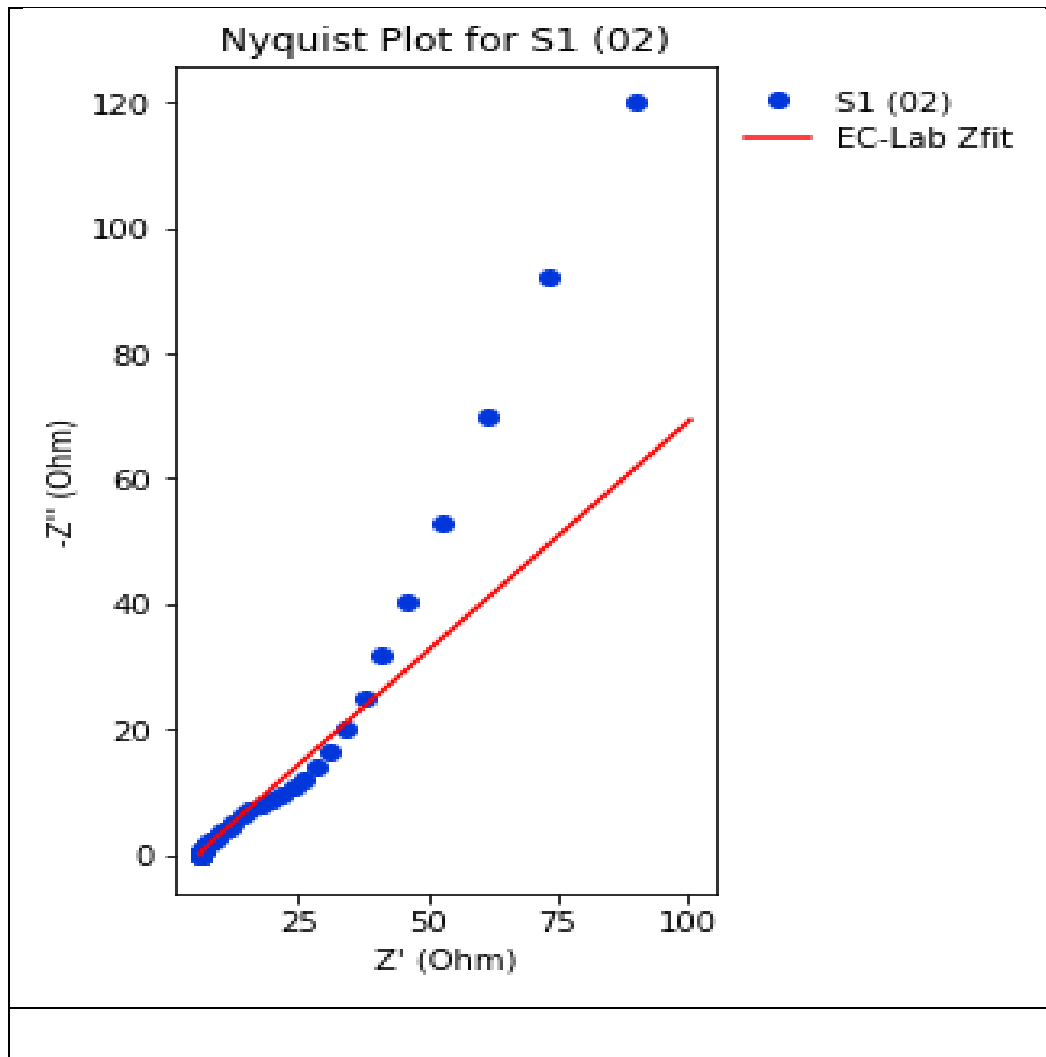


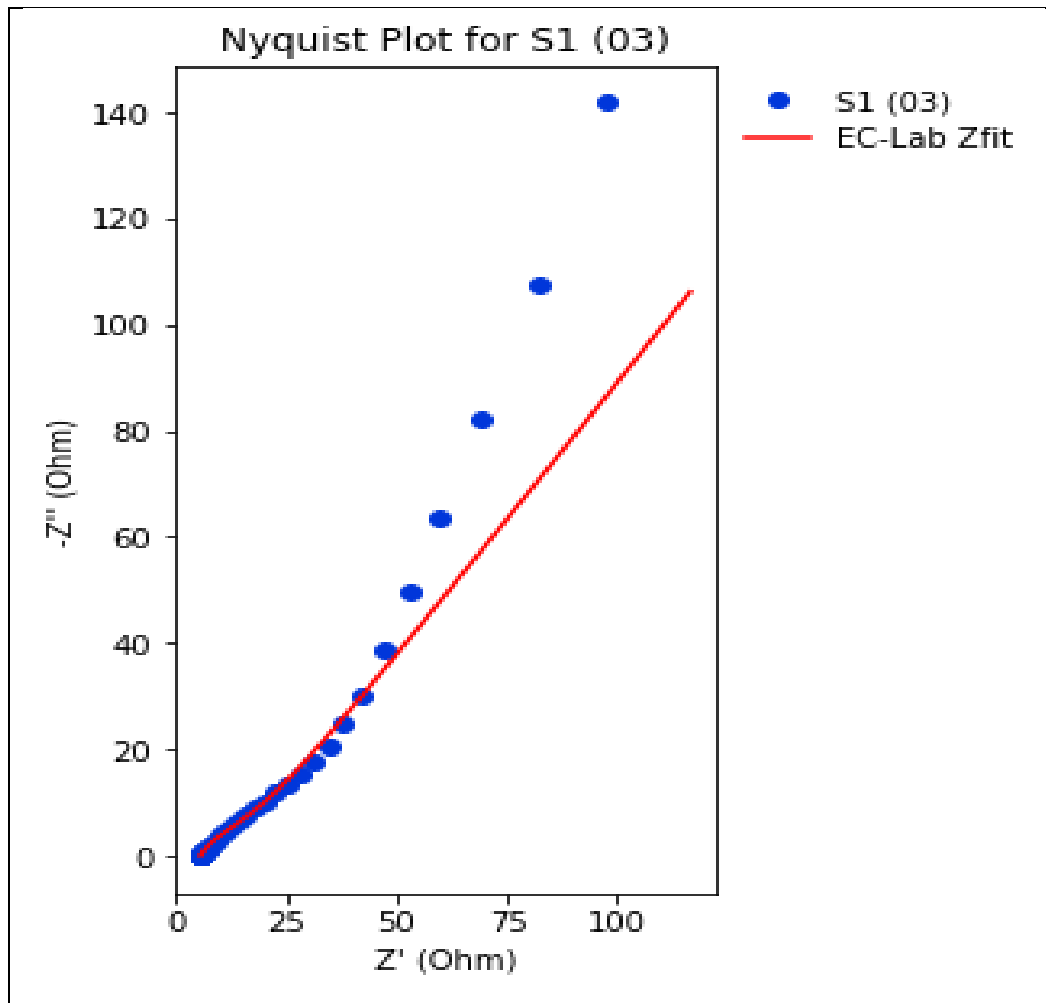


S1 : Nyquist full



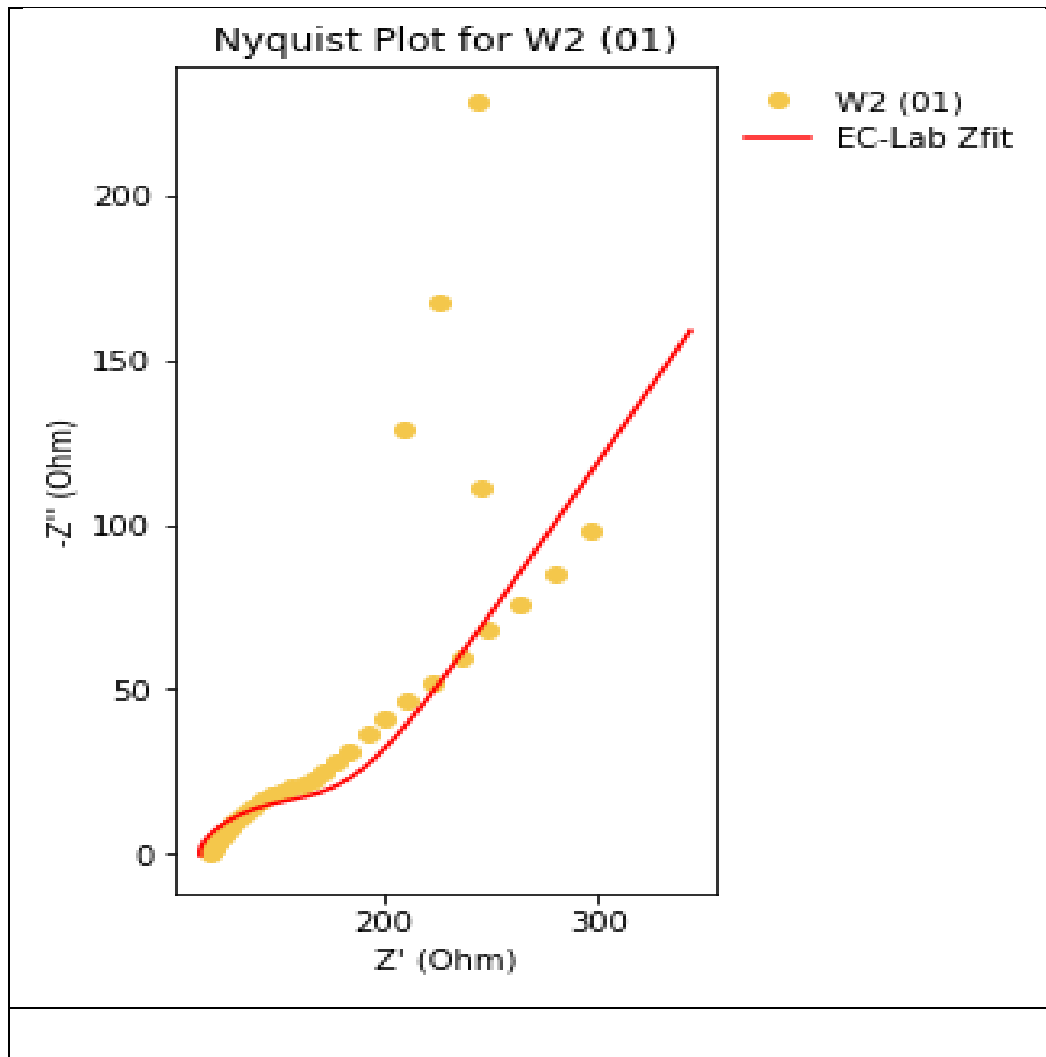


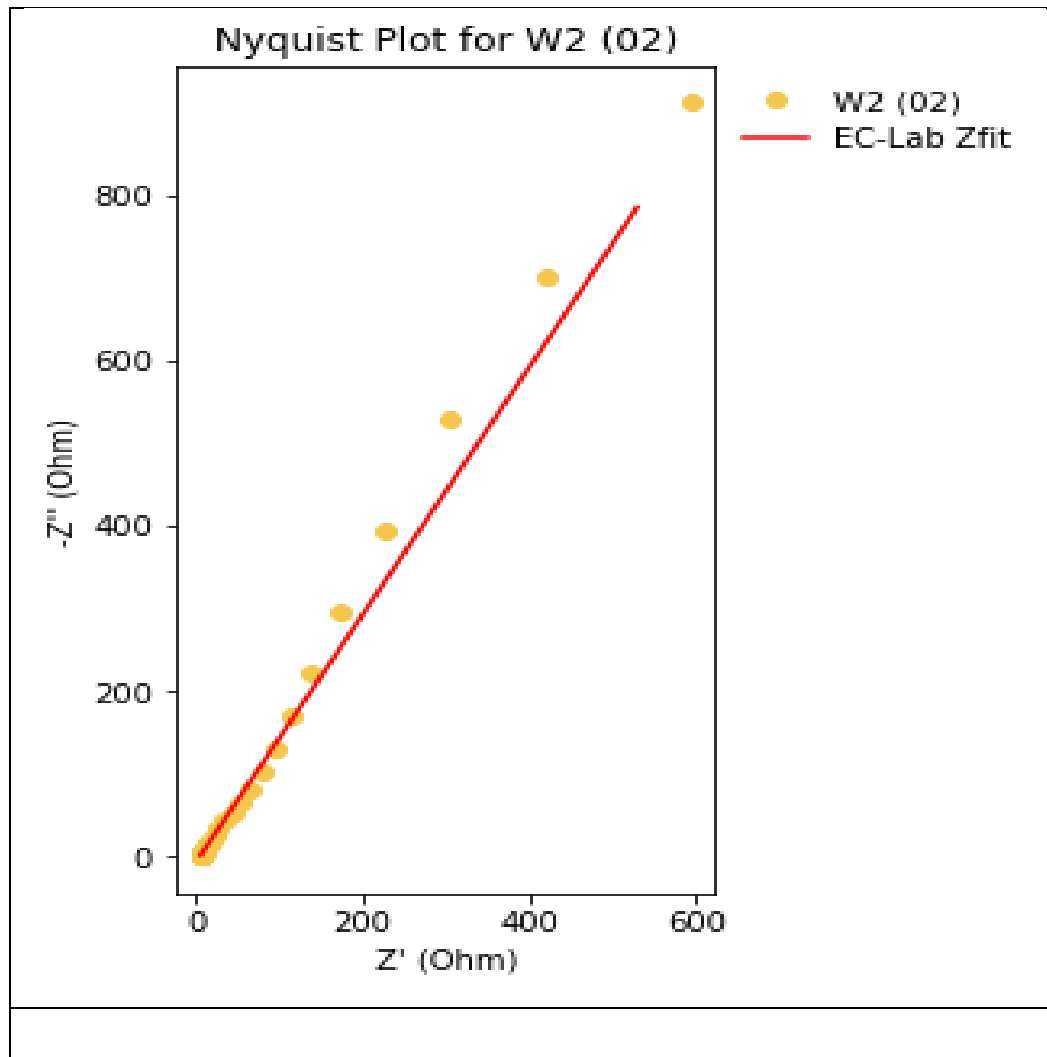


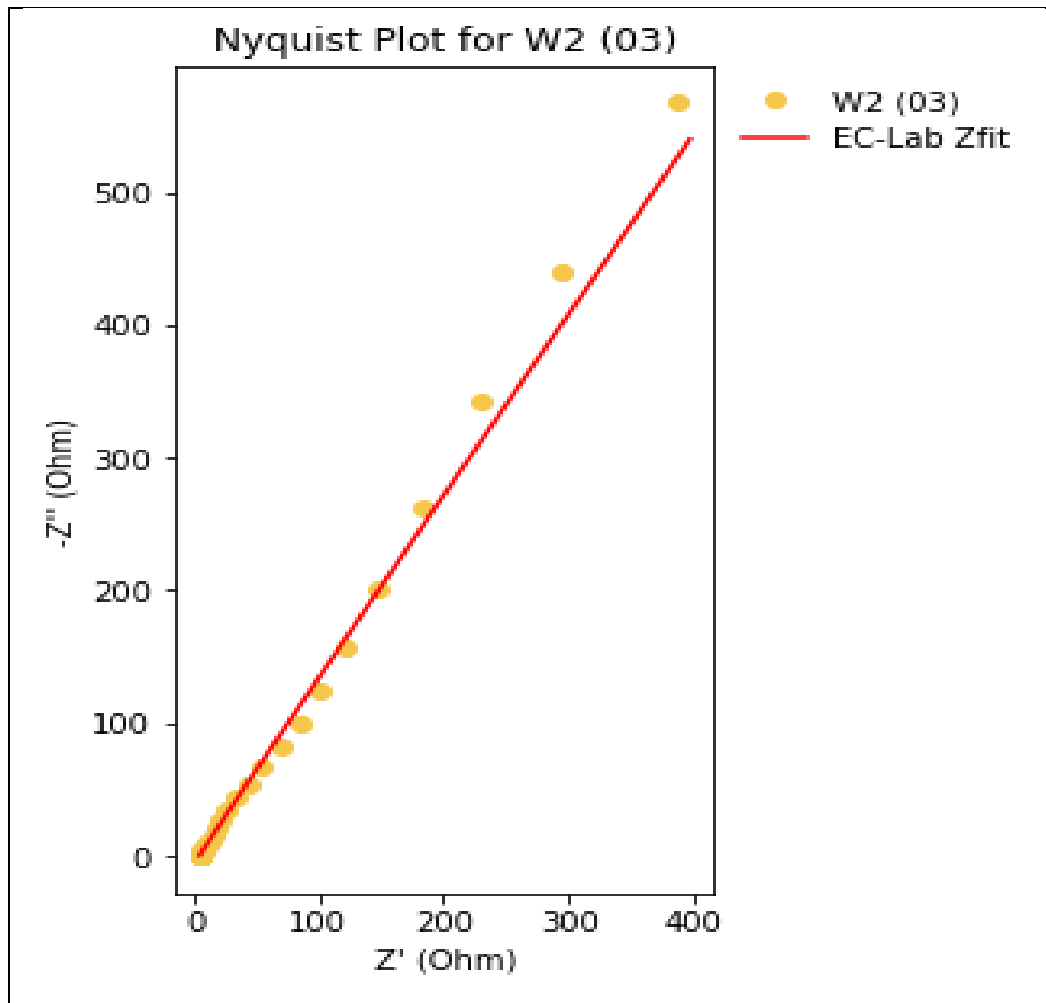


W2 : Nyquist full



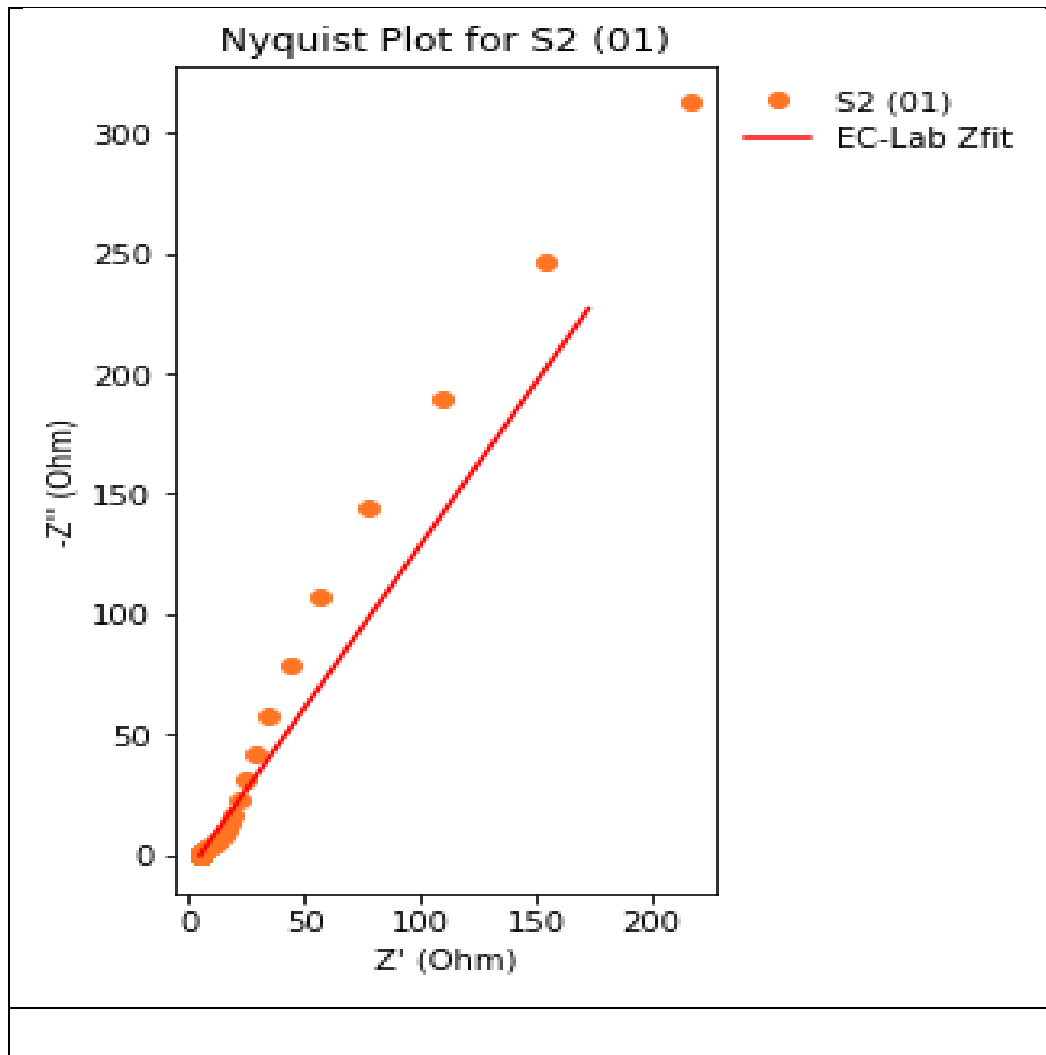


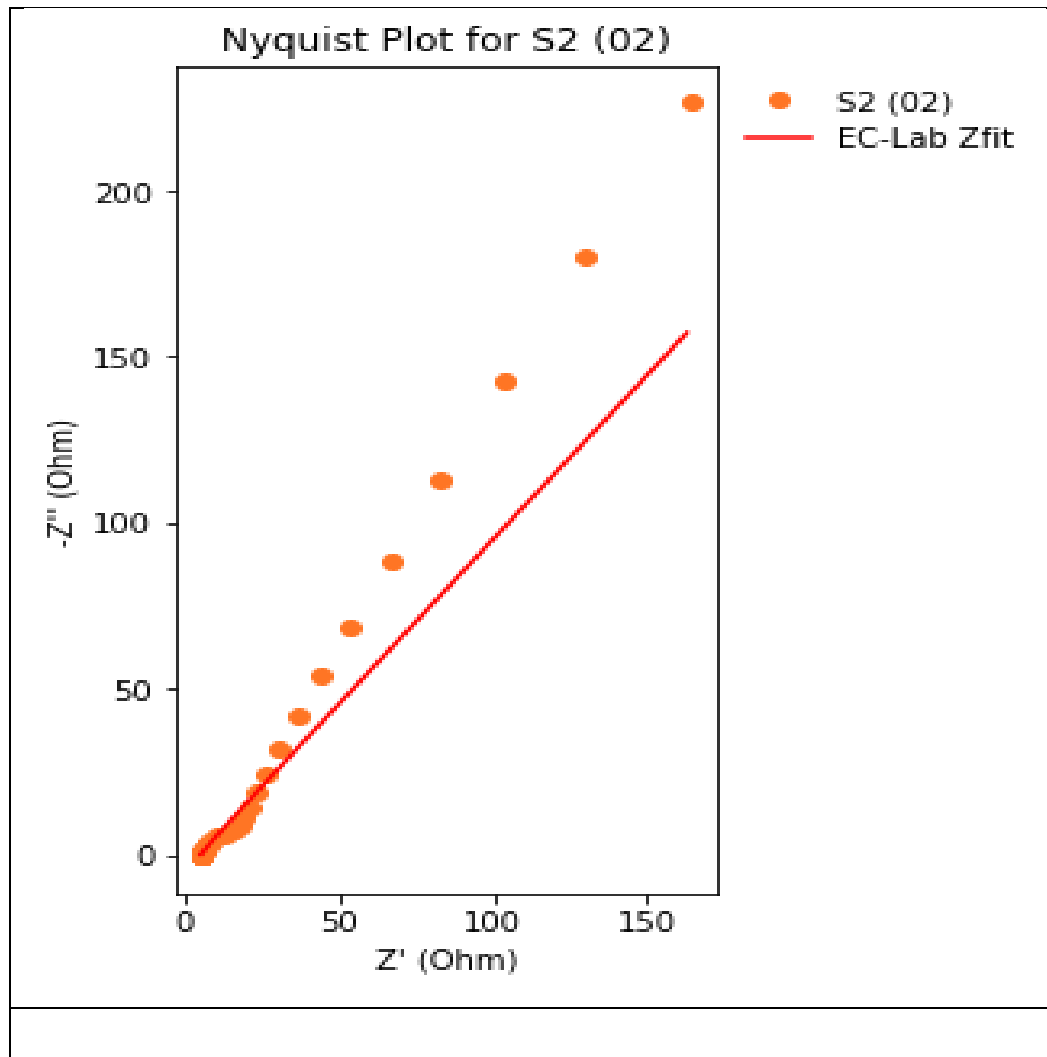


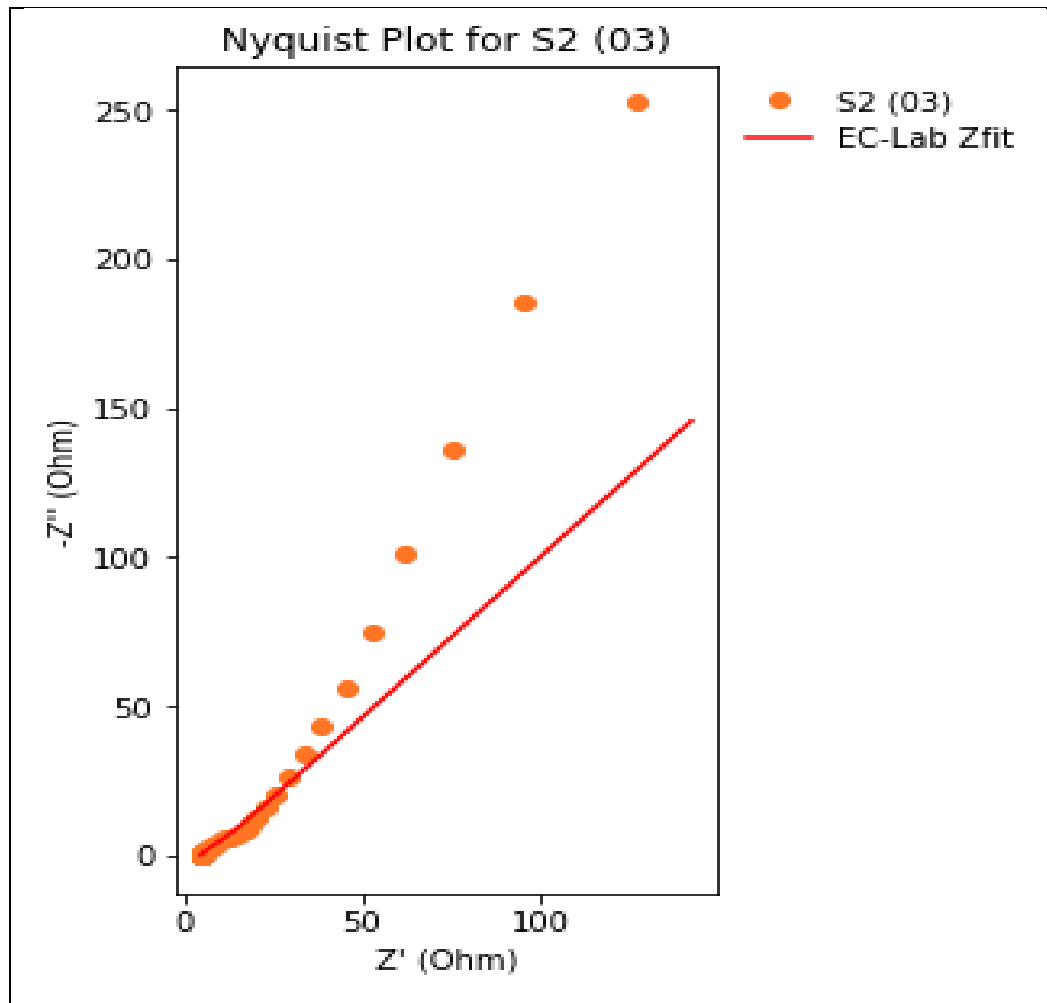


S2 : Nyquist full



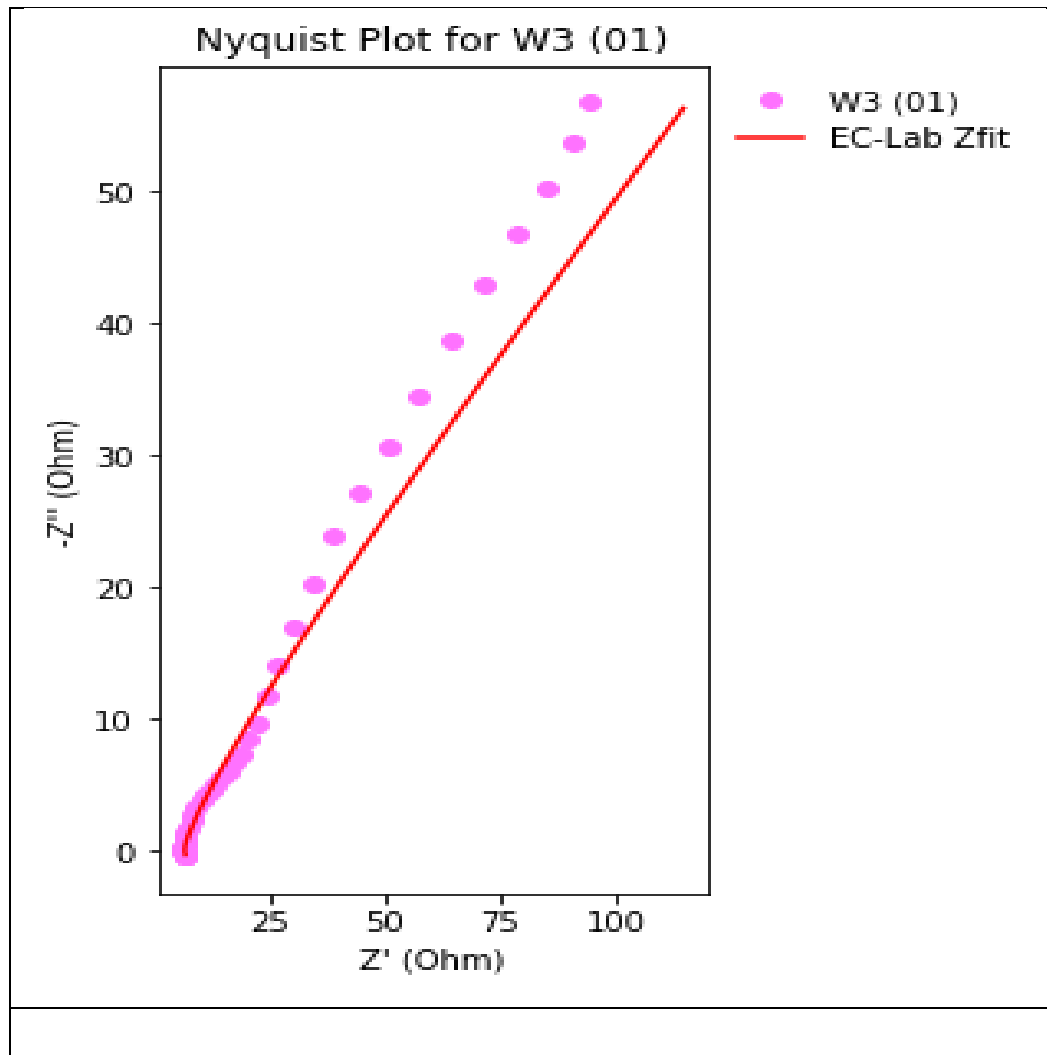


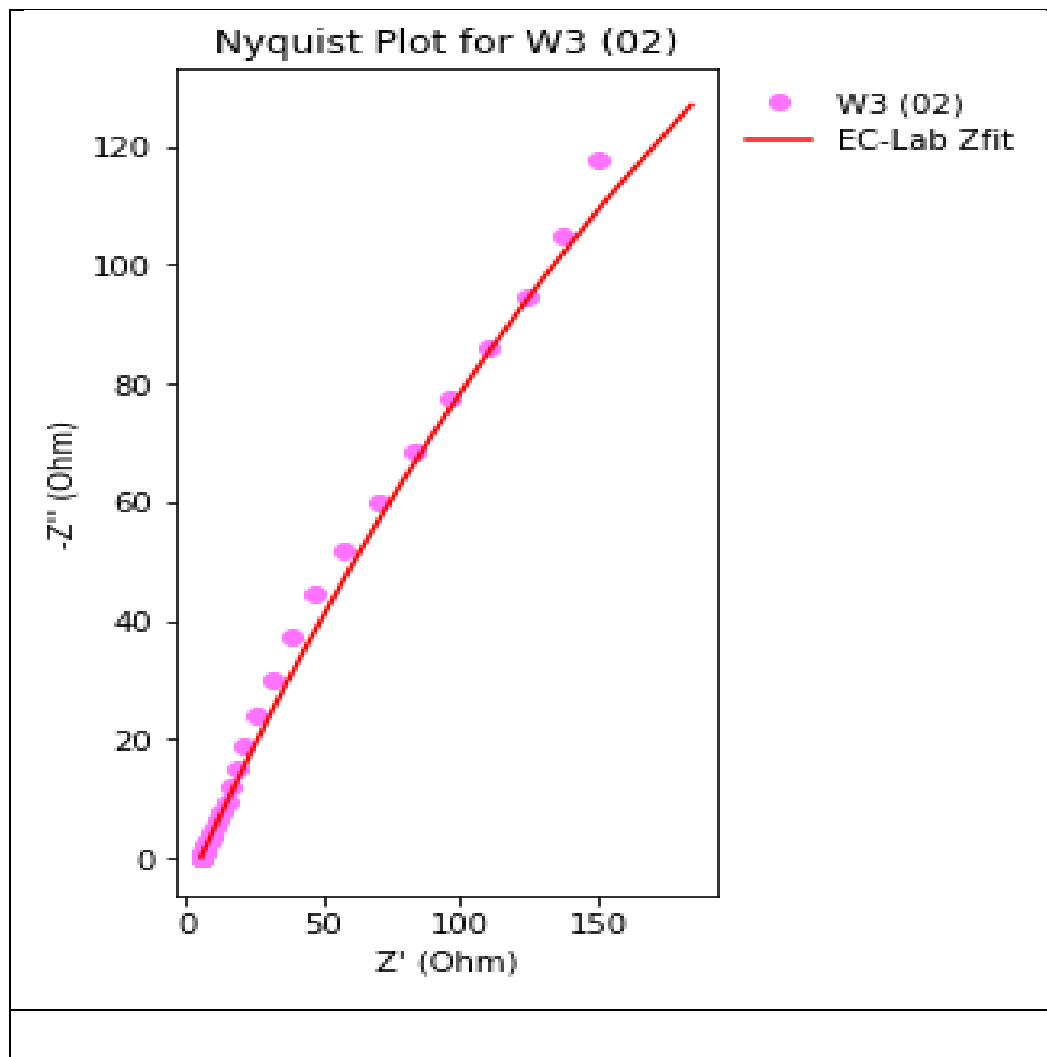


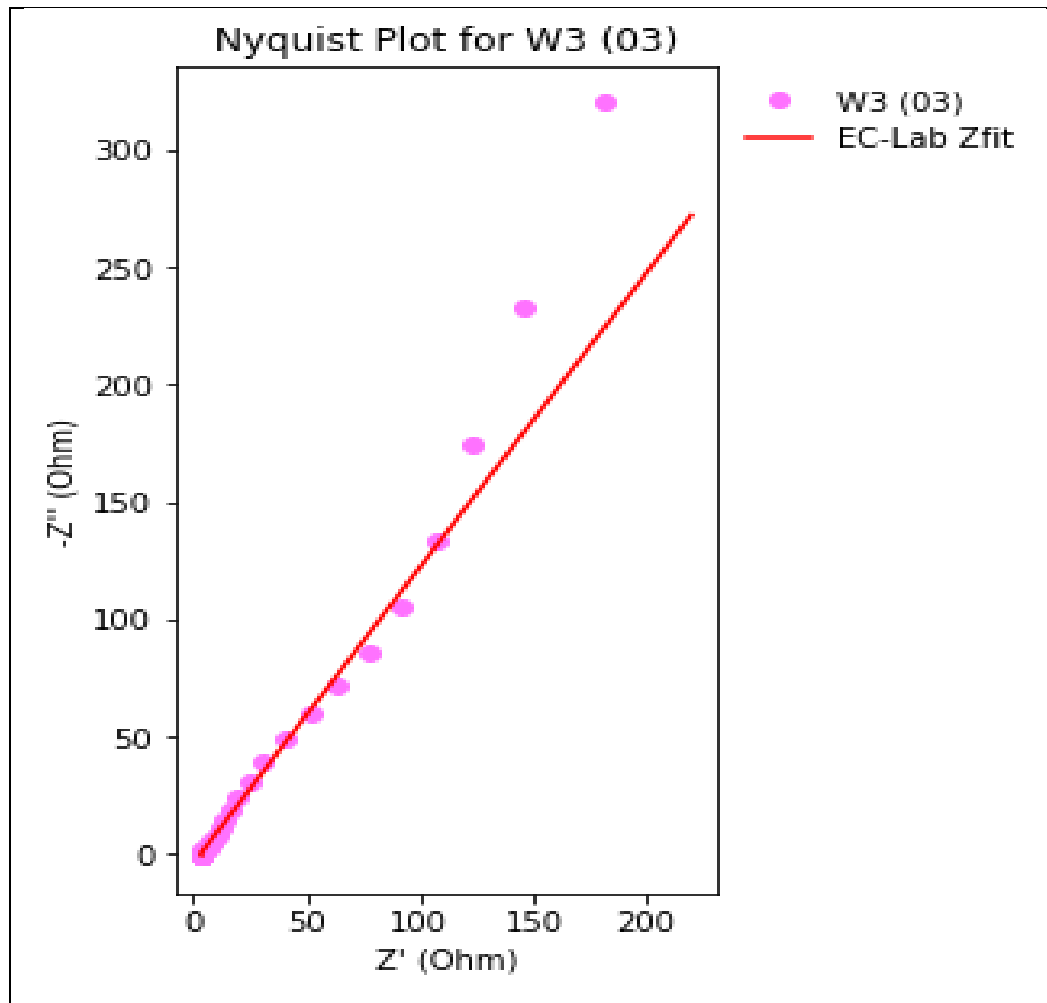


W3 : Nyquist full



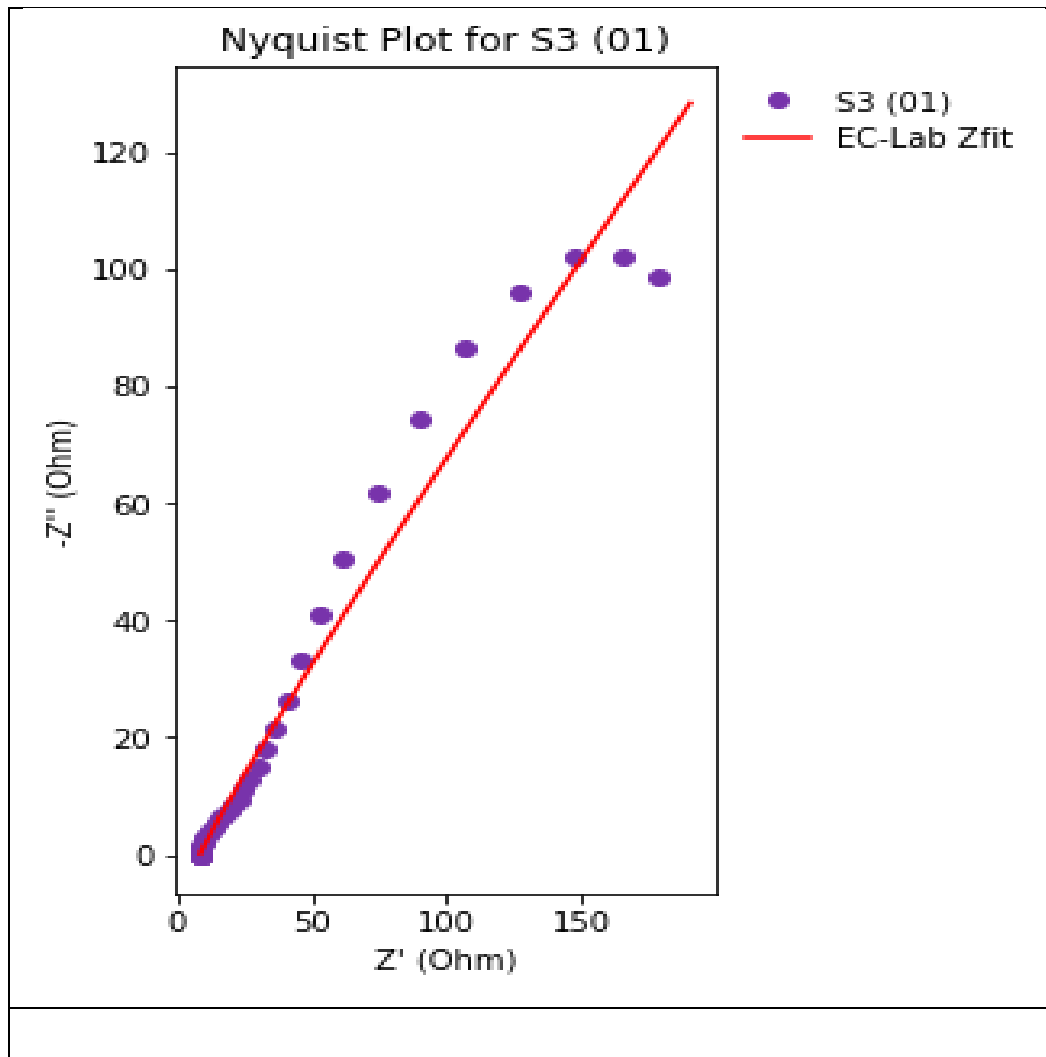


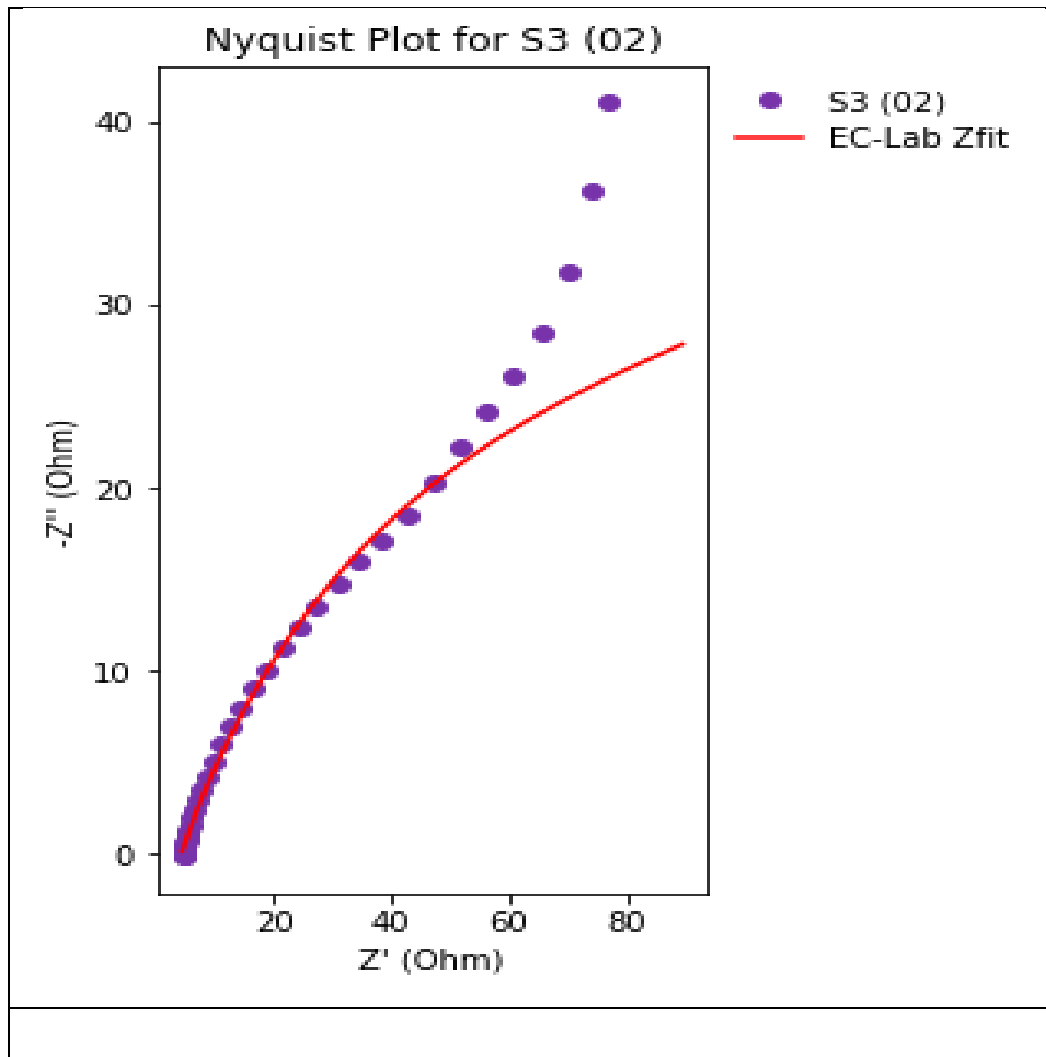


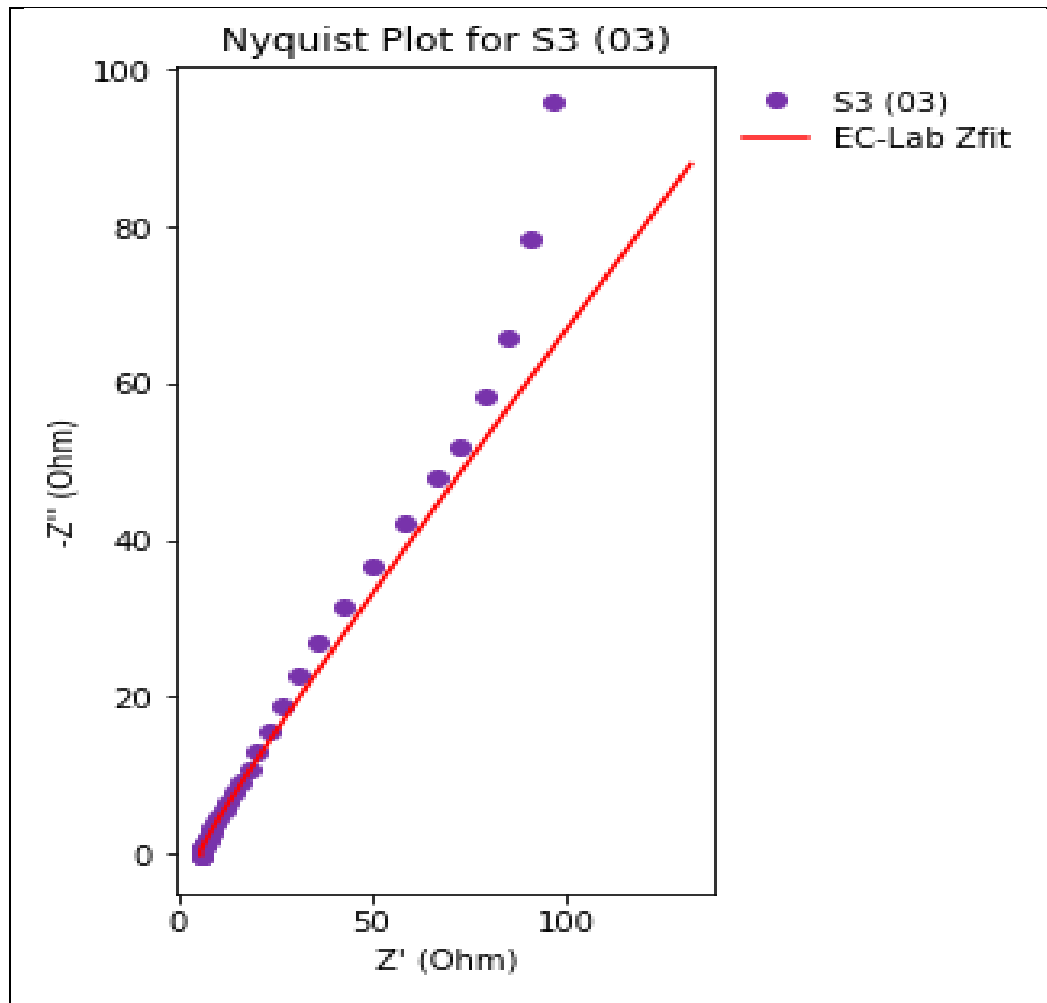


S3 : Nyquist full



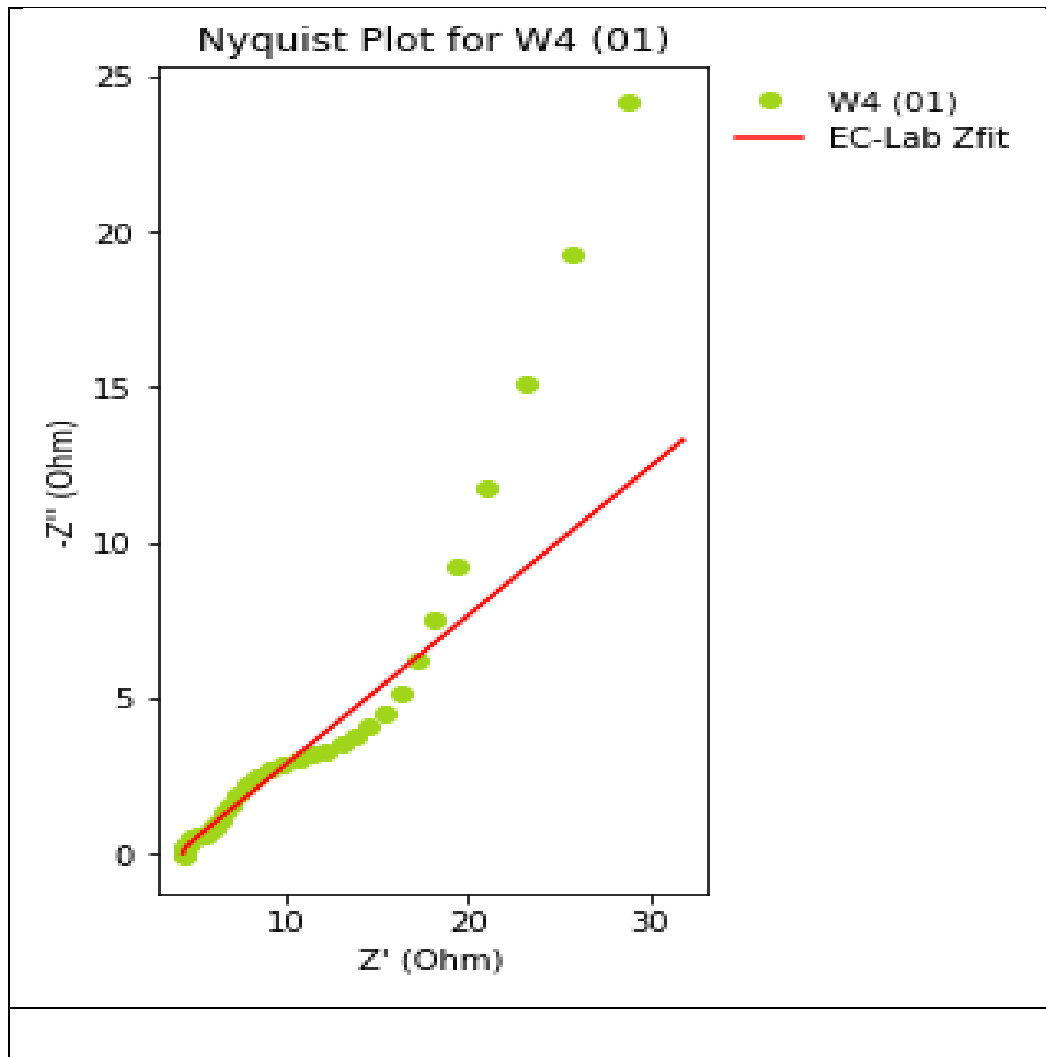


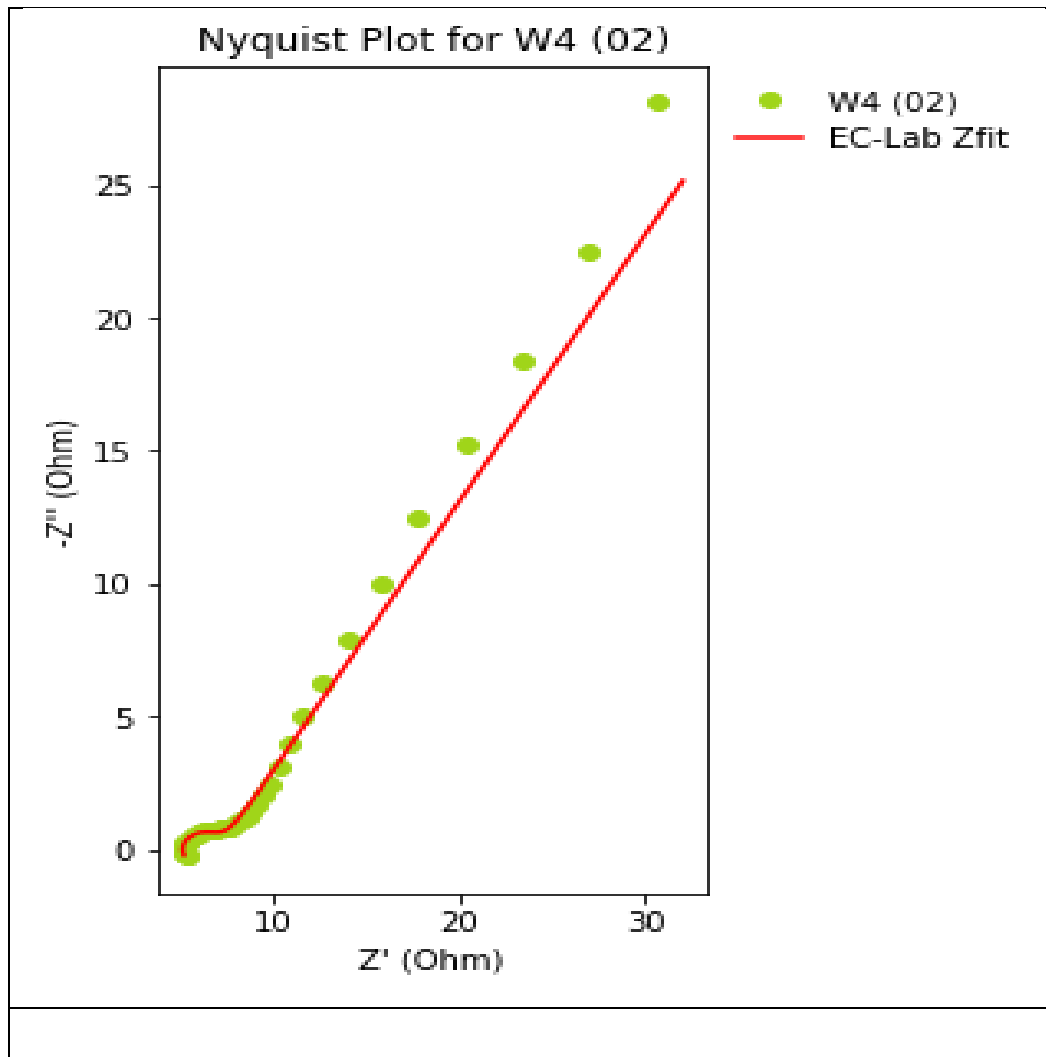


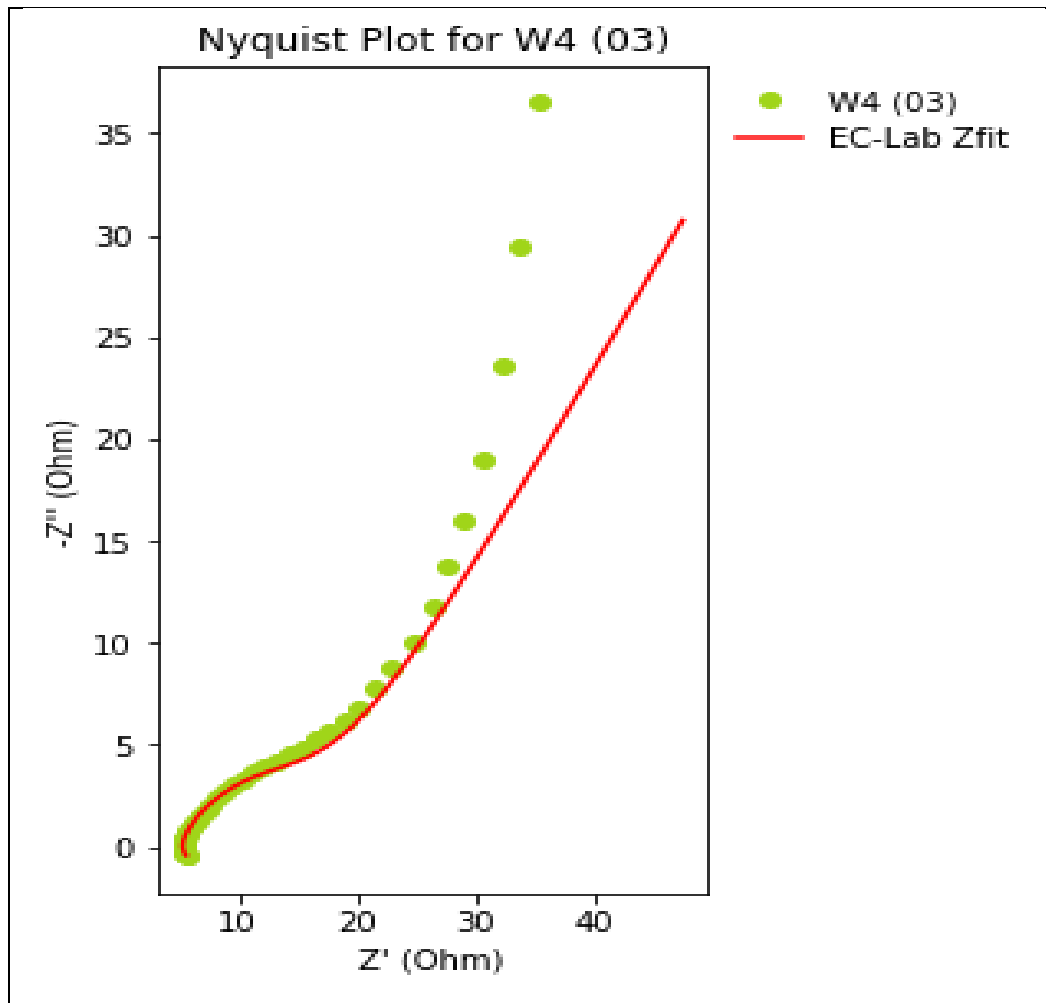


W4 : Nyquist full



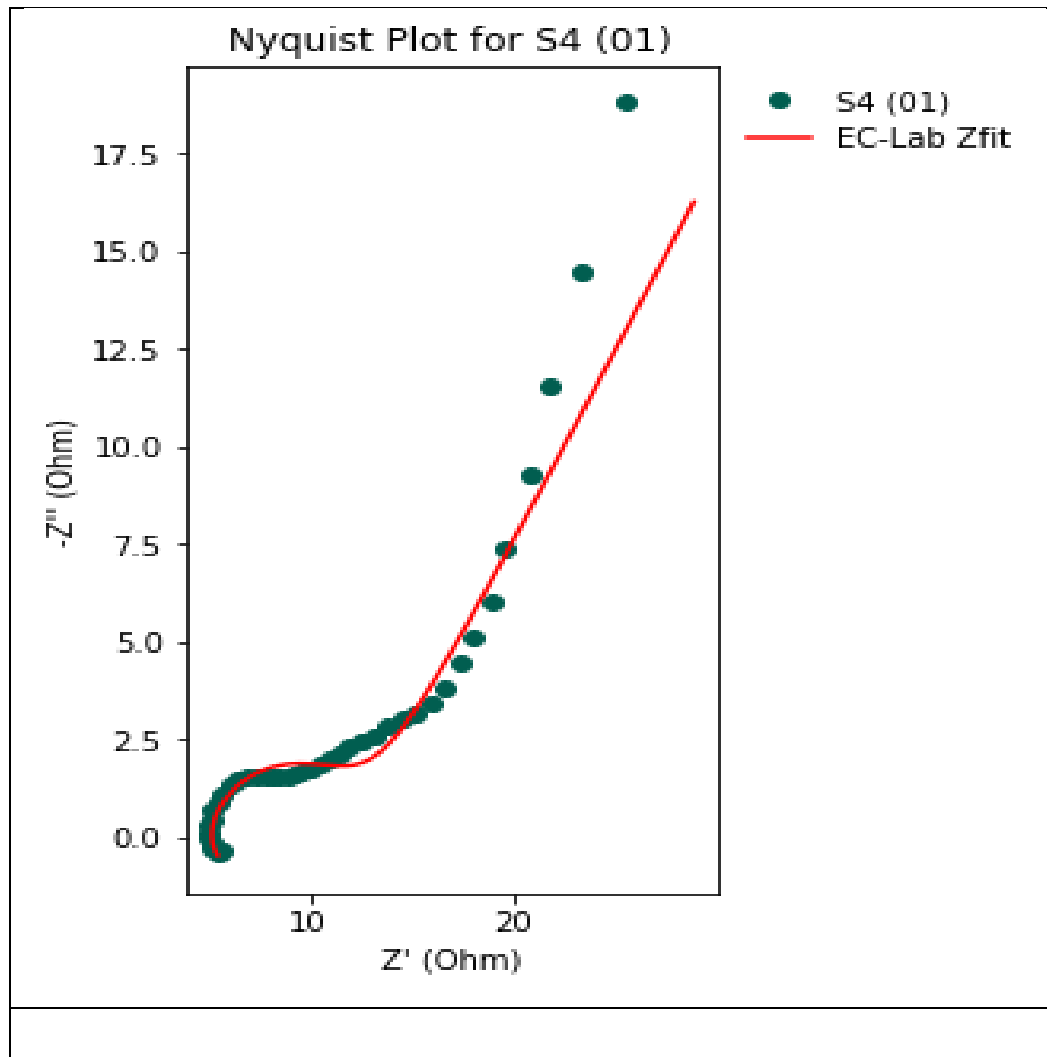


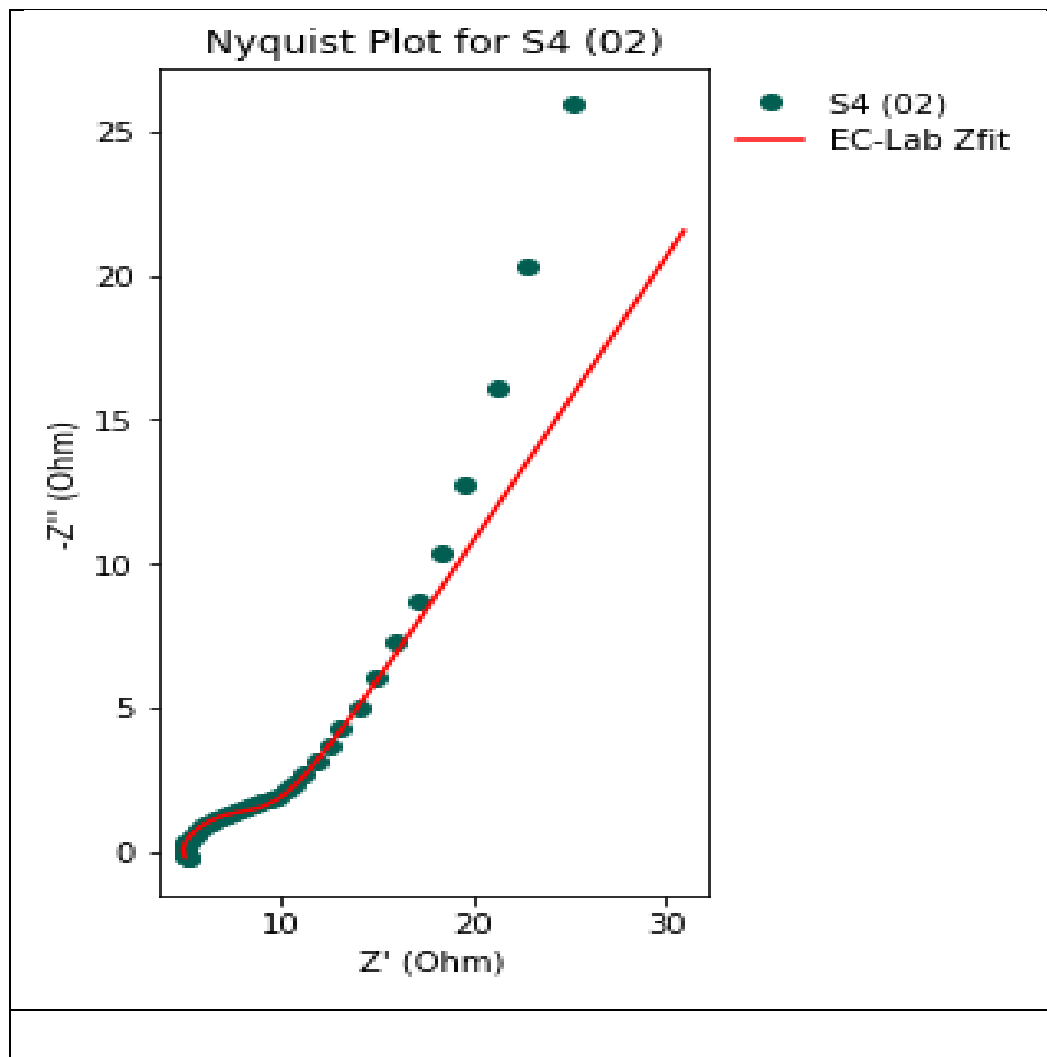


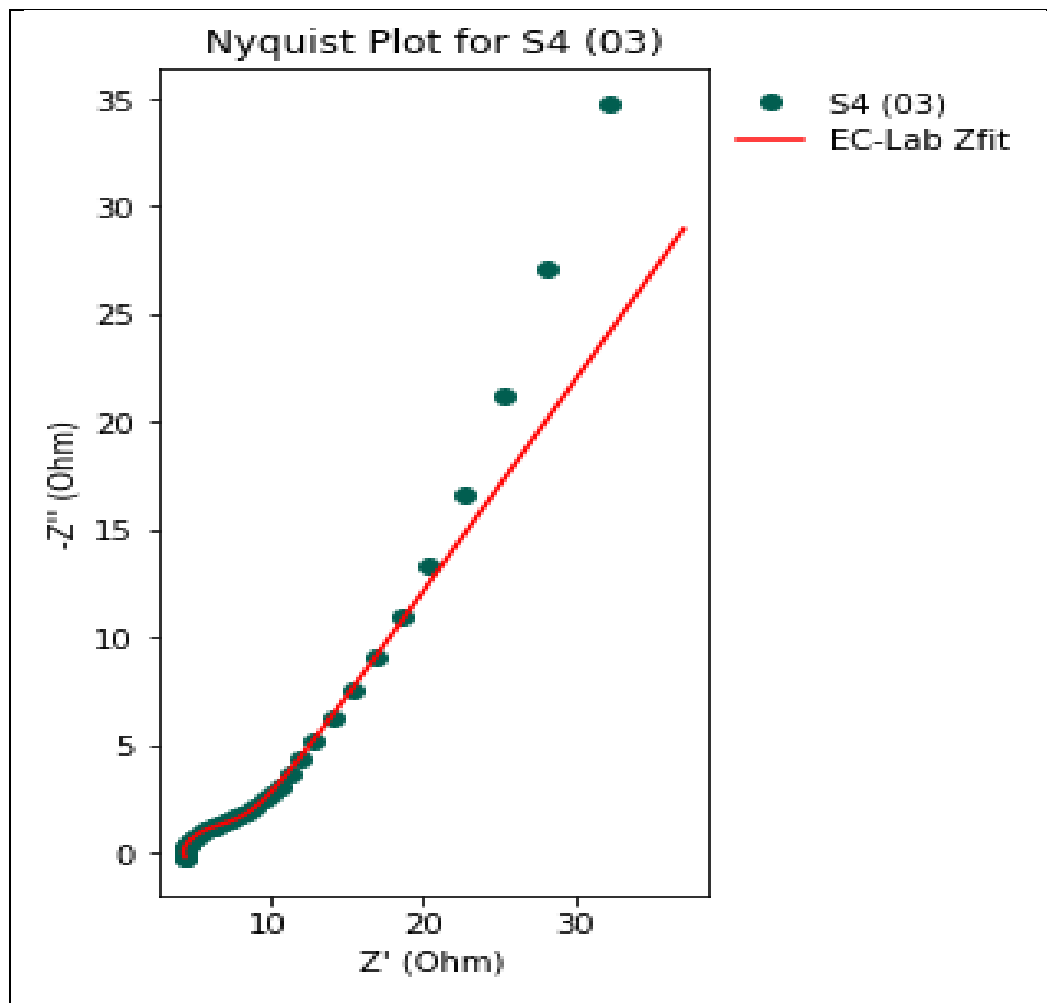


S4 : Nyquist full









H.2 Equivalent Circuit Fitting Data

W1 (01)

Fitting Parameters up to 1 Hz

circuit parameter	value	standard error	unit
L1	1.54e-08	0.02	$H.s^{(a-1)}$
a1	0.104	0.207	
R1	4.54	0.0301	Ohm
Q2	0.0123	0.00293	$F.s^{(a - 1)}$
a2	0.324	0.0653	
R2	5.19e-14	1.7e+09	Ohm
s1	66.7	2.48e+14	$Ohm.s^{-1/2}$

Fitting Parameters for full range: 10mHz to 100kHz

circuit parameter	value	standard error	unit
-------------------	-------	----------------	------

L1	1.54e-08	0.02	$H.s^{(a-1)}$
a1	0.104	0.207	
R1	4.54	0.0301	Ohm
Q2	0.0123	0.00293	$F.s^{(a - 1)}$
a2	0.324	0.0653	
R2	5.19e-14	1.7e+09	Ohm
s1	66.7	2.48e+14	$Ohm.s^{-1/2}$

W1 (02)

Fitting Parameters up to 1 Hz

circuit parameter	value	standard error	unit
L1	0	1.38e-24	$H.s^{(a-1)}$
a1	0.000161	0.000655	
R1	5.4	0.0405	Ohm
Q2	0.00422	0.00109	$F.s^{(a - 1)}$
a2	0.674	0.0299	
R2	21.9	4.72	Ohm
s1	17.4	2.22	$Ohm.s^{-1/2}$

Fitting Parameters for full range: 10mHz to 100kHz

circuit parameter	value	standard error	unit
L1	0	1.38e-24	$H.s^{(a-1)}$
a1	0.000161	0.000655	
R1	5.4	0.0405	Ohm
Q2	0.00422	0.00109	$F.s^{(a - 1)}$
a2	0.674	0.0299	
R2	21.9	4.72	Ohm
s1	17.4	2.22	$Ohm.s^{-1/2}$

W1 (03)

Fitting Parameters up to 1 Hz

circuit parameter	value	standard error	unit
L1	1.71e-16	0.0309	$H.s^{(a-1)}$
a1	0.0155	0.339	
R1	4.2	0.427	Ohm

Q2	6.99e-05	0.0323	$F.s^{(a - 1)}$
a2	0.732	0.156	
R2	1.11	1.89e+12	Ohm
s1	1.94	0.492	$Ohm.s^{-1/2}$

Fitting Parameters for full range: 10mHz to 100kHz

circuit parameter	value	standard error	unit
L1	1.71e-16	0.0309	$H.s^{(a-1)}$
a1	0.0155	0.339	
R1	4.2	0.427	Ohm
Q2	6.99e-05	0.0323	$F.s^{(a - 1)}$
a2	0.732	0.156	
R2	1.11	1.89e+12	Ohm
s1	1.94	0.492	$Ohm.s^{-1/2}$

S1 (01)

Fitting Parameters up to 1 Hz

circuit parameter	value	standard error	unit
L1	0.0174	0.014	$H.s^{(a-1)}$
a1	0.343	0.0419	
R1	2.86	0.229	Ohm
Q2	0.0189	0.000478	$F.s^{(a - 1)}$
a2	0.364	0.00899	
R2	1.18e+03	1.14e+03	Ohm
s1	5.48e+17	2.24e+26	$Ohm.s^{-1/2}$

Fitting Parameters for full range: 10mHz to 100kHz

circuit parameter	value	standard error	unit
L1	0.0174	0.014	$H.s^{(a-1)}$
a1	0.343	0.0419	
R1	2.86	0.229	Ohm
Q2	0.0189	0.000478	$F.s^{(a - 1)}$
a2	0.364	0.00899	
R2	1.18e+03	1.14e+03	Ohm
s1	5.48e+17	2.24e+26	$Ohm.s^{-1/2}$

S1 (02)

Fitting Parameters up to 1 Hz

circuit parameter	value	standard error	unit
L1	0.102	0.136	$H.s^{(a-1)}$
a1	0.154	0.0499	
R1	5.17	0.287	Ohm
Q2	0.0257	0.00236	$F.s^{(a - 1)}$
a2	0.401	0.022	
R2	3.04	0.292	Ohm
s1	$6.95e+15$	$1.66e+22$	$Ohm.s^{-1/2}$

Fitting Parameters for full range: 10mHz to 100kHz

circuit parameter	value	standard error	unit
L1	0.102	0.136	$H.s^{(a-1)}$
a1	0.154	0.0499	
R1	5.17	0.287	Ohm
Q2	0.0257	0.00236	$F.s^{(a - 1)}$
a2	0.401	0.022	
R2	3.04	0.292	Ohm
s1	$6.95e+15$	$1.66e+22$	$Ohm.s^{-1/2}$

S1 (03)

Fitting Parameters up to 1 Hz

circuit parameter	value	standard error	unit
L1	$1.86e-15$	0.0355	$H.s^{(a-1)}$
a1	0.114	0.418	
R1	5.53	0.0493	Ohm
Q2	0.00774	0.00239	$F.s^{(a - 1)}$
a2	0.568	0.0314	
R2	18.2	34.1	Ohm
s1	33.6	6.06	$Ohm.s^{-1/2}$

Fitting Parameters for full range: 10mHz to 100kHz

circuit parameter	value	standard error	unit
L1	$1.86e-15$	0.0355	$H.s^{(a-1)}$

a1	0.114	0.418	
R1	5.53	0.0493	Ohm
Q2	0.00774	0.00239	$F.s^{(a - 1)}$
a2	0.568	0.0314	
R2	18.2	34.1	Ohm
s1	33.6	6.06	$Ohm.s^{-1/2}$

W2 (01)

Fitting Parameters up to 1 Hz

circuit parameter	value	standard error	unit
L1	76.3	4.34	$H.s^{(a-1)}$
a1	0.0264	0.00348	
R1	0.367	0.56	Ohm
Q2	0.00157	0.000891	$F.s^{(a - 1)}$
a2	0.329	0.048	
R2	135	150	Ohm
s1	51.1	82.5	$Ohm.s^{-1/2}$

Fitting Parameters for full range: 10mHz to 100kHz

circuit parameter	value	standard error	unit
L1	76.3	4.34	$H.s^{(a-1)}$
a1	0.0264	0.00348	
R1	0.367	0.56	Ohm
Q2	0.00157	0.000891	$F.s^{(a - 1)}$
a2	0.329	0.048	
R2	135	150	Ohm
s1	51.1	82.5	$Ohm.s^{-1/2}$

W2 (02)

Fitting Parameters up to 1 Hz

circuit parameter	value	standard error	unit
L1	9.94e-20	6.13e-17	$H.s^{(a-1)}$
a1	0.926	0.00511	
R1	5.57	0.025	Ohm
Q2	0.00598	9.39e-05	$F.s^{(a - 1)}$

a2	0.626	0.00467	
R2	0.22	0.00807	Ohm
s1	1.42e+17	1.46e+17	Ohm.s ^{-1/2}

Fitting Parameters for full range: 10mHz to 100kHz

circuit parameter	value	standard error	unit
L1	9.94e-20	6.13e-17	H.s ^(a-1)
a1	0.926	0.00511	
R1	5.57	0.025	Ohm
Q2	0.00598	9.39e-05	F.s ^(a - 1)
a2	0.626	0.00467	
R2	0.22	0.00807	Ohm
s1	1.42e+17	1.46e+17	Ohm.s ^{-1/2}

W2 (03)

Fitting Parameters up to 1 Hz

circuit parameter	value	standard error	unit
L1	1.96e-31	4.66e-28	H.s ^(a-1)
a1	0.993	0.000933	
R1	4.43	0.0136	Ohm
Q2	0.00669	0.000774	F.s ^(a - 1)
a2	0.627	0.0132	
R2	2.65	2.4e+08	Ohm
s1	548	1.08e+16	Ohm.s ^{-1/2}

Fitting Parameters for full range: 10mHz to 100kHz

circuit parameter	value	standard error	unit
L1	1.96e-31	4.66e-28	H.s ^(a-1)
a1	0.993	0.000933	
R1	4.43	0.0136	Ohm
Q2	0.00669	0.000774	F.s ^(a - 1)
a2	0.627	0.0132	
R2	2.65	2.4e+08	Ohm
s1	548	1.08e+16	Ohm.s ^{-1/2}

S2 (01)

Fitting Parameters up to 1 Hz

circuit parameter	value	standard error	unit
L1	3.07e-07	3.06e-08	H.s ^(a-1)
a1	1	9.52e-10	
R1	4.8	0.0213	Ohm
Q2	0.0184	0.0011	F.s ^(a - 1)
a2	0.595	0.0205	
R2	2.35e+09	1.8e+17	Ohm
s1	5.57e+16	5.43e+27	Ohm.s ^{-1/2}

Fitting Parameters for full range: 10mHz to 100kHz

circuit parameter	value	standard error	unit
L1	3.07e-07	3.06e-08	H.s ^(a-1)
a1	1	9.52e-10	
R1	4.8	0.0213	Ohm
Q2	0.0184	0.0011	F.s ^(a - 1)
a2	0.595	0.0205	
R2	2.35e+09	1.8e+17	Ohm
s1	5.57e+16	5.43e+27	Ohm.s ^{-1/2}

S2 (02)

Fitting Parameters up to 1 Hz

circuit parameter	value	standard error	unit
L1	0.666	0.529	H.s ^(a-1)
a1	0.123	0.033	
R1	1.47e-07	0.282	Ohm
Q2	0.000928	0.00147	F.s ^(a - 1)
a2	0.441	0.0851	
R2	3.74	0.315	Ohm
s1	42.2	3.64	Ohm.s ^{-1/2}

Fitting Parameters for full range: 10mHz to 100kHz

circuit parameter	value	standard error	unit
L1	0.666	0.529	H.s ^(a-1)
a1	0.123	0.033	

R1	1.47e-07	0.282	Ohm
Q2	0.000928	0.00147	$F.s^{(a - 1)}$
a2	0.441	0.0851	
R2	3.74	0.315	Ohm
s1	42.2	3.64	$Ohm.s^{-1/2}$

S2 (03)

Fitting Parameters up to 1 Hz

circuit parameter	value	standard error	unit
L1	6.97e-07	0.0112	$H.s^{(a-1)}$
a1	0.104	0.267	
R1	4.69	0.0219	Ohm
Q2	0.00713	0.0056	$F.s^{(a - 1)}$
a2	0.613	0.106	
R2	9.42	3.84e+11	Ohm
s1	46.7	6.43e+13	$Ohm.s^{-1/2}$

Fitting Parameters for full range: 10mHz to 100kHz

circuit parameter	value	standard error	unit
L1	6.97e-07	0.0112	$H.s^{(a-1)}$
a1	0.104	0.267	
R1	4.69	0.0219	Ohm
Q2	0.00713	0.0056	$F.s^{(a - 1)}$
a2	0.613	0.106	
R2	9.42	3.84e+11	Ohm
s1	46.7	6.43e+13	$Ohm.s^{-1/2}$

W3 (01)

Fitting Parameters up to 1 Hz

circuit parameter	value	standard error	unit
L1	0.0739	0.14	$H.s^{(a-1)}$
a1	0.222	0.0661	
R1	5.32	0.405	Ohm
Q2	0.0143	0.000788	$F.s^{(a - 1)}$
a2	0.265	0.0194	

R2	1.89e-15	0.00167	Ohm
s1	132	16.9	Ohm.s ^{-1/2}

Fitting Parameters for full range: 10mHz to 100kHz

circuit parameter	value	standard error	unit
L1	0.0739	0.14	H.s ^(a-1)
a1	0.222	0.0661	
R1	5.32	0.405	Ohm
Q2	0.0143	0.000788	F.s ^(a - 1)
a2	0.265	0.0194	
R2	1.89e-15	0.00167	Ohm
s1	132	16.9	Ohm.s ^{-1/2}

W3 (02)

Fitting Parameters up to 1 Hz

circuit parameter	value	standard error	unit
L1	1.79e-06	0.0248	H.s ^(a-1)
a1	0.761	0.331	
R1	5.06	0.0539	Ohm
Q2	0.00108	0.000223	F.s ^(a - 1)
a2	2.22e-16	6.3e-16	
R2	0	0	Ohm
s1	47.6	1.04	Ohm.s ^{-1/2}

Fitting Parameters for full range: 10mHz to 100kHz

circuit parameter	value	standard error	unit
L1	1.79e-06	0.0248	H.s ^(a-1)
a1	0.761	0.331	
R1	5.06	0.0539	Ohm
Q2	0.00108	0.000223	F.s ^(a - 1)
a2	2.22e-16	6.3e-16	
R2	0	0	Ohm
s1	47.6	1.04	Ohm.s ^{-1/2}

W3 (03)

Fitting Parameters up to 1 Hz

circuit parameter	value	standard error	unit
L1	0.00112	0.00172	$H.s^{(a-1)}$
a1	0.516	0.0597	
R1	3.34	0.0624	Ohm
Q2	0.0121	0.00247	$F.s^{(a - 1)}$
a2	0.589	0.0245	
R2	19.6	$5.49e+13$	Ohm
s1	345	$6.22e+15$	$Ohm.s^{-1/2}$

Fitting Parameters for full range: 10mHz to 100kHz

circuit parameter	value	standard error	unit
L1	0.00112	0.00172	$H.s^{(a-1)}$
a1	0.516	0.0597	
R1	3.34	0.0624	Ohm
Q2	0.0121	0.00247	$F.s^{(a - 1)}$
a2	0.589	0.0245	
R2	19.6	$5.49e+13$	Ohm
s1	345	$6.22e+15$	$Ohm.s^{-1/2}$

S3 (01)

Fitting Parameters up to 1 Hz

circuit parameter	value	standard error	unit
L1	$3.2e-31$	$1.71e-19$	$H.s^{(a-1)}$
a1	0.838	0.0209	
R1	8.28	0.0453	Ohm
Q2	0.00643	0.00136	$F.s^{(a - 1)}$
a2	0.315	0.0425	
R2	0	0.121	Ohm
s1	95.9	243	$Ohm.s^{-1/2}$

Fitting Parameters for full range: 10mHz to 100kHz

circuit parameter	value	standard error	unit
L1	$3.2e-31$	$1.71e-19$	$H.s^{(a-1)}$
a1	0.838	0.0209	
R1	8.28	0.0453	Ohm

Q2	0.00643	0.00136	$F.s^{(a - 1)}$
a2	0.315	0.0425	
R2	0	0.121	Ohm
s1	95.9	243	$Ohm.s^{-1/2}$

S3 (02)

Fitting Parameters up to 1 Hz

circuit parameter	value	standard error	unit
L1	5.21e-23	1.98e-23	$H.s^{(a-1)}$
a1	1	1.64e-14	
R1	4.24	0.0469	Ohm
Q2	0.013	0.000535	$F.s^{(a - 1)}$
a2	0.127	0.022	
R2	1.2e-14	0.00316	Ohm
s1	75.9	3.13	$Ohm.s^{-1/2}$

Fitting Parameters for full range: 10mHz to 100kHz

circuit parameter	value	standard error	unit
L1	5.21e-23	1.98e-23	$H.s^{(a-1)}$
a1	1	1.64e-14	
R1	4.24	0.0469	Ohm
Q2	0.013	0.000535	$F.s^{(a - 1)}$
a2	0.127	0.022	
R2	1.2e-14	0.00316	Ohm
s1	75.9	3.13	$Ohm.s^{-1/2}$

S3 (03)

Fitting Parameters up to 1 Hz

circuit parameter	value	standard error	unit
L1	0.163	0.0808	$H.s^{(a-1)}$
a1	0.155	0.0241	
R1	4.67	0.204	Ohm
Q2	0.011	0.00184	$F.s^{(a - 1)}$
a2	0.33	0.0477	
R2	3.05e-125	0.0136	Ohm

s1	85.4	9.25e+12	Ohm.s ^{-1/2}
----	------	----------	-----------------------

Fitting Parameters for full range: 10mHz to 100kHz

circuit parameter	value	standard error	unit
L1	0.163	0.0808	H.s ^(a-1)
a1	0.155	0.0241	
R1	4.67	0.204	Ohm
Q2	0.011	0.00184	F.s ^(a - 1)
a2	0.33	0.0477	
R2	3.05e-125	0.0136	Ohm
s1	85.4	9.25e+12	Ohm.s ^{-1/2}

W4 (01)

Fitting Parameters up to 1 Hz

circuit parameter	value	standard error	unit
L1	3.69e-07	0.0144	H.s ^(a-1)
a1	0.995	0.152	
R1	4.02	0.118	Ohm
Q2	0.0712	0.00373	F.s ^(a - 1)
a2	0.284	0.0106	
R2	9.96e+16	1.97e+17	Ohm
s1	0.425	0.00791	Ohm.s ^{-1/2}

Fitting Parameters for full range: 10mHz to 100kHz

circuit parameter	value	standard error	unit
L1	3.69e-07	0.0144	H.s ^(a-1)
a1	0.995	0.152	
R1	4.02	0.118	Ohm
Q2	0.0712	0.00373	F.s ^(a - 1)
a2	0.284	0.0106	
R2	9.96e+16	1.97e+17	Ohm
s1	0.425	0.00791	Ohm.s ^{-1/2}

W4 (02)

Fitting Parameters up to 1 Hz

circuit parameter	value	standard error	unit
L1	0.743	0.107	$H.s^{(a-1)}$
a1	0.102	0.00688	
R1	2.17	0.191	Ohm
Q2	0.00399	0.000501	$F.s^{(a - 1)}$
a2	0.491	0.0117	
R2	4.35	0.114	Ohm
s1	6.56	0.108	$Ohm.s^{-1/2}$

Fitting Parameters for full range: 10mHz to 100kHz

circuit parameter	value	standard error	unit
L1	0.743	0.107	$H.s^{(a-1)}$
a1	0.102	0.00688	
R1	2.17	0.191	Ohm
Q2	0.00399	0.000501	$F.s^{(a - 1)}$
a2	0.491	0.0117	
R2	4.35	0.114	Ohm
s1	6.56	0.108	$Ohm.s^{-1/2}$

W4 (03)

Fitting Parameters up to 1 Hz

circuit parameter	value	standard error	unit
L1	0.0741	0.0723	$H.s^{(a-1)}$
a1	0.234	0.0355	
R1	4.02	0.272	Ohm
Q2	0.00971	0.0015	$F.s^{(a - 1)}$
a2	0.479	0.0171	
R2	16.4	1.91	Ohm
s1	8.65	0.744	$Ohm.s^{-1/2}$

Fitting Parameters for full range: 10mHz to 100kHz

circuit parameter	value	standard error	unit
L1	0.0741	0.0723	$H.s^{(a-1)}$
a1	0.234	0.0355	
R1	4.02	0.272	Ohm

Q2	0.00971	0.0015	$F.s^{(a - 1)}$
a2	0.479	0.0171	
R2	16.4	1.91	Ohm
s1	8.65	0.744	$Ohm.s^{-1/2}$

S4 (01)

Fitting Parameters up to 1 Hz

circuit parameter	value	standard error	unit
L1	0.777	0.158	$H.s^{(a-1)}$
a1	0.129	0.015	
R1	1.04	0.254	Ohm
Q2	0.00579	0.000536	$F.s^{(a - 1)}$
a2	0.436	0.00965	
R2	11.8	0.36	Ohm
s1	4.28	0.185	$Ohm.s^{-1/2}$

Fitting Parameters for full range: 10mHz to 100kHz

circuit parameter	value	standard error	unit
L1	0.777	0.158	$H.s^{(a-1)}$
a1	0.129	0.015	
R1	1.04	0.254	Ohm
Q2	0.00579	0.000536	$F.s^{(a - 1)}$
a2	0.436	0.00965	
R2	11.8	0.36	Ohm
s1	4.28	0.185	$Ohm.s^{-1/2}$

S4 (02)

Fitting Parameters up to 1 Hz

circuit parameter	value	standard error	unit
L1	0.143	0.0727	$H.s^{(a-1)}$
a1	0.173	0.0268	
R1	3.53	0.245	Ohm
Q2	0.0105	0.0021	$F.s^{(a - 1)}$
a2	0.456	0.0189	
R2	6.75	0.525	Ohm

s1	5.99	0.275	Ohm.s ^{-1/2}
----	------	-------	-----------------------

Fitting Parameters for full range: 10mHz to 100kHz

circuit parameter	value	standard error	unit
L1	0.143	0.0727	H.s ^(a-1)
a1	0.173	0.0268	
R1	3.53	0.245	Ohm
Q2	0.0105	0.0021	F.s ^(a - 1)
a2	0.456	0.0189	
R2	6.75	0.525	Ohm
s1	5.99	0.275	Ohm.s ^{-1/2}

S4 (03)

Fitting Parameters up to 1 Hz

circuit parameter	value	standard error	unit
L1	0.0385	0.0199	H.s ^(a-1)
a1	0.241	0.025	
R1	3.56	0.126	Ohm
Q2	0.011	0.00209	F.s ^(a - 1)
a2	0.479	0.0183	
R2	5.67	0.427	Ohm
s1	8.29	0.32	Ohm.s ^{-1/2}

Fitting Parameters for full range: 10mHz to 100kHz

circuit parameter	value	standard error	unit
L1	0.0385	0.0199	H.s ^(a-1)
a1	0.241	0.025	
R1	3.56	0.126	Ohm
Q2	0.011	0.00209	F.s ^(a - 1)
a2	0.479	0.0183	
R2	5.67	0.427	Ohm
s1	8.29	0.32	Ohm.s ^{-1/2}

H.2.1 High Error Samples from Fitting

Parameter: L1 (High Error Samples: 3)

sample	parameter	error > value	error > 5 x value	error	value
S1_02	L1	True	False	0.136	0.102
W3_01	L1	True	False	0.14	0.0739
W3_03	L1	True	False	0.0017	0.0011

Parameter: a1 (High Error Samples: 5)

sample	parameter	error > value	error > 5 x value	error	value
W1_01	a1	True	False	0.207	0.104
W1_02	a1	True	False	0.00066	0.00016
W1_03	a1	True	True	0.339	0.0155
S1_03	a1	True	False	0.418	0.114
S2_03	a1	True	False	0.267	0.104

Parameter: R1 (High Error Samples: 1)

sample	parameter	error > value	error > 5 x value	error	value
W2_01	R1	True	False	0.56	0.367

Parameter: Q2 (High Error Samples: 1)

sample	parameter	error > value	error > 5 x value	error	value
S2_02	Q2	True	False	0.00147	0.00093

Parameter: R2 (High Error Samples: 8)

sample	parameter	error > value	error > 5 x value	error	value
W1_03	R2	True	True	1890000000000.0	1.11
S1_03	R2	True	False	34.1	18.2
W2_01	R2	True	False	150.0	135.0
W2_03	R2	True	True	240000000.0	2.65
S2_01	R2	True	True	1.8e+17	2350000000.0
S2_03	R2	True	True	384000000000.0	9.42
W3_03	R2	True	True	5490000000000.0	19.6

W4_01	R2	True	False	1.97e+17	9.96e+16
-------	----	------	-------	----------	----------

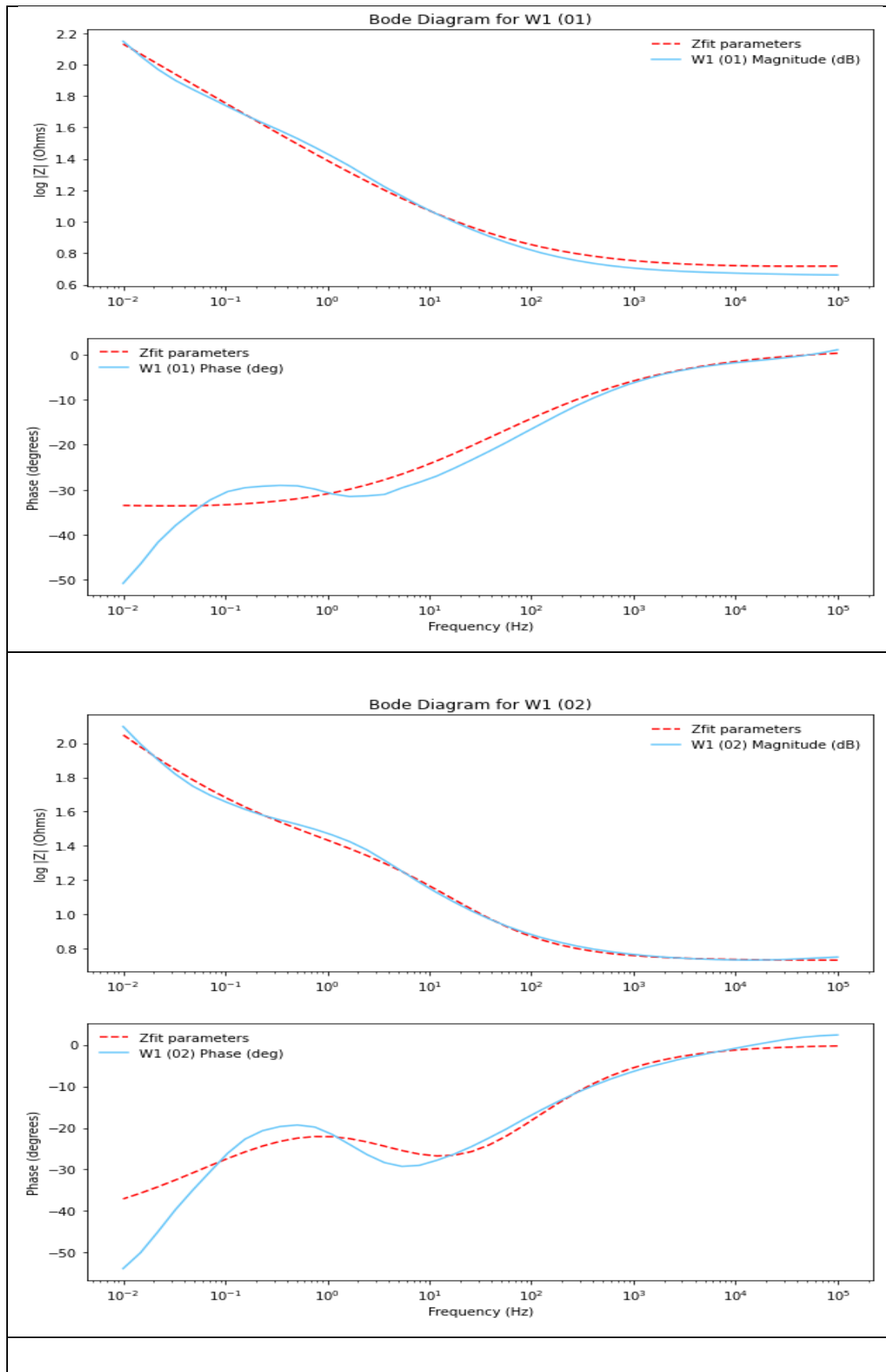
Parameter: s1 (High Error Samples: 11)

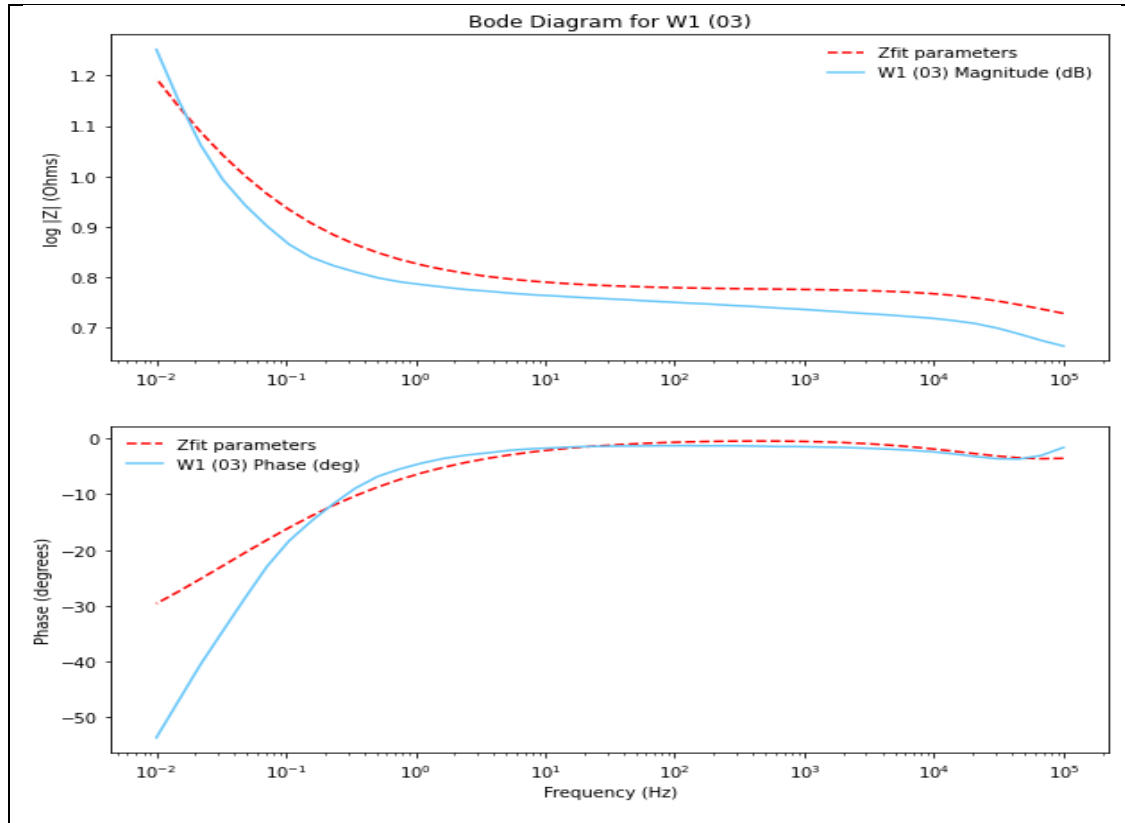
sample	parameter	error > value	error > 5 x value	error	value
W1_01	s1	True	True	2480000000000000.0	66.7
S1_01	s1	True	True	2.24e+26	5.48e+17
S1_02	s1	True	True	1.66e+22	6950000000000000.0
W2_01	s1	True	False	82.5	51.1
W2_02	s1	True	False	1.46e+17	1.42e+17
W2_03	s1	True	True	1.08e+16	548.0
S2_01	s1	True	True	5.43e+27	5.57e+16
S2_03	s1	True	True	643000000000000.0	46.7
W3_03	s1	True	True	6220000000000000.0	345.0
S3_01	s1	True	False	243.0	95.9
S3_03	s1	True	True	92500000000000.0	85.4

H.3 Bode Diagrams

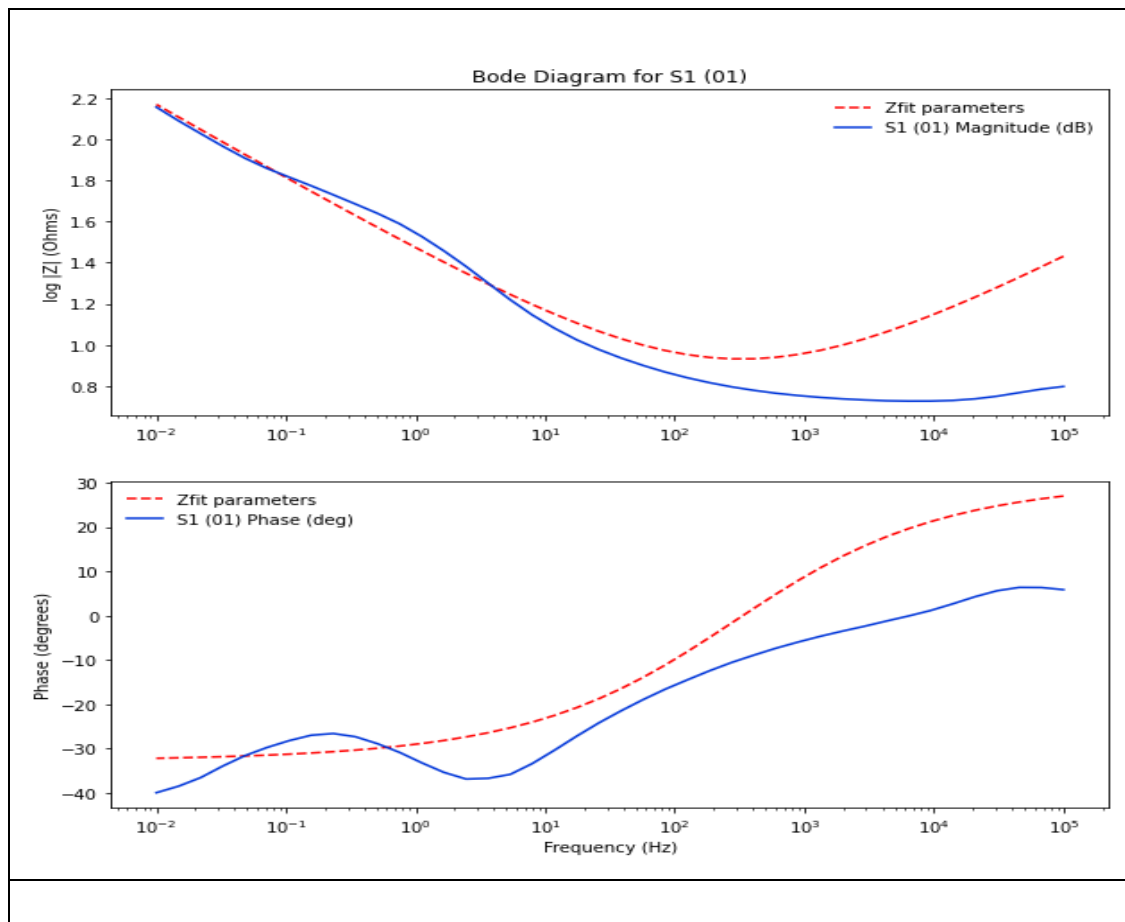
W1 : Bode Diagrams

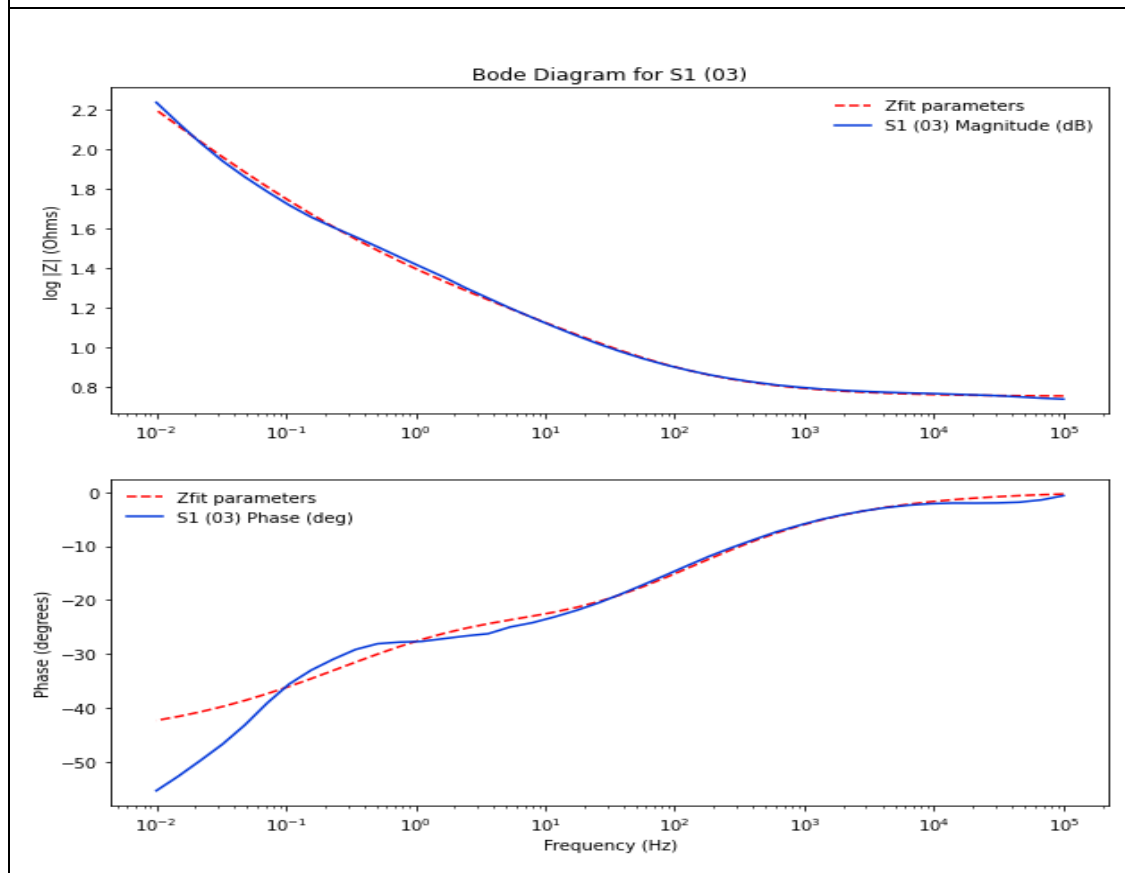
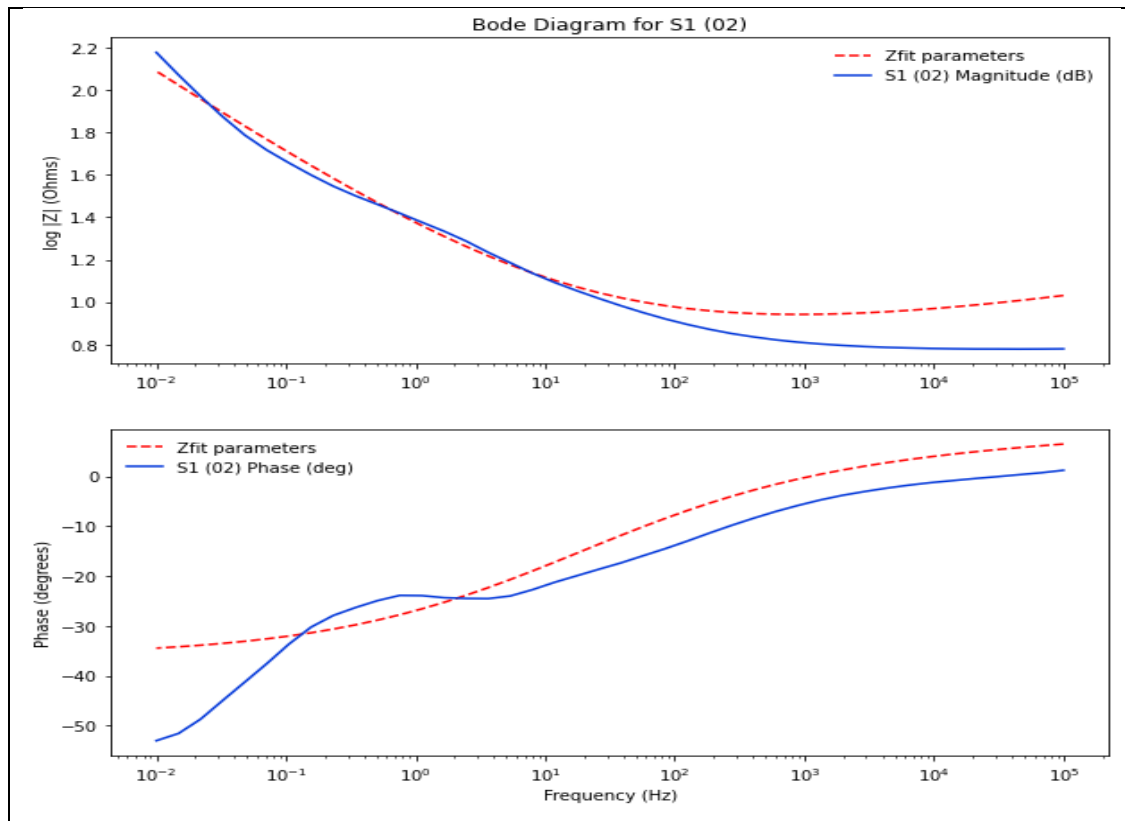
--





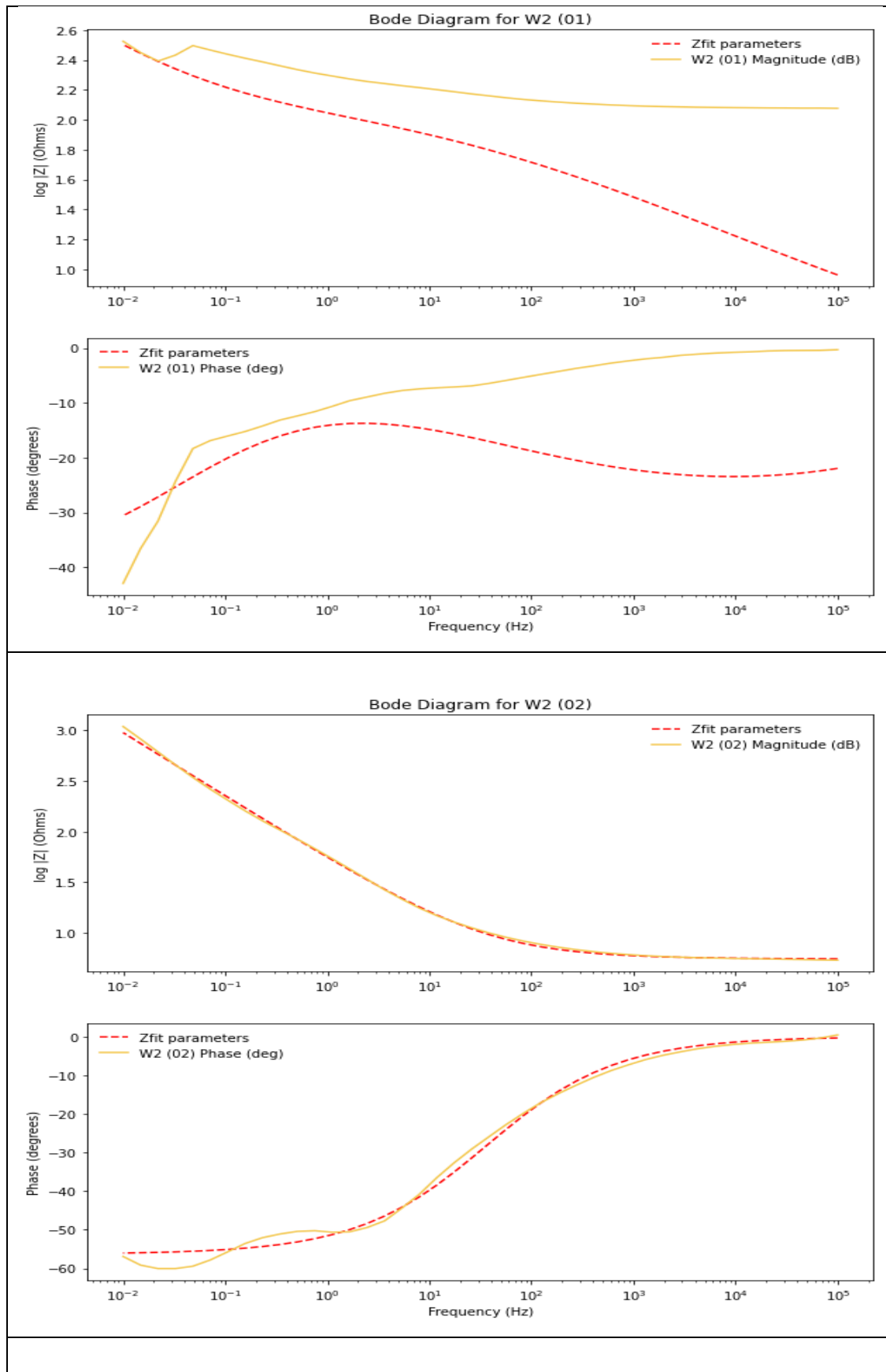
S1 : Bode Diagrams

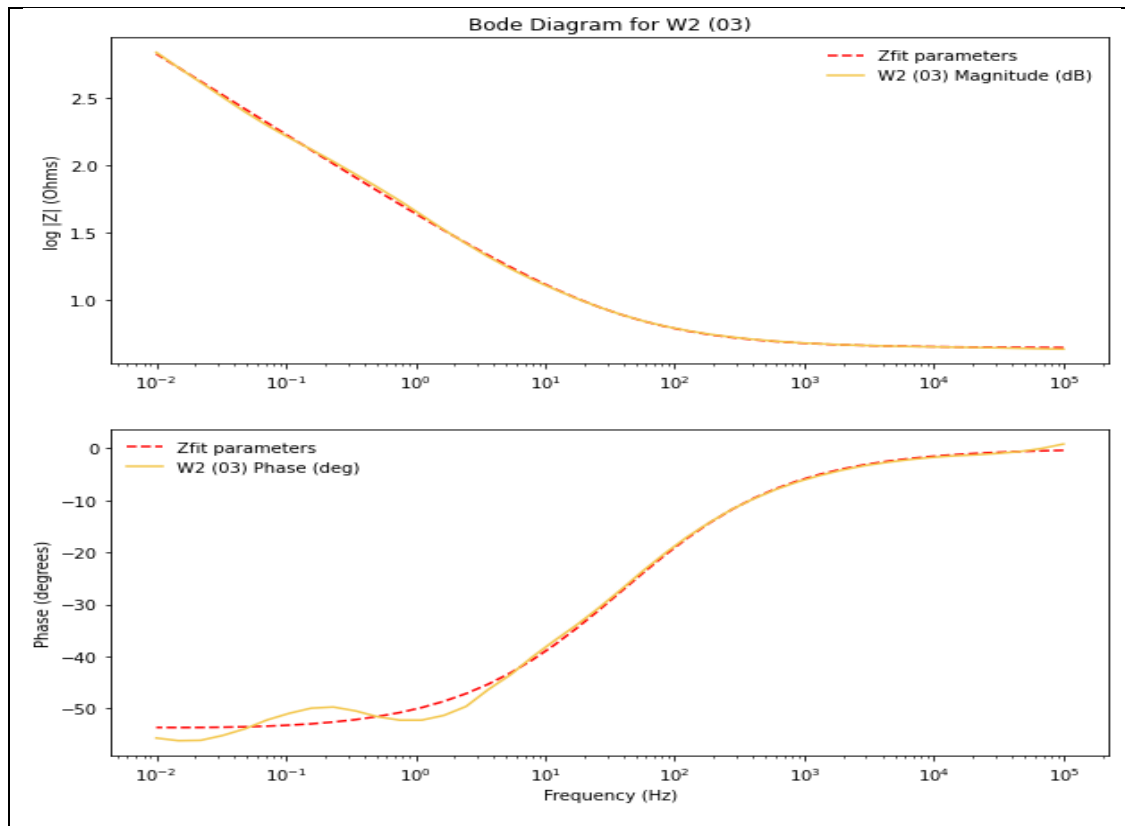




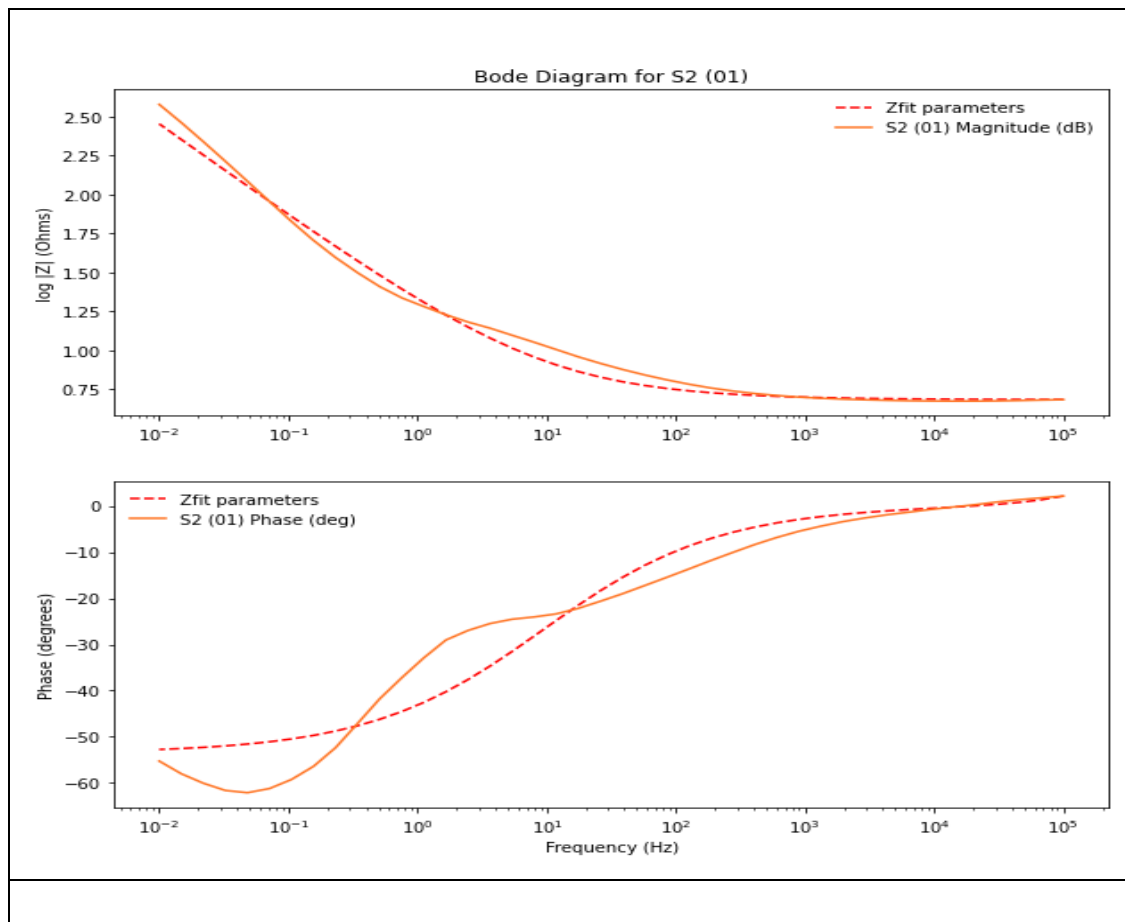
W2 : Bode Diagrams

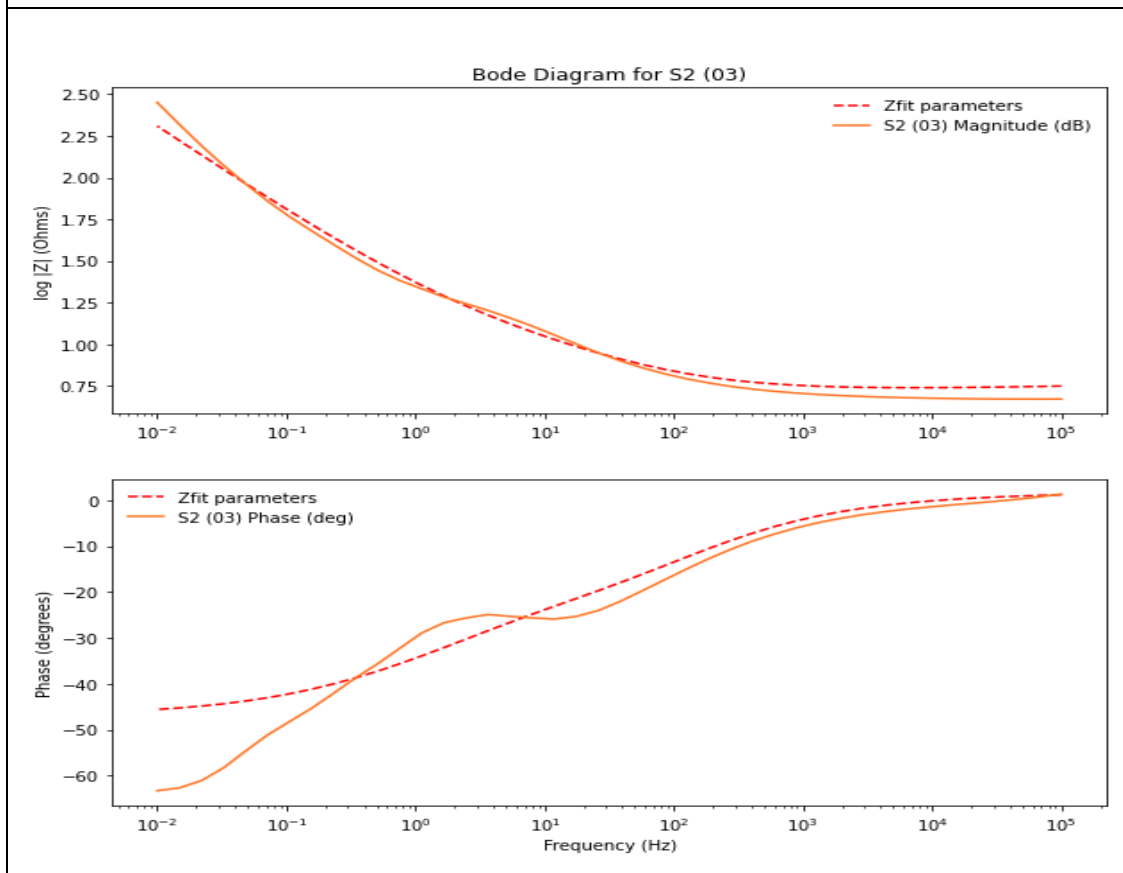
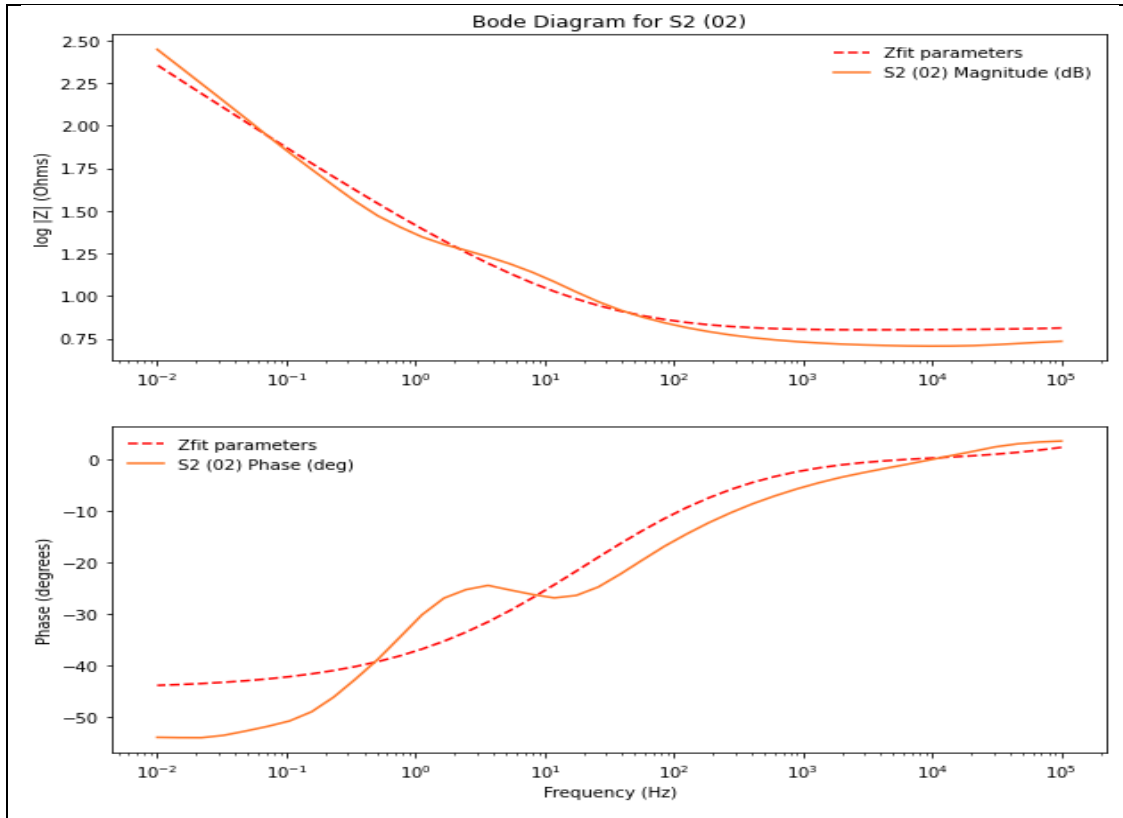






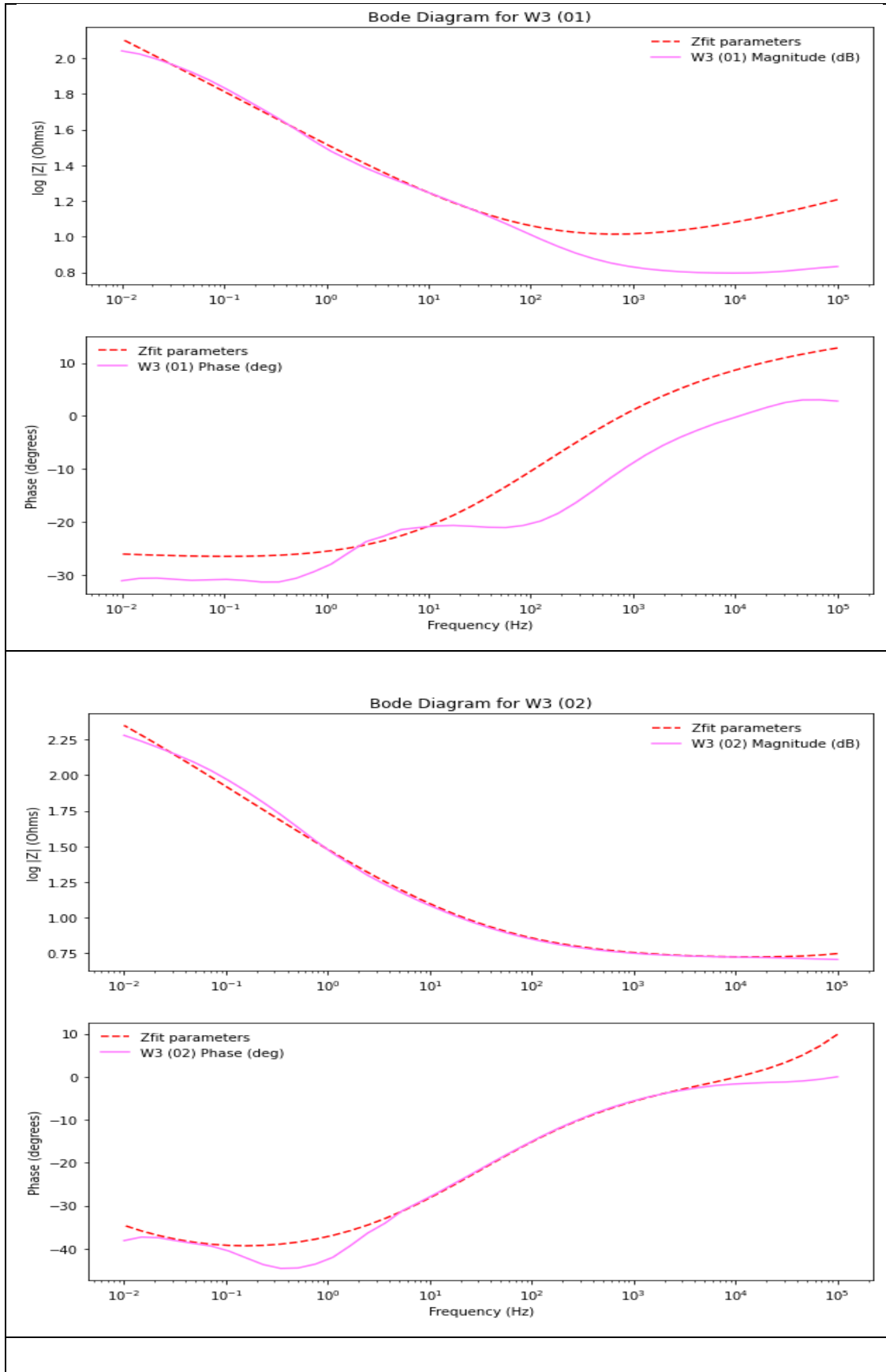
S2 : Bode Diagrams

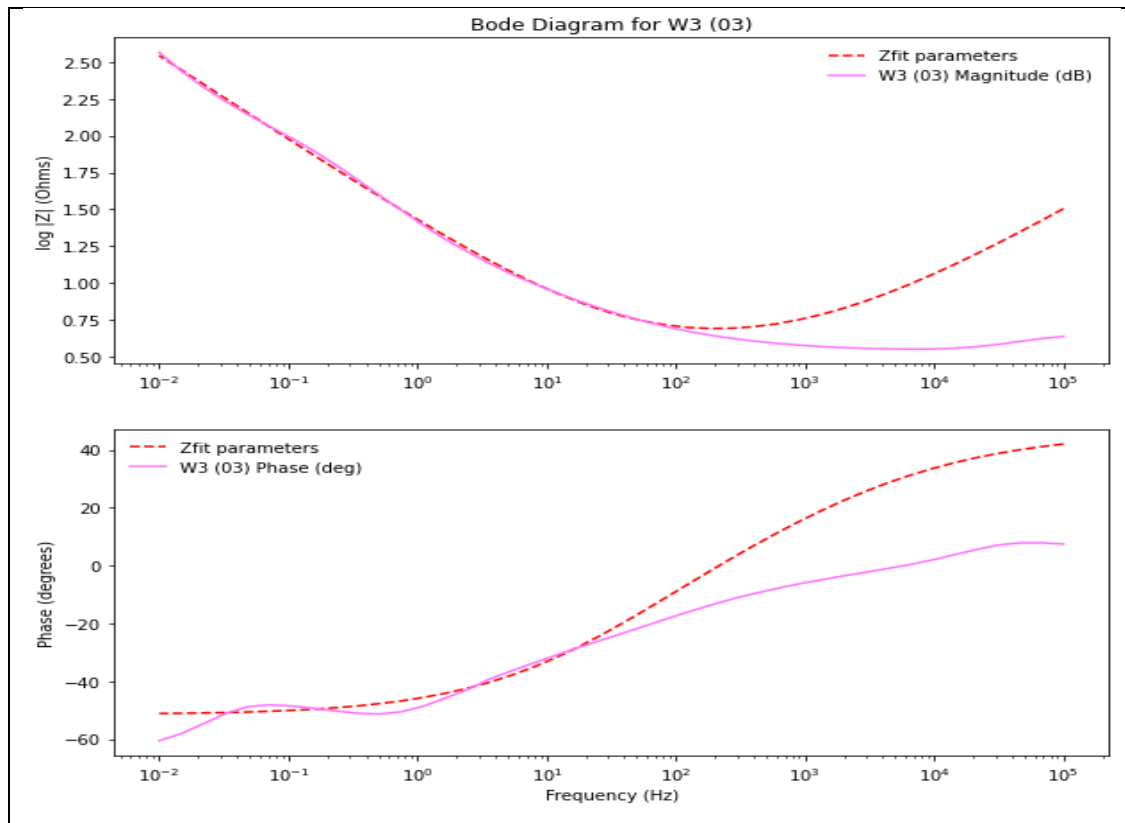




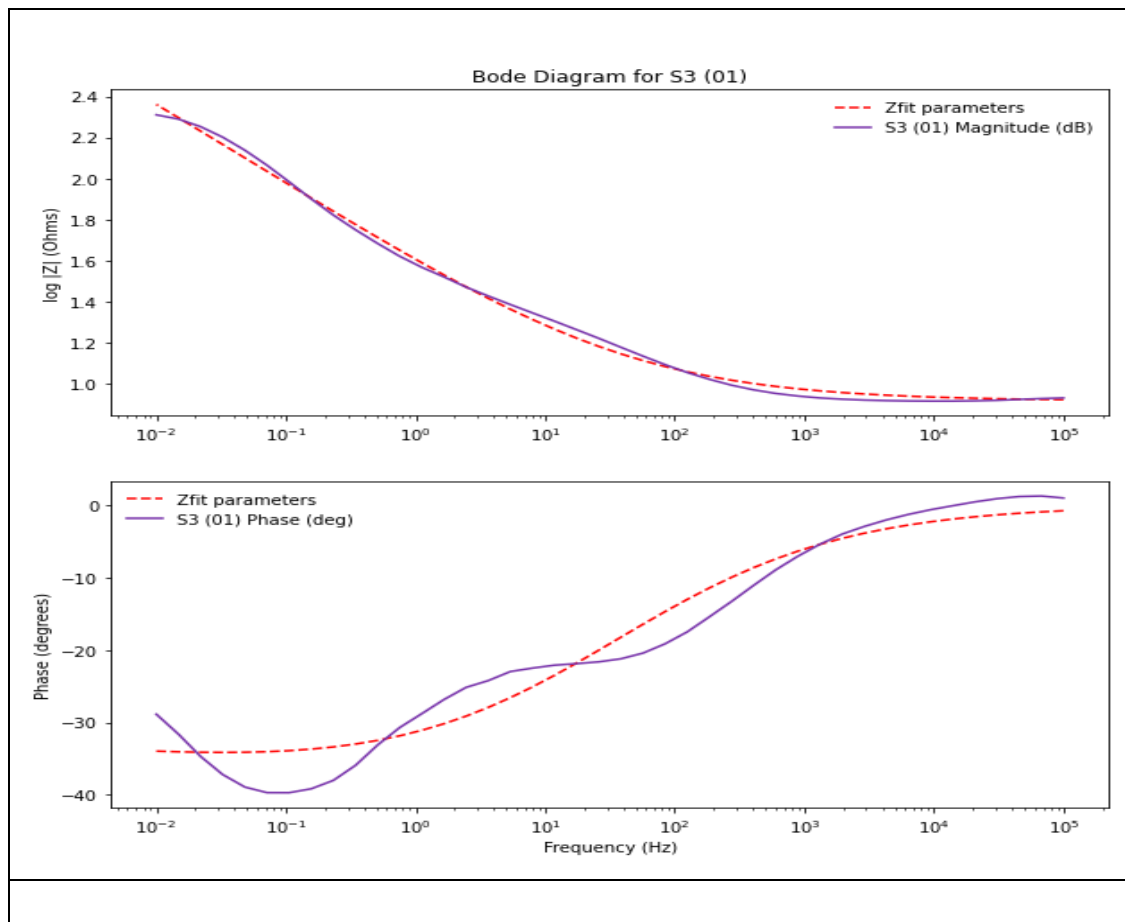
W3 : Bode Diagrams

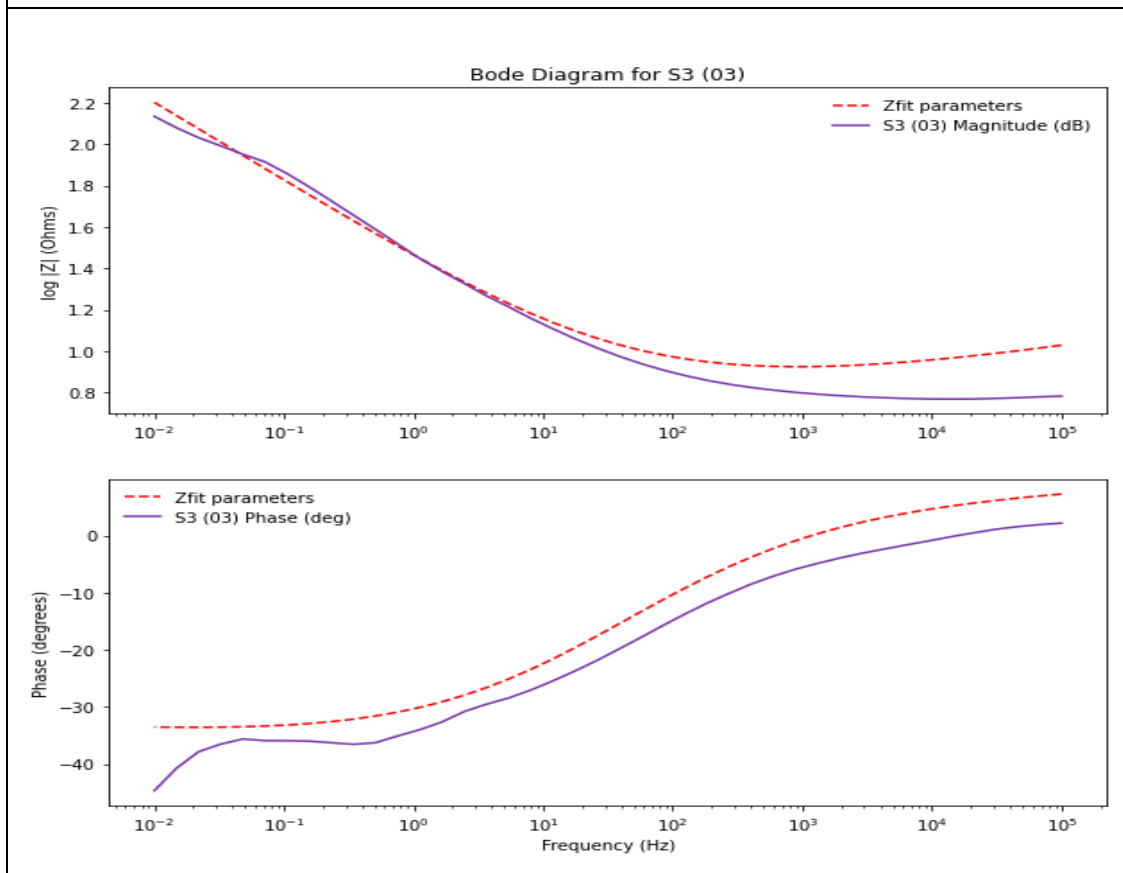
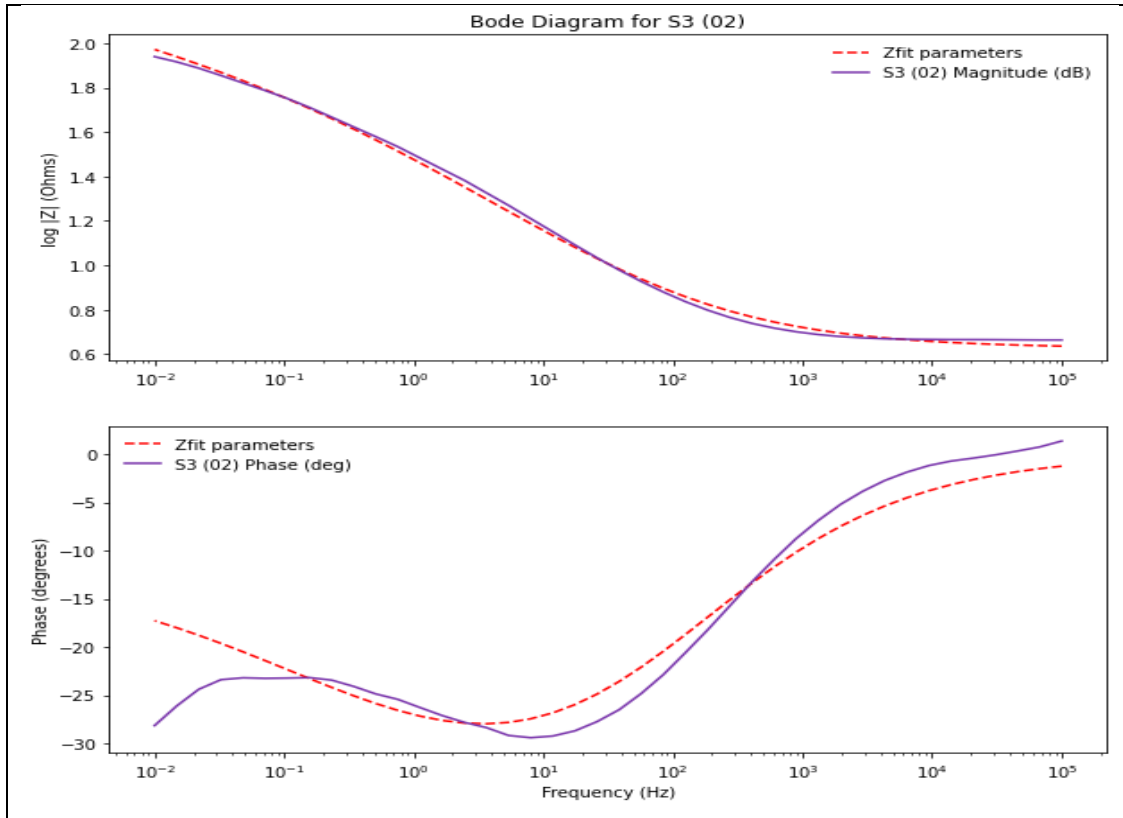






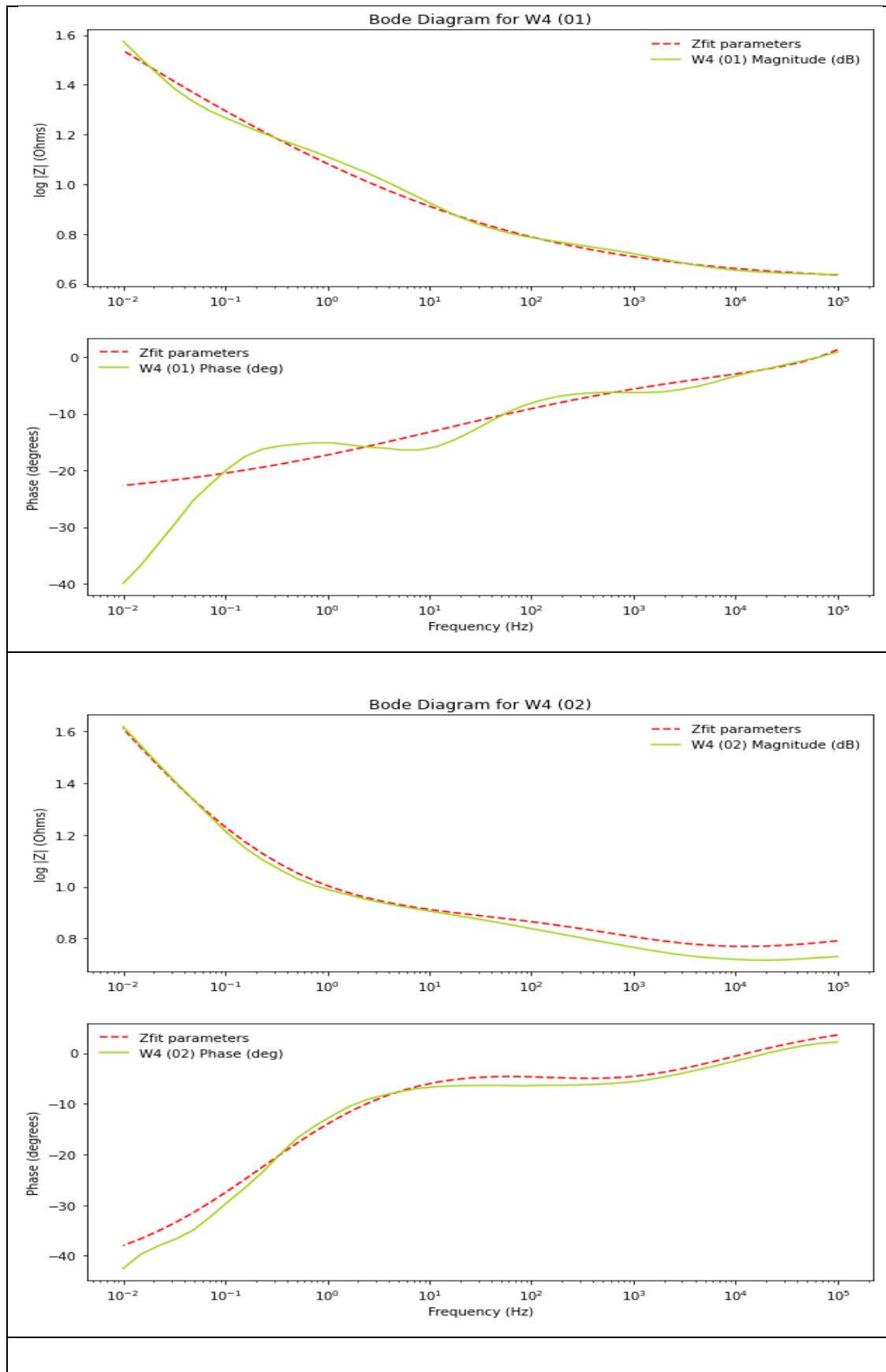
S3 : Bode Diagrams

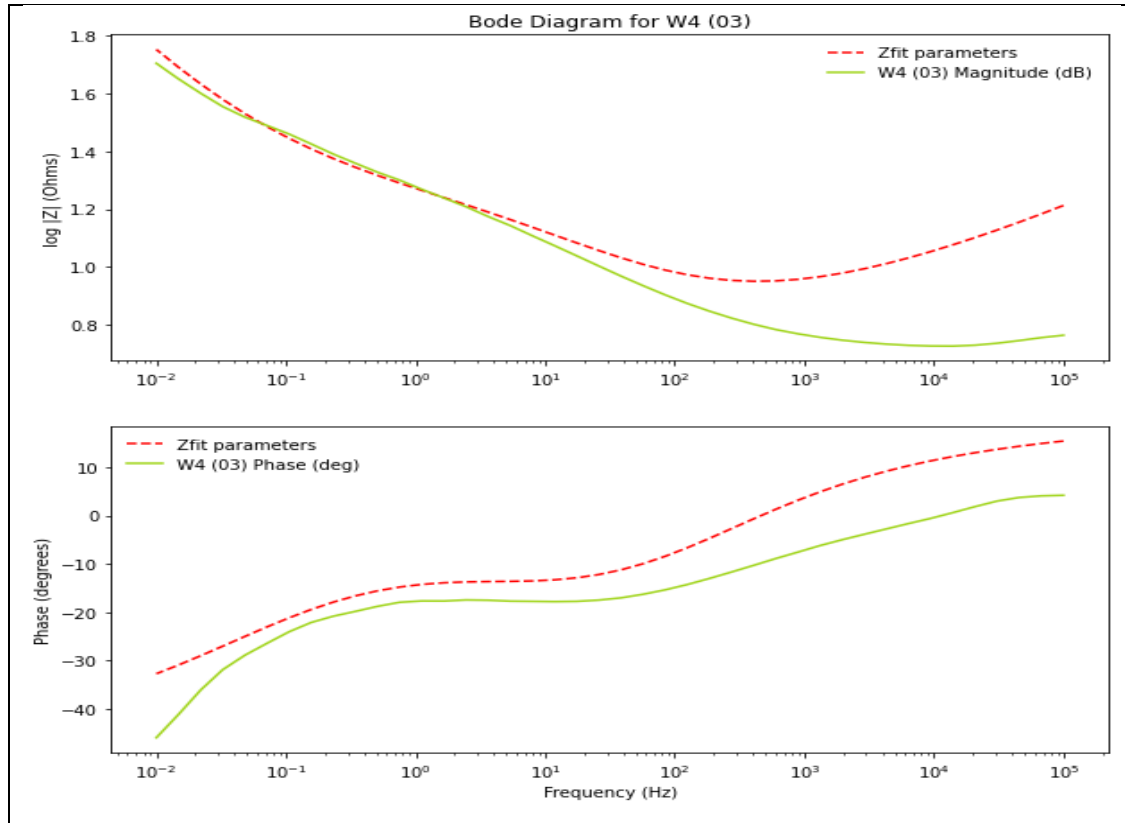




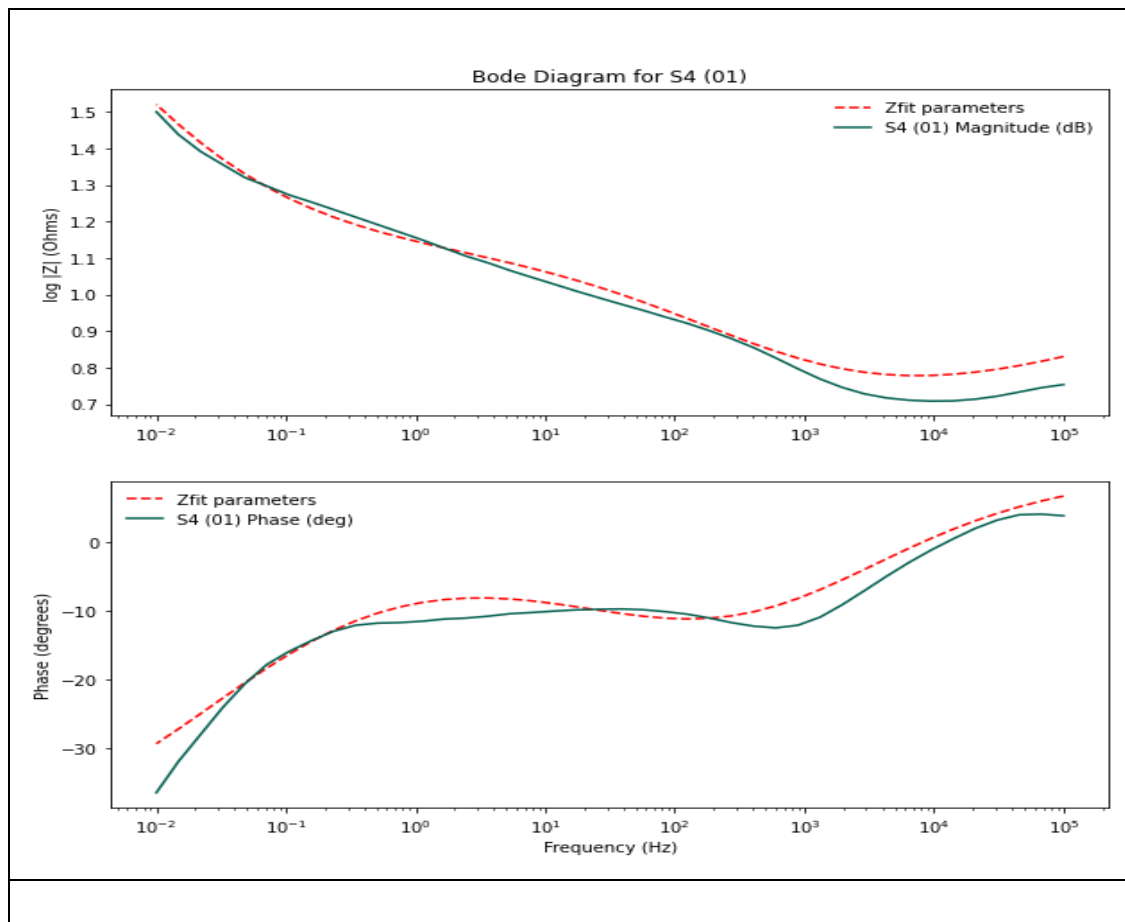
W4 : Bode Diagrams

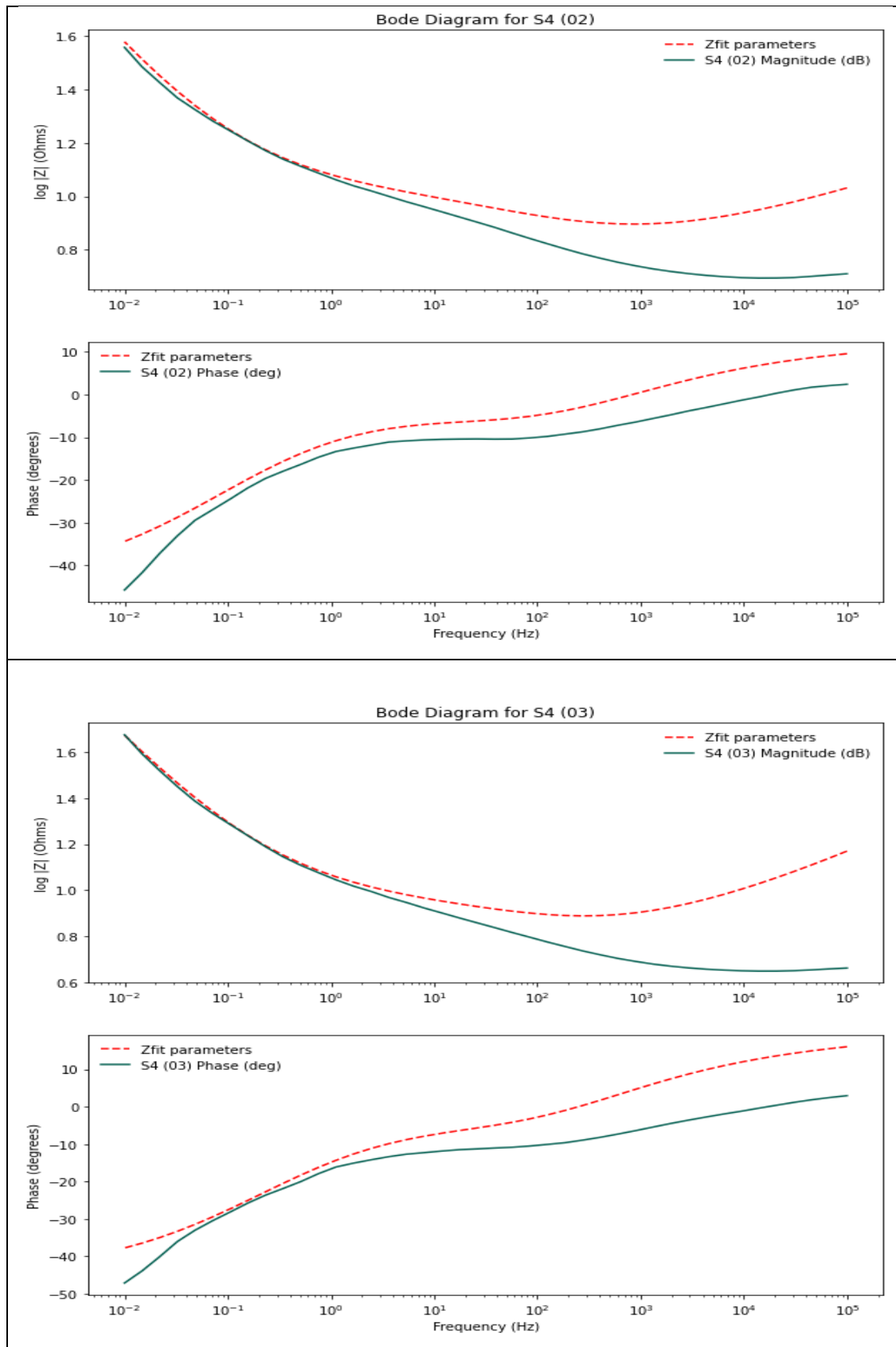






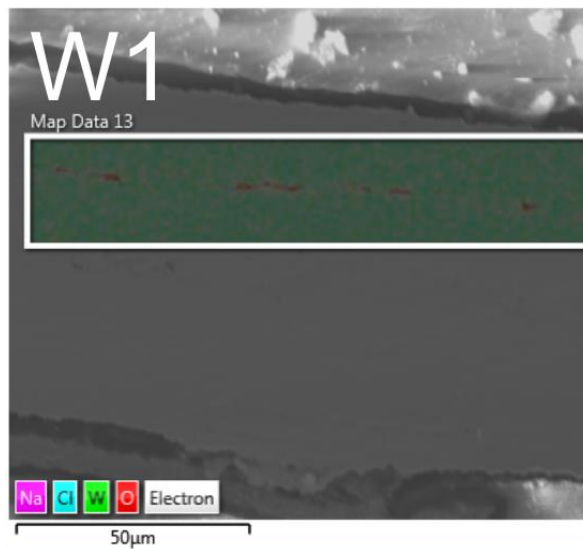
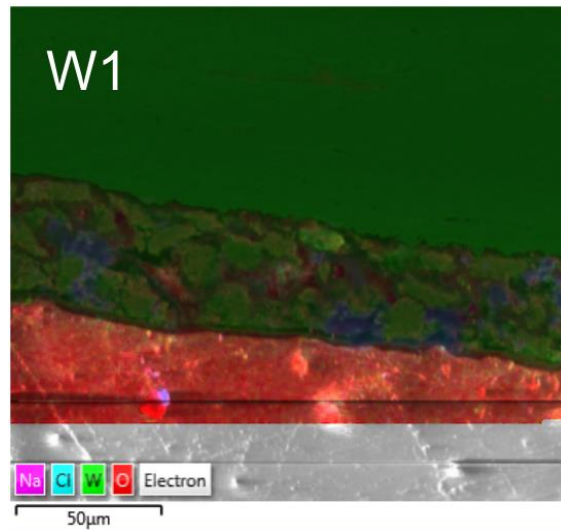
S4 : Bode Diagrams



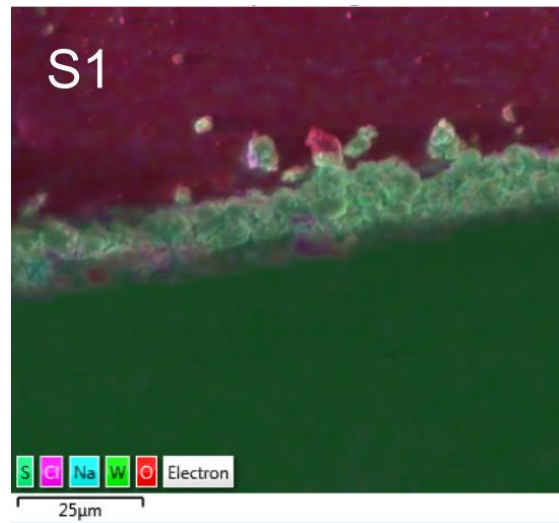
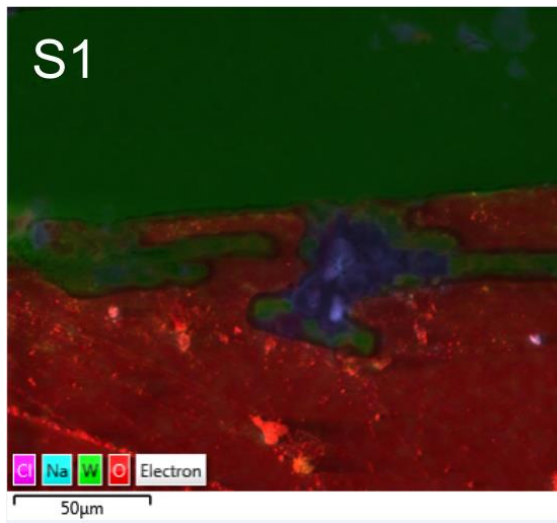


Appendix I EDX Data of samples from Chapter 4

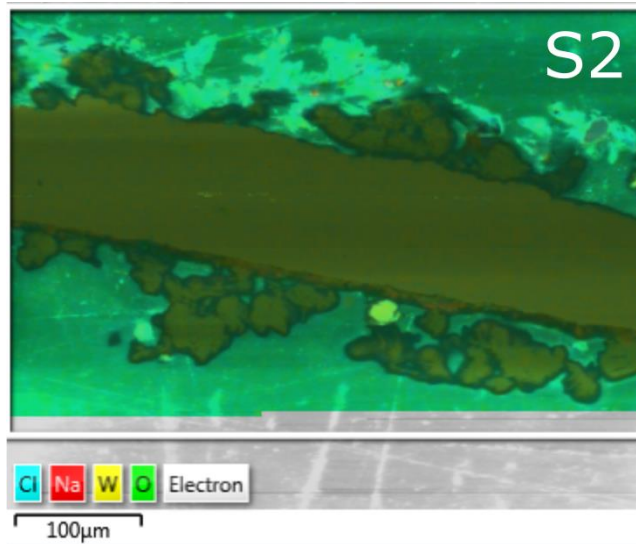
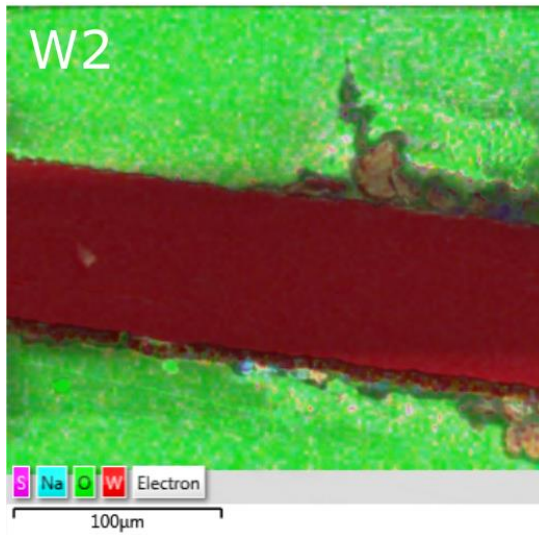
I.1.1 NaCl



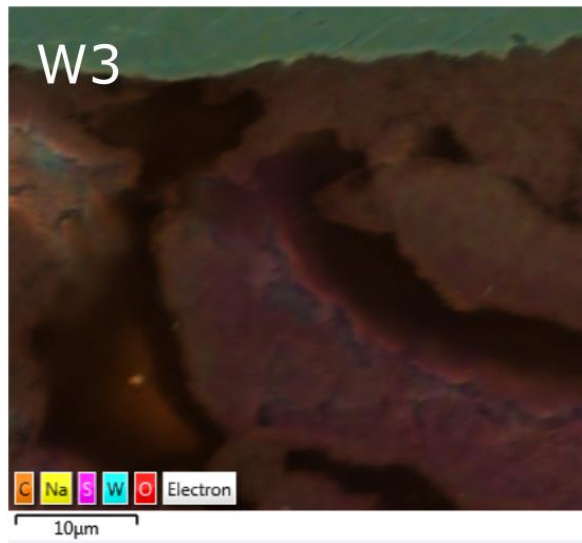
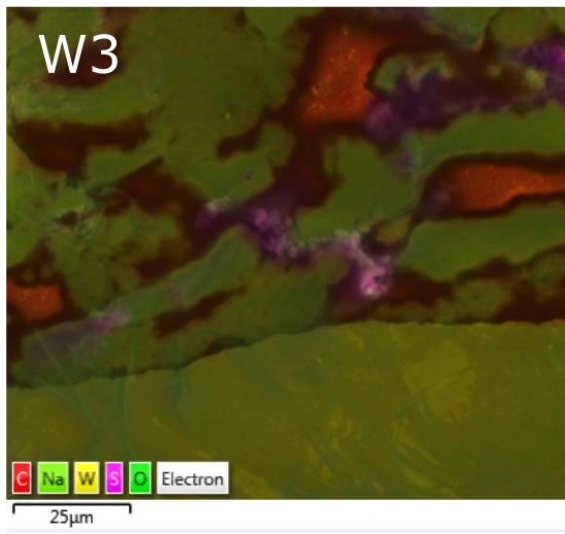
I.1.2 S1



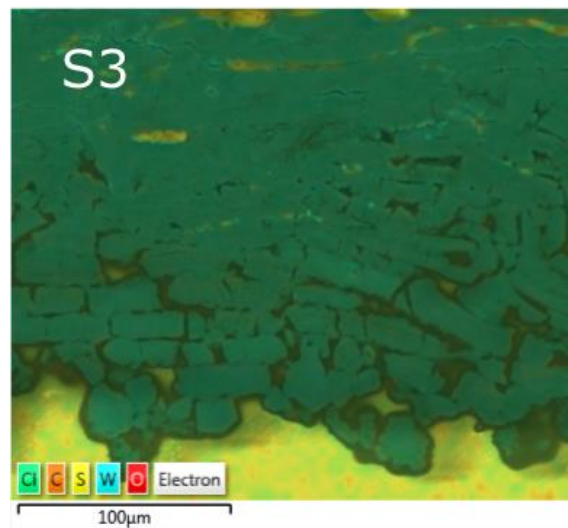
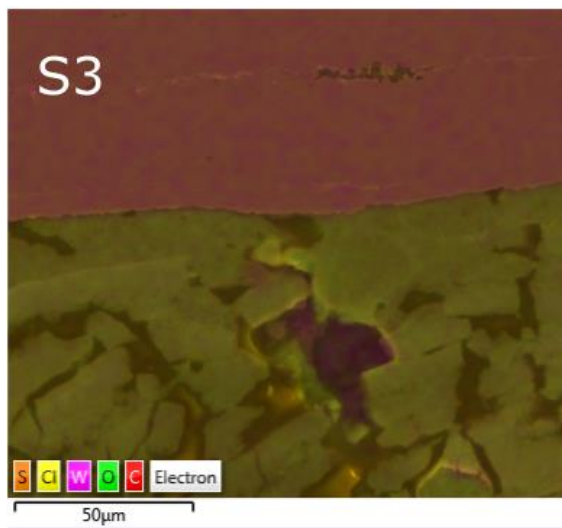
I.1.3 Na₂SO₄ Samples W2 and S2



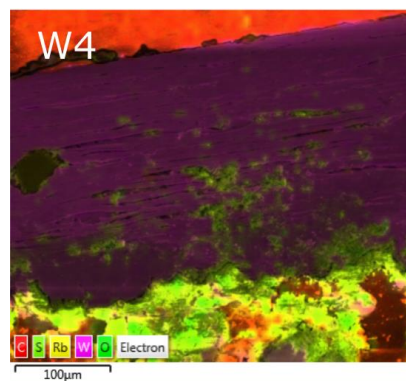
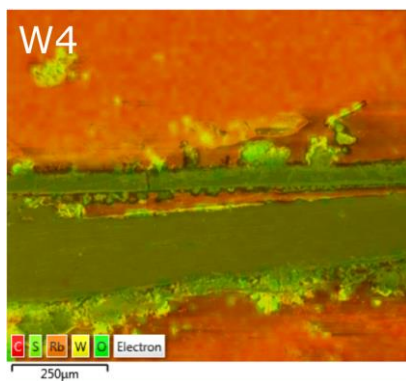
I.1.4 W3

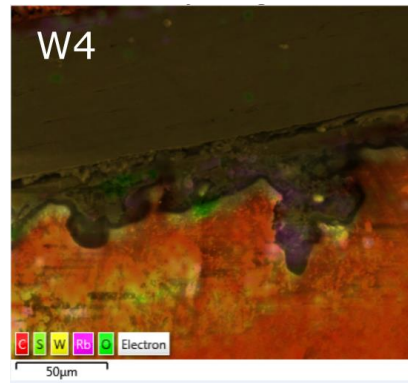
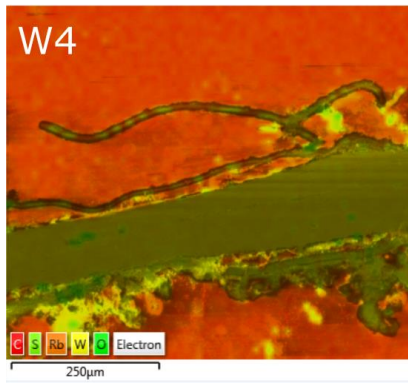


I.1.5 S3

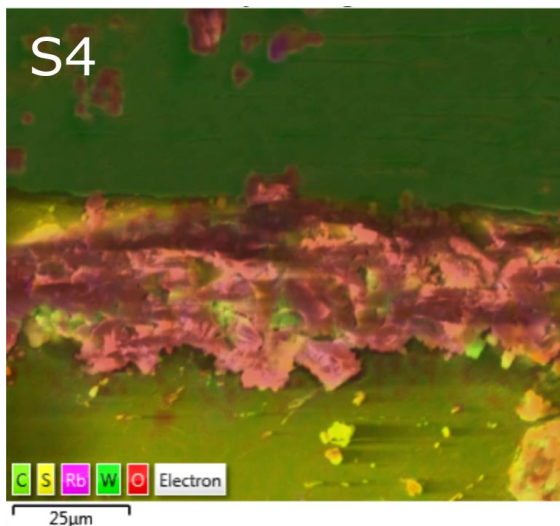
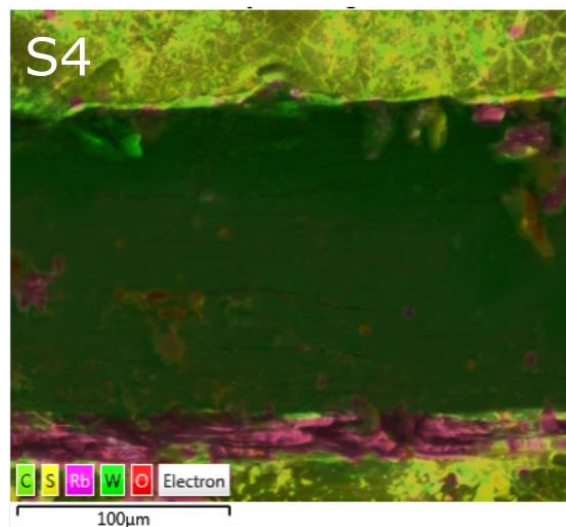
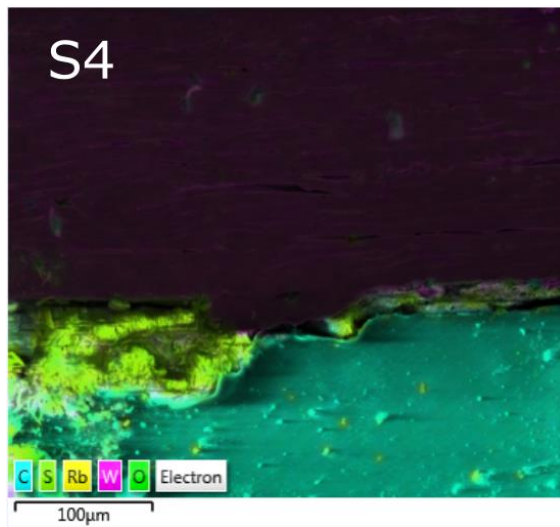


I.1.6 W4





I.1.7 S4

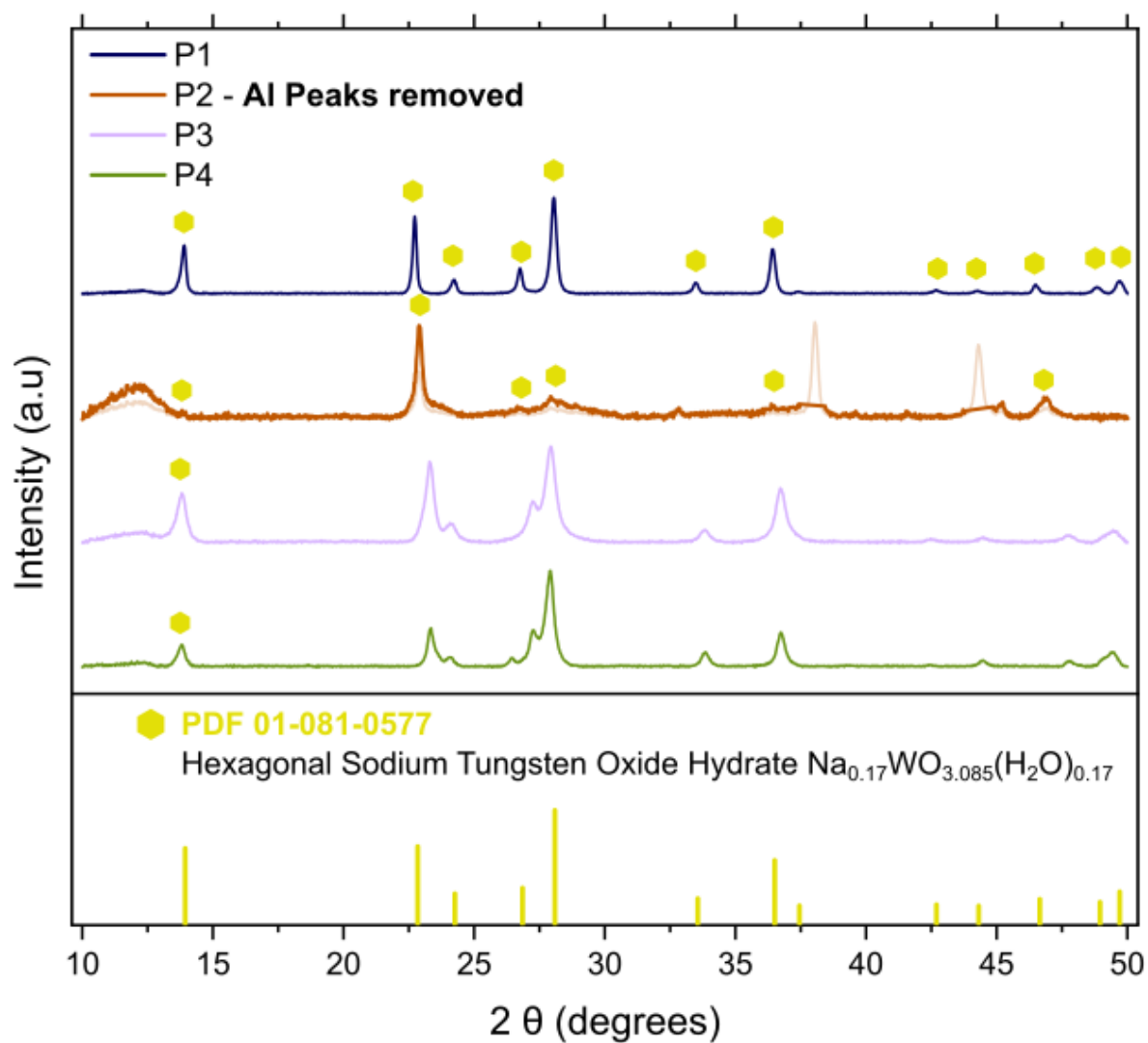


I.2 Cross Sectional SEM Thickness Results

Sample	Measured Data (μm)					Mean Value (μm)
W	147.624	148.594	152.44	149.527	148.594	149.36
S	73.955	72.643	71.581	72.933	74.257	73.07
W1	77.982	74.505	74.276	75.107	76.672	75.71
S1	no data					
W2	76.13	76.27	75.33	74.48	75.55	75.55
S2	101.12	103.94	106.86	95.54	100.01	101.49
W3	76.529	78.079	81.694	72.897	75.48	76.94
S3	73.963	65.495	70.531	115.325	82.635	81.59
W4	245.031	251.979	262.011	253.214	240.121	250.47
S4	142.961	145.091	144.532	138.782	144.9	143.25

Appendix J X-ray diffraction Additional PDF Files

J.1 Aluminium Peaks present in Na₂SO₄-directed samples



Appendix K Active masses of binder-free powder electrodes

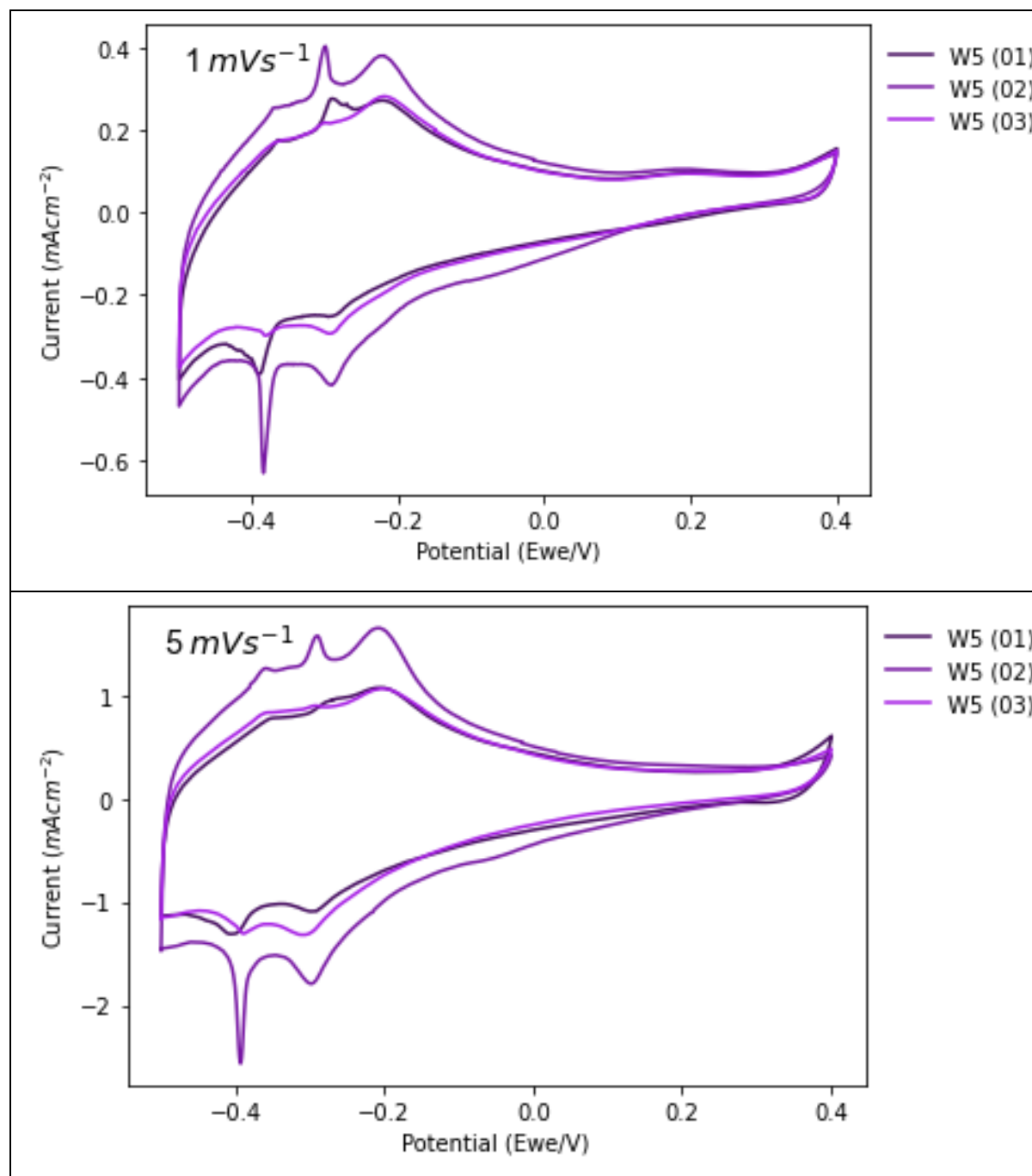
sample	Active mass (mass)
1 P1 (01)	0.0019
2 P1 (02)	0.0039
3 P1 (03)	0.0019
4 P2 (01)	0.0024
5 P2 (02)	0.0023
6 P2 (03)	0.0018
10 P3 (01)	0.0023

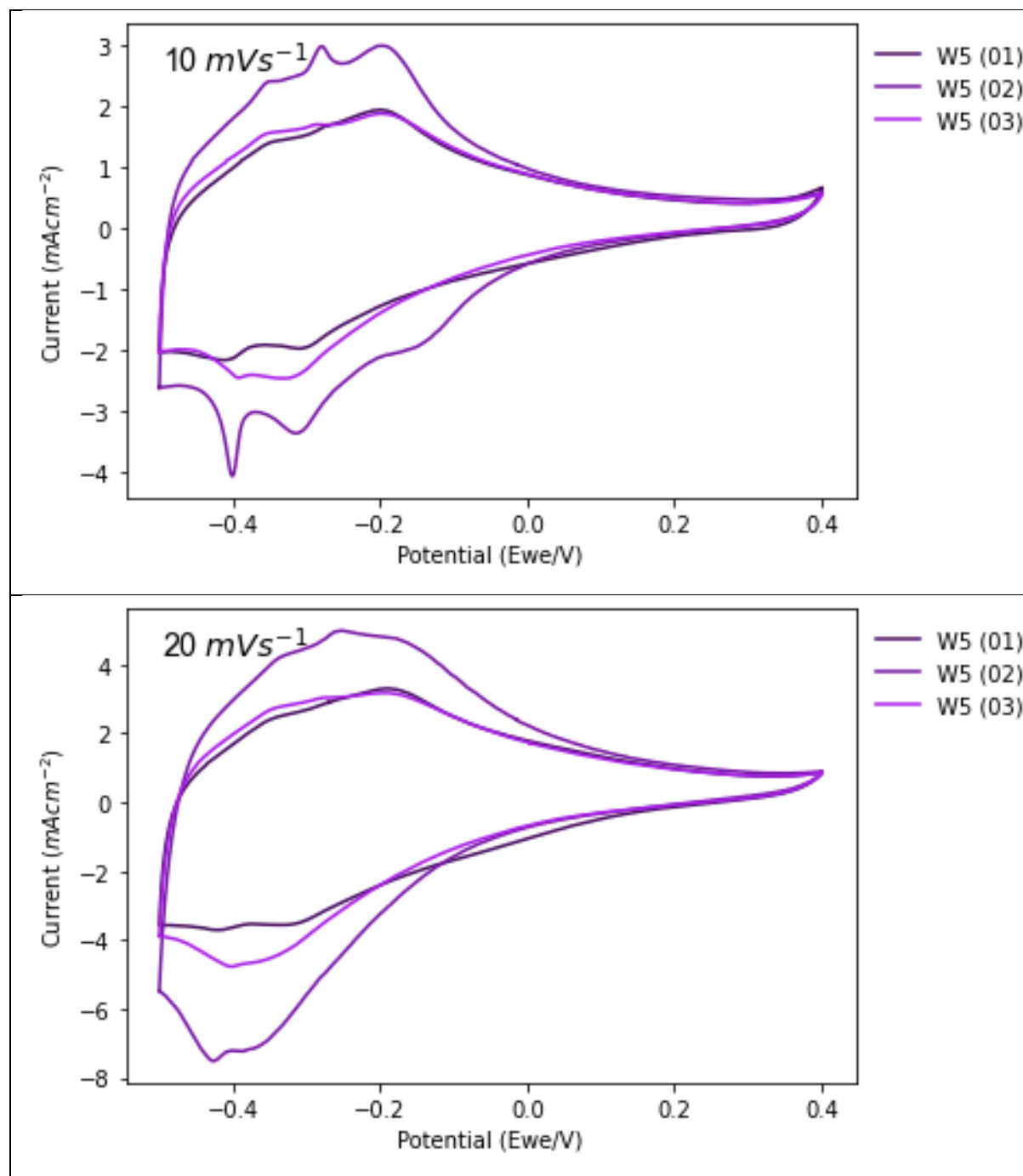
11	P3 (02)	0.0032
12	P3 (03)	0.0021
13	P3 (04)	0.0032
7	P4 (01)	0.0052
8	P4 (02)	0.0020
9	P4 (03)	0.0021
6	S1 (01)	0.0200
8	S1 (02)	0.0400
10	S1 (03)	0.0200
0	S2 (01)	0.0200
2	S2 (02)	0.0300
4	S2 (03)	0.0400
12	S3 (01)	0.2600
14	S3 (02)	0.1800
16	S3 (03)	0.1500
18	S4 (01)	0.0300
20	S4 (02)	0.0300
22	S4 (03)	0.0600
7	W1 (01)	0.0100
9	W1 (02)	0.0300
11	W1 (03)	0.0200
1	W2 (01)	0.0200
3	W2 (02)	0.0300
5	W2 (03)	0.0200
13	W3 (01)	0.2000
15	W3 (02)	0.1100
17	W3 (03)	0.1400
19	W4 (01)	0.0500
21	W4 (02)	0.0500
23	W4 (03)	0.0400

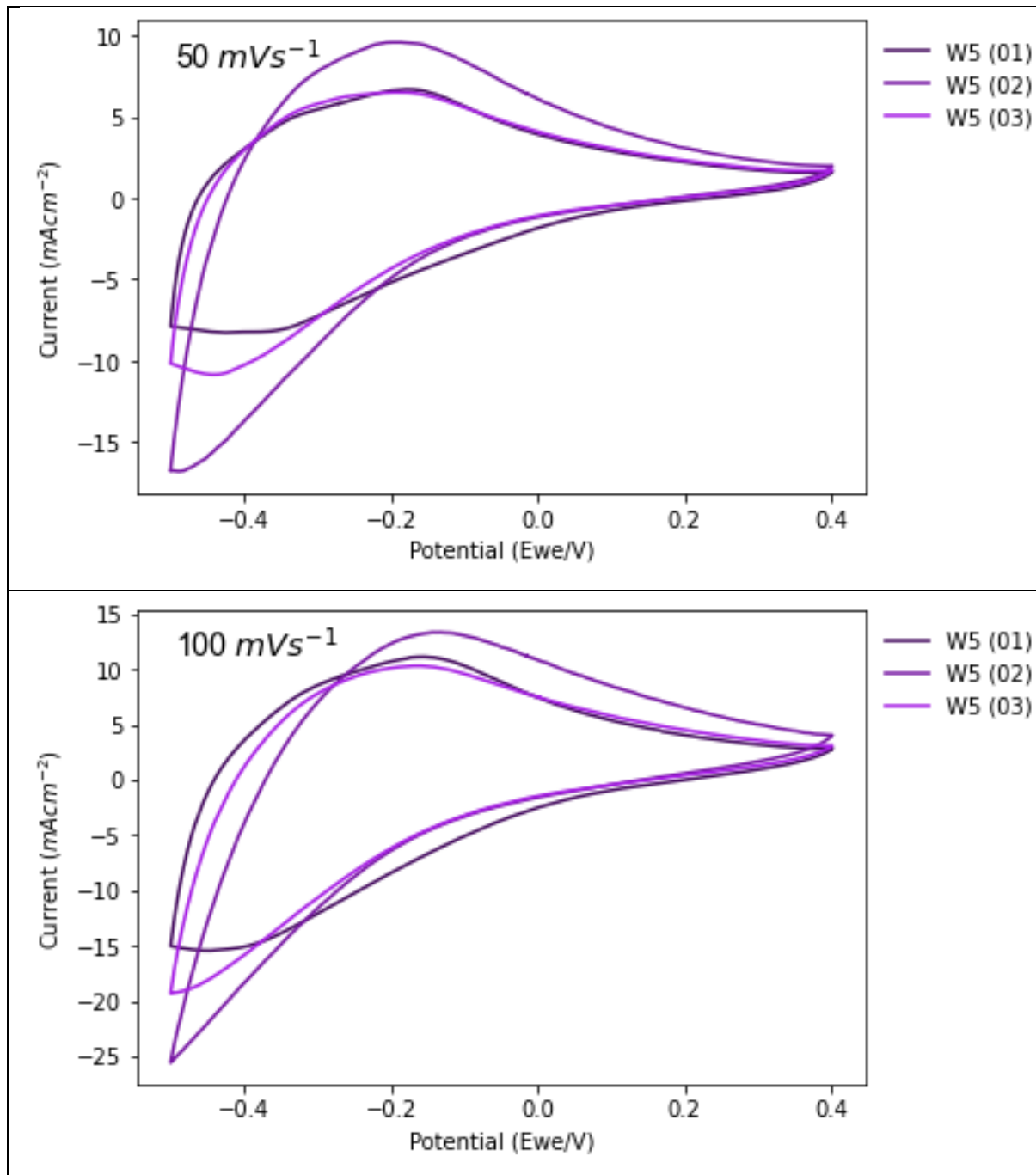
Appendix L Full Cyclic Voltammetry data from Chapter 6

L.1 Iteration 1

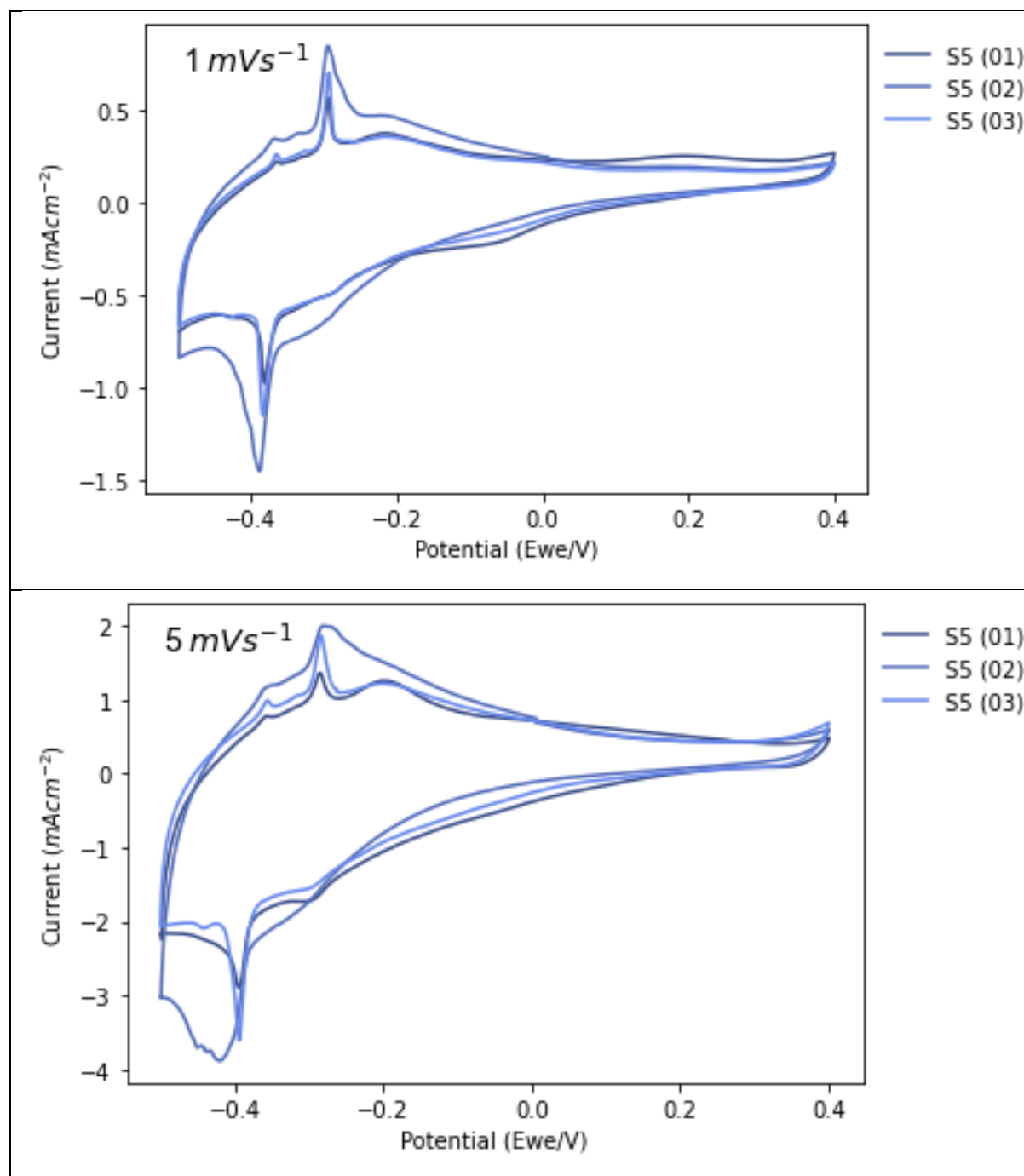
L.1.1 W5

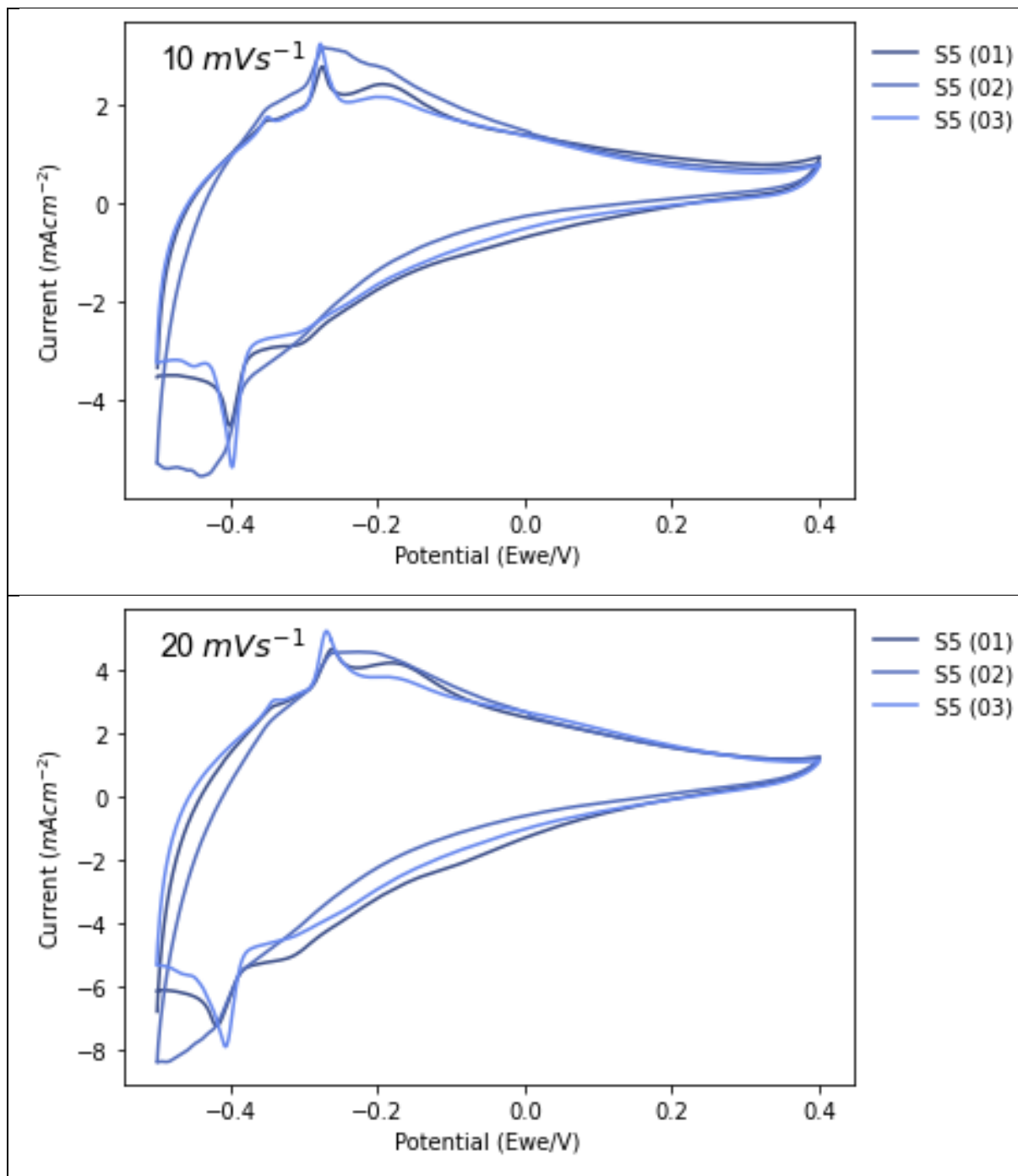


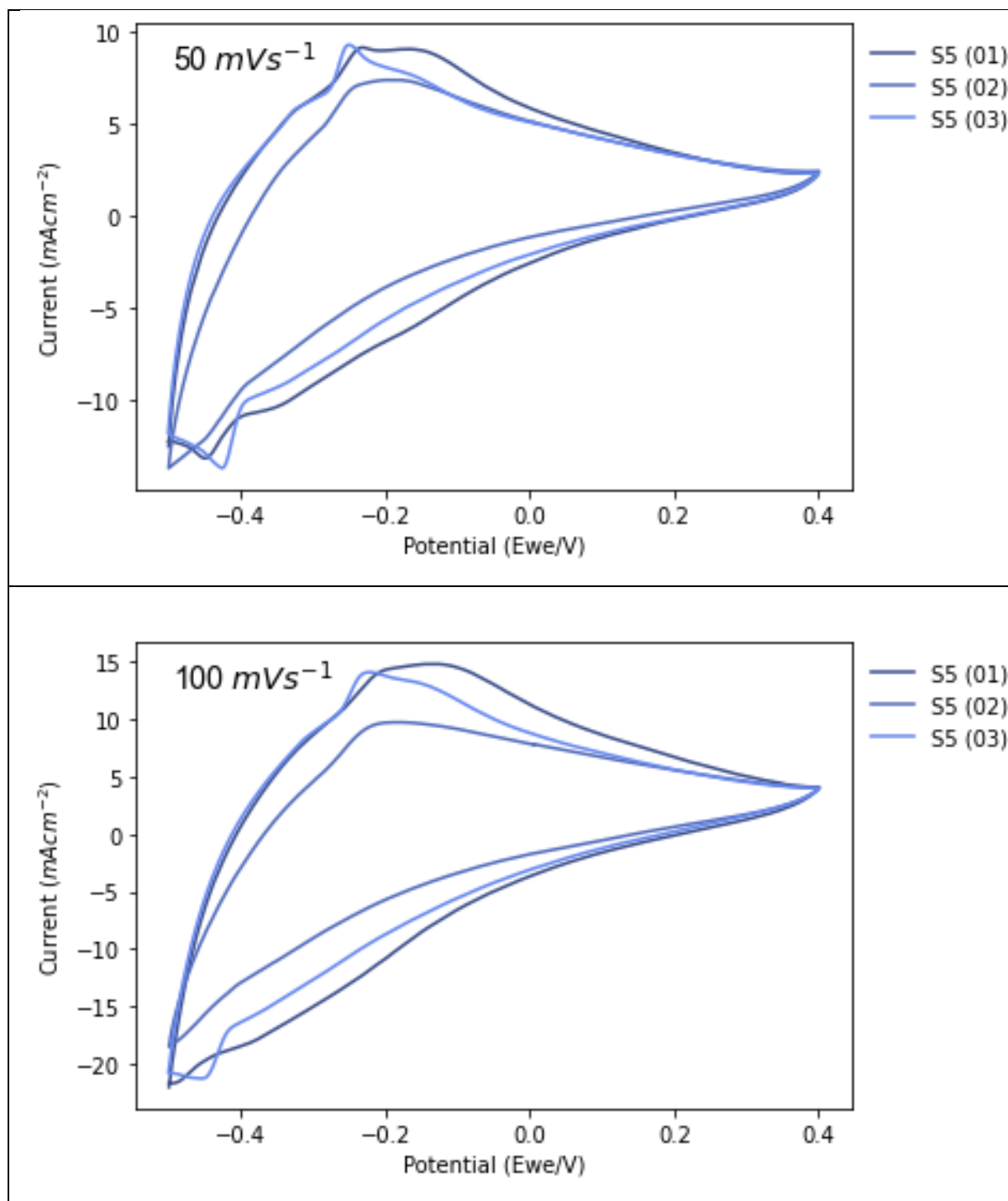




L.1.2 S5

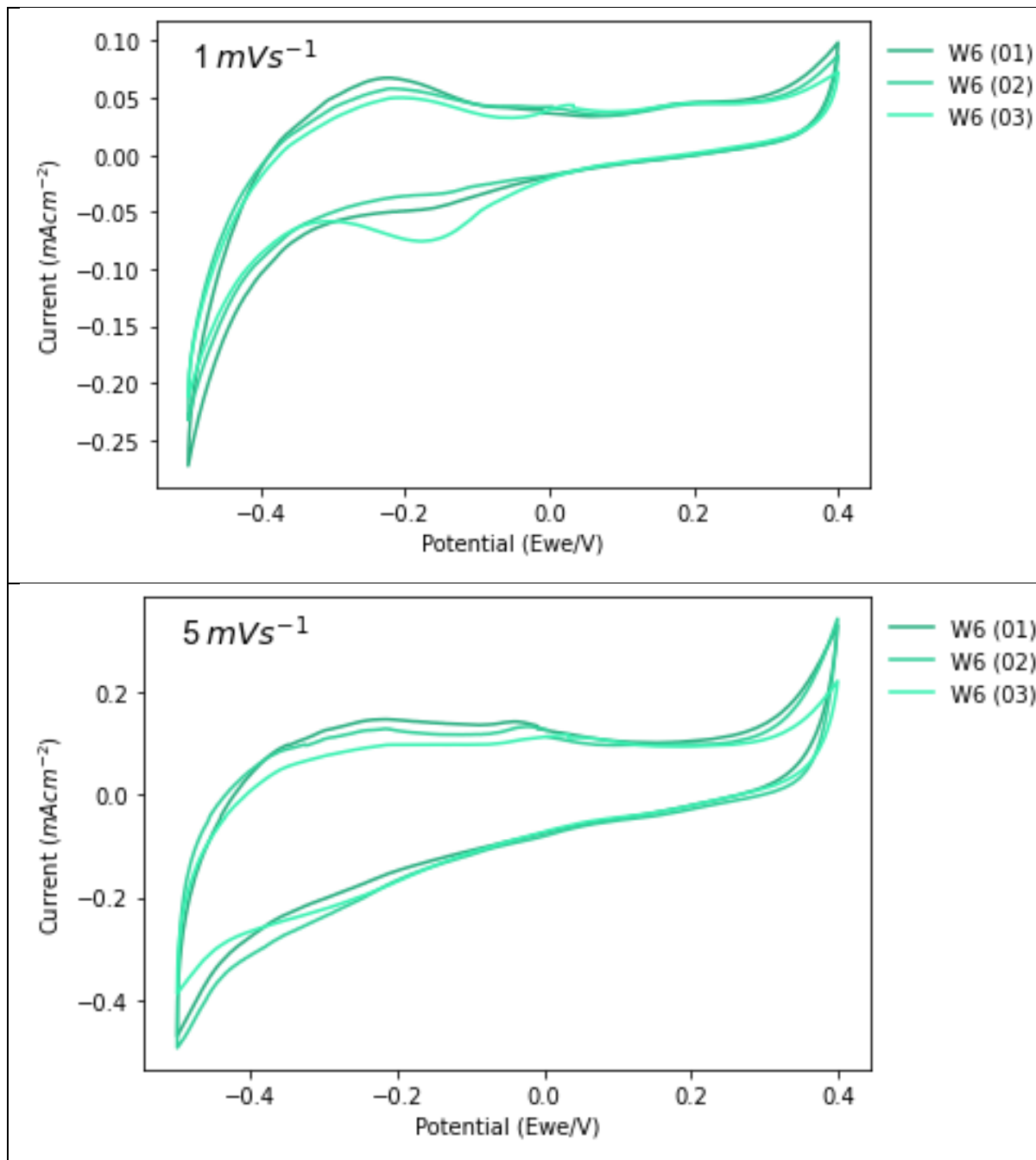


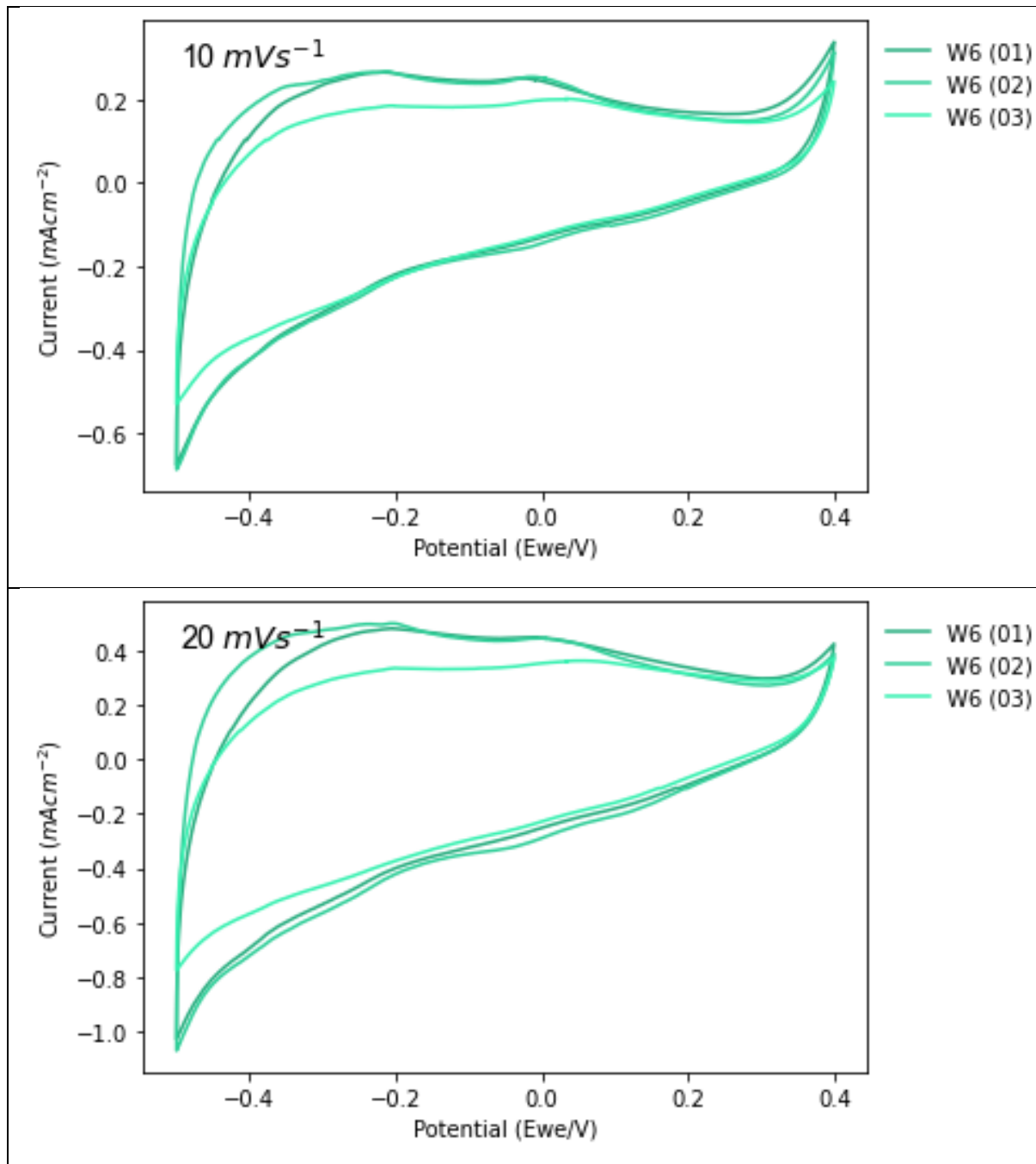


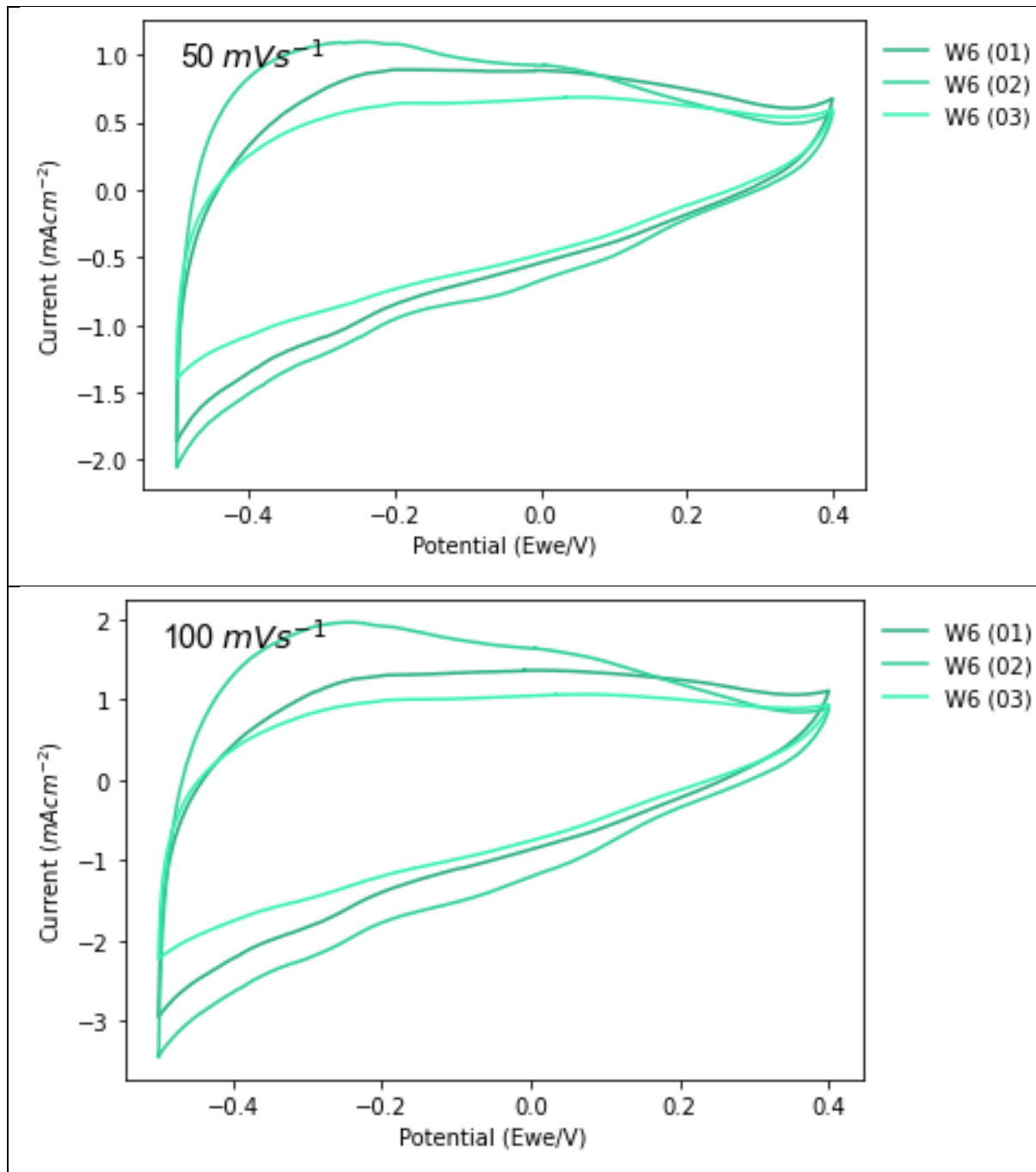


L.2 Iteration 2

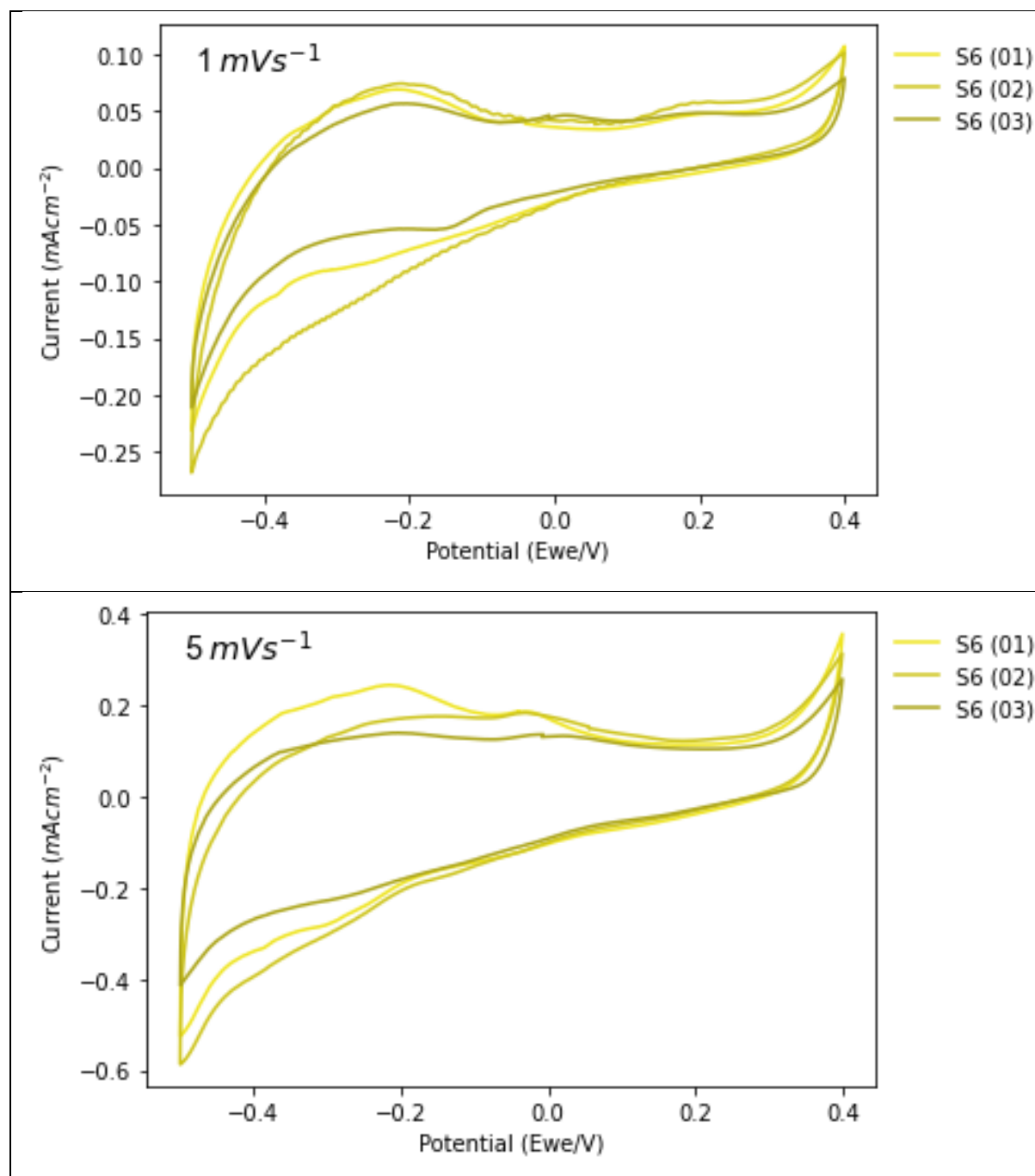
L.2.1 W6

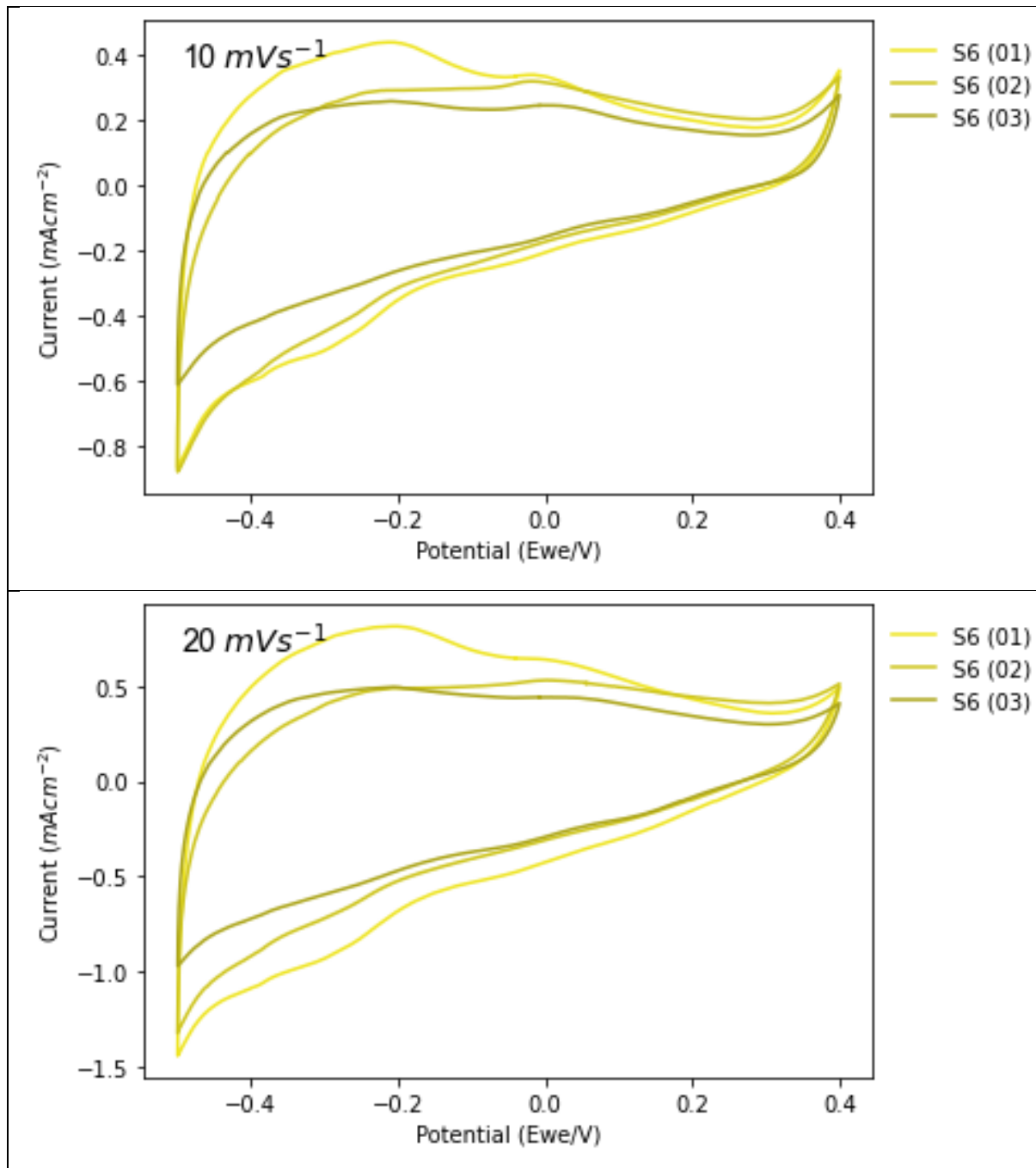


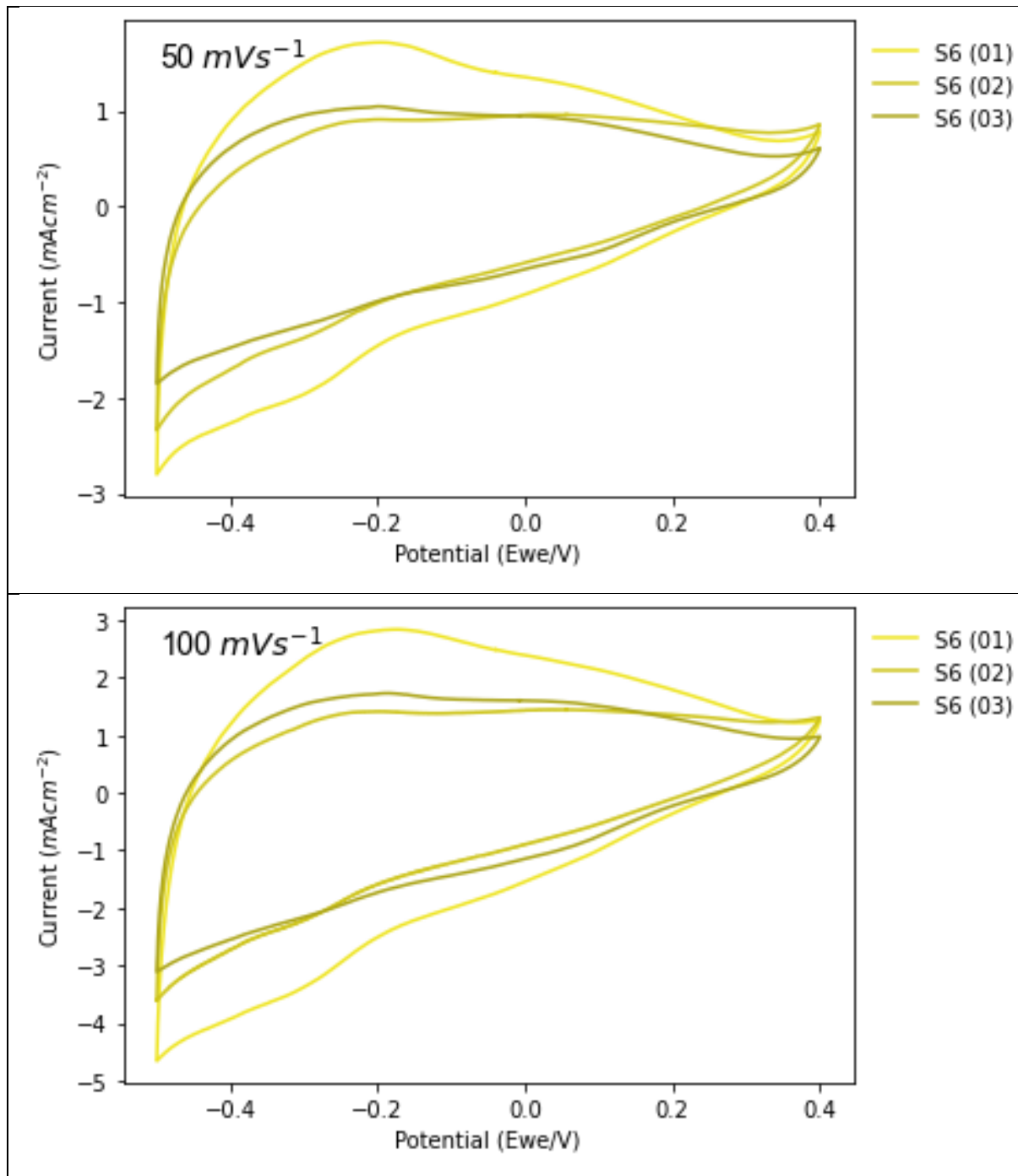




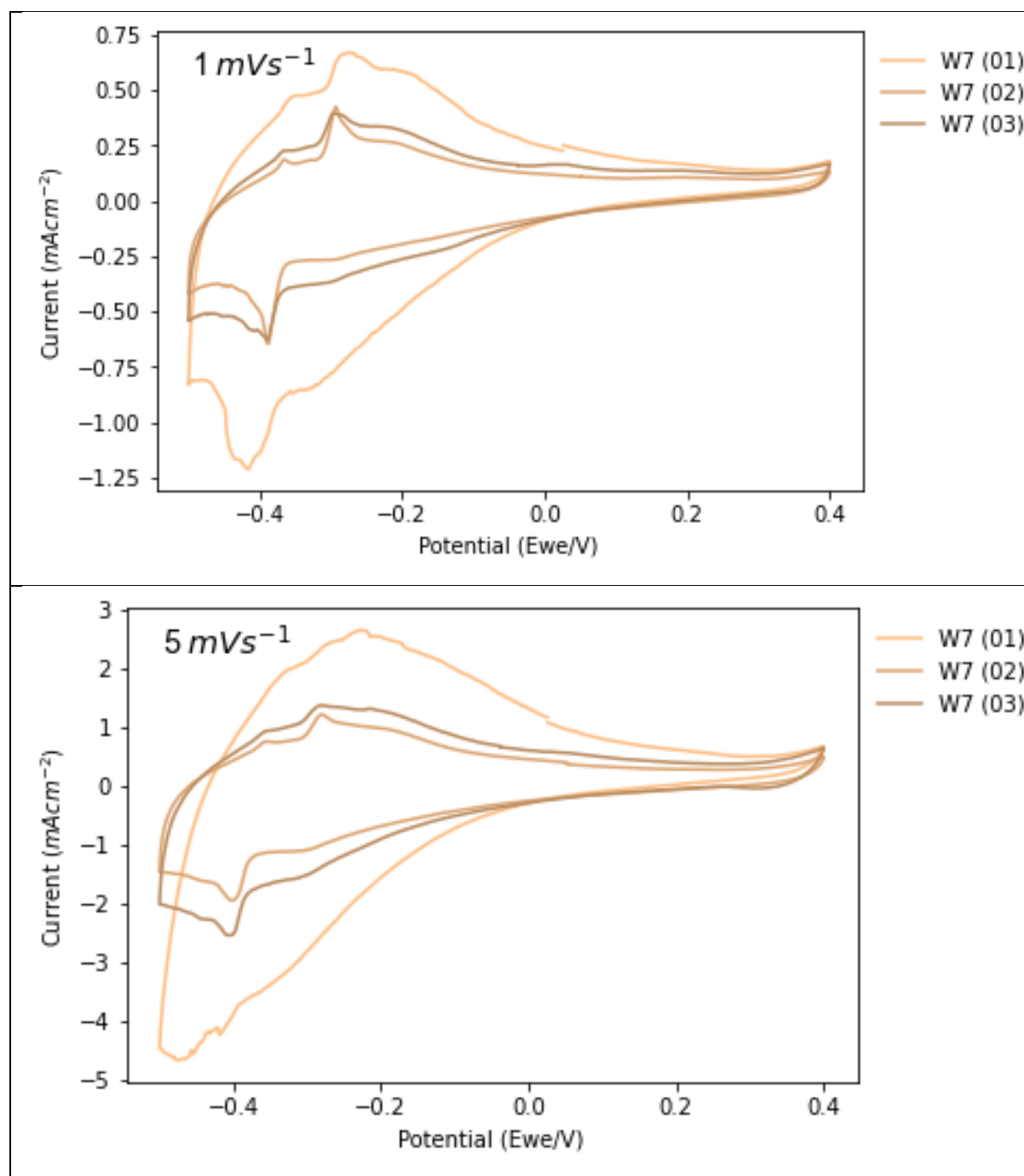
L.2.2 S6

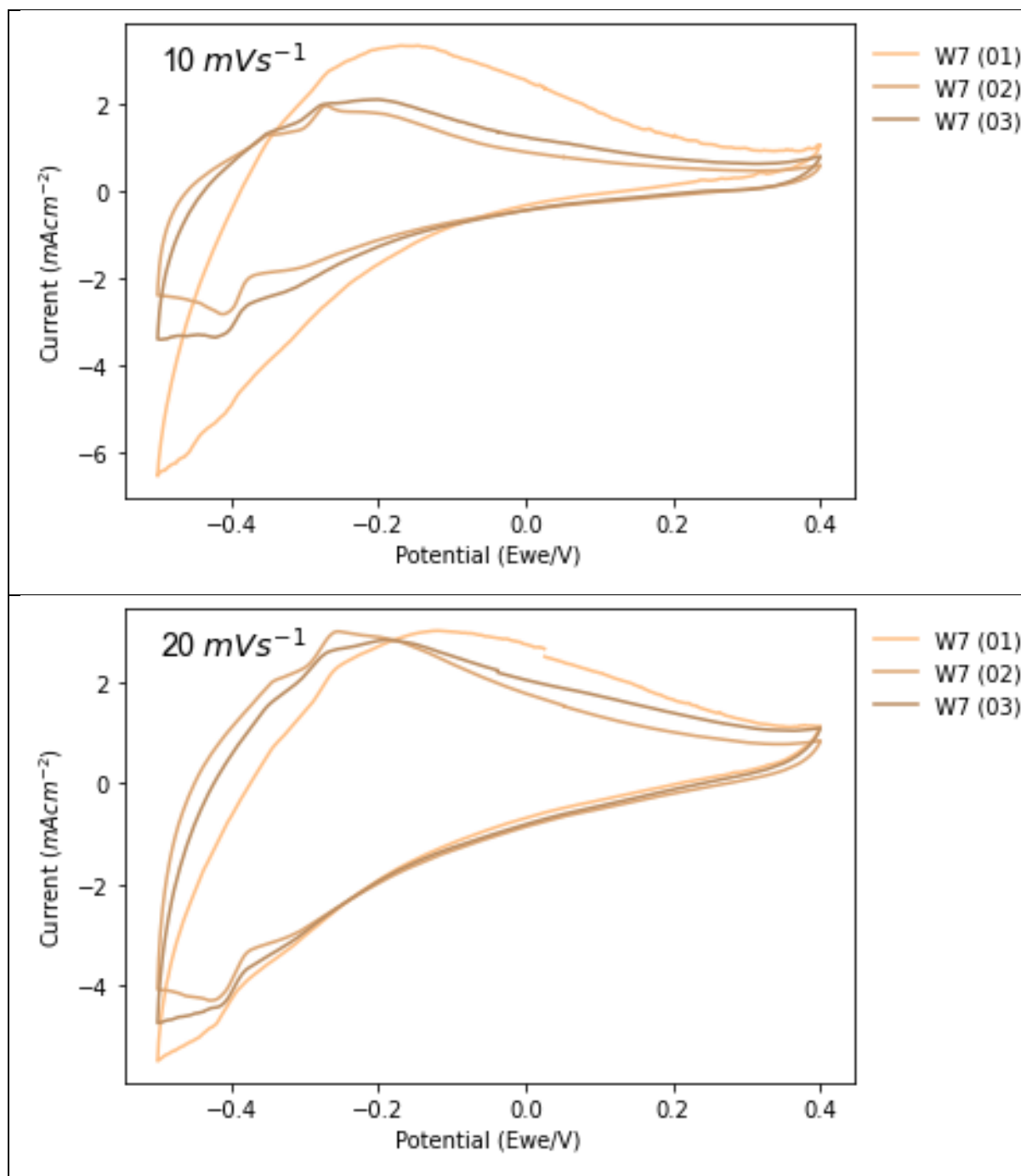


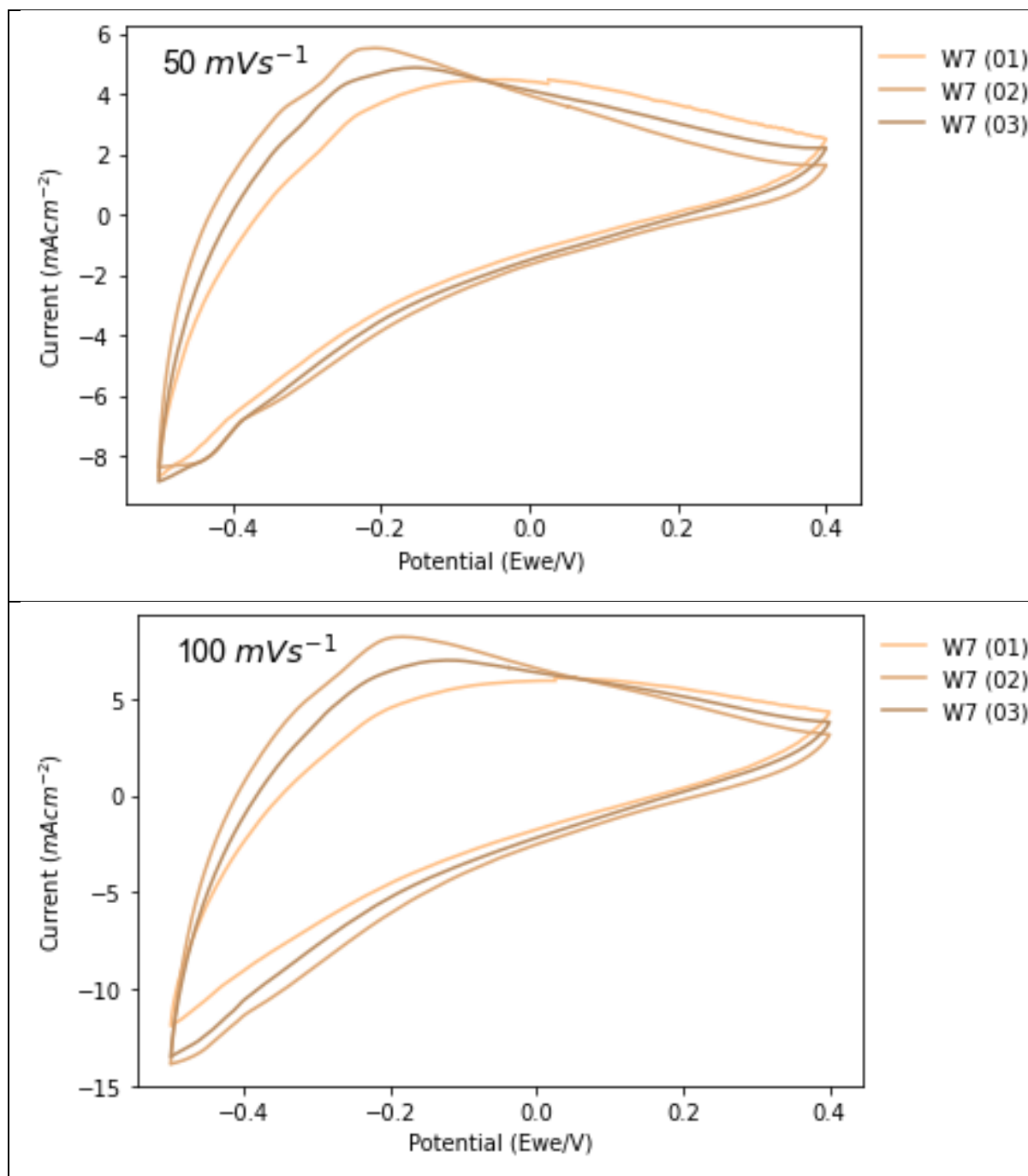




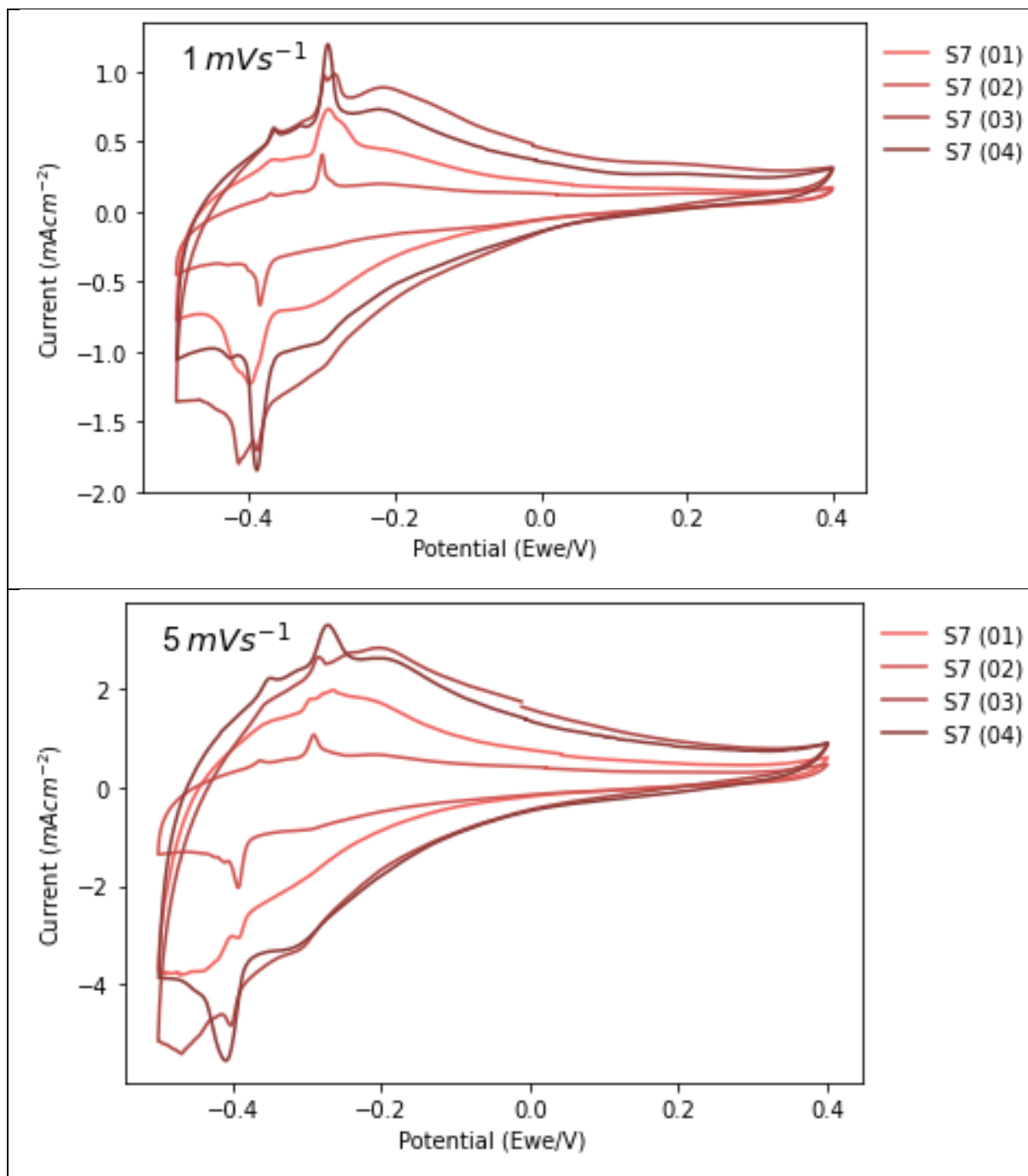
L.3 Iteration 3

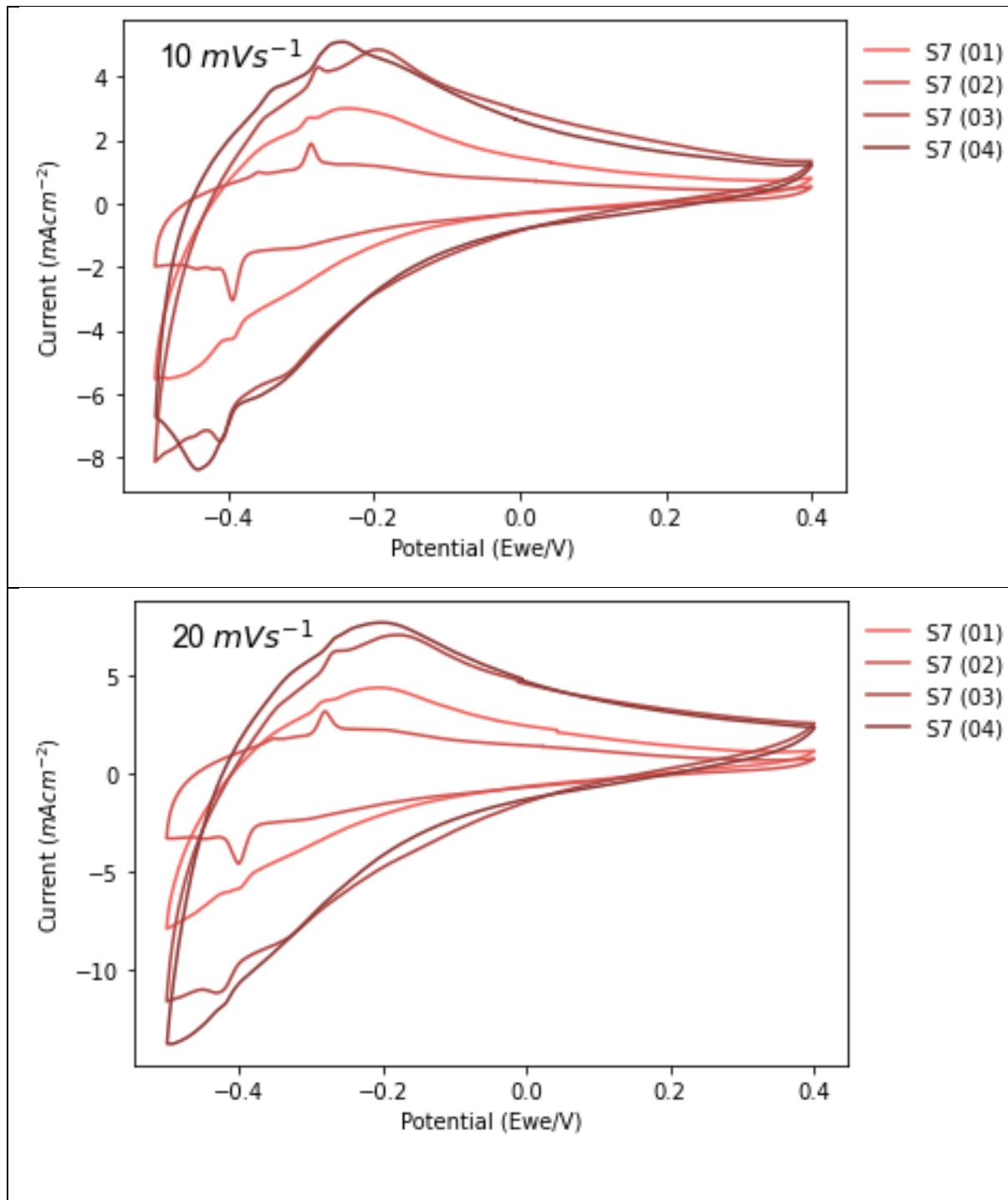


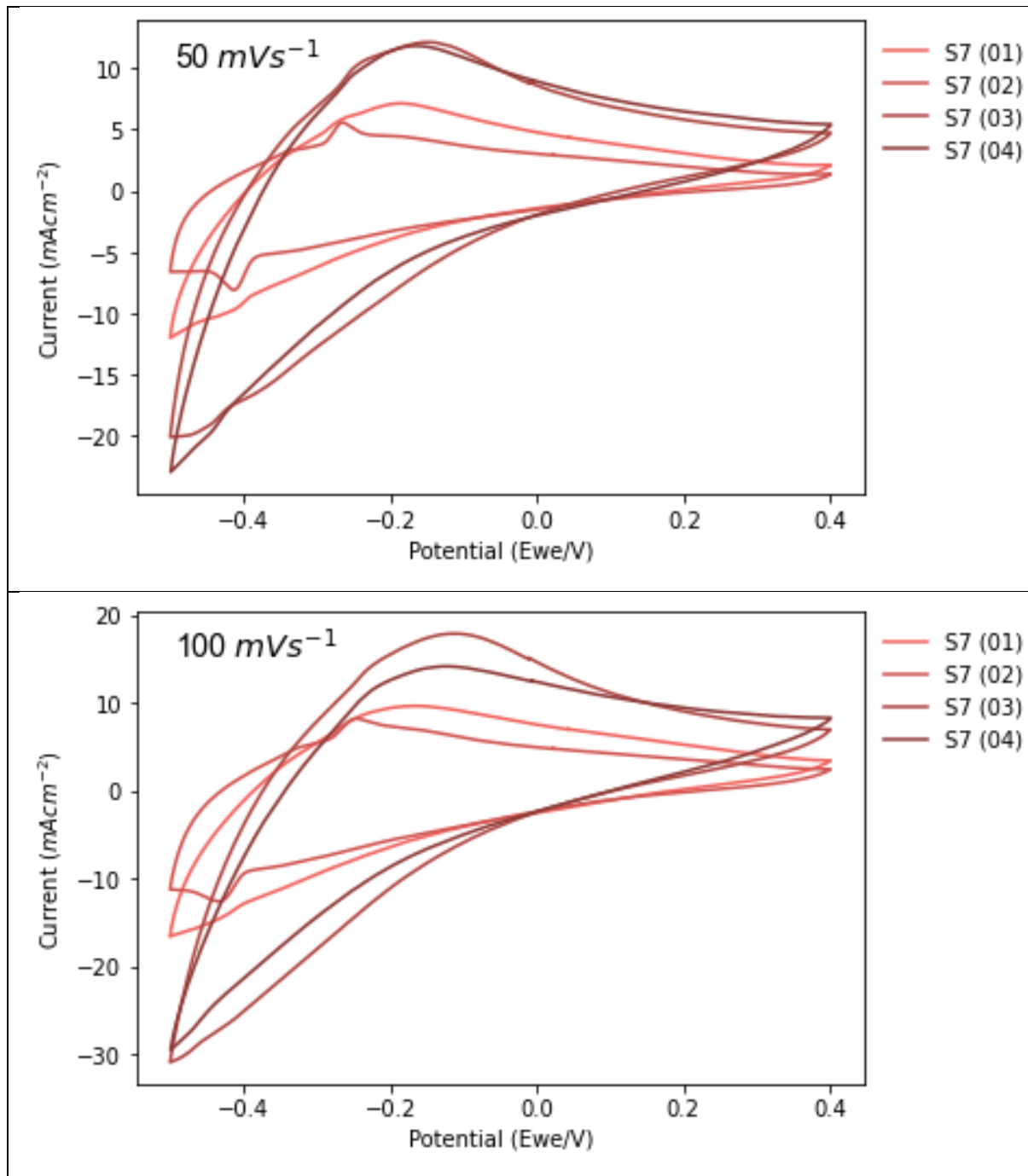




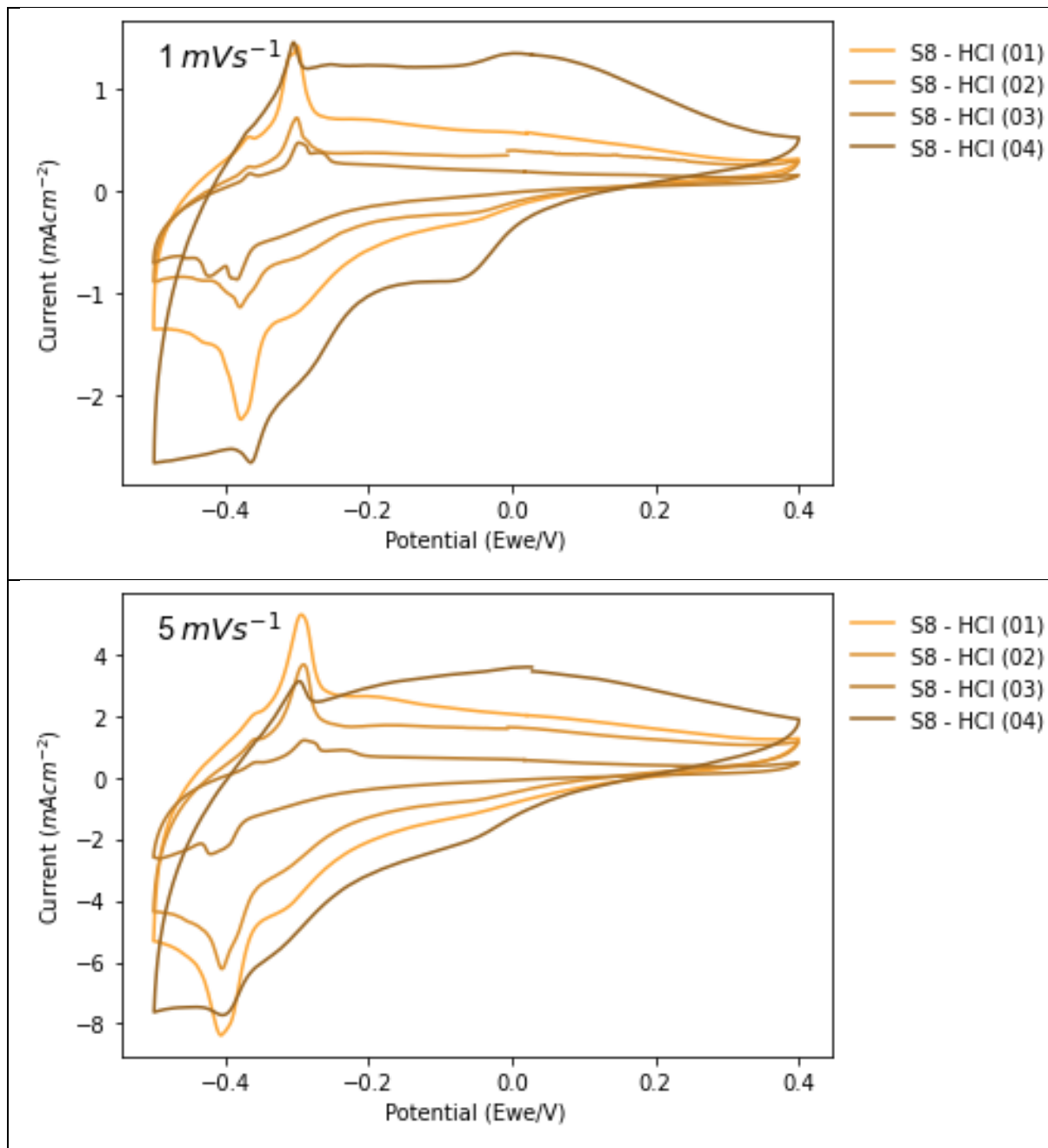
L.3.1 S7

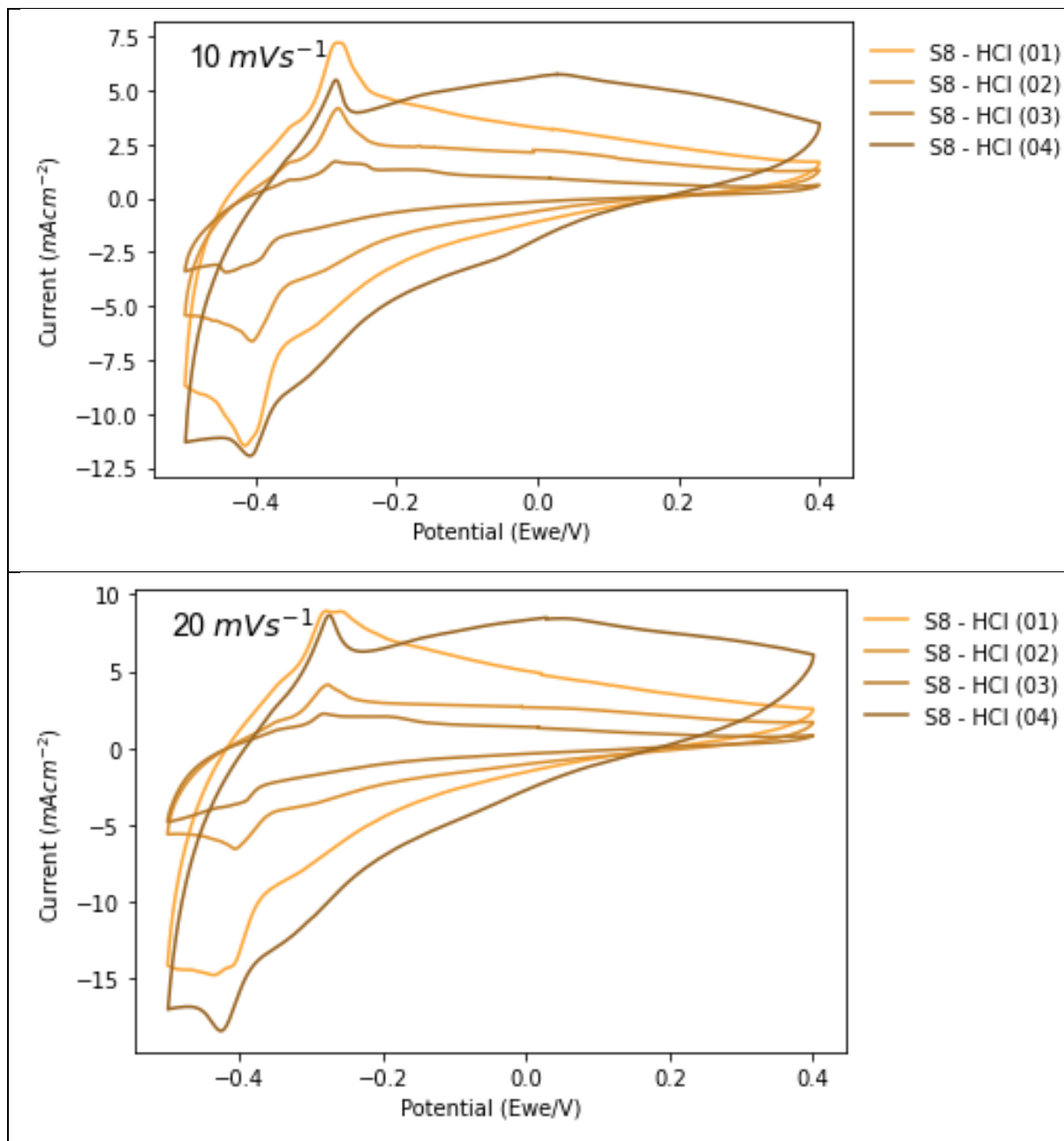


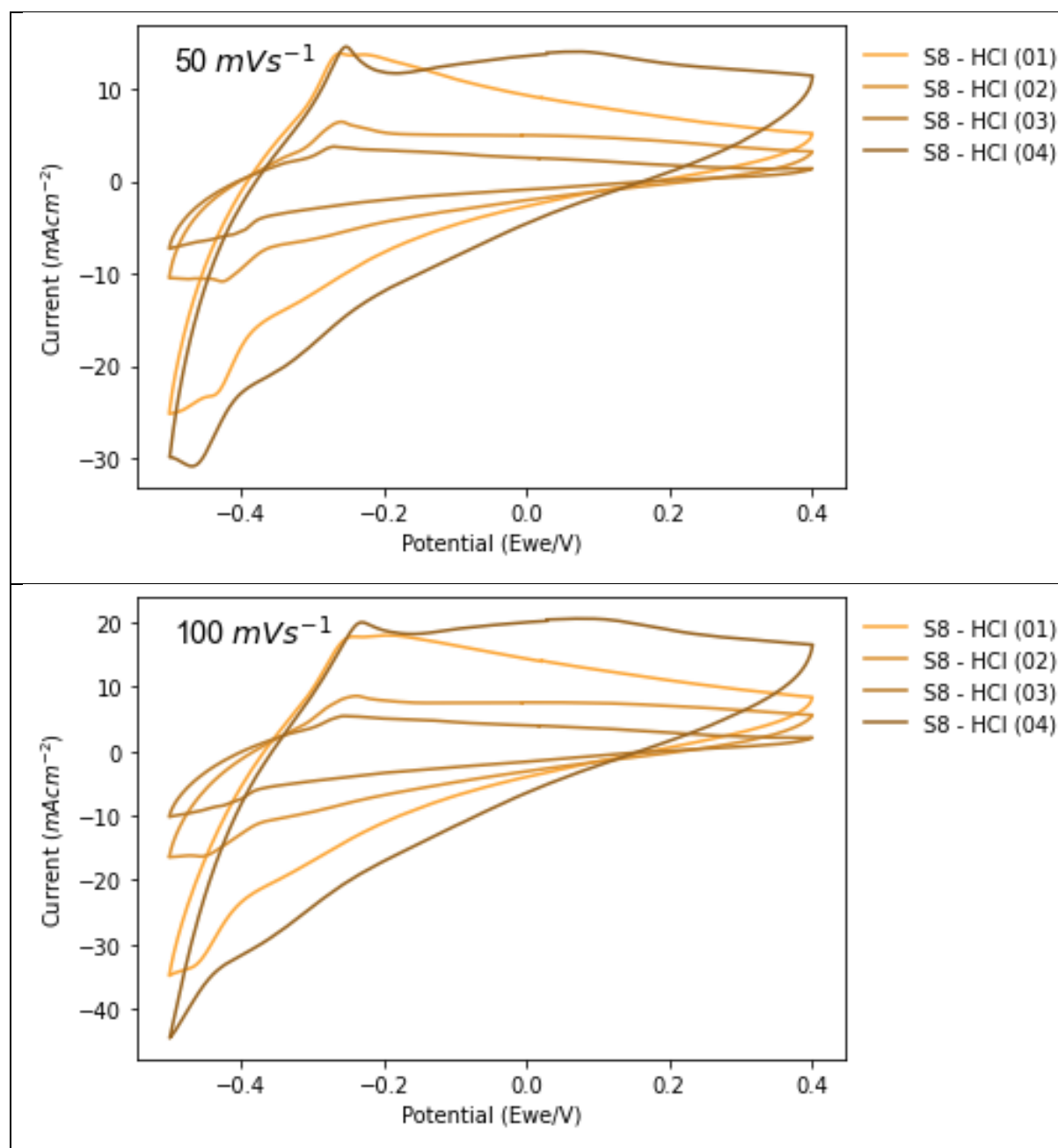




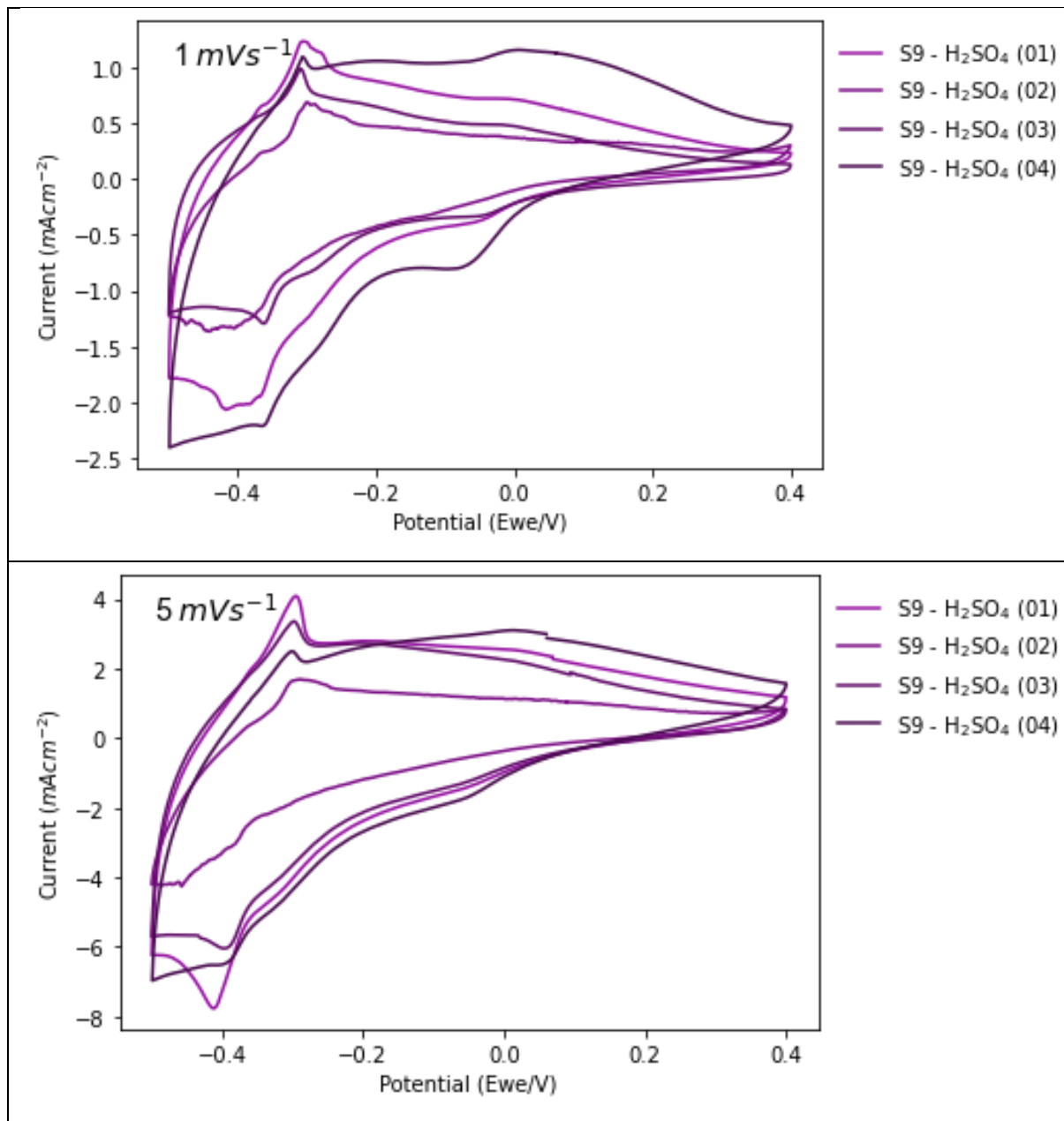
L.4 Iteration 4

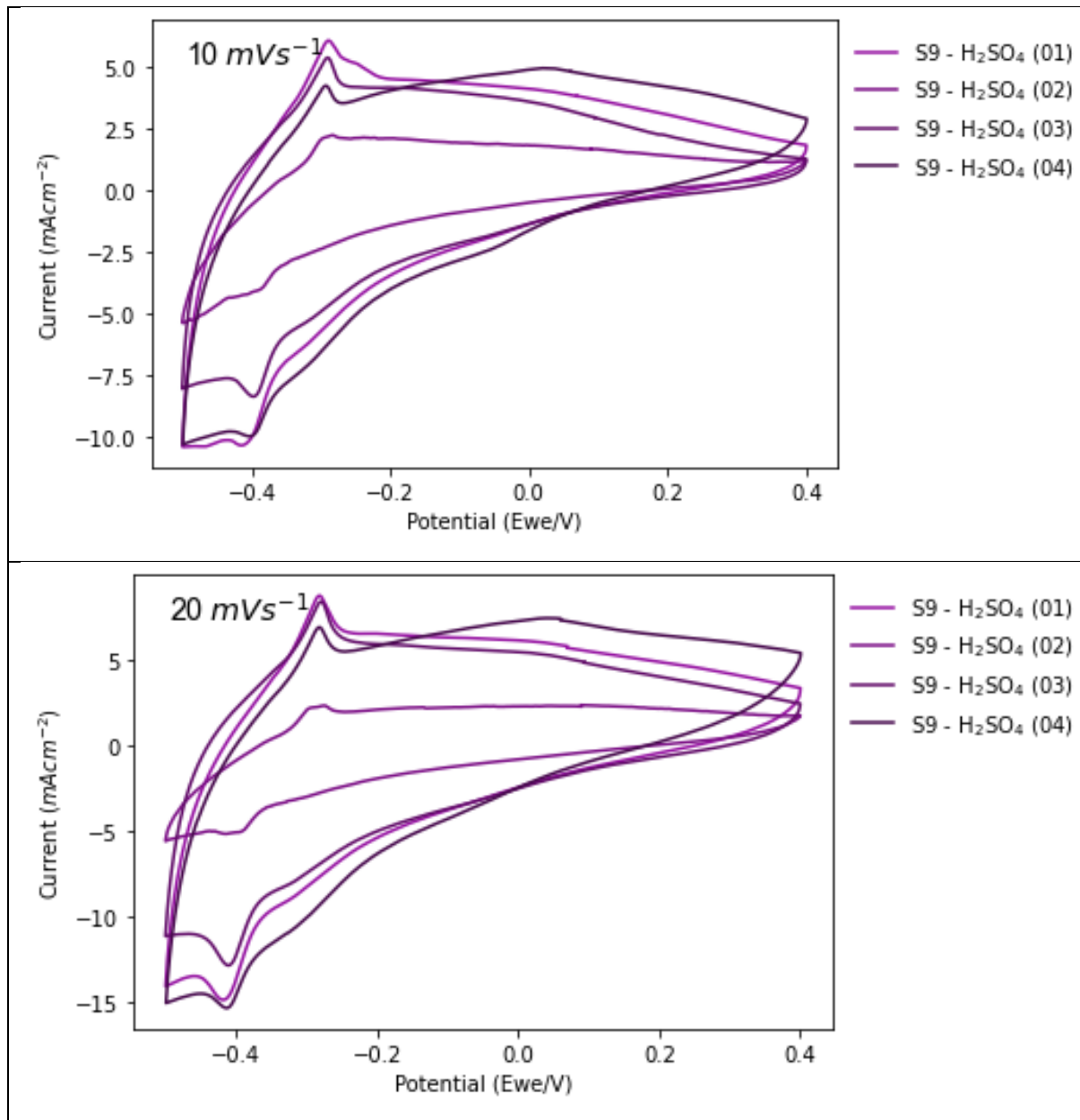


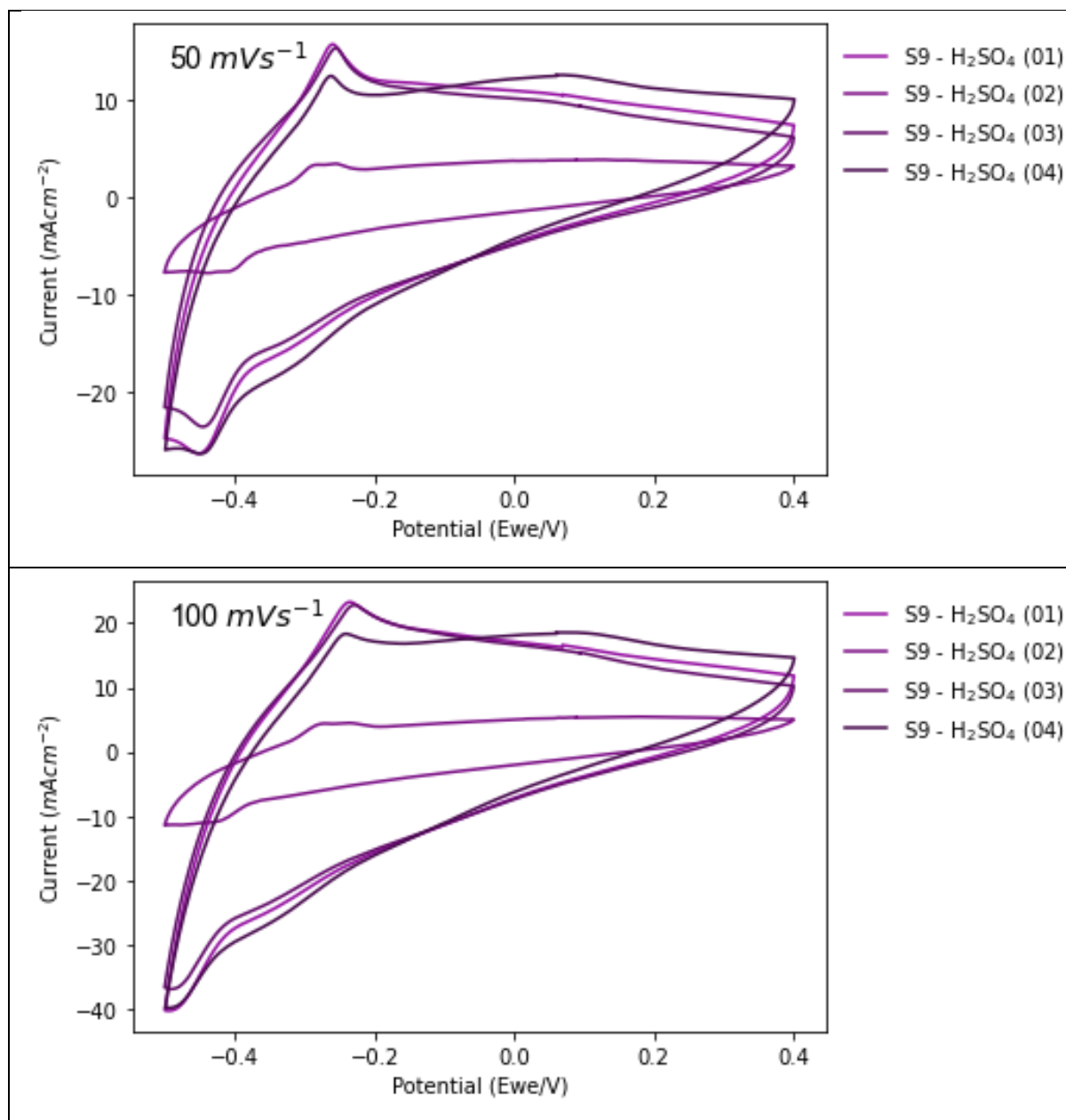




L.5 Iteration 5







L.6 Summary Table of Capacities and Capacitances

Sample	run	Scanrate (mV/s)	Capacity (mAh/cm ²)	Capacitance (F/cm ²)
S	1	1	0.053	0.212
S	1	5	0.047	0.188
S	1	10	0.042	0.168
S	1	20	0.037	0.148
S	1	50	0.028	0.112
S	1	100	0.022	0.088
S5	1	5	0.069	0.276

S5	1	10	0.064	0.256
S5	1	1	0.111	0.444
S5	1	20	0.055	0.22
S5	1	50	0.045	0.18
S5	1	100	0.036	0.144
W5	1	5	0.05	0.2
W5	1	10	0.045	0.18
W5	1	1	0.061	0.244
W5	1	20	0.041	0.164
W5	1	50	0.034	0.136
W5	1	100	0.028	0.112
S5	2	5	0.078	0.312
S5	2	10	0.064	0.256
S5	2	1	0.131	0.524
S5	2	20	0.049	0.196
S5	2	50	0.032	0.128
S5	2	100	0.022	0.088
W5	2	5	0.071	0.284
W5	2	10	0.066	0.264
W5	2	1	0.083	0.332
W5	2	20	0.06	0.24
W5	2	50	0.043	0.172
W5	2	100	0.028	0.112
S5	3	5	0.068	0.272
S5	3	10	0.06	0.24
S5	3	1	0.103	0.412
S5	3	20	0.054	0.216
S5	3	50	0.041	0.164
S5	3	100	0.031	0.124
W5	3	5	0.051	0.204
W5	3	10	0.047	0.188
W5	3	1	0.061	0.244
W5	3	20	0.042	0.168
W5	3	50	0.034	0.136
W5	3	100	0.025	0.1

S6	1	5	0.015	0.06
S6	1	10	0.014	0.056
S6	1	1	0.022	0.088
S6	1	20	0.013	0.052
S6	1	50	0.011	0.044
S6	1	100	0.009	0.036
W6	1	5	0.011	0.044
W6	1	10	0.009	0.036
W6	1	1	0.017	0.068
W6	1	20	0.008	0.032
W6	1	50	0.006	0.024
W6	1	100	0.005	0.02
S6	2	5	0.014	0.056
S6	2	10	0.012	0.048
S6	2	1	0.025	0.1
S6	2	20	0.01	0.04
S6	2	50	0.007	0.028
S6	2	100	0.006	0.024
W6	2	5	0.012	0.048
W6	2	10	0.009	0.036
W6	2	1	0.017	0.068
W6	2	20	0.009	0.036
W6	2	50	0.008	0.032
W6	2	100	0.007	0.028
S6	3	5	0.012	0.048
S6	3	10	0.01	0.04
S6	3	1	0.017	0.068
S6	3	20	0.009	0.036
S6	3	50	0.007	0.028
S6	3	100	0.006	0.024
W6	3	5	0.009	0.036
W6	3	10	0.008	0.032
W6	3	1	0.017	0.068
W6	3	20	0.007	0.028
W6	3	50	0.005	0.02

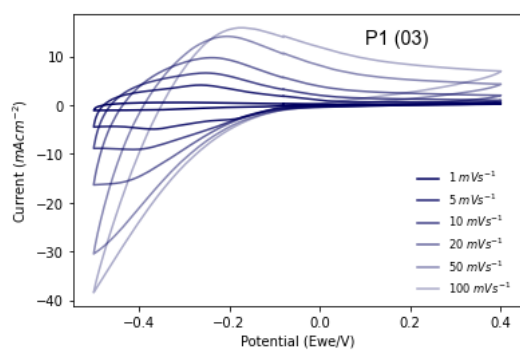
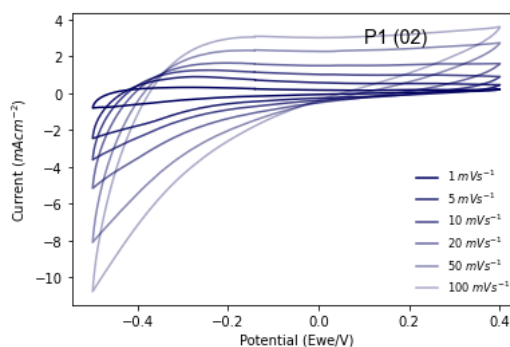
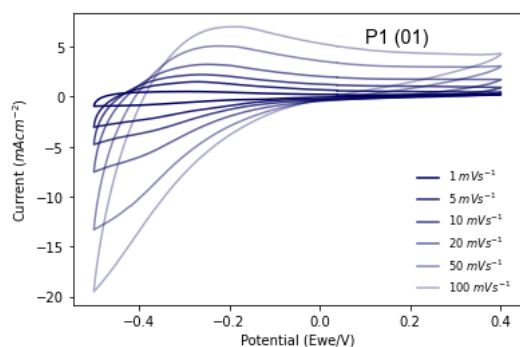
W6	3	100	0.004	0.016
W7	1	5	0.118	0.472
W7	1	10	0.073	0.292
W7	1	1	0.156	0.624
W7	1	20	0.037	0.148
W7	1	50	0.024	0.096
W7	1	100	0.016	0.064
W7	2	5	0.051	0.204
W7	2	10	0.044	0.176
W7	2	1	0.069	0.276
W7	2	20	0.037	0.148
W7	2	50	0.029	0.116
W7	2	100	0.022	0.088
W7	3	5	0.068	0.272
W7	3	10	0.052	0.208
W7	3	1	0.086	0.344
W7	3	20	0.038	0.152
W7	3	50	0.027	0.108
W7	3	100	0.019	0.076
S7	1	5	0.083	0.332
S7	1	10	0.063	0.252
S7	1	1	0.128	0.512
S7	1	20	0.045	0.18
S7	1	50	0.031	0.124
S7	1	100	0.023	0.092
S7	2	5	0.039	0.156
S7	2	10	0.034	0.136
S7	2	1	0.061	0.244
S7	2	20	0.03	0.12
S7	2	50	0.024	0.096
S7	2	100	0.02	0.08
S7	3	5	0.137	0.548
S7	3	10	0.113	0.452
S7	3	1	0.231	0.924
S7	3	20	0.085	0.34

S7	3	50	0.056	0.224
S7	3	100	0.039	0.156
S8 - HCl	1	5	0.186	0.744
S8 - HCl	1	10	0.139	0.556
S8 - HCl	1	1	0.242	0.968
S8 - HCl	1	20	0.097	0.388
S8 - HCl	1	50	0.062	0.248
S8 - HCl	1	100	0.043	0.172
S8 - HCl	2	5	0.126	0.504
S8 - HCl	2	10	0.08	0.32
S8 - HCl	2	1	0.139	0.556
S8 - HCl	2	20	0.048	0.192
S8 - HCl	2	50	0.034	0.136
S8 - HCl	2	100	0.025	0.1
S8 - HCl	3	5	0.045	0.18
S8 - HCl	3	10	0.034	0.136
S8 - HCl	3	1	0.081	0.324
S8 - HCl	3	20	0.025	0.1
S8 - HCl	3	50	0.017	0.068
S8 - HCl	3	100	0.013	0.052
S9 - H2SO4	1	5	0.196	0.784
S9 - H2SO4	1	10	0.15	0.6
S9 - H2SO4	1	1	0.283	1.132
S9 - H2SO4	1	20	0.11	0.44
S9 - H2SO4	1	50	0.078	0.312
S9 - H2SO4	1	100	0.057	0.228
S9 - H2SO4	2	5	0.086	0.344
S9 - H2SO4	2	10	0.059	0.236
S9 - H2SO4	2	1	0.161	0.644
S9 - H2SO4	2	20	0.037	0.148
S9 - H2SO4	2	50	0.023	0.092
S9 - H2SO4	2	100	0.016	0.064
S9 - H2SO4	3	5	0.174	0.696
S9 - H2SO4	3	10	0.129	0.516
S9 - H2SO4	3	1	0.203	0.812

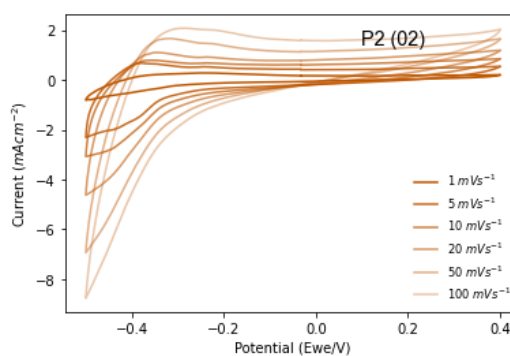
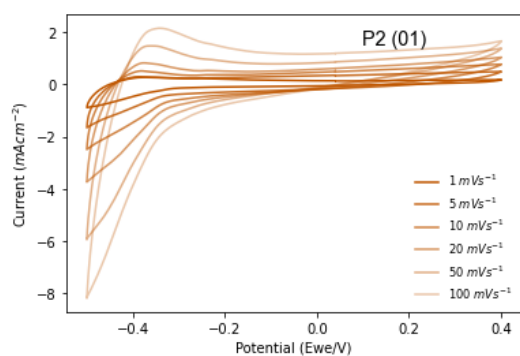
S9 - H ₂ SO ₄	3	20	0.102	0.408
S9 - H ₂ SO ₄	3	50	0.074	0.296
S9 - H ₂ SO ₄	3	100	0.056	0.224

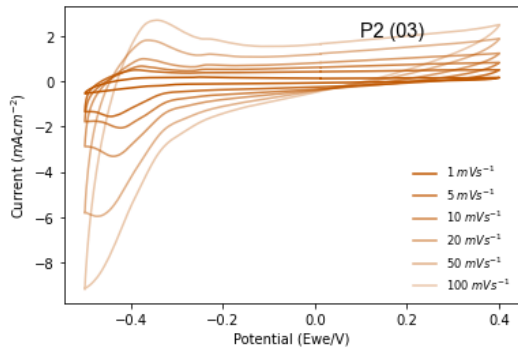
Appendix M Cyclic Voltammetry data from Chapter 7

M.1 P1

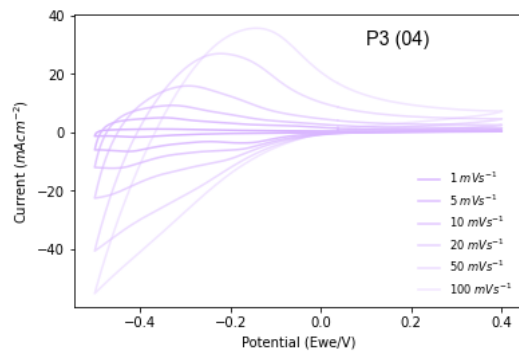
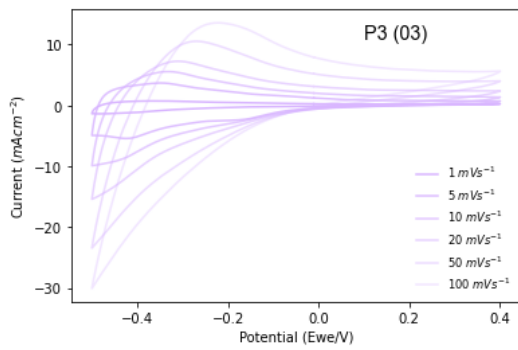
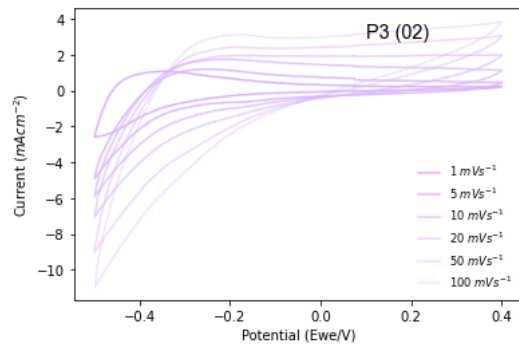
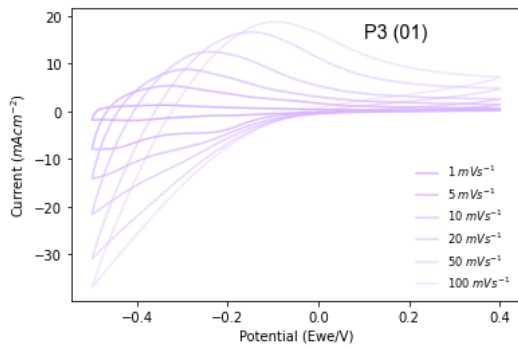


M.2 P2

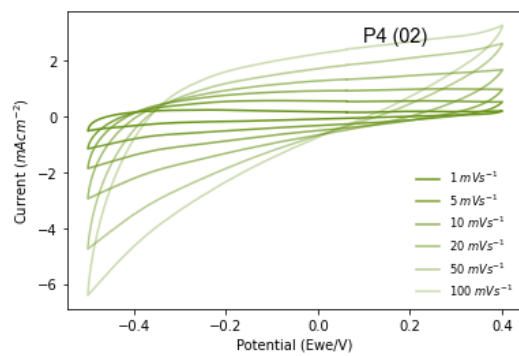
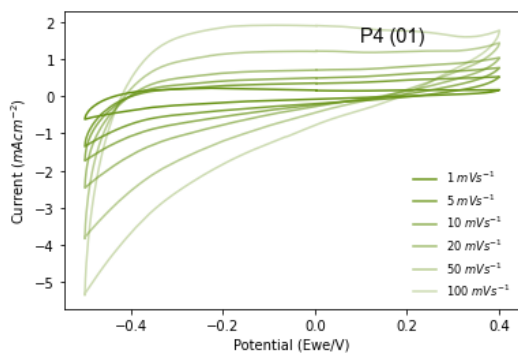


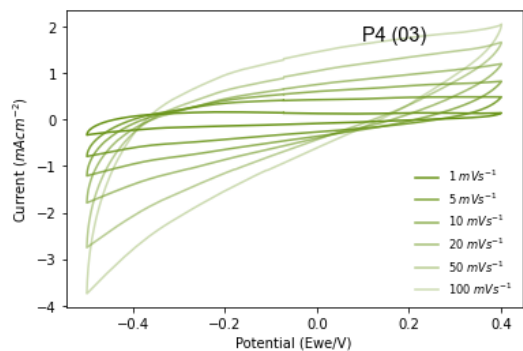


M.3 P3

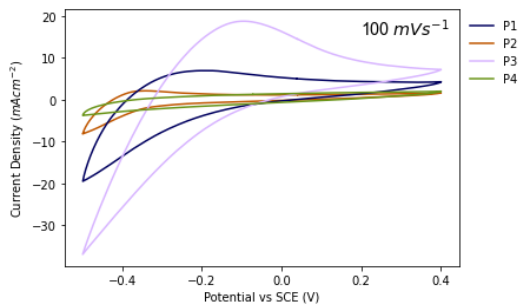
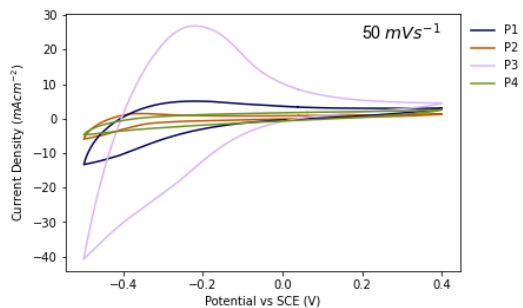
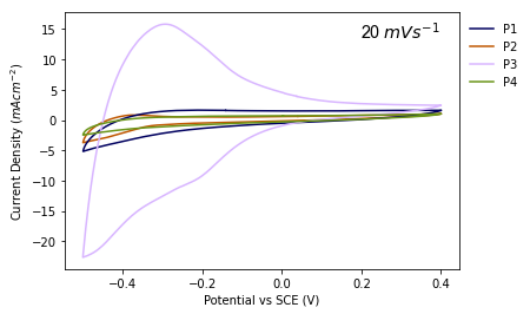
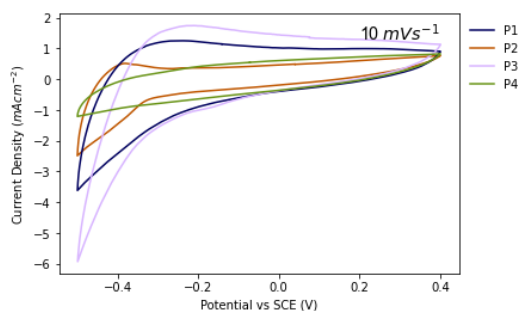
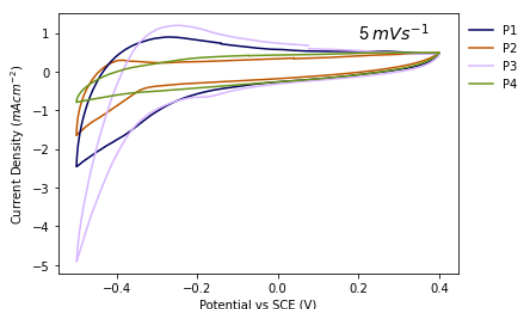
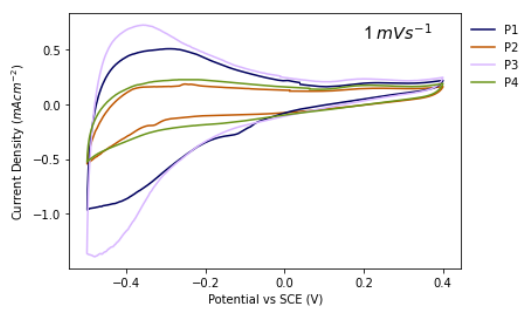


M.4 P4





M.5 Comparison of median CV samples across powders



M.6 Summary Table of Capacities and Capacitances from CV Data

Sample	Run	Scanrate/ mV/s	Area/ mAV	Mass/ g	Charge Q/ Coulombs	Specific Capacity/ mAhg	Specific Capacitance/ Fg
P1	01	1.0	0.48	0.0	0.48	70.95	283.81
P1	01	5.0	1.32	0.0	0.26	39.02	156.1
P1	01	10.0	2.09	0.0	0.21	30.89	123.58
P1	01	20.0	3.13	0.0	0.16	23.13	92.53
P1	01	50.0	4.74	0.0	0.1	14.01	56.05
P1	01	100.0	6.09	0.0	0.06	9.0	36.01
P1	02	1.0	0.33	0.0	0.33	22.92	91.67
P1	02	5.0	0.98	0.0	0.2	13.61	54.44
P1	02	10.0	1.45	0.0	0.14	10.07	40.28
P1	02	20.0	1.99	0.0	0.1	6.91	27.64
P1	02	50.0	2.71	0.0	0.05	3.76	15.06
P1	02	100.0	3.33	0.0	0.03	2.31	9.25
P1	03	1.0	0.54	0.0	0.54	79.82	319.28
P1	03	5.0	2.95	0.0	0.59	87.21	348.85
P1	03	10.0	4.85	0.0	0.48	71.69	286.76
P1	03	20.0	7.08	0.0	0.35	52.33	209.31

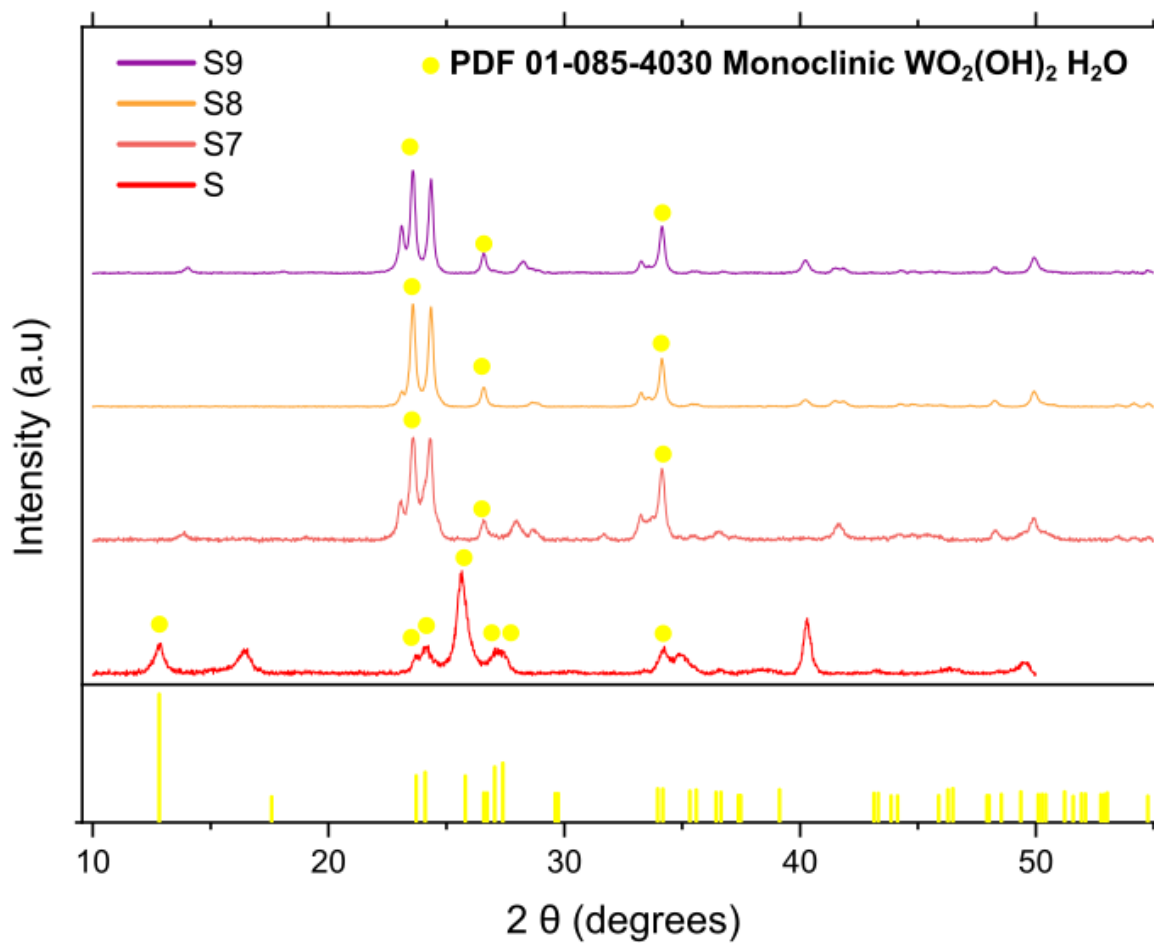
P1	03	50.0	9.54	0.0	0.19	28.2	112.81
P1	03	100.0	10.09	0.0	0.1	14.92	59.66
P2	01	1.0	0.25	0.0	0.25	29.04	116.14
P2	01	5.0	0.5	0.0	0.1	11.61	46.46
P2	01	10.0	0.71	0.0	0.07	8.25	32.98
P2	01	20.0	0.91	0.0	0.05	5.28	21.14
P2	01	50.0	1.29	0.0	0.03	3.0	11.98
P2	01	100.0	1.73	0.0	0.02	2.01	8.04
P2	02	1.0	0.26	0.0	0.26	31.32	125.26
P2	02	5.0	0.74	0.0	0.15	17.83	71.3
P2	02	10.0	0.96	0.0	0.1	11.56	46.25
P2	02	20.0	1.21	0.0	0.06	7.29	29.15
P2	02	50.0	1.55	0.0	0.03	3.73	14.94
P2	02	100.0	1.92	0.0	0.02	2.31	9.25
P2	03	1.0	0.2	0.0	0.2	30.97	123.88
P2	03	5.0	0.69	0.0	0.14	21.37	85.48
P2	03	10.0	0.97	0.0	0.1	15.02	60.08
P2	03	20.0	1.33	0.0	0.07	10.3	41.19
P2	03	50.0	1.99	0.0	0.04	6.16	24.65
P2	03	100.0	2.6	0.0	0.03	4.03	16.1
P3	01	1.0	1.05	0.0	1.05	126.46	505.86

P3	01	5.0	3.91	0.0	0.78	94.19	376.74
P3	01	10.0	6.09	0.0	0.61	73.35	293.4
P3	01	20.0	8.19	0.0	0.41	49.32	197.28
P3	01	50.0	10.23	0.0	0.2	24.64	98.57
P3	01	100.0	10.91	0.0	0.11	13.14	52.56
P3	02	1.0	0.74	0.0	0.74	63.33	253.31
P3	02	5.0	1.05	0.0	0.21	17.97	71.88
P3	02	10.0	1.68	0.0	0.17	14.38	57.51
P3	02	20.0	2.12	0.0	0.11	9.07	36.28
P3	02	50.0	2.64	0.0	0.05	4.52	18.08
P3	02	100.0	3.21	0.0	0.03	2.75	10.99
P3	03	1.0	0.61	0.0	0.61	79.35	317.38
P3	03	5.0	2.93	0.0	0.59	76.22	304.9
P3	03	10.0	4.25	0.0	0.42	55.28	221.13
P3	03	20.0	5.57	0.0	0.28	36.23	144.9
P3	03	50.0	7.45	0.0	0.15	19.38	77.52
P3	03	100.0	9.1	0.0	0.09	11.84	47.35
P3	04	1.0	0.85	0.0	0.85	72.74	290.96
P3	04	5.0	3.79	0.0	0.76	64.87	259.47
P3	04	10.0	6.6	0.0	0.66	56.48	225.93
P3	04	20.0	10.37	0.0	0.52	44.37	177.49

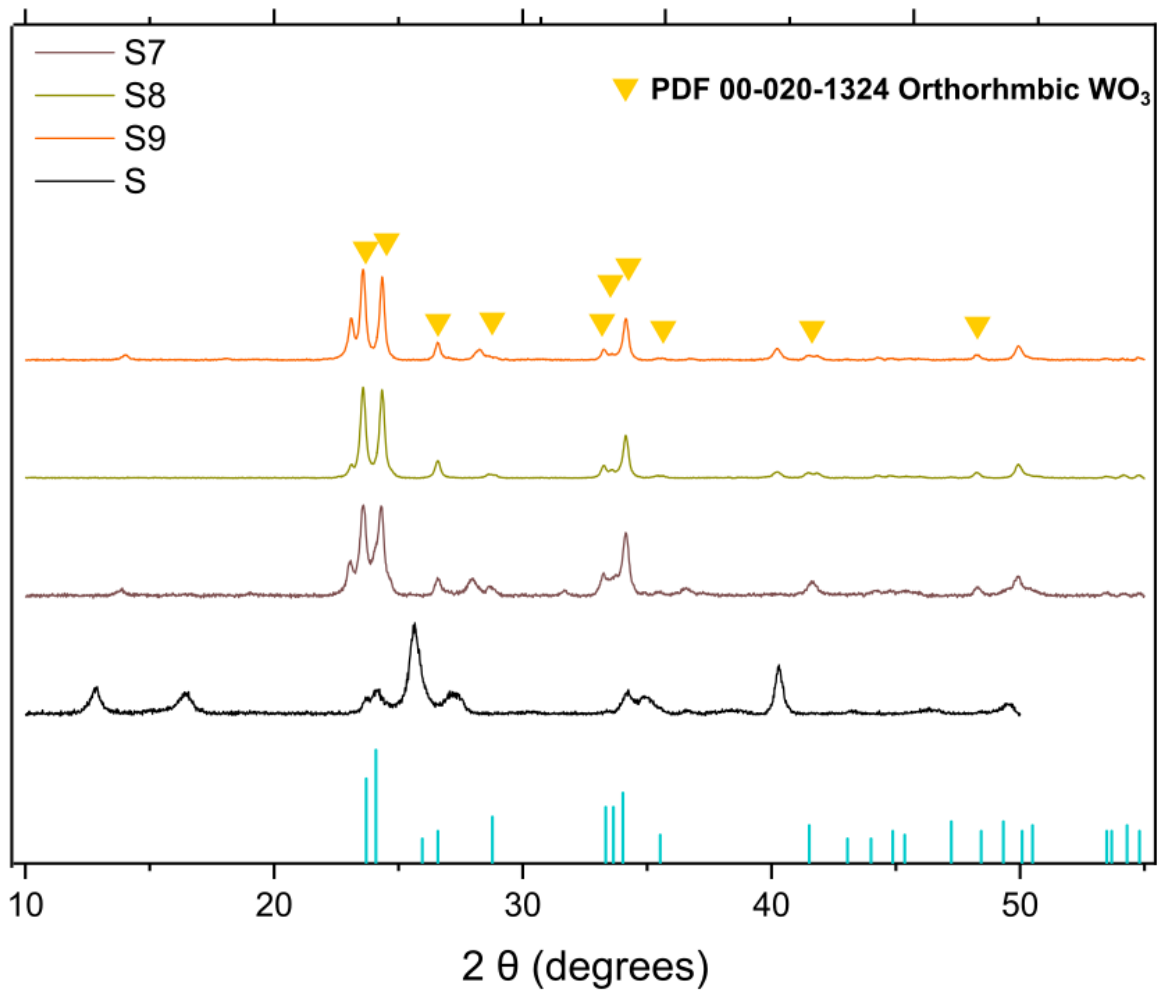
P3	04	50.0	16.29	0.0	0.33	27.88	111.52
P3	04	100.0	20.56	0.0	0.21	17.6	70.38
P4	01	1.0	0.25	0.01	0.25	13.33	53.31
P4	01	5.0	0.48	0.01	0.1	5.12	20.47
P4	01	10.0	0.66	0.01	0.07	3.52	14.07
P4	01	20.0	0.92	0.01	0.05	2.45	9.81
P4	01	50.0	1.52	0.01	0.03	1.62	6.48
P4	01	100.0	2.38	0.01	0.02	1.27	5.08
P4	02	1.0	0.26	0.0	0.26	36.76	147.05
P4	02	5.0	0.72	0.0	0.14	20.36	81.44
P4	02	10.0	1.15	0.0	0.12	16.26	65.04
P4	02	20.0	1.55	0.0	0.08	10.96	43.83
P4	02	50.0	1.99	0.0	0.04	5.63	22.51
P4	02	100.0	2.52	0.0	0.02	3.56	14.25
P4	03	1.0	0.19	0.0	0.19	25.74	102.98
P4	03	5.0	0.53	0.0	0.11	14.36	57.45
P4	03	10.0	0.73	0.0	0.07	9.89	39.56
P4	03	20.0	0.9	0.0	0.04	6.1	24.39
P4	03	50.0	1.2	0.0	0.02	3.25	13.01
P4	03	100.0	1.68	0.0	0.02	2.28	9.1

Appendix N XRD Spectra of S, S7, S8 & S9

N.1 Reference pattern PDF 01-085-4030 Monoclinic $\text{WO}_2(\text{OH})_2 \cdot \text{H}_2\text{O}$

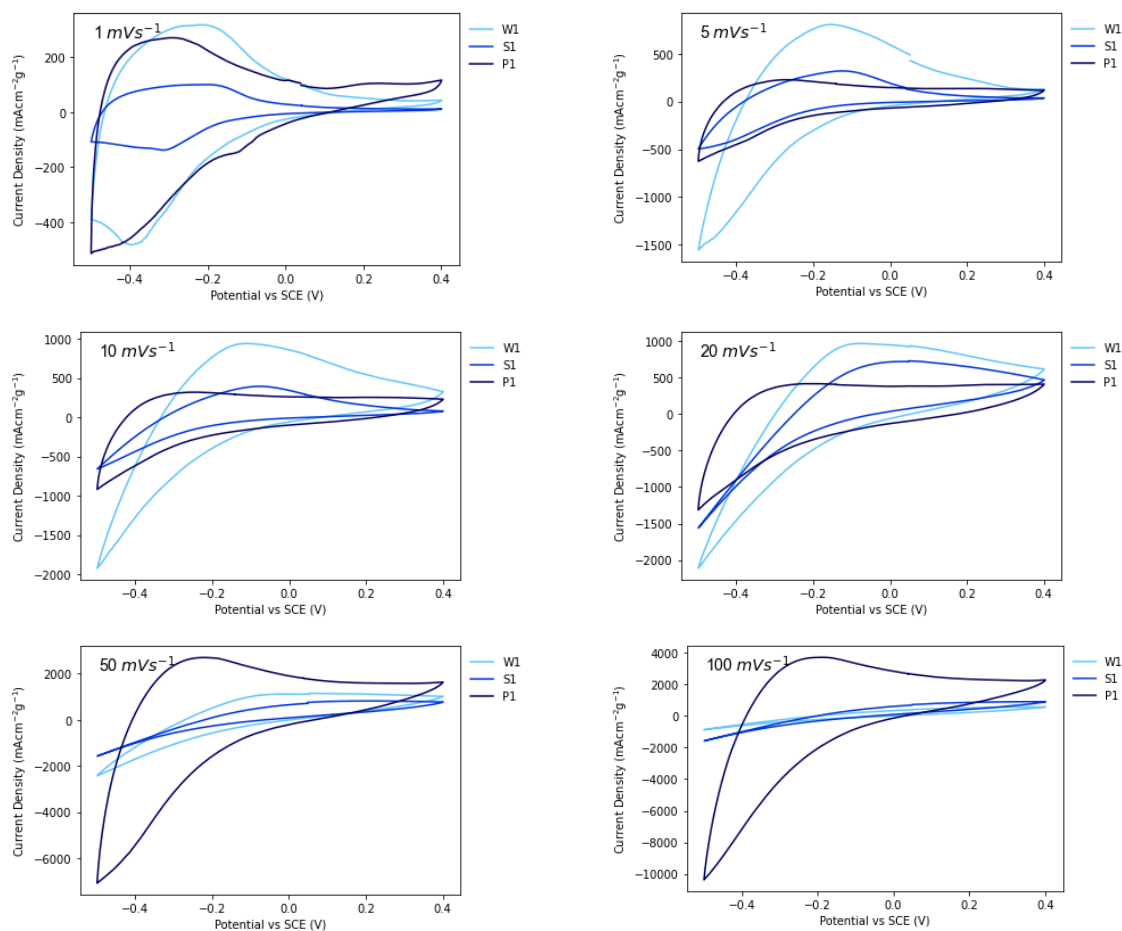


N.2 PDF 00-020-1324 Orthorhombic WO₃

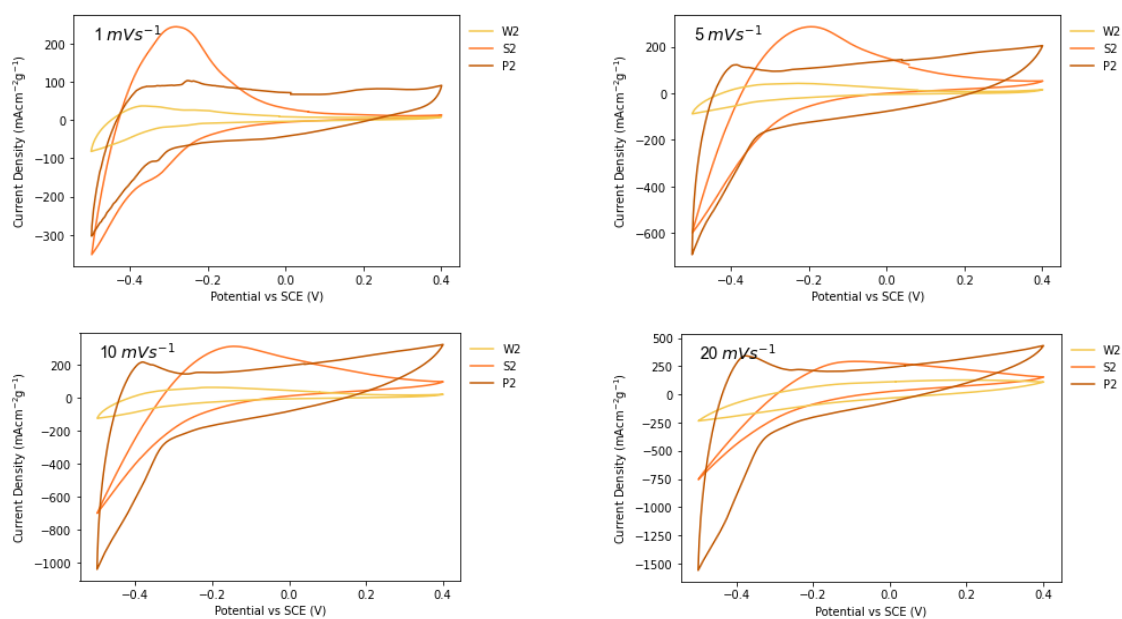


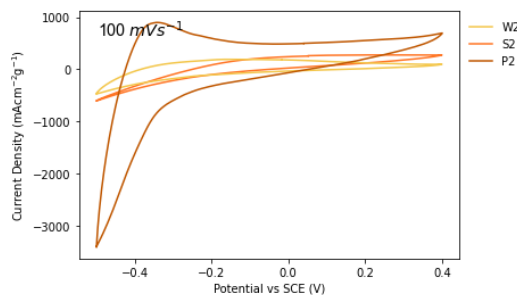
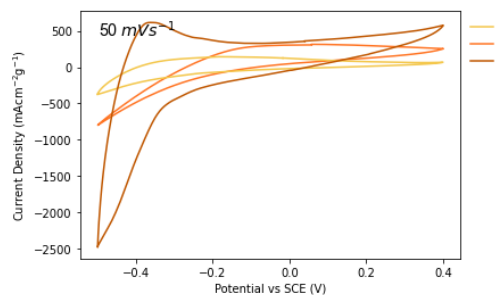
Appendix O CV Comparison of P and W & S electrodes

O.1 NaCl Samples: W1, S1 & P1

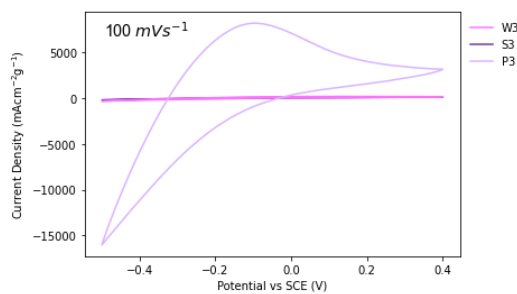
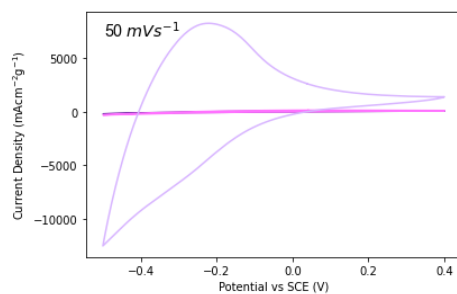
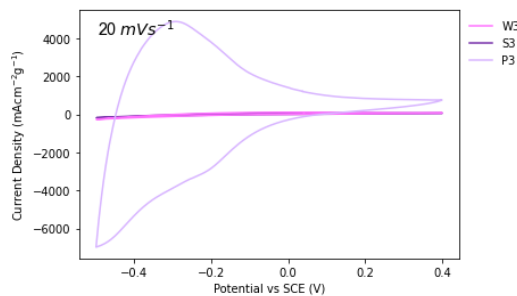
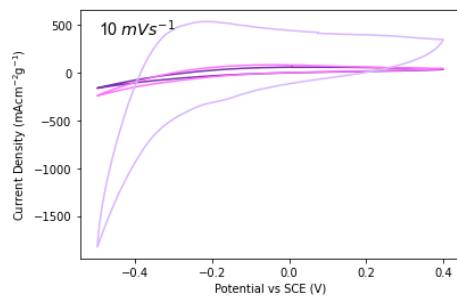
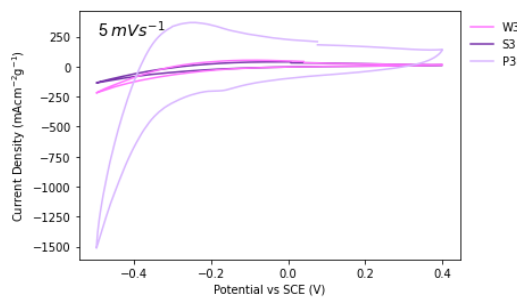
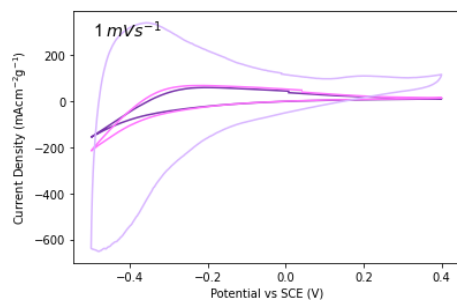


O.2 Na₂SO₄ Samples: W2, S2 and P2

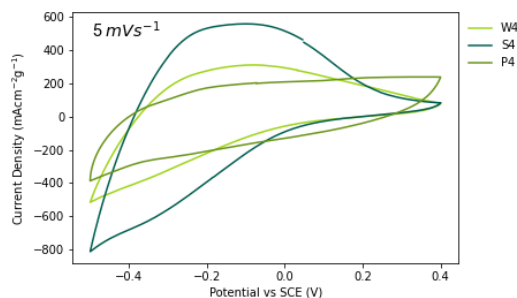
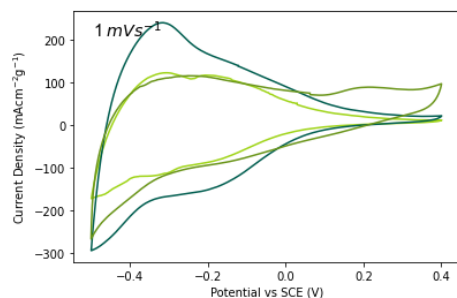


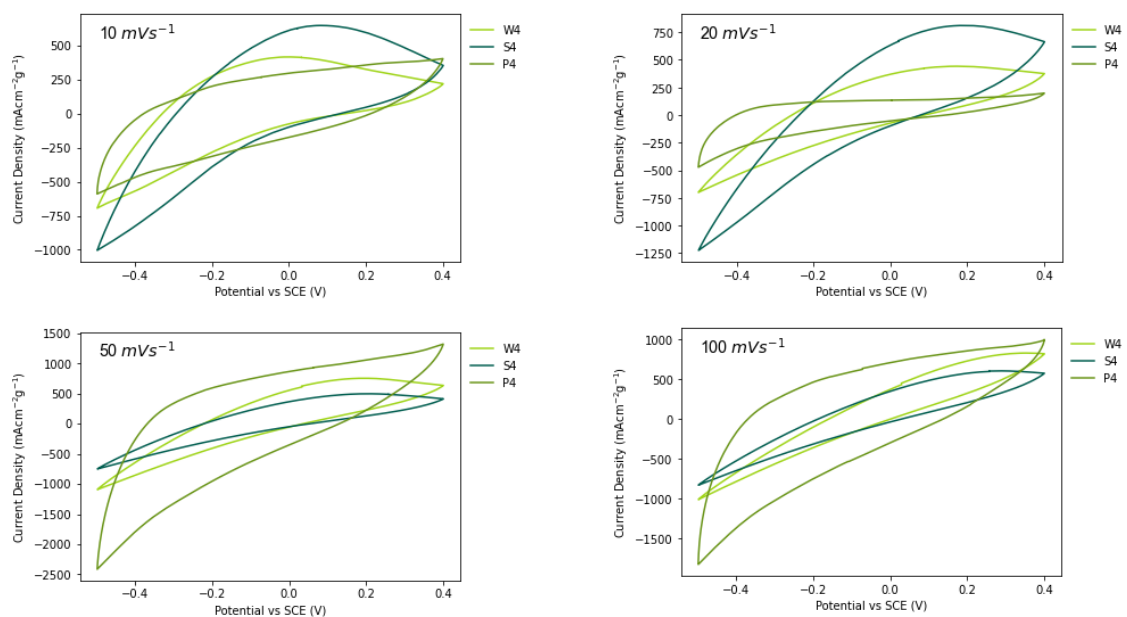


O.3 (NH₄)₂SO₄ Samples: W3, S3 & P3

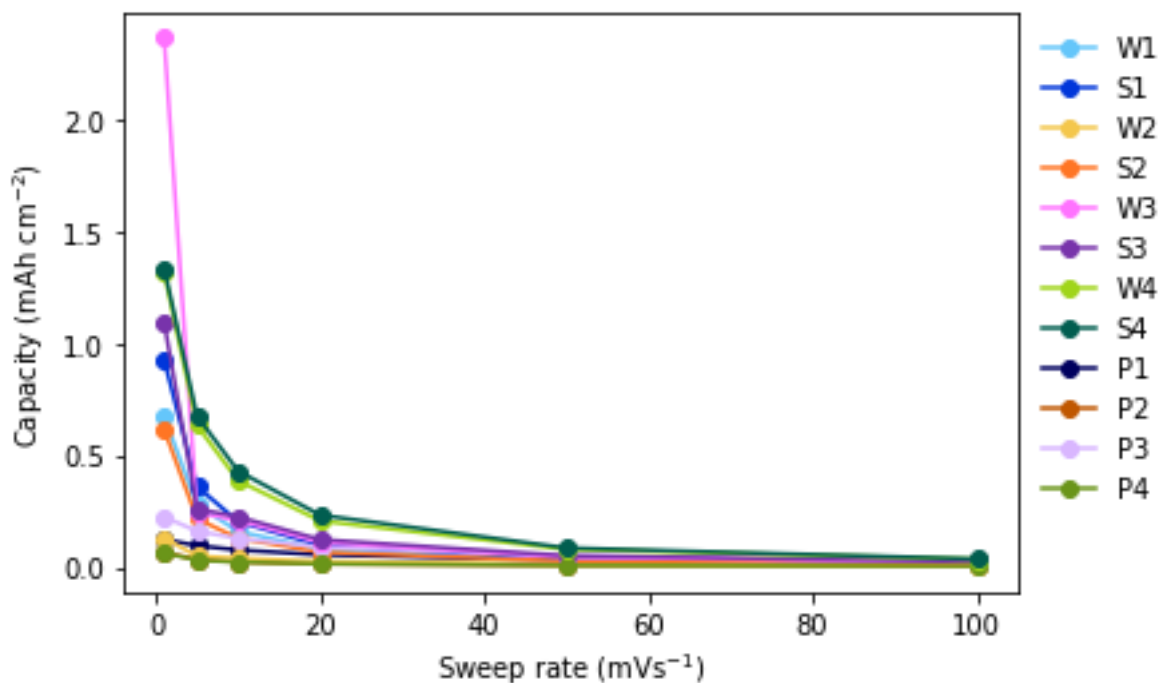


O.4 Rb₂SO₄ Samples: W4, S4 & P4



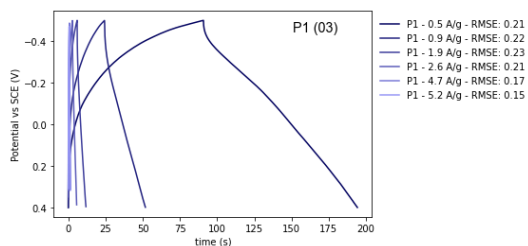
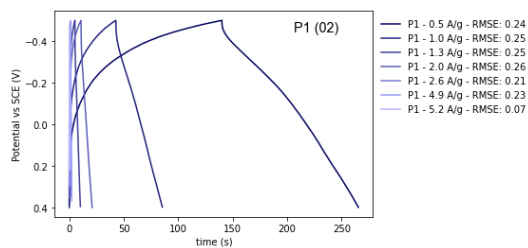
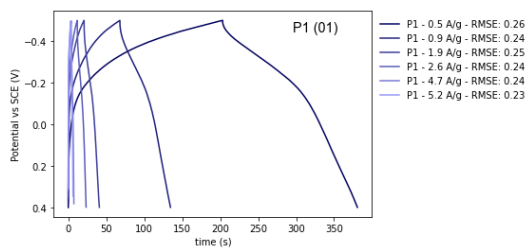


0.5 Powder Samples Areal Capacity Compared with Binder-Free Samples

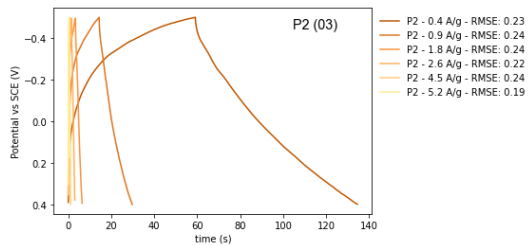
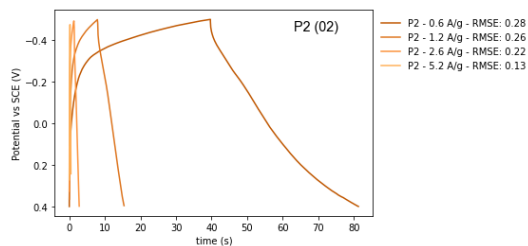
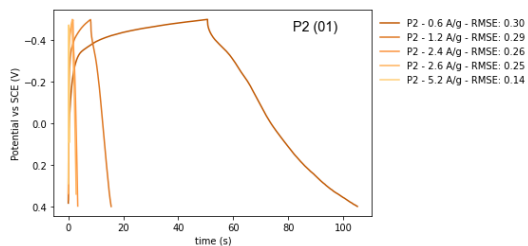


0.6 GCD Data for Powder Electrodes

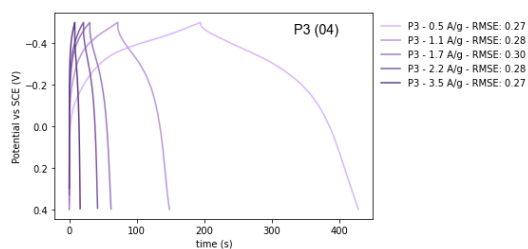
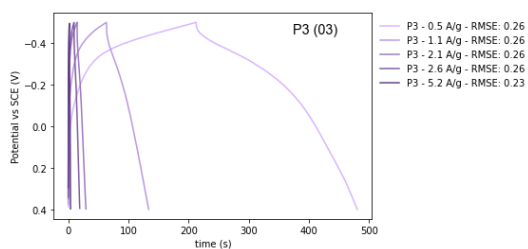
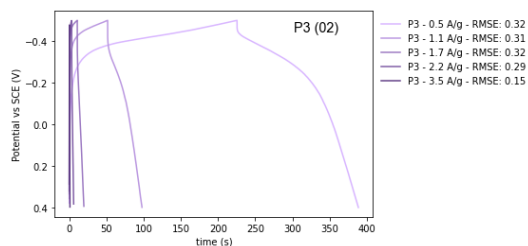
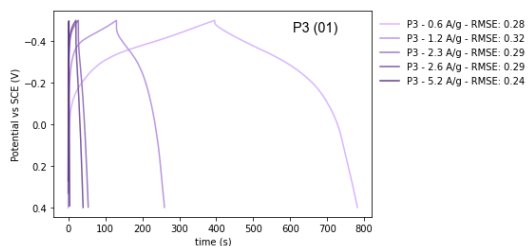
0.6.1 P1



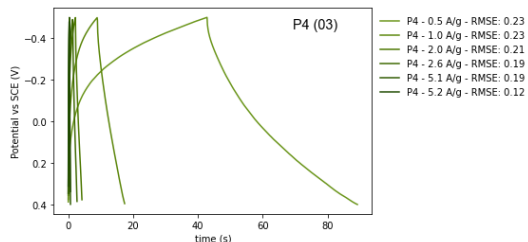
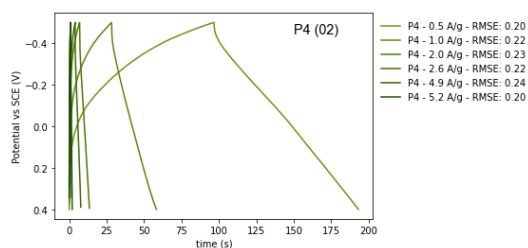
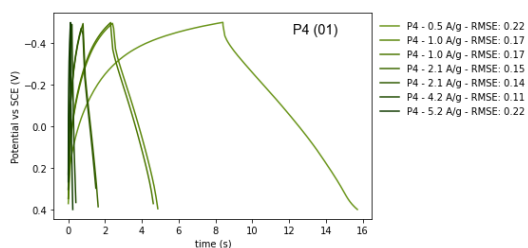
0.6.2 P2



0.6.3 P3

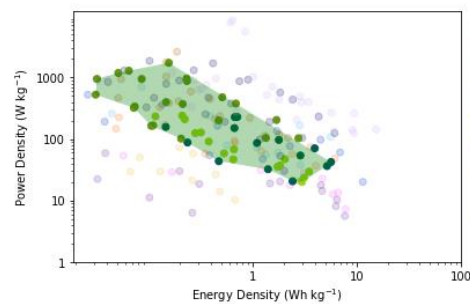
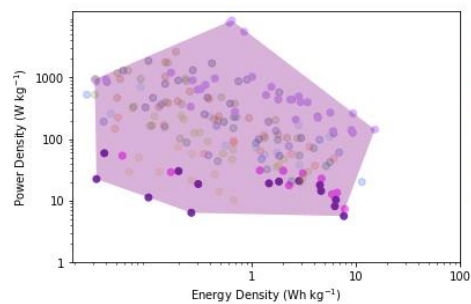
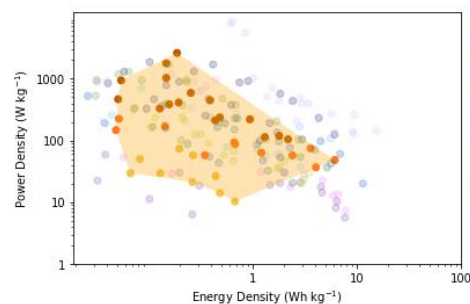
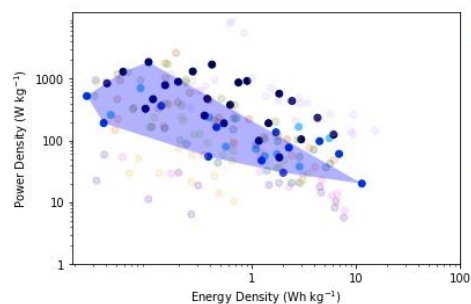


0.6.4 P4

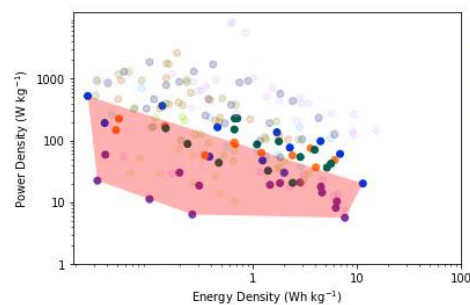
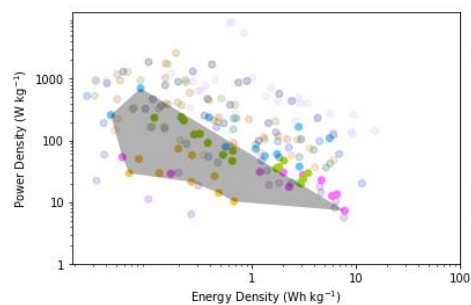


0.7 Ragone Diagrams

0.7.1 By capping agent

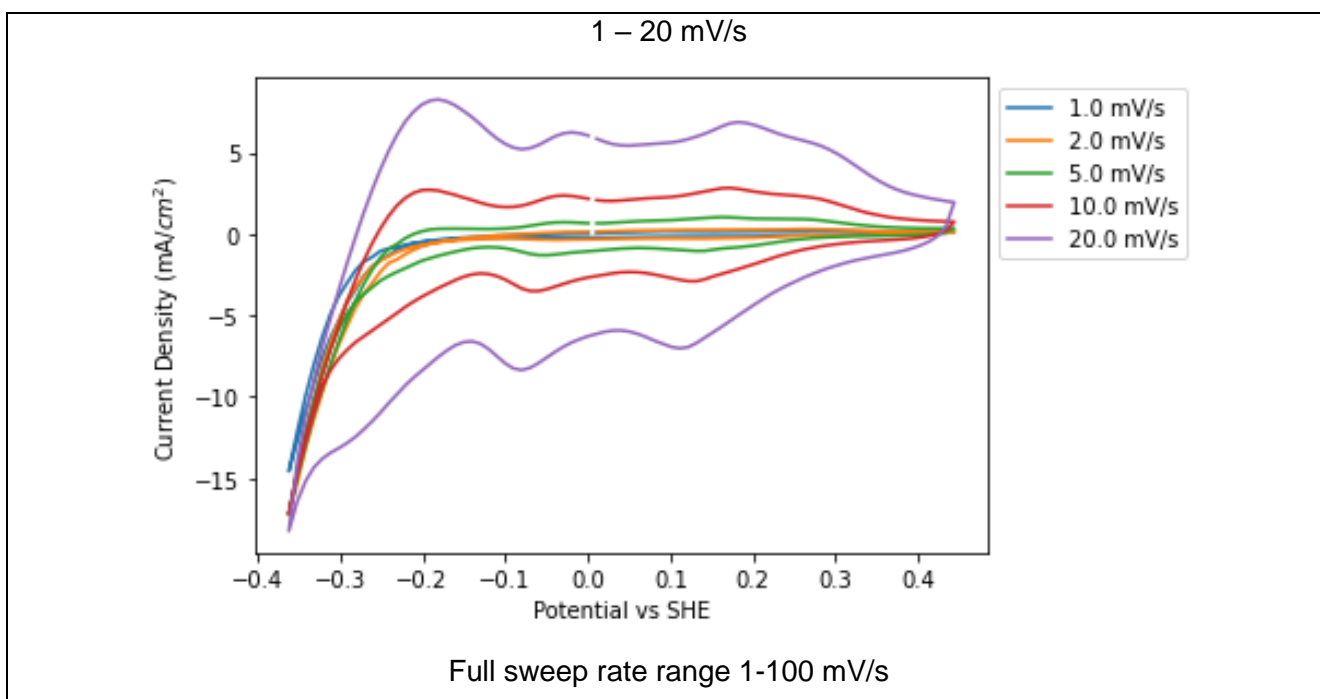


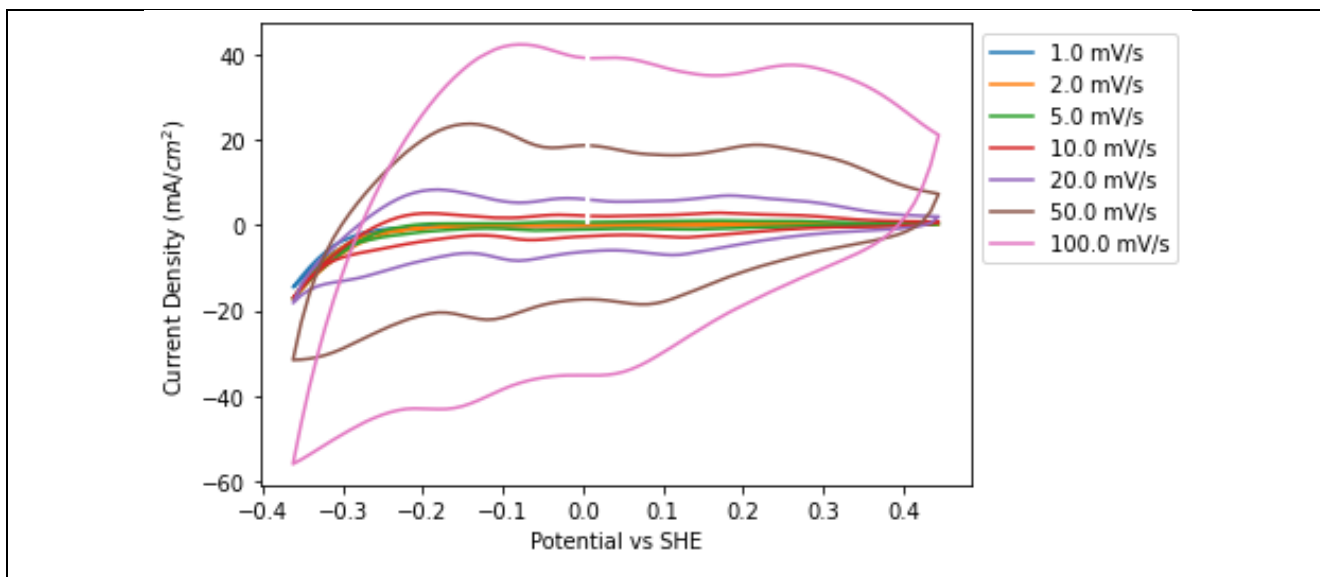
0.7.2 By substrate type



Appendix P Molybdenum – Molybdenum Oxide CV data at different potential ranges

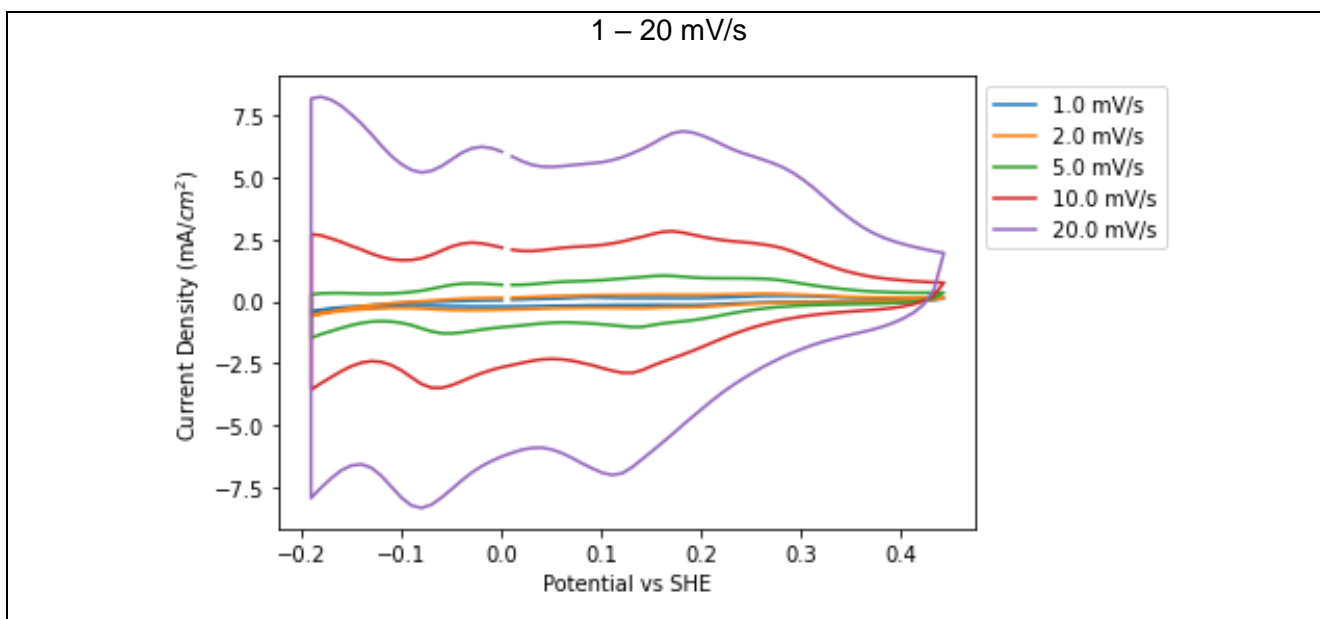
P.1 Lower potential -0.359V vs SHE

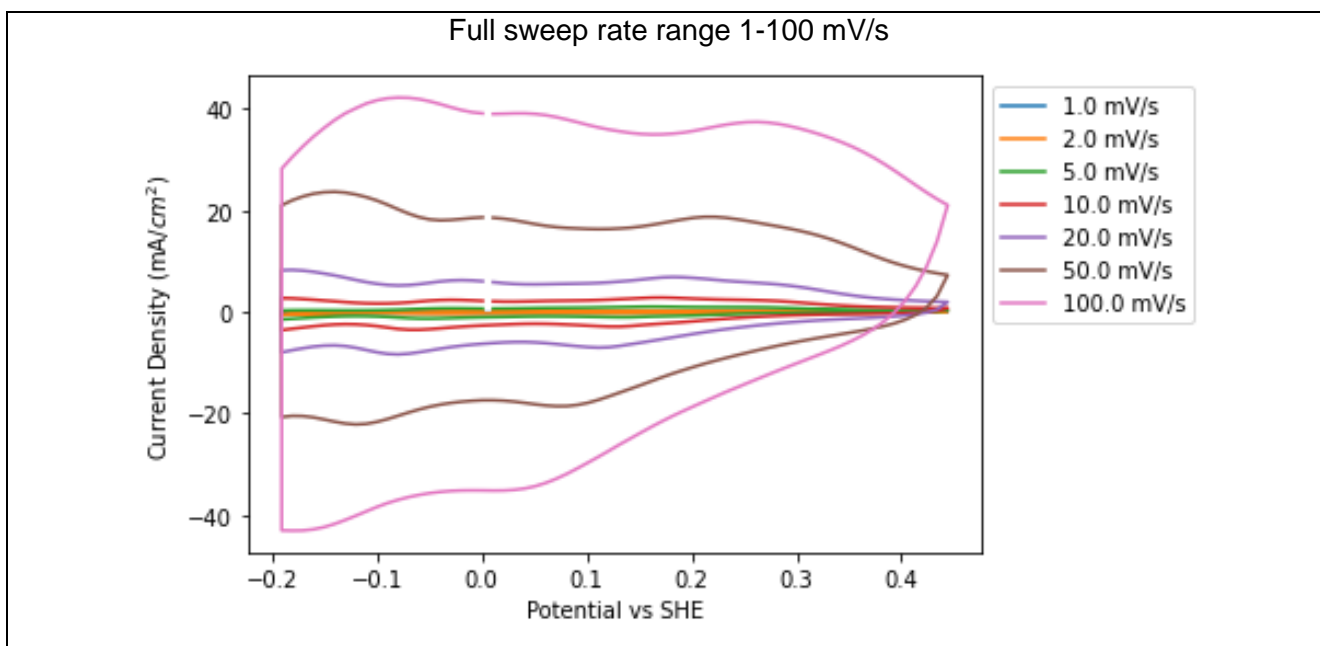




Scan rate (mVs ⁻¹)	Capacity (mAhcm ⁻²)	Capacitance (mFcm ⁻²)
1	0.003	14.22
2	0.01	45.51
5	0.052	232.18
10	0.087	391.28
20	0.117	526.17
50	0.135	605.6
100	0.125	561.21

P.2 Lower potential -0.2V vs SHE





Scan rate (mVs ⁻¹)	Capacity (mAhcm ⁻²)	Capacitance (mFcm ⁻²)
1	0.04	205.85
2	0.03	169.68
5	0.05	265.76
10	0.07	388.60
20	0.09	506.83
50	0.11	596.25
100	0.10	584.85